

University of Warwick institutional repository: <http://go.warwick.ac.uk/wrap>

A Thesis Submitted for the Degree of PhD at the University of Warwick

<http://go.warwick.ac.uk/wrap/60269>

This thesis is made available online and is protected by original copyright.

Please scroll down to view the document itself.

Please refer to the repository record for this item for information to help you to cite it. Our policy information is available from the repository home page.

A Catalytic and Solid State Study of Lanthanum Doped Ceria

By

**Mark Francis Wilkes
B.Sc. (Hons), M.Sc.**

**A thesis submitted in fulfilment of the requirements for the degree of
Doctor of Philosophy**

**Centre for Catalytic Systems and Materials Engineering
School of Engineering
University of Warwick**

August 1999

Contents

Page

i - v	Contents
1	Acknowledgements
1	Declaration
2	Abstract
3	Chapter 1 Introduction
10	Chapter 2 Literature Review
10	2.1 Materials
11	2.1.1 Structure
11	2.1.1.1 Ceria
13	2.1.1.1.1 Ceria - A Non-stoichiometric oxide
13	2.1.1.1.2 Solid/Gas Equilibrium
17	2.1.1.2 Lanthana
19	2.1.1.3 Aliovalent Doped Ceria Solid Solutions
21	2.1.1.4 Microstructure - Dopant Effects
22	2.1.1.5 Defect Reactions
23	2.1.1.6 Defect Interactions
25	2.1.1.7 Phase Diagrams for Binary Eutectic
29	2.1.1.8 Solute Incorporation
31	2.1.1.9 Solid State Reaction Techniques
34	2.1.2 Transport Studies - Ionic Conductivity
34	2.1.2.1 Theory
41	2.1.2.2 Conductivity Measurements
43	2.1.2.3 Conductivity of Fluorite Oxides
44	2.1.2.3.1 Undoped Ceria
45	2.1.2.3.2 Doped Ceria
50	2.1.3 Surface Composition and Enrichment
56	2.1.3.1 Surface Composition Modelling
57	2.2 Catalysis
59	2.2.1 Interactions with CO
65	2.2.2 Interactions with O ₂
69	2.2.3 Interactions with CH ₄
71	2.2.4 Catalytic Oxidation of CO
78	2.2.5 Catalytic Oxidation of CH ₄

Page

89	Chapter 3	Experimental
89	3.1	Materials Preparation
89	3.1.1	Ceramic
90	3.1.2	Coprecipitation
93	3.2	X-ray Powder Diffraction
93	3.2.1	Introduction
93	3.2.2	Theory
94	3.2.3	Experimental Applications
94	3.2.3.1	Phase
94	3.2.3.2	Lattice Parameters
95	3.2.3.3	Crystallite Size
96	3.2.4	Instrumentation and Procedure
97	3.2.5	Errors and Reproducibility
98	3.3	Surface Area Measurement
98	3.3.1	Introduction
99	3.3.2	Apparatus and Instrumentation
101	3.3.3	Sample Preparation
102	3.3.4	Single Point Measurement
102	3.3.4.1	Calibration
103	3.3.4.2	Experimental Procedure
104	3.3.5	Errors and Reproducibility
105	3.4	X-ray Photoelectron Spectroscopy
105	3.4.1	Introduction
106	3.4.2	Apparatus and Instrumentation
107	3.4.3	Analysis of Spectra
108	3.4.4	Errors and Reproducibility
108	3.5	Catalytic Measurements
108	3.5.1	Apparatus
111	3.5.2	Experimental Determination Of Mass Transfer Limitations
112	3.5.3	Error and Reproducibility
112	3.6	Temperature Programmed Desorption
113	3.6.1	Apparatus
114	3.6.2	Experimental Procedure
115	3.6.3	Error and Reproducibility
115	3.7	<i>In Situ</i> Diffuse Reflectance Infrared Fourier Transform Spectroscopy
115	3.7.1	Introduction
116	3.7.2	Apparatus
117	3.7.3	Experimental Procedure
118	3.7.4	Errors and Reproducibility

Page

119	Chapter 4	Results and Discussion
119	4.1	X-ray Diffraction and Surface Area Studies
119	4.1.1	Ceramic Materials
126	4.1.2	Coprecipitated Materials
126	4.1.3	Calcination Parameters - Investigation and Optimisation
134	4.1.4	Systematic Study
144	4.1.5	Sintering Study
155	4.2	XPS Surface Composition Studies
156	4.2.1	Segregation with Temperature
159	4.2.2	Segregation with Time
162	4.2.3	Segregation with Bulk Composition
165	4.2.3.1	Analysis and Discussion
165	4.2.3.1.1	Segregation Modelling
165	4.2.3.1.1.1	McLean Model
168	4.2.3.1.1.2	Mackrodt and Tasker Model
173	4.2.3.1.1.3	Wynblatt and Ku Model
183	4.2.3.1.1.4	Summary
184	4.3	Temperature Programmed Desorption Studies
184	4.3.1	Basicity Study - CO ₂
192	4.3.2	CH ₄
192	4.3.3	CO
192	4.3.3.1	Blank Runs
193	4.3.3.2	Temperature Effects Study
193	4.3.3.2.1	Ceria
194	4.3.3.2.2	Lanthana
195	4.3.3.2.3	Quantitative Analysis
196	4.3.3.3	Effect of Oxygen
197	4.3.3.3.1	Ceria
200	4.3.3.3.2	Lanthana
203	4.3.3.3.3	Summary
205	4.3.3.4	Effect of Catalyst Composition
210	4.3.3.5	Summary
211	4.4	In Situ Diffuse Reflectance Infrared Fourier Transform Spectroscopy
211	4.4.1	Experimental Methodology
212	4.4.2	Results Analysis
212	4.4.2.1	Initial Spectra - Compositional Variations
215	4.4.2.2	Final Spectra - Compositional Variations
216	4.4.2.3	CO Oxidation - Compositional Variations
217	4.4.2.4	CH ₄ Oxidation - Compositional Variations
219	4.4.2.5	Spectral Variations with Cell Environment
219	4.4.2.5.1	Ceria
222	4.4.2.5.2	Lanthana
224	4.4.2.5.3	Ce _{0.95} La _{0.05} O _{1.975}
225	4.4.2.5.4	Ce _{0.05} La _{0.95} O _{1.5+x}
225	4.4.2.6	Summary

Page

226	4.5	Catalysis Study
227	4.5.1	Preliminary Experiments
227	4.5.1.1	Investigation of Rate Diffusion Limitations
230	4.5.2	Ternary Oxide Study
231	4.5.3	CO Oxidation - Systematic Study
233	4.5.3.1	CO Oxidation - Standard Activity Measurements
236	4.5.3.2	CO Oxidation - Arrhenius Studies
242	4.5.3.3	CO Oxidation - Compensation Effect
244	4.5.3.4	CO Oxidation - Kinetic Studies
245	4.5.3.4.1	Ceria
245	4.5.3.4.1.1	The Effect of CO Partial Pressure
247	4.5.3.4.1.2	The Effect of O ₂ Partial Pressure
249	4.5.3.4.1.3	The Effect of CO ₂ Partial Pressure
250	4.5.3.4.1.4	Mechanistic Discussion
252	4.5.3.4.2	Lanthana
254	4.5.3.4.2.1	The Effect of CO Partial Pressure
258	4.5.3.4.2.2	The Effect of O ₂ Partial Pressure
259	4.5.3.4.2.3	The Effect of CO ₂ Partial Pressure
260	4.5.3.4.2.4	Mechanistic Discussion
266	4.5.3.4.3	Ce _{1-x} La _x O _{2-x/2} Mixed Oxides
266	4.5.3.4.3.1	The Effect of CO Partial Pressure
270	4.5.3.4.3.2	The Effect of O ₂ Partial Pressure
271	4.5.3.4.4	Summary - Nature of the Active Species
273	4.5.4	CH ₄ Oxidation - Systematic Study
275	4.5.4.1	CH ₄ Oxidation - Standard Activity Measurements
279	4.5.4.2	CH ₄ Oxidation - Arrhenius Studies
282	4.5.4.3	CH ₄ Oxidation - Compensation Effect
284	4.5.4.4	CH ₄ Oxidation - Kinetic Studies
285	4.5.4.4.1	Ceria
285	4.5.4.4.1.1	The Effect of CH ₄ Partial Pressure
286	4.5.4.4.1.2	The Effect of O ₂ Partial Pressure
287	4.5.4.4.1.3	The Effect of CO ₂ Partial Pressure
288	4.5.4.4.1.4	Mechanistic Discussion
293	4.5.4.4.2	Lanthana
294	4.5.4.4.2.1	The Effect of CH ₄ Partial Pressure
295	4.5.4.4.2.2	The Effect of O ₂ Partial Pressure
296	4.5.4.4.2.3	The Effect of CO ₂ Partial Pressure
297	4.5.4.4.2.4	Mechanistic Discussion
300	4.5.4.4.3	Ce _{1-x} La _x O _{2-x/2} Mixed Oxides
305	4.5.3.4.4	Summary - Nature of the Active Species
308	Chapter 5	Summary and Conclusions
308	5.1	Solid State Studies
310	5.2	Surface Studies
317	5.3	Catalytic Studies
318	5.3.1	CO Oxidation Systematic Study
324	5.3.2	CH ₄ Oxidation Systematic Study
328	Chapter 6	References

Page**Appendices**

336	Appendix 2.1	Kröger-Vink Notation
338	Appendix 3.1	Raw Materials
339	Appendix 3.2	XRD Theory
339	A3.2.1	The Production of X-Rays
343	A3.2.2	The Properties of X-Rays
344	A3.2.3	Diffraction
345	A3.2.4	The Bragg Law
349	A3.2.5	Crystallography
351	A3.2.6	Crystal Planes Involved in Diffraction
355	Appendix 3.3	XRD Reference Patterns
357	Appendix 3.4	Surface Area Measurement by Gas Adsorption - Theory
362	Appendix 3.5	XPS Theory
370	Appendix 3.6	Catalysis Experimental Theory
370	A3.6.1	Experimental Theory and Calculation of Reaction Rate
374	A3.6.2	Limitations of the Plug Flow Model Approximations and Assumptions
374	A3.6.2.1	Wall Effects
377	Appendix 3.7	DRIFTS Theory
377	A3.7.1	General Description
377	A3.7.2	Diffuse Reflectance Theory
379	A3.7.3	Kubelka - Munk Theory
379	A3.7.4	Fourier Transform Spectroscopy
384	Appendix 4.1	Patent Study
384	A4.1.1	Patent Study
387	A4.1.2	Ternary Oxide Catalytic Study
387	A4.1.2.1	Experimental
388	A4.1.2.2	Results Summary
388	A4.1.2.2.1	CH ₄ Oxidation
390	A4.1.2.2.2	CO Oxidation

Acknowledgements

I wish to thank my project supervisors: Dr Percy Hayden MBE, for all of his time and efforts which have been greatly appreciated, especially given the difficult working circumstances over the last two years of the project; and Dr Ashok Bhattacharya for allowing me to use the facilities within the Centre for Catalytic Systems and Materials Engineering. I would also like to thank the technical staff within the group: John Pillier, Richard Reynolds and Ellen Williams for the excellent support and technical assistance they have provided throughout the project. In addition to the technical staff I would also like to express my gratitude to members of the academic staff within the group, particularly Dr James Sarginson and Alex Kinniburgh for their help and camaraderie. Outside the University I also wish to thank Dr Isla Mathieson at the Institute of Surface Science and Technology (Loughborough University), for providing X-Ray Photoelectron Spectroscopy derived surface composition data on a consultancy basis.

On a personal note, I would also like to express my eternal gratitude to my mother, father, and especially my girlfriend Kate Wood, who have provided me with love and support throughout the duration of the project.

Declaration

I do hereby declare that this thesis is my own work, and has not been submitted for a degree at another university.

Abstract

In this study of the catalytic oxidation of CO and CH₄ over lanthanum doped ceria, it is demonstrated that dopant concentration is the dominant factor in the variation in catalytic properties. This composition dependency of catalytic properties is correlated with the variations in solid state and adsorption properties. The aim of the thesis is to determine precisely which of the dopant concentration dependent material properties are the major influencing factors in catalytic property variations.

As heterogeneous catalysis is a surface phenomenon, full characterisation of the surface of the materials is necessary in a fundamental study. Surface composition is shown to vary significantly from that of the bulk, due to a surface segregation phenomenon which is studied in detail. A known model based on electrostatic interactions and atomistic simulations is successfully used to rationalise surface segregation. Catalytic properties and other surface characterisation data are subsequently interpreted with respect to surface composition. Catalyst surface composition studies are also used to estimate the variation in surface free oxide anion vacancy concentration with composition, based on the assumption that surface conductivity varies with composition similarly as does bulk conductivity. Surface conductivity is thus derived from literature bulk conductivity data.

In the case of the catalytic oxidation of CO the addition of lanthanum dopant retards catalytic activity under the standard reaction conditions. The catalytic reaction rate equation activation energy and specific pre-exponential factor are demonstrated to vary similarly, peaking strongly at the surface composition coincident with maximum free oxide anion vacancy concentration. The catalytic properties are therefore proposed to be dependent on the free oxide anion vacancy population in the surface.

In the case of the catalytic oxidation of CH₄ the addition of lanthanum dopant is shown to promote activity under the standard reaction conditions. A synergistic promotion effect is demonstrated for surface base and redox functionalities which is shown to be maximised at the equicationic surface composition. The base function is shown to be enhanced with lanthanum surface concentration and is proposed to result in enhanced methane activation activity by acid/base site deprotonation. The Ce^{IV} ↔ Ce^{III} redox function is attributed to surface cerium, resulting in enhanced oxidation of the methyl fragment following deprotonation on an adjacent acid/base site.

Chapter 1 Introduction

Ceria (CeO_2) is a fluorite structured oxide, which depending on temperature and oxygen partial pressure is able to exist in a range of oxygen stoichiometries of the general formula CeO_{2-x} . The range of compositions occurs by virtue of a facile $\text{Ce}^{\text{III}} \leftrightarrow \text{Ce}^{\text{IV}}$ redox, thus limiting the compositional range between the dioxide (CeO_2), and the sesquioxide (Ce_2O_3). The redox properties of cerium are the basis of several industrial applications as a heterogeneous catalyst.

As a consequence of reduction of ceria, the incorporation of oxide anion vacancies into the fluorite lattice occurs. Within a given range of concentrations, these vacancies give rise to significant levels of anionic conductivity. The production of anion vacancies can similarly be achieved under non-reducing conditions by substitutional incorporation of trivalent dopants, such as lanthanide cations, in the fluorite lattice. In this case, anion vacancies are formed as charge compensating defects during the solid solution formation reaction. The resulting solid solution series can be described in terms of the trivalent lanthanide (Ln), dopant concentration, x , as $\text{Ce}_{1-x}\text{Ln}_x\text{O}_{2-x/2} V_{\text{O}}^{\bullet\bullet}$ where Ln is the trivalent lanthanide species and $V_{\text{O}}^{\bullet\bullet}$ is an oxide anion vacancy, one of which is introduced into the lattice as a charge compensating defect for every two trivalent Ln cations.

The substitutional incorporation of lanthanide cations into the fluorite structured ceria lattice, and the resulting solid solutions, have been a focus of both academic and industrial interest over the last 40 years. The large range of lanthanide dopant concentrations able to be accommodated by the ceria lattice has rendered such systems ideal for the production of solid oxide anionic conductors, which show variations in conductivity properties with dopant type and concentration. Likewise, the correlation between anionic conductivity and catalytic activity for several different test reactions has also been a research goal for several different groups over the last four decades.

The main industrial application of ceria is in 'three-way' vehicle emission control catalyst, in which ceria plays several roles. These include as a stabiliser for the

high surface area alumina washcoat, as a promoter of the water-gas shift reaction ($\text{CO} + \text{H}_2\text{O} \rightarrow \text{CO}_2 + \text{H}_2$), and as an oxygen storage component. The uses of ceria as an oxidation, partial oxidation and oxidative coupling catalyst have been the major focus of recent research on doped ceria systems, in order that catalytic reactions can be better understood and that the catalyst materials can be optimised.

Despite the obvious interest over the years in the mechanistic implications of promotion of catalytic reactions over ceria, and particularly lanthanide doped ceria, the exact nature of the empirically observed activity promotions are still not exactly defined. Several possible factors involved in the dopant dependency of catalytic activity over ceria have been proposed in the literature, including enhancement of surface basicity and adsorption properties, enhancement of conductivity properties, and modification of catalyst composition dependent morphological properties. However in previous studies the direct correlation of all of these properties with catalytic activity has not as yet been achieved, thus it has not been determined which of these factors are the most important factors in the promotion of catalytic activity. It is also likely that for reactions with different mechanisms, the factors dominating the variations in catalytic activity will also differ.

Looking in more detail at specific prior art, a particular synergistic promotion of catalytic CH_4 oxidation activity was reported in a US patent by W. C. Mackrodt (USP 3, 070, 165. 1991). In the patent, the variation in CH_4 oxidation activity with dopant concentration for various combinations of lanthanide dopants was investigated in terms of activity per unit weight of catalyst. The addition of lanthanide dopants was determined to result in an increase in activity, which was generally found to be maximised for a dopant concentration of 20 - 30 cation % lanthanum in the bulk. A synergistic promotion effect was claimed for a combination of lanthanum and praseodymium dopants at this pre-determined optimum total dopant concentration, with respect to either of the dopants separately at the same optimum total dopant concentration. The claimed synergistic effect of the combination of dopants was promissory with regards elucidation of significant and fundamental implications, and was worthy of further investigation.

Preliminary work was carried out in which the synergistic CH_4 activity promotion effects reported in the patent were reproduced, the results of which are reported in Appendix 4.1. Further characterisation of the catalyst in terms of specific surface area was also completed in order to express the activity of the materials in terms of specific activity, effectively eliminating the influences of gross morphological differences between the catalysts. Subsequent analysis of the relative specific activities of the doped and undoped materials revealed that the synergistic effect claimed was actually due to dopant dependent morphological differences between the catalysts. A significant promotion of specific activity was observed on the addition of dopants in comparison with the undoped ceria, but catalysts doped at the same concentration with different lanthanides were found to have the same specific activity as each other. It was clear from these initial results that the concentration of the lanthanide dopant was the dominant factor in terms of variations in catalytic activity, rather than the type of dopant.

The primary aim of the work reported in this thesis was to determine which of these dopant dependent factors are dominant with regards variation in catalytic properties, and to assess the interplay between such factors within selected catalytic reaction systems. In order to better understand the nature of the dopant induced promotion of catalytic activity, it was necessary to complete a systematic catalytic study of the lanthanum doped ceria binary oxide system. To this end, the dependence of morphological, surface and solid state properties on dopant concentration within the binary catalyst series was investigated, and correlated where possible with specific catalytic activity and kinetic data for CH_4 oxidation and for CO oxidation. The CO oxidation reaction was included in the study to provide a comparison with the CH_4 oxidation reaction in terms of ease of reactant activation and catalytic reaction mechanism. Within the preliminary experiments it was determined that the inclusion of lanthanide dopants in ceria had a detrimental effect on the CO oxidation reaction catalytic activity of ceria, in stark contrast to the promotion effect observed with the CH_4 oxidation reaction. This emphasised the differing dependencies of the two reactions on lanthanide dopant concentration in ceria, and so the study of the variation

in CO catalytic oxidation properties with lanthanum dopant concentration was continued to provide comparative catalytic data to compliment the CH₄ oxidation study. Solid state characterisable properties include specific surface area, bulk phase, lattice parameter, crystallite size, oxide anion vacancy concentration, anionic conductivity and surface composition. Additionally, the dopant concentration dependence of surface adsorption properties was also investigated in temperature programmed desorption, and *in situ* diffuse reflectance infrared spectroscopy studies. Kinetic studies were completed for each reaction over a range of catalyst compositions, in order to elucidate and compare reaction mechanisms for both reactions over similar catalysts, and to determine the variation in reaction mechanism with catalyst composition for each individual reaction. Correlation of solid state, surface adsorption and catalytic data was then attempted, in order to determine the physical nature of the dependence of catalytic properties on dopant concentration.

This thesis is divided into several chapters. Chapter 2 provides a general overview of prior art within the open literature. The ceria/lanthana binary oxide catalyst system is described in terms of the phase structures of the series end members and solid solutions of intermediate compositions. The formation of doped ceria solid solutions and the effects of dopant type and concentration on phase, structure and morphology are reviewed, along with the known effects of dopant concentration with respect to anionic conductivity. The known trends and models for surface composition variation with temperature and bulk dopant concentration are also examined for the mixed oxide materials. Finally, surface adsorption and catalytic properties of the ceria/lanthana series are addressed and the current understanding of both CO and CH₄ catalytic oxidation over ceria, lanthanum doped ceria and lanthana catalysts is reviewed.

A notable omission within the literature is the description of catalytic activity in terms of surface composition of the Ce_{1-x}La_xO_{2-x/2} materials. The prior art has identified that surface segregation occurs with most mixed oxides, and since catalysis is a surface phenomenon, a fundamental description of the catalytic action of these mixed oxides requires determination of the variation in catalytic activity with surface

composition. One of the aims of this thesis was to determine this variation over a range of mixed oxide compositions for both CH_4 and CO oxidation reactions. A further aim has been to identify the factors influencing surface segregation in the ceria/lanthana mixed oxides, to describe surface segregation quantitatively, and to compare the predictive abilities of theoretical models of surface segregation.

The preparation and characterisation techniques for the catalyst materials used in the present study are addressed in chapter 3. Materials were made using a ceramic processing technique and a coprecipitation technique, the latter of which was adopted for the systematic catalyst composition variation study. Three different experimental techniques were used in the study to characterise solid state properties including X-ray powder diffractometry (bulk phase, lattice parameter and crystallite size studies), surface area (N_2 adsorption techniques), and surface composition, (X-ray photoelectron spectroscopy). Surface adsorption properties were investigated in order to bridge the gap between solid state, surface composition and catalytic measurements. This included CO , CH_4 and CO_2 temperature programmed desorption experiments to determine the type, strength and surface density of reactant/product adsorption sites, and *in situ* diffuse reflectance infrared spectroscopy studies to determine the nature of adsorbed species under both catalytic oxidation reaction conditions. Finally, the micro-reactor based catalytic measurements used in the present study are discussed. This includes a detailed account of the apparatus and experimental techniques used to determine specific activity, activation energy and active site density data.

The results of the various characterisation methods are presented and discussed in chapter 4. Initial experiments were completed in order to determine the solid solution limits within the ceria/lanthana binary oxide system and to optimise/standardise the catalyst preparation technique with respect to the requirements of the characterisation and catalytic activity measurement apparatus available. The major requirements for the catalysts were a specific surface area greater than $5\text{m}^2\text{g}^{-1}$ coupled with morphological stability at high reaction temperatures. This minimum surface area was determined in order to avoid experimental error due to apparatus detection limits in the surface area, temperature programmed desorption and

catalytic studies. Of the preparation techniques assessed, a coprecipitation technique was determined to best meet the requirements of the study. The coprecipitate processing parameters were subsequently optimised, thus deriving a standard preparation method for catalysts used in the systematic compositional study. A full systematic compositional variation series of catalysts was then prepared using the standard preparation method. The resulting series of catalysts were subsequently characterised using the techniques described in chapter 3.

A major achievement of the solid state studies was the experimental characterisation and subsequent rationalisation of surface segregation processes in the ceria/lanthana solid solution ranges, in terms of a known model based on electrostatic interaction theory and atomistic simulations. Further analysis using an alternative model based on lattice energy calculations demonstrated that the variation in the free energy of segregation with composition was predominantly due to composition dependent variation in the solute-solvent interaction energy, thus ratifying the use of the electrostatic model.

CH_4 and CO oxidation reactions were used for the systematic catalyst compositional studies, due to the potential of very different reaction mechanisms. The rate determining steps for the two reactions being generally categorised within the open literature as base catalysed deprotonation in the case of CH_4 oxidation, and electron transfer in the case of CO oxidation. The potential development of a low temperature combustion catalyst for these two important reactions was also in mind throughout the study, as a possible commercial application for the binary oxide materials.

In the case of CO oxidation, sharply defined variations in reaction activation energy and specific pre-exponential factor were observed; the coincident peaks of which also coincided with the estimated compositional dependent maxima in both surface anionic conductivity, and electronic conductivity. An experimental study of the variation in surface conductivity with composition was attempted using ac. impedance spectroscopy methods. This method allows the factorisation of the contributions toward total conductivity, from both bulk and surface/grain boundary processes.

Unfortunately, suitable samples could not be prepared at the standard catalyst calcination temperature. Although direct measurement of surface conductivity was not possible in the present study, physical reasoning indicated that bulk and surface conductivity within the catalyst materials were likely to differ, due to the aforementioned segregation dependent compositional differences, based on the reasonable assumption that bulk and surface conductivities exhibit similar compositional dependencies. It was thus possible to use the surface segregation study data, in combination with literature regarding the variations in conductivity with bulk composition for the $\text{Ce}_{1-x}\text{La}_x\text{O}_{2-x/2}$ series, to rationalise the dependence of the measured catalytic properties on both bulk and surface catalyst composition and conductivity. The study demonstrated that the CO catalytic oxidation activation energy and specific pre-exponential factor exhibited a dependence on the surface free oxide anion vacancy population.

The known dependency of CH_4 activation activity on surface basicity required characterisation of the systematic compositional series of catalysts in terms of specific basicity, in order to rationalise compositional variations in the measured CH_4 oxidation reaction catalytic properties. A synergistic activity promotion effect by basic and redox surface functionalities was determined for the CH_4 oxidation reaction using parametric response modelling techniques. This was explained in terms of surface composition and cerium/lanthanum surface cationic functions.

The conclusions of the project are described in chapter 5, in which the results described in chapter 4 are collated and discussed in terms of the aims of the project.

Chapter 2 Literature Review

2.1 Materials

The materials used as catalysts throughout this study are based on ceria, lanthanum doped ceria and lanthana. (In some cases ceria has also been doped with other lanthanides). (In this text the term lanthanide is used as the collective name for the 15 elements from 57 (La) through to 71 (Lu) - the 4f elements. Occasionally the term rare earth is also used in reference to Sc, Y, La and Lu).

Both cerium and lanthanum were discovered by C. G. Mosander in 1885. Cerium is characterised by having two stable oxidation states Ce^{3+} (cerous) and Ce^{4+} (ceric). The latter ion is a powerful oxidising agent, but is completely stabilised when associated with the strong coordinating ligand oxygen in the CeO_2 oxide. The bulk of the world's cerium is derived from two minerals; bastnasite (LnFCO_3) and monazite ($\text{Ln, Th} \text{PO}_4$) which are found in economically significant deposits in California USA and in Baiyunebo in Inner Mongolia, China. The lanthanides are generally separated from the ore by acid extraction and precipitation methods to yield a mixed lanthanide solution. The individual lanthanide fractions are then further separated by solvent extraction, selective precipitation and using ion exchange extraction techniques.¹ The electronic structure of the lanthanides is difficult to define as the atomic spectra are complex, but are generally $[\text{Xe}]4f^n5d^06s^2$. The outer electron configuration of neutral cerium is $[\text{Xe}]4f^15d^16s^2$, in the case of neutral lanthanum it is $[\text{Xe}]4f^05d^16s^2$. In the case of cerium the sudden contraction and reduction in energy of the 4f orbitals immediately after La is not sufficient to avoid occupancy of the 5d orbital. The predominant oxidation state for lanthanide chemistry is therefore +3, except in the cases of Ce and Pr where the +4 oxidation states are also common.^{1, 2} The doping of ceria with other rare earth cations results in the formation of solid solutions in which the host oxide structure is retained at relatively high dopant loadings, thus allowing the effect of isostructural dopant concentration variations on material and catalytic properties to be determined for a wide range of compositions. In order to demonstrate

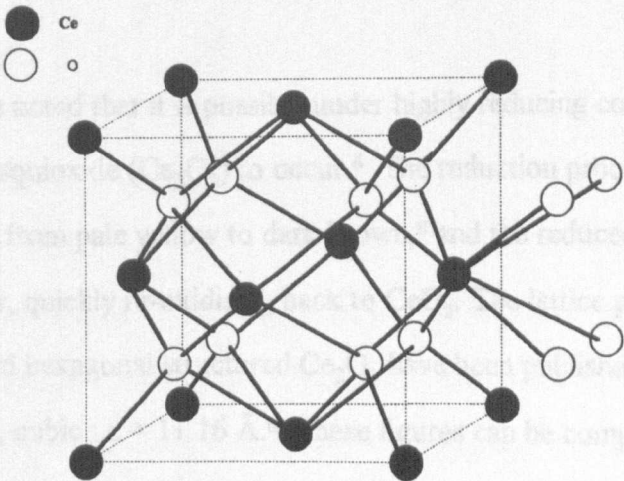
the formation and material properties of solid solutions it is first necessary to define the structures of the host and dopant materials.

2.1.1 Structure

2.1.1.1 CeO_2

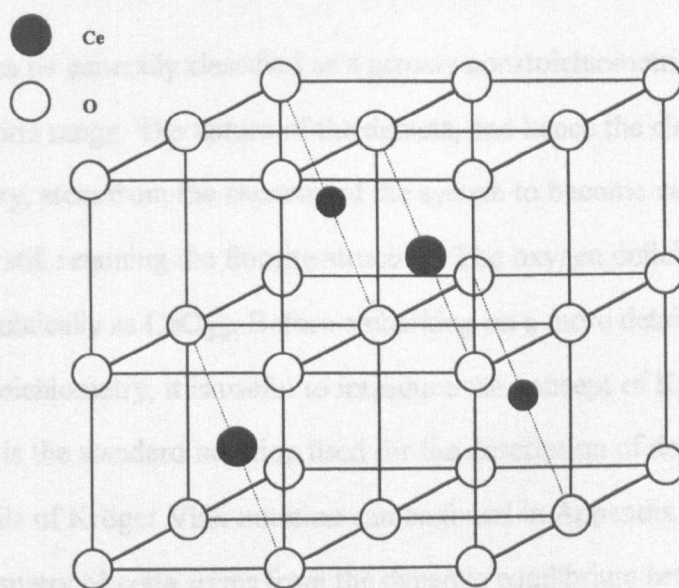
Compounds such as ceria are based on face-centre cubic structure packing of cations with all of the tetrahedral sites filled by anions.^{3,4} Since there are twice as many tetrahedral sites as there are atoms, the stoichiometry of the material must be MX_2 , as is the case with ceria. This structure is known as fluorite (named after the mineral fluorite, CaF_2). In the case of ceria, the fluorite structure is stable from room temperature up to the melting point.⁵ This structure is particularly common for binary compounds in which the cation is large, such that eight-fold coordination is preferred. The coordination of cations around anions is 4, and thus the bond strength contributed by each cation is $4/8$. As four cations surround each anion, the sum of bond strengths is 2, which is the valence of the anion. In turn, the anionic bond strength is $2/4$. As each cation is coordinated with eight anions, the sum of bond strengths is 4, which is the valence of the cation. Thus charge neutrality of the structure is preserved. The fluorite structure of ceria is presented in figure 2.1 below.

Figure 2.1 The fluorite structure of CeO_2 .³



The FCC cation packing of the fluorite structure is emphasised by the superimposed cubic framework (dotted lines). The four-fold coordination of cations around each anion is clear within the FCC framework and the eight-fold coordination of anions around each cation is demonstrated by the inclusion of the full complement of anions around the face-centre cation in the right-hand side face. The unit cell of the fluorite structure consists of a cube made up of 8 individual cubes where the vertices are anion positions. The cation positions within the unit cell are at the body centre position within diagonally opposed individual anion cubes. This unit cell is complicated and difficult to present schematically and is therefore generally presented in the literature as half of the true unit cell for reasons of clarity.^{6,7} However, the full unit cell is represented in figure 2.2 below.

Figure 2.2 A diagram of the fluorite ceria unit cell.



It should be noted that it is possible under highly reducing conditions for the formation of the sesquioxide (Ce_2O_3) to occur.⁶ The reduction process is accompanied by a colour change from pale yellow to dark brown,⁸ and the reduced Ce_2O_3 is known to be unstable in air, quickly re-oxidising back to CeO_2 . The lattice parameters for both cubic structured and hexagonal structured Ce_2O_3 have been published; hexagonal : $a = 3.89 \text{ \AA}$, $c = 6.07 \text{ \AA}$, cubic : $c = 11.16 \text{ \AA}$.⁶ These figures can be compared with the cubic fluorite lattice parameter for CeO_2 reported by Touzelin (1981)⁹ as $c = 5.4105 \pm$

0.0005 Å. 5.411 Å from JCPDS cards⁸, and 5.426 by Sanchez and Gazquez.¹⁰ The cubic form of Ce_2O_3 has been determined as containing 32 metal atoms and 48 oxygen atoms per unit cell related to a double edge fluorite structure with one quarter of the oxygen sites vacant and regularly ordered.⁶ It should be noted that this structure/composition combination is not common, and is the least well known of the rare earth sesquioxides. The structures of the various rare earth oxides are discussed further in the excellent review by Adachi and Imanaka (1988).⁶ The reducibility of CeO_2 will be discussed further later in this section, but as under general preparation (calcination in air), and catalytic experimental conditions (high P_{O_2}), reduction of the material is unlikely, further discussion of the sesquioxide is beyond the scope of this text.

2.1.1.1.1 Ceria - a Nonstoichiometric Oxide

Ceria can be generally classified as a grossly nonstoichiometric oxide with a broad composition range. The nature of the defects, and hence the classification of the nonstoichiometry, stem from the capacity of the system to become vastly oxygen deficient whilst still retaining the fluorite structure. The oxygen deficiency is generally expressed formulaically as CeO_{2-x} . Before embarking on a more detailed account of the nature of nonstoichiometry, it is useful to introduce the concept of Kröger Vink notation which is the standard notation used for the description of defects in ionic materials. Details of Kröger Vink notation can be found in Appendix 2.1. The nature of the nonstoichiometry of ceria stems from the dynamic equilibrium between the solid and gaseous oxygen.

2.1.1.1.2 Solid/Gas Equilibrium

In the case of fluorite structured oxides generally, oxygen is known to diffuse far more rapidly than the metal cations. Oxygen diffusion coefficients in CeO_{2-x} have been measured in the literature.¹¹ A summary of oxygen diffusion data on fluorite materials compiled by Matzke (1981)⁷ found that all stoichiometric and

nonstoichiometric oxides exhibited similar behaviour with diffusion coefficients and activation enthalpies proportional to their melting temperature. In all cases of sub- and super-stoichiometric compositions, diffusion was faster than for stoichiometric compounds, as would be expected. (In super-stoichiometric compounds oxygen diffusion is by an oxygen interstitialcy mechanism). Little reliable data exists within the literature on the metal diffusion rate within fluorite oxides, and due to relatively low diffusion coefficients compared with oxygen, is only relevant to the preparation of these materials.

The predominant defects in oxides of the fluorite structure, and hence in nonstoichiometric CeO_{2-x} are doubly ionised oxygen vacancies.¹²⁻¹⁴ Substoichiometric CeO_{2-x} contains predominantly oxygen vacancies rather than metal interstitials as previously thought,¹⁵ as confirmed by X-ray and neutron diffraction studies.¹⁶⁻¹⁷ In the case of CeO_{2-x} , reduction of the cation from Ce^{IV} to Ce^{III} creates localised Ce^{3+} cations and the charge balance of the crystal is then restored by the creation of a relatively positively charged anion vacancy. The reduction process has been determined as being rate controlled by the rate of oxide ion diffusion.¹⁸ Equilibration of the surface with the atmosphere by a fast reduction stage is followed by a uniform reduction rate, limited by the rate of oxide ion transport; the diffusion constant for the oxide ions being independent of the concentration gradient within the solid material. The activation energy for the reduction process was reported as $27.2 \text{ kcal mol}^{-1}$ ($113.9 \text{ kJ mol}^{-1}$) which is in good agreement with the oxygen self diffusion activation energy of $24.8 \pm 3.5 \text{ kcal mol}^{-1}$ ($103.8 \pm 14.7 \text{ kJ mol}^{-1}$) reported by Steele and Floyd¹¹ for CeO_2 with $P_{\text{O}_2} = 0.21 \text{ atm}$. The formation of cation interstitials as an alternative charge compensating species is unlikely in fluorite structured oxides as the cation Frenkel energy is high in ionic oxides.¹⁹ The presence of anion vacancies in fluorite type oxides is general has been shown to occur at concentrations up to 17% of the oxygen sub-lattice, before any phase change. The reason for the high activation energy for anionic mobility is that the ratio between the opening between adjacent cations that effectively cage the oxide ions and the oxide ion diameter is usually 0.682. The cation lattice therefore provides a continuous barrier to anion mobility.¹⁰

In such systems the interactions between the vacancies and other species within the lattice play an important role in the defining material properties, such that the properties of the materials are probably better described in terms of defect complexes rather than point defects. The variations in oxygen mobility and oxide ion conductivity are probably the most important property typical of nonstoichiometric fluorite oxides, as these properties govern the uses of such materials in applications such as catalysis, solid oxide fuel cells and sensors.¹² The quasi-chemical equation expressing the formation of doubly charged oxygen vacancies can be written;



In the case of nonstoichiometric ceria the change in oxidation state from Ce^{IV} to Ce^{III} occurs readily, facilitating the reaction. Applying the law of mass action;

$$K_{\text{V}_\text{O}^{**}} = [\text{V}_\text{O}^{**}] \cdot [\text{Ce}'_\text{Ce}]^2 \cdot \text{P}_{\text{O}_2}^{1/2} \quad (2.2)$$

In order to preserve charge neutrality $[\text{Ce}'_\text{Ce}] = 2[\text{V}_\text{O}^{**}]$, thus the law of mass action equation can be rewritten in terms of vacancy concentration and oxygen partial pressure such that;

$$K_{\text{V}_\text{O}^{**}} = 4[\text{V}_\text{O}^{**}]^3 \cdot \text{P}_{\text{O}_2}^{1/2} \quad (2.3)$$

The vacancy concentration can now be expressed in terms of the fraction of unoccupied sites in the oxide anion lattice, i.e., x in CeO_{2-x} such that $[\text{V}_\text{O}^{**}] = \frac{1}{2}x$. The mass action law equation can thus be further expressed as;

$$K_{\text{V}_\text{O}^{**}} = \frac{1}{2}x^3 \text{P}_{\text{O}_2}^{1/2} \quad (2.4)$$

It can thus be seen that the formation of doubly charged oxide anion vacancies in the fluorite ceria lattice depends on oxygen partial pressure such that;

$$x \propto P_{O_2}^{-1/6} \quad (2.5)$$

Other types of defects and indeed defect clusters would give rise to other exponents of the general form;

$$x \propto P_{O_2}^{-1/n} \quad (2.6)$$

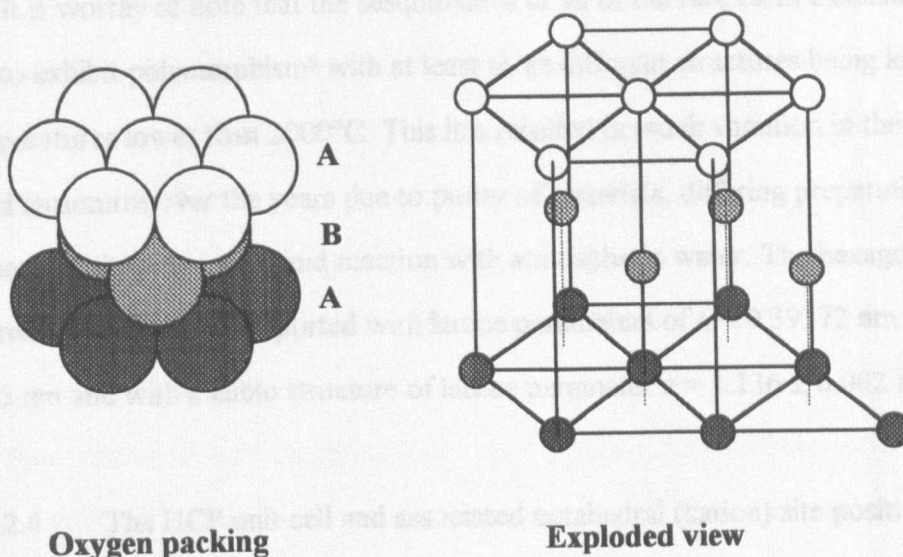
where n is characteristic of the type of defect, for example for a neutral defect $n = 2$ and for a singly charged oxygen vacancy $n = 4$.²⁰ The main flaw in this model is that it is assumed in the law of mass action that the defects are randomly distributed through the material and do not interact with each other. This assumption is generally only true however for very small deviations from stoichiometry. The association of defects can however be considered as being the formation of new defect complex species, to which the mass action law may be applied at intermediate defect concentrations. At high defect concentrations, extensive ordering of defects will preclude further use of the law. The association of defects is discussed further later in this chapter in section 2.1.1.6. The ordering of defects results in the formation of a homologous series of metastable substoichiometric phases depending on oxygen partial pressure and temperature. Several discrete phases within the homologous series have been determined in the literature²¹ including Ce_7O_{12} , Ce_9O_{16} , $Ce_{11}O_{20}$, $Ce_{16}O_{30}$, $Ce_{19}O_{34}$, $Ce_{29}O_{52}$, $Ce_{39}O_{70}$, $Ce_{40}O_{72}$ and $Ce_{62}O_{112}$, and the existence of further members of the series is highly probable. A phase diagram for CeO_{2-x} for $0 < x < 0.5$ has been determined by Touzelin (1981).⁹ and Korner et al, (1989).²² The reductive behaviour of the CeO_{2-x} system has been reviewed in greater depth by Trovarelli, (1996),²³ including the temperature programmed reduction (TPR) of ceria with hydrogen and carbon monoxide. Temperature programmed reduction studies of ceria and doped ceria was studied by Zotin et al (1993).²⁴ The conclusion of the study was that the TPR was difficult to quantify due to complications involved in the reduction of add-species such as adsorbed surface carbonates. The stability of the add-species was likewise also a function of the preparation process of the material, specifically the precursor materials and the thermal history. For example, nitrate species were found to

increase the stability of surface add-species following reaction with them to form new species.

2.1.1.2 La_2O_3

The sesquioxide of lanthanum is known to have a hexagonal structure above c. 590°C ²⁵ This structure is similar to that of corundum ($\alpha\text{Al}_2\text{O}_3$). The structure can be best described as hexagonally close packed oxygen with two thirds of the octahedral sites filled with La^{3+} cations, and is shown below in figure 2.3. The structure can thus be thought of as consisting of linked LaO_6 octahedra.

Figure 2.3 The hexagonal close packing in La_2O_3 .



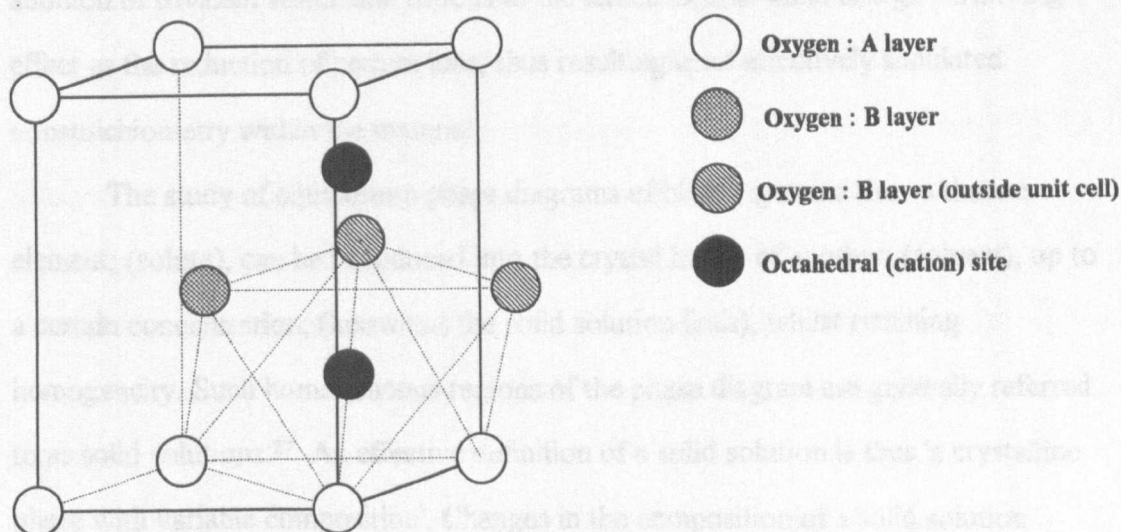
In figure 2.3, only the oxygen packing is shown, for the sake of simplicity.²⁶ The hexagonal packed second layer fit into the hollows in the first hexagonal packed layer. Atoms in the third layer are directly above those in the first layer, resulting in an A B A B stacking sequence. This structure differs from that of a face-centred cubic structure in that the third layer atoms are placed in the hollows in the third layer resulting in an A B C A B C repeating sequence. The atom positions of the FCC structure first layer repeat every fourth layer, rather than every third layer as is the case with the HCP structure. The incorporation of the cationic sites into the HCP oxygen

crystal structure is difficult to represent graphically and is beyond the scope of this text, although such representations can be found in the literature.⁴

In close packed structures the octahedral sites are found to form a hexagonal array, centred halfway between the adjacent close packed layers and with the same periodicity as the close packed atoms. The sites are found to be neither directly above or directly below the atoms in the close packed layers A and B in HCP materials, but are found to be co-linear with the third layer (C) in FCC materials. The ratio of octahedral sites to atoms within the unit cell is unity for close packed structures. In each hexagonal unit cell there can be found two octahedral sites which form continuous rows oriented normal to the close packed atom planes of the HCP structure. The HCP unit cell is presented in figure 2.4, including the positions of the octahedral sites.

It is worthy of note that the sesquioxides of all of the rare earth elements are known to exhibit polymorphism⁶ with at least three different structures being known for temperatures lower than 2000°C. This has resulted in much variation in the reported structures over the years due to purity of materials, differing preparative processes and the adsorption and reaction with atmospheric water. The hexagonal structured La_2O_3 has been reported with lattice parameters of $a = 0.39372 \text{ nm}$ and $c = 0.61295 \text{ nm}$ and with a cubic structure of lattice parameter $c = 1.136 \pm 0.002 \text{ nm}$.⁶

Figure 2.4 The HCP unit cell and associated octahedral (cation) site positions.



The rare earth sesquioxides are also known to become hydrated and carbonated if they are exposed to atmospheric carbon dioxide and water vapour at ambient temperature and pressure.⁶ Oxides that belong to the lighter rare earth series (La_2O_3 , Nd_2O_3 , Sm_2O_3) transform partially to carbonated hydroxides under such conditions, although in contrast to the hydration, the carbonation process is limited to the outer layers of the oxides. In this study, all samples were inevitably exposed to atmospheric air under storage conditions and the formation of carbonated hydroxides during storage was therefore highly probable. In order to ensure test materials were oxides only, each 800°C calcined material was heated to 600°C for approximately 30 minutes immediately prior to use in order to decompose the carbonated hydroxides to oxides.

2.1.1.3 Aliovalent Cation Doped Ceria Solid Solutions.

Earlier in this chapter the solid/gas equilibrium and nature of nonstoichiometry in anion deficient ceria (CeO_{2-x}) was discussed in terms of essentially intrinsic defects. The reduction of Ce^{IV} to Ce^{III} (using reduced oxygen partial pressures/reductants at elevated temperature), charge compensated by the formation of anion vacancies was used to explain the nature of the nonstoichiometry. It is also possible, however to alter the charge balance of fluorite materials by the substitutional addition of aliovalent dopant ions the lattice, thereby inducing a charge compensating defect population within the material, exactly as in nonstoichiometric systems.¹⁹ In the case of ceria, the addition of trivalent lanthanide cations to the lattice has the same charge perturbing effect as the reduction of cerium ions, thus resulting in an effectively simulated nonstoichiometry within the material.

The study of equilibrium phase diagrams of binary systems shows that an element; (solute), can be introduced into the crystal lattice of another; (solvent), up to a certain concentration; (known as the solid solution limit), whilst retaining homogeneity. Such homogeneous regions of the phase diagram are generally referred to as solid solutions.²⁷ An effective definition of a solid solution is thus 'a crystalline phase with variable composition'. Changes in the composition of a solid solution generally result in modification of the material properties. These phenomena can be

characterised, rationalised and used to design and engineer new materials with desired properties, and to enhance such properties in existing materials. There are numerous examples of such technology in present use, for example, several thermo-mechanical and electrical applications of magnesia, alumina and zirconia based their solid solutions.²⁸

In this present study, the addition of various concentrations of lanthanum solute to a fluorite structured ceria host material has been studied in order to correlate solute concentration with variations in measurable physical and catalytic properties for the heterogeneous oxidation of methane and carbon monoxide.

The addition of trivalent dopant ions to a ceria-host solid solution results in changes in the lattice parameters of the materials.²⁹ Modelling of the lattice parameter variations with composition involves determining the expansion of the lattice if the dopant cations are larger than that of the host, and an accompanying contraction of the lattice due to the creation of cation vacancies as charge compensating species. This contraction can be thought of as an effective decrease in the effective anionic radius with increasing dopant concentration.²⁹ In the case of doped ceria, an empirical equation for the lattice parameter variation with dopant concentration has been reported by Kim (1989);

$$d_{Ce} = 0.5413 + m[0.0220(r_{dopant} - r_{host}) + 0.00015(Z_{dopant} - Z_{host})] \quad (2.7)$$

for the case of a single dopant. In the equation, m is the cation % of dopant in the solid solution, r denotes cationic radius in nm, and Z the valence state. In the case of lanthanum doped ceria, the highest reported solid solution limit is 68 cation %³⁰. (The solubility of lanthanide dopants is very high in comparison with other common dopants e.g., 25 cation % Ca as reported by Adham and Hammou, (1983)³¹) and Arai et al (1986)³². Substitution of the ionic radii data into the empirical equation results in a theoretical maximum lattice parameter (for a saturated solid solution of lanthanum in ceria) of 5.553352 Å.

It should also be noted that there is also a more limited solubility of cerium cations in the lanthana structure, as determined by Rienäcker et al, (1962).³³ In this

study, additions of up to approximately 5 cation % Ce to lanthana resulted in single phase solid solutions. The solubility of cerium in lanthana has also been reported by Eyring.³⁴

2.1.1.4 Microstructure - The Effect of Dopants

There are four main techniques available for the characterisation of the microstructure of oxide materials. These include electron microscopy, density measurement, surface area/porosity measurement and the estimation of primary crystallite size using x-ray techniques. In this study the materials are primarily characterised as catalysts and therefore the latter two of the four aforementioned techniques were most appropriate. Suitable apparatus for accurate density measurement was not available in this study, and the insulating nature of the oxide rendered electron microscopy studies unsuitable due to sample charging effects.

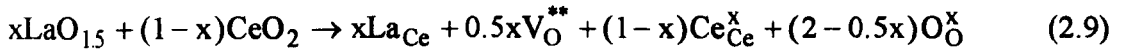
The effects of lanthanum doping of ceria has been investigated with respect to surface area stability by Pijolat et al (1993)³⁵ The sintering of ceria based materials was determined to be the result of a loss in microporosity accompanied by an increase in crystallite size. For pure ceria, the kinetic rate of crystallite growth was found to vary as a function of $P_{O_2}^{-1/6}$. The addition of lanthanum dopants was observed to slow the rate of crystallite growth. The crystal growth inhibiting effect was observed to increase with dopant level up to 10 cation %. This was explained in terms of retardation of the rate determining step (ambipolar diffusion of oxygen and electrons), by lanthanum. Another study by Rienäcker and Wu (1962)³³ also observed that additions of lanthanum to ceria up to a level of approximately 10 cation % resulted in a significant increase in surface area resistance to sintering. Higher lanthanum dopant levels were found to result in a progressive decrease in the surface area stability with respect to sintering, up to approximately 60 cation % where results were similar to those of pure ceria.

2.1.1.5 Defect Reactions

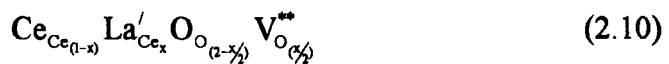
All processes involving the formation of defects or a reaction in a crystal may be expressed as defect chemical reactions. In the case of aliovalent solute incorporation, as is the case with lanthanum doping of ceria, the valence difference between host and solute cationic species must be compensated for by the formation of further defects. (As a result of this, the free energy of solution for aliovalent solutes also includes the energy of formation of the associated compensating defects). In the case of lanthanum incorporation in the ceria lattice, the general defect reaction can be written as⁸ ;



or



As can be seen, an oxide anion vacancy is introduced into the lattice as charge compensation for the substitutional incorporation of two lanthanum cations at host cation sites in the ceria lattice. It is possible for the defects to exhibit multiple valence states; in the case of oxygen vacancies relative 2+, 1+ charges and neutrality with respect to the "perfect crystal lattice" are possible, although generally one valence is predominant at any given temperature. The resulting formulation of the nonstoichiometric oxide simulated by aliovalent cation doping can be expressed similarly to other chemical formulae with the use of Kröger - Vink notation. For ceria doped with trivalent lanthanum ions the formulation of the solid solution phase can be written;

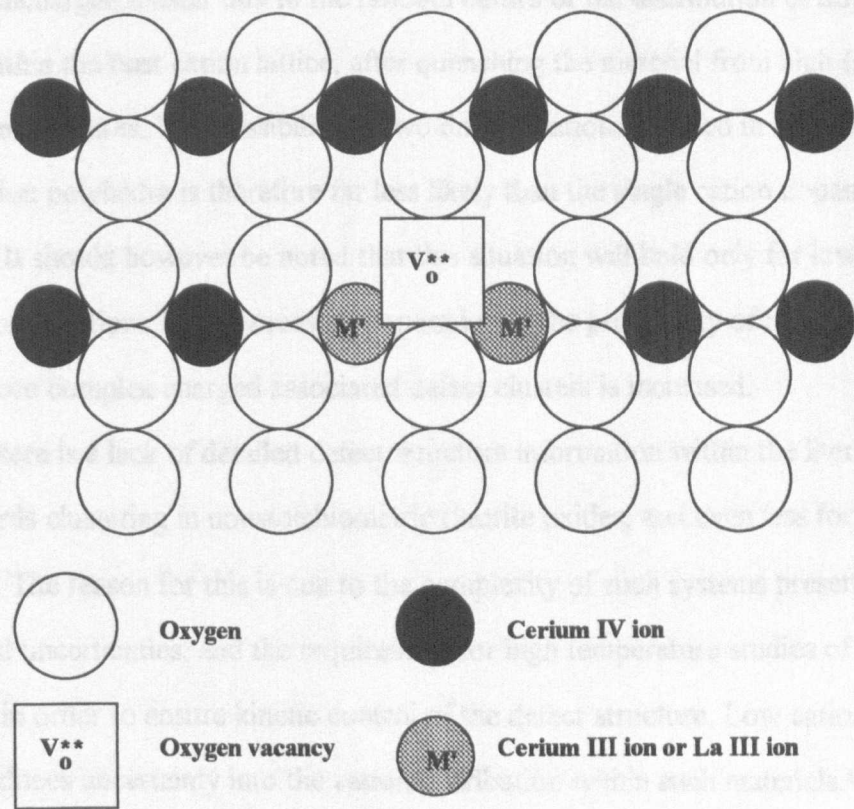


This general formulation is used to represent the catalyst material series in an abbreviated fashion such that any material can be defined with respect to its composition by quoting x, the lanthanum dopant cation fraction.

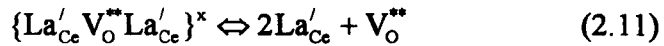
2.1.1.6 Defect Interactions

The interaction and clustering of defects in nonstoichiometric oxides has considerable influence over the thermodynamic, transport and associated material properties. Generally for defect concentrations exceeding 0.5 - 1 %, defect interactions occur.⁷ The mechanisms of stabilisation of the high levels of disorder associated with high defect concentrations can be classified in terms of aggregation (kinetically controlled Coulombic interaction between a dopant ion and its associated charge compensation species), and elimination (crystallographic shearing processes along shear planes consisting of defect aggregates). The type of mechanism adopted by the oxide is dependent largely on the metal - oxygen interaction potentials. The simplest clusters consist of dopant - charge compensating defect pairs, but these are generally replaced by more complex structures at higher defect concentrations. A defect cluster is represented schematically in figure 2.5.⁷

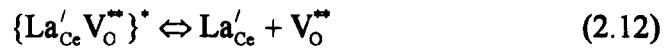
Figure 2.5 A schematic representation of a defect cluster in a nonstoichiometric oxide.



The simplest possible neutral cluster consists of one vacancy and two trivalent (reduced or aliovalent dopant) cations and effectively has the M_2O_3 formula. Such M_2O_3 nuclei can grow incrementally by doubling, tripling, etc., in size to form the many substoichiometric phases within the ceria (and also other fluorite oxides) phase diagram.³⁶⁻³⁷ The defect association reaction for the simple neutral cluster in the case of the ceria/lanthana system can be written;



It is also possible for a charged defect cluster to form, the defect association reaction for which can be written;



The probability of formation of these two associated defect clusters has been discussed in the literature by Kilner and Steele (1981)³⁸ and further by Kilner (1983).³⁹ They concluded that the formation of the charged defect cluster would be favoured over the uncharged cluster due to the random nature of the distribution of dopant cations within the host cation lattice, after quenching the material from high (mobile cation) temperatures. The possibility of two dopant cations situated in adjacent anion coordination polyhedra is therefore far less likely than the single cation dopant situation. It should however be noted that this situation will hold only for low dopant cation concentrations; with increasing dopant levels the probability of neutral, and further more complex charged associated defect clusters is increased.

There is a lack of detailed defect structure information within the literature, with regards clustering in nonstoichiometric fluorite oxides, and even less for doped materials. The reason for this is due to the complexity of such systems presenting many theoretical uncertainties, and the requirement for high temperature studies of doped materials in order to ensure kinetic control of the defect structure. Low cation mobility also introduces uncertainty into the cation distribution within such materials.¹⁹ There

is however a plethora of data regarding transport studies (see later section), of fluorite oxide materials which provides supporting evidence for defect interaction theories.

2.1.1.7 Phase Diagrams for a Typical Binary Eutectic

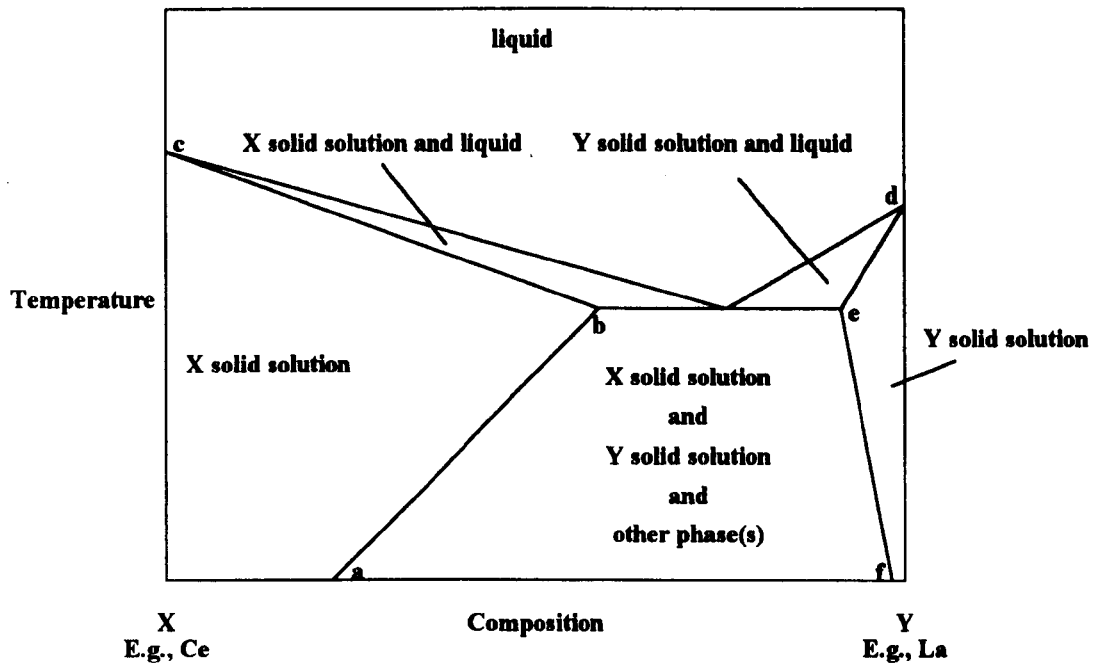
The simplest form of solid solution system is one in which complete miscibility of both solid and liquid states occurs, such that solid solutions can be formed at all compositions. In most binary eutectic solid solution systems, (as in the case of ceria/lanthana), the crystalline phases only exhibit partial solubility within each other. A general phase diagram representative of this type of system is shown in figure 2.6.

Crystals of Y (e.g. La_2O_3) dissolve in crystals of X (e.g. CeO_2) forming a solid solution. The composition limit of solid solution is dependent on temperature and is denoted by the lines *abc* (for solutions of Y in X), and *def* (for solutions of X in Y). Near the melting point of each pure material, the composition limit of solubility is reduced due to melting of the other material, resulting in solid solutions of reducing solute composition and liquid solute. As temperature is reduced, a maximum in the solution composition limit is reached at point *b* (for solutions of Y in X) and point *e* (for solutions of X in Y). In each case, this temperature is known as the solidus temperature. As temperature is further reduced, so do the solid solution composition limits along the lines *ab* and *ef*. The region described by *abef* consists of at least two phases, saturated solid solutions of Y in X and X in Y, and possibly other intermediate phases. It should be noted that this phase diagram is meant only to provide a general description of an ideal binary phase diagram and is not meant to accurately represent the phase diagram for the ceria/lanthana binary system which is yet to be reported in the literature. Certain features in the phase diagram are however deliberately representative of the system, for example, the solubility of lanthanum in ceria is much greater than that of cerium in lanthana, and is represented by the relative compositions at *b* and *e*. Ceria and lanthana also have similar melting points denoted by *c* and *d* (2750°C for ceria⁴⁰. and $2304 \pm 5^\circ\text{C}$ for lanthana³⁴).

Solid solutions can generally be further classified into three broad types; substitutional solid solutions (where solute atoms occupy normal lattice sites within the

host crystal lattice), interstitial solid solutions (where solute atoms occupy positions in the interstices of the host crystal lattice - generally limited to solute species of small ionic radii), and defect solid solutions (where sites within the host lattice remain vacant, usually in order to charge-compensate for aliovalent solute atoms).

Figure 2.6 An example phase diagram for a binary eutectic system with limited solid solubility of end members in each other.



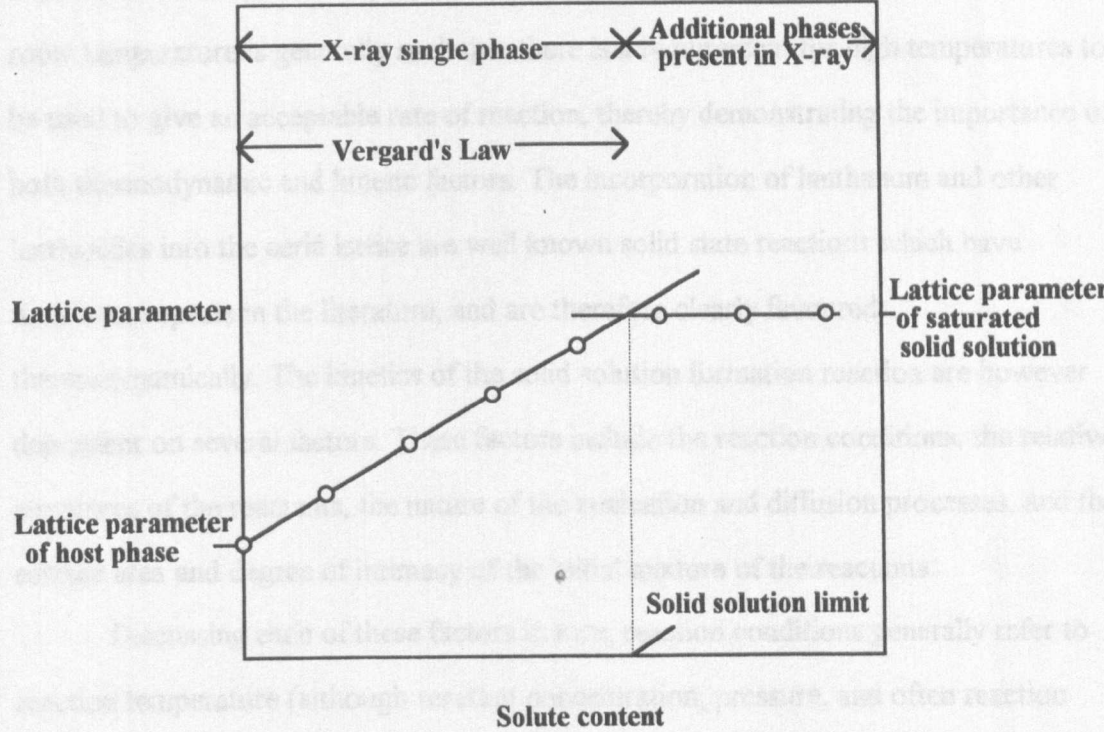
Generally, it can be assumed that the ability of given materials to form solid solutions depends on structure (and bonding), and the degree of closeness in ionic size of the solvent and solute ions (usually the larger ion should be less than 15% larger than the smaller ion). Discussing these factors in turn, the bonding in two isostructural materials is not necessarily the same - in order to form a solid solution it is generally necessary for the bonding of both materials to be either predominantly ionic or covalent in nature. The fact that the materials are isostructural does not in itself ensure the possibility of solid solution formation. It is also known for materials with different structures exhibiting similar bonding to form at least partial solid solutions over limited compositional ranges, provided that the bonding in both materials is similar. This is the case in the formation of ceria/lanthana solid solutions.

The main implication of an ionic size miss-match between solute and solvent atoms is the introduction of an element of local lattice strain, which in turn results in either an expansion or contraction (depending on the dopant cation radius), of the mean lattice parameter of the host lattice with solute addition. In continuous solid solutions of ionic salts, the lattice parameter of the solution is directly proportional to the atomic fraction of solute ions present in the solution - a relationship known as Vergard's Law.²⁶ Deviation from the Vergard's Law relationship between lattice parameter and solute fraction is an indication of the formation of a defect solution. For example, beyond a certain level of substitution, further increases in the solute concentration may result in either a phase change in the solid solution, or in the formation of an additional phase along with what can be described as a saturated solid solution. Under such conditions, the lattice parameter of the solution can be observed to undergo a sudden departure from the constant slope predicted by Vergard's Law, at a specific solid solution composition. This composition is known as the solid solution limit. The ionic radius for lanthanum (La^{3+} 103.2 pm⁴¹) is within 18.6% of that of cerium (Ce^{4+} 87 pm⁴¹) and therefore lies slightly outside that of the previously mentioned 15% general limitation.

Experimentally determined lattice parameter data can be used to produce a solvus curve - a curve forming the boundary between the single phase solid and two phase solid regions of the binary phase diagram. In the case of ionic materials this is generally achieved by producing a series of solid solutions of increasing, accurately known solute content using a fixed method, and measuring the lattice parameter using X-ray diffraction techniques (see experimental chapter section 3.2 and Appendix 3.2). A parametric model can be constructed based on these observations such that the variation in lattice parameter with composition can be determined for that system and preparative method. For the formation of a limited solid solution with a defined solid solution limit, the system should exhibit a discontinuity from a linear relationship between lattice parameter and composition at the solid solution limit solute concentration, beyond which the lattice parameter should remain constant at the saturated solution value. Furthermore, observation of the diffraction patterns should confirm the presence of a second phase within the sample material for solute contents

beyond the solution limit. An example of such a plot is shown below in figure 2.7. The solid solution limit of lanthanum in ceria has been estimated in the literature as being between 50⁴² and 68³⁰ cation % lanthanum.

Figure 2.7 An example plot of the variation in lattice parameter with solute content for a typical oxide solid solution.



From the above figure, the solid solution limit at the given preparation temperature is given by the intersection of the two branches of the parameter curve. The effect of variations in preparation temperature are to produce similar curves but shifted such that for a lower temperature, the Vergard's Law branch would be shorter and the solid solution branch would be found at a lower lattice parameter.²⁶ All other points on the solvus curve can then be determined by equilibrating one of the fixed composition materials at various temperatures. Measured parameters can then be used in conjunction with the parameter/solute content plot to determine the solute content at the other equilibrium temperatures, effectively using the portion of the parameter curve which obeys Vergard's Law as a master curve for the determination of the whole solvus. It should be noted that the solvus curve only represents one phase boundary

within the phase diagram which would require full phase analysis at all temperatures and compositions to be complete.

2.1.1.8 Solute Incorporation.

The most widely used method of preparation of polycrystalline materials is the solid state direct reaction of precursor materials. The rate of solid state reactions at room temperature is generally such that there is a requirement for high temperatures to be used to give an acceptable rate of reaction, thereby demonstrating the importance of both thermodynamic and kinetic factors. The incorporation of lanthanum and other lanthanides into the ceria lattice are well known solid state reactions which have numerous reports in the literature, and are therefore clearly favoured thermodynamically. The kinetics of the solid solution formation reaction are however dependent on several factors. These factors include the reaction conditions, the relative structures of the reactants, the nature of the nucleation and diffusion processes, and the surface area and degree of intimacy of the initial mixture of the reactants.

Discussing each of these factors in turn, reaction conditions generally refer to reaction temperature (although reactant concentration, pressure, and often reaction atmosphere can also have significant influence over reaction rate). The temperature required for a given reaction rate depends entirely on the other factors (discussed next) and can only be determined experimentally. Experiments determining the rate of reaction over a range of temperatures allow the derivation of a reaction enthalpy by the Arrhenius method.

The role of the structures of the reactants is to determine the degree of structural reorganisation required in product formation, and the ease of nucleation of the product. The thermally activated diffusive migration of atomic species is limited by structural constraints, effectively trapping them in their appropriate lattice sites. The thermal energy required for such species to move is therefore dependent on the species involved in the process and the lattice structure.

Nucleation of the product material occurs at the interface between two of the reactant crystals which are in intimate contact across a shared face - known as a grain

boundary. At a sufficiently high temperature, the first stage of the solid state reaction is the formation of a layer of reacted product at the grain boundary which may be isostructural with one or both of the reactant crystals, or may have a completely different structure. This nucleation process is rate limited by the difficulty of structural change (if any), the breaking and forming of bonds required by the reaction and the diffusion rate of the species required to migrate. The ease of nucleation also depends on the surface structure (and therefore surface reactivity) of the reacting phases, which can vary significantly from the bulk material, and from crystal face to crystal face. The reactivity of the surfaces also depends on surface crystal defects, especially in the product phase.

The next stage of the solid state reaction process involves the propagation of the reactant/product boundary layer into the bulk of the reactant crystals, in order to allow the product layer to grow. In the case of the ceria/lanthana solid solution formation, this requires the counter diffusion of cerium and lanthanum cations through the bulk solid solution material to the propagating reaction interfaces. The rate limiting step for the solid solution reaction will be the diffusion of the slowest diffusing species. The presence of lattice vacancies in the product material (which is in turn dependent on lanthanum content in the present study), often enhances the diffusion of ions through it. This inter-diffusion followed by reaction process is known as the Wagner Mechanism.⁴³ A complete account of diffusion in ceramic materials is beyond the scope of this text but several excellent reviews exist in the literature which provide excellent background reading on this subject.⁴⁴⁻⁴⁸ From this discussion, as well as ionic diffusion rates and the rate of product nucleation, it is also clear that the rate of reaction will also be proportional to the intimacy of the reactant mixture. As the reaction rate is dependent on contact between reactant grains, the total contact area has a great influence on the rate of reaction. Higher reactant surface areas result in higher contact areas and therefore rates. In practice, contact between all of the reactant surfaces can be improved by pelleting.

2.1.1.9 Solid State Reaction Techniques

The principles of solid state reactions are derived taking into account the principles of diffusion theory, typically to produce an intimate mixture of suitable reactant materials and to then subject the mixture to a thermal treatment in order to drive the solid state reaction. The theory of the technique is simple, yet there are several complicating factors which must be taken into consideration. The most important factors are the choice of reactant materials, purity, and the method used to produce the initial intimate mixture.

The purity of the starting materials is generally dictated by the end use of the product material. During thermal treatment, many impurities are known to segregate to the surface and grain boundaries of the material, thus changing the solid state reaction and sintering properties, (e.g., the work of Pijolat et al, (1993)³⁵ investigating the effect of lanthanum doping on the sintering properties of ceria), and the grain boundary conductivity (e.g., the increase in grain boundary resistance caused by segregated silicon in doped ceria as determined by Gerhardt and Nowick, (1986)⁴⁹ which was said to form a liquid/glassy phase at the grain boundaries by Tanaka et al (1987)⁵⁰). For refractory materials the presence of minute levels of impurity can have a large influence over the microstructural and therefore mechanical, electrical and surface properties of the product material. In the case of ceria/lanthana, the major impurities in cerium based materials are known to be other lanthanides due to the difficulties associated with lanthanide separation. In order that the composition of the solid solution materials at low lanthanum levels could be accurately estimated, only materials of > 99.99 % purity were considered to be suitable for use in this study.

In the case of the preparation of doped oxidic materials, the simplest reactants to use are the oxides comprising the desired product, mixed in the correct proportions to provide the desired composition. However, there are several problems implicit with this method. Taking the ceria/lanthana system as an example, the reaction of the oxides to form a solid solution is complicated due to the difficulty in forming an intimate mixture of the oxides in the starting material. Ceria in particular is a hard material, its abrasive properties making grinding to form grains of small enough dimensions for

solid state reactions laborious and time consuming. Even ball-milling for many hours often does not provide a satisfactorily intimate mixture and thus prolonged high temperature treatment is necessary in order to produce a solid solution. The solid solution limit of lanthanum in ceria is thus apparently reduced in comparison with those previously reported for identical materials prepared by other techniques, even after a severe thermal treatment history. This is demonstrated by the presence of multiple phases in the X-ray diffraction patterns in the study by Rienäcker and Wu (1962).³³

The use of high temperature treatments is undesirable for other reasons, both general and specific to this study. In this study, catalytic and surface area measurements are two of the primary characterisation techniques utilised and after severe thermal treatment, materials were found to be highly sintered with very low specific surface areas. Due to the experimental limitations of both the surface area measurement apparatus and catalytic activity measurement apparatus, very low surface area materials (i.e. less than $5\text{m}^2\text{g}^{-1}$) were unsuitable for testing due to the inevitable increases in error associated with the characterisation of such samples.

Other methods of producing a more intimate mixture of oxide materials suitable for solid state reactions at lower temperatures were therefore used in this study. Two separate methods were used; the 'ceramic method', and a coprecipitation method. Both of these experimental methods are discussed in detail in section 3.1. In these methods, soluble compounds of the required metal cations are mixed in solution. The resulting solution was then either chemically or solvent evaporation precipitated to yield a precursor material with a high degree of homogenisation and a high surface area, such that the solid state reaction will proceed at much lower temperatures than with the mixed oxides method. The homogeneity of the precursor solution is effectively on the near atomic scale. In the case of the ceria/lanthana solid solution formation reaction, mixtures of the hydrated metal nitrates, weighed in the correct proportions were dissolved in distilled water. The resulting solution was then either evaporated to dryness and then thermally decomposed at 450°C before calcination (ceramic method), or precipitated with ammonia solution or ammonium bicarbonate solution, filtered, washed, dried and decomposed at 450°C before calcination (coprecipitation method).

Both methods result in similar precursor oxide materials of accurately known composition, with cationic mixing on the atomic scale.

There are possible problems associated with both methods; in the ceramic method the drying and decomposition process must be slow in order to avoid 'spitting' and possible loss of product material. In the coprecipitation method, the possibility of selective precipitation of one of the components prior to the other is significant if the precipitation of each occurs at a significantly different pH. The resulting material in such circumstances could effectively be described as one metal precipitate encapsulated in the metal precipitate which precipitates at the higher pH. This problem can be avoided by precipitation at constant pH, effected by dropwise addition of the metal nitrate solution to a large excess of the alkaline solution, with rapid stirring.

Once the precursor material has been prepared, heat treatment is required in order to drive the solid state reaction. The calcination temperature, time, atmosphere and reaction vessel are selected for each reaction on the basis of requirements of the product material. The minimum calcination temperature and time can only be determined experimentally for a given reaction, using X-ray powder diffraction phase analysis of the product. Once this has been determined, further consideration of the reaction vessel material and the calcination atmosphere is necessary. The reaction vessel material should be chemically inert with respect to the reactants and product materials under the thermal treatment conditions used, in order to avoid cross contamination. The choice of materials is generally limited to platinum (melting point approximately 1700°C) for very high temperature treatments, or refractory materials such as α -alumina or stabilised ZrO_2 .

Finally, the atmosphere of the reaction can also significantly affect the composition of the reaction products and the kinetics of the reaction. For example, (as mentioned previously), the gross nonstoichiometry of ceria is critically dependent on both temperature and the partial pressure of oxygen. At low partial pressures and high temperatures (effectively reducing conditions), the formation of materials such as fluorite structured CeO_{2-x} are possible due to the $\text{Ce}^{\text{IV}} \rightarrow \text{Ce}^{\text{III}}$ redox reaction. Under sufficiently forcing conditions the formation of the HCP structured sesquioxide Ce_2O_3 is favoured. Under high and low oxygen partial pressures materials with different bulk

and surface structures are formed, which on reaction with HCP structured lanthanum sesquioxide would probably have a different solid state reaction rates, and could possibly form different products with different structures and compositions. As the fluorite structured solid solution material is the desired product in this study, it was necessary to maintain high oxygen partial pressures during the solid state reaction - effected by performing the reaction in atmospheric air.

The last part of the experimental procedure is analysis of the product material. For solid state reactions, X-ray powder diffraction is the technique of choice allowing the determination of phase(s) present. This in turn allows the product to be identified, and the extent of the reaction to be assessed. The presence of reactant phases and the measurement of lattice parameter variations can be used to determine the solid solution limit of a given system under given reaction conditions; and within the solid solution limit, the extent of reaction can be determined with temperature and time.

2.1.2 Transport Studies - Ionic Conductivity

2.1.2.1 Theory

In the following section is a brief outline of the theory, key concepts and analytical principals involved in ionic conductivity. The discussion is general, but where possible the ceria/lanthana system studied in this work has been used as an illustrative example. It should be noted that most of the existing theory and atomistic simulation techniques discussed are only strictly valid for very dilute solid solutions. In this study, many of the materials have been doped in order to exhibit large deviations from the stoichiometry of the host material, and thus analysis by traditional theoretical techniques discussed in this section would be considered questionable over such large compositional ranges. This section does however provide valuable background information and insight into the possible effects on such systems of high dopant concentration, and is of use in the classification and interpretation of other characterisation data, (e.g., catalytic activity), if over rather more limited compositional ranges.

Ceria and aliovalent cation doped ceria fall into a class of materials loosely described as superionic conductors (or fast ion conductors). To be classified as such the transport of ions through the material must be such that the conductivity (σ) $> 10^{-4} \Omega^{-1} \text{cm}^{-1}$ at the test temperature, whilst under the same conditions electronic conductivity is negligible. In such materials the application of an electric field results in material transport - effectively behaving as a solid electrolyte.⁵¹ Generally the conductivity is limited to one mobile ionic species, (which in the case of the ceria/lanthana series is the oxide anion), and is defined in terms of an electrolytic domain. This is the temperature and electroactive species chemical potential range over which the transport number of the electroactive species is ≈ 1 .

In anion deficient fluorite oxides in general, the total conductivity can be divided into three distinct regions.^{38, 52 - 53} At extreme values of P_{O_2} the conductivity is electronic in nature. At high P_{O_2} oxygen tends to be incorporated into the lattice resulting in the formation of positive holes such that;



It can be shown that under such conditions $[\text{Hole}^{\bullet}] \propto P_{O_2}^{1/4}$.

Conversely, at low P_{O_2} oxygen tends to be lost from the lattice resulting in the formation of electrons, such that;



It can be shown that under such conditions $[e'] \propto P_{O_2}^{-1/4}$

At intermediate P_{O_2} the conductivity is predominantly ionic in nature. The range of P_{O_2} where ionic conductivity dominates (the ionic domain), is dependent on temperature and anion vacancy concentration, (which is in turn dependent on intrinsic cationic reducibility and the concentration of extrinsic aliovalent cations). The concentrations of both positive holes and electrons increase with temperature, thus the

ionic domain is diminished with temperature.³⁸ Under the conditions used in this study, both for conductivity studies and for catalytic studies, the conductivity of the ceria/lanthana solid solution system is known to be predominantly ionic in nature,^{5, 53} although the total conductivity will always contain electronic contributions, such that;

$$\sigma_{\text{total}} = \sigma_{\text{O}^{2-}} + \sigma_{\text{electronic}} \quad (2.15)$$

The proportion of the total conductivity accounted for by each conducting species is known as its transference (or transport) number. For the oxide anion in the present study this is given by⁵³ ;

$$t_{\text{O}^{2-}} = \frac{\sigma_{\text{O}^{2-}}}{\sigma_{\text{total}}} \quad (2.16)$$

and is generally determined by the EMF method.⁵¹ Within the ionic domain, the oxide anion transport number is approximately unity.

In all fluorite structured materials anion mobility is several orders of magnitude greater than cation mobility. The anion mobility is further enhanced by the anion deficiency within the structure. Ionic conductivity in such materials has attracted great interest over the years due to the applications of such materials as solid state electrolytes in solid oxide fuel cells, sensors, batteries, and increasingly in other areas encompassing pollution monitoring and control, energy conservation and conversion.⁵

⁵¹ Ionic conductivity within these materials is found to vary as a function of composition, temperature and experimental atmospheric conditions.

The mechanism of ionic conductivity is generally described as a 'hopping' process.⁵⁴ The motion of the oxide anions in anion deficient fluorite structured oxides can be described as a succession of distinct discrete events or "hops". There are four preconditions for this mechanism, such that the residence time at a given anion site must be much greater than the jump event duration, and must be much greater than the thermal vibration time. The hopping distance (d), must be significantly greater than the thermal vibrational motion amplitude, and the change in potential energy due to the particle rearrangement accompanying the hop (ΔE , essentially a temperature

independent term), must be greater than kT . If these conditions are met then the diffusion coefficient (D), can be defined in terms of n , the number of potential hop species, ν , a term for the hopping event attempt frequency, d and ΔE ;

$$D \propto n \nu d^2 \exp^{-(\Delta E/kT)} \quad (2.17)$$

The hopping model is generally considered to be validated for a given system by two criteria; the measured Arrhenius energy should be of much greater magnitude than kT (i.e., not 'liquid-like' properties). The conductivity (or diffusion coefficient) should also be strongly affected by the presence of dopants (- effectively proof of defect migration).⁵⁴ Further evidence can also be gained by structural studies.

Experimentally, conductivity is usually measured as a function of temperature, such that an activation energy for the conduction process may be determined using the Arrhenius method. Empirically, the temperature dependence of conductivity can be expressed as;

$$\sigma T = A \exp^{(-E_a/kT)} \quad (2.18)$$

Where A is a constant, E_a the activation energy - effectively the enthalpy of ion migration,⁵¹ and k the Boltzmann constant. A plot of $\log(\sigma T)$ vs. $1/T$ is usually a straight line with slope $-E_a/k$ and the intercept on the y axis is $\log(\sigma T)$.³⁸

The activation energy often does not necessarily remain constant at all temperatures, exhibiting a lower activation energy for ionic conduction at higher temperatures. This results in the appearance of two straight line portions of different slope on the plot of $\log(\sigma T)$ vs. $1/T$.³⁸ This effect has been attributed to the dissociation of vacancy clusters at higher temperatures reducing the contribution to the activation energy required to dissociate the vacancy from the cluster.¹⁹ The temperature dependence of the ionic conductivity (and thus E_a), is determined by the temperature dependence of the anionic mobility (μ). In turn μ is dependent on the Gibbs free energy for the migratory jump process (ΔG_{jump}), such that for unassociated vacancies³⁸ ;

$$\mu \propto \exp^{(-\Delta G_{\text{jump}}/kT)} \quad (2.19)$$

As $\Delta G = \Delta H - T\Delta S$, and assuming that ΔS is temperature independent, it can be said;

$$\mu \propto \exp^{(-\Delta H_{\text{jump}}/kT)} \quad (2.20)$$

In most cases, the assumption that vacancies are free is unreasonable, therefore in addition to the ionic mobility contribution ΔH_{jump} , the activation energy also encompasses a separate contribution from the associate binding energy, (ΔH_{ABE}) such that;

$$E_a = \Delta H_{\text{jump}} + \Delta H_{\text{ABE}} \quad (2.21)$$

For isothermal experiments the associate binding energy should remain constant, as should the activation energy for the jump process. However, depending on the defect associate binding energy, full association can persist to high temperatures.⁵⁵ Changes in the activation energy with composition are therefore indicative of changes in the nature of the defect complex association, or in the anionic conduction mechanism. At high temperatures the associate binding energy should effectively fall to zero, thus the measured activation energy should be a direct measure of the activation energy for the jump process.³⁸ The associate binding energy will also change if there are any variations in the nature of the defect associate. Because of the charged nature of the associate pair with trivalent dopants, the binding energy of the defect associate pair is dopant concentration dependent due to Coulombic interactions and will generally exhibit a minimum,³⁹ corresponding to $r_{\text{dopant}} = r_{\text{host}}$.²⁹ In a homologous series of materials such as doped fluorite oxides, the differences in conductivity are generally determined by the differences in activation energy, the most significant contribution to which is the associate binding energy.³⁹ Dopant ion size effects therefore have a large effect on the association energy, and therefore the ionic conductivity.⁵⁶ In the case of the ceria/lanthana system, at high lanthana (and therefore anion vacancy)

concentrations, doubling, trebling, etc., of the defect complexes is possible, resulting in the possibility of ordered phases of various dopant concentration dependent stoichiometries, as found in the simpler CeO_{2-x} system mentioned previously. The energy state of oxygen vacancies within defect associates can be classified into three groups; isolated, associated and deeply trapped, each with successively stronger (defect concentration dependent) association interactions.⁵⁷ The temperature dependence of the conductivity can be further described by the temperatures above which each of the association interactions successively disappear.⁵ These temperatures will be characterised by a convergence in the straight line (Arrhenius) plots of $\log \sigma T$ vs. $1/T$. The associate binding energy has been determined for several trivalent dopants in ceria in the literature^{5, 58} and for lanthanum was determined to be $3.226 \text{ kcal mol}^{-1}$ ($13.507 \text{ kJ mol}^{-1}$).

Changes in the conduction mechanism are also often associated with structural changes. For example in the case of the ceria/lanthana system, beyond the solid solution limit, the fluorite structure of the ceria host can no longer accommodate further additions of lanthanum. Thus, the formation of a two phase material is most likely, consisting of a fluorite saturated solid solution phase and a hexagonal lanthana phase. The presence of the second phase can either aid or hinder the conduction process, thereby causing a change in the activation energy for the conduction process. Within the solid solution compositional range, it is also possible to observe discontinuities in the Vergard's law plot at critical dopant concentrations, which may correspond to dopant vacancy associate ordering.³⁹ Although this is a purely empirical observation, correlation with dopant concentration dependent conductivity data could prove of use in future studies.

The pre-exponential factor, A , is dependent on several temperature independent variables derived from the ionic mobility and on other variables such as the number of orientations of the association complex involved.³⁸ In the case of the ceria/lanthana system. the pre-exponential factor is assumed proportional to the number of conducting species, (i.e., $[V_O^{**}]$), which is in turn proportional to the aliovalent dopant concentration. Thus, variations in A with composition can be used to

determine approximate trend variations in concentration of the conducting species with composition.

There are significant differences between the anionic transport behaviour of reduced and doped nonstoichiometric oxides.¹¹ Larger variations in the activation energy with composition are found with CeO_{2-x} than with lanthanide doped analogues due to the high mobility of conduction band electrons in the CeO_{2-x} compared with the low mobility of dopant cations. The activation energy for motion in nonstoichiometric ceria decreases with increasing anion vacancy concentration, whereas the activation energy for trivalent lanthanide doped ceria is relatively independent of anion vacancy concentration and similar to that of near stoichiometric ceria ($19.4 \text{ kcal mol}^{-1}$ (81.2 kJ mol^{-1})) for $\text{Ce}_{0.8}\text{La}_{0.2}\text{O}_{1.9}$ ⁵⁹). The work of Balazs and Glass (1995)⁵⁹ did demonstrate the existence of a fall and then rise in activation enthalpy with composition for Y doped ceria, the minimum occurring between approximately 8 and 15 cation % doping.

The high mobility of vacancies and electrons in CeO_{2-x} ensures that thermodynamically stable defect clusters form in the reduced material. In the doped material the low cation mobility results in kinetically controlled defect clustering which is unlikely to be thermodynamically stable, except at very high temperatures where cation mobility is significantly increased. Further evidence for the doped materials not being at thermodynamic equilibrium is the maximum observed in plots of anion conductivity with dopant concentration,⁶⁰ and the atomistic simulation study by Catlow (1983)⁵⁴ Equilibrium distribution of clusters should result in the concentration of mobile dissociated vacancies increasing with the total vacancy concentration, therefore some amount of kinetic control of the defect structure and clustering is the only explanation for the observation. The atomistic interpretation of this phenomenon is that as dopant concentration is increased, simple clusters (single vacancy - isolated dopant cation), will give way to more complex clusters which may involve several dopant cations, (e.g., shear plane formation as discussed previously). The higher coulombic attraction between vacancies and more complex clusters results in a reduction in the mobility of the vacancy, leading to the observed reduction in the anionic conductivity.

The dopant/defect interactions in highly concentrated dopant solutions have been interpreted atomistically by Catlow (1984).⁵⁶ Rather than describing the ordering

(and stabilisation) of defect clusters, anion sites were classified in terms of the number of dopant ions in the immediate surrounding cation environment. This number can vary between 0 and 4 for the fluorite structure. A random distribution of dopants was assumed and the dopant/host cation radius ratio was used to modify the dopant/vacancy associate binding energy. The resulting model of the variation in conductivity with composition, (derived from the model of the variation of the dopant/vacancy associate binding energy with composition), was found to agree well with experimental data. The decrease in conductivity at higher dopant concentration levels was explained by the immobilisation of vacancies by the formation of 'deep traps' - anion sites with a large number of surrounding dopant cations. Deep traps can effectively be thought of as an atomistic (point defect) description of microdomains with an ordered structure. In a real system a thermodynamic equilibrium between microdomains and point defects is likely to occur. The atomistic simulation study of Catlow (1983)⁵⁴ concluded that the deep traps were anion sites surrounded by two or more dopant cations. Beyond a critical dopant concentration, (assuming a random distribution of dopants), the concentration of such deep traps increases resulting in the immobilisation of more vacancies and a decrease in conductivity.

2.1.2.2 Conductivity Measurements.

Early conductivity measurements of solid oxide materials were based on dc. methods⁵¹ using highly sintering ceramic processing methods to prepare samples. This technique was flawed due to the inability of the method to distinguish between the electrode, grain boundary and bulk contributions to the overall measured conductivity. The grain boundary contribution is dependent on the microstructure of the ceramic samples, which is difficult to control with good reproducibility and to quantify. This resulted in often significant errors in interpretation of conductivity measurements. Further developments of the dc. technique included the use of the four probe technique⁵¹ rather than the two probe used previously, which eliminated electrode effects but did not resolve bulk and grain boundary contributions. This problem was only relatively recently overcome in the early 1970's, using Impedance Spectroscopy

methods.⁵¹ This relatively new technique uses complex plane impedance analysis to separate and quantify the individual contributions to total conductivity in the frequency domain. The reader unfamiliar with the technique is also directed to excellent reviews of the subject by Kilner and Steele (1981),³⁸ Subbarao and Maiti (1984),⁵ and a review of superionic conductor science by Badwal (1994).⁵¹

As mentioned previously, the microstructure of materials has a great effect on both the magnitude of, and the relative bulk/grain boundary contribution ratio in the total conductivity. Microstructure is in turn determined by processing parameters such as purity, thermal history, and composition. Impurities in materials can segregate to the surface and grain boundaries under sintering conditions which can have significant effects on the conductivity of the grain boundary. In addition, by affecting transport properties across the grain boundaries impurity segregation also affects the sintering (and thus microstructure) of ceramicised materials, as discussed previously in section 2.1.1.9. The degree of sintering, as determined using surface area, porosity and density measurements also affects the relative contributions toward the total conductivity - highly porous materials generally have a higher grain boundary concentration, and thus a more significant grain boundary contribution to total conductivity than a less porous material. Grain boundary composition, (and therefore sintering properties and microstructure), are also dependent on the composition of the material as dopants and associated defects are able to modify diffusion processes in ceramic materials. All of the diffusion processes determining the aforementioned parameters are activated processes, and therefore also temperature dependent.

Finally, the conductivity of fluorite oxides is also dependent on the experimental atmosphere, particularly with regards the ambient oxygen partial pressure. As discussed previously in the solid/gas equilibrium (section 2.1.1.1), reduction of CeO_{2-x} results in the formation of oxygen vacancies as charge compensating defects and it can be calculated that $x \propto P_{\text{O}_2}^{1/6}$ for the formation of the V_{O}^{**} species as the sole charge compensating defect species. A more complex dependence on P_{O_2} will be the case for extrinsically doped ceria, therefore experimental work is generally carried out under constant oxygen partial pressure (a constant flow of dry air) in order to be able to effectively treat this variable as constant. Full

theoretical analysis of the effect of P_{O_2} and temperature on conductivity is beyond the scope of this work, but an excellent review can be found in the literature by Kilner and Steele (1981).³⁸ Studies have determined, however, that there is a dependence of the critical oxygen partial pressure - a measure of the reducibility of oxides, (and thus the electrolytic domain and resistance to reduction) on the ionic size of the dopant cation. This dependence is very similar to that of conductivity on the dopant ionic size, with Sm_2O_3 doping resulting in the greatest stability against reduction.³⁰

2.1.2.3 Conductivity of Fluorite Oxides - Literature Data

There is a large scatter in the conductivity and activation energies reported in the literature arising from different material purity, preparation techniques and measurement techniques.³⁰ There is also often a lack of characterisation data, such as microstructural and phase analysis with which to correlate conductivity data. The omnipresent complicating factor in the comparison of literature data is that of measurement temperature. The vacancy and dopant/vacancy associations as well as the relative magnitude of electronic and ionic conductivity contributions are all temperature dependent. Even in the case of the ionic contribution alone, the ratio between the bulk and grain boundary contributions are also temperature dependent. For these reasons, comparison between measurements made by different researchers, and in some cases even comparison between materials within a single study, can be subjective. It is therefore imperative that the reviewed data were generated in a systematic fashion, preferably within a single study, in the comparison of materials of varied composition. In this review of the literature, the few studies that have determined the effects of a systematic composition variation on conductivity have been reviewed, along with other more general conclusions made from the conductivity literature as a whole.

The ability of the fluorite lattice to accommodate large additions of alkaline earth and rare earth cations in solid solution allows the formation of uncommonly high concentrations of oxygen vacancies. This highly defective structure, coupled with

relatively high ionic mobilities result in high ionic conductivities ($\sim 10^{-2} - 10^{-1} \Omega^{-1} \text{ cm}^{-1}$), with negligible contributions from electronic conductivity pathways.^{61, 53}

The conductivity of doped fluorite structured oxides is typified by a peak in the conductivity vs. dopant concentration plot.^{53, 62} The peak conductivity generally coincides with a minimisation in the activation energy for anion transport.^{63, 59} However, the variation in dopant complex association energy with composition (and thus the variation in activation energy with composition), is often dissimilar to the variation in the pre-exponential term with composition for different dopants, i.e. no compensation effect is observed. As the total conductivity is dependent on both pre-exponential factor and activation energy, the maximum in the total conductivity and the minimum in activation energy often do not correspond exactly.³⁰ The concentration dependence of the pre-exponential factor in doped fluorite oxides has not been well understood as yet and may be determined by a concentration dependent entropic factor of the free energy of defect association.³⁰

The observed behaviour is discussed in the following sections in terms of two concentration ranges; the dilute range where conductivity rises with increasing dopant level up to the peak conductivity figure, and the concentrated range where the conductivity falls with increasing dopant level beyond that corresponding to the peak conductivity. The major difference between fluorite oxide materials with respect to their conductivity behaviour is their relative compositional stability with respect to oxidising and/or reducing environments.

2.1.2.3.1 Undoped CeO_2

As discussed previously, cerium dioxide (CeO_{2-x}) exhibits a wide range of nonstoichiometric compositions due to the ease of reduction of the Ce^{IV} cation to Ce^{III} . At low oxygen partial pressures (and high temperatures), the reduction produces an oxygen deficient n-type semiconductor.⁶¹ Measurements of conductivity variations with temperature and oxygen partial pressure, coupled with other characterisation data have shown that $V_{\text{O}}^{\bullet\bullet}$ is the dominant defect at low defect concentrations ($x < 10^{-3}$). At

higher defect concentrations V_O^* becomes dominant.¹³ Ionic conductivity in pure ceria is however so low as to be effectively negligible.⁵

2.1.2.3.2 Doped CeO_2

The substitutional addition of lower valent cations to the ceria lattice results in an increase in the concentration of oxygen vacancies to well above that of electronic defects and the material becomes a predominantly ionic conductor. A significant increase in the oxide ion transference number toward unity is observed, as well as an increase in the total conductivity by several orders of magnitude with doping, compared with undoped ceria.^{53, 64} Under high oxygen partial pressure conditions and at temperatures below approximately 1000°C , ceria is predominantly an ionic conductor for dopant levels greater than around 1 cation %.⁶¹ At significantly reduced oxygen partial pressures, a component of conductivity $\propto P_{\text{O}_2}^{-1/4}$ is always observed, indicating the onset of n-type electronic conductivity. The onset of the n-type electrical conductivity is observed to occur at successively higher oxygen partial pressures with successively higher temperatures,⁶⁵ as would be expected from the reductive mechanism mentioned previously in section 2.1.2.1. The n-type conductivity takes place by small polaron transport through a hopping mechanism in which electrons jump from a Ce^{III} to a neighbouring Ce^{IV} ion.⁵ Substitutional incorporation of higher valent cation dopants by the formation of $\text{CeO}_2/\text{Nb}_2\text{O}_5$ solid solutions results in increased n-type conductivity.⁶⁶ (The solid solution limit of Nb in the ceria lattice is approximately 1.6 cation %. Beyond this concentration a monoclinic structure attributable to a fergusonite phase (CeNbO_4) is present in X-ray patterns⁶⁷). The possible charge compensation mechanisms are reduction of host cerium cations or the formation of oxygen interstitials. The defect structure of ceria doped with penta- and hexavalent dopants to promote n-type conductivity has been modelled in greater detail by DeGuire et al, (1992).⁶⁸

A study by Yahiro et. al. (1989)⁶⁴ concluded that ionic conductivity is also dependent on the lanthanide dopant cation radius for samples of constant anion vacancy concentration. As variations in the oxide ion mobility are the only possible

explanation for this variation, the maximum conductivity was correlated to a minimisation in the binding energy between the dopant and host cations, further corresponding to proximity of the dopant cation radius to that of the Ce^{IV} ionic radius, i.e., conductivity is maximised by doping with cations that minimise the expansion or contraction of the lattice, (lattice strain effect).²⁹ It was also found in this study that the P_{O_2} range for ionic conductivity and the resistance to reduction also exhibited maxima corresponding to that observed with conductivity. The optimum ionic radius of the dopant cation, results in an intercationic void with a radius, r_{crit} , known as the critical radius. This void radius results in the maximisation of conductivity, (which gives the minimum association enthalpy between dopant ion and oxygen vacancy). The corresponding cation critical radius can thus be determined.³⁰ In the case of fluorite oxides, Kilner and Brook (1982),⁶⁹ developed a calculation for the determination of the critical radius. The lattice parameter is given by $a_0 = 4/\sqrt{3}(r_{\text{cation}} + r_{\text{anion}})$. The calculation assumes that the migrating anion passes between the two nearest neighbour cations through the centre of a line joining them, (length $a_0/2\sqrt{2}$). The critical radius can thus be determined;

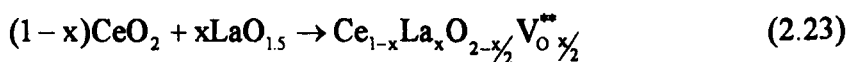
$$r_c = (a_0/2\sqrt{2}) - r_{\text{anion}} = (2/\sqrt{6})(r_{\text{cation}} + r_{\text{anion}}) - r_{\text{anion}} \quad (2.22)$$

In the case of doped ceria, several published studies^{70, 58, 64, 71} are in existence, several of which have been reviewed.^{30, 39} Doping with Sm^{3+} or Gd^{3+} (ionic radii 95.8Å and 93.8Å, respectively),⁷² was determined to give the highest conductivity for trivalent doping at 10 mole % (18.2 cation %), of the trivalent sesquioxide. Of the trivalent lanthanides, these cations have ionic radii most similar to that of Ce^{IV} . Atomistic simulation work and defect complex binding energy modelling studies by Butler et al (1983)⁷³ resulted in theoretical binding energies similar to those derived experimentally, predicting a minimum at a critical dopant cation radius. In the case of small dopants, the increase in binding energy with decreased dopant cation radius was explained in terms of relaxation of the dopant towards the oxygen vacancy increasing the stability of the dopant/vacancy complex. For larger dopants, there is an energy associated with the reduction in crystal strain when an oxygen vacancy is introduced

into a neighbouring site. These two opposing effects lead to a minimum in the plot of binding energy with lanthanide dopant radius at Gd^{III} for a ceria host.

The most recent study by Balazs and Glass (1995)⁵⁹ concluded however, that there is no real determinable trend in the variation in conductivity with dopant cation radius. This apparent contradiction of the conclusions of previous studies were explained in terms of grain boundary effects. The conductivity measurements were thus said to be dominated by microstructure which was in turn a measure of the effects of processing conditions, i.e., impurity concentration and sintering. This basic observation is crucial to the interpretation and significance allocated to literature data.

The best example of a systematic experimental study of lanthanum doped ceria in the literature for the isothermal variation in conductivity with composition is the study by Takahashi et al (1965).⁶² This work was further compared with data from other research and with data from other systems to produce a definitive review by Takahashi (1972).⁵³ In the study, the total conductivity of samples sintered at 1600°C were measured for compositions such that $x = 0, 0.05, 0.1, 0.2, 0.3, 0.5, 0.7$ and 1. The conductivity at each composition was measured from 400°C to 1200°C at 100°C intervals in order to determine the variation with temperature of conductivity with composition. The oxide ion transference numbers were determined by an electromotive force method⁵¹ with a cathodic P_{O_2} fixed at 1 atmosphere, and a cathodic P_{O_2} / anodic P_{O_2} ratio of 50. The system studied was represented as in this study by the reaction product of the solid solution formation reaction;



At all temperatures, the total conductivity variation with composition plots were observed to rise sharply to a peak with addition of lanthanum dopant. This proportionality of conductivity to vacancy concentration in the dilute solid solution range is predicted (providing mobility is independent of concentration), and has been demonstrated for other analogous doped fluorite systems.⁵ The composition at the peak is observed to shift steadily from approximately $x = 0.13$ at a measurement temperature of 400°C, to $x = 0.17$ at 600°C, which are typical reaction temperatures

for the CO and CH₄ catalytic oxidation reactions, respectively, in the present study. Similar maxima in the conductivity variation with composition plot have been found for Y₂O₃ doped ceria between approximately $x = 0.1$ (Wang et al, (1981) measured at 550°C)⁶³ and $x = 0.15$ (Adham and Hammou (1983) measured between 500°C and 600°C).⁷⁴ The composition corresponding to the maximum in conductivity is also known to be dependent on the type of dopant.³⁰

The magnitude of the increase in the total conductivity with lanthanum dopant addition between $x = 0$ and the peak conductivity is observed to decrease with temperature. At 400°C the increase is more than two orders of magnitude, whereas at 1200°C the increase is less than one order of magnitude. This effect can be attributed to the increase in the concentration of intrinsic anion vacancies with temperature as $\text{CeO}_2 \xrightarrow{\text{heat}} \text{CeO}_{2-x}$. This is supported by a relative five orders of magnitude increase in the conductivity of ceria between 400°C and 1200°C, compared with less than three orders of magnitude increase for lanthana. Beyond the peak conductivity composition, further increases in lanthanum content result in a decrease in the total measured conductivity. This is explained by the ordering of the vacancies beyond the critical concentration denoted by the peak conductivity. The introduction of more dopant ions results in a concomitant increase in the vacancy concentration and resulting increase in vacancy association. The resulting loss of disorder in the theoretical distribution of oxide ion vacancies effectively reduces the mobility of the free vacancies and thus ionic conductivity. This agrees with the theoretical discussion in this section and the discussion of defect interaction theories, earlier in this chapter.

The oxide ion transference number was determined for samples where $x = 0.2$, 0.3, 0.4 and 0.5, all at 600°C, 800°C and 1000°C. At all temperatures the isothermal transference number was observed to increase with lanthanum content, and to decrease with temperature for each given composition. The increase in transference number with lanthanum content can be explained in terms of ionic conduction increasing with vacancy concentration. Beyond the critical vacancy concentration where vacancy association results in a decrease in conductivity with further increases in the vacancy population, the transference number was not observed to decrease as would be expected. This is likely due to stabilisation of the Ce^{IV} oxidation state by the addition

of lanthanum to the fluorite ceria lattice. The decrease in oxide ion transference number with temperature is due to an increase in the magnitude of electronic conductivity with temperature, as thermally activated intrinsic defects are created. This effect is enhanced by a reduction in P_{O_2} as it has previously been shown that

$$\sigma_{n\text{-type}} \propto P_{O_2}^{-1/4}$$

A further, (and probably the original) study of the variation in conductivity with dopant level should be mentioned in this review. The effect of lanthanum doping of ceria on conductivity and on CO oxidation catalyst activity was studied by Rienäcker and Wu (1962).³³ There are however factors associated with this original work which make comparisons with later work difficult. For example the solid solution limit as determined in the study is approximately half of the maximum estimated in other studies, undoubtedly due to the mixed oxide preparation. The main deficiency of the study, as stated by the author was the lack of surface composition data with which to correlate results. The conductivity measurements were made using the 2-probe dc. method which was generally considered to be unsuitable by later researchers. With addition of lanthanum, the peak conductivity was determined to occur for approximately 15 to 18 cation % lanthanum, which is in excellent agreement with those of Takahashi (1965).⁶² The dopant level corresponding to the peak conductivity was not observed to vary significantly with measurement temperature over the experimental range (87°C - 292°C), which considering the relatively small temperature range is unremarkable. The activation energy of the conductive process was found to vary with composition in the range 20 - 30 kcal mole⁻¹ (83.7 - 125.6 kJ mol⁻¹) which is also similar to other reported values.^{11, 59}

Perhaps the most interesting feature of this study is in the correlation between the pre-exponential factor and measured activation energy for conductivity, as determined by the Arrhenius method. When a plot of log pre-exponential factor vs. activation energy is examined, there is a simultaneous decrease in both terms up to a lanthanum content of approximately 15 cation % lanthanum. For dopant levels beyond this level, there is a simultaneous increase in both terms up to a dopant concentration of approximately 33 cation % lanthanum. All of the points between 0 and 33 cation % lanthanum lie on a line, which for catalytic measurements would be described in terms

of a compensation effect plot. The compensation effect phenomenon is discussed in the catalysis section of this chapter (section 2.2), and in the results chapter (section 4.5). From the X-ray data it can also be determined that 0 - 33 cation % lanthanum is the single phase solid solution range. Beyond 33 cation % lanthanum there is a discontinuity in the plot up to a lanthanum content of approximately 90 cation %. Between this level and pure lanthanum, a plot of activation energy vs. specific pre-exponential factor fall on a line parallel to the first line, all points in this region also being determined as single phase with the lanthanum (HCP) structure. The main conclusion to be drawn from these observations are that conductivity behaviour variations (and therefore mechanisms), are consistent within both single phase regions of the ceria/lanthana system. Both single phase regions exhibit similar compensation behaviour, showing parallel plots, bridged by points from two-phase intermediate compositions. This observation is of particular interest as the two solid solution regions in the ceria/lanthana system have quite different structures, and one would expect, dissimilar conductivity behaviour.

It should be noted that for the conductivity variations in the HCP (lanthana) structured solid solution region. The addition of cerium to lanthana results in an isolated minimum in the conductivity with composition plot at approximately 10 cation % Ce, which is potentially of interest as it is effectively the composition with the minimum conductivity for the whole system. However, close inspection of the data reveals that this conclusion would be based on a single data point, and therefore further experimental studies would be desirable to further investigate this point.

2.1.3 Surface Composition and Enrichment

The surface composition of ceramic materials, and the composition of internal surfaces known as grain boundaries can often differ significantly from that of the bulk material. The behaviour of the surfaces and interfaces of ceramic materials has a profound influence over many properties, and thus, the applications of such materials. It is therefore necessary to characterise the interface layer as well as the bulk phase of ceramic materials in order to evaluate and explain the properties and performance of

such materials in real scientific terms. The difference between surface and bulk properties are caused mainly by segregation and adsorption, resulting in the formation of composition gradients within the interface region. These gradients and resulting electric fields strongly influence local properties including reactivity (due to changes in ionic transport properties),⁷⁵⁻⁷⁶ and the structure of the interface, which may exhibit significant differences to that of the bulk. Such interfacial structural re-ordering occurs when the concentration of a segregated species exceeds the local solution limit, resulting in the formation of bi-dimensional interface structures.⁷⁷ The implications of the tendency for the compositions of interfaces to be different to the bulk are numerous and encompass many fields of application, including heterogeneous catalysis, materials and engineering. In the field of heterogeneous catalysis, the catalytic reactivity and selectivity is determined by the surface properties of a material. The surface properties are in turn determined by the material preparation and activation processes used.⁷⁸ As well as segregation from the bulk material, processing temperature and interactions between the material and gas phase in all stages of preparation can exert a profound influence over the composition and phase of the near surface layer of oxide materials.⁷⁹ Other solid state properties are also determined by surface segregation properties of ceramic materials, such as corrosion,⁸⁰ (where the interfacial properties of the surface oxide layer determine the resistance to corrosion of the metal beneath), sintering,^{81, 82} adhesion,⁸³ fracture,⁸⁴ and tribological behaviour.⁸⁵

The driving force for segregation is the reduction of surface free energy as a consequence of the changed composition. Segregation phenomena have been extensively studied and recently reviewed over oxide systems.^{86, 87} Segregation processes have been shown to have many parallels with adsorption processes and can be termed as adsorption from the solid phase. Segregation is thus governed by analogous laws as those which apply to adsorption from the gas phase.⁸⁸ The similarity between both adsorption and segregation has led to several relationships developed for adsorption processes being applied to segregation in solids. However, although this type of theoretical approach has been shown to apply to alloy systems,⁸⁹ in the case of ionic solid systems the application of such theoretical models has been limited due to their complex nature.^{82, 86, 88}

In the present study, the application of a known model for surface segregation in binary alloys, the McLean regular solution model,⁹⁰ (based on the Langmuir adsorption isotherm), to the simple binary oxide solid solution system, $\text{Ce}_{1-x}\text{La}_x\text{O}_{2-x/2}$ was investigated. The application of other surface segregation models was also tested in order to determine how best to best describe the surface segregation phenomena in an oxide solid solution system. As discussed previously, lanthanum doped ceria forms solid solutions with the ceria fluorite structure over a wide range of compositions, therefore making it well suited to application the McLean model.⁴² Modifications of the McLean model have been previously attempted by Lea and Seah, (1977)⁹¹ where the constant value of the surface enrichment factor was replaced by a surface concentration dependent variable, and by Rowlands and Woodruff⁹² who further developed the model by including terms to account for the physical driving forces for segregation such as the diffusion coefficients and the heat of segregation.

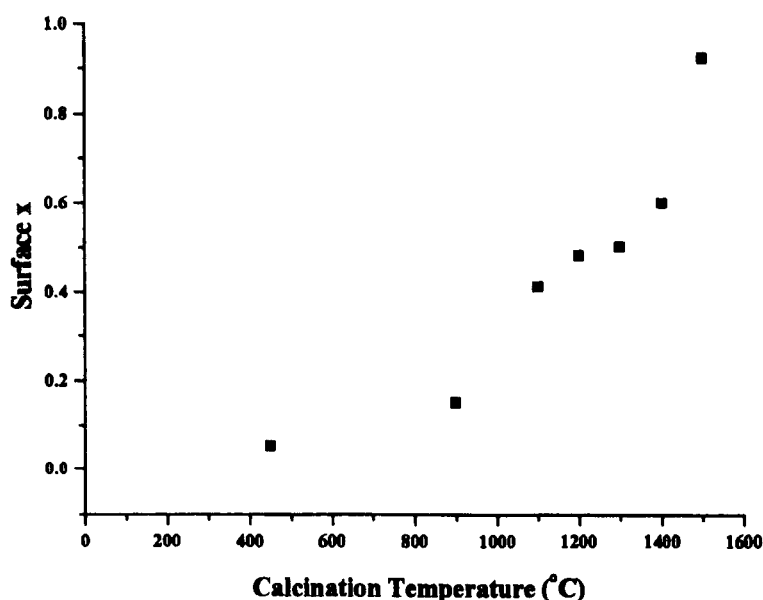
The variation in oxide ion conductivity of ceria based solid solutions has been discussed earlier in this chapter in terms of bulk conductivity. Grain boundary conductivity has been studied specifically by several researchers^{31, 49, 50, 93} and it has been demonstrated that the surface segregation of dopants has a great influence on grain boundary conductivity, which in turn has implications for the applications of such materials. Such applications include electrochemical sensors for medical, industrial and automotive use,⁹⁴ solid oxide fuel cell technology,^{71, 95 - 96} and possibly in the production of catalysts where (oxygen) ionic transport is determined to be associated with the rate limiting step.

The phenomenon of surface segregation of lanthanide dopants in ceria based materials has been reported previously,^{97 - 98} however the semi-quantitative nature of the reported work did not lend itself well to detailed modelling of the segregation process and thus, was not interpreted in this way. It was concluded in the latter reference that the mechanism of segregation of lanthanum in ceria was dependent on preparation method; in coprecipitated materials segregation is via macrodefects in the lattice, whilst in sol-gel materials the mechanism is one of bulk diffusion. Derived activation energies from Arrhenius type plots of \ln (surface cation ratio) vs. reciprocal temperature (ΔH_{seg}) were reported as falling in the range 6 - 11 kcal mol⁻¹ (25 - 45 kJ

mol^{-1}). However, it was also noted that these were probably not thermodynamic equilibrium values and that the activation energies should be interpreted as an indication of the activation energy involved in the transport mechanism. Clearly, the ability to model the surface composition, and therefore the surface properties of these materials would provide an invaluable tool for the design and manufacture of new materials, allowing them to be tailored for optimum performance within targeted applications.

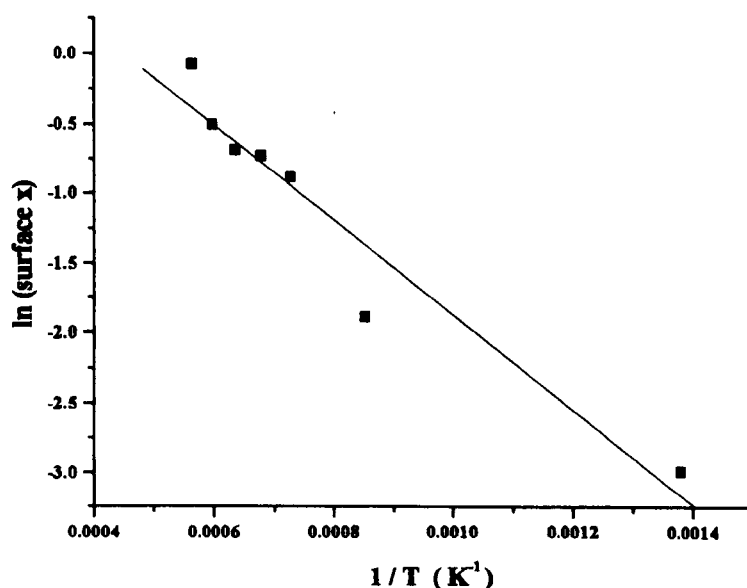
A further study was reported in a US Patent by Mackrodt, W. C., (1991).⁹⁹ In this work, the variation in surface lanthanum content with 4 hour isochronous calcinations at temperatures between 900°C and 1500°C for a fixed 5 cation % lanthanum bulk composition material was determined. Experiments were performed at 100°C intervals and the surface composition was determined by XPS. At all temperatures the surface was significantly enriched with lanthanum, the level of enrichment increasing with temperature. This data is presented graphically in figure 2.8 below. The precursor material calcined at 400°C was found to have a surface composition identical to that of the bulk.

Figure 2.8 The variation in surface lanthanum content with calcination temperature for bulk $x = 0.05$ material calcined for 8 hours at 1200°C using data derived from Mackrodt Patent.⁹⁹



The temperature coefficient of the segregation process was not determined in the patent, but using the experimental data presented and the Arrhenius method, this was determined to be 6.7 kcal mol⁻¹ (28.1 kJ mol⁻¹), which is in excellent agreement with the value reported by Harrison (1993)⁹⁸ as mentioned previously. The Arrhenius plot from which this value is derived is shown in figure 2.9 below.

Figure 2.9 Arrhenius plot using surface segregation of lanthanum from ceria data. Data derived from the Mackrodt patent.⁹⁹



As can be seen in the above plot, the fit of the data to a linear plot is not perfect (measured r^2 of 0.965). Observations from the plot are that over the full temperature range a linear fit is reasonable, indicating that the segregation mechanism is invariant with temperature. The magnitude of the temperature coefficient being comparable with cation diffusion processes. At higher temperatures, the gradient of the Arrhenius plot does appear to increase suggesting that there is a change in the cation diffusion mechanism at temperatures above 1400°C, but further data points in the high temperature region would be necessary to resolve this point. A possible explanation at higher temperatures for the change in the cation diffusion mechanism could be due to the loss of oxygen by the ceria lattice at high temperatures and the subsequent incorporation of anion vacancies into the lattice, resulting in the creation of alternative cation diffusion pathways. Several experiments were also carried out to investigate the

simultaneous surface segregation of two dopant cations, with lanthanum and praseodymium. From the limited number of experiments, the segregated surface ratio of the two dopants was found to be roughly proportional to the bulk ratio.

In the present study, samples were analysed by XPS to determine the Ce/La surface ratios. The theoretical and experimental details of this study can be found in Appendix 3.5 and the experimental chapter (section 3.4), respectively.

General concepts for the interpretation of segregation phenomenon have previously been reviewed for alloy systems¹⁰⁰ and for oxide systems.⁸⁶⁻⁸⁷ In summary, both processes of adsorption and segregation were historically first described using the Gibbs approach which involves the relationship between the surface excess number and the surface tension.¹⁰¹ This approach predicts that the surface will be enriched in the lattice component that results in a decrease in surface tension. The main shortcoming of this approach to describing segregation processes is the assumption that the solute surface excess concentration is independent of the bulk concentration of the solute. The next major advance in segregation theory was made by McLean,⁹⁰ who applied a regular solution model to grain boundary segregation in alloys. A regular solution was defined as a solution in which the only entropy contribution to the free energy of mixing is the ideal entropy of random mixing. Unlike an ideal solution, a regular solution is assumed to have a finite, non-zero enthalpy of mixing. Despite the simplicity of this model it has been successful in predicting a wide variety of properties in simple solid solutions. The simplest form of the model applies to a two component substitutional solid solution which is assumed to consist of a segregated surface monolayer in equilibrium with a semi-infinite bulk of uniform composition. This can be expressed as:

$$\frac{X_s^2}{X_s^1} = \frac{X_b^2}{X_b^1} \exp \left(\frac{-\Delta G_{\text{seg}}}{RT} \right) \quad (2.24)$$

Where X_s^2 and X_s^1 are segregating solute and solvent species respectively, at the surface, and X_b^2 and X_b^1 are segregating solute and solvent species respectively in the bulk, ΔG_{seg} is the free energy of segregation, K is the Boltzmann constant and T is Kelvin temperature.

The form of the model equation is very similar to the Langmuir Gas Adsorption Isotherm.¹⁰² As with the Langmuir Isotherm, there are a number of implicit assumptions, which are:

1. All surface sites are identical and differ in free energy from the bulk.
2. ΔH_{seg} remains constant with increasing surface coverage, i.e., interaction between segregant species will produce deviation from the model behaviour.
3. The segregating species is distributed randomly, both at the surface and in the bulk, i.e., there is no clustering or ordering.
4. The model applies only to a two component system.

Despite the invalidity of these approximations in most real systems, the McLean model does provide a useful analytical tool for the interpretation of segregation phenomena.

2.1.3.1 Surface Segregation Modelling

Application of a model based on the McLean equation forces the assumption that the exponential term in the equation remains constant for all bulk compositions. This is analogous to the assumption that all surface sites are identical, as in the Langmuir isotherm. As in adsorption studies the assumption of energetic equivalence is unrealistic for real systems. Non-Langmuir segregation behaviour has been previously reported in the literature by Sayle et al,¹⁰³ for atomistic simulation studies of platinum and palladium segregation in ceria. Their studies confirmed that the segregation energies were coverage dependent, and the deviation from Langmuir behaviour was explained in terms of an increase in defect - defect interactions as the impurity concentration was increased. The model used in their study was based on the Mackrodt and Tasker (1989)¹⁰⁴ coverage dependent segregation isotherm which is also adopted in the present study and is discussed at length in the results chapter, (section 4.2 and subsections therein). It was also noted that the formation of different structured solid solutions or different phases as the impurity concentration was varied

was a possible complication in the simulation studies. Further atomistic simulation studies of the segregation of isovalent impurities in MgO and CaO by P. W. Tasker et al (1985),¹⁰⁵ noted again that the McLean (Langmuir) model, although of use in systems where ΔG_{seg} remained relatively constant with surface coverage, was generally not applicable to real systems. Their calculated free energies of segregation as a function of fractional coverage were found to have a highly non-linear dependence. These phenomena were explained in terms of surface reconstruction and the formation of overlayers. Furthermore, it was suggested that the energy of reconstruction could be an appreciable fraction of the total segregation energy.

The free energy of surface segregation of a dopant has been correlated with its atomic fraction in the mixed oxide in an expression derived by Wynblatt and Ku (1977)¹⁰⁶ from an essentially bond model approach but wherein bond quantities have been replaced by empirical parameters such as surface energies and heat of mixing. Whereas the overall treatment is less preferred than an alternative based on an electrostatic (atomistic) model, it enables factorisation of the major contributions to the free energy of surface segregation. This model is also adopted by and adapted to the present study, as an alternative to compare with the Mackrodt and Tasker model¹⁰⁴ and in order to attempt to factorise the contributions to the driving force for the segregation process. The derivation and application of a model applicable to the present study from the Wynblatt and Ku bond model can be found in the results chapter, (section 4.2 and subsections therein).

2.2 Catalysis

The principles of oxidative catalysis on solid oxides has been reviewed by Sokolovskii (1990)¹⁰⁷ and Satterfield (1991)¹⁰⁸ The characterisation of oxide catalysts is generally more complicated than, for example, supported metal catalysts. This is due to several factors mainly related to structure and composition, which can combine to make elucidation of active sites and reaction mechanisms difficult. Several different catalytic reaction mechanisms are known to exist over different catalysts, and for different reactions. Most catalytic oxidation reactions can, however, be interpreted in

terms of a redox mechanism.¹⁰⁸ This mechanism, (also known as the Mars and van Krevelen mechanism) assumes a two step reaction in which the reactant is first oxidised by oxygen from the catalyst, resulting in a reduction of the catalyst surface. Following desorption of the reaction product, the reduced catalyst is subsequently re-oxidised by gas phase oxygen. The rates of both steps are identical under steady state reaction conditions. This type of reaction mechanism generally results in a zero-order dependence on the to-be oxidised reactant partial pressure, and a positive order dependence on oxygen partial pressure. This general rule applies to systems where the rate determining step is the re-oxidation of the catalyst. However, in cases where the activation energy for the re-oxidation step is high, and under high temperature operating conditions the reaction can become zero-order on oxygen and positive order on the to-be-oxidised reactant. The concept of redox mechanisms can also be applied to systems in which the cation exhibits variable oxidation states, as in such materials the reaction would result in no structural changes in the catalyst.

In the redox mechanism, the oxygen species involved is not specified, but is generally assumed to be lattice O^{2-} as the behaviour of chemisorbed species is often better represented by other models, such as the Langmuir-Hinshelwood, Rideal-Eley or other mechanisms.¹⁰⁹ The oxygen species involved, and indeed the source of the reacting oxygen may also vary with experimental conditions and temperature. Dependence on P_{O_2} and temperature particularly influences the anionic mobility, especially within fluorite oxides, (as discussed previously in section 2.1.2 and subsections therein). This in turn influences the rate of transport, formation and activation of the oxygen species involved in the reaction, and consequently also influences the kinetics and selectivity of the reaction. The extent of reduction of the oxide catalyst has also been frequently shown to correlate with catalytic activity, more reduced samples generally being more active.¹⁰⁸

The applications of oxidative catalysis encompass total oxidation of toxic materials as a solution to ecological problems, exemplified by the three-way automotive catalysts,^{110 - 111} and selective or partial oxidation of materials as a vital synthetic method for the production of many important feedstock chemicals. Over the years, a plethora of literature has been accumulated from which certain principles of

heterogeneous oxidative catalysis have been developed. These include the adsorption and activation of oxygen species, of the species to be oxidised, the formation of surface reaction intermediate species, the possible mechanisms of oxidation reactions, and the influence of catalyst properties and experimental conditions. In this section, a review of such principles and prior art is presented with particular relevance to the ceria/lanthana system.

There are several interesting features of ceria and ceria-based solid solutions which have attracted much attention in recent years, particularly in the field of heterogeneous catalysis, as reviewed recently by Trovarelli, (1996).²³ The utilisation of ceria as a key component in three-way catalysts for the treatment of automotive exhaust emissions¹¹⁰⁻¹¹¹ is the most economically and technologically important application, and as such, has driven much research in this area, as well as applications as a catalyst for other oxidation reactions.¹¹²⁻¹¹⁴ However, despite its obvious importance, a more detailed mechanistic understanding (at the atomic level) on how cerium affects catalytic processes is still a matter of considerable debate. There are however certain key facts which have been established, including the activity of the redox couple $\text{Ce}^{\text{IV}} \leftrightarrow \text{Ce}^{\text{III}}$ (and thus the high oxidising power of the Ce^{IV} cation), and the formation of surface and bulk vacancies which can be rationalised with respect to their influence on catalysis. The main other area of study regarding ceria and ceria based solid solutions has been based on ionic conductivity properties of such materials and the use of ion and mixed conducting oxides as catalysts has been reviewed in great detail by Gellings and Bouwmeester (1992).¹¹⁵

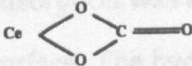
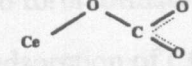
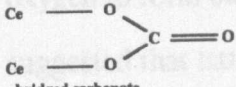
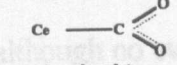
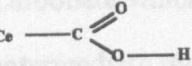
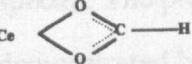
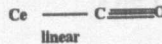
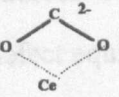
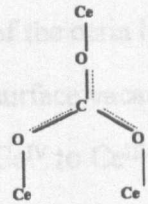
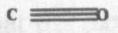
2.2.1 Interactions with Carbon Monoxide

The interaction of ceria with carbon monoxide has been reviewed by Trovarelli (1996).²³ The adsorption of CO on the surface of ceria is accompanied by reduction of surface oxygen and the formation of surface oxygen vacancies. Reduction of ceria by CO occurs readily - at lower temperatures than reduction by hydrogen, but is very sensitive to the morphology of the sample. As CO does not diffuse into the bulk, reduction occurs by a chemical-pump mechanism involving the diffusion of oxygen

toward the surface followed by subsequent elimination by the formation of oxygen vacancies. Davydov (1984)¹¹⁶ provides an excellent general review of IR studies of CO adsorption on metal oxides, including the formation of carbonate and carboxylate surface complexes. However, in this section only the literature specific to the ceria/lanthana system will be discussed from hereon.

The first significant infrared study of the adsorption of CO on ceria was published by Li et al (1989)¹¹⁷ in which the adsorption of CO and CO₂ was investigated with respect to surface species formed. The adsorption of CO was found to result in the formation of several surface carbonate species, as well as linearly adsorbed CO. The adsorption experiments were completed on both hydroxylated and dehydroxylated ceria surfaces, the presence of surface hydroxyl groups determined by characteristic IR absorption bands at 3664, 3629 and 3427 cm⁻¹. Desorption experiments following the CO and CO₂ adsorption experiments were also completed in order to determine the relative thermal stability of the adsorbed species and to provide further evidence for band assignation. The thermal stability of the surface carbonate species was determined to vary such that; Bridged Carbonate < Bidentate Carbonate < Inorganic Carboxylate < Unidentate Carbonate. The bridged carbonate species was formed by CO₂ adsorption, but not by CO adsorption. The adsorption of CO with P_{CO} was found to obey a Langmuir type relationship. The IR absorption bands were attributed to surface species, which along with data from other studies are summarised in figure 2.11. Results of the same adsorption experiments over hydroxylated ceria did not form the same strongly absorbing species as CO adsorption over the dehydroxylated ceria, suggesting that the surface hydroxyl groups hinder the CO from forming adsorbed species, especially at temperatures below 200°C. The formation of formate species by reaction between surface hydroxyl and adsorbed CO species was demonstrated over the hydroxylated ceria. No linearly adsorbed CO was observed over the hydroxylated ceria leading to the conclusion that the CO is linearly adsorbed at dehydroxylated cation sites.

Figure 2.11 A Summary of IR Absorptions for Adsorbed CO species on CeO_2 .

Species	Frequency (wavenumbers) (Trovarelli 1996 Ref. 23)	Frequency (wavenumbers) (Bozon-Verduraz 1994 Ref 118)
 bidentate carbonate	854 (856), 1028 (1011) 1286, 1562 (1586) 1460 - 1480 1360 - 1380 1070, 850	830-860, 1030, 1250-1310 1580-1610
 unidentate carbonate	854 (856), 1062 (1045) 1348 (1354), 1454 1420 - 1480 1350 - 1400 880, 1060	850, 1070 1360-1380 1460-1480
 bridged carbonate	(1600), (1325), (1040) (1132), (1219), (1396), (1728) 1700 - 1750, 1180	1180 1700-1750
 inorganic carboxylate	(1481), (1420) 1310 (weak), 1510 (1506) 1560 - 1580 1350 - 1400	1350-1400 1560-1580
 acid carboxylate	1628	
 formate	771, 1329, 1369, 1558, 1587 2852, 2944	1307, 1369, 1558, 1576, 2848, 2939
 linear	2156, 2177 2150, 2165	
 carbonite	1266, 1071, 773 1317, 1150	
 bulk polydentate	880, 1060, 1350-1400 1420-1480	880 1060 1350-1400 1420-1480
 Gas Phase	2143	

Out-gassing at temperatures in excess of 800°C was found to be necessary to produce a surface completely clear of all hydrocarbons in a later study by Bozon-Verduraz et al (1994).¹¹⁸ In this study, adsorption of CO on partially reduced ceria was found to result in the formation of carbonite and formate species. Carbonite species were observed to be converted to carbonate on heating such that overall, either two CO species disproportionate to C and CO_2 (Boudouard-type reaction), or carbonates are formed by the sub-surface ceria (effectively forming bulk carbonate).

The formation of carbonate and carboxylate species demonstrated that ceria can be partially reduced by CO, even at room temperature. The extent of CO adsorption was also found to be dependent on the degree of dehydroxylation of the surface. The hydroxyl groups were shown to react with adsorbed CO that did adsorb to form formate species, similarly to as reported by Li et al.¹¹⁷ A mechanism for the adsorption of CO on dehydroxylated cations and subsequent reaction with capping oxygen to form bidentate carbonate was proposed. At higher temperatures it was suggested that lattice oxygen could migrate to the surface to compensate for the reduction of the surface by CO and form bulk carbonate and carboxylate species, although no evidence for this specifically was presented in the study. The bidentate carbonate which is the first to be formed on CO adsorption was proposed to be an intermediate, which is converted into unidentate carbonate and inorganic carboxylate species. The presence of carbonate species even on degassed ceria surfaces was further demonstrated by a temperature programmed reduction study by Zotin et al (1993).²⁴

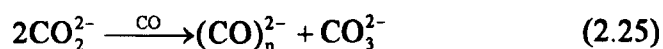
The role of oxygen vacancies on ceria surfaces in the oxidation of CO has been addressed by Sayle et al (1994)¹¹⁹ using computer simulation techniques. In this study, defect equilibria and energies were compared in the bulk and at various crystalline surfaces. The oxidation of CO by oxygen originating from ceria (effectively reduction of the ceria by CO), was examined and it was assumed to involve the creation of surface vacancies - effectively a reduction of the lattice accompanied by reduction of Ce^{IV} to Ce^{III} as charge compensation. It was determined that the formation of vacancies at the surfaces was thermodynamically more favourable than in the bulk, and that the oxygen vacancy formation energy (and therefore ease of reduction), differs from surface to surface. It was concluded that processing conditions which favour the formation of surfaces which are more easily reduced, result in materials with enhanced activity towards redox oxidation of CO. This also emphasises the relevance of conductivity measurements, particularly pertaining to material surfaces, the ease of reduction and re-oxidation theoretically being proportional to the oxide anion conductivity.

The adsorption of CO on partially reduced ceria was investigated by Arai et al (1993)¹²⁰ The amount of strongly adsorbed CO was found to increase with the degree

of reduction. XPS was used to determine that the concentration of Ce^{III} increased with the degree of reduction, but that the concentration of Ce^{III} was invariant with CO adsorption. This result should however be interpreted within the context of possible surface reduction by under the UHV conditions required for XPS analysis, resulting in an overall reduction in the average surface cationic oxidation state. The amount of CO adsorbed was found to be directly proportional to the concentration of Ce^{III} . The implications of this are that reduced ceria provides the strong adsorption sites for CO, but adsorption does not cleave the C-O bond, which would result in oxidation of the reduced cation.

The higher adsorption strength of CO on Ce^{III} than on Ce^{IV} was also reported in an IR study of CO adsorption on ceria by Bozon-Verduraz et al (1994).¹¹⁸ The distribution of the carbonate species formed by CO adsorption was found to be dependent on the pre-treatment history of the material. For example the bidentate carbonate and inorganic carboxylate species are preferentially formed on samples previously reduced by hydrogen. Mention was also made of the characteristic absorption bands of adsorbed oxygen species including the superoxide species (O_2^-) where $\nu(\text{O-O}) = 1126 \text{ cm}^{-1}$, and the peroxide species (O_2^{2-}) where $\nu(\text{O-O}) = 883 \text{ cm}^{-1}$.

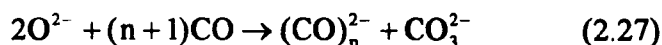
The formation of the carbonite (CO_2^-) species by CO adsorption on ceria and lanthana has been investigated by Binet et al (1994).¹²¹ The presence of dioxygen was found to remove the characteristic IR absorption bands from *in situ* spectra, therefore the presence of such species stable under the oxygen excess conditions of the present study is very unlikely. However, the presence of such species as reaction intermediates is a possibility. The fate of the carbonite species on oxygen addition is the formation of carbonate species. Two possible mechanisms for the formation of carbonate from carbonite species were proposed. The first mechanism involves oxidation by a surface oxygen species, which would be accompanied by the reduction of a cation in the oxide material. Alternatively, the disproportionation of two carbonite species could occur;



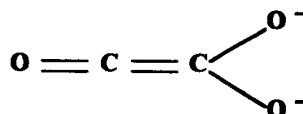
This mechanism is supported by the carbonite \rightarrow carbonate reaction occurring over irreducible oxides, but is not proven. An alternative (Boudouard reaction type) disproportionation could occur involving carbon deposition. Evidence for CO disproportionation by such a mechanism was reported by Li et al (1991).¹²² CO₂ was found to be produced by the reaction of CO over partially reduced ceria. The disproportionation reaction scheme was reported as;



The formation of carbonite species on lanthana has also been reported by Bailes et al (1996).¹²³ On more basic oxides (e.g. lanthana), CO coupling to form C₂O₃²⁻ and larger anions consisting of several CO units was reported. This reaction was represented as a disproportionation over a low coordinate surface oxide ion.



The formation of bulk lanthanum oxycarbonate (La₂O₂CO₃) was reported to be facile due to the hexagonal structure of lanthana, the decomposition of the oxycarbonate being then effected only at temperatures greater than 500°C. The adsorption of CO₂ on the surface of lanthana results in the formation of carbonate by reaction with surface O²⁻ ions. (IR absorptions at 850, 1060, 1390 and 1500 cm⁻¹). By contrast, adsorption of CO on the same surface resulted in the formation of carbonite species. (IR absorptions at 987 and 1390 cm⁻¹). As with carbonite species on ceria, oxygen sensitivity precludes the presence of stable carbonite species on the lanthana rich materials under the reaction conditions used in the present study. It was concluded in Bailes's study that the dimeric anion C₂O₃²⁻ formed by the coupling of adsorbed CO was stable in the presence of dioxygen. The dimer was expected to have a ketenic structure as shown in figure 2.10. Bands observed at 2075 and 1367 cm⁻¹ were assigned to the ketenic dimer.

Figure 2.10 Ketenic structure of $\text{C}_2\text{O}_3^{2-}$ 

UV studies by Zecchina and Stone (1978)¹²⁴ investigated CO adsorption on alkaline earth oxides. The conclusions of this work were that adsorbed CO formed anionic CO clusters of dimeric and polymeric proportions. The mechanism for the formation of the anionic clusters proposed was an earlier version of that proposed by Bailes (1996)¹²³. In this mechanism, the carbonate formed by the oxidation of the carbonite species or the polymeric species and subsequent thermal decomposition of such species can be reduced to the $2\text{CO} \rightarrow \text{C} + \text{CO}_2$ reaction. The basicity of the oxide material determines the reactivity toward CO.

2.2.2 Interaction with oxygen

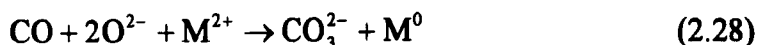
For the characterisation of oxygen species on oxide surfaces, there are two definitive reviews. In Che and Tench (1982)¹²⁵ the mononuclear species are reviewed, and in Che and Tench (1983)¹²⁶ molecular species are addressed. The general nature of both of these references provides an excellent background to surface oxygen species which is beyond complete review in this thesis. The following review is focused on oxygen species on the surfaces of the ceria/lanthana system specifically.

Correlations between rates of catalytic oxidation and oxygen binding energy have generally established that the weaker the oxygen binding with the catalyst surface, the more efficient is complete oxidation with a given catalyst.¹⁰⁷ The most reactive oxygen species are atomic or molecular radical ions, however their role in catalysis is unclear.¹⁰⁷ It is generally thought that following activation of a surface oxygen species, such species may be incorporated into the lattice and thus be strongly bound to the catalyst surface. Such species are often participant in the formation of selective oxidation products. As shown previously in the solid/gas equilibrium review (section 2.1.1.1), interaction between oxygen and the catalyst is a dynamic process, with

competitive rates between the activation of surface oxygen species and either reaction, or incorporation into the lattice. The relative rates of these processes under given conditions therefore determine the catalytic properties of the material.

Complete oxidation catalysts must provide a high rate of primary activation (binding) of oxygen. Under conditions of oxygen excess in the reactant mixture, the rate of the primary activation of oxygen is generally much higher than the rate of its incorporation into the lattice. The reaction rate under such conditions will depend primarily on the rate constant of the interaction of the to-be-oxidised species (and therefore its rate of activation), with the active oxygen species.

The adsorption of oxygen onto oxides has been reviewed by Spivey (1987)¹²⁷ Oxygen adsorption occurs more readily on p-type oxides because electrons are easily removed from the cations to form active species such as O^- , whereas on n-type oxides, oxygen adsorbs on pre-reduced surfaces effectively re-oxidising the surface. These examples were illustrated with two different mechanisms for the oxidation of CO, one over each type of material. Over p-type oxides (e.g., NiO), O^- forms from O_2 adsorption, which then reacts with adsorbed CO to form CO_2 . The variable valence cation is first oxidised by donating an electron to form O^- and then reduced back to the original oxidation state on reaction between the adsorbed CO and the O^- . On n-type oxides (e.g., ZnO), the mechanism for the oxidation of CO involved reaction with lattice O^{2-} . The mechanism can be represented;



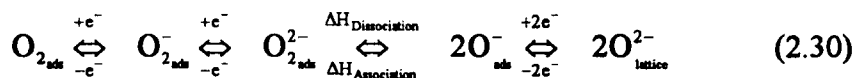
Then



The different mechanisms, and particularly the source of oxygen for the oxidation reactions results in vast differences in the activity for the same reaction over n-type and p-type materials. It is interesting to note the formation of an adsorbed carbonate intermediate in the n-type oxide mechanism, as observed as stable species in the case of the ceria/lanthana system in the present study, (discussed previously in section 2.1.1). The formation of a carbonate intermediate may also be interpreted in

terms of the more conventional redox cycle, involving the alternate reduction and re-oxidation of the oxide.

Characterisation of the oxygen species adsorbed on ceria has determined the formation of O_2^- (superoxide) species (IR absorbtion at 1126 cm^{-1}), and O_2^{2-} (peroxide) species (IR absorbtion at 883 or 853 cm^{-1}).²³ Both of these species are intermediates in the dissociative adsorption mechanism of incorporation of gas phase oxygen into the reduced ceria lattice;



The higher the state of reduction of the ceria surface, the more the equilibrium favours peroxide formation.

The superoxide species, (O_2^-), forms from the adsorption of an oxygen molecule on a single unsaturated surface Ce^{III} ion to give $(Ce^{4+} - O_2^-)$.¹²⁸ Superoxide species on the surface of heat-treated ceria were studied by Zhang and Klabunde (1992)¹²⁹ who determined that at least three different forms of adsorbed O_2^- existed, corresponding to different adsorption sites. It was determined that end-on bonded superoxide species were specifically involved in the process of incorporation of oxygen from the gas phase into the lattice. The rate of formation of superoxide species from gas phase oxygen was determined as first order with P_{O_2} , but further reduction to lattice oxygen was dependent on the availability of electrons and a suitable reaction pathway to fill oxide ion vacancies. Interaction between O_2^- and CO was also investigated, although the results were inconclusive.

A further FTIR study of adsorbed dioxygen on ceria reported by Li et al (1989)¹³⁰ confirmed that O_2^- was formed on coordinatively unsaturated cerium. Characteristic IR bands were reported for O_2^- at 1126 and 2112 cm^{-1} . The reduction of the superoxide species to the peroxide species was determined to be faster than the dissociation of the peroxide species into $2O^-$, which was suggested to be the rate determining step for the incorporation of oxygen into the lattice. Further investigation by Li et al (1990)¹³¹ in a follow-up study investigating oxygen exchange over ceria using FTIR concluded that exchange between lattice and gas phase oxygen, and

peroxide and gas phase oxygen, was far slower than exchange between gas phase oxygen and superoxide species.

In addition to the superoxide on ceria following dioxygen adsorption, as reported by Li et al (1989),¹³⁰ an additional band attributed to the peroxide species (O_2^{2-}) was also reported at 883 cm^{-1} . The concentration of peroxide species was found to increase proportionally with the degree of reduction of the ceria surface. From this it was deduced that the formation of peroxide species was associated with reduced cerium cation sites. The formation of peroxide species, (O_2^{2-}) increasing with further reduction of the ceria surface was also associated with a pair of reduced cerium ions or a single oxygen vacancy by Liu and Flytzani-Stephanopoulos (1995).¹²⁸

As regards the relative reactivity of the various surface oxygen species, O^{2-} ions are known to be less reactive than O^- ions¹²⁶ with respect to the catalytic oxidation of CO and methane. It was suggested by Che and Tench (1982)¹²⁵ that there could well be little distinction however, between O^- and O^{2-} under catalyst operating conditions.

The stability of the O^- species was reported to be very low and under CO oxidation reaction conditions is therefore expected to be a reactive transient species. The presence of bulk O^{2-} is unquestionable, but the existence of such species in low coordinate sites at surfaces, although likely, is difficult to prove. Both CO and CO_2 react with O^- to form CO_2^- and CO_3^- , respectively. Alkanes react with O^- readily, and more slowly with O^{2-} . Both species are capable of activation of hydrocarbons by hydrogen abstraction. There are three possible ways in which oxygen can be involved in oxidation reactions; activation of a hydrocarbon by abstraction of a hydrogen, direct nucleophilic attack on an adsorbed hydrocarbon by a negatively charged oxygen ion, and in replenishing lattice oxygen to a reduced catalyst in a Mars-van Krevelen redox mechanism type reaction.

The dioxygen species are generally either superoxide or peroxide. The superoxide species is also able to activate hydrocarbons, similarly to O^- and O^{2-} , although evidence for activation by peroxide is thin. The peroxide species is, as mentioned previously, an important intermediate in the incorporation of gas phase oxygen into the lattice, as would be required during a steady state catalytic reaction

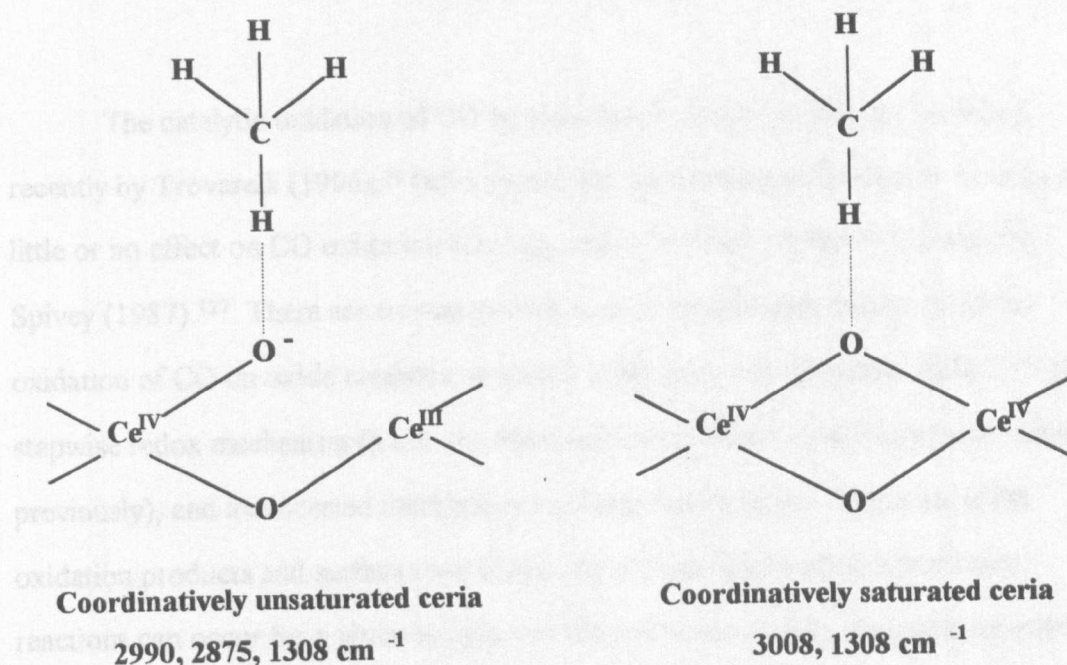
with the Mars-van Krevelen redox mechanism. This would be favoured at higher temperatures where the anionic mobility within doped ceria is significant.

2.2.3 Interaction with Methane

The subject of the catalytic interaction between oxides and hydrocarbons has been studied extensively over the last 10 to 15 years due to the importance of catalytic oxidation reactions in automotive and industrial emission control, and was reviewed by Trovarelli (1996).²³ Methane activation was said to occur by several possible mechanisms including interaction with coordinatively unsaturated sites, interaction with lattice oxygen, interaction with various activated oxygen surface species (including V_O^{\bullet}), and by an surface acid-base dissociative adsorption mechanism. This range of suggested mechanisms is undoubtedly due to the variety of preparative methods and experimental conditions used, which clearly have great bearing on the methane activation mechanism. In this section, the literature regarding the activation of methane is reviewed, paying close attention to the experimental conditions used in each study, and the kinetic characteristics of each mechanism. Other data, such as the characterisation and identification of intermediate species is also presented, with a view to formulation of a reaction mechanism under the experimental conditions of the present study.

A recent infrared study by Li and Xin (1992)¹³² determined that there are two distinct adsorption sites for methane on outgassed ceria as shown in figure 2.12. The adsorption bond strength in the case of the coordinatively unsaturated surface may be enough to activate the methane under relatively mild reaction conditions. Other possible mechanisms suggested for the activation of methane include activation over acid-base pairs, such as low coordination surface crystalline defects. The activation of the methane is generally by hydrogen abstraction, (dissociative adsorption) to give either ionic or radical species. Coadsorbed CO was found to have no effect on the IR spectrum of adsorbed methane, lending further support to the interaction of methane with surface anions exclusively.

Figure 2.12 Methane adsorption on the two sites on the ceria surface, as proposed by Li and Xin (1992)¹³²



It should be noted that the adsorption experiments were carried out at 0°C or less and the IR absorptions were observed to disappear at higher temperatures, demonstrating their thermal instability due to weak adsorption. It was concluded that the hydrogen abstraction from methane is via either of the two adsorbed intermediates, which are formed by adsorption of methane on surface lattice oxygen and coordinatively unsaturated oxygen. The lifetime of such intermediates under reaction conditions was stated to be so short as to render them undetectable.

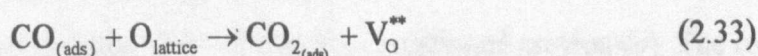
Further studies by Ito et al (1989)¹³³ investigated the adsorption and oxidation of methane over an irreducible oxide, MgO. The findings of this study were also that coordinatively unsaturated MgO surface species were important in chemisorption and catalysis, being able to dissociate CH_4 into CH_3^- and H^+ . It was concluded that the methyl anion thus produced is easily oxidised by O_2 into one of two methoxide ion (OCH_3^-) species, one of which is significantly more stable than the other. O_2 is reduced to O_2^- . Both of the OCH_3^- species are then either decomposed to hydrogen and CO, or further oxidised by the action of O_2^- to yield OCH_2^- and bidentate CO_3^{2-} species, however these species thermally decomposed between 77°C and 277°C .

2.2.4 Carbon Monoxide Catalytic Oxidation



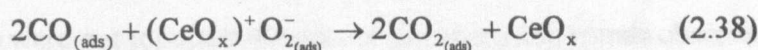
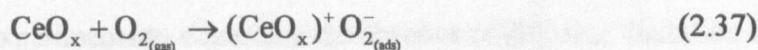
The catalytic oxidation of CO by ceria based materials has been reviewed recently by Trovarelli (1996),²³ (who stated that the addition of lanthanum to ceria had little or no effect on CO oxidation activity), and by a wider variety of materials by Spivey (1987).¹²⁷ There are two commonly known mechanisms for the catalytic oxidation of CO on oxide catalysts, as stated in the review by Davydov (1984);¹¹⁶ the stepwise redox mechanism (a.k.a. the Mars and van Krevelen mechanism as mentioned previously), and a concerted mechanism involving simultaneous formation of the oxidation products and surface re-oxidation by oxygen. Generally both of these reactions can occur for a given system, but the redox mechanism is usually prevalent at high reaction temperatures. The dissociative adsorption of oxygen to give several active surface oxygen species occurs readily at low temperatures (generally below the reaction temperature), thus resulting in a zero-order dependence on P_{O_2} . The various forms of surface oxygen species are able to react and form surface complexes with CO, such as carbonate and carboxylate species, which are subsequently thermally decomposed at the reaction temperatures to yield the oxidation reaction products.

The redox reaction mechanism relies on the alternative oxidation and reduction of the ceria surface and involves the formation of V_O^{**} species which are re-oxidised by molecular oxygen from the gas phase:²³



The concerted mechanism involves adsorption and reaction of CO with the catalyst itself to form similar carbonate or carboxylate compounds as in the redox

mechanism. Effectively, adsorbed CO can react with an activated surface oxide species (e.g., superoxide):²³



At the lower temperatures where this mechanism is prevalent, the rate determining step is subsequent decomposition of the surface complex species under the action of molecular oxygen. The transition between the two mechanisms with increasing temperature is due mainly to the increased rate of thermal decomposition of the carbonate species, which at higher reaction temperatures are of a transient intermediate nature. This point is further supported by the correlation between CO oxidation activity and the stability of adsorbed CO surface complex species.¹³⁴

The original systematic study of lanthanum doped ceria catalysts for the oxidation of CO was published by Rienäcker and Wu (1962)³³ who determined that lattice oxygen from the ceria could be involved in the catalytic oxidation mechanism. The aim of the study was to determine the relationship between composition, conductivity, CO catalytic oxidation activity, structure, and particularly to determine whether there was a link between the oxide anion mobility of the oxide catalysts and the catalytic activity. There are several significant differences between the work of Rienäcker and this present study. The materials used by Rienäcker exhibited a limited solid solution range (a solid solution limit of approximately 35 cation % compared with 68 cation % as reported by Inaba et al, (1996),³⁰ as mentioned previously). The reason for the limited solubility was undoubtedly a result of the material processing. The major deficiency of the Rienäcker study however, was a lack of surface composition data. Consequently, all variations in characterised trends were reported with respect to bulk compositional variations. (In the present study, materials made by a coprecipitation method resulted in a solid solution limit in the 55 - 60 cation % La in

ceria range. Samples were also characterised in terms of surface composition using XPS).

In the Rienäcker study, the CO oxidation activity was measured in terms of temperature required to yield 10 %, 20 % and 31.6 % conversions from a 3 % CO / 97 % air feed mixture. Experiments to determine the absence of diffusion limitation of the catalytic reaction rate were not reported. Results of this study and trends observed are therefore described in this context.

Light-off temperatures were observed to increase in an almost linear fashion with the lanthanum dopant concentration. This type of light-off analysis however does not take account of surface area differences between samples. From the measured surface areas, there is a factor of 5.5 difference between the highest surface area ($22.5 \text{ m}^2\text{g}^{-1}$ for 10 cation % La) and the lowest surface area ($4.1 \text{ m}^2\text{g}^{-1}$ for 99.75 cation % La). The observed high activity drop with small additions of lanthanum up to 10 cation % is accompanied by a large surface area stabilisation effect, (effectively doubling the surface area between pure ceria and 10 cation % lanthanum doped ceria), which makes the already rapid decrease in activity with lanthanum addition even more significant when expressed in specific rate terms.

There are two observed maxima in the plot of the variation in activation energy with lanthanum concentration, separated by a broad minimum (falling to $11.6 \text{ kcal mol}^{-1}$ (48.6 kJ mol^{-1}) at 57 cation % lanthanum). The first maximum (of approximately 20 kcal mol^{-1} (83.7 kJ mol^{-1})) occurring at between 10 and 18 cation % lanthanum, the second (also approximately 20 kcal mol^{-1} (83.7 kJ mol^{-1})) between 95 and 97.5 cation % lanthanum. The similarity in the shape of this plot and that of the corresponding electrical resistance variation with composition is striking, although the minimum in the conductivity plot occurs between 18 and 33 cation % lanthanum.

A plot of the variation in pre-exponential factor with activation energy terms as determined for CO catalytic oxidation over the full series of materials was also observed to exhibit striking similarities with the analogous plot of the conductivity factors. For both parameters, two parallel compensation-type plots are obtained corresponding to the single- and two-phase regions in the ceria/lanthana system. In the case of the catalytic measurements however, the bridging points marking the transition

between the two regimes occur at between 10 and 18 cation % lanthanum, which is a significantly lower dopant concentration than the analogous region (18 - 33 cation % lanthanum), for the conductivity measurements.

Two possible mechanisms were proposed by Rienäcker, the first involving the formation and reaction of ionic adsorbed CO^+ and O^- species to form CO_2 , the second involving the formation and reaction of the same species, but stepwise such that two O^- anions react with one CO^+ cation to form a CO_3^- anion, which then reacts further with another CO^+ cation to yield 2CO_2 . In both cases, adsorption and electron abstraction from the CO and dissociative adsorption of oxygen were said to be rate determining steps, the significance of each to the overall rate being dependent on the variation in the vacancy structure of the materials with composition. However, in the absence of further characterisation data, (particularly catalytic reaction kinetic data and surface composition data), better interpretation was deemed impossible in that study.

A similar study was published in 1972 by Breysse et al¹³⁵ which sought to answer some of the questions left unanswered by the Rienäcker study.³³ The Breysse study concentrated on elucidation of the mechanism for the catalytic oxidation of CO by undoped ceria, and particularly the correlation between catalytic activity and electrical conductivity. In this study, the adsorption of CO was found to be accompanied by a reduction of the ceria, the CO being oxidised simultaneously to CO_2 . The dissociative adsorption of oxygen on the reduced ceria, effectively re-oxidising the material was found to be rapid. The proposed mechanism therefore involved the alternating reduction and oxidation of the ceria surface. The experimental work in the Breysse study was quite original as the apparatus used allowed the simultaneous measurement of catalytic activity and conductivity (2-probe dc.), under the experimental conditions. The rate response to linear gas velocity variations were determined in this experiment in order to ensure measurements were made in the absence of diffusion limitations of rate. The method used in this study to ensure adequate linear gas velocity to avoid limitation of reaction rate by diffusion effects was also used in the present study.

The reaction order with respect to oxygen was found to be zero, and a partial order of 0.84 ± 0.06 was determined for CO partial pressure variations. The activation

energy was determined to be $20 \pm 1 \text{ kcal mol}^{-1}$ ($83.7 \pm 4.2 \text{ kJ mol}^{-1}$), which was comparable to the activation energy determined in the same study for conductivity of $25 \pm 1 \text{ kcal mol}^{-1}$ ($104.7 \pm 4.2 \text{ kJ mol}^{-1}$). The conductivity was found to increase with P_{CO} , such that a plot of $\log 1/\text{resistance}$ vs. $\log P_{\text{CO}}$ was a straight line of slope 0.4 ± 0.03 , whereas almost the opposite effect was found for variations in P_{O_2} , such that an analogous plot resulted in a straight line of slope -0.5 ± 0.03 . The rate was found to be retarded by small amounts of CO_2 added to the reaction mixture, but further increases in the CO_2 level were found to have negligible effect. The decrease in the activity for CO oxidation with the addition of lanthanum to ceria as determined by Rienäcker (1962)³³ and the proposed mechanism for CO oxidation over ceria as determined by Breysse (1972)¹³⁵ were linked by Castiglioni et al (1992).¹³⁶ The strong oxidising properties attributed to ceria were cited as being a result of the ease of the cerium cation redox process. The formation of ceria/lanthana solid solutions was therefore interpreted as effectively moderating the oxidising character by reducing the concentration of variable valence cerium cations in the surface of the material, due to displacement by lanthanum cations. A use dependent deactivation of ceria/lanthana CO oxidation catalysts was explained in terms of the formation of carbonate species, observed using FTIR spectroscopy.

The most recent work investigating the use of lanthanum doped ceria based materials in CO oxidation catalysis, generally use such materials as promoted supports for dispersed metal catalysts. In many of these studies, the effect of the dopant on ceria is of secondary importance to the aims of the studies which are generally to determine the catalytic activity of the metal dispersion. Perhaps the best (and most recent), example of such a study is the excellent work published in two parts by Liu and Flytzani-Stephanopoulos (1995),^{112, 128} in which the total oxidation of both CO and CH_4 was investigated over fluorite oxide supported dispersed transition metal oxide catalysts. In a previous study, Liu and Flytzani-Stephanopoulos (1994)¹³⁷ had determined that for the catalytic reduction of sulphur dioxide by CO, activity was enhanced by the addition of rare earth dopants to ceria. (Similarly to CO oxidation, this reaction is also thought to proceed via a redox mechanism involving surface oxygen/vacancy participation). In the later study,^{112, 128} the activity of rare earth doped

ceria catalysts for CO oxidation did not show any correlation with the calculated bulk oxygen vacancy concentration or the oxygen mobility (determined from analysis of literature dopant/vacancy association energies^{58, 73}).

In the Liu and Flytzani-Stephanopoulos (1995) study,^{112, 128} the lanthanum dopant concentration added to $\text{Cu}_{0.15}\text{Ce}_{0.85}\text{O}_x$ was varied between 0 and 10 cation %. The results of these experiments were inconclusive, with large variations in the low doped catalyst activities which was attributed to variability in the catalyst preparation. The study did conclude however that the addition of 10 cation % lanthanum resulted in a decrease in CO catalytic oxidation activity, which was attributed to excessive enrichment of the surface with lanthanum. (XPS measurements determined a surface content of 18 cation % lanthanum for the 10 cation % bulk lanthanum material).

The kinetic measurements made by Liu and Flytzani-Stephanopoulos (1995) were made over Cu/ceria catalysts which contained approx. 3 cation % lanthanum. The reaction order with respect to oxygen partial pressure was found to be close to zero - in good agreement with the Breyse study (1972).¹³⁵ The order of reaction with respect to CO partial pressure was found to decrease from one to zero with increasing P_{CO} . The order of 0.84 ± 0.06 also reported by Breyse (1972)¹³⁵ clearly falls into this range. The experimental data were represented by Liu and Flytzani-Stephanopoulos by the equations;

$$R_{\text{CO}} = \frac{k_{\text{CO}} K_{\text{CO}} P_{\text{O}}^n}{1 + K_{\text{CO}} P_{\text{CO}}} \quad \text{where } k_{\text{CO}} = A \exp^{(-E_a/RT)} \text{ and } K_{\text{CO}} = K \exp^{(Q/RT)} \quad (2.31)$$

k_{CO} is the reaction rate constant, K_{CO} is the CO adsorption equilibrium constant.

Application of the above equations to the experimental data resulted in n approximating to zero, E_a was in the range 17.4 - 22.5 kcal mol⁻¹ (73 - 94 kJ mol⁻¹), and Q was in the range of 6.7 - 14.6 kcal mol⁻¹ (28 - 61 kJ mol⁻¹).

The oxidation of CO was said to proceed by a Langmuir-Hinshelwood mechanism, the active site for CO adsorption being a Cu^+ species stabilised by incorporation into the ceria lattice.¹³⁸ The presence of Cu^+ at the surface was confirmed by XPS analysis. The enhanced catalytic activity was attributed to a concerted enhancement of both CO adsorption and oxygen activation. The active

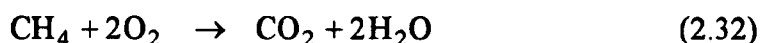
oxygen species was said to be the superoxide species O_2^- which is discussed further in the following section.

For many oxidation catalysts the formation of carbonate and/or carboxylate surface species has been determined with the use of *in situ* IR studies.¹⁰⁷ Such species are often found to be stable under inert or vacuum conditions, but are readily decomposed to CO_2 in the presence of oxygen. At higher temperatures, the presence of oxygen is not required for the carbonate decomposition to occur. The rates of carbonate decomposition and of CO oxidation measured under identical conditions have been demonstrated to be almost identical,¹⁰⁷ confirming the participation of such surface species as intermediates in the catalytic reaction. The mechanism of carbonate decomposition is thought to be by reduction of the oxide surface, followed by surface re-oxidation by oxygen from the gas phase, (or at lower temperatures, preceded by the oxidation of reduced cations which were produced by the formation of the carbonate). At a given temperature, the total rate of reaction will be determined by either the rate of decomposition in the presence of oxygen (low temperature mechanism), the rate of thermal (spontaneous) decomposition (high temperature mechanism), or by a combination of both, (intermediate temperatures).

Although attempts to correlate the CO oxidation catalytic activity with conductivity by both Rienäcker (1962)³³ and Breysse (1972)¹³⁵ were both inconclusive, further evidence relating CO oxidation activity and oxide ion conductivity was reported in a study by Chan et al (1994)¹³⁹ who investigated CO oxidation over a series of perovskite mixed oxides. For CO oxidation by a stoichiometric gas mix with oxygen, at low temperatures catalytic activity was determined to be a function of the lattice oxygen mobility. The oxidation reaction rate order on oxygen partial pressure for the perovskite materials was found to be < 1 , and was found to decrease with increasing reaction temperature. This was explained such that at low temperature the contribution to the rate by a gas phase oxygen mechanism is higher than the contribution from a lattice oxygen mechanism. As reported by Liu and Flytzani-Stephanopoulos (1995),^{112, 128} the Langmuir-Hinshelwood model was used. The reduction in oxidation reaction rate order on P_{O_2} with temperature was explained in terms of thermal activation of oxide ion mobility in the lattice, allowing exchanges

between surface and lattice oxygen species to become significant. In cases where the rate order was found to be independent of temperature, the participation of mobile lattice and/or surface lattice oxygen was deemed likely. The order with respect to CO was found to be positive in all cases, and the oxidation reaction was found to proceed in the absence of gas phase oxygen, confirming the participation of lattice oxygen.

2.2.5 Methane Catalytic Oxidation



The oxidation of hydrocarbons over oxide catalysts involves a successive fragmentation of the hydrocarbon chain, up to the formation of surface formate species. The oxidation reaction then proceeds by oxidative decomposition, similarly to the decomposition of surface carbonate intermediates in the case of CO oxidation.¹⁰⁷ At low temperatures the decomposition rate is increased by the presence of molecular oxygen, whilst at higher temperatures the decomposition is spontaneous. In both cases the decomposition is accompanied by the formation of carbon dioxide and water products. At any given temperature, the total rate of reaction will be determined by either the rate of decomposition in the presence of oxygen (low temperature mechanism), the rate of thermal (spontaneous) decomposition (high temperature mechanism), or by a combination of both, (intermediate temperatures). Historically, the first studies regarding the use of lanthanide oxides as hydrocarbon oxidation catalysts were focused on comparisons of the activity of the individual oxides, such as the study using butane oxidation as the test reaction by Hattori et al (1976)¹⁴⁰. In this study general trends in activity were determined under reducing conditions (approximately 75% of O₂ feed required for stoichiometric reaction), and correlated with other physical properties. Activity variations, in this case were found to correlate well with the conductivity variations across the series and with the variation in the fourth ionisation potential - this was interpreted as oxidation of the cation from the 3+ to the 4+ oxidation state being rate limiting. Under the net reducing conditions cerium,

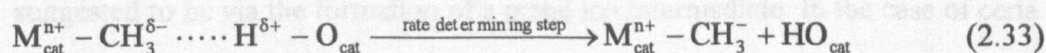
praseodymium and terbium were most active due to the relatively easy oxidation from the 3+ to the 4+ oxidation state, in comparison with the other lanthanide oxides.

Later studies were more focused on supported noble and transition metal catalysts, primarily investigating the effects of lanthanide oxides as promoters. Much of this work stemmed from the development of the three-way automotive exhaust emissions catalyst, and on other clean (low temperature) burn technologies to reduce pollutant emissions.¹²⁷ In this section, such studies will be reviewed with specific regard to literature with direct relevance to the present study which focuses on the total oxidation of methane.

The addition of lanthanum to ceria results in an increase in selectivity of the oxidation reaction toward methane dimerisation products.¹³⁶ This can be explained similarly to the reduction in CO oxidation activity as discussed previously - the cerium cation redox process favour the formation of total oxidation products. The addition of lanthanum, which is a poor radical scavenger (thought to be the activated form of methane following hydrogen abstraction) compared with cerium cations, results in an increase in dimerisation products due to an increase in the number of $\bullet\text{CH}_3$ radical species into the gas phase.

Carbonation of the surface of ceria based materials was not found to be as significant for CH_4 oxidation as for CO oxidation, due mainly to the higher reaction temperatures resulting in spontaneous thermal decomposition of carbonate species.¹³⁶

In the study by Liu and Flytzani-Stephanopoulos (1995)^{112, 128} the catalytic CH_4 oxidation light-off temperature was reduced, (and therefore activity was increased), with successive 1 and 4.5 cation % lanthanum dopant additions. Further lanthanum addition to 10 cation % resulted in a decrease in the catalytic activity, similar to that reported for CO oxidation. The role of the dopant was proposed such that CH_4 activation (by hydrogen abstraction) would be promoted over more basic oxides. The basic site onto which the hydrogen is abstracted is generally thought to be a surface oxygen species, the negatively charged residual being stabilised by an acid (metal) site;



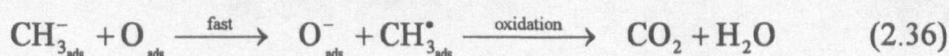
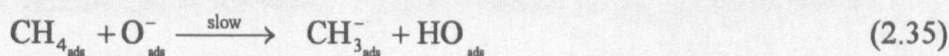
The methyl intermediate species were found to be easily oxidised and became radical species by loss of an electron back to the catalyst. The strength and geometry of the acidic and basic sites are therefore crucial for CH₄ activation accounting for both the increase, and maximum in activity with increasing basicity (on lanthanum addition).

The kinetic measurements made by Liu and Flytzani-Stephanopoulos (1995)^{112, 128} were made over copper/ceria catalysts which contained 3 cation % lanthanum. The reaction kinetics were found to be similar to the CO oxidation kinetics, discussed earlier. The experimental data were found to be best represented by the equations;

$$R_m = \frac{k_{CH_4} K_{CH_4} P_{CH_4} P_{O_2}^{0.18 \pm 0.04}}{1 + K_{CH_4} P_{CH_4}} \quad (2.34)$$

The values of E_a and Q (see equation 2.31 in section 2.2.4), as determined by the Arrhenius method were -0.00934 and -14.2 respectively.

With regards the mechanism of methane oxidation over the 15 cation % Cu : 85 cation % Ce (trace lanthanum) material, a Langmuir-type adsorption dependence on P_{CH_4} was cited as evidence that the rate determining step involves adsorbed methane. The dependence of the reaction rate on P_{O_2} was observed to obey a power law dependence, leading to the conclusion that complex oxygen sources exist for the reaction. The mechanism for methane oxidation was thus proposed as;



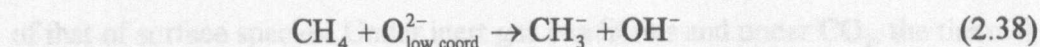
The rate determining step was determined to be the abstraction of a hydrogen from the adsorbed methane by a basic superoxide species. The resulting negative charge on the methyl group formed is then quickly transferred to an uncharged adsorbed oxygen. The mechanism of this charge transfer during the formation of the methyl radical was suggested to be via the formation of a metal ion intermediate. In the case of ceria catalysts, this would be facilitated by the ease of the Ce^{III} - Ce^{IV} redox;



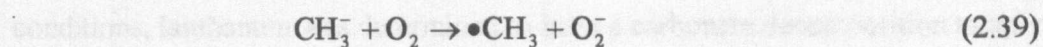
Other mechanisms reported in the literature describe the direct reaction of gaseous methane with the catalyst surface, but at the low temperatures used in the Liu and Flytzani-Stephanopoulos study, this was thought to be unlikely and that the formation of an adsorbed methyl intermediate was said to be more probable.

Although the rate expressions for CO and methane oxidation were determined to be similar, the large difference in pre-exponential factors suggested fundamental differences in the respective mechanisms. It was concluded that the methane oxidation mechanism was more complex than that of CO oxidation and that the adsorption sites for CO and methane were different.

Catalysts and reaction mechanisms for the oxidative coupling of methane were reviewed by Maitra (1993).¹⁴¹ In this review, in addition to the O^- active site mechanism as discussed previously in this section, (as reported by Liu and Flytzani-Stephanopoulos (1995)),^{112, 128} a further mechanism was discussed involving O^{2-} with a low coordination number as the active site. In this case the abstraction of a hydrogen from CH_4 occurs effectively as an acid-base reaction which can be represented¹⁴¹;



Methyl radicals can be formed by a further reaction of the carbanion with O_2 ;



The catalytic production of methyl radicals from CH_4 was studied by Campbell et al (1988)¹⁴² (following an earlier study by the same group Lin et al (1986)¹⁴³), using a matrix isolation electron spin resonance technique. Lanthana was determined to have a far higher activity for methyl radical formation than ceria and it was concluded that the ability of the cerium cation to exhibit multiple oxidation states was not important in the activation of methane. Basicity was said to influence the formation of surface oxygen species such as O_2^- and O_2^{2-} , which are in turn capable of activating methane.

This acid-base mechanism results in the activation of methane via heterolytic cleavage.^{141, 144} As a consequence, if this is the reaction mechanism, then there should exist a correlation between catalytic activity and catalyst basicity.

Generally, basicity increases with increased coordinative unsaturation of surface metal-oxygen ionic species and is dependent on the cation species present.¹⁴¹ The population of low coordinated sites in turn is dependent on surface morphology and thus, surface composition. As well as CH₄ adsorption, CO, CO₂ and O₂ are also adsorbed on strongly basic low coordinate oxide sites leading to retardation of the CH₄ activation process. Retardation due to poisoning by CO₂ particularly has been demonstrated in several studies, and has been attributed to the formation of carbonate species, which has previously been discussed in this chapter with respect to CO interaction with the present study catalysts.

Basicity measurements of oxide surfaces are possible by a variety of different methods, including XPS methods to determine oxygen binding energy, carbonate decomposition temperature measurements (TGA), and acidic gas (CO₂) adsorption/desorption (TPD) measurements. The general assumption with the two latter (and more common) techniques is that the carbonate decomposition temperature is proportional to the basicity of the material, and that bulk behaviour is representative of that of surface species. Under inert gas conditions and under CO₂, the thermal decomposition temperature for lanthanide carbonates was determined by Maitra (1990).¹⁴⁵ The decomposition temperature was found to be greatly increased in the presence of CO₂, as would be expected by Le Chatellier's principle. Under the inert gas conditions, lanthanum was determined to have a carbonate decomposition temperature of approximately 700°C, much higher than the analogous value for cerium carbonate (approximately 500°C) - a difference of 225°C. Under the CO₂ gas conditions, the temperature difference was even greater - a difference of approximately 370°C. The basicity of lanthanum cations was therefore concluded to be far higher than that of cerium cations - in fact lanthana was determined to be the most basic of the lanthanide oxides.

The acid and base strength distribution of ceria and lanthana were further investigated by NH₃ and CO₂ temperature programmed desorption experiments in a

study by Choudhary and Rane (1991).¹⁴⁶ In this study, the determination of the desorbed CO_2 was by a stepped temperature method, each step over a range of 100°C , and by a secondary adsorption gravimetric analysis technique. This method is relatively inadequate for the determination of the energy distribution of adsorption sites, but is adequate as a tool to determine the broad differences in the basic sites. Lanthanum was observed to desorb far more CO_2 than ceria, and generally at higher temperatures, indicating the presence of more and stronger basic sites on lanthanum than ceria. This result agrees with those of Maitra (1990).¹⁴⁵

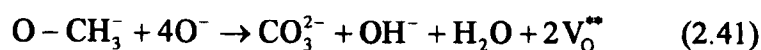
A later study by Maitra et al (1992)¹⁴⁷ further investigated the influence of basicity on the catalytic activity for the oxidative coupling of CH_4 . The formation of acidic CO_2 was found to retard the catalytic reaction rate as the CO_2 reacts with the basic sites on the surface. CO_2 retardation effects were found to be more pronounced over more basic materials. Lanthana was confirmed as the most basic of the lanthanide oxide cations, the predilection of cerium, praseodymium and terbium to higher oxidation states being cited as the reason for suppression of basicity in these materials under oxidising conditions.

The most recent mechanistic study of CH_4 and O_2 activation for the OCM reaction over lanthana was reported by Lacombe et al (1995).¹⁴⁸ Isotope exchange experiments determined an exchange between CH_4 and CD_4 which increased with temperature. The exchange products were CH_3D and CHD_3 indicating reversible methane activation with a low degree of equilibration. CO_2 was found to significantly reduce the equilibration, supporting the previous argument by Maitra et al (1992)¹⁴⁷ that CO_2 poisons the active (basic) sites for methane activation. The CH_4 activation mechanism was determined to be reversible following the isotopic exchanges observed, and thus reaction with activated oxygen was determined to be the irreversible step in the CH_4 activation mechanism.

Further oxygen isotopic exchange experiments by Lacombe et al (1995).¹⁴⁸ determined that gaseous O_2 adsorbed dissociatively was recombined statistically before desorption. Isotopic mixing of all the oxygen atoms of the oxide was determined to be fast enough throughout the bulk for isotopic equilibrium between the gas and the solid phase to be achieved. Pre-adsorption of CO_2 resulted in a decrease in the mean

residence time of the oxygen on the catalyst, an effect which was attributed to carbonate formation. The conclusions from these experiments were that the activation of oxygen occurred on the same basic sites as CH_4 activation, via a dissociative adsorption process. Several possibilities for the activation mechanism and for the active species itself, including O^- , O_2^- and O^{2-} were discussed, but no firm conclusions were made due to the likely equilibrium between such species.

The total oxidation of CH_4 was investigated by Lacombe et al (1994)¹⁴⁹ which concluded that associated low coordination lattice oxygen atoms and oxygen vacancies were the active sites for the total oxidation of methyl radicals through a series of successive steps involving O^- . It was determined that oxycarbonate species could exist under OCM conditions. The main conclusion of this IR study was that during the OCM reaction, methoxide ions were formed as intermediate species over lanthana of the form $\text{La} - \text{O} - \text{CH}_3$. Several carbonate species were formed as temperature was increased up to around 700°C , beyond this temperature thermal decomposition of the carbonate species occurs. Under reaction conditions, the catalyst surface was determined to remain free of stable adsorbed carbonate or hydroxyl groups, showing that any carbonate or such species formed are of a transient nature, acting as intermediates in fast catalytic cycles. The activation of methane and the subsequent formation of methoxide ion intermediate species was suggested to occur on specific paired sites such as $\text{O}^{2-} - \text{V}_\text{O}^{\bullet\bullet}$, possibly formed by the dehydroxylation of specific coordinatively unsaturated terminal La-OH groups. A mechanism for the oxidation reaction was subsequently suggested where gaseous methyl radicals could react with coordinatively unsaturated surface oxygen, resulting in the formation of $\text{O} - \text{CH}_3^-$ methoxide ions. Subsequently, the methoxide ion would be oxidised by a series of reactions leading to the formation of carbonate groups;



The active sites for methane activation were thus determined to be oxygen species O^- or the dimer O_2^{2-} . A further kinetic study by Otsuka et al (1987)¹⁵⁰ also concluded that the active oxygen species responsible for the activation of methane in oxidative coupling were diatomic; O_2 , O_2^- or O_2^{2-} .

The best example of a systematic study of the effect of lanthanum (and other lanthanide) dopants on the catalytic oxidation of CH_4 properties of ceria in the open literature, is a US patent by Mackrodt, W. C., (1991).⁹⁹ In this study, materials were prepared by the addition of 2M NH_4HCO_3 solution to a 1M aqueous solution of mixed metal nitrates of the desired composition. Following calcination at 1200°C for 8 hours, the catalytic activity for CH_4 oxidation by air was determined as the rate of formation of CO_2 per gram of catalyst at 600°C (a temperature at which the conversion was relatively low so that the catalyst bed approximated to isothermal conditions). The incorporation of Pr, Tb, Nd, Sc, Yb, Gd, Sm and La were tested, both individually and in various combinations. The presence of dopants resulted in significant increases in the activity of the materials with respect to pure ceria, praseodymia, terbia and lanthana, which to all intents and purposes had zero activity at 600°C. The most marked improvement in activity for a single dopant was observed with La, activity peaking between 12.5 and 25 cation % lanthanum at levels approximately 30 times greater than that of undoped ceria. It is interesting to compare this result with a study by Machida and Enyo (1987)¹⁵¹ in which a series of Yb doped ceria catalysts were tested for OCM activity. Their results show a minimum in the selectivity for C_2 products at around the same dopant concentration (9.5 - 18 cation % Yb) as the maximisation in total oxidation activity reported in the Mackrodt patent. Returning to the patent by Mackrodt, a comparable increase in activity was also observed for 25 cation % praseodymium doping. The results of the single dopant modified catalysts led to a further investigation into the effects of combinations of the best dopants, La and Pr. In these experiments, a different preparation was used and therefore measured activities (measured per unit weight rather than per unit area of catalyst), are unfortunately not comparable with the single dopant results. The trend in these results however with total dopant content was similar to that with single dopants, the peak in activity occurring for a 25 cation % total dopant level. The La : Pr ratio was varied from 3 : 1

to 1 : 1 to 1 : 3 at a total dopant level of 40 cation %. The optimum ratio for the promotion of activity was 1 : 1 (although this was based on only three experimental data-points).

There were several fundamental deficiencies in this study which preclude further analysis of the variations in activity with dopant concentration and type. In the initial catalytic study to determine the effects of single dopants on the methane catalytic activity, no exact surface areas were reported (except all were reported as $> 1\text{m}^2\text{g}^{-1}$). In later experiments reported in the patent, significant variations in the surface areas of doped and undoped ceria were reported, and indeed at constant dopant concentration, from dopant to dopant. The reported differing degrees of dopant surface area stabilisation do not account for the large orders of magnitude increases in activity, but do make meaningful comparison of absolute activity between different dopants subject to considerable error, as differentiation between a chemical promotion and a material morphology promotion is not possible. An example of this type of miss-interpretation of data can be found in a study by Zamar, (1995)¹¹³ in which the incorporation of isovalent dopants into ceria was claimed to give rise to great increases in methane combustion activity based on light off temperatures. Further analysis of the data presented in the article revealed that when the catalyst surface areas were taken into account, the promotion of rate was almost entirely due to a surface area stabilisation effect of the dopant. The synergistic effects of combinations of dopants claimed within the Mackrodt (1991)⁹⁹ patent are therefore reviewed in this context.

During the preparation of the doped ceria materials dopant surface segregation was observed. It was suggested by Mackrodt, (1991)⁹⁹ that the active species at the surface may be comprised of regions of material of different phase and structure from the bulk fluorite lattice, for example in the case of the ternary system tested in the patent pyrochlore structure $(\text{Ce}_{1-x}\text{Pr}_x)\text{La}_2\text{O}_7$, PrO_{2-x} , or La_2O_3 .

The most recent study which included the effect of lanthanum doping on CH_4 total oxidation properties of ceria was a further study by Kundakovic and Flytzani-Stephanopoulos (1998).¹⁵² In this study the earlier work on modified ceria supported copper was extended by testing the effect of support crystallite size on activity. The effect of lanthanum and zirconium dopants on the support sintering, reducibility and

metal support synergistic effects during the oxidation reaction were tested. Catalytic activity was determined using the light-off mode and kinetic measurements were made using the reactor in the differential mode. The results of the kinetic study over lanthanum doped ceria showed a strong linear increase in activity with P_{CH_4} under constant P_{O_2} , and a slow increase in rate with increasing P_{O_2} under constant P_{CH_4} conditions. The experimental data was represented by;

$$r = \frac{k_{CH_4} K_{CH_4} P_{CH_4} P_{O_2}^{0.23}}{(1 + K_{CH_4} P_{CH_4})} \quad (2.44)$$

where k_{CH_4} is the reaction rate expressed such that $k_{CH_4} = A \exp(-E_a/RT)$, and K_{CH_4} is the methane adsorption equilibrium constant, such that $K_{CH_4} = K \exp(Q/RT)$

The Langmuir type adsorption dependence on P_{CH_4} was cited as evidence that the rate determining step involved adsorbed CH_4 . The power order dependence on P_{O_2} was cited as evidence of multiple oxygen sources during the reaction. E_a was determined to be 27 kcal mol⁻¹ (113.0 kJ mol⁻¹) and the pre-exponential factor was determined to be 5.7×10^8 for 10 cation % La doped ceria. The heat of adsorption was determined to be low (approximately 5.7 kcal mol⁻¹ (24 kJ mol⁻¹)) and thus allowed simplification of the kinetic equation to;

$$r = k'_{CH_4} P_{CH_4} P_{O_2}^{0.23} \quad \text{where } k'_{CH_4} = A' \exp(-E'_a/RT) \quad (2.45)$$

This is consistent with the redox (Mars-van Krevelen mechanism) of oxidation with slow reduction and fast oxidation steps, which was further supported by the demonstration of the reduction of ceria based catalysts by CH_4 . The nature of the active site was determined to be dependent on the thermal history of the sample which was explained in terms of the surface enrichment of lanthanum, (although this conclusion was not investigated in great depth.

It was determined that the coordinatively unsaturated oxygen species were responsible for CH_4 activation on doped ceria. Surface defects on ceria were determined to be sites for oxygen adsorption. Three factors were cited as important in controlling the activity of ceria in redox catalysis, these being crystallite size/surface

area stabilisation, the formation of defects, and the modification of the reduction behaviour. The modification of the reduction behaviour was said to be directly related to the ionic conductivity which is in turn significantly modified by the addition of dopants. The catalytic activity is also determined by the ability of the surface to activate CH_4 by hydrogen abstraction. This process leads to a reduction of the surface of the ceria based material, and therefore the ability of the material surface to become re-oxidised either by anionic transport from the bulk (conductivity related), or by dissociative adsorption of oxygen from the gas phase, is also a key determining factor in the overall activity. Lanthanum doping was determined to stabilise the crystallite size and create extrinsic oxygen vacancies, both of which were found to result in enhanced activity with respect to pure ceria and enhancement of the pre-exponential factor by an order of magnitude.

In conclusion, CH_4 oxidation activity was determined to depend on surface oxygen availability, and therefore to be promoted by enhanced reducibility achieved by doping. The addition of lanthanum to ceria also further enhanced catalytic activity due to the introduction of oxygen vacancies in the surface.

Chapter 3 Experimental

3.1 Materials Preparation.

In the present study, two different methods were generally used in order to prepare mixed ceria/lanthana oxide precursor materials which were then subjected to suitable thermal treatments, depending on intended usage. With the exception of specific experiments to determine the effects of pelletisation on sintering properties, all samples were in the form of powders. For the sintering studies, some samples were prepared in the form of a self supporting cylindrical pellets by isostatic pressing.

3.1.1 Ceramic preparation.

The ceramic preparation is a mixed nitrate preparation method that can be regarded as perhaps the simplest method of forming solid solution materials, other than high temperature mixed oxides methods. In the ceramic method, crystalline cerium (III) nitrate hexahydrate and lanthanum(III) nitrate hexahydrate were used exclusively as raw materials. The standard preparation method required mixing of the metal nitrates (in the correct proportion) by grinding together in an agate pestle and mortar. The reactants were then placed in a Pyrex beaker covered with a Pyrex watch-glass and placed in a furnace at room temperature. The furnace was then heated at a rate of $60^{\circ}\text{C hour}^{-1}$ up to a temperature of 450°C in order to drive off the water of crystallisation and decompose the nitrate precursors to form intimately mixed oxides.

A further development of this method was introduced in order to maximise the intimacy of cation mixing. The mixed nitrate precursors were dissolved together in a minimum volume of distilled water, rather than just relying on mechanical mixing. This mixed nitrate solution was then gently evaporated to dryness over a hot-plate in order to form an intimate mixture of nitrates. This precursor material was subsequently thermally decomposed using the same method as described previously.

In order to form single phase solid solution materials, further thermal treatment was necessary after formation of the mixed oxide precursors. The precursor material

was pelleted in order to maximise grain packing, (and thus grain boundary contact area), to ensure efficient formation of a solid solution by high temperature solid state reaction. Pelletisation was generally done on 1g aliquots of material which were isostatically pressed at 5000 kg. Pelleted samples were placed in an alumina boat and calcined in air at 1400°C for 24 hours. Following calcination, samples were reground in an agate pestle and mortar and then stored in an air-tight vial before further characterisation and testing.

3.1.2 Coprecipitation method

The development of the preparation method from the ceramic technique discussed above, to a coprecipitation method came about for two main reasons. The first and most important reason was due to the low surface areas of the materials formed by the ceramic method (see Results Chapter, section 4.1 and subsections therein). The low surface areas resulted in several experimental difficulties, associated with material characterisation and catalytic activity testing. As the surface areas were all $< 1\text{ m}^2\text{g}^{-1}$, accurate determination of surface area and porosity measurements using the best available (Micromeritics ASAP) apparatus was not possible due to an experimental requirement of a total sample surface area of 15 m^2 . Thus, surface area measurements of the ceramic materials could not be considered accurate. With regards the catalytic activity measurements, the low surface area combined with a limitation on catalyst bed volume (due to the apparatus available), resulted in the requirement for high temperatures ($> 800^\circ\text{C}$ in the case of methane oxidation), to give significant conversions. Once more the limitations of the apparatus - in this case the reactor furnace maximum temperature - resulted in the necessity to develop an alternative preparative method which would yield samples of higher specific surface area.

The coprecipitation method used in the initial study of the Mackrodt patent (1991)⁹⁹ (Appendix 4.1), resulted in surface areas $> 10\text{ m}^2\text{g}^{-1}$, and thus seemed suitable for the present study. The method was similar to the ceramic technique in that the starting materials were mixed nitrates. However, once mixed in the correct proportions, they were dissolved in sufficient distilled water to form an approximately

molar solution. The mixed cations were then precipitated by addition of excess 2M NH_4HCO_3 (ammonium bicarbonate) solution with vigorous stirring, at room temperature. The precipitation reaction resulted in the formation of a white precipitate of metal hydroxide (metal oxide hydrate) dispersed in a solution, which was stirred for a further 30 minutes before filtration under vacuum. Further addition of alkali to the mother liquor did not result in any further precipitation, and there was no characteristic yellow colouration of cerium ions in solution, therefore all of the metal cations were assumed to be precipitated. The precipitate was washed until free of alkali (by smell), by re-dispersion in approximately 1 litre of distilled water followed by filtration under vacuum. The filtrate was subsequently dried overnight in air at 110°C . The resulting powder was then placed in a covered Pyrex beaker and heated in air from room temperature to 450°C at a rate of $60^\circ\text{C hour}^{-1}$ in order to drive off remaining water and decompose remaining carbonate species, or residual ammonium bicarbonate. The mixed oxide sample was then calcined immediately.

The initial calcination treatments were based on the procedure in the Mackrodt patent; 8 hours at 1200°C in air. Further experiments were completed to investigate first the effect of calcination temperature, and then the effect of pelleting, on surface area and sintering properties. From these experiments (see results chapter, section 4.1 and subsections therein), the calcination process was optimised with respect to surface area and thermal stability under catalytic reaction conditions. As catalytic activity is a function of catalyst surface area use dependent changes in the catalyst materials, such as sintering, must be avoided as far as possible. In order to achieve this aim, it was determined that the calcination temperature should be of the order of 200°C higher than the maximum temperature that the catalyst would be expected to see, under low conversion reaction conditions. The figure of 200°C was thought to be adequate to allow for any exotherm occurring during reaction, and was supported by no reduction in surface area observed for any of the selected samples measured before and after catalytic reaction, providing the reaction temperature did not exceed approximately 600°C . The result of the trial and error study determined that an 8 hour calcination at 800°C in air of unpelleted precursor mixed oxide material was the optimum

preparation for the catalytic study, and was made standard for all samples undergoing catalytic activity measurement.

Other calcination regimes were also used on occasion, such as isothermal calcinations with calcination time varied, and isochronous calcinations at various temperatures. These samples were specifically used in the sintering properties and XPS studies and details of specific variations in preparation for these samples can be found in the relevant sections in the results chapter.

There are two intrinsic factors associated with the coprecipitation method, which with hindsight could have been avoided, but due to time limitations on the experimental work were unavoidable. Both factors relate to the precipitation reaction itself, and specifically the precipitant and the reaction sequence. Addressing the use of ammonium bicarbonate as the precipitant, although the material used was 99% grade, the introduction of impurities was significantly higher than with ammonia solution. However as the decomposition process of the ammonium bicarbonate precipitated material could result in a material with a significantly different morphology (i.e., surface area) than if another precipitant were used, and because it was specified in the Mackrodt patent,⁹⁹ the use of ammonium bicarbonate was continued. The second factor relates to the way in which the precipitation was carried out. In the Mackrodt patent, the ammonium bicarbonate solution was added to the nitrate solution. This would result in a rapid swing from low to high pH during the addition of the precipitant. The implication of this is that the two different metals could possibly be precipitated at two different pH's, thus resulting in what is effectively a two stage (selective) precipitation. The seeding of crystal growth of the last precipitated metal on the crystals of the metal precipitate that is formed at the lower pH is likely to form discrete encapsulated particles of the precipitate of one metal within the other. The solution to this problem is to slowly add the metal nitrates solution to the excess bicarbonate solution, effectively precipitating both metals instantaneously, and more importantly simultaneously. Although from the formation of solid solutions this effect appears negligible, (solid solutions being formed at much lower temperatures than by use of the ceramic method, due to a superior intimacy of cationic mixing), the effect may have some significance with regards the surface composition.

Due to time and raw material limitations, it was decided that it was not feasible to deviate from the Mackrodt patent method. Thus the standard preparation was used throughout the systematic catalytic study.

3.2 X-Ray Powder Diffraction (XRD)

3.2.1 Introduction

X-ray diffraction is undoubtedly the most useful and important technique available to the Solid State Chemist. The use of the technique, aided by the labour saving use of micro-computers, has now allowed the development of X-ray diffraction beyond structure determination alone. Additional uses of the technique include chemical and phase analysis, the estimation of crystallite/particle size and the determination of crystalline orientation.

X-ray powder diffraction analysis has been used extensively in the present studies for the characterisation of materials in terms of phase analysis of ceria/lanthana materials, and the estimation of lattice parameter and crystallite size. The use of XRD allows the determination of the solid solution limits of the system, and characterisation of sintering and solute incorporation processes, both as a function of material composition and of preparative process parameter variations.

3.2.2 Theory

A detailed general account of all X-ray diffraction techniques within this text would be unfeasible due to a plethora of applications based texts, each addressing a particular applied aspect of the technique. There are however several excellent literature references which provide good general descriptions of the theory and techniques of X-ray diffraction, and its application.^{26, 43, 153 - 159} An overview of the technique, including a general account of the main principles involved is presented in Appendix 3.2

3.2.3 Experimental Applications Used in the Present Study

3.2.3.1 Phase Studies.

The X-ray diffraction pattern of a material, in terms of line positions can be generally used for routine identification of materials. The phases present in the cerium/lanthanum oxide solid solutions were determined by comparison of the experimentally determined X-ray diffraction patterns with the library patterns, (Appendix 3.3). The presence of any peaks other than those characteristic of the (dopant induced lattice expansion shifted) characteristic cubic fluorite peaks, indicated the presence of a second phase present within the sample. The onset of a second phase appearing in the solid solution patterns with increasing lanthanum levels was used to estimate the solid solution limits within the binary oxide system.

3.2.3.2 Lattice Parameter Studies

Four major peaks in the X-ray diffraction pattern for ceria and the lanthanum cerium oxide solid solutions were used in the determination of lattice parameters; (111), (200), (220) and (311). These peaks were chosen as they remain strong and well resolved over the solid solution range. The peaks were identified and indexed by comparison with the standard library pattern for Ceria, (Appendix 3.3). The average lattice parameter was then determined over the four peaks using the equation

$$a = d_{hkl} \times \sqrt{h^2 + k^2 + l^2} \quad (3.1)$$

For each peak, d_{hkl} was determined using the instrumentation software, rather than the simple Bragg Equation, as the software allows for additional instrument factors, and is therefore more accurate. No internal standard was available to calibrate the measured 2θ values, therefore measured values are not considered absolute. However, the main purpose of the lattice parameter determinations is as a systematic characterisation of the solid solution system as a function of composition and preparative treatment, rather

than as a tool in the determination of the (known) crystal structure. As such, determined lattice parameters within the experimental data set can be considered comparable.

3.2.3.3 Crystallite Size Estimation by Line Broadening

For crystallite sizes below approximately 2000Å, a broadening effect on the diffracted beam is observed. The explanation of the broadening effect requires consideration of diffraction of a beam where the angle of incidence to the diffracting plane is slightly different to the Bragg Angle (θ). For an incident beam $\theta + \delta\theta$, there exists a phase lag of $\lambda + \delta\lambda$ for rays diffracted from subsequent planes. By the n^{th} plane, the cumulative incremental phase lag eventually reaches $\lambda/2$. Thus, the reflections from the first and the n^{th} plane are perfectly out of phase and destructive interference occurs, the two reflections annihilate each other. If the crystal is made up of $2n$ planes, then the net diffracted beam intensity from $\theta + \delta\theta$ also equals zero as the diffracted rays from planes 1 to n , exactly cancel the diffracted beam from the $n+1^{\text{th}}$ to the $2n^{\text{th}}$ plane. Thus, the intensity of the diffracted beam falls in intensity from its maximum at θ , to zero at $\theta + \delta\theta$. Similarly, there is a lower limiting angle at $\theta - \delta\theta$. The magnitude of the angular range $\theta + \delta\theta$ to $\theta - \delta\theta$ is hence governed by the number of planes, and therefore the thickness of the crystal. For crystals where the number of planes is very large, $\delta\lambda$ (and by default $\theta + \delta\theta$ to $\theta - \delta\theta$) becomes vanishingly small, and therefore no significant broadening contribution is observed from the crystal size effect. Even in the absence of crystal size broadening, the diffracted line still has a finite thickness due to the focusing geometry of the instrument and the lack of 100% monochromatic $K\alpha$ X-rays. A perfectly parallel beam, as is modelled under Bragg conditions does not actually exist, as there will always be an element of convergence or divergence under experimental conditions. The generally accepted formula for the determination of crystallite size by line broadening is given in the Scherrer equation;

$$t = \frac{0.9\lambda}{B \cos\theta_B} \quad (3.2)$$

where t denotes the thickness of the crystal (\AA), θ_B is the Bragg Angle and B is the full width at half median for the experimental peak (radians). The crystallite size estimations in this work were calculated using the specific equation;

$$t = \frac{79.44}{B \cos \theta_B^\circ} \quad (3.3)$$

where θ_B is measured in degrees. The numerator allows for the constant, λ (1.5405\AA for $\text{CuK}\alpha$), and the $180/\pi$ degrees to radians conversion factor. The full width at half median was measured for experimental peaks following a $\text{CuK}\alpha_2$ subtraction and then a Gaussian peak fitting to the experimental data points, all of which are functions of the Phillips instrumentation software package.

3.2.4 Instrumentation and Experimental Procedure

All X-ray diffraction patterns in this study were collected and analysed using a Phillips diffractometer (model PW1710) using a Micro-Vax with VMS computer with Phillips APD 1700 software, which includes a Phillips instruments, Inc. CD-ROM database (1987). The database is based on the PDF 2 database from JCPDS.

X-rays are produced using a copper target, tungsten filament and a current of 40 mA. The electron accelerating voltage was 40kV. X-rays pass through a beryllium window and a 4° fixed collimator. A nickel filter is used to remove $K\beta$ and the continuous spectrum. The diffracted beam positions and intensities were recorded using a scintillation detector (proportional), with 0.2mm collimating slits.

All samples were prepared for X-ray diffraction analysis by thorough grinding of the pre-calcined materials in an agate pestle and mortar. Samples were then loaded into the instrument sample holder, which consists of a plate with a rectangular cup of approximately 2 mm depth machined on one side. The surface of the sample in the holder was levelled flush with the surface of the holder using a glass microscope slide. The sample holder was then introduced to the instrument chamber. The rest of the experiment was then controlled from the instrument computer work-station. For general scans, used for phase and lattice parameter determination experiments, the

diffractometer was used in continuous scan mode. Samples were scanned between 10° and 80° in 2θ , with a scan speed of approximately 0.02°s^{-1} . This resulted in a total scan time of approximately 1 hour. For line broadening experiments, smaller scan ranges were used for 1 hour scans in order to improve the accuracy of the Gaussian curve fitting when determining the full width at half median. The line positions analysed varied with composition of the solid solution materials, but were always over a range of 15° , using a scan speed of approximately 0.005°s^{-1} .

3.2.5 Errors and Reproducibility

In the data supplied by the manufacturer, in the absence of an internal standard the measured lattice parameters should be quoted to three decimal places in the angstrom range, for example; a calculated lattice parameter of 5.40489\AA should be quoted as $5.404(9)\text{\AA}$. It was not specific in the literature whether this value was derived from multiple scans of a static sample, or whether sample unloading/reloading variations had been tested. It was therefore necessary to conduct experiments to determine the error inherent in the sample packing procedure.

In a set of experiments, the same sample of ceria was run ten times, unloading and reloading the sample for each scan. Determination of the standard deviation of the ten lattice parameter measurements (each measured over four peaks) resulted in an error of $\pm 0.00626\text{ \AA}$ with a mean lattice parameter of $5.399(9)\text{ \AA}$. Lattice parameters are therefore quoted hereon with an error of $\pm 0.007\text{ \AA}$. Thus the mean lattice parameter from the study is quoted as $5.400 \pm 0.007\text{ \AA}$.

Further calculations to determine the error in the estimation of crystallite size were also carried out based on the same ten scans. For an average estimated crystallite size of 425 \AA , the standard deviation was determined to be 22 \AA . All quoted crystallite sizes are therefore subject to a sample to sample error of $\pm 5\%$. It should be reiterated that these measurements are estimations and therefore this calculated error is with respect to comparative values of a series of samples, not with respect to the absolute crystallite size.

3.3 Surface Area Measurement

3.3.1 Introduction

The determination of specific surface area is an invaluable tool in the study of catalytic systems, without which the determination of specific activities of catalysts would not be possible. As long as the rate of transport of reactants to, and products from the surface are faster than the catalysed reaction, then the rate of reaction should be proportional to the surface area of the active phase of the catalyst.¹⁶⁰ This characterisation technique allows the study of true specific catalytic activity of surfaces in terms of comparable measurements, (activity per unit area) rather than more empirical comparisons (activity per unit weight).

The advantages of this type of comparison are that morphological factors due to differing catalyst system properties and preparative techniques are eliminated. For a given series of similar catalysts, the reaction rate measurement can be standardised with respect to surface area and true variations in the surface chemistry across the series can be evaluated.

Other applications of surface area measurements are in the standardisation of measurements of other surface properties, such as temperature programmed adsorption/desorption and temperature programmed oxidation/reduction studies. In these applications the measurements derived from these techniques can also be standardised with respect to surface area, giving directly comparable figures for different materials. This allows further comparative chemical analysis of surfaces in a series of catalysts and is particularly of use when surface chemical composition is also known. When the results from these “specific” characterisation techniques are correlated with XPS surface composition data, valuable insights into the surface chemistries of catalytic systems can be derived.

So far, the advantages of surface area determination as a method of eliminating morphological differences from the measurement of chemical and catalytic properties of surfaces have been discussed, however the measurement of morphological variations in a series of materials is also valuable with respect to solid state studies. It is also

possible to follow the variation in surface area with preparation technique and with composition. For example, the variation in surface area with calcination temperature and firing time can be determined for a material of a given composition, and the variation with composition for a fixed preparation technique can be determined. When this data is correlated with X-ray powder diffraction study results which can estimate crystallite size, lattice parameter and phase composition, and with XPS studies to determine surface composition, a detailed overview of a solid state chemical system can be determined with respect to sintering characteristics. This information can then be used to provide further insight into the surface and catalytic chemistry of a system, and may be used as a tool to optimise further catalyst systems and material preparative techniques.

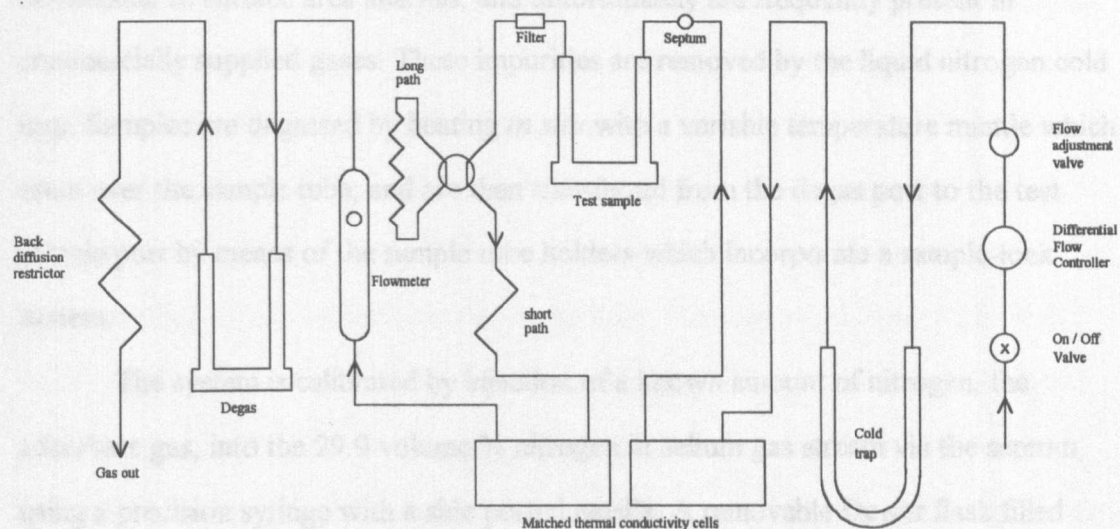
This brief introduction to the applications of surface area measurement in the field of catalysis is followed by an outline of the experimental methodology used. A brief review of the theory and experimental methodology of surface area measurement by gas adsorption techniques is presented in Appendix 3.4.

3.3.2 Experimental Apparatus / Instrumentation

Surface Area measurements were made using a commercially available Micromeritics Flowsorb II 2300 instrument for the determination of single point surface area. Figure 3.1 shows a schematic diagram of the apparatus.

The surface area of solid materials is measured by determining the quantity of gas that adsorbs as a monolayer at the boiling point of the adsorbate gas. Under the experimental conditions the area covered by each adsorbed gas molecule is known, therefore the total surface area of the sample can be calculated from the number of adsorbed molecules.

Figure 3.1 A Schematic diagram of the Micromeritics Flowsorb 2300 Apparatus.



The apparatus allows measurements to be made from a flowing stream of a helium/nitrogen gas mixture. The mixture is flowed over the sample and the composition of the exhaust is monitored by a thermal conductivity detector with an integrator/recorder. When the sample is cooled in liquid nitrogen, physisorption of nitrogen from the gas mixture results in the detection of a negative peak with respect to the baseline until the adsorption process is complete, whereupon the signal returns to the baseline level. On removal of the cooling trap, the sample returns to room temperature thus desorbing the physisorbed nitrogen. This results in the detection of a positive peak with respect to the baseline until the desorption process is complete whereupon the signal returns to the baseline level. The areas under each of these peaks, (which should be identical), are proportional to the amount of nitrogen adsorbed and desorbed. The peak areas can be calibrated by the addition of a known amount of nitrogen to the gas mixture, or by comparison with a known adsorbent sample of certified surface area.¹⁶¹ It has been found experimentally that for the helium/nitrogen mixture which is used by the instrument, that a mixture of 30 volume % nitrogen is most favourable for monolayer formation under the atmospheric pressure/liquid nitrogen adsorption temperature conditions used.

The Flowsorb II 2300 instrument allows a regulated flow of dry 29.9 vol. % (certified) nitrogen in helium to be passed at a constant flow rate through the instrument and over the sample under test, and the sample at the degas port

simultaneously. Traces of moisture and other impurities in the inlet gas stream are very detrimental to surface area analysis, and unfortunately are frequently present in commercially supplied gases. These impurities are removed by the liquid nitrogen cold trap. Samples are degassed by heating *in situ* with a variable temperature mantle which seats over the sample tube, and are then transferred from the degas port to the test sample port by means of the sample tube holders which incorporate a sample-lock system.

The system is calibrated by injection of a known amount of nitrogen, the adsorbate gas, into the 29.9 volume % nitrogen in helium gas stream via the septum, using a precision syringe with a side ported needle. A removable Dewar flask filled with liquid N₂ can be supported beneath the test sample tube holder to allow adsorption of nitrogen from the 29.9 vol. % nitrogen in helium gas stream onto the sample, and desorption of nitrogen back into the 29.9 volume % nitrogen in helium gas stream. The position of the Dewar flask supporting platform also incorporates a switch which compels the detector/integrator system into the correct mode regarding nitrogen lean (adsorption) measurements and nitrogen rich (desorption) measurements.

The detector consists of matched thermal conductivity cells operating at a fixed temperature of 42 ± 1 °C for gas concentration detection. The detector signal is calibrated to indicate the instantaneous difference in percent nitrogen between the reference flow path and the flow from the sample path.

The display of the Flowsorb II 2300 instrument has multiple functions. It can be used to monitor the detector signal, the degas temperature or the surface area for a single point measurement. The surface area displayed is a measure of the total surface area of the test sample. This value must be divided by the sample weight in order to derive the specific surface area for the sample (m²g⁻¹).

3.3.3 Sample Preparation

The Flowsorb II 2300 instrument can reliably measure surface areas with total surface areas between 0.1 and 280 m², but results are most accurately and quickly determined if the sample quantity is such that the total surface area is between 0.5 and

25m². Thus, the amount of sample required for each test must be determined experimentally. The specific sample surface area was derived from the total measured surface area and the weight of the sample, the true weight of the sample being determined after the sample has been degassed (i.e. after the adsorption/desorption experiment has been completed). The clean dry sample tube and stoppers were weighed before adding the powder to be analysed, ensuring that some free space was left above the sample for the unimpeded gas flow. The sample tube was then fitted to the sample holder and installed at the degas port. The heating mantle was then fitted around the sample tube and the degas temperature selected using the push-button controller. The samples were degassed at the highest temperature possible, within the thermal stability range of the samples. In the case of the ceria/lanthana based oxides, this corresponds to a temperature of approximately 200 °C. Higher temperatures in an inert atmosphere (such as the 29.9 volume % nitrogen in helium), cause a reduction of the sample which is characterised by a visible darkening from a light yellow colour to brown. This was avoided at 200 °C and yet the degas rate was sufficient for the samples to be completely dry after 30 minutes (as determined by repeated weighing experiments).

3.3.4 Single Point Surface Area Measurement

3.3.4.1 Calibration

The Flowsorb II 2300 instrument is calibrated by injecting an exact 1ml volume of nitrogen into the instrument through a septum using a syringe with a side ported needle. 1ml of nitrogen gas corresponds to 2.84 m² of sample when using a 30 vol. % nitrogen in helium mixture, when the adsorption is at liquid nitrogen temperature, and when the ambient conditions are 22°C and 760 mmHg. The gas supplied for use with the equipment is however certified 29.9 vol. % nitrogen in helium and therefore the 1ml surface coverage was recalculated to take this into account, as shown in the theory section. The surface coverage of 1ml nitrogen for the actual experimental conditions used was determined to be 2.85 m² as shown in the calculations in appendix 3.4.

The instrument was calibrated before use until a steady surface area reading of $2.85 \pm 0.01 \text{ m}^2$ was obtained for three successive injections of 1 ml N_2 , (obtained by filling the syringe under liquid N_2). Before calibration, gas flow through the instrument was initiated in order to purge the system and the detector was switched on and allowed to reach its equilibrium temperature which was indicated by a steady response. The conductivity cell response was then standardised with respect to the gas mixture in accordance with the manufacturers instructions (i.e. gives a reading of 29.9 for the 29.9% nitrogen in helium gas mixture used).

3.3.4.2 Experimental procedure

Once degassed, samples were transferred to the test sample port. At this point the cold trap was replenished as necessary in order to ensure identical conditions for each sample, and a fresh sample was loaded onto the degas port in preparation for the next experiment. During the transfer it was inevitable that some air was introduced into the system. This required approximately 15 minutes to purge through the apparatus before each experiment.

Once purged, the detector response was zeroed as was the surface area display. A dewar of liquid nitrogen was then placed around the test sample and topped up to the brim in order to ensure identical adsorption conditions for each sample. There was immediately a marked decrease in the flow, (indicated by the flowmeter), as nitrogen from the 29.9% nitrogen in helium gas mixture was adsorbed onto the sample. After a few seconds, the flow recovers and eventually returns to normal as the sample achieves monolayer coverage. After a further 10 minutes, the detector response begins and the instrument integrator accumulates the total surface area data for the sample. The end of this stage of the experiment is signified by the return of the detector response signal to zero. The surface area is then noted, the surface area display zeroed, and the liquid nitrogen dewar removed from the sample tube in order to initiate the desorption process.

On desorption there is a marked increase in the rate of gas flow through the flowmeter due to the desorption of the adsorbed nitrogen into the 29.9% nitrogen in

helium gas stream. Again, the flow recovers after a short time signifying the desorption process is complete. The total surface area is accumulated similarly to the adsorption data, and the result noted. The adsorption and desorption stages were both repeated in order to confirm results. The sample tube was then removed from the apparatus and replaced with a pre-prepared sample from the degas port.

The weight of the sample was calculated by difference between the empty tube (as determined before sample addition) and the tube with the degassed sample inside. The average of the four total surface area figures from the repeated adsorption and desorption experiments was then divided by the sample weight in order to provide a specific surface area in m^2g^{-1} .

3.3.5 Accuracy, reproducibility and error

Instrument specifications for the Micromeritics Flowsorb II 2300 are quoted as typically better than $\pm 3\%$ for low specific surface areas and improve for higher specific surface areas. The instrument also has a minimum surface area of 0.1m^2 and a minimum specific surface area of approximately $0.01\text{m}^2\text{g}^{-1}$. These figures made this instrument ideal for the samples tested, several of which had surface areas below $10\text{m}^2\text{g}^{-1}$. Access to a more advanced Micromeritics Automated Surface Area and Porosity (ASAP) instrument was available, but this required a minimum total surface area of 15m^2 and had a throughput of 1 sample per day, and therefore was unsuitable for use due to the large number of samples to be tested, and the low specific surface area of the samples. However, reference samples and some test samples were tested on both machines which were found to agree within 3.3% for a $214\text{m}^2\text{g}^{-1}$ standard sample. Most of the samples which were used for catalytic studies were re-tested on separate occasions in order to determine error. The results were generally found to be reproducible within approximately 4% on average for repeat runs. Agreement between adsorption and desorption figures was generally found to be very good, averaging at $\pm 2.63\%$ for the systematic series of $\text{Ce}_{1-x}\text{La}_x\text{O}_{2-x/2}$ catalytic samples prepared by coprecipitation and calcination in air at 800°C for 8 hours.

3.4 X-Ray Photoelectron Spectroscopy

3.4.1 Introduction

Generally, the surface composition and often the surface structure of a solid material is known to differ significantly from that of the bulk material. In the field of heterogeneous catalysis the composition and structure of these outermost atomic layers are of far greater importance than that of the bulk material as all catalytic reactions occur at the solid/gas interface. This being known, the use of electron emission spectroscopic techniques has been wide-spread in recent years for the characterisation of the surfaces of industrial catalysts,¹⁶² and in many academic studies investigating the properties of catalyst, semiconductor and materials with many other applications. Several reviews of surface characterisation science combining electron spectroscopic techniques with other surface and bulk characterisation exist,^{163 - 165} and provide excellent experimental and interpretational reference material for many systems.

The emission of electrons from surfaces induced by a photon or electron beam is one of the most successful means of learning about composition and bonding at the atomic level in surfaces. Electrons can be emitted readily from a solid by incident photons or electrons with energies of the emitted electrons greater than the work function (a few electron volts). Electron beams have the fortuitous property of low penetrative power (due to low kinetic energies) which means that they are only able to escape from the outermost layers of a solid, thus rendering them ideal for surface studies. Electrons emitted from atomic layers beneath the topmost layers, lose their energies by collisions before exiting the surface.¹⁶⁶

In electron spectroscopic techniques, the analyte is irradiated with either a beam of X-radiation, electrons or short wavelength UV radiation. The excitation of the analyte results in the emission of electrons and photons, the former of which is measured and classified as a function of energies and intensities. There are three common types of electron spectroscopy in common usage. Auger Electron Spectroscopy (AES) generally uses an electron beam as the excitation source

(although x-rays can be used), Ultraviolet Photoelectron Spectroscopy (UPS) uses a beam of ultraviolet radiation to stimulate electron ejection from the analyte, and X-ray photoelectron spectroscopy (XPS). This is the most popular of the electron spectroscopic techniques which uses X-radiation as the excitation source, and was used to determine the surface composition of catalytic samples in these research studies. An overview of the technique including an account of the main theoretical principles is presented in Appendix 3.5.

3.4.2 Experimental Apparatus / Instrumentation

Most of the surface analysis for this study was completed on a service basis by the Institute of Surface Science and Technology (ISST), an analytical consultancy company operating from the Physics Department at Loughborough University, Leicestershire.

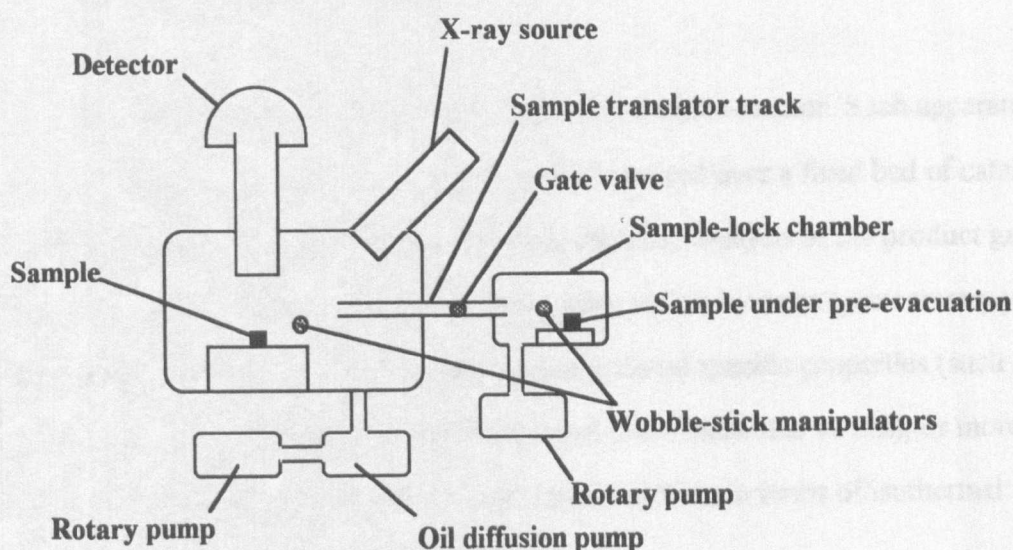
The work was completed using a VG ESCA_{lab} Mk I instrument. The X-ray source was non-monochromated Mg K α (1253.6 eV) with an electron emission current of 20mA and an accelerating voltage of 10kV resulting in an X-ray power of 200W. Scans were recorded with a take off angle of 90° to the sample over the range 830eV to 930eV with a step size of 0.1eV and a 20ms dwell time. A detector slit diameter of 10mm was used and the pass energy was 100eV. The final spectra were averaged over 30 scans.

Samples were submitted as fine powders mounted on 10mm diameter cupped-top sample studs. The loaded sample stubs were introduced to the analysis chamber of the instrument via an evacuable sample-lock chamber. This arrangement allows quick introduction of samples into the analysis chamber through a gate valve, without loss of vacuum in the main analysis chamber. After introduction to the sample lock chamber, samples were evacuated for approximately 15 minutes in order to degas the surface. Sample manipulation within the instrument was effected using "wobble-sticks" and externally driven sample translators in order to transfer the sample from the sample lock chamber, through the gate valve, and into the analysis chamber. Once the sample is in position, all further experimental control was via the PC based instrument

software and associated instrument control units. The scan time for each sample was approximately 15 minutes, and the set-up of the apparatus allowed the degas of subsequent samples during analysis. A schematic of the instrument set-up is shown in figure 3.2.

Analysis of the four $x = 0.2$ samples (for the variation in calcination temperature study only), were performed in-house using a Kratos XSAM instrument using similar conditions to those described above. The only significant difference between the two instrument techniques being the requirement for a greater scan average with the Kratos instrument due to a lower detector response. This resulted in a scan time of approximately one hour for each sample.

Figure 3.2 Schematic of XPS instrument set-up



3.4.3 Analysis of spectra

The cerium/lanthanum ratio was quantified by measurement of the $3d_{5/2}$ peaks (Ce $3d_{5/2}$ 884eV, La $3d_{5/2}$ 834eV) following subtraction of a manually assigned Shirley type background. No internal standard was required as the instrument specific quantification factors for cerium and lanthanum were the same, and therefore the ratio of peak areas could be taken directly as the cation ratio in the analysed surface layer.

3.4.4 Error and reproducibility

Due to the service nature of this analysis, no error and reproducibility studies were possible in this study. Results from the ISST were quoted to the nearest 0.1% and therefore the error is assumed to be $\pm 0.05\%$ point for all samples. The main source of error associated with the technique is in the manual baseline assignment. Error increases in significance with the more extreme ratios where the accuracy of the peak area measurement has a greater dependence on the peak start and end points. However, the accuracy of the reported results was determined by error and reproducibility studies performed by ISST on other systems, and therefore results are quoted as supplied.

3.5 Catalytic Measurements

All catalytic measurements were made using a micro-reactor. Such apparatus allows precisely known reactant gas mixtures to be passed over a fixed bed of catalyst under either steady state or temperature flux conditions. Analysis of the product gas stream, generally by calibrated gas chromatography and or by mass spectrometry yields reaction rate data which can be used to measure material specific properties (such as activation energies and Arrhenius method derived pre-exponential values), or more simply to compare the performance of a group of materials in terms of isothermal specific rates or reaction light off temperatures.

3.5.1 Micro-Reactor Apparatus

Gases of known composition are introduced from cylinders via Brooks 5850 Mass Flow Controllers. The use of mass flow controllers allows precise metering of gases in order to produce accurate inlet gas mixtures with pre-determined compositions and volumetric flow rates. The construction of the micro-reactor consists of quarter, eighth, and sixteenth inch stainless steel tube connected using Swagelok™ fittings. The system is operated at atmospheric pressure, with negligible (assumed)

pressure drop across the catalyst bed. The reactant gases were mixed in the manifold section, aided by flow perturbation caused by the 7 μ m filter. Once beyond the filter, a two-way tap is used to divert the gas mixture flow to the desired application; the Diffuse Reflectance Infra-red Fourier Transform Spectrometer (DRIFTS) environment cell, (see section 3.6 and subsections therein), or to the micro-reactor reaction tube, as described presently.

Once beyond the tap, gases are pre-heated to 120°C in the stainless line on entering the oven section. Gases then enter the quartz reaction tube within the vertical tube furnace and pass upwards through the catalyst where reaction occurs at elevated temperature. Product stream gases (reactant and product), then return to the oven section where the temperature returns to 120°C. On leaving the oven, the gas line is maintained at 120°C using heating tape to prevent condensation of water (a product of methane combustion). The product stream gas is then fed through a Valco™ Valve incorporating a fixed volume sample loop, to allow injection of samples from the product stream into the GC (Hewlett Packard model 5890) using a Carboxen 1000 column. Finally, a small proportion of the product stream is bled through a porous frit/needle-valve into the Mass Spectrometer (Fisons Instruments), whilst the remainder is vented. A schematic diagram of the micro-reactor apparatus is presented in figure 3.3. Figure 3.4 presents a schematic diagram of the reaction tube apparatus which is housed inside an oven maintained at 120°C. The apparatus is encased in shaped blocks of a refractory material both to support the weight of the apparatus and to provide thermal insulation.

Reactant gases preheated to 120°C enter the bottom of the quartz reaction tube and proceed vertically upwards into the heated zone of the tube furnace, and into the catalyst bed. The fixed catalyst bed consists of a cylindrical plug of 200-400 μ m catalyst particles of dimensions 10mm length (approx.) x 4mm diameter. The catalyst is constrained by two plugs of 14 μ m fibre diameter quartz wool at each end of the bed. The upper quartz wool plug is butted against the end of an α -alumina thermocouple sheath in order to prevent any upwards movement of the catalyst bed due to the upward flow of gas through it. The thermocouple itself is then placed inside the sheath,

Figure 3.3 Micro-reactor Schematic Diagram

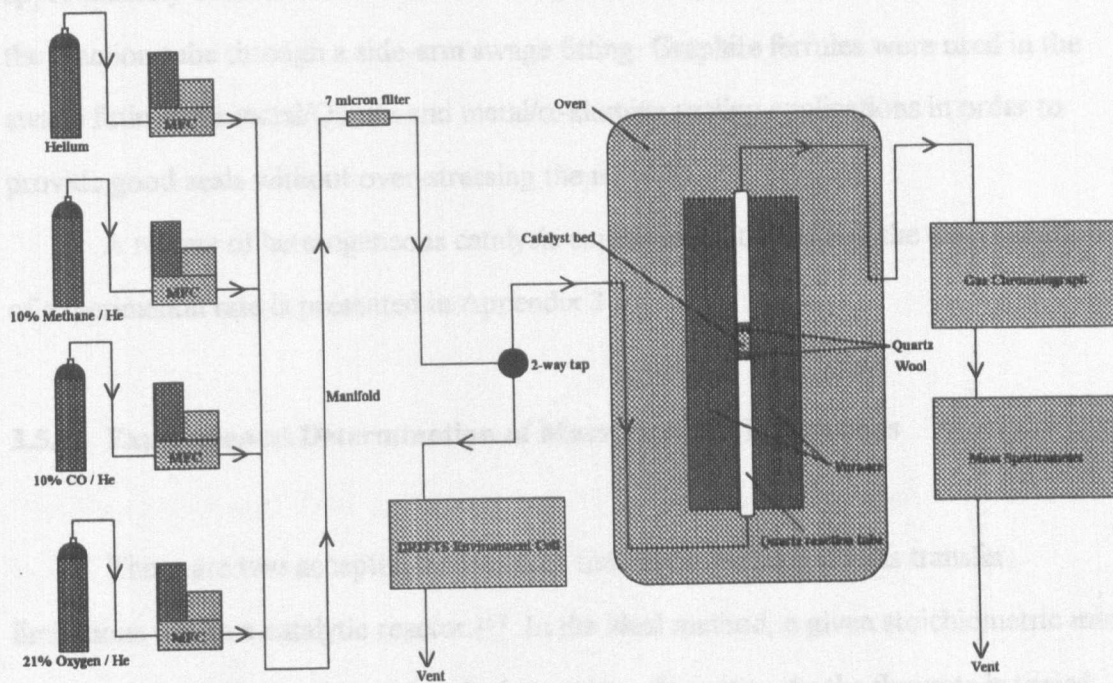
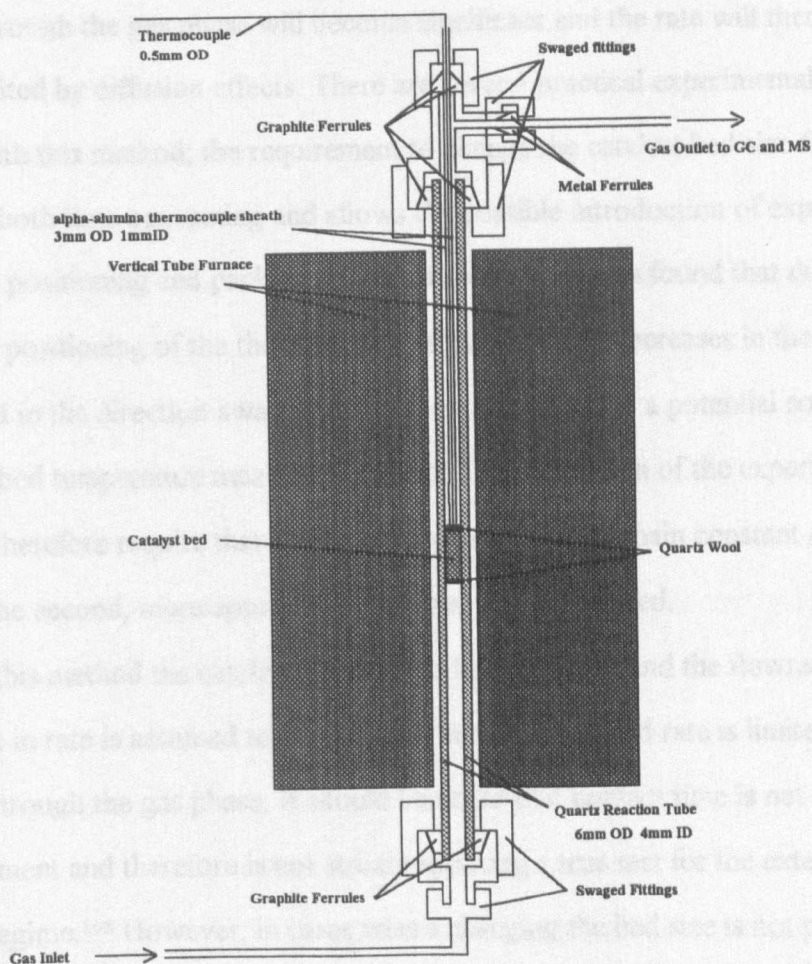


Figure 3.4 A schematic diagram of the micro-reactor reaction tube.



the probe tip being separated from the uppermost part of the catalyst bed by approximately 1mm α -alumina. Once through the catalyst bed, the product gases exit the reaction tube through a side-arm swage fitting. Graphite ferrules were used in the swage fittings for metal/Quartz and metal/ α -alumina sealing applications in order to provide good seals without over-stressing the more fragile materials.

A review of heterogeneous catalysis experimental theory and the determination of experimental rate is presented in Appendix 3.6.

3.5.2 Experimental Determination of Mass Transfer Limitations

There are two accepted methods for the determination of mass transfer limitations within a catalytic reactor.¹⁶⁷ In the ideal method, a given stoichiometric mix of gases is passed over the catalyst bed at various flowrates, As the flowrate is varied, so is the catalyst bed mass such that the ratio of the two remains constant, thus maintaining a constant contact time for each flowrate In the absence of significant diffusion effects, conversion will remain constant. Below a given flowrate the rate of diffusion through the gas phase will become significant and the rate will therefore become limited by diffusion effects. There are several practical experimental problems however with this method; the requirement to change the catalyst bed size for each flowrate is both time consuming and allows the possible introduction of experimental error in the positioning and packing of the catalyst bed. It was found that due to the end-of-bed positioning of the thermocouple, that significant increases in the size of the catalyst bed in the direction away from the thermocouple was a potential source of significant bed temperature measurement error. This limitation of the experimental apparatus therefore require that the size of the bed should remain constant and therefore the second, more approximate method should be used.

In this method the catalyst bed mass is held constant and the flowrate is varied. A decrease in rate is assumed to be evidence that the observed rate is limited by diffusion through the gas phase. It should be noted that contact time is not constant for this experiment and therefore is not strictly speaking a true test for the external diffusion regime.¹⁶⁸ However, in cases where changing the bed size is not practicable,

this method is adequate and has been reported¹⁶⁷ and used experimentally¹³⁵ in the literature. Once the mass transfer limitations have been determined for a given catalyst/reaction/reactor system, standard flowrate and catalyst bed mass conditions can be established for further experimentation and the influence of diffusion through the gas phase on rate can be considered negligible.

3.5.3 Error and Reproducibility

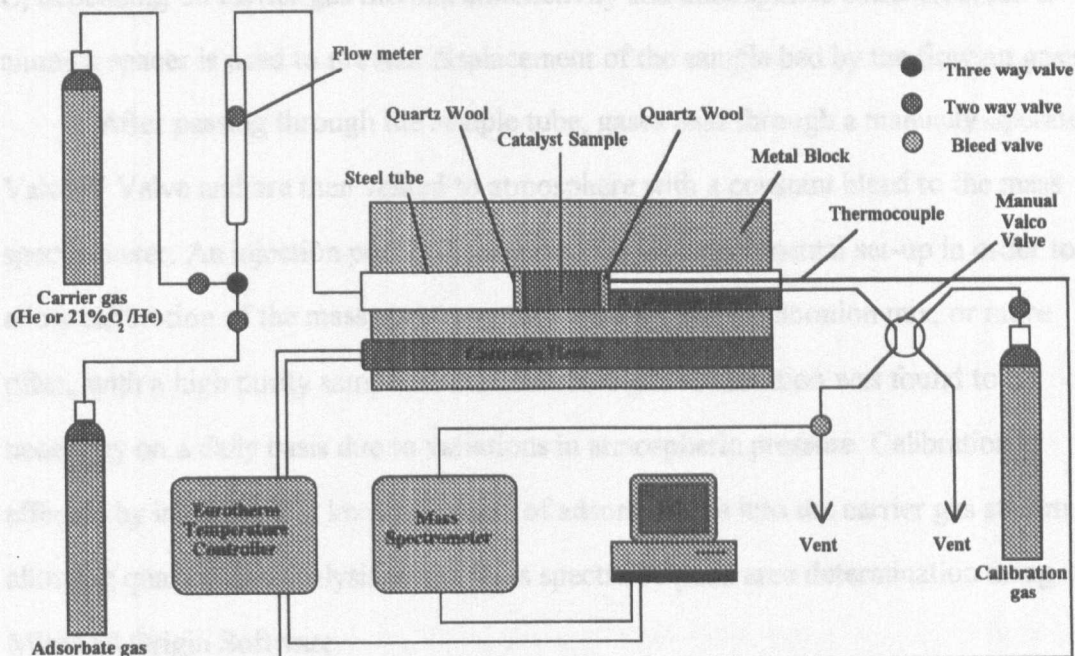
Under steady state reaction conditions (generally achieved within 30 - 40 minutes equilibration time), gas chromatograph results were determined to have an error of approximately $\pm 2\%$ on an injection to injection basis. Sample to sample reproducibility was estimated to be approximately $\pm 5\%$ based on analysis of data from repeated samples. It should be noted that this error could be compounded by use dependent changes in the catalyst materials, such as reduction of the ceria based materials, which were generally found to result in non-steady state rate measurements. Good equilibration procedures (1 hour standard equilibration time), were found to minimise this error to within acceptable limits.

3.6 Temperature Programmed Desorption Studies. (TPD)

Temperature programmed desorption studies are of great value when correlated with catalytic data. Such studies allow the adsorption of reactants and products involved in a particular reaction scheme to be characterised in terms of the extent of adsorption (which can be determined by quantitative analysis of the desorbed species), and the adsorption strength (which can be determined by the observed desorption temperature). Other material properties can also be studied, such as surface acidity by the use of basic adsorbate probe molecules, (such as ammonia), and surface basicity by the use of acidic probe molecules, (such as carbon dioxide). Such studies can characterise the acidic/basic surface sites in terms of strength and site density. If the specific surface area of the test material is also determined, the number of surface sites per unit area (the specific adsorptivity), can be determined to provide a method of

characterisation of trends in quantifiable surface properties within a systematic series of materials.

Figure 3.5 Temperature Programmed Desorption Apparatus.



3.6.1 Apparatus

As can be seen from the schematic diagram of the TPD apparatus presented in figure 3.5, the layout is similar to that of the micro-reactor. The main differences are that the TPD apparatus does not require the accuracy of reactant gas delivery met by use of mass flow controllers in the micro-reactor system. Instead, gases are metered by a simple ball-float flow meter, the feed to which is switchable between carrier gas and adsorbate gas supplies.

In common with the micro-reactor apparatus, all pipework is $\frac{1}{4}$ " stainless steel with Swagelok™ fittings and joints. Due to the rapid sample turnover and the mechanical stresses on the sample tube (which is clamped in the heating block), quartz tubing was deemed unsuitable and steel tube was used in its place. ($\frac{1}{4}$ " O.D., 4mm I.D, approx.). The heater unit is comprised of a steel block in which the sample tube and a cartridge heater are clamped. The cartridge heater is controlled using a Eurotherm control unit, and the sample temperature is determined using an unsheathed k-type

thermocouple placed at the end of the sample bed. The temperature controller temperature output is also recorded for each mass spectrum scan. Thus the variation in signal intensity with temperature for each mass monitored was recorded continuously. The maximum temperature achievable by the system is in the region of 800°C to 850°C, depending on carrier gas thermal conductivity and atmospheric conditions. An α -alumina spacer is used to prevent displacement of the sample bed by the flowing gases.

After passing through the sample tube, gases pass through a manually operated Valco™ Valve and are then vented to atmosphere with a constant bleed to the mass spectrometer. An injection port is incorporated in the experimental set-up in order to allow calibration of the mass spectrometer with a certified calibration mix, or more often, with a high purity sample of the adsorbate gas. Calibration was found to be necessary on a daily basis due to variations in atmospheric pressure. Calibration is effected by injection of a known volume of adsorbate gas into the carrier gas stream allowing quantitative analysis of the mass spectra by peak area determination using Microcal Origin Software.

3.6.2 Experimental Procedure

In all experiments, 0.4g of sample with a 200-400 μ m particle size range was used. The surface areas of all samples tested were determined prior to the TPD experiments. Repeat measurements after the TPD experiments on selected samples showed negligible change in surface area. In order to "clean" the surface of the sample, a "pre-TPD" was performed. The aim of this procedure was to remove adsorbed water, carbon dioxide and any other air-borne species which may have adsorbed on the sample during the sample preparation. The pre-TPD was completed under the same conditions as the post adsorption TPD, i.e., under the same carrier gas and temperature program. Repeat runs of the pre-TPD on selected samples showed no evidence of further desorption and the procedure was therefore deemed effective as a method for standardising the sample materials prior to adsorption.

Various types of TPD experiment were completed in order to determine surface basicity (CO₂ TPD), CO adsorption properties (CO TPD) and methane

adsorption properties (CH_4 TPD). The effects of the presence of gaseous O_2 on the adsorption/desorption properties of the ceria/lanthana materials were tested by using both helium and a 21 vol. % O_2 in He (Heliox) mixture as carrier gases. The adsorption conditions (temperature, adsorbate concentration and adsorbate exposure time), were optimised prior to systematic testing. The exact procedures completed and the experimental details are presented along with the results in section 4.3 and subsections therein.

3.6.3 Errors and Reproducibility

The Temperature programmed desorptions were determined to be reproducible with sample to sample error estimated to be $\pm 5\%$, based on comparison of quantifications of non-oxidative, and non-oxidative plus oxidative TPD experiments.

3.7 Diffuse Reflectance Infrared Fourier Transform Spectroscopy. (DRIFTS)

3.7.1 Introduction

Diffuse Reflectance IR spectroscopy is a valuable source of information regarding the physicochemical properties of surface species. This information can be generally classified into the study of surface adsorption on materials, and the molecular changes during adsorption. Data regarding the orientation of the adsorption and the dissociative or non-dissociative nature of the adsorption processes is of great importance in the elucidation of the mechanisms for both adsorption processes and catalytic reactions. It should be noted that the proved existence of a surface species does not necessarily prove its participation as an intermediate in a particular process, as often such species have a high degree of stability. However, when DRIFTS data can be augmented by other surface adsorption characterisation data such as temperature programmed desorption studies and catalytic reaction kinetic studies, the evidence for mechanistic involvement of observed adsorbed species can be lent further support.

In this study, the use of a temperature controlled environment cell has allowed a series of *in situ* "snapshots" of the surface adsorption of the catalyst species under reaction conditions for both CH₄ and CO oxidation reactions. The aim of this characterisation is to provide observed evidence for surface complexes which may participate in the reactions, and to further observe how the nature of the surface complexes vary with catalyst composition. Surface composition data for the catalysts was determined using X-ray photoelectron spectroscopy (see sections 3.4, 4.2 and Appendix 3.5) allowing correlation of observed surface adsorption phenomena with accurate surface compositions, rather than less accurate estimations based on the bulk compositions. Further correlation with temperature programmed desorption data (see sections 3.6 and 4.3) and catalytic data (see sections 3.5, 4.5 and Appendix 3.6) can be used to investigate the mechanisms involved in the catalytic reactions. A brief review of the theory of diffuse reflectance infrared Fourier transform spectroscopy is presented in Appendix 3.7.

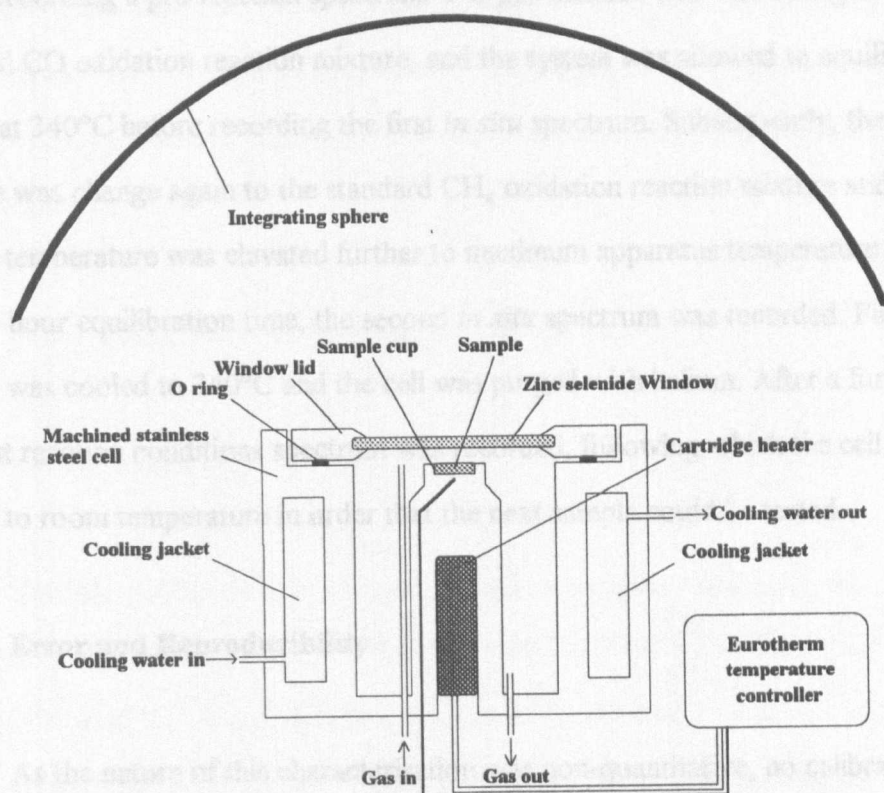
3.7.2 Experimental apparatus

In this study a temperature controlled environment cell (Graseby Specac) was used for all measurements, including sample preconditioning. The environment cell consists of a 3mm depth sample cup mounted in heated metal block. This in turn is encased in a machined stainless steel water-cooled casing. Access to the sample is gained by a removable lid incorporating a zinc selenide window which is infrared transparent in the range 17000cm⁻¹ to 720cm⁻¹. The window lid is affixed to the cell using Allen headed bolts, and sealing is effected using a compressible O-ring.

The temperature of the sample cup block is controlled and monitored using an internal thermocouple and a Graseby Specac control unit utilising a Eurotherm™ controller. The gas environment in the cell is also controllable. In this set-up, gas mixtures of known composition are fed from the micro-reactor system (see section 3.5.1) and through the environment cell. The ability to vary both the temperature and gas environment of the sample allowed the collection of spectra *in situ* under reaction conditions. A schematic diagram of the environment cell is presented in figure 3.6.

Use of the DRIFTS environment cell required the use of the Mattson Galaxy 7020 FTIR spectrometer in transmittance mode, as if recording a transmittance spectrum. 1024 scan averages were recorded for each spectrum between 750cm^{-1} and 4000cm^{-1} , with a resolution of 4cm^{-1} .

Figure 3.6 A schematic diagram of the infrared environment cell



3.7.3 Experimental procedure

The experimental procedure for the DRIFTS analysis of the ceria/lanthana materials was confined to the determination of *in situ* spectra under CO and CH_4 oxidation reaction conditions, and the determination of pre-reaction and post-reaction spectra in order to determine if materials underwent use dependent changes following catalytic reaction.

Before testing each day, desiccated KBr was loaded into the environment cell. The temperature was elevated to 340°C and the cell was purged with helium for 1 hour

before recording a background spectrum. The cell was subsequently cooled to room temperature and the KBr was replaced with the test sample which had been calcined at 600°C for 30 minutes immediately prior to use. This was done in order to ensure decomposition of carbonate material and the removal of adsorbed water, which were an inevitable consequence of storing the materials under atmospheric conditions. Again the temperature was elevated to 340°C and the cell was purged with helium for 1 hour before recording a pre-reaction spectrum. The gas mixture was next changed to the standard CO oxidation reaction mixture, and the system was allowed to equilibrate for 1 hour at 340°C before recording the first *in situ* spectrum. Subsequently, the gas mixture was change again to the standard CH₄ oxidation reaction mixture and the sample temperature was elevated further to maximum apparatus temperature of 500°C. After 1 hour equilibration time, the second *in situ* spectrum was recorded. Finally, the sample was cooled to 340°C and the cell was purged with helium. After a further hour, the post reaction conditions spectrum was recorded, following which the cell was cooled to room temperature in order that the next sample could be tested.

3.7.4 Error and Reproducibility

As the nature of this characterisation was non-quantitative, no calibration or error measurements were considered necessary. The resolution of the instrument under the experimental conditions was 4 cm⁻¹ and the observed absorption bands were observed to be in excellent agreement with reported literature.

Chapter 4 Results and Discussion

This chapter gives account of the results of the characterisation and catalytic studies from experimental work done during the present study. The results are discussed in terms of analogous results in the literature, and with regards development of the experimental methodology. The first results discussed are related to bulk properties of the materials. These results derived from XRD and surface area measurements were of particular relevance to development of the catalyst preparation method and are discussed in terms of chronological development of the materials preparation.

4.1 X-ray Diffractometer and Surface Area Studies

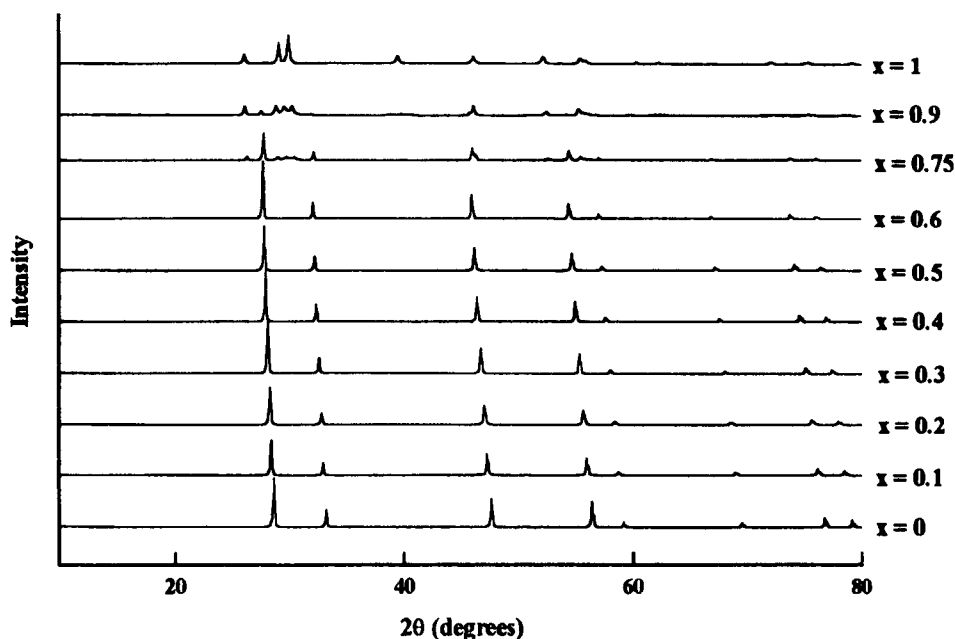
4.1.1 Ceramic samples

The initial XRD studies were performed on samples made using the ceramic method (section 3.1.1) and can be represented by the general formula $\text{Ce}_{1-x}\text{La}_x\text{O}_{2-x/2}$. Values of x were 0, 0.1, 0.2, 0.3, 0.4, 0.5, 0.6, 0.75, 0.9 and 1. Scans were performed between 2θ values of 10° and 80° over a period of 1 hour. The resulting data were used to determine phase composition, lattice parameter and to estimate crystallite size, all with respect to bulk composition. The resulting scans are presented comparatively as an Intensity vs. 2θ plot in figure 4.1. The intensity axis is unitless as each scan has been displaced along this axis for clarity, however, the relative intensities between scans are in proportion.

With regards phase analysis, the characteristic XRD pattern of the cubic fluorite structure is maintained between $x = 0$ and approximately $x = 0.6$, thus confirming the formation of a range of cubic fluorite structured solid solutions of lanthanum in ceria up to a lanthanum concentration of 60 cation %. There is slight evidence at $x = 0.6$ for the presence of a second phase in the appearance of further peaks not characteristic of the fluorite phase. Based on this, the solid solution limit of

lanthanum in ceria can be tentatively estimated as being between $x = 0.5$ and 0.6 . This result is in excellent agreement with literature values.^{42, 50}

Figure 4.1 XRD patterns for $\text{Ce}_{1-x}\text{La}_x\text{O}_{2-x/2}$ for various compositions ($0 < x < 1$), for samples prepared by the ceramic method.



Further observations of the x-ray diffraction patterns show that with increasing lanthanum content between $0 < x < 0.6$ there is a steady shift in the characteristic cubic fluorite peak positions toward lower 2θ values. This is due to the incorporation of a progressively larger concentration of lanthanum cations into the ceria lattice. The larger lanthanum cations (in comparison with cerium cations)⁴¹ result in an expansion of the cubic fluorite lattice, and hence a shift in peak positions toward lower 2θ values. This variation in lattice parameter is discussed next.

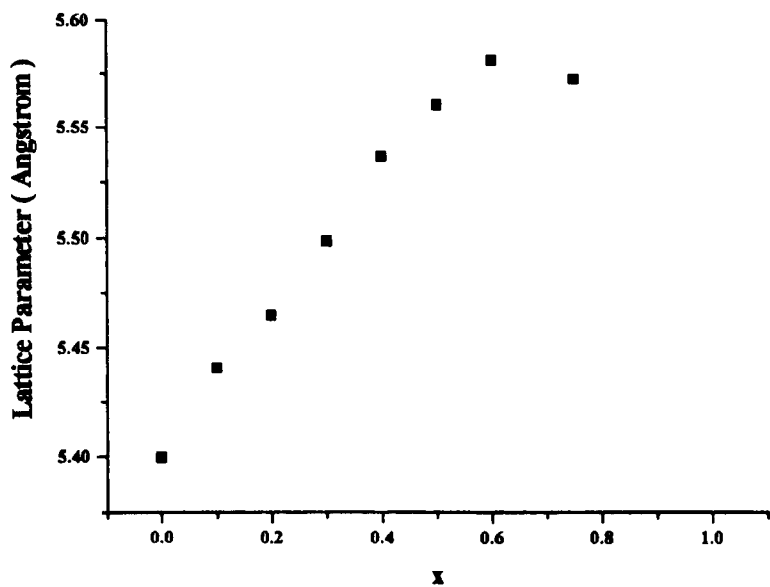
Lattice parameters were determined using the method described in section 3.2.3.2. The lattice parameters thus determined are presented in table 4.1. A full account of the method used for the determination of the average lattice parameter measurements and an error analysis can be found in the X-ray powder diffraction section of the experimental chapter (section 3.2 and subsections therein, and Appendix 3.2).

Table 4.1 Lattice parameter calculations for $\text{Ce}_{1-x}\text{La}_x\text{O}_{2-x/2}$ prepared using the ceramic method.

x	d111	d200	d220	d311	a111 (Å)	a200 (Å)	a220 (Å)	a311 (Å)	Average LP (Å)
0	3.1146	2.6985	1.9097	1.6292	5.395	5.397	5.401	5.403	5.399
0.1	3.1385	2.7198	1.9242	1.6413	5.436	5.440	5.442	5.444	5.440
0.2	3.1496	2.7305	1.9335	1.6498	5.455	5.461	5.469	5.472	5.464
0.3	3.1702	2.7476	1.9452	1.6597	5.491	5.495	5.502	5.505	5.498
0.4	3.1947	2.7670	1.9578	1.6699	5.533	5.534	5.537	5.538	5.536
0.5	3.2065	2.7794	1.9666	1.6775	5.554	5.559	5.562	5.564	5.560
0.6	3.2173	2.7887	1.9747	1.6845	5.572	5.577	5.585	5.587	5.581
0.75	3.2091	2.7834	1.9722	1.6835	5.558	5.567	5.578	5.584	5.572

A more accurate estimation of the solid solution limit by use of a Vergard's law plot can then be determined by examining the variation in average lattice parameter with lanthanum content, as shown in figure 4.2.

Figure 4.2 A plot of lattice parameter variation with lanthanum content for $\text{Ce}_{1-x}\text{La}_x\text{O}_{2-x/2}$ ($0 > x > 1$) prepared by the ceramic method.



It can be observed that with addition of lanthanum to ceria, there is a linear increase in lattice parameter with lanthanum concentration up to approximately $x =$

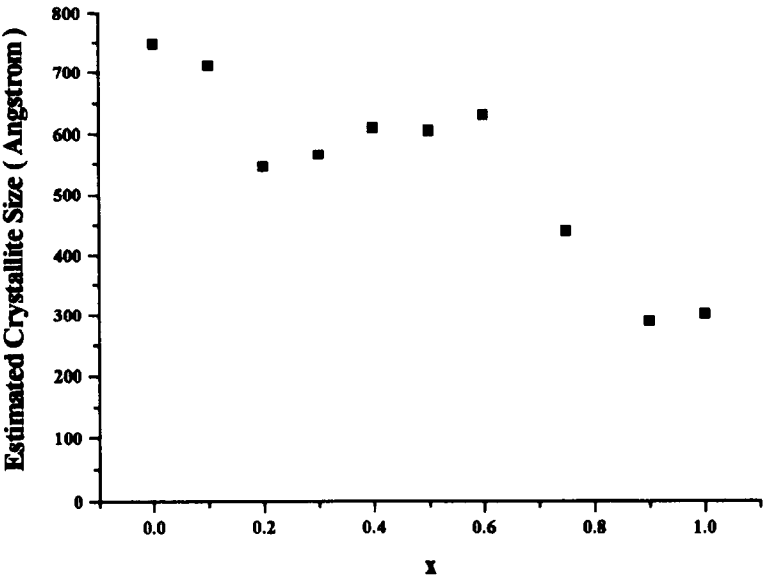
0.6, as would be expected in accordance with Vergard's Law.²⁶ At lanthanum concentrations greater than $x = 0.6$, the lattice parameter of the cubic phase does not show any further increase with further lanthanum additions. The cubic fluorite characteristic peaks were not discernible for $x = 0.9$, therefore only values up to and including $x = 0.75$ were included in the plot. The concentration at which the Vergard's Law linear variation in lattice parameter with lanthanum content is discontinued corresponds to the solid solution limit of lanthanum in ceria; in this case between $x = 0.55$ and 0.6 . The value of x cannot be determined more accurately than this due to only two points being on the constant lattice parameter section. This result is again in excellent agreement with literature data^{30, 42} and with the crude estimate of solid solution limit based on phase analysis. The absolute values of lattice parameters measured were also in good agreement with literature values.^{8 - 10} At the lanthanum rich end of the series, on addition of 10 cation % cerium to lanthana a shift in the characteristic hexagonal close packed (HCP) peaks to higher 2θ values can be observed. This observation is evidence for the incorporation of cerium cations into the lanthana HCP lattice. It would appear that the solubility of cerium in lanthanum is far less than the solubility of lanthanum in ceria.

Finally, the variation in estimated crystallite size with lanthanum content was also investigated in order to gain information regarding the effect of lanthanum doping on sintering properties. The method used for estimation of crystallite size and an error analysis can be found in the X-ray powder diffraction section of the experimental chapter in section 3.2.3.3. The peak selected for analysis was the well resolved 220 reflection which is found in a range of 2θ values below the 47.6° observed for pure ceria. The scans for line broadening were conducted separately to the phase analysis/lattice parameter scans. In order to improve resolution and increase the accuracy of the peak-fitting software, 1 hour scans were completed over a range of 15° in 2θ , centred around the 220 peak position. The summary of the calculations and results of the crystallite size estimation are presented in table 4.2. The variation in crystallite size with lanthanum dopant concentration is presented in figure 4.3.

Table 4.2 Crystallite size estimation calculations and results for $Ce_{1-x}La_xO_{2-x/2}$ prepared using the ceramic method.

x	2θ	θ	cos θ	Constant	FWHM	Crystallite size (Å)
0	47.585	23.793	0.9150	79.44	0.116	748
0.1	47.291	23.646	0.9160	79.44	0.122	711
0.2	46.931	23.466	0.9173	79.44	0.159	545
0.3	46.600	23.300	0.9184	79.44	0.153	565
0.4	46.423	23.212	0.9191	79.44	0.142	609
0.5	46.085	23.043	0.9202	79.44	0.143	604
0.6	45.927	22.964	0.9208	79.44	0.137	630
0.75	45.882	22.941	0.9209	79.44	0.196	440
0.9	46.189	23.095	0.9199	79.44	0.299	289
1	46.256	23.128	0.9196	79.44	0.286	302

Figure 4.3 A plot of the variation in estimated crystallite size with composition for $Ce_{1-x}La_xO_{2-x/2}$ prepared by the ceramic method.



The first observation from the plot of variation in estimated crystallite size with lanthanum dopant concentration is the reduction in crystallite size in comparison with pure ceria caused by the successive additions of 10 and 20 cation % lanthanum dopant. This result suggests that up to an optimum doping level of approximately $x = 0.2$, lanthanum has a significant stabilisation effect with respect to sintering on ceria.

Lanthanum additions between $0.2 < x < 0.6$ result in a near linear reduction in

the sintering stabilisation effect, although there is still a significant stabilisation effect even at $x = 0.6$ in comparison with pure ceria. The reason for the appearance of a minimum in the estimated crystallite size (and therefore a maximum in the stabilisation with respect to sintering) in the $0 < x < 0.6$ solid solution range is unclear, although similar effects have been reported previously in the literature.³⁵ The interpretation of the phenomenon in the literature was due to lanthanum blocking the rate determining step for the sintering process at grain boundaries by the formation of a phase boundary at the contact planes. The rate limiting step was said to be the transfer of oxide ions across the grain boundaries. Such theories do not explain the reduction in the stabilisation effect beyond the peak concentration, and are therefore suspect.

Conductivity measurements⁵³ have determined that oxide ion conductivity in bulk materials is maximised at similar concentrations of lanthanum dopant in ceria, and therefore a tenuous correlation between the two factors is suggested, however the fact that oxide ion conductivity is maximised at a similar concentration to that at which the stabilisation effect is maximised, would suggest that the assignment of oxide ion conductivity as being the rate determining step for the sintering process³⁵ is unlikely.

Beyond $x = 0.6$, there is a discontinuity in the curve pointing to a rapid increase in resistance toward sintering as lanthanum content is increased. The reason for the discontinuity in the sintering behaviour curve at the already determined solid solution limit of approximately $x = 0.6$ is that beyond this level, the estimated average crystallite size will be weighted by the increasing concentration of segregated lanthana. Therefore the reduction in crystallite size observed between $0.6 < x < 1$ can be attributed to what is effectively a dilution of the saturated solid solution crystals within a mass of lanthanum which has an average estimated crystallite size of 302\AA .

Surface area measurements of the materials prepared by the ceramic method were completed using a Micromeritics Single Point Surface Area instrument which was suitable for low specific surface area applications. The theory, operation, calibration and experimental methodology can be found in the experimental chapter, along with an error analysis for the technique, (section 3.3 and subsections therein).

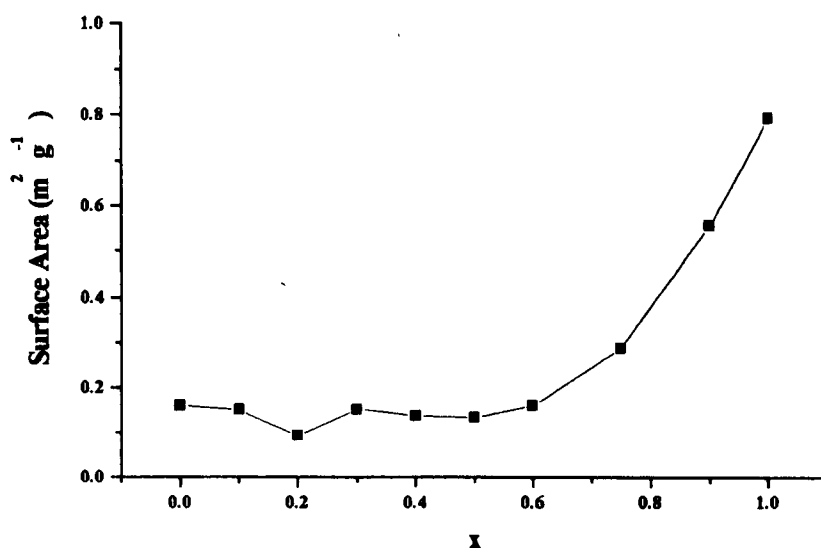
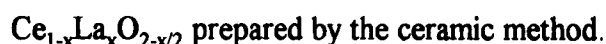
The surface area variation with composition is presented in table 4.3 and plotted in figure 4.4

Table 4.3 Experimental results for specific surface area measurements of ceramic



x	0	0.1	0.2	0.3	0.4	0.5	0.6	0.75	0.9	1
Surface area (m ² g ⁻¹)	0.16	0.15	0.09	0.15	0.14	0.13	0.16	0.29	0.56	0.79

Figure 4.4 A plot of the variation in specific surface area with composition for



It was observed from the results that all measured surface areas for materials prepared by the ceramic method were $< 1 \text{ m}^2\text{g}^{-1}$. No correlation between measured surface area and estimated crystallite size was observed. The low specific surface areas were found to cause detection limit related problems in temperature programmed desorption studies, and cause a requirement for high reaction temperatures in catalytic testing. Due to apparatus limitations the ceramic samples were deemed unsuitable for further testing. The requirement for higher specific surface area materials was met by use of a coprecipitation technique to prepare catalysts which is discussed in the materials preparation section. A further reason for adopting the coprecipitation method was in order to preserve continuity with the initial work to reproduce the results of Mackrodt et al,⁹⁹ the results of which are detailed in Appendix 4.1

4.1.2 Coprecipitated samples

Initial investigations into material and catalytic properties of materials prepared by the coprecipitation method were completed in order to attempt to reproduce literature data reported by Mackrodt.⁹⁹ The reasons for this were twofold so as to validate the experimental set-up and methodology, and to perform a preliminary investigation into the claimed synergistic promotion of catalytic methane oxidation activity by a combination of lanthanum and praseodymium dopants in ceria. The results of these preliminary experiments are presented and discussed in Appendix 4.1.

4.1.3 Calcination Parameters - Investigation and Optimisation.

In the preliminary coprecipitated material study (Appendix 4.1) and to a lesser extent the study of ceramic materials (section 4.1.1), three factors were identified as determining material morphology; dopant (type and concentration), calcination temperature, and the effect of sample pelletisation before calcination. In this section, these factors are investigated in terms of their effect on surface area and estimated crystallite size. The sintering properties of the materials had already been determined by the preliminary study (Appendix 4.1), to be dependent on the presence of lanthanum dopant, such that the dopant retards sintering. As the main limiting factor with respect to optimisation of the preparation process is preservation of surface area, it was necessary to investigate undoped ceria, which was most easily sintered and susceptible to loss of surface area. In order to determine the effect of the presence of dopant over a range of temperatures, 20 cation % lanthanum doped ceria was also investigated. The study on the ceramic samples did not indicate that higher levels of lanthanum resulted in significantly different effects on the sintering behaviour of the material, and therefore 20 cation % lanthanum was assumed to be representative of other dopant concentrations. Finally, the effect of pelletisation of the sample before calcination was also experimentally determined.

The experimental plan was thus devised to investigate the variation in surface area and estimated crystallite size with calcination temperature from a 450°C

decomposition firing (held at temperature for approximately 30 minutes), and then from 500°C to 1400°C at 100°C intervals. Calcination times for the 500°C to 1400°C experiments were 8 hours with 2 hour work-up and work-down times. Pelletisation was effected on 1g aliquots, using a 16mm die, and isostatic pressing at a pressure of 5 tonnes (as used in the ceramic method). The materials investigated were coprecipitated CeO_2 and $\text{Ce}_{0.8}\text{La}_{0.2}\text{O}_{1.9}$.

All pelleted materials were subsequently analysed by XRD, (section 3.2). Scans were performed between 2θ values of 40° and 55° over a period of 1 hour. The resulting data were used to estimate crystallite size. Lattice parameters were not determined as they were not considered relevant to this particular study. Surface areas were determined for all samples using the single point method, (section 3.3).

All materials were assumed to be single phase with the cubic fluorite structure. The experimental results and calculations for the crystallite size estimations are presented in table 4.4. Surface area results for pelleted and unpelleted samples are presented in table 4.5, along with the estimated crystallite sizes for the pelleted materials as calculated in table 4.4.

Table 4.4 Experimental results and estimation of crystallite size for CeO_2 and $\text{Ce}_{0.8}\text{La}_{0.2}\text{O}_{1.9}$ samples calcined unpelleted at various temperatures.

Temp (°C)	x	2 θ	θ	cos θ	Constant	FWHM	Crystallite size Unpelleted (Å)
450(D)	0	47.387	23.6935	0.9157	79.44	0.942	92
500	0	47.445	23.7225	0.9155	79.44	0.827	105
600	0	47.463	23.7315	0.9154	79.44	0.585	148
700	0	47.502	23.751	0.9153	79.44	0.399	218
800	0	47.523	23.7615	0.9152	79.44	0.225	386
1000	0	47.544	23.7720	0.9152	79.44	0.105	827
1200	0	47.529	23.7645	0.9152	79.44	0.085	1012
1400	0	47.549	23.7745	0.9151	79.44	0.097	895
450(D)	0.2	46.918	23.4590	0.9173	79.44	1.414	61
500	0.2	46.941	23.4705	0.9173	79.44	1.313	66
600	0.2	46.913	23.4565	0.9174	79.44	1.044	83
700	0.2	46.905	23.4525	0.9174	79.44	0.728	119
800	0.2	46.861	23.4305	0.9175	79.44	0.503	172
900	0.2	46.892	23.4460	0.9174	79.44	0.368	235
1000	0.2	46.964	23.4820	0.9172	79.44	0.286	303
1100	0.2	46.910	23.4550	0.9174	79.44	0.229	378
1200	0.2	46.926	23.4630	0.9143	79.44	0.160	541
1300	0.2	46.909	23.4545	0.9174	79.44	0.133	651
1400*	0.2	47.000	23.5000	0.9171	79.44	0.27	321
1400#	0.2	46.967	23.4835	0.9172	79.44	0.201	431

Notes

D Decomposition firing only - approximately 30 minutes at 450°C in air.

* XRD scan performed on silica slide due to small amount

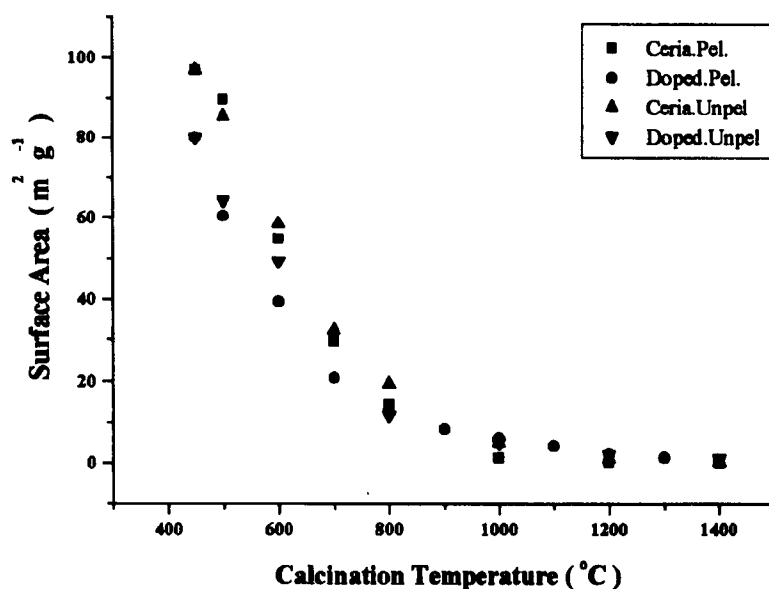
Previous scan of 1400 * using larger amount. Scanned over 10° - 80° in 1 hour.

Table 4.5 Surface area results and estimated crystal sizes for pelleted and unpelleted CeO_2 and $\text{Ce}_{0.8}\text{La}_{0.2}\text{O}_{1.9}$ samples calcined at various temperatures.

Temp (°C)	x	Crystallite size Unpelleted (Å)	Surface Area Pelleted (m^2g^{-1})	Surface Area Unpelleted (m^2g^{-1})
450(D)	0	92	96.8	96.8
500	0	105	89.6	85.3
600	0	148	54.7	58.4
700	0	218	29.5	32.1
800	0	386	14.2	19.4
1000	0	827	1.1	4.8
1200	0	1012	0.1	0.9
1400	0	895	< 0.1	0.1
450(D)	0.2	61	79.9	79.9
500	0.2	66	60.3	64.2
600	0.2	83	39.3	49.2
700	0.2	119	20.8	-
800	0.2	172	12.8	11.5
900	0.2	235	8.2	-
1000	0.2	303	5.8	4.9
1100	0.2	378	4.1	-
1200	0.2	541	2.2	1.9
1300	0.2	651	1.2	-
1400*	0.2	321	0.6	0.9
1400#	0.2	431	0.6	0.9

As would be expected, there is a general increase in estimated crystallite size with calcination temperature, which is accompanied by a decrease in surface area. This data is plotted in figures 4.5 and 4.6.

Figure 4.5 A plot of the variation in specific surface area with calcination temperature for pelleted and unpelleted CeO_2 and $\text{Ce}_{0.8}\text{La}_{0.2}\text{O}_{1.9}$.



It is observed from figure 4.5 that the pelletisation process has negligible influence over the post calcination surface areas, when compared with unpelleted analogues. It was thus decided that pelletisation was an unnecessary step in the preparation procedure, therefore all samples prepared henceforth were calcined unpelleted. In these experiments, the stabilisation of higher surface areas by dopant retardation of the sintering rate was not evident, indeed the surface areas of the undoped materials was consistently higher than that of the doped materials up to temperatures approximately $> 800^\circ\text{C}$. The reason for this was not clear, as all samples of the same composition were calcined simultaneously in the same furnace. At temperatures $> 800^\circ\text{C}$, little difference in surface area was observed between any of the samples calcined at a given temperature, indicating that the rate of sintering at such temperatures was effectively composition independent. Beyond 1000°C , there is little observed change in surface area with increasing calcination temperature, indicating that the materials are at, or very near theoretical density.

With regards optimisation of the preparation process, there were several factors for consideration. Regarding characterisation apparatus, the maximum temperature that any catalyst test could be run at was 700°C , although to optimise longevity of the apparatus, 600°C was set as an arbitrary limit. In order to avoid use

dependent changes in the catalyst materials, (particularly due to exposure to temperatures above the calcination temperature), the minimum catalyst calcination temperature should be significantly higher than the catalytic reaction temperature. Due to the possibility of an exotherm in the catalyst bed, it was decided that 200°C would be an adequate calcination/reaction temperature margin. Therefore, the minimum calcination temperature was derived as 800°C.

In contrast to this, the accuracy of the measurement of surface area, and indeed the accuracy of the measured activity of the catalyst are proportional to the surface area of the catalyst. It was therefore also desirable to use as low a calcination temperature as possible in order to preserve the maximum possible surface area. It was thus decided to use the minimum calcination temperature (as decided with regards the maximum catalytic reaction temperature), 800°C, as the optimum calcination temperature. With reference to figure 4.5, a calcination temperature of 800°C results in materials with surface areas in the approximate range 10 - 20 m²g⁻¹. Assuming that other materials with different dopant concentrations would not deviate significantly from this range, this surface area range was deemed adequate.

The variation in crystallite size with calcination temperature for the same unpelleted samples used for the surface area study was also determined. The variation in estimated crystallite size with calcination temperature is shown in figure 4.6. For both doped and undoped ceria, estimated crystallite size is observed to increase with calcination temperature, as expected. Beyond approximately 1300°C there is a discontinuity in the plots for both materials, but this is most likely to be due to experimental error due to small sample sizes. The 20 cation % lanthanum doped material is observed to be stabilised with respect to sintering at all temperatures, with respect to undoped ceria. This stabilisation is not reflected in the relative surface areas between doped and undoped materials, as discussed previously. It is of interest at this point to compare the variation in surface area with estimated crystallite size for both the lanthanum doped and undoped material. This comparison is shown in figure 4.7.

Figure 4.6 A plot showing variation in crystallite size with calcination temperature for CeO_2 and $\text{Ce}_{0.8}\text{La}_{0.2}\text{O}_{1.9}$, calcined unpelleted for 8 hours.

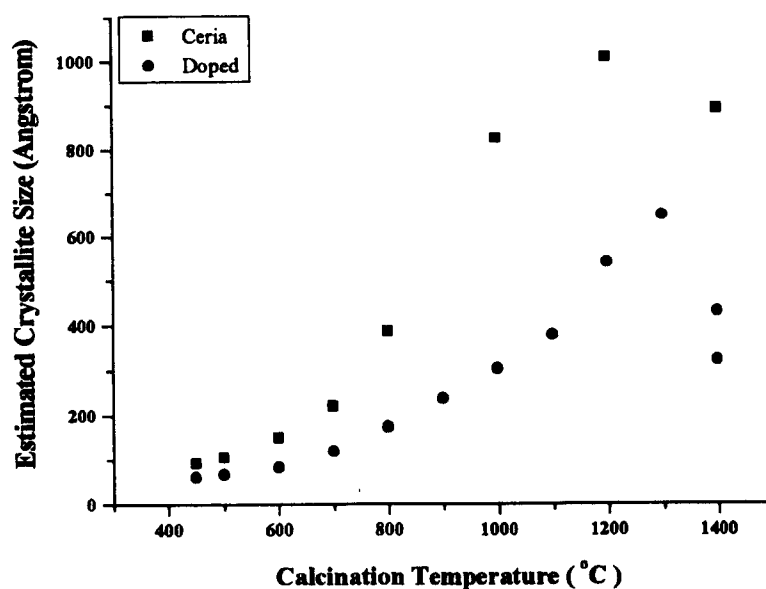
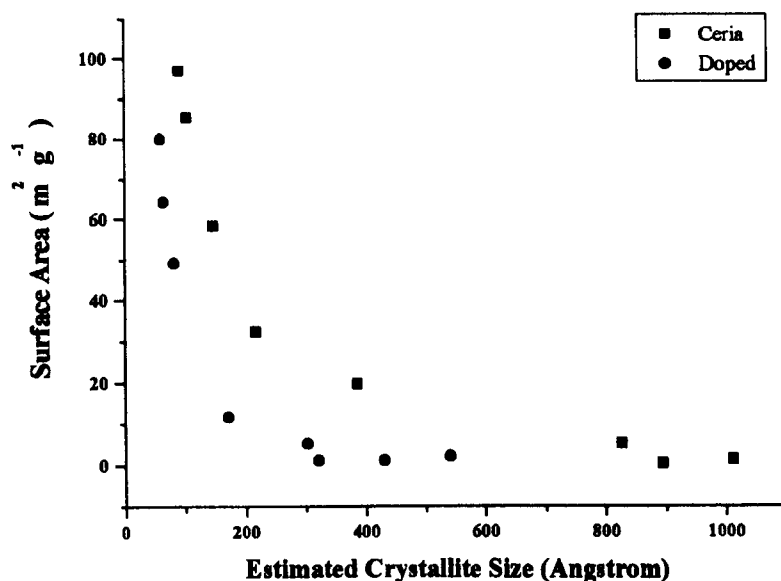


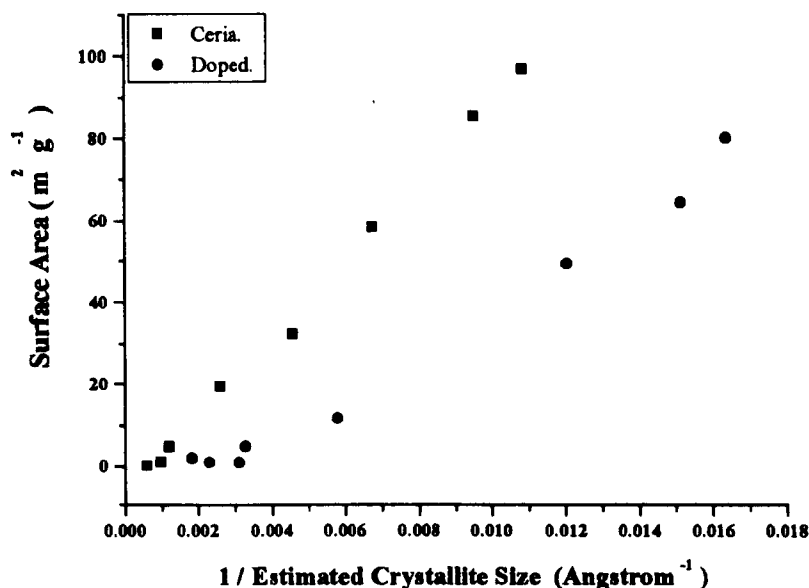
Figure 4.7 A plot of the variation in surface area with crystallite size for 20 cation % lanthanum doped and undoped ceria.



The variation in surface area is found to be inversely proportional to that of estimated crystallite size. A plot of surface area vs. $1/\text{estimated crystallite size}$ is shown in figure 4.8 to demonstrate this point. It can be observed that surface area varies linearly for both materials with $1/\text{estimated crystallite size}$, up to higher temperatures where the plot breaks down due to experimental error and the limitations of the crystallite size estimation process. Each material has a different slope indicating that the relationship

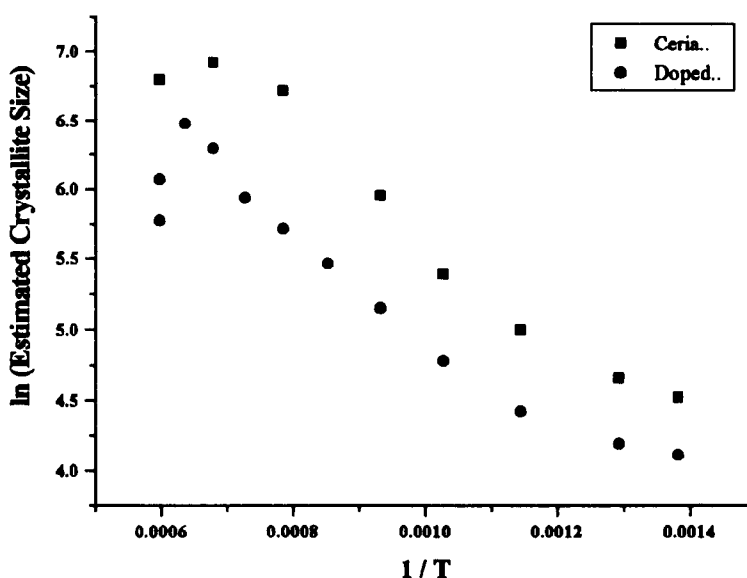
between surface area and crystallite size is not the same for both materials. The plots converge at high temperature due to the reduction in the rate of change in surface area with crystallite size as theoretical density is approached. The experimental limitations of the surface area measurements also become more significant for the lower surface area materials.

Figure 4.8 A plot of the variation in surface area with $1/\text{estimated crystallite size}$ for unpeletted ceria and 20 cation % lanthanum doped ceria.



It is possible at this point to determine an enthalpy for the sintering process for each material by use of the Arrhenius method, plotting $\ln(\text{estimated crystallite size})$ vs. $1/T$. The slope of the graph is proportional to the enthalpy of the sintering process. Arrhenius plots for both ceria and 20 cation % lanthanum doped ceria are presented in figure 4.9. It can be observed from figure 4.9 that if the high and low temperature regions are ignored, the linear portions of both plots are roughly parallel. This indicates that the sintering process in both doped and undoped materials is likely to be similar. The sintering process enthalpies of both materials are determined by the Arrhenius method to be approximately $6.5 \text{ kcal mol}^{-1}$ (27.2 kJ mol^{-1}), which is of the order expected for ionic diffusion processes.

Figure 4.9 Arrhenius-type plots for the sintering process in ceria and 20 cation % lanthanum doped ceria.

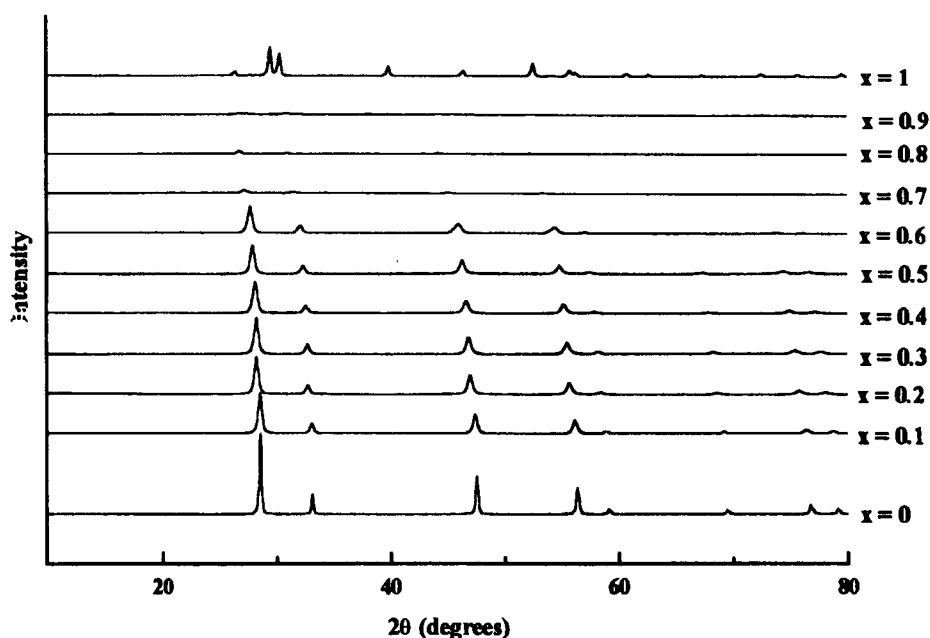


4.1.4 Systematic Study

Following the above study on the variation in surface area and crystallite size with calcination temperature pelleting and the presence of dopant on coprecipitated samples, the calcination procedure was standardised. All samples discussed hereon were calcined at 800°C for 8 hours in air, unpelleted, unless specifically stated otherwise. These samples were used for the systematic characterisation and catalytic studies which are discussed later in this chapter.

XRD studies were performed on a series of samples made using the coprecipitation method (section 4.1.2) using the now standard calcination procedure. Values of x were 0, 0.1, 0.2, 0.3, 0.4, 0.5, 0.6, 0.7, 0.8, 0.9 and 1. Scans were performed between 2θ values of 10° and 80° over a period of 1 hour. The resulting data were used to determine phase composition, lattice parameter and to estimate crystallite size, all with respect to bulk composition. The resulting scans are presented comparatively as an Intensity vs. 2θ plot in figure 4.10. The intensity axis is unitless as each scan has been displaced along this axis for clarity, however, the relative intensities between scans are in proportion.

Figure 4.10 XRD patterns for $\text{Ce}_{1-x}\text{La}_x\text{O}_{2-x/2}$ for compositions $0 < x < 1$, samples prepared by the standard coprecipitation method.



With regards phase analysis, the characteristic XRD pattern of the cubic fluorite structure is maintained between $x = 0$ and $x = 0.6$, (similarly to materials prepared by the ceramic method), again confirming the formation of a range of cubic fluorite structured solid solutions of lanthanum in ceria up to a lanthanum concentration of 60 cation %. There is little evidence at $x = 0.6$ for the presence of a second phase, the appearance of further peaks not characteristic of the fluorite phase becoming apparent at $x = 0.7$. Based on this, the solid solution limit of lanthanum in ceria can be tentatively estimated as $x = 0.6$. This result is again in good agreement with literature values^{30, 42} and with the previous results from analogous materials prepared by the ceramic method.

The somewhat surprising result of the solid solution limit of lanthanum in ceria appearing to be slightly higher for the coprecipitated materials than for the ceramic materials can be explained in terms of the relative crystallinity of the secondary phase between the two methods, which is in turn dependent on the temperature of calcination. The ceramic materials were calcined in air at 1400°C for 24 hours, whereas the coprecipitated samples were calcined for just 8 hours at 800°C . At lanthanum concentrations exceeding the solid solution limit, the second phase in the

coprecipitated materials is bound to be more amorphous than in the case of the ceramic materials, due to the reduced level of sintering inherent from the more gentle thermal treatment. The result of this is that the second phase will not become determinable by XRD phase analysis until higher concentrations are reached in the coprecipitated materials than would be required for the ceramic materials.

Further observations of the x-ray diffraction patterns show that with increasing lanthanum content between $0 < x < 0.6$ there is a steady shift in the characteristic cubic fluorite peak positions toward lower 2θ values. As mentioned previously, this is due to the incorporation of progressively larger concentrations of lanthanum cations into the ceria lattice. The larger lanthanum cations (in comparison with cerium cations)⁴¹ result in an expansion of the cubic fluorite lattice, and hence a shift in peak positions toward lower 2θ values.

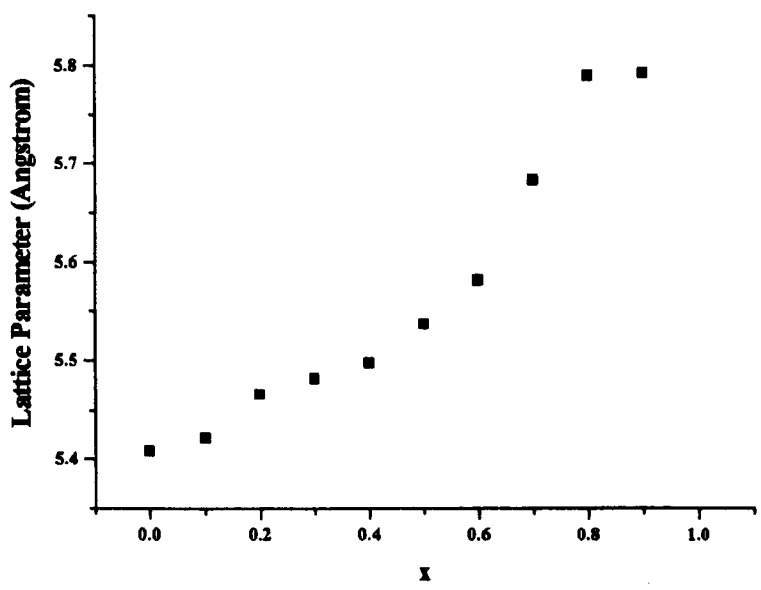
Lattice parameters were determined using the method described in section 3.2.3.2. The lattice parameters thus determined are presented in table 4.6. A full account of the method used for the determination of the average lattice parameter measurements and an error analysis can be found in the X-ray powder diffraction section of the experimental chapter in section 3.2.

Table 4.6 Lattice parameter calculations for $\text{Ce}_{1-x}\text{La}_x\text{O}_{2-x/2}$ prepared using the coprecipitation method.

x	d111	d200	d220	d311	a111 (Å)	a200 (Å)	a220 (Å)	a311 (Å)	Average LP (Å)
0	3.1200	2.7046	1.9122	1.6311	5.404	5.409	5.409	5.410	5.408
0.1	3.1295	2.7062	1.9189	1.6357	5.420	5.412	5.427	5.425	5.421
0.2	3.1581	2.7305	1.9313	1.6492	5.470	5.461	5.463	5.470	5.466
0.3	3.1642	2.7366	1.9389	1.6546	5.481	5.473	5.484	5.488	5.481
0.4	3.1625	2.7480	1.9432	1.6641	5.478	5.496	5.496	5.519	5.497
0.5	3.1894	2.7637	1.9610	1.6733	5.524	5.527	5.547	5.550	5.537
0.6	3.2108	2.7863	1.9763	1.6889	5.561	5.573	5.590	5.601	5.581
0.7	3.2809	2.8330	2.0095	1.7191	5.683	5.666	5.684	5.702	5.684
0.8	3.3370	2.8899	2.0516	1.7487	5.780	5.780	5.803	5.800	5.791
0.9	3.3389	2.8911	2.0505	1.7507	5.783	5.782	5.800	5.806	5.793

A more accurate estimation of the solid solution limit by use of a Vergard's law plot can then be made by examining the variation in average lattice parameter with lanthanum content, as shown in figure 4.11.

Figure 4.11 A plot of lattice parameter variation with lanthanum content for $Ce_{1-x}La_xO_{2-x/2}$ ($0 > x > 1$) prepared by the coprecipitation method.



It can be observed that with addition of lanthanum to ceria, there is a linear increase in lattice parameter with lanthanum concentration up to approximately $x = 0.5$ to 0.6 , as would be expected in accordance with Vergard's Law.²⁶ The linearity of the plot is not as well defined as was observed with the materials prepared by the ceramic method, but is adequate. At lanthanum concentrations greater than $x = 0.6$, the lattice parameter of the cubic phase as measured increases rapidly with further lanthanum additions. The lattice parameter was not observed to reach a constant maximum value with increasing lanthanum concentration in this study of the coprecipitated materials, mainly due to complications in peak identification due to the onset of the appearance of additional peaks from the second phase from approximately $x = 0.7$ onwards. Several of these peaks were near coincident with the shifted peaks characteristic of the saturated solid solution. As it was not possible to determine a constant cubic fluorite saturated solid solution lattice parameter beyond $x = 0.6$, a 'best estimation' approach was thus used - effectively continuing to follow the shifts of the 'same' peaks, although

it is likely that their assignment changed from a characteristic cubic peak to that of a characteristic HCP peak with increasing lanthanum concentration. The discontinuity in the linear plot in the Vergard's Law region (approximately $0 < x < 0.6$) and the linear region beyond this (approximately $0.7 < x < 0.9$), allowed the determination of the solid solution limit, similarly to the situation where the discontinuity is characterised by a constant lattice parameter corresponding to a saturated solid solution. The solid solution limit of lanthanum in ceria made by the coprecipitation method was therefore determined to be between $x = 0.55$ and 0.6 , again in agreement with literature values,^{30, 42} the estimated value based on phase analysis observations, and the value determined for materials made by the ceramic process, as discussed previously.

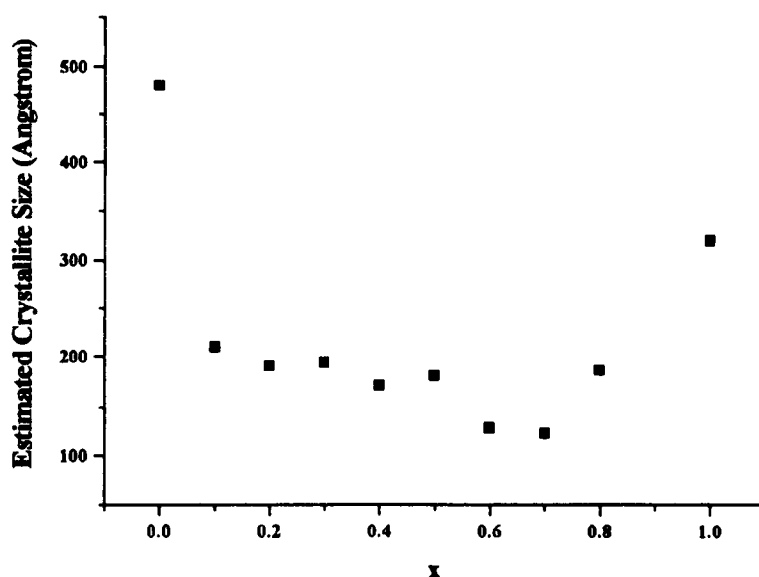
As with the materials prepared by the ceramic method, at the lanthanum rich end of the series, on addition of 10 cation % cerium to lanthana a shift in the characteristic hexagonal close packed (HCP) peaks to higher 2θ values was observed. A further addition of 20 cation % cerium to lanthana resulted in a complicated diffraction pattern which prevented accurate peak assignment. This observation is presented as limited evidence for the incorporation of cerium cations into the lanthana HCP lattice. It would appear to confirm that the solubility of cerium in lanthanum, although significant, is far less than the solubility of lanthanum in ceria.

The variation in estimated crystallite size with lanthanum content was also investigated in order to gain information regarding the effect of lanthanum doping on sintering properties. The method used for estimation of crystallite size and an error analysis can be found in the X-ray powder diffraction section of the experimental chapter in section 3.2. The peak selected for analysis was the well resolved 220 reflection which is found in a range of 2θ values below the 47.6° observed for pure ceria. The scans for line broadening were conducted separately to the phase analysis/lattice parameter scans in order to improve resolution and increase the accuracy of the peak-fitting software. Scans were completed over a range of 15° in 2θ , centred around the 220 peak position and were conducted over 1 hour. The summary of the calculations and results of the crystallite size estimation are presented in table 4.7. The variation in crystallite size with lanthanum dopant concentration is presented in figure 4.12.

Table 4.7 Crystallite size estimation calculations and results for $\text{Ce}_{1-x}\text{La}_x\text{O}_{2-x/2}$ prepared using the standard coprecipitation method.

x	2θ	θ	$\cos \theta$	Constant	FWHM	Crystallite size (Å)
0	47.510	23.755	0.9153	79.44	0.182	477
0.1	47.354	23.677	0.9158	79.44	0.416	209
0.2	46.933	23.467	0.9173	79.44	0.457	190
0.3	46.790	23.395	0.9178	79.44	0.449	193
0.4	46.577	23.289	0.9185	79.44	0.508	170
0.5	46.243	23.122	0.9197	79.44	0.479	180
0.6	45.903	22.952	0.9208	79.44	0.674	128
0.7	45.070	22.535	0.9236	79.44	0.702	123
0.8	44.134	22.067	0.9267	79.44	0.460	187
1	46.391	23.196	0.9192	79.44	0.270	320

Figure 4.12 A plot of the variation in estimated crystallite size with composition for $\text{Ce}_{1-x}\text{La}_x\text{O}_{2-x/2}$ prepared by the standard coprecipitation method.

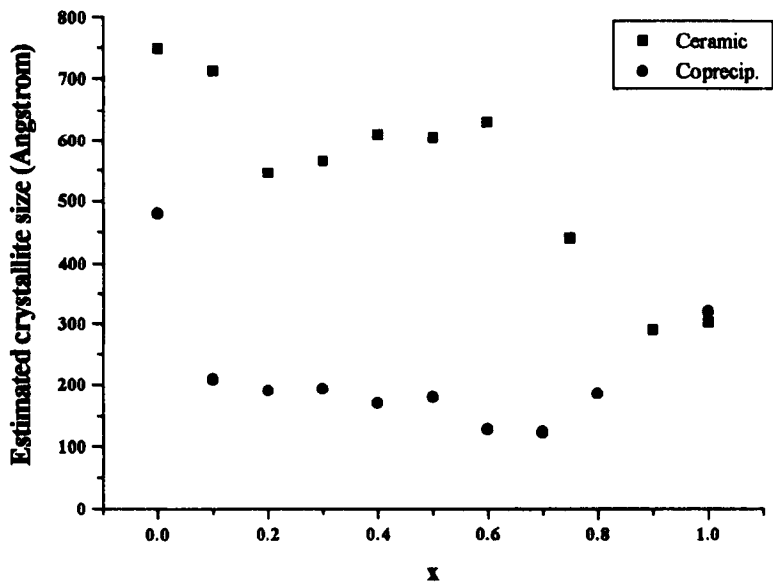


The first observation from the plot of variation in estimated crystallite size with lanthanum dopant concentration is that crystallite sizes are far smaller than for the analogous materials prepared using the ceramic method. This result is as expected given that the higher temperature treatment involved in the ceramic preparation should result in increased levels of sintering. A dramatic reduction in crystallite size in comparison with pure ceria is observed on addition of 10 cation % lanthanum dopant.

Further additions of lanthanum up to the solid solution limit of lanthanum in ceria ($x = 0.6$) result in a further slight increase in the stabilisation effect with respect to sintering, with increasing lanthanum dopant concentration. This progressive effect is, however, much less marked than that between $x = 0$ and $x = 0.1$. It would appear that in contrast with the higher temperature ceramic preparation, the lower temperature treatment used in the coprecipitation method is far more sensitive to the effect of small concentrations of lanthanum dopant. The magnitude of the stabilisation effect of lanthanum doping with respect to sintering is also greater for the coprecipitated samples. At lanthanum dopant levels between $0.7 < x < 1$, a discontinuity in the approximately linear variation in crystallite size with increasing lanthanum content is observed, similarly to that observed in the study of materials prepared by the ceramic method. However, in the case of coprecipitated materials, the crystallite size varies in a linear fashion toward a higher value with increasing lanthanum content, rather than toward a lower value as observed with the ceramic materials. The discontinuity originates at the solid solution limit and in this case the estimated average crystallite size is again weighted by the crystallite size of the increasing concentration of segregated lanthana above the solid solution limit. The linear increase in crystallite size observed between $0.7 < x < 1$ can thus be attributed to what is effectively a dilution of the saturated solid solution crystals within a separate lanthana phase (which has an average estimated crystallite size of 320\AA). It is interesting at this point to compare the estimated crystallite sizes of ceria and lanthana prepared by the ceramic and coprecipitation method. With regards ceria, the ceramic material has a far higher crystallite size (748\AA), than the coprecipitated material (477\AA). This can be attributed to increased sintering under the higher temperature regime of the ceramic process. However, in the case of lanthana, the ceramic material has a crystallite size which is effectively the same as that prepared by the coprecipitation method. The values for the ceramic material (302\AA) and the coprecipitated material (320\AA) are separated by only 18\AA . As each of the measured values has been determined to have an estimated error of $\pm 5\%$ (i.e., approximately 16\AA), these values are effectively identical. The independence of lanthana crystallite size with respect to preparation technique, and particularly to thermal history was an unexpected result and indicative of significantly different ionic transport mechanisms in

the cubic fluorite and HCP structures. The relative difference between the estimated crystallite sizes for materials prepared by the ceramic and coprecipitation method, with lanthanum dopant concentration is presented in figure 4.13.

Figure 4.13 A comparative plot of the variation in estimated crystallite size with x for $Ce_{1-x}La_xO_{2-x/2}$ for ceramic and coprecipitated materials.



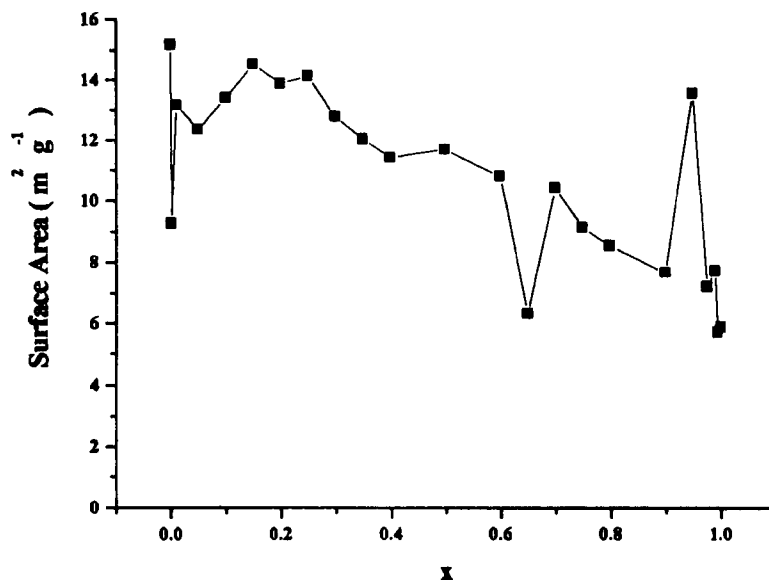
Finally, the variation in surface area with composition was investigated for samples prepared by the coprecipitation method using the standard calcination. Surface areas were determined using the single point method (section 3.3 and subsections therein), and the results of the experimental work are presented (alongside the results of the estimated crystallite sizes), in table 4.8. This table contains the surface area data for all samples made by the coprecipitation method using the standard calcination treatment. The samples include the full systematic study of lanthanum doped ceria, and ceria doped with other selected lanthanides.

Table 4.8 A comparison between surface area and crystallite size variations with composition for $\text{Ce}_{1-x}\text{La}_x\text{O}_{2-x/2}$ ($0 < x < 1$) and other selected dopants at the indicated levels, prepared by the standard coprecipitation method.

x	Estimated Crystallite Size (Å)	Surface Area (m²g⁻¹)
0.000	477	15.2
0.001	-	9.3
0.010	-	13.2
0.050	-	12.4
0.100	209	13.4
0.150	-	14.5
0.200	190	13.9
0.250	-	14.1
0.300	193	12.8
0.350	-	12.1
0.400	170	11.4
0.500	180	11.7
0.600	128	10.8
0.650	-	6.3
0.700	123	10.4
0.750	-	9.1
0.800	187	8.5
0.900	-	7.7
0.950	-	13.6
0.975	-	7.2
0.990	-	7.7
0.995	-	5.7
1.000	320	5.9
0.200 Pr	-	17.9
0.200 Gd	-	18.6
0.100 La + 0.100 Pr	-	19.0
Nb	-	15.0

The variation in surface area with composition for $\text{Ce}_{1-x}\text{La}_x\text{O}_{2-x/2}$ ($0 < x < 1$) prepared by the coprecipitation method using standard calcination is shown in figure 4.14.

Figure 4.14 A plot showing the variation in surface area with composition for $\text{Ce}_{1-x}\text{La}_x\text{O}_{2-x/2}$ ($0 < x < 1$) prepared by the standard coprecipitation method.



It can be observed from figure 4.14 that surface areas for the $\text{Ce}_{1-x}\text{La}_x\text{O}_{2-x/2}$ ($0 < x < 1$) series fall in the approximate range of 5 - 15 m^2g^{-1} . This range of surface areas is therefore between 1 and 2 orders of magnitude greater than analogous materials prepared using the ceramic method. There is a general trend within the series for a decrease in surface area with x , although there is less than a factor of three difference between the lowest and highest measured surface areas. There are three discontinuities in the surface area trend with composition. At low lanthanum doped ceria, at low cerium doped lanthana, and at $x = 0.65$, marked deviations are observed. At $x = 0.65$ there is a sharp spike in the trend toward lower surface areas. This is of interest as $x = 0.65$ has been determined to be the approximate solid solution limit for lanthanum in ceria and thus is worthy of note, however as the spike is based on a single data-point alone, it is possible that the deviation is due to experimental error in either the preparation or surface area measurement. Of more interest are the deviations at low and high x . It should be noted that once more the two deviations are also based on single data-points at $x = 0.001$ and at $x = 0.95$, although the general trend in the points surrounding both of these regions suggest that the observed effects may be real rather than caused by experimental error. When placed in context of solid state materials

characterisation only, the magnitude of the variations in surface area, the trend across the series and the deviations mentioned are relatively insignificant. The exact values of the surface area are however crucial in the determination of specific catalytic activity and specific basicity, both of which are discussed later in this chapter in section 4.5. No correlations between surface area and estimated crystallite size were observed for the $\text{Ce}_{1-x}\text{La}_x\text{O}_{2-x/2}$ ($0 < x < 1$) series.

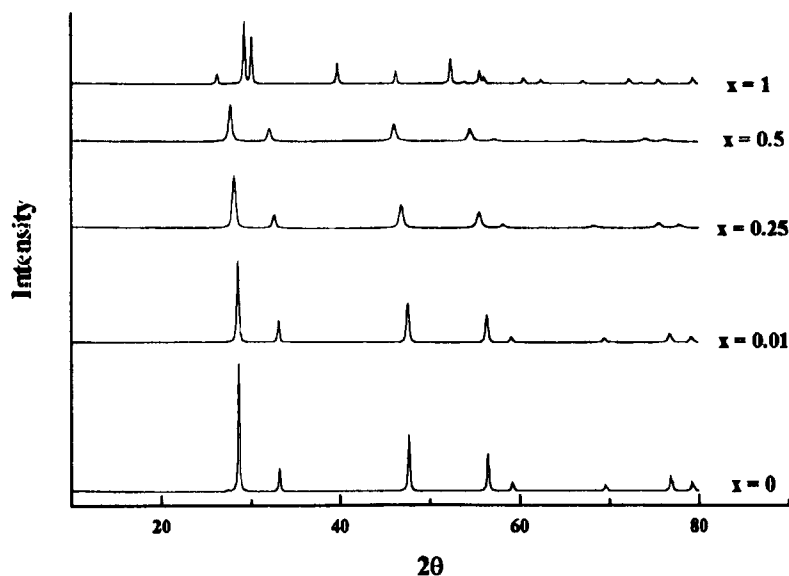
4.1.5 Sintering study

The previous section described the differences in sintering behaviour between the ceria/lanthana series of materials prepared by the ceramic method and the coprecipitation method. In order to further investigate the solid state properties of these materials, a further set of experiments were performed on materials prepared using the coprecipitation method. The effect of variations in calcination temperature and calcination time were investigated for selected compositions.

In order to investigate the effect of calcination temperature, materials of selected compositions were examined after initial decomposition at 450°C (oxide precursors), and then after 8 hours at 600°C, 800°C and 1000°C. Five different compositions were selected for the temperature variation study; pure ceria and pure lanthana were selected first. As end-members of the ceria/lanthana mixed oxide materials, these samples were intended to function as reference samples for the other compositions within the series. The rest of the selected samples were chosen so as to investigate the effect of solid solution composition. As it had been previously observed that the addition of just 10 cation % lanthanum to ceria resulted in significant changes in sintering properties for coprecipitated materials, the effect of very low lanthanum dopant concentration on the sintering properties of ceria was determined with a 1 cation % concentration ($x = 0.01$). It was also of interest to determine the effect of high and middling lanthanum levels within the solid solution range. As the solid solution concentration limit had been previously determined for lanthanum in ceria as approximately $x = 0.55$ to 0.6 , lanthanum concentrations of 50 cation % ($x = 0.5$) and 25 cation % ($x = 0.25$) were selected.

Calcinations were performed in air for 8 hours, as in the standard coprecipitation method used for the systematic composition variation study. As with the previous XRD studies, phase analysis, lattice parameter and crystallite size were determined for all samples. With regards phase analysis, all materials were determined to be single phase; all ceria/lanthana material diffraction patterns were characteristic of the cubic fluorite structure, whilst all of the $x = 1$ samples were determined to be HCP. Single phase solid solutions were found to form after the initial decomposition process at 450°C , even for lanthanum concentrations as high as $x = 0.5$. As lanthanum concentrations were increased, a shift in diffraction pattern peaks was observed, due to the incorporation of lanthanum into the ceria lattice. An example of peak shift with increasing lanthanum concentration is shown in figure 4.15 for materials prepared at 800°C .

Figure 4.15 Diffraction patterns for $\text{Ce}_{1-x}\text{La}_x\text{O}_{2-x/2}$ for $x = 0, 0.01, 0.25, 0.5$ and 1, all calcined at 800°C

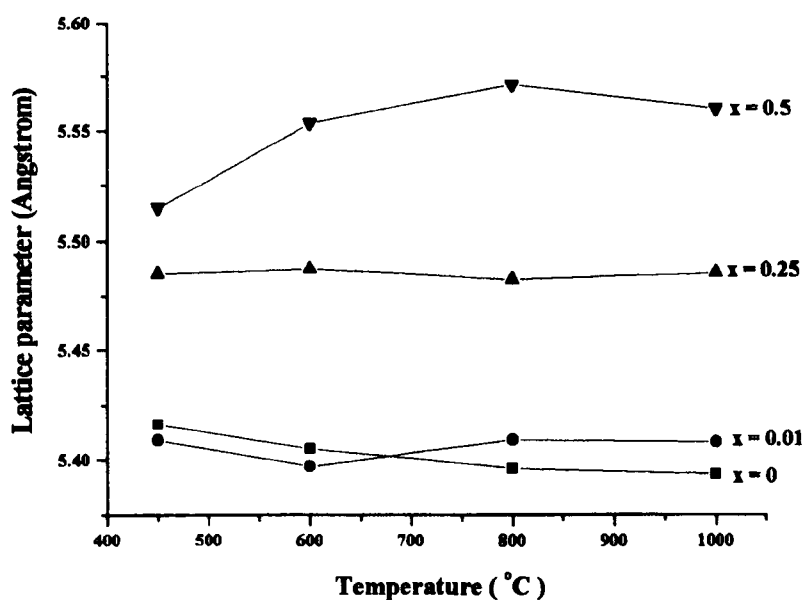


Lattice parameters were determined for the cubic structured materials ($x = 0, 0.01, 0.25$ and 0.5). The calculations for the variation in lattice parameter with temperature is shown in table 4.9, and the results are presented in figure 4.16.

Table 4.9 Lattice parameter calculations for the variation in lattice parameter with calcination temperature for cubic fluorite solid solutions $Ce_{1-x}La_xO_{2-x/2}$.

Temp (°C)	x	d111	d200	d220	d311	a111 (Å)	a200 (Å)	a220 (Å)	a311 (Å)	Av. LP (Å)
450	0	3.1133	2.7046	1.9209	1.6373	5.392	5.409	5.433	5.430	5.416
600	0	3.1216	2.7010	1.9113	1.6292	5.407	5.402	5.406	5.403	5.405
800	0	3.1112	2.6961	1.9092	1.6290	5.389	5.392	5.400	5.403	5.396
1000	0	3.1088	2.6949	1.9085	1.6284	5.385	5.390	5.398	5.401	5.393
450	0.01	3.1165	2.7026	1.9150	1.6326	5.398	5.405	5.416	5.415	5.409
600	0.01	3.1053	2.7038	1.9107	1.6272	5.379	5.408	5.404	5.397	5.397
800	0.01	3.1194	2.7036	1.9135	1.6319	5.403	5.407	5.412	5.412	5.409
1000	0.01	3.1192	2.7032	1.9126	1.6316	5.403	5.406	5.410	5.411	5.408
450	0.25	3.1578	2.7488	1.9409	1.6527	5.470	5.498	5.490	5.481	5.485
600	0.25	3.1730	2.7445	1.9379	1.6532	5.496	5.489	5.481	5.483	5.487
800	0.25	3.1628	2.7409	1.9389	1.6535	5.478	5.482	5.484	5.484	5.482
1000	0.25	3.1636	2.7407	1.9406	1.6550	5.480	5.481	5.489	5.489	5.485
450	0.5	3.2774	3.1350	1.9514	1.3856	5.677	6.270	5.519	4.596	5.515
600	0.5	3.2034	2.7765	1.9634	1.6761	5.548	5.553	5.553	5.559	5.553
800	0.5	3.2159	2.7794	1.9719	1.6816	5.570	5.559	5.577	5.577	5.571
1000	0.5	3.2065	2.7762	1.9712	1.6770	5.554	5.552	5.575	5.562	5.561

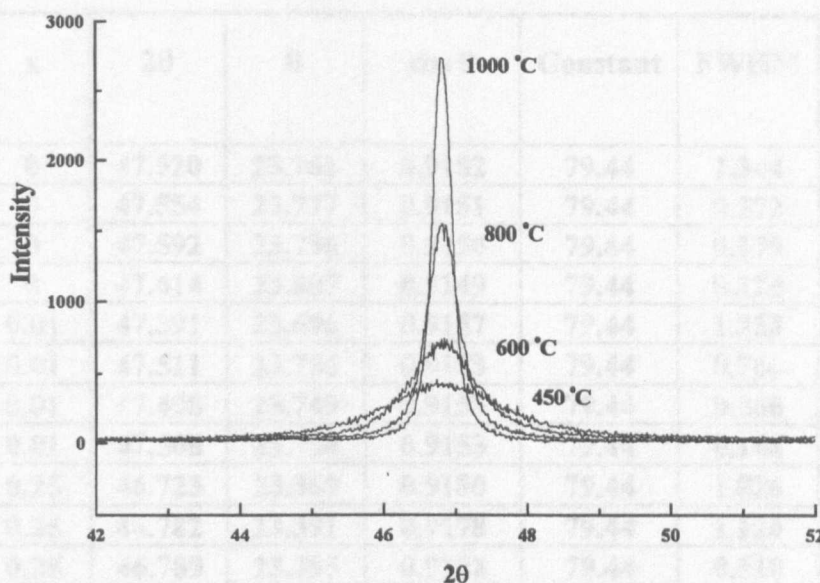
Figure 4.16 A plot of the variation in lattice parameter with calcination temperature for cubic fluorite solid solutions $Ce_{1-x}La_xO_{2-x/2}$.



The first observation from figure 4.16 is that for $x = 0, 0.01$ and 0.25 , there is little variation in lattice parameter with calcination temperature. At $x = 0.5$ however, an increase in lattice parameter is observed with temperature, up to between 600°C and 800°C . This suggests that the more concentrated solid solutions require more forcing conditions for complete solution formation. From this result, it would be expected that phase analysis of the $x = 0.5$ samples would reveal evidence of multiple phase composition for the lower temperature calcinations, and marked peak shifts to lower 2θ values with increasing temperature. This was not observed in the diffraction patterns, however, even after the 450°C decomposition firing. This is probably due to the second phase concentration detection limit of the XRD apparatus, in combination with relatively low crystallinity resulting in no observed characteristic HCP reflections. There is a general increase in lattice parameter with increasing lanthanum dopant concentration, as expected, although at the $x = 0.01$ level the increase is not observed below approximately 700°C . The reason for this is probably due to an initial lattice contraction with increasing sintering temperature. This effect is clearly observed for undoped ceria, and for 1 cation % lanthanum doped ceria at lower calcination temperatures, however the dopant incorporation seems to reduce this effect at higher calcination temperatures. The reason for the lattice contraction with calcination temperature for undoped ceria is perhaps due to the formation of substoichiometric phases of the form CeO_{2-x} at higher calcination temperatures. This discussion of this phenomenon can be found in the literature review chapter in section 2.1.1 and subsections therein.

Crystallite size estimations were completed for all materials, again using the method mentioned previously. For each composition, peaks were observed to become sharper and more intense with increasing calcination temperature, due to the increase in crystallinity during sintering. A typical example of this phenomenon is shown in figure 4.17 for the $x = 0.25$ sample calcined at various temperatures.

Figure 4.17 A plot showing the variation in 220 diffraction peak shape as a function of calcination temperature.



The experimental results and calculations are presented in table 4.10 and the estimated crystallite sizes are plotted with temperature and composition in figure 4.18.

Looking in detail at figure 4.18, the first observations are that the solid solution materials are all stabilised with respect to sintering in comparison with the series end-members, ceria and lanthana. The variations in estimated crystallite size with calcination temperature for ceria and lanthana with respect to sintering are similar, both demonstrating near-linear increases in crystallite size with increasing calcination temperature. The retardation of sintering demonstrated by the reduced rate of increase in crystallite size of the doped samples with temperature, in comparison with ceria and lanthana, is marked even for 1 cation % lanthanum. The variation in dopant retardation of sintering with temperature is illustrated in figure 4.19.

Table 4.10 Experimental results and calculations of estimated crystallite size for



Temp (°C)	x	2θ	θ	cos θ	Constant	FWHM	Crystallite size (Å)
450	0	47.520	23.761	0.9152	79.44	1.344	65
600	0	47.554	23.777	0.9151	79.44	0.572	152
800	0	47.592	23.796	0.9150	79.44	0.175	496
1000	0	47.614	23.807	0.9149	79.44	0.124	700
450	0.01	47.391	23.696	0.9157	79.44	1.253	69
600	0.01	47.511	23.756	0.9153	79.44	0.786	110
800	0.01	47.498	23.749	0.9153	79.44	0.260	334
1000	0.01	47.508	23.754	0.9153	79.44	0.144	603
450	0.25	46.723	23.369	0.9180	79.44	1.826	47
600	0.25	46.782	23.391	0.9178	79.44	1.126	77
800	0.25	46.789	23.395	0.9178	79.44	0.510	170
1000	0.25	46.777	23.389	0.9178	79.44	0.259	334
450	0.5	45.890	22.945	0.9209	79.44	1.903	45
600	0.5	46.206	23.103	0.9198	79.44	1.953	44
800	0.5	46.014	23.007	0.9205	79.44	0.546	158
1000	0.5	46.080	23.040	0.9202	79.44	0.353	245
450	1	51.963	25.982	0.8989	79.44	1.446	61
600	1	52.596	26.298	0.8965	79.44	0.361	245
800	1	52.328	26.164	0.8975	79.44	0.212	418
1000	1	52.292	26.146	0.8977	79.44	0.125	708

Figure 4.18 A plot of the estimated crystallite size variation with temperature for

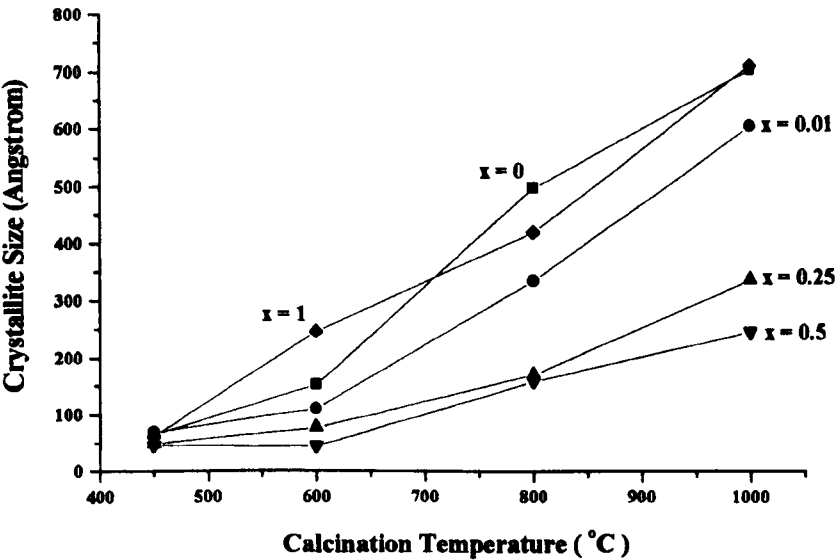
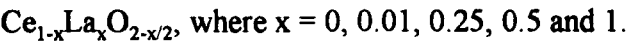
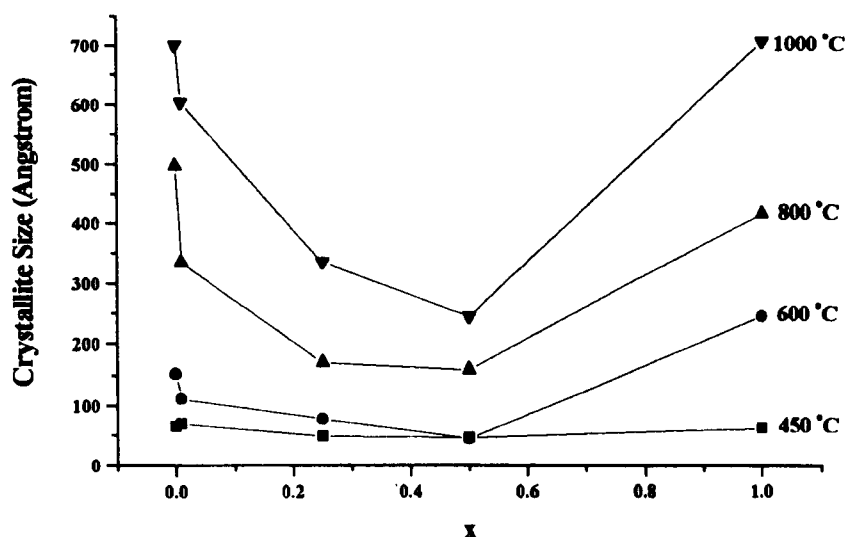


Figure 4.19 A plot showing the variation in crystallite size with lanthanum content for different calcination temperatures.



It is clear from figure 4.19 that the magnitude of the sintering retardation effect of lanthanum dopants does not vary linearly with lanthanum concentration. Relative to concentration, smaller dopant levels have a larger retarding effect on sintering than subsequently larger dopant levels. The reason for this phenomenon is unclear, but a possible explanation does exist. It is known from literature data that when lanthanum is incorporated into ceria, the surface and grain boundary regions become enriched with lanthanum due to temperature dependent surface segregation.⁹⁷⁻⁹⁸ It has also been proposed in the literature³⁵ that the sintering mechanism for ceria based oxide anion conducting materials involves migration of ionic species across grain boundaries, a process which is retarded by the presence of enhanced levels of lanthanum at the grain boundaries. The results of the present study are supported by such literature evidence. Furthermore, the reduction in the sintering retardation effect with increased bulk dopant level would also suggest primarily a grain boundary effect, as further bulk additions would have successively less effect on the surface composition, which would reach a lanthanum saturation concentration before the bulk does. It was proposed in the literature³⁵ that the rate determining step for the sintering process was the migration of oxide anions across the grain boundaries. However, other literature sources⁵³ have also determined that oxide anion conductivity is optimised for a bulk lanthanum concentration in ceria of approximately $0.1 < x < 0.2$. With regards the

present study, there are no observed maxima in the rate of sintering (except at $x = 0$ and 1), therefore casting doubt on this theory. If the rate determining step was oxide anion mobility, then assuming that the anion conductivity varies similarly with lanthanum dopant concentration at the surface as in the bulk, and assuming that the level of surface enrichment of lanthanum is not vastly removed from the bulk lanthanum concentration, then it would be reasonable to expect the rate of sintering to increase with a bulk lanthanum concentration of 1 cation %. As this is not observed in the experimental results for any of the calcination temperatures used, the theory is discounted. In addition to this, further evidence discounting this theory exists in the literature as it is widely known that cationic diffusion constants are orders of magnitude lower than anion diffusion in fluorite oxide materials, as discussed previously in the literature review. This would suggest that the rate limiting step for the sintering process is far more likely to be related to cationic diffusion than anionic diffusion (conductivity).

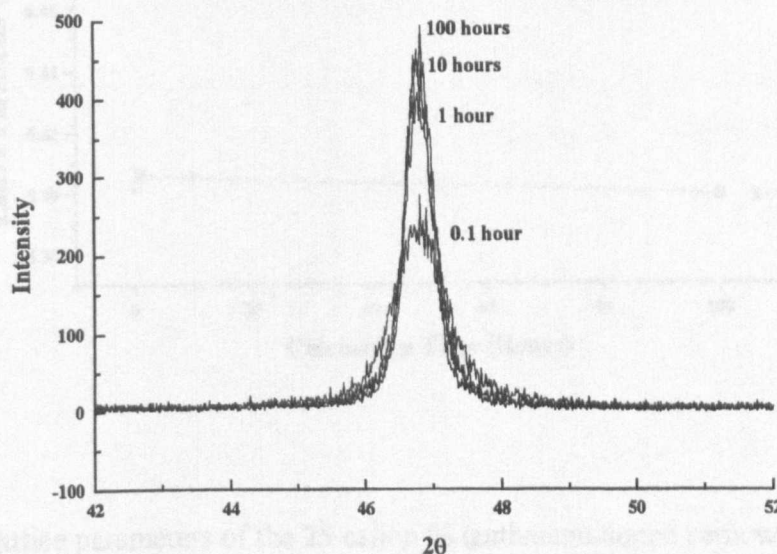
General theories on sintering mechanisms tend to suggest that the rate limiting process is the progression of the grain boundary through one of a pair of grains.³ This process would be limited by ionic diffusion of the slowest diffusing species. It would be expected that given the larger size of lanthanum in comparison with ceria, that diffusion of lanthanum through the ceria lattice should be slower than the diffusion of cerium based on ionic size alone. This effect would be significant even for low bulk lanthanum concentrations, and higher concentrations would have successively less effect. This theory provides a better explanation of the experimental results than the conductivity based theory.

Finally, a further set of experiments was completed in order to investigate calcination time. The aim of these experiments was to determine the equilibration time associated with the calcination process by determining the time required to achieve constant lattice parameter and estimated crystallite size values at a typical calcination temperature. These experiments were performed over ceria (to provide a reference), and 25 cation % lanthanum doped ceria, (a representative sample for the solid solution materials and to investigate the effect of lanthanum dopant addition on equilibration time). A calcination temperature of 800°C was used, as in the standard preparation

method. Calcination time was varied from a minimum time of 0.1 hour to 100 hours. The minimum time chosen was thought to be the shortest time possible for a calcination in which the heat-up and cool-down times would be insignificant in comparison with the time at the calcination temperature. In order to ensure that heat-up and cool-down times were as short as possible, samples were all calcined as fine powders which were spread evenly (and thinly - to a depth of approximately 0.5mm or less) over the bottom of the alumina calcination boat in order to make heat transfer from the gas phase as efficient and fast as possible. Samples were all introduced to pre-heated furnaces, and removed to atmospheric temperature after the requisite calcination time had elapsed. Thus, the cooling process was ensured to be as fast as possible. Following processing, samples were stored in air tight vials until analysed by XRD.

All samples were determined to be single phase with the cubic fluorite structure, as expected. With increased calcination time, diffraction peaks were observed to sharpen and become more intense, (similarly as was observed with increasing calcination temperature in figure 4.17), this time demonstrating an increase in crystallinity with increasing calcination time. The change in peak shape with calcination time for the 220 peak of the 25 cation % lanthanum doped ceria sample is shown in figure 4.20.

Figure 4.20 A plot of the variation in 220 peak shape with calcination temperature.

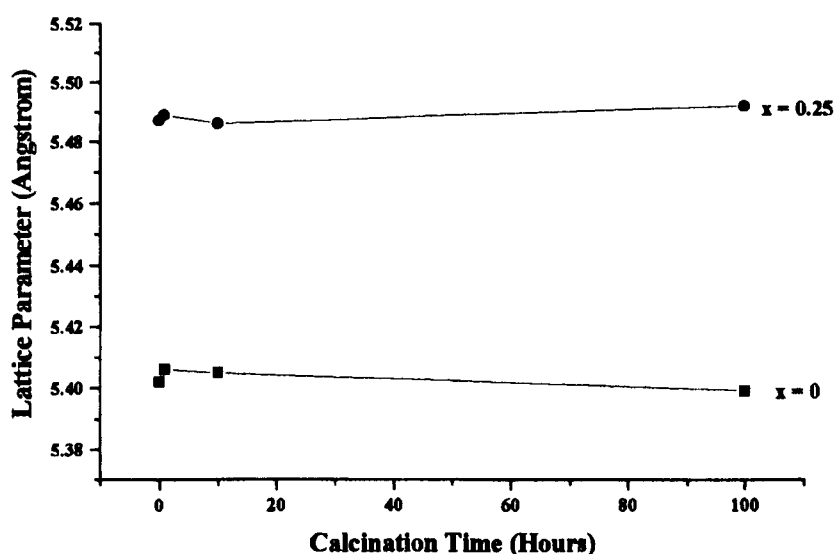


Lattice parameters were determined using the method described previously. Experimental results and calculations are presented in table 4.11 and variations in lattice parameter with calcination time are presented in figure 4.21.

Table 4.11 Experimental results and lattice parameter determination calculations for the calcination time dependency experiments.

Time (hr)	x	d111	d200	d220	d311	a111 (Å)	a200 (Å)	a220 (Å)	a311 (Å)	Av. LP (Å)
0.1	0	3.1194	2.7024	1.9107	1.6268	5.403	5.405	5.404	5.395	5.402
1	0	3.1189	2.7032	1.9118	1.6309	5.402	5.406	5.407	5.409	5.406
10	0	3.1173	2.7028	1.9120	1.6306	5.399	5.406	5.408	5.408	5.405
100	0	3.1130	2.6987	1.9101	1.6296	5.392	5.397	5.403	5.405	5.399
0.1	0.25	3.1741	2.7441	1.9356	1.6541	5.498	5.488	5.475	5.486	5.487
1	0.25	3.1677	2.7431	1.9411	1.6564	5.487	5.486	5.490	5.494	5.489
10	0.25	3.1666	2.7460	1.9384	1.6537	5.485	5.492	5.483	5.485	5.486
100	0.25	3.1705	2.7480	1.9406	1.6557	5.491	5.496	5.489	5.491	5.492

Figure 4.21 A plot showing the variation in lattice parameter with calcination time for ceria and 25 cation % lanthanum doped ceria.



The lattice parameters of the 25 cation % lanthanum doped ceria was found to be significantly higher than that of undoped ceria due to the incorporation of the

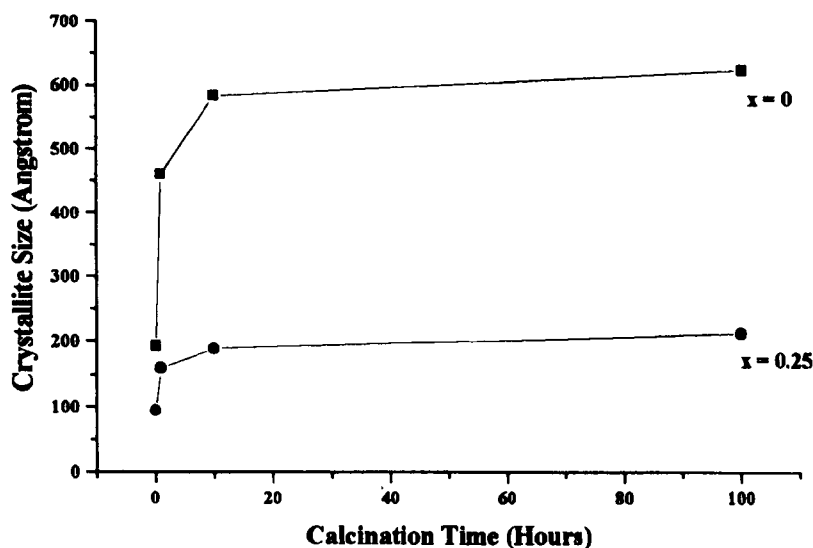
lanthanum cations into the ceria lattice, as expected. It can be observed from figure 4.21 that there is a brief induction period in the sintering process in which there is a small but significant increase in lattice parameter. If this was observed only with the doped material, then it would suggest further incorporation of lanthanum into the ceria lattice causing the observed lattice expansion. This in turn would infer that formation of the solid solution was not complete following the 450°C decomposition step in the material preparation. However, as this feature is also common to the undoped material, it must be assumed that the cause is an artefact of either the preparation method, or indeed the X-ray measurements and was not investigated further. There is no significant change in the lattice parameters of both lanthanum doped and undoped ceria after 1 hour, suggesting that there are no further time dependent phase changes or solid state reactions. It was therefore assumed that thermodynamic equilibrium was achieved after 1 hour at 800°C, at least with respect to formation of a solid solution and any further solid state reaction.

The variation in crystallite size with calcination time was also investigated. Experimental results and calculations for the estimation of the crystallite sizes is presented in table 4.12 and the variation in crystallite size with calcination time for both 25 cation % lanthanum doped and undoped ceria is presented in figure 4.22.

Table 4.12 Experimental data and calculations of crystallite size for the experiments to determine the variation in crystallite size with calcination time for ceria and 25 cation % lanthanum doped ceria.

Time (Hr)	x	2 θ	θ	cos θ	Constant	FWHM	Crystallite size (Å)
0.1	0	47.537	23.769	0.9152	79.44	0.451	192
1	0	47.513	23.757	0.9153	79.44	0.189	459
10	0	47.526	23.763	0.9152	79.44	0.149	583
100	0	47.570	23.785	0.9151	79.44	0.139	625
0.1	0.25	46.724	23.362	0.9180	79.44	0.917	94
1	0.25	46.748	23.374	0.9179	79.44	0.541	160
10	0.25	46.730	23.365	0.9180	79.44	0.458	189
100	0.25	46.755	23.378	0.9179	79.44	0.406	213

Figure 4.22 A plot of the variation in estimated crystallite size with calcination time for undoped and 25 cation % lanthanum doped ceria.



The first observation from figure 4.22 is that for any given calcination time, the 25 cation % lanthanum doped ceria samples are significantly less sintered than the undoped samples, as was expected based on the previous results in this section. Secondly, as calcination time is increased, both doped and undoped materials vary similarly with a rapid initial increase in crystallite size over the first 10 hours, followed by a much slower increase with further calcination time. It is unclear from these results whether the crystallite size actually reaches a constant value with prolonged calcination, but the low rate of change in crystallite size beyond approximately 10 hours would suggest that this was the case. It was therefore assumed that the ceria and ceria based solid solutions are at approximate thermodynamic equilibrium with respect to sintering after approximately 10 hours.

4.2 XPS Surface Composition Studies.

Surface segregation from $\text{Ce}_{1-x}\text{La}_x\text{O}_{2-x/2}$ ($0 < x < 1$) was investigated using XPS. The theory and experimental methodology for this technique is discussed in section 3.4 and subsections therein. The experimental work was performed mostly on a service basis at the Institute for Surface Science and Technology at Loughborough

University. The experiments to determine the variation in surface composition with calcination temperature were completed in-house.

This section of the solid state study was completed with three aims; to determine the effects of calcination temperature, calcination time and the effects of bulk composition on the surface segregation properties of lanthanum doped ceria. The segregation of lanthanum from ceria has been previously reported in the literature⁹⁷⁻⁹⁸ and is discussed in the literature review (section 2.1.3). This present systematic study was completed in order to be able to quantify the segregation phenomena.

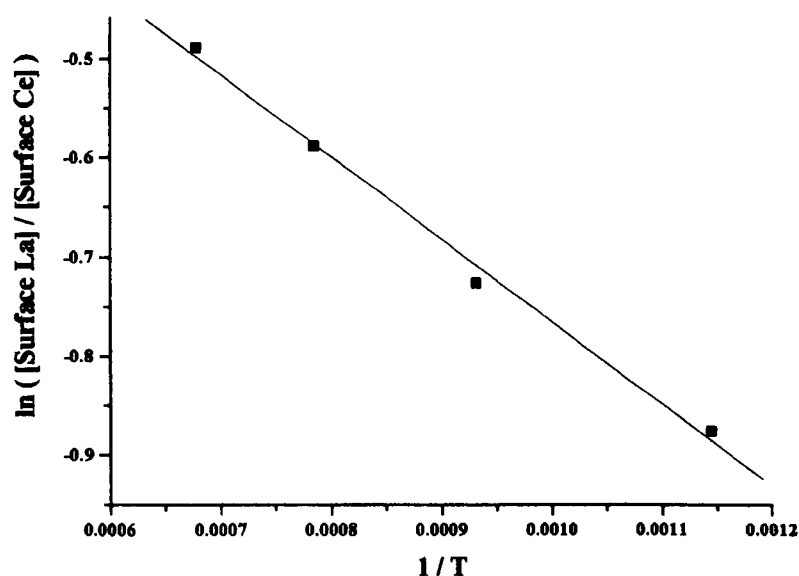
4.2.1 Segregation as a Function of Calcination Temperature

In order to investigate the variation in surface composition with calcination temperature, a batch of $\text{Ce}_{0.8}\text{La}_{0.2}\text{O}_{1.9}$ was prepared using the coprecipitation technique and decomposed to oxides by heating to 450°C in air. Samples were then calcined in air in 1g aliquots. The 20 cation % lanthanum level was chosen specifically to provide a sample typical of the $\text{Ce}_{1-x}\text{La}_x\text{O}_{2-x/2}$ system, but the composition was deliberately kept below the middle of the solid solution range in order to reduce the chance of lanthanum saturation of the surface at high calcination temperatures. For each calcination temperature, work-up and work-down was completed over 2 hours from a base temperature of 200°C. The temperature was maintained at the required level for each calcination for 8 hours in all cases. The calcination temperatures tested were 600°C, 800°C, 1000°C, and 1200°C. The XPS analysis for these experiments was completed in-house. Samples were also characterised using XRD. The experimental results for the variation in surface composition with calcination temperature are presented in table 4.13, and shown in the form of an Arrhenius-style plot in figure 4.23.

Table 4.13 Experimental results for the experiments to determine the variation in surface composition with calcination temperature for $\text{Ce}_{0.8}\text{La}_{0.2}\text{O}_{1.9}$.

Calcination Temperature ($^{\circ}\text{C}$)	Lanthanum Surface Fraction (x)
600	0.294
800	0.326
1000	0.357
1200	0.380

Figure 4.23 A plot of the variation in \ln (surface ratio) with reciprocal calcination temperature for $\text{Ce}_{0.8}\text{La}_{0.2}\text{O}_{1.9}$.



It is observed from table 4.13 that all samples are significantly enriched with lanthanum at the surface, in comparison with the bulk composition. It is thus possible to calculate a segregation enthalpy using the Arrhenius method. On this basis a value of $1.6 \text{ kcal mol}^{-1}$ (6.9 kJ mol^{-1}) was derived from the slope of a plot of \ln (surface ratio) vs. $1/T$. The response is similar to that reported in the literature ($6 - 11 \text{ kcal mol}^{-1}$ reported by Harrison^{97, 98}), but the quantitative value is significantly lower. All samples were determined to be single phase by XRD analysis, and there was no shift in lattice parameter from a mean value of 5.465 \AA with increasing calcination temperature. It should be noted at this point that as this set of experimental data was obtained using a different instrument to the following surface composition analysis data, direct

comparison of absolute values of the two sets of data must be exercised with caution.

However, sample to sample comparisons within each experimental group are valid.

Further experiments were carried out at a later date at ISST Loughborough to determine the effect of composition on the response of surface composition to temperature. To this end, further samples of low and high lanthanum concentrations ($x = 0.001$ and $x = 0.5$, respectively) were calcined similarly to the $x = 0.2$ samples. In this case the calcination time was 10 hours and the calcination temperatures were 450°C , 800°C and 1400°C . The results of this additional study are presented in table 4.14 and are shown in figure 4.24 along with the $x = 0.2$, 8 hour calcination data for comparison.

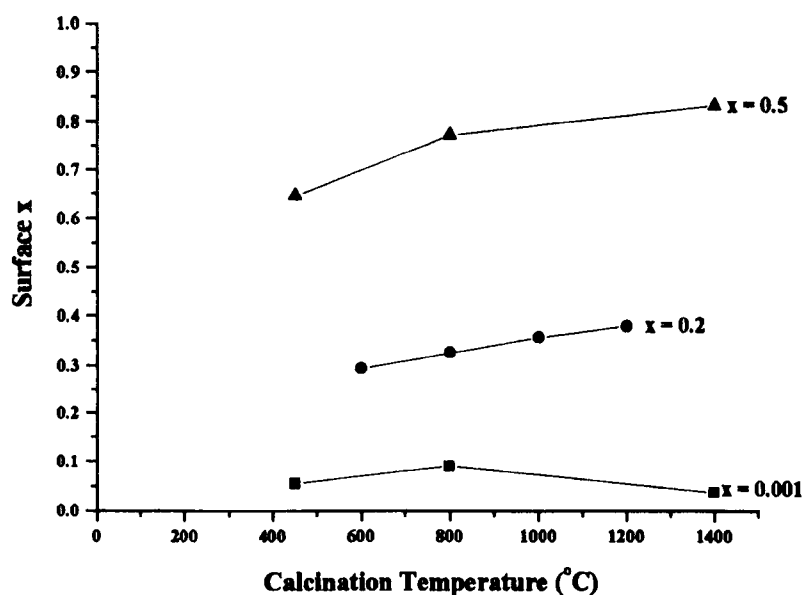
Table 4.14 Additional experimental results for the determination of the variation in surface composition with calcination temperature for samples $x = 0.001$ and $x = 0.5$, (10 hour calcinations).

Calcination Temperature ($^{\circ}\text{C}$)	Lanthanum surface fraction ($x = 0.001$ bulk material)	Lanthanum surface fraction ($x = 0.5$ bulk material)
450	0.053	0.643
800	0.080	0.769
1400	0.037	0.834

It is observed that for $x = 0.5$, surface lanthanum concentration is significantly enhanced with respect to bulk composition at all calcination temperatures, and that the level of enrichment increases with calcination temperature, (as observed previously with sample $x = 0.2$). The results for the $x = 0.001$ sample do not clearly demonstrate the systematic variation in surface composition with calcination temperature, but this is most likely due to significant surface composition measurement error, inherent at vanishingly high and low surface concentrations, due to baseline fitting error. The results for $x = 0.001$ are therefore not considered further beyond this point. An enthalpy for the segregation process was determined using the Arrhenius method for

the $x = 0.5$ sample. A value of $2.6 \text{ kcal mol}^{-1}$ (10.9 kJ mol^{-1}) was derived from the slope of an plot of $\ln(\text{surface ratio})$ vs. $1/T$, which as in the case of the $x = 0.2$ sample, is still significantly less than, but of the same order as the data reported by Harrison⁹⁷⁻⁹⁸. No XRD studies were completed for these samples, although from the other studies both the $x = 0.001$ and the $x = 0.5$ samples can be assumed to be single phase solid solutions.

Figure 4.24 A plot of the variation in surface composition with calcination temperature for samples $x = 0.001$ and $x = 0.5$ (10 hour calcinations) and for sample $x = 0.2$ (8 hour calcination).



4.2.2 Segregation as a Function of Calcination Time.

The time dependency of the surface segregation process was also examined at bulk lanthanum compositions corresponding to $x = 0.001$, $x = 0.25$ and $x = 0.5$ which were prepared using the coprecipitation method and decomposed to oxide at 450°C before calcination. These lanthanum levels were selected as being representative of the solid solution range. The calcination temperature used for all samples was 800°C , as used in the standard calcination method for coprecipitated materials. Four 1g aliquots of the decomposed oxide materials were calcined separately as powders for 0.1, 1, 10 and 100 hours. In each experiment, the samples were introduced to the pre-heated

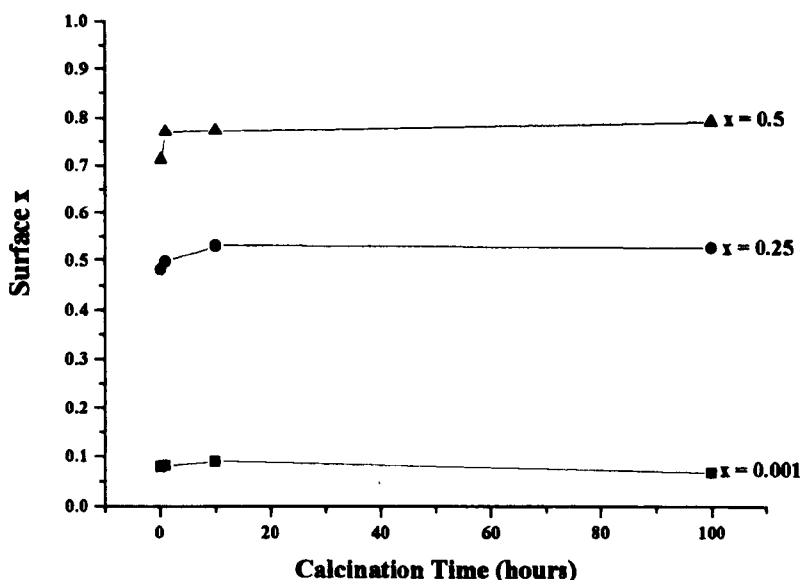
furnace and removed to room temperature after the required time had elapsed. In each case, the decomposed oxide powder was spread thinly across the bottom of an alumina boat, resulting in a layer of less than 0.5 mm depth. This was done to minimise the heat-up and cool-down times, which could significantly affect the true time at the required calcination temperature. There was no direct method available to determine the heat-up and cool-down rates for these experiments, but it was expected to be in the order of seconds rather than minutes. The 0.1 hour calcination result is therefore assumed to be the result of an accurate calcination time, but is reported with the proviso of possible error. The experimental results of the isothermal calcination time dependency experiments are presented in table 4.15. The variation in surface composition with calcination time is shown in figure 4.25.

Table 4.15 Experimental results for the isothermal (800°C) calcination time dependency experiments.

Calcination Time (hours)	Surface x (Bulk x = 0.001)	Surface x (Bulk x = 0.25)	Surface x (Bulk x = 0.5)
0.1	0.079	0.481	0.711
1	0.080	0.497	0.769
10	0.089	0.531	0.772
100	0.067	0.527	0.793

XRD analysis of the $x = 0.25$ samples were assumed representative of the sample series. All $x = 0.25$ samples were determined to be single phase with the cubic fluorite structure by XRD. Peak shifts toward lower 2θ values were observed compared with pure ceria, confirming that the lanthanum was incorporated into the ceria lattice forming a solid solution even after just 0.1 hour. Accordingly, the average lattice parameter for the four $x = 0.25$ samples was determined to be 5.488Å compared with a value of 5.408Å determined for pure ceria.

Figure 4.25 A plot of the variation in surface composition with calcination time at 800°C for samples $x = 0.001$, $x = 0.25$ and $x = 0.5$



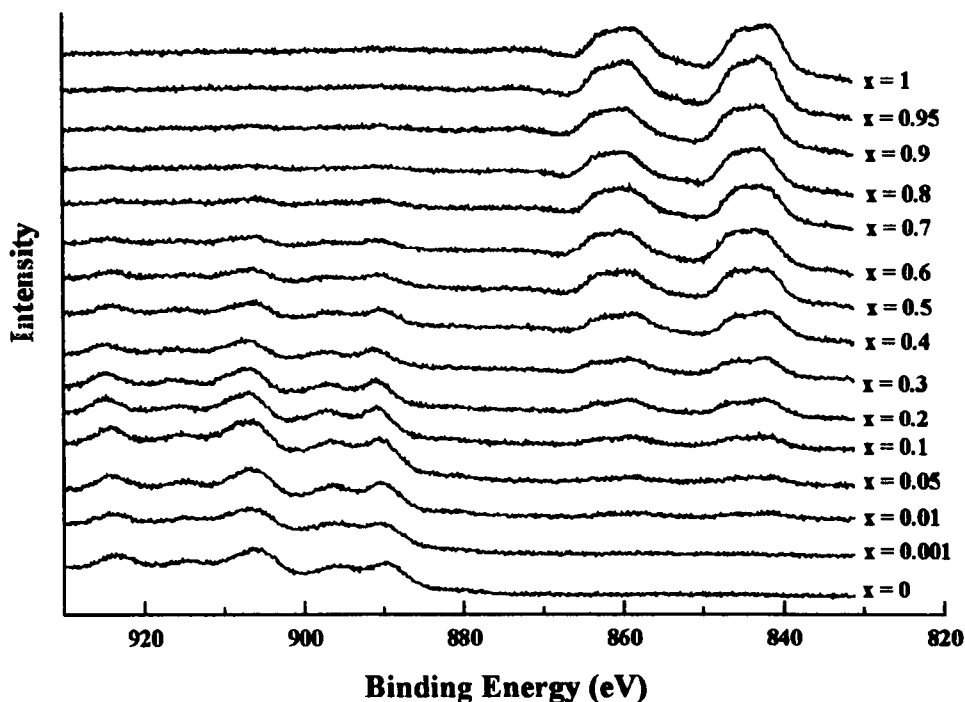
In all samples tested, the surface was significantly enriched with lanthanum in comparison with the bulk composition. The surface concentration of lanthanum was observed to increase rapidly with time, reaching a constant value after approximately 5 hours. Computer aided curve fitting of the data, using a best fit routine allowed evaluation of surface lanthanum concentration for intermediate calcination times. The result of this analysis determined that following an 8 hour calcination, the surface lanthanum concentration was within 0.2 % of the steady state (thermodynamic equilibrium) concentration.

The interpretation of this data is that the surfaces of the 0.1, 25 and 50 cation % lanthanum doped ceria samples all reach a thermodynamic equilibrium surface lanthanum concentration after the standard 8 hours at 800°C calcination. The observed variation in the surface lanthanum concentration with calcination temperature (section 4.2.1), can be attributed to significant shifts in the equilibrium surface lanthanum concentration with calcination temperature. It is assumed for all bulk compositions, that surface compositions are at thermodynamic equilibrium after the standard 8 hours at 800°C calcination.

4.2.3 Segregation as a Function of Bulk Composition

A series of samples of $\text{Ce}_{1-x}\text{La}_x\text{O}_{2-x/2}$ of various compositions ($0 < x < 1$) were prepared by the coprecipitation method and were subjected to the standard calcination treatment; 8 hours in air at 800°C . Samples were subsequently analysed by XRD (as reported previously in section 4.1.4), and by XPS to determine the surface cation ratio. The resulting XPS spectra are shown in figure 4.26.

Figure 4.26 XPS spectra for the variation in bulk composition in $\text{Ce}_{1-x}\text{La}_x\text{O}_{2-x/2}$ for ($0 < x < 1$).



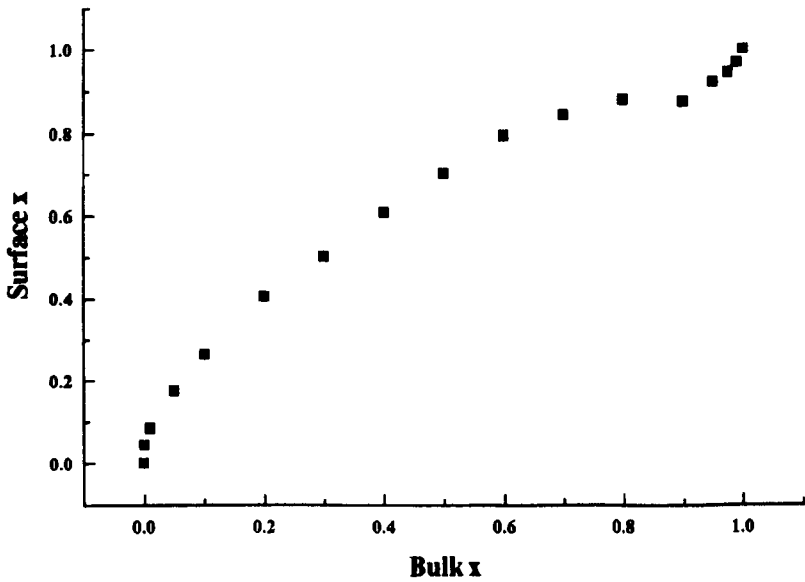
The experimental results are presented in table 4.16. The lanthanum surface enrichment factor (defined as the ratio of surface lanthanum to bulk lanthanum), is also included in the table in order to indicate both the magnitude and enriched species. Lanthanum enrichment factors greater than unity signify segregation of lanthanum from the bulk material, factors less than unity signify segregation of cerium from the bulk material. The greater the magnitude of the enrichment factor, the greater the degree of segregation in proportion to the bulk concentration. The variation in surface

composition with bulk composition is shown in figure 4.27, and the variation in lanthanum surface enrichment factor with composition is shown in figure 4.28.

Table 4.16 Experimental results for XPS surface composition analysis.

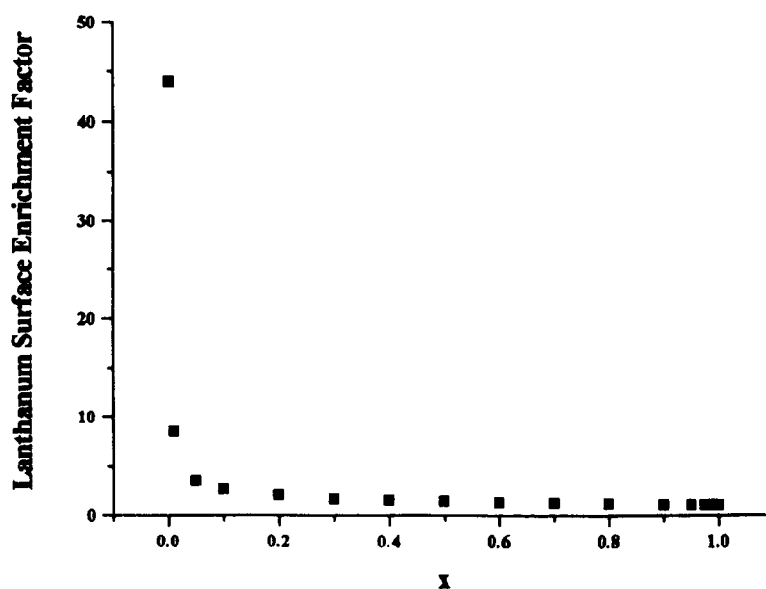
Bulk La x_b	Bulk Ce $1-x_b$	Surface La x_s	Surface Ce $1-x_s$	Enrichment factor x_s / x_b
0.001	0.999	0.044	0.956	44.00
0.01	0.99	0.085	0.915	8.50
0.05	0.95	0.176	0.824	3.52
0.1	0.9	0.265	0.735	2.65
0.2	0.8	0.407	0.593	2.04
0.3	0.7	0.504	0.496	1.68
0.4	0.6	0.609	0.391	1.52
0.5	0.5	0.701	0.299	1.40
0.6	0.4	0.790	0.210	1.32
0.7	0.3	0.839	0.161	1.20
0.8	0.2	0.876	0.124	1.10
0.9	0.1	0.873	0.127	0.97
0.95	0.05	0.920	0.080	0.97
0.975	0.025	0.943	0.057	0.97
0.99	0.01	0.969	0.031	0.98

Figure 4.27 A plot of the variation in surface composition with bulk composition for $Ce_{1-x}La_xO_{2-x/2}$ ($0 < x < 1$)



It is observed from the variation in surface composition with bulk composition (figure 4.27), and in the variation in surface lanthanum enrichment factor with bulk composition (figure 4.28), that the surfaces of the $\text{Ce}_{1-x}\text{La}_x\text{O}_{2-x/2}$ materials are enriched with lanthanum in comparison with the bulk composition for bulk compositions $0 < x < 0.8$, (corresponding approximately to the solid solution composition range of lanthanum in ceria). Between $0.9 < x < 1$, (corresponding approximately to the solid solution composition range of cerium in lanthana), the surface of the materials are observed to be enriched with cerium, with respect to the bulk composition. This result allows the surface composition data to be effectively split into two data-sets for analysis; $0 < x < 0.8$ (La in CeO_2 solid solution compositional range) for segregation of lanthanum from a ceria structured bulk, and $0.9 < x < 1$ (Ce in La_2O_3 solid solution estimated compositional range) for segregation of cerium from a lanthana structured bulk. The $0.8 < x < 0.9$ dopant concentration region comprises the phase transition composition zone in which the bulk structure changes from cubic fluorite to hexagonal close packed with increasing lanthanum concentration, and is therefore not included in further analysis.

Figure 4.28 A plot of the variation in enrichment factor with bulk composition for $\text{Ce}_{1-x}\text{La}_x\text{O}_{2-x/2}$ ($0 < x < 1$).



With regards the variation in enrichment factor with bulk composition, it can be observed in figure 4.28 that the level of enrichment is maximised at low bulk lanthanum compositions. With increasing bulk lanthanum concentrations, the level of enrichment is observed to fall rapidly from the maximum. The decline in enrichment factor was determined to vary in an approximately logarithmic fashion, (determined as a 'best fit' using curve-fitting software).

4.2.3.1 Analysis and Discussion

The aim of this analysis is to rationalise the segregation process in terms of known theory and segregation models. Several models have been proposed as generally suitable for the description of such experimental data, the most basic of which is the McLean regular solution model,⁹⁰ (based on the Langmuir gas adsorption isotherm). The basic assumption of this model is that the surface enrichment factor (and thus the enthalpy of segregation), remains constant and is independent of either bulk or surface composition.

4.2.3.1.1 Surface Segregation Modelling

4.2.3.1.1.1 McLean model

The surface and bulk compositions of the ceria-lanthana mixed oxides have been compared according to the McLean (Langmuir) equation to extract the free energies of segregation. As discussed previously in the literature review chapter in section 2.1.3.1, the McLean equation for a regular solution (dilute solution range only) can be expressed;

$$\frac{X_s^2}{X_b^1} = \frac{X_b^2}{X_s^1} \exp^{(-\Delta H_{\text{seg}}/RT)} \quad (4.1)$$

In the case of real systems, the enthalpy of segregation denoted in the regular solution model is more correctly expressed in terms of a free energy of segregation;

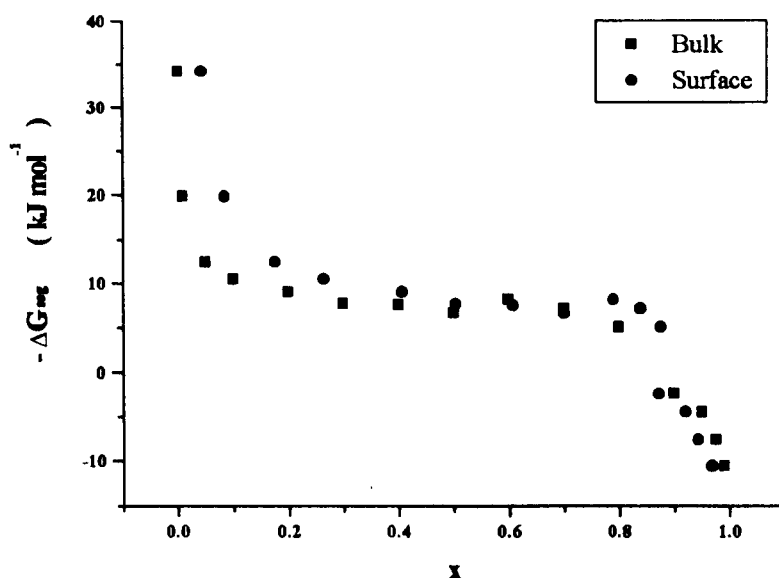
$$\frac{X_s^2}{X_s^1} = \frac{X_b^2}{X_b^1} \exp^{(-\Delta G_{\text{Seg}}/RT)} \quad (4.2)$$

The results of the determination of free energy of segregation with composition are presented in table 4.17 and figure 4.29.

Table 4.17 Free energies of segregation for the $\text{Ce}_{1-x}\text{La}_x\text{O}_{2-x/2}$ series determined using the McLean model (equation 4.2).

Bulk x	Surface x	$-\Delta G_{\text{Seg}}$ (kJ mol ⁻¹)
0	0	-
0.001	0.044	34.157
0.010	0.085	19.798
0.050	0.176	12.498
0.100	0.265	10.503
0.200	0.407	9.011
0.300	0.504	7.703
0.400	0.609	7.572
0.500	0.701	6.603
0.600	0.790	8.204
0.700	0.839	7.169
0.800	0.876	5.075
0.900	0.873	-2.404
0.950	0.920	-4.479
0.975	0.943	-7.650
0.990	0.968	-10.577
1	1	-

Figure 4.29 A plot of the variation in ΔG_{seg} (derived using equation 4.2), with surface composition for the $\text{Ce}_{1-x}\text{La}_x\text{O}_{2-x/2}$ series



From table 4.17 and figure 4.29 it is clear that the free energy is strongly coverage-dependent; that is to say, the McLean model is not applicable over the whole range of mixed oxides studied here. At low coverages, the free energy of segregation decreases rapidly as the lanthanum coverage is increased: at high coverages, it becomes almost independent of the coverage. However the free energy of segregation exhibits a localised discontinuity at bulk $x = 0.6$ (surface $x = 0.79$). The data in Section 3.4 shows the solubility limit of lanthana in ceria to be in the bulk concentration range $0.6 < x < 0.7$. Accordingly the evaluation of the data is preferably limited to bulk $x = 0.6$.

In conclusion, the McLean model was determined to be unsuitable for representation of the experimental data, due to the observed coverage dependence of derived free energy of segregation.

Several alternative adsorption isotherms have been developed to allow for variations in adsorption enthalpy with surface coverage. These include the Temkin isotherm, which assumes a linear variation in adsorption enthalpy with surface coverage, and the Freundlich isotherm which assumes a logarithmic variation. With regards the application of such adsorption models to the present segregation study, of these models, the Freundlich isotherm was determined to provide the best fit, returning

an order of 0.63. The power law function of the Freundlich isotherm is an empirical function which allows for a logarithmic variation in adsorption enthalpy. The reasonable fit obtained therefore suggests that the variation in the free energy of segregation varies with composition is approximately logarithmic.

4.2.3.1.1.2 Mackrodt and Tasker Model¹⁰⁴

Surface segregation in the ceria/lanthana system evaluated according to the McLean equation⁹⁰, has shown a clear coverage-dependence of the free energy of surface segregation. The rationalisation of the experimental data by a relationship derived from the Mackrodt and Tasker model¹⁰⁴ is investigated in the following analysis.

Mackrodt and Tasker (1989)¹⁰⁴ adapted Liu and King's electrostatic model¹⁶⁹ to derive, (using atomistic lattice simulations), a non-Arrhenius segregation isotherm from a statistical thermodynamic analysis of two component systems comprising single types of surface and bulk sites, modified to accommodate solute-solute interactions at the surface.

The Mackrodt-Tasker model is;

$$\frac{X_s^2}{X_s^1} = \frac{X_b^2}{X_b^1} \exp \left(\frac{-[\Delta G^0 + X_s(X_s + 1) \times (d\Delta G/dX_s)]}{RT} \right) \quad (4.3)$$

where ΔG^0 is the free energy of segregation in the absence of solute-solute interactions. We now consider a representation of the observed variation of ΔG_{Seg} in terms of coverage and seek solutions to the equation;

$$\Delta G^0 + [X_s(X_s + 1) \times (d\Delta G/dX_s)] = \Delta G^{X_s} \quad (4.4)$$

where ΔG^0 is a constant; $X_s = X_s^2/X_s^1$ and ΔG^{X_s} is the free energy of segregation when the solute/solvent ion ratio at the surface is X_s .

In the McLean model, $d\Delta G/dX_s = 0$ and $\Delta G^{X_s} = \Delta G^0$. However the general solution is

$$\Delta G^{X_s} = \Delta G^0 + C(1 + 1/X_s) \tag{4.5}$$

where ΔG^0 and C are constants.

Hence $\Delta G^{X_s} = B + \frac{C}{X_s}$ where, $B = \Delta G^0 + C$ (4.6)

The free energies of segregation evaluated according to the McLean model (table 4.17) have been computer curve fitted to equation 4.5. In each case the range of data fitted has been from bulk $x = 0.001$ to several values, up to a maximum of bulk $x = 0.8$. The results of the statistical model-fitting analysis are summarised in table 4.18 which shows that the model is robust over the bulk concentration range $0.001 < x < 0.7$, although exhibiting a lower quality of fit when bulk x exceeds 0.5. The XRD studies in section 4.1.4 has determined a solubility limit for La in $Ce_{1-x}La_xO_{2-x/2}$ in the range $0.5 > x < 0.6$. The evaluated free energies are therefore limited to the model based on the curve fit of experimental data between $0.001 < \text{bulk } x < 0.5$.

Table 4.18 Free Energy of Segregation of Lanthana as a function of surface composition from $x = 0.001$ to $x = 0.4 - 0.8$ - a statistical model-fitting analysis summary.

Bulk x	Surface x	ΔG^0 (kJ mol ⁻¹)	C (kJ mol ⁻¹)	r ²	F-statistic
0.4	0.609	-5.521	-1.251	0.999	4773
0.5	0.701	-5.583	-1.247	0.999	5478
0.6	0.79	-5.766	-1.236	0.997	2790
0.7	0.84	-5.756	-1.236	0.998	3335
0.8	0.88	-5.474	-1.255	0.992	1166

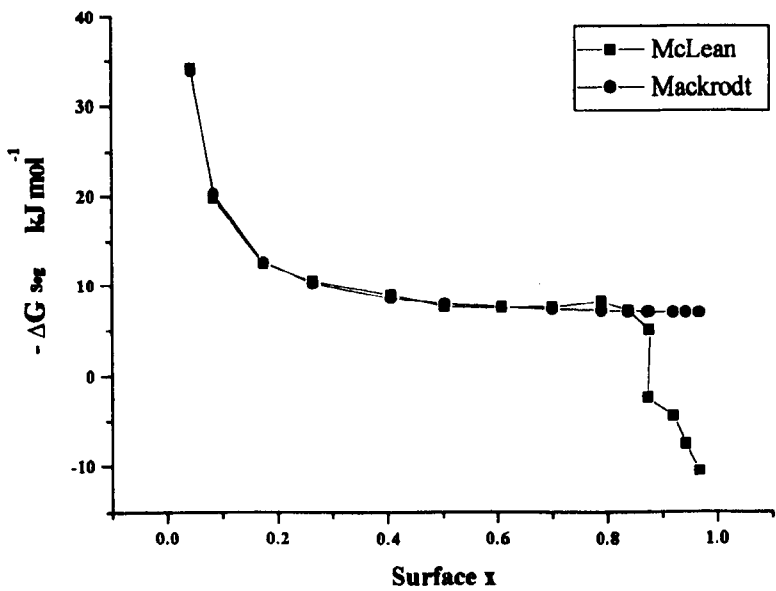
The measured (McLean equation derived), and modelled (Mackrodt and Tasker) free energies as a function of surface composition up to surface $x = 0.88$ are presented and compared in table 4.19 and figure 4.30. (The modelled free energies

were derived using the ΔG^0 and C values derived from the best fit evaluation of the experimental data, which was over the bulk concentration range $0.001 < x < 0.5$).

Table 4.19 Measured (McLean), and modelled (Mackrodt & Tasker) free energy variations with surface composition for La segregation.

Bulk x	Surface x	$-\Delta G_{\text{seg}}$ Measured kJ mol ⁻¹ .	$-\Delta G_{\text{seg}}$ Modelled kJ mol ⁻¹ .
0.001	0.044	34.157	33.924
0.010	0.085	19.798	20.254
0.050	0.176	12.498	12.668
0.100	0.265	10.503	10.289
0.200	0.407	9.011	8.647
0.300	0.504	7.703	8.057
0.400	0.609	7.572	7.631
0.500	0.701	7.603	7.362
0.600	0.790	8.204	7.161
0.700	0.839	7.169	7.069
0.800	0.876	5.075	7.007
0.900	0.873	-2.404	7.011
0.950	0.920	-4.479	6.938
0.975	0.943	-7.650	6.905
0.990	0.968	-10.577	6.871

Figure 4.30 A plot of measured (McLean), and Modelled (Mackrodt & Tasker), free energy variations with surface composition for La segregation.



It can be concluded that the Mackrodt and Tasker model provides a good description of the coverage-dependent free energy of segregation of lanthana from its solid solution in ceria. The model in figure 4.30 is based on the coefficients for the $0 < x < 0.5$ evaluation (best fit evaluation). It should be noted that application of the model beyond the solid solution range is not strictly valid, but has been extrapolated over the full $0 < x < 1$ for illustrative purposes. It is observed that as the solid solution limit is approached $\Delta G_{\text{seg}} \rightarrow \Delta G^0 + C$, which is effectively equivalent to the difference between the bulk and surface lattice strain energies. This can be explained in terms of the bulk composition and structure approaching to that of the surface, near the solid solution limit - the expanded character of the host lattice approaches that of the surface with increasing lanthanum dopant incorporation, resulting in the observed minimisation in the free energy of segregation at $\Delta G^0 + C$ at the solid solution limit.

A further study was made of segregation of ceria from its solid solution in lanthana, based on the surface compositions of samples with bulk lanthanum concentration between $0.9 < x < 1$. (The opposite signs of ΔG_{seg} , the free energies of segregation at low concentrations of solute, for lanthanum segregation from ceria, and for cerium segregation from lanthana, reflects the difference in solute/solvent cationic radii: 103.2 pm La^{3+} , and 87 pm Ce^{4+}). With the exception of the measurement on the most dilute solution of ceria ($1-x = 0.01$), the measured free energy of segregation conforms with equation 4.5. (The error associated with the $1-x = 0.01$ sample can be explained in terms of error in XPS baseline allocation at a vanishingly low concentration of cerium cations in the surface). The summary of the evaluation of the ΔG_{seg} of cerium from lanthana using equation 4.5, (from which the modelled data is derived), is presented in table 4.20.

Table 4.20 Free Energy of Segregation of Ceria - a Statistical Model Fit Analysis Summary.

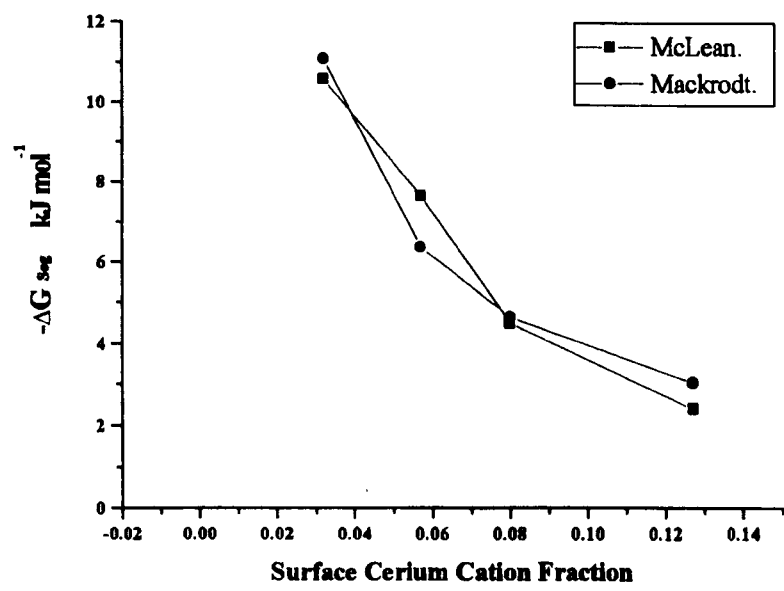
ΔG^0 (kJ mol ⁻¹)	C (kJ mol ⁻¹)	r ²	F-statistic
-0.329	-0.344	0.940	31

It can be observed that the limiting value of ΔG_{seg} ($\Delta G^0 + C$) for the segregation of cerium from lanthana is approximately one order of magnitude less than that determined for the segregation of lanthanum from ceria. At any given dopant level, the driving force for segregation of cerium cations from the HCP lanthana matrix is much less than for the segregation of lanthanum from the cubic ceria lattice. This is most probably due to the relative cationic radii of cerium and lanthana, the incorporation of the smaller cerium cations into lanthana resulting in far less lattice strain than in the case of the substitutional incorporation of (larger) lanthanum cations into ceria. The facile $\text{Ce}^{\text{III}} - \text{Ce}^{\text{IV}}$ redox also allows the incorporation of cerium into the lanthana matrix as an isovalent dopant, requiring neither the formation of cation vacancies or oxygen interstitials as charge balancing species. This is reflected in the very small interaction coefficient (C), (in comparison with that determined for lanthanum segregation from ceria), which is dependent on both host/dopant cationic radii and charge differences. Table 4.21 and Figure 4.31 present data for the comparison of measured and modelled (Mackrodt and Tasker) free energies as a function of surface composition between zero and 10 bulk cation % cerium.

Table 4.21 Measured (McLean equation derived), and modelled (Mackrodt and Tasker) free energy variations with surface composition for Ce segregation.

Bulk Ce (1-x)	Surface Ce (1-x)	ΔG_{seg} Measured kJ mol ⁻¹ .	ΔG_{seg} Modelled kJ mol ⁻¹ .
0	0	-	-
0.010	0.032	-10.577	-11.079
0.025	0.057	-7.650	-6.364
0.050	0.080	-4.479	-4.629
0.100	0.127	-2.404	-3.038

Figure 4.31 A plot of measured (McLean), and Modelled (Mackrodt & Tasker), free energy variations with surface composition for Ce segregation.



Summary

Whilst remaining single phase solid solutions up to lanthanum contents between $0.5 < x < 0.6$, lanthanum ions preferentially segregate to the surface; segregation being more pronounced from dilute solutions. The free energy of segregation was determined to be strongly coverage-dependent within the single phase solid solution regions, in a manner which was modelled by an expression derived by Mackrodt and Tasker, based on atomistic lattice simulations of solute-solute interactions. Similarly, the preferential segregation of cerium with composition from lanthana in the HCP (lanthana host) single phase region ($0.9 < x < 1$), was also observed to conform to the Mackrodt and Tasker model derived expression, but with smaller coefficients.

4.2.3.1.1.3 Wynblatt and Ku Model¹⁰⁶

At equilibrium, the surface and grain boundary compositions of a mixture will, in general, differ from the bulk composition. At least four different types of driving force have been recognised as determining such surface segregation in solids: surface tension, strain energy, electrostatic potential and spread in the Madelung potential. In

the previous analysis of surface segregation in mixed oxides of ceria and lanthana, the experimental results were interpreted in terms of an electrostatic model quantified by a statistical-mechanical treatment by atomistic lattice simulation methods.¹⁰⁴ It is of interest to compare models based on the different types of driving force. Here, a unified segregation model based on macroscopic properties such as surface tension and strain energy¹⁰⁶ is contrasted with the atomistic model due to Mackrodt and Tasker.¹⁰⁴

The ideal solution model (equation 4.22), comprises two contributions to the free energy of the solution: an entropy term arising from the random distribution of atoms and an enthalpy term arising from mixing contributions. The model assumes a semi-infinite system consisting of two phases: a two-component solid solution and a surface plane of atoms. Complete treatment of the equilibrium surface composition of solids will minimise the total free energy of the system (i.e., equation 4.2 holds), with contributions from surface energy, binary solution interaction and elastic solute strain energy. Of the several treatments available, two forms of the regular solution model for alloys, developed by Defay et al, (1966)¹⁷⁰ and by McLean (1957),⁹⁰ respectively, are the preferred versions of several treatments. The present analysis follows a unified formalism of these two forms¹⁰⁶ and applies them to mixed oxides.

Defay¹⁷⁰ adopted a lattice model and calculated the energy of the system in terms of nearest neighbour bond energies. Wynblatt and Ku¹⁷¹ modified Defay's approach to reflect better the physical concept of the problem. The energy of a crystal was computed as a sum over all nearest neighbour bonds, assigned energies ϵ_{AA} , ϵ_{BB} , and ϵ_{AB} , for bonds between AA, BB, and AB, respectively. They expressed the average energy change of removing an A-atom from a bulk alloy to be:

$$-[Z_L \{X_b^A \epsilon_{AA} + (1 - X_b^A) \epsilon_{AB}\} + \{2Z_V [X_b^A \epsilon_{AA} + (1 - X_b^A) \epsilon_{AB}\}]] \quad (4.7)$$

where Z_L = number of lateral bonds made by A within its lattice layer

and Z_V = number of vertical bonds made by A to each of its adjacent lattice layers.

Likewise, the average energy change of returning an A-atom to the surface is:

$$[Z_L \{X_s^A \epsilon_{AA} + (1 - X_s^A) \epsilon_{AB}\} + Z_V \{X_b^A \epsilon_{AA} + (1 - X_b^A) \epsilon_{AB}\}] \quad (4.8)$$

An interaction parameter is defined in terms of the bond energies, thus:

$$\omega = \epsilon_{AB} - \frac{(\epsilon_{AA} + \epsilon_{BB})}{2} \quad (4.9)$$

On combining equations 4.7 and 4.8, their equivalents for the B-atom exchange, and equation 4.9 then the heat of segregation, ΔH_{seg} is:

$$\Delta H_{\text{seg}} = \frac{Z_V (\epsilon_{BB} - \epsilon_{AA})}{2} + 2\omega Z_L (X_b^A + X_s^A) + 2\omega Z_V (X_b^A - 0.5) \quad (4.10)$$

The surface energy of pure component A (γ_A) is:

$$\gamma_A = \frac{-Z_V \epsilon_{AA}}{2\sigma} \quad (4.11)$$

where σ = surface area per atom.

$$\omega = \frac{\Delta H_M}{ZX_b^A X_b^B} \quad (4.12)$$

where Z = coordination number in the solid solution and ΔH_M = heat of mixing.

Substituting equation 4.11, its equivalent for pure B, and equation 4.12 into equation 4.10, then:

$$\Delta H_{\text{seg}} = (\gamma_A - \gamma_B)\sigma + \frac{2\Delta H_M \{Z_L (X_b^A - X_s^A) + Z_V (X_b^A - 0.5)\}}{ZX_b^A X_b^B} \quad (4.13)$$

McLean also applied a regular solution model to the problem of segregation to grain boundaries in dilute alloys. He proposed that the strain energy associated with a solute atom in a solid solution would be eliminated by the exchange of a solute atom from the solution with a solvent atom from the surface. Accordingly McLean equated ΔH_{seg} to the dissipation of the solute strain energy in the solid solution, ϵ_{El} ; that is:

$$\Delta H_{\text{seg}} = -\epsilon_{\text{El}} = -\frac{24 \pi K G r_0 r_1 (r_1 - r_0)^2}{3Kr_1 + 4Gr_0} \quad (4.14)$$

where K = bulk modulus of the solute, G = shear modulus of the solvent, r_0 = radius of solvent atom, r_1 = radius of solute atom.

Although this model was developed for segregation at grain boundaries, its use for segregation at surfaces may be rationalised by assuming that the solute strain energy is dissipated on exchanging a bulk solute atom with a surface solvent atom. Since the geometric constraints at a surface are fewer than at a grain boundary, this extension of the argument is not unreasonable.

On the basis that any model must involve minimisation of the total free energy of the system, which includes surface energies, "alloy" interactions, and solute strain energy, Wynblatt and Ku¹⁰⁶ equated the heat of segregation to the sum of the right-hand sides of equations 4.13 and 4.14; that is

$$\Delta H_{\text{seg}} = (\gamma_A - \gamma_B)\sigma + \frac{2\Delta H_M \{Z_L(X_b^A - X_s^A) + Z_V(X_b^A - 0.5)\}}{ZX_b^A X_b^B} - \frac{24 \pi K G r_0 r_1 (r_0 - r_1)^2}{3Kr_1 + 4Gr_0} \quad (4.15)$$

Taking component A as the solute, r_0 and r_1 in equation 4.15 may be replaced by r_B and r_A , respectively.

As Wynblatt and Ku¹⁰⁶ point out, equation 4.15 may appear to have an element of inconsistency in that ΔH_M of a solid already includes any solute strain energy contributions. In deriving equation 4.13, ΔH_M was assumed to be the same in both the

bulk and surface phases. This infringes the surface analogue of the McLean model which supposes surface solute strain energy is low, however as a consequence of combining equations 4.13 and 4.14, equation 4.15 may be taken as providing some correction for this supposition. The appearance of an enthalpy term rather than a free energy term in equation 4.1 is a consequence of the use of an ideal solution model where the entropy term arises from a random distribution of ions in the solid solution. In actual solid solutions, equation 4.1 becomes:

$$\frac{X_s^A}{X_s^B} = \frac{X_b^A}{X_b^B} \times \exp^{(-\Delta G_{seg}/RT)} = \frac{X_b^A}{X_b^B} \times \exp^{(\Delta S_{seg}/R)} \times \exp^{(-\Delta H_{seg}/RT)} \quad (4.16)$$

where ΔG_{seg} and ΔS_{seg} are the free energy and entropy of segregation, respectively.

Since the entropy terms must parallel the enthalpy terms in equation 4.15, ΔS_{seg} may be formulated to be:

$$\Delta S_{seg} = (S_A - S_B)\sigma + \frac{2\Delta S_M^E \{Z_L(X_b^A - X_s^A) + Z_V(X_b^A - 0.5)\}}{ZX_b^A X_b^B} + \frac{d}{dT} \times \frac{24\pi KGr_0r_1(r_0 - r_1)^2}{3Kr_1 + 4Gr_0} \quad (4.17)$$

where S_A and S_B are the specific surface entropies of the pure components, and ΔS_M^E is the excess entropy of mixing.

Over a range of compositions of solid solutions of components A and B and at a constant temperature, equations 4.15 and 4.17 may be represented by equations 4.18 and 4.19:

$$\Delta H_{seg} = k_1\sigma + k_2 \frac{[k_3(X_b^A - X_s^A) + k_4(X_b^A - 0.5)]}{X_b^A(1 - X_b^A)} + k_5 \quad (4.18)$$

where;

$$k_1 = \gamma_A - \gamma_B \quad k_2 = 2\Delta H_M \quad k_3 = \frac{Z_L}{Z} \quad k_4 = \frac{Z_V}{Z} \quad \text{and} \quad k_5 = \frac{24 \pi K G r_0 r_1 (r_0 - r_1)^2}{3Kr_1 + 4Gr_0}$$

and;

$$\Delta S_{\text{seg}} = k_6 \sigma + k_7 \frac{k_3(X_b^A - X_s^A) + k_4(X_b^A - 0.5)}{X_b^A(1 - X_b^A)} + k_8 \quad (4.19)$$

where

$$k_6 = S_A - S_B \quad k_7 = 2\Delta S_M^E \quad k_8 = \frac{d}{dT} \times \frac{24 \pi K G r_0 r_1 (r_0 - r_1)^2}{3Kr_1 + 4Gr_0}$$

Thus the free energy of segregation may be represented by:

$$\Delta G_{\text{seg}} = k_1 \sigma + k_2 \frac{k_3(X_b^A - X_s^A) + k_4(X_b^A - 0.5)}{X_b^A(1 - X_b^A)} + k_5 + k_9 \sigma + k_{10} \frac{k_3(X_b^A - X_s^A) + k_4(X_b^A - 0.5)}{X_b^A(1 - X_b^A)} + k_{11} \quad (4.20)$$

where;

$$k_9 = k_6 T \quad k_{10} = k_7 T \quad k_{11} = k_8 T$$

At constant temperature, equation 4.20 may be re-written as:

$$\Delta G_{\text{seg}} = k_{12} \sigma + k_{13} \frac{k_3(X_b^A - X_s^A) + k_4(X_b^A - 0.5)}{X_b^A(1 - X_b^A)} + k_{14} \quad (4.21)$$

where;

$$k_{12} = k_1 + k_9 \quad k_{13} = k_2 + k_{10} \quad k_{14} = k_5 + k_{11}$$

The aim of the experimental programme was to measure ΔG_{seg} , σ , and X_s^A as

functions of X_b^A where X_b^A is the equilibrium atom fraction of component A in the bulk solid solution. The bulk and surface composition results, along with surface area and ΔG_{seg} data derived using the McLean model (equation 4.2) are re-presented in table 4.22.

Table 4.22 Surface area, surface composition and experimentally derived ΔG_{seg} for the $\text{Ce}_{1-x}\text{La}_x\text{O}_{2-x/2}$ material series.

X_b^A	X_b^B	X_s^A	X_s^B	Surface Area (m^2g^{-1})	Experimental $-\Delta G_{\text{seg}}$ (kJ mol^{-1})
0	1	0	1	15.2	-
0.001	0.999	0.044	0.956	9.3	34.157
0.010	0.990	0.085	0.915	13.2	19.798
0.050	0.950	0.176	0.824	12.4	12.498
0.100	0.900	0.265	0.735	13.4	10.503
0.200	0.800	0.407	0.593	13.9	9.011
0.300	0.700	0.504	0.496	12.8	7.703
0.400	0.600	0.609	0.391	11.4	7.752
0.500	0.500	0.701	0.299	11.7	7.603
0.600	0.400	0.790	0.210	10.8	8.204
0.700	0.300	0.839	0.161	10.4	7.169
0.800	0.200	0.876	0.124	8.5	5.075
0.900	0.100	0.873	0.127	7.7	-2.404
0.950	0.050	0.920	0.080	13.6	-4.479
0.975	0.025	0.943	0.057	7.2	-7.650
0.990	0.010	0.968	0.032	7.7	-10.577
1	0	1	0	5.9	-

The surface area of these materials (SA), may be reasonably represented by :

$$\text{SA} = 11.5 + 6.6 \times X_b^A - 11.7 \times (X_b^A)^2 \tag{4.22}$$

In a further simplification of the Wynblatt and Ku model, it is assumed that the surface geometry, and hence the planer atom density over this range of mixed oxides is constant .

This data may be fitted to a Freundlich-style adsorption isotherm;

$$X_s^A = k \times (X_b^A)^n \qquad \text{where } n < 1$$

The experimental data may be reasonably represented as;

$$X_s^A = 1.06 \times (X_b^A)^{0.6} \quad (4.23)$$

The empirical relationships 4.22 and 4.23 may be substituted into equation 4.21 to express ΔG_{seg} in terms of X_b^A ;

$$\Delta G_{seg} = k_{14} + k_{12}[11.5 + 6.6X_b^A - 11.7(X_b^A)^2] + k_{13} \frac{k_3(X_b^A - 1.06(X_b^A)^{0.6}) + k_4(X_b^A - 0.5)}{X_b^A(1 - X_b^A)} \quad (4.24)$$

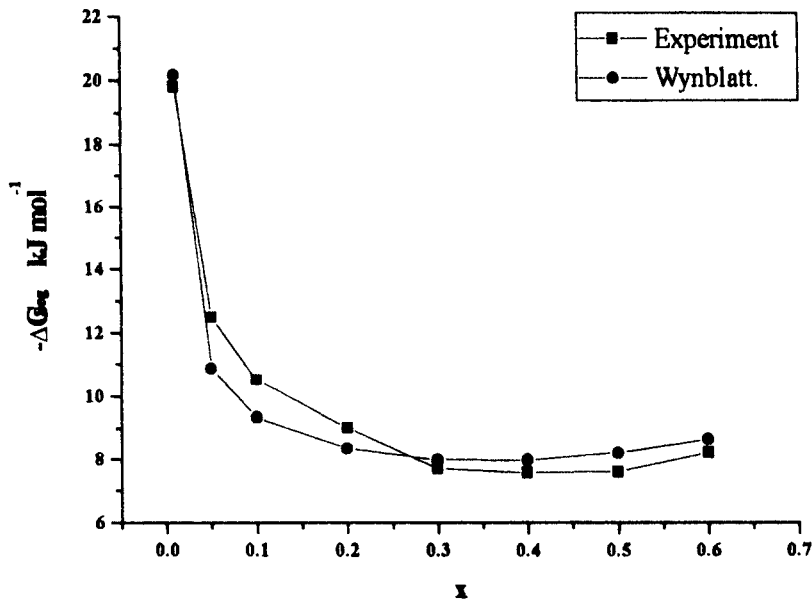
In the determination of the structure and surface crystal face bond coordination factors, the application of equation 4.24 to an oxide system rather than an alloy presents several complications. In an alloy, only metal-metal bonds exist and the coordination environment of all metal atoms in the alloy can be assumed to remain constant, irrespective of composition. On the other hand, in an ionic oxide such as the ceria/lanthana system, all cations are bonded to (and therefore coordinated with), oxide anions. In order to apply the Wynblatt and Ku¹⁰⁶ model, it is therefore necessary to apply the coordination concept with respect to cation-anion 'molecules'. This concept was applied to segregation by Wynblatt and McCune (1988)⁸⁶ for the isovalent solution of CaO doped MgO in which (by analogy), equation 4.24 would represent the surface energy change when one 'molecule' of CaO in the bulk is exchanged with a molecule of MgO in the surface. This surface energy was demonstrated to be identical to that of just a cation exchange. In the present system a further complication is introduced by the aliovalency of the lanthanum dopant which inevitably introduces oxide anion vacancies into the structure. This complication is not specifically allowed for in the Wynblatt and Ku model,¹⁰⁶ but the effects of the dopant aliovalency will be incorporated into the variations in the solute strain and solute-solvent interaction energy contributions. The cationic structure of cerium oxide has the fluorite structure, the face centre cubic structure which allows the constants k_3 and k_4 to be set; $k_3 = Z_L/Z = 6/12$ and $k_4 = Z_V/Z = 3/12$ for the 111 surface, thus permitting equation 4.24 to be re-presented as:

$$\Delta G_{\text{seg}} = k_{14} + k_{12}(11.5 + 6.6X_b^A - 11.7(X_b^A)^2) + k_{13} \frac{0.5(X_b^A - 1.06(X_b^A)^{0.6} + 0.25(X_b^A - 0.5))}{X_b^A(1 - X_b^A)}$$

(4.25)

Fitting the experimental data over the solid solution range; $0.01 < X_b^A < 0.6$ to equation 4.25 results in $k_{14} = -18214$, $k_{12} = 870$, and $k_{13} = 788$. The experimental and modelled (equation 4.25) free energy of segregation as a function of X_b^A , the atomic fraction of lanthanum in the bulk is presented in figure 4.32.

Figure 4.32 A plot of experimental and modelled (Wynblatt and Ku Model) ΔG_{seg} as a function of x , for $0.01 < x < 0.6$.



Comparison of the quality of the statistical analysis of the Mackrodt & Tasker¹⁰⁴ model with the Wynblatt and Ku¹⁰⁶ model is made in table 4.23.

Table 4.23 Comparison of statistical indices of the electrostatic and bond models

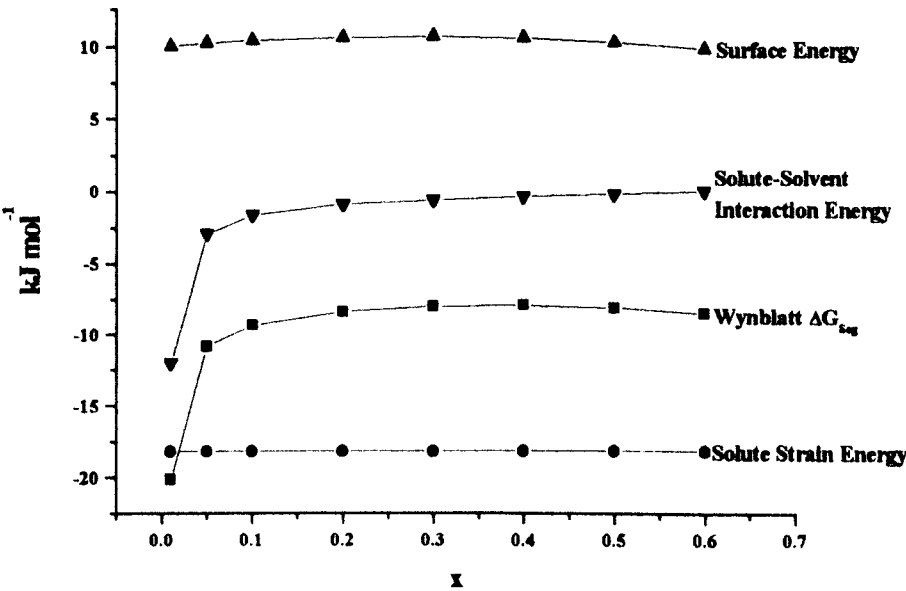
Model	r ²	F-statistic
Electrostatic (Mackrodt and Tasker)	0.998	2800
Bond (Wynblatt and Ku)	0.95	50

From an overall point of view, the electrostatic model is preferred. However an advantage of the bond model is that it enables factorisation of the contributions to the free energy of segregation into a surface energy, a binary solution interaction factor and an elastic solute strain energy. Table 4.24 and Figure 4.33 present these factorised contributions derived from the experimental data.

Table 4.24 Contributory factors to ΔG_{seg} for $\text{Ce}_{1-x}\text{La}_x\text{O}_{2-x/2}$ for $0.01 < x < 0.6$

Bulk x	Solute Strain Energy kJ mol ⁻¹	Surface Energy kJ mol ⁻¹	Solute-Solvent Interaction Energy kJ mol ⁻¹	ΔG_{seg} (Modelled) (Wynblatt & Ku) kJ mol ⁻¹	ΔG_{seg} (McLean) kJ mol ⁻¹
0.01	-18.214	10.061	-12.014	-20.167	-19.798
0.05	-18.214	10.267	-2.909	-10.856	-12.498
0.10	-18.214	10.477	-1.603	-9.340	-10.503
0.20	-18.214	10.746	-0.871	-8.338	-9.011
0.30	-18.214	10.811	-0.590	-7.993	-7.703
0.40	-18.214	10.673	-0.430	-7.970	-7.572
0.50	-18.214	10.331	-0.314	-8.197	-7.603
0.60	-18.214	9.786	-0.214	-8.642	-8.204

Figure 4.33 A plot of the variations in magnitude of the contributory factors to ΔG_{seg} for $\text{Ce}_{1-x}\text{La}_x\text{O}_{2-x/2}$ for $0.01 < x < 0.6$



It is observed that the solute strain energy is independent of the composition of the solid solution, whereas the magnitudes of both of the other contributions decrease as the solid solution is progressively surface enriched with lanthana. The strain energy associated with a solute cation in a solid solution arises from the difference between the solute and solvent cationic volumes and is eliminated on the exchange of a solute cation in the bulk with a solvent cation at the surface. This is evaluated as favouring segregation and is determined to be invariant with composition of the solid solution.

The surface energy term is related to the heats of sublimation of the pure oxides, and their heat of mixing. This is evaluated as not favouring segregation, and was determined to be weakly dependent on the composition of the solid solution.

The solute-solvent interaction energy was evaluated as favouring segregation and was found to be strongly dependent on the composition of the solid solution, asymptotically tending toward a low value (possibly zero) as the solid solution limit composition is approached. In algebraic terms, the variation in the solute-solvent interaction energy was found to vary with composition according to an exponential expression.

The factorisation of the contributions further shows that the main determinant of the dependency of the free energy of segregation on the composition of the solid solution is the solute-solvent interaction energy: in percentile terms, its contribution toward the modelled ΔG_{seg} decreases from approximately 30% to 1% as the atomic fraction of lanthanum in the solid solution is increased from $x = 0.01$ to $x = 0.6$. This solute-solvent interaction energy contribution depends predominantly on coulombic and compensatory vacancy interactions caused by the aliovalency of the lanthanum dopant. This conclusion lends support to the Mackrodt and Tasker electrostatic model¹⁰⁴ in which such interactions are the basis of the theoretical variation in ΔG_{seg} with solid solution composition.

4.2.3.1.1.4 Summary

The free energy of segregation and surface area of this range of mixed oxides are strongly dependent on the composition of the mixed oxide. The free energy of

surface segregation of lanthanum has been correlated with its atomic fraction in the mixed oxide in an expression derived by Wynblatt and Ku¹⁰⁶ from an essentially bond model approach but wherein bond quantities have been replaced by empirical parameters such as surface energies and heat of mixing. Whereas the overall treatment is less preferred than an alternative based on an electrostatic model, it enables factorisation of the major contributions to the free energy of surface segregation. The major factor generating the composition dependency of the free energy is the binary ceria/lanthana interaction energy. It is concluded that surface segregation in the present study is best described in terms of the solute-solute interactions accommodated in the electrostatic model developed by Mackrodt and Tasker,¹⁰⁴ rather than the bond model developed by Wynblatt and Ku.¹⁰⁶

4.3 Temperature Programmed Desorption Studies

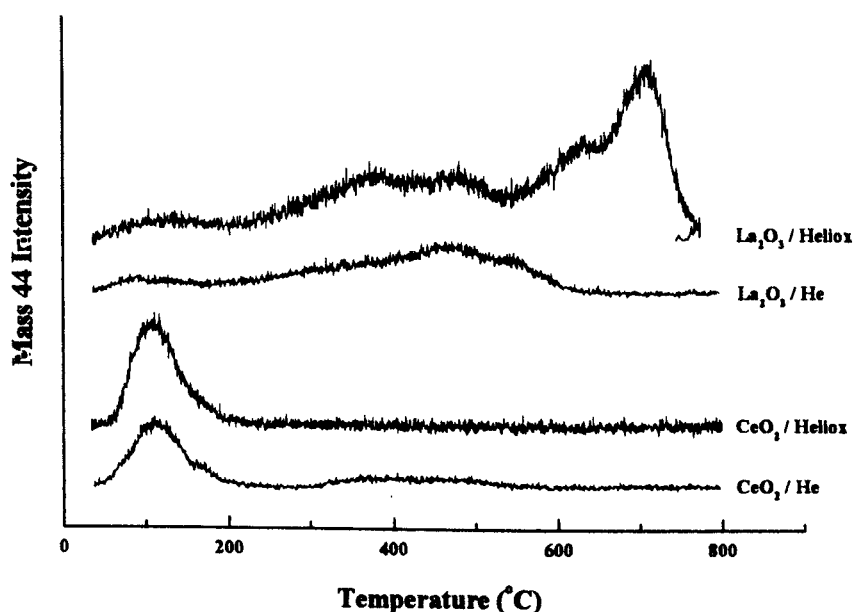
4.3.1 Basicity Measurements by CO₂ TPD

Initial experiments were designed to investigate CO₂ temperature programmed desorption (TPD) over the solid solution system end-members (CeO₂ and La₂O₃) in order to determine a suitable experimental methodology. Due to the known tendency of the lanthanide oxides to adsorb moisture and carbon dioxide from the atmosphere and form bulk hydroxide and carbonate materials, it was considered necessary to incorporate a 'pre-TPD' in order to decompose the materials to oxides *in situ*, before the adsorption study. The first experiments were therefore to determine the most suitable carrier gas and adsorption gas. The choice of carrier gas was between He and 21% O₂ in He, (Heliox). Helium would generally be the preferred choice due to its inert nature, however the reducibility of ceria based solid solutions under inert conditions was a possible cause of error. The formation of a reduced surface would not be representative of the materials under the high P_{O₂} catalytic reaction conditions, and therefore use of He was compared with similar experiments using Heliox. The choice of adsorbent gas was between 2% CO₂/Ar and pure CO₂.

The adsorbent gases were investigated first, over lanthana following pre-TPD in Heliox. There was no significant difference between the two desorptions following one hour exposures to both gases at room temperature. Further experiments were therefore completed using pure CO_2 as the adsorbant gas in order to simplify the experimental procedure. A matrix of experiments was then completed in order to determine the effect of carrier gas on CO_2 TPD over ceria and lanthana. In these experiments the pre-TPD results are not compared as some were performed over fresh samples and some were performed over previously used samples which had been stored *in situ* in the experimental apparatus. Experiments were performed following pre-TPD in the appropriate carrier gas, cooling to room temperature under the flowing carrier gas and then exposure to flowing CO_2 for 1 hour at room temperature. The appropriate carrier gas flow was then resumed and the temperature program started. The desorption of other species was not observed with the lanthana samples, although significant desorptions of water were observed in the CO_2 TPD for the ceria experiments, particularly when Heliox was used as a carrier gas. This would seem to indicate that there may be trace water present in the Heliox which was adsorbed more efficiently by the ceria sample than by the lanthana. This could have been removed with the use of molecular sieves, but as this was not done for the catalytic study, it was not appropriate to do so for the TPD study. The results of these experiments are shown in figure 4.34.

CO was observed in the mass spectrometer trace for all samples, but only in the presence of CO_2 . The CO/CO_2 ratio was that expected from CO_2 fragmentation in the mass spectrometer, and therefore the desorption of CO as a distinct species was ruled out. It should be noted that due to atmospheric and other experimental variables the intensity of the uncalibrated mass spectrometer signals is not truly quantitative, but the general trends observed can be reasonably compared. Later quantitative studies are based on results following calibration of the mass spectrometer.

Figure 4.34 A plot showing the variation in TPD of CO_2 over CeO_2 and La_2O_3 , using He and Heliox carrier gases, (room temperature adsorption).



It is observed from figure 4.34 is that several adsorption sites exist, with different strengths, both from material to material, and on each individual material. The strength of the main CO_2 adsorptions on ceria are notably less than on lanthana. On ceria, the main desorption of CO_2 occurs at just over 100°C , irrespective of TPD carrier gas. This indicates that the bonds between CO_2 and the surface are weaker for ceria than in the case of lanthana (main desorption beginning at approximately 250°C). This is expected due to the higher basicity of lanthana.^{141, 146 - 147} The effect of basicity is also demonstrated by the observed increase in CO_2 adsorbed, and adsorption strength over the ceria surface pre-reduced by pre-TPD in He. On the reduced ceria surface a second higher temperature desorption is observed above 300°C which is not observed with the oxidised material. This is due to the increase in the concentration of surface basic sites as a consequence of reduction in the inert carrier pre-TPD. There is no discernible CO_2 desorption above approximately 200°C over the (assumed) fully oxidised material.

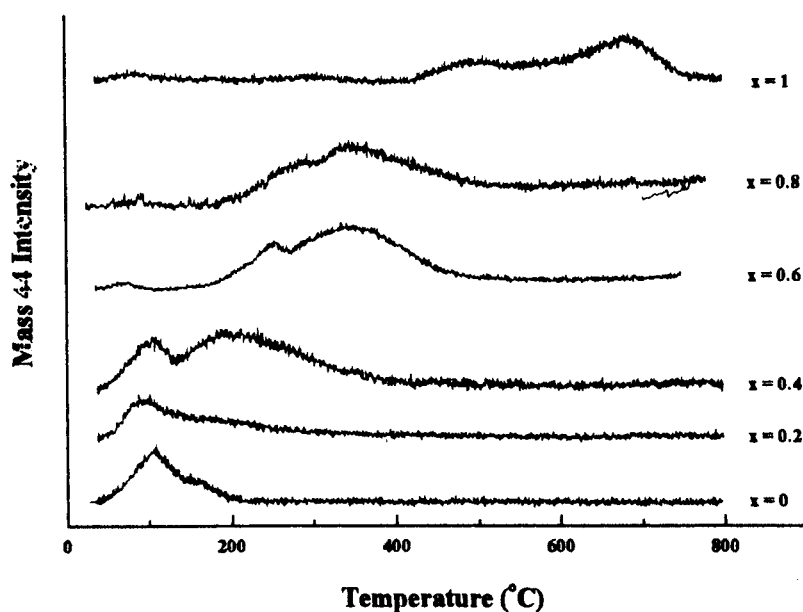
There is also a notable difference between the results from the lanthana experiments under different carrier gases. The amount of CO_2 adsorbed and the strength of adsorption are increased after the oxidative pre-TPD. As lanthana can effectively be considered irreducible, the logical conclusion is that the oxidative pre-

treatment resulted in an increase in the concentration of basic surface adsorption sites. The most likely explanation for this observation is that the oxidative pre-TPD is more efficient than the reductive pre-treatment in forming basic adsorption sites; the surface of lanthana is known to be easily carbonated, and the presence of oxygen in the carrier during the pre-TPD would facilitate oxidative decomposition of the surface carbonate species. In the case of the He pre-TPD, decomposition would be retarded due to the requirement of reduction of the (irreducible) lanthana being the only source of oxygen. It is likely that the decomposition of the lanthana surface carbonate species occurs by different mechanisms, depending on the partial pressure of oxygen in the carrier gas, and the oxidative decomposition proceeds at lower temperatures than the reductive mechanism.

As the aim of the TPD studies was to determine the adsorption/desorption characteristics of the catalyst materials under conditions approximating to the catalytic reaction conditions, all experiments from this point onward were conducted using Heliox as the carrier gas in order to simulate the oxidative reaction environment. A small scale study was completed to determine the effect of adsorption temperature on the CO₂ adsorption/desorption properties of the catalyst series end-members. No significant effect of temperature was observed for either material between room temperature and 200°C adsorptions. All experiments in the following series were therefore performed using Heliox carrier and adsorption was for 1 hour at room temperature.

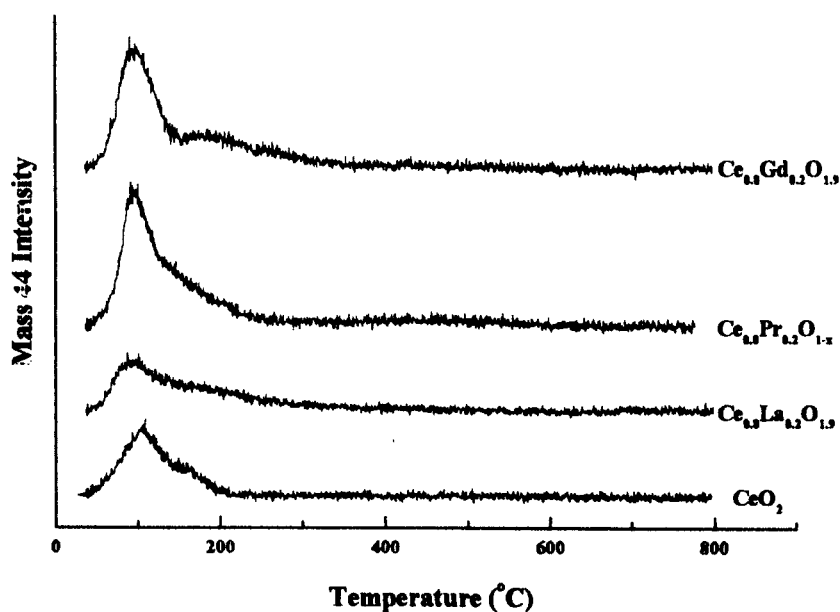
The following set of experiments were performed in order to investigate and quantify the variation in basicity with composition for the catalyst materials. The effect of lanthanum concentration was investigated with materials $x = 0, 0.2, 0.4, 0.6, 0.8$ and 1 . The effect of dopant type was also investigated using praseodymium and gadolinium dopants at the $x = 0.2$ concentration. The amount of CO₂ desorbed was quantified, and as the surface areas of the materials were also determined, the specific basicity was determined. The strength of the basic sites was compared from material to material by comparison of desorption temperature, as shown in figure 4.35.

Figure 4.35 A plot showing the variation in TPD of CO₂ adsorbed at room temperature with composition, over Ce_{1-x}La_xO_{2-x/2} (x = 0, 0.2, 0.4, 0.6, 0.8 and 1), using Heliox carrier gas.



It can be observed in figure 4.35 that the CO₂ adsorption strength increases with lanthanum content of the catalyst material. This can be deduced by the increase in the temperature at which the main CO₂ desorption occurs. Up to lanthanum concentrations of x = 0.4, the presence of two peaks in the desorption spectra is evidence for two CO₂ adsorption sites, the intensity of the stronger of the two increasing with lanthanum content. Beyond x = 0.4, there is no evidence for weakly bound adsorbed CO₂ which is characteristic of the ceria rich materials. Knowing that the solid solution limit in the bulk material is approximately x = 0.6, this result suggests that the lanthanum content of the surface is significantly higher than in the bulk material. This is supported by the surface composition analysis data in the previous section in which surface segregation of lanthanum was observed. The effect of different dopants on CO₂ TPD is shown in figure 4.36 in which Ce_{0.8}La_{0.2}O_{1.9} is compared with Ce_{0.8}Pr_{0.2}O_{2-x} and Ce_{0.8}Gd_{0.2}O_{1.9}. It is observed from figure 4.36 that the variation in the type of lanthanide dopant results in only subtle effects on the CO₂ TPD spectra.

Figure 4.36 A plot showing the variation in TPD of CO_2 adsorbed at room temperature with composition, over $\text{Ce}_{0.8}\text{La}_{0.2}\text{O}_{1.9}$, $\text{Ce}_{0.8}\text{Pr}_{0.2}\text{O}_{2-x}$ and $\text{Ce}_{0.8}\text{Gd}_{0.2}\text{O}_{1.9}$, using Heliox carrier gas.



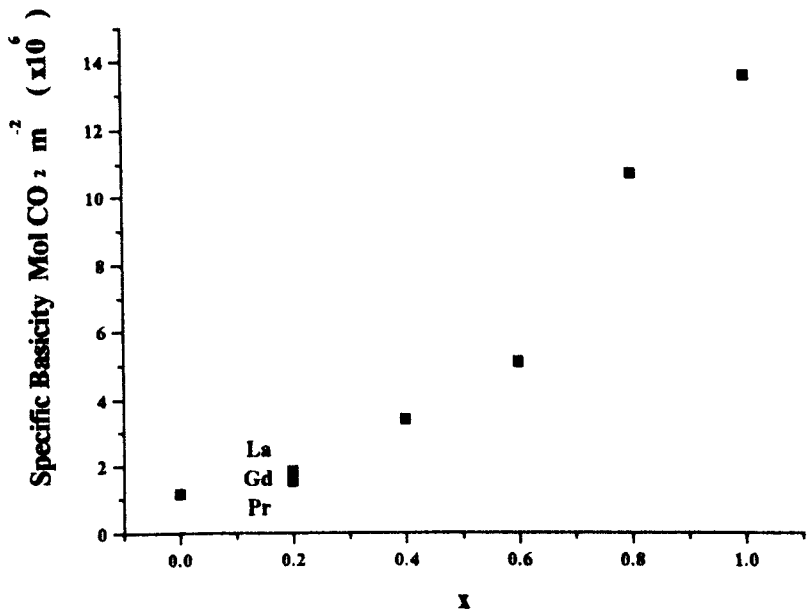
Lanthana is known to be the most basic of the lanthanide oxides. Assuming that the lanthanide cations segregate to the surface of ceria in a similar fashion, then it could be reasonably expected that for a given dopant concentration the dopant with the most basic oxide would result in the largest promotion of surface basicity in the doped material. This is indeed observed in this study; with lanthanum having the most pronounced high temperature desorption peak in comparison with the low temperature desorption peak. Gadolinium doped ceria has a significantly promoted basicity with respect to undoped ceria, although to a lesser extent than lanthanum doped ceria, whilst praseodymium doped ceria exhibits similar adsorption / desorption characteristics to the undoped material. It would appear that the facile $\text{Pr}^{\text{III}} \rightarrow \text{Pr}^{\text{IV}}$ oxidation state change results in less promotion of surface basicity than by the trivalent lanthanide dopants. The quantitative analysis of the CO_2 TPD experimental results are presented in table 4.25.

Table 4.25 Experimental results and determination of specific basicity expressed as mol CO₂ adsorbed m⁻² for Ce_{1-x}La_xO_{2-x/2} (x = 0, 0.2, 0.4, 0.6, 0.8 and 1), Ce_{0.8}Pr_{0.2}O_{2-x} and Ce_{0.8}Gd_{0.2}O_{1.9}.

Material	Surface Area (m ² g ⁻¹)	Volume adsorbed per gram ml CO ₂ g ⁻¹	Volume adsorbed per m ² ml CO ₂ m ⁻²	Nº moles adsorbed per gram mol CO ₂ g ⁻¹	Nº moles adsorbed per m ² mol CO ₂ m ⁻²
CeO ₂	15.185	0.385	0.0254	1.72 × 10 ⁻⁵	1.133 × 10 ⁻⁶
Ce _{0.8} La _{0.2} O _{1.9}	13.879	0.562	0.0405	2.51 × 10 ⁻⁵	1.808 × 10 ⁻⁶
Ce _{0.6} La _{0.4} O _{1.8}	11.418	0.585	0.0751	3.83 × 10 ⁻⁵	3.354 × 10 ⁻⁶
Ce _{0.4} La _{0.6} O _{1.7}	10.826	1.229	0.1135	5.49 × 10 ⁻⁵	5.071 × 10 ⁻⁶
Ce _{0.2} La _{0.8} O _{1.6}	8.531	2.052	0.2405	9.16 × 10 ⁻⁵	10.737 × 10 ⁻⁶
La ₂ O ₃	5.894	1.800	0.3054	8.03 × 10 ⁻⁵	13.624 × 10 ⁻⁶
Ce _{0.8} Pr _{0.2} O _{2-x}	17.934	0.599	0.0334	2.67 × 10 ⁻⁵	1.489 × 10 ⁻⁶
Ce _{0.8} Gd _{0.2} O _{1.9}	18.595	0.670	0.0360	2.99 × 10 ⁻⁵	1.608 × 10 ⁻⁶

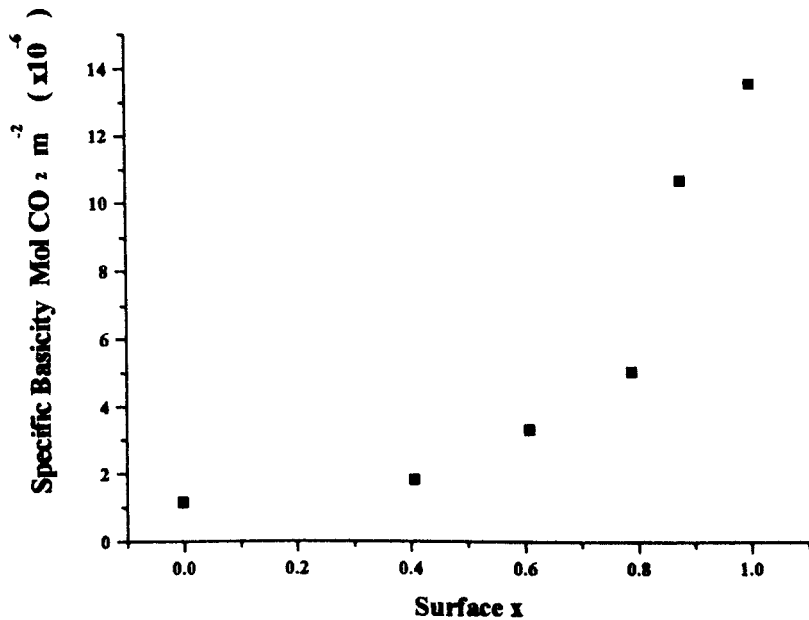
The variation in specific basicity (expressed as number of moles of CO₂ adsorbed m⁻²), with bulk composition and type of dopant is shown in figure 4.37.

Figure 4.37 The variation in specific basicity with bulk composition and dopant.



Specific basicity is observed to increase by over one order of magnitude with increasing lanthanum concentration in ceria in a smooth non-linear fashion. It is known that lanthanum preferentially segregates to the surface of lanthanum doped ceria solid solutions. The variation in specific basicity (expressed as moles of CO_2 adsorbed m^{-2}), with surface composition is shown in figure 4.38. The variation in specific basicity does not parallel the variation in surface composition with bulk composition (section 4.2.3), thus it can be deduced that the adsorption site for CO_2 is not directly proportional to the concentration of lanthanum cations at the surface, but rather to the concentration of some particular arrangement of lanthanum cations at the surface which is favoured at higher lanthanum concentrations.

Figure 4.38 A plot showing the variation in specific basicity with surface composition.



It was suggested in the previous surface composition analysis (section 4.2.3) that the solid solution limit at the surface of the lanthanum doped ceria solid solution system appeared to be of the order of $x = 0.8$. This value is in excess of the previously determined bulk solid solution limit which was determined to be approximately $x = 0.6$, and was explained in terms of the surface free energy stabilising the fluorite solid solution structure at higher dopant levels than is possible in the bulk material which is governed by the lattice energy. It can be observed in figure 4.38 that there is a rapid

rise in specific basicity beyond a surface composition of $x = 0.8$ which corresponds well with the previously derived surface solid solution limit. This correlation suggests that the sharp rise in specific basicity beyond the bulk composition of $x = 0.6$ (surface composition $x = 0.8$) is actually due to segregated lanthana on the surface of the saturated solid solution.

4.3.2 CH₄ TPD measurements.

The measurement of CH₄ adsorption and desorption was investigated over the two end members of the catalyst series; ceria and lanthana. The experiments were completed using Heliox carrier gas and 1 hour adsorption times. No desorption spectra were obtained from these experiments, even with elevated temperature adsorptions. It was therefore concluded that the adsorption of CH₄ on the catalysts used in the present study is of a transient nature and was beyond further investigation using temperature programmed desorption techniques.

4.3.3 CO TPD measurements.

4.3.3.1 Blank runs

Due to the known ease of activation of CO in comparison with hydrocarbons such as methane, it was deemed necessary to complete an experimental 'blank run' in order to determine the reactivity of CO toward the experimental apparatus itself. In the experiment the adsorption and TPD were completed with quartz wool only in the steel sample tube. The experiment was completed using an adsorption temperature of 340°C, typical of the oxidation reaction conditions.

It was observed that negligible adsorption/desorption activity occurred for an adsorption temperature of 340°C. Quantification of the blank run and comparison with typical catalyst adsorption/desorption run quantification, determined that in the case of the lowest specific adsorptivity material (ceria), the desorption from the apparatus was negligible. In the case of the other materials which were subsequently determined to

have significantly higher specific adsorptivities, the negligible error caused by this phenomenon, caused by contribution from adsorption on the internal surfaces of the apparatus is reduced in all cases in comparison with ceria. The highest adsorption temperature used in this study was limited to 340°C on the basis of this study, in order that the effects of activated adsorptions on the internal surfaces of the apparatus could be eliminated. It should also be noted that there were no discrete desorptions of CO - all desorptions were mass 44 (CO₂) due to oxidation of the adsorbed CO by the heliox carrier gas.

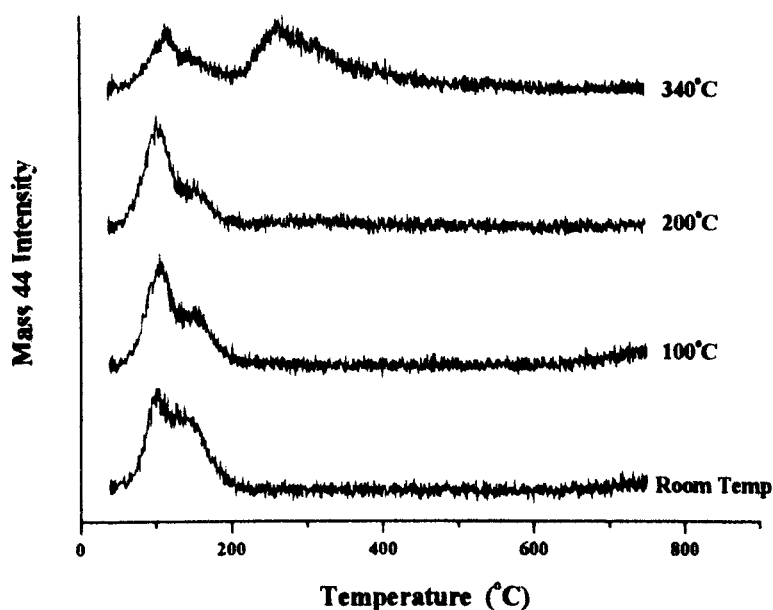
4.3.3.2 Temperature Effects

The aim of the next set of experiments was to determine the CO adsorption/desorption properties of ceria, lanthana and selected solid solution compositions. Initially, the effects of adsorption temperature were investigated.

4.3.3.2.1 Ceria

Variation in CO-TPD with adsorption temperature over ceria is shown in figure 4.39.

Figure 4.39 The variation in CO-TPD spectra of ceria with adsorption temperature.

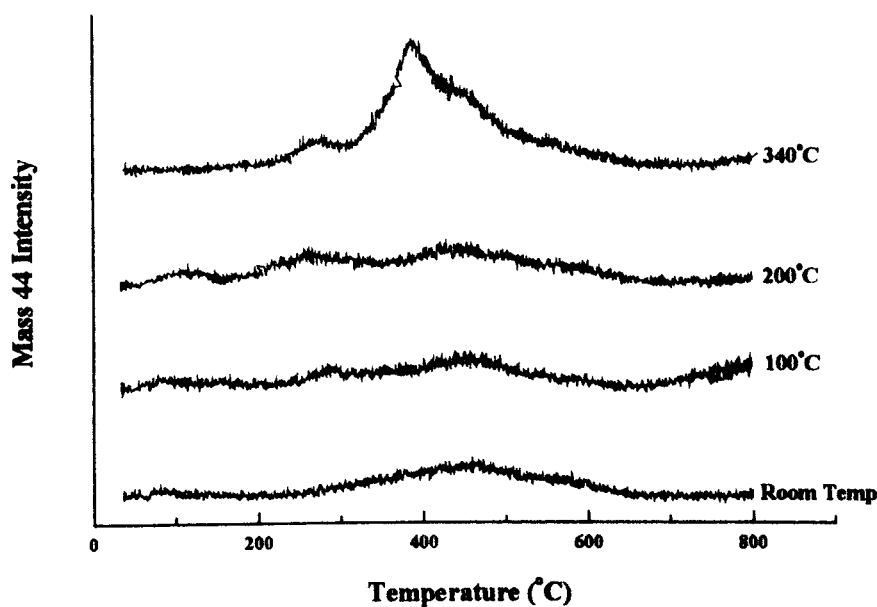


Two low temperature (approx. 100°C and 150°C) desorption peaks are observed for CO-TPD over ceria which are relatively invariant with adsorption temperature, (although the 150°C peak is noted to reduce in intensity as adsorption temperature is increased). This observation suggests that the weak adsorption sites responsible for the low temperature desorption peak do not require thermal activation. As the adsorption temperature is increased from 200°C to 340°C, a further higher temperature desorption peak is observed at approximately 250°C. It can be concluded that at least two well resolved CO adsorption sites are thermally activated under the catalytic reaction conditions over ceria.

4.3.3.2.2 Lanthana

A similar plot of the variation in CO-TPD spectra with adsorption temperature over lanthana is shown in figure 4.40.

Figure 4.40 A plot showing the variation in CO-TPD spectra of lanthana with adsorption temperature.



In the case of CO-TPD over lanthana, there is no low temperature desorption observed, regardless of the adsorption temperature. At room temperature a broad low-intensity desorption is observed between approximately 300°C and 650°C, which is

resolved with increasing adsorption temperature up to 200°C into separate desorption peaks at approximately 100°C, 250°C and 450°C. Following CO adsorption at 340°C, three intense and well resolved desorptions are observed at 275°C, 400°C and 450°C. It can be concluded that at least three well resolved CO adsorption sites are thermally activated under the catalytic reaction conditions over lanthana.

4.3.3.2.3 Quantitative Analysis

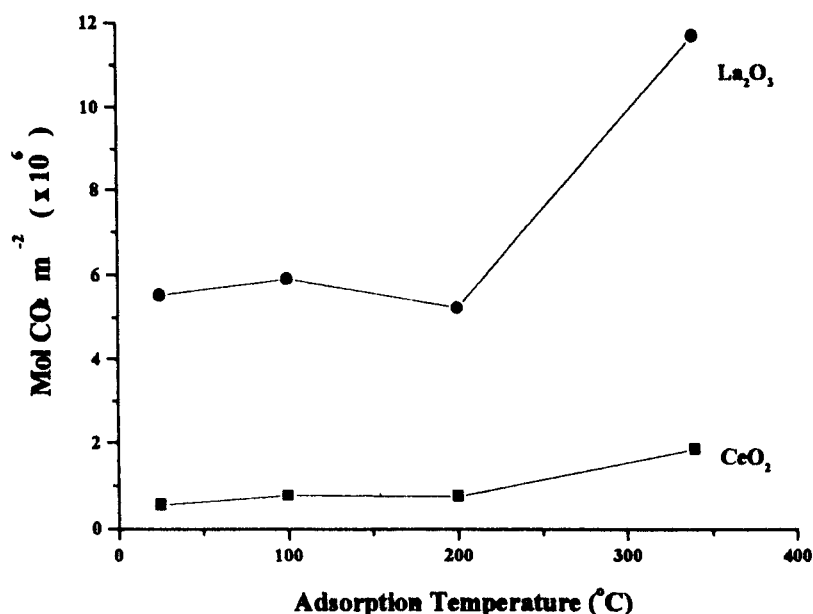
Quantitative analysis of variation in the CO₂ desorbed from both ceria and lanthana with adsorption temperature was also completed, the results of which are presented in table 4.26. The variation in CO-TPD with adsorption temperature for ceria (9.868 m²g⁻¹) and lanthana (5.894m²g⁻¹) is shown in figure 4.41.

Table 4.26 Quantitative analysis of CO-TPD adsorption temperature experiments.

Adsorption Temperature (°C)	CeO ₂ mol CO ₂ g ⁻¹	CeO ₂ mol CO ₂ m ⁻²	La ₂ O ₃ mol CO ₂ g ⁻¹	La ₂ O ₃ mol CO ₂ m ⁻²
25	5.55×10^{-6}	5.62×10^{-7}	32.60×10^{-6}	5.53×10^{-6}
100	7.65×10^{-6}	7.75×10^{-7}	34.90×10^{-6}	5.92×10^{-6}
200	7.48×10^{-6}	7.58×10^{-7}	31.00×10^{-6}	5.26×10^{-6}
340	18.60×10^{-6}	1.88×10^{-6}	68.80×10^{-6}	1.17×10^{-5}

It is observed from figure 4.41 that the number of CO adsorption sites increases with adsorption temperature for both ceria and lanthana, with significant increases beginning from approximately 200°C - 340°C. The room temperature adsorption CO adsorption site density of lanthana is approximately one order of magnitude greater than that of ceria. The thermal activation of further CO adsorption sites is also observed to be more rapid with increasing temperature for lanthana than ceria.

Figure 4.41 A plot showing the variation in total specific desorption with adsorption temperature for CeO_2 and La_2O_3 .



4.3.3.3 Effect of Oxygen

In the CO-TPD experiments thus far, the only desorbed species observed was CO_2 , undoubtedly due to the presence of oxygen in the Heliox carrier gas. Further experiments were therefore completed in order to determine the CO-TPD characteristics under an inert carrier. The reason for these experiments was to determine whether any adsorbed CO would be oxidatively adsorbed. A study of oxidative adsorption over the reducible ceria materials was of interest in order to determine the extent of reducibility of the catalyst material by the reactants, and the effect of oxygen partial pressure on catalyst reducibility. It was postulated that under reducing conditions CO would still be at least partially oxidatively adsorbed on ceria, resulting in a reduction of the bulk material. The reduction of the bulk material by CO should be progressively reduced with increasing oxygen partial pressure. The extent of oxidative adsorption should also be a function of adsorption temperature, higher temperatures facilitating the reduction of bulk ceria by CO.

Experiments were performed using ceria and lanthana materials in order to gain contrasting results for reducible and irreducible oxides, respectively. Two adsorption temperatures were used in each case which had been shown in the previous section to

yield low (25°C), and high (340°C), adsorption site densities in the test materials. In each case, following CO adsorption, the TPD experiment was run using He carrier gas in order to determine CO-TPD spectra under inert conditions. Following the initial inert carrier TPD, the sample was subsequently cooled in the He carrier and the TPD experiment was immediately repeated under heliox in order to determine whether any adsorbed CO species were not desorbed under the inert carrier, were desorbed under oxidative conditions.

4.3.3.3.1 Ceria

In the case of ceria, the variation in the CO and CO₂ desorption after CO adsorption, with adsorption temperature under He carrier is shown in figure 4.42. The quantification of the CO and CO₂ desorptions are presented in table 4.27.

Figure 4.42 A plot showing the variation in CO and CO₂ desorption following CO adsorption, with adsorption temperature under He.

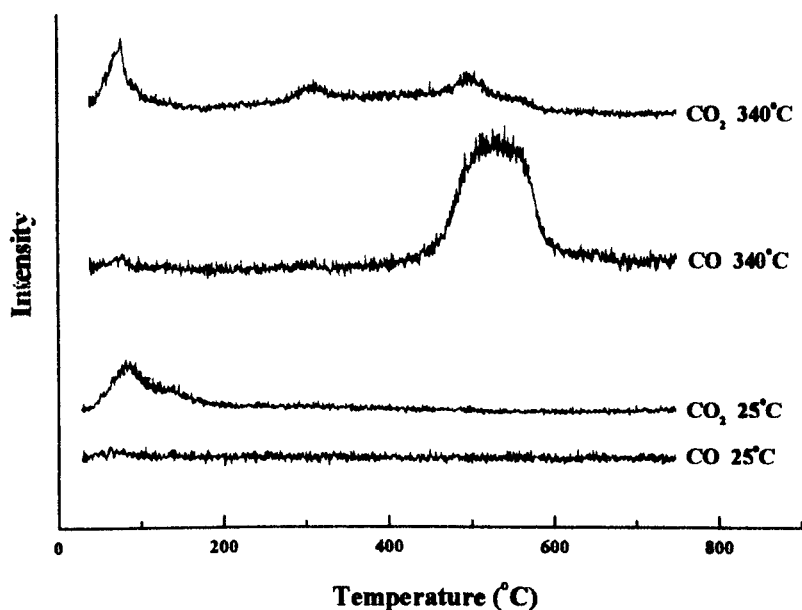


Table 4.27 CO and CO₂ desorption quantification for figure 4.42

Adsorption Temperature (°C)	CO Desorption μmol g ⁻¹	CO ₂ Desorption μmol g ⁻¹	Total CO _x Desorption μmol g ⁻¹
25	0	11.3	11.3
340	24.3	21.0	45.3

It is observed from figure 4.42 that both the amount of oxidatively and non-oxidatively adsorbed CO, and the strength of the adsorption increases with adsorption temperature. The amount of CO oxidatively adsorbed (as measured by CO₂ desorption quantification) is observed to double over the adsorption temperature range studied, confirming that the reduction of ceria by adsorbed CO is a thermally activated process. Two separate high temperature oxidative desorptions are observed at approximately 300°C and 500°C. From this it can be ascertained that two strong oxidative adsorption sites exist on the ceria surface in the absence of gaseous oxygen, clearly corresponding to two separate surface oxygen species. The observed appearance of a single CO desorption at the higher CO adsorption temperature (and therefore with increasing extent of reduction of the ceria surface), suggests that cerium (III) cations at the surface provide the non-oxidative CO adsorption sites. The concentration of these sites increases with the extent of reduction of the ceria.

A similar plot showing the variation in the CO and CO₂ desorption under Heliox, after CO adsorption and desorption under inert carrier (He), with adsorption temperature is shown in figure 4.43. Quantification of the CO and CO₂ desorptions during the subsequent oxidative desorption are presented in table 4.28.

Under the Heliox carrier gas conditions, no desorptions of CO were observed, and therefore no CO quantification was done for these experiments. It should be noted that all observed CO desorptions under the oxidative carrier were coincident with the observed CO₂ desorptions, and of the correct order to be attributed to CO₂ fragmentation in the Mass Spectrometer.

Figure 4.43 A plot showing the variation in CO and CO₂ desorption following CO adsorption, with adsorption temperature under Heliox

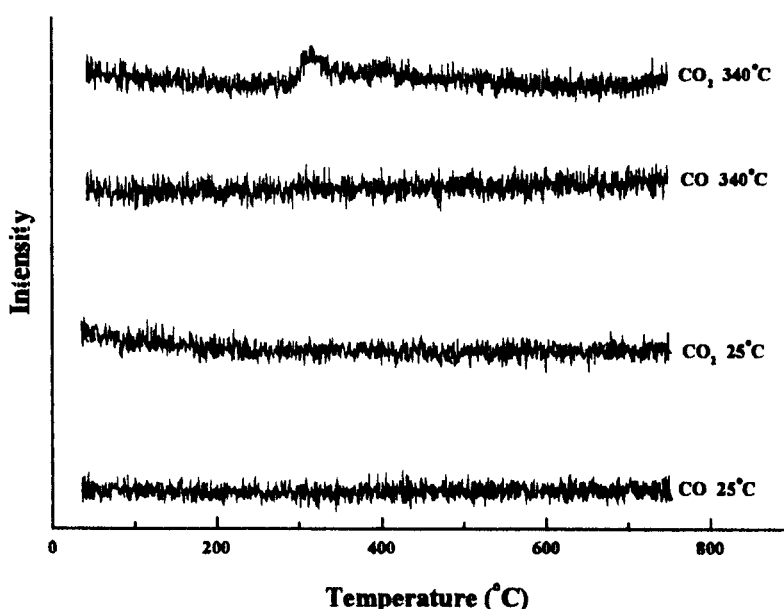


Table 4.28 CO and CO₂ desorption quantification for figure 4.43.

Adsorption Temperature (°C)	CO Desorption $\mu\text{mol g}^{-1}$	CO ₂ Desorption $\mu\text{mol g}^{-1}$
25	-	-
340	-	2.6

The observation of two CO₂ desorption at approximately 300°C and 400°C in the Heliox TPD following the He TPD indicates that not all of the adsorbed CO was thermally desorbed under the inert carrier within the 25°C - 750°C TPD range. The CO₂ desorption quantification indicates that the amount of carbonaceous residue following CO adsorption not desorbed under inert carrier TPD conditions is thermally activated with CO adsorption temperature, (and therefore with the extent of reduction of the ceria). The presence of two separate desorptions suggests that the residue remaining following the inert carrier TPD is adsorbed on two different sites. As the capping oxygen has been cited as the oxidative adsorption site, it is inferred that the residue is adsorbed on cation sites, the two desorptions observed under Heliox being due to two different adsorption sites on Ce^{III} and Ce^{IV} surface cations. Following CO adsorption at 340°C, the amount of CO₂ desorbed under the second Heliox carrier

TPD following the initial TPD under He corresponded to approximately 5% of the total desorption. This suggests that the ratio between the sites responsible for the He carrier desorptions and the sites responsible for the Heliox desorptions varies with adsorption temperature, and thus with the extent of reduction of the surface.

With regards the nature of the residual adsorbed species, it is possible that a Boudouard reaction type disproportionation ($2\text{CO} \rightarrow \text{CO}_2 + \text{C}$) occurs, resulting in carbon deposition. The deposited carbon being subsequently oxidised at low temperature in the presence of gaseous oxygen. It is plausible that the CO_2 resulting from oxidation of the carbonaceous residue is thermally desorbed at a temperature similar to that observed for desorptions under the heliox carrier gas, as shown in figure 4.39. Evidence for such a disproportionation reaction occurring is presented in the literature review chapter, section 2.2.1.

4.3.3.3.2 Lanthana

Similar experiments were subsequently completed over lanthana. A plot showing the variation in CO and CO_2 desorption following CO adsorption, with adsorption temperature under He is shown in figure 4.44. Quantification results of the CO and CO_2 desorptions are presented in table 4.29.

The presence of three strong CO desorptions at 100°C, 350°C and 500°C following CO adsorption at 340°C can be observed, indicative of the presence of at least three different CO adsorption sites on lanthana, as opposed to one desorption at 500°C for the analogous experiment over ceria (figure 4.42). As reduction of lanthanum is not possible with increasing CO adsorption temperature, (as is the case with ceria), it is more likely that the increase in CO adsorption with temperature is due to a progressive dehydroxylation of the surface cations.^{117 - 118} The adsorption strength and quantification figures show that lanthana has a higher site density for CO adsorption under inert conditions than ceria, although at 340°C the strengths of the main adsorptions on both materials are similar, having desorption temperatures of approximately 500°C.

Figure 4.44 A plot showing the variation in CO and CO₂ desorption following CO adsorption, with adsorption temperature under He

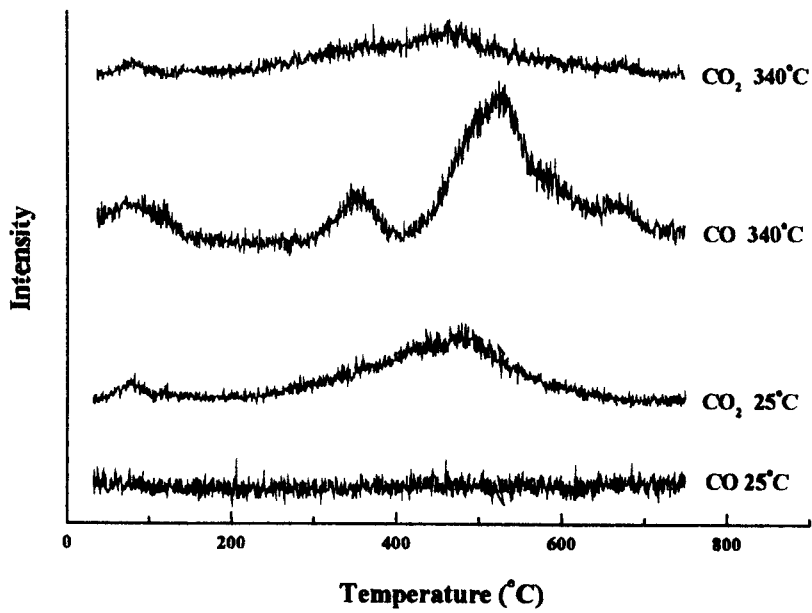


Table 4.29 CO and CO₂ desorption quantification for figure 4.44

Adsorption Temperature (°C)	CO Desorption $\mu\text{mol g}^{-1}$	CO ₂ Desorption $\mu\text{mol g}^{-1}$	Total CO _x Desorption $\mu\text{mol g}^{-1}$
25	0	30.6	30.6
340	51.6	27.2	78.8

With regards oxidative adsorption of CO (as characterised by CO₂ desorption under the inert carrier), quantification shows that this phenomenon remains largely invariant with adsorption temperature, as does the desorption temperature at approximately 450°C. This result suggests that within the adsorption temperature range tested, a fixed amount of surface oxygen is available for the oxidative adsorption of CO. It can be further surmised that this finite amount of oxygen is related to a particular surface oxygen species, such as capping oxygen.

A similar plot showing the variation in the CO and CO₂ desorption under Heliox, after CO adsorption and desorption under inert carrier (He), with adsorption

temperature is shown in figure 4.45. Quantification of the CO and CO₂ desorptions during the subsequent oxidative desorption are presented in table 4.30.

Figure 4.45 A plot showing the variation in CO and CO₂ desorption following CO adsorption, with adsorption temperature under Heliox

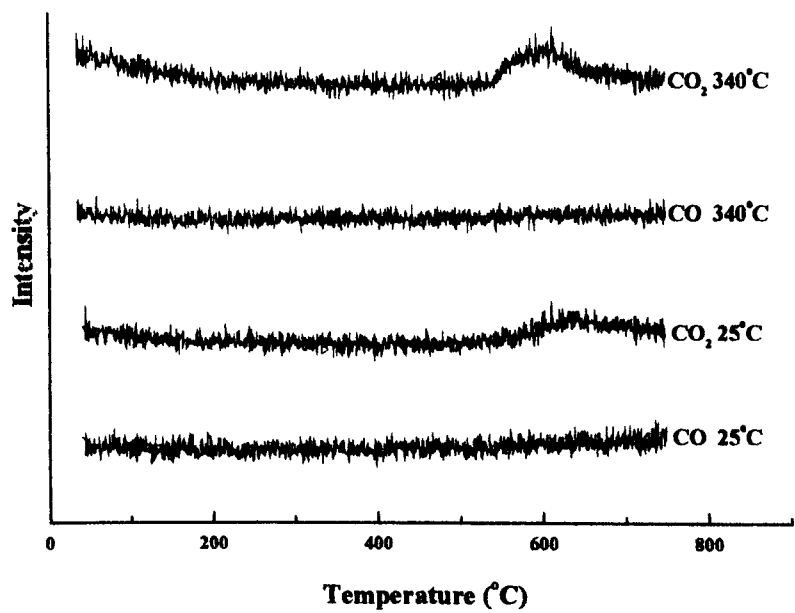


Table 4.30 CO and CO₂ desorption quantification for figure 4.45

Adsorption Temperature (°C)	CO Desorption μmol g ⁻¹	CO ₂ Desorption μmol g ⁻¹
25	-	4.0
340	-	10.8

Under the Heliox carrier gas conditions, no desorptions of CO were observed, and therefore no CO quantification was done for these experiments. It should be noted that all observed CO desorptions were coincident with the observed CO₂ desorptions, and of the correct order to be attributed to CO₂ fragmentation in the Mass Spectrometer.

As determined with ceria, it can be similarly concluded that not all of the CO adsorbed on lanthana is thermally desorbed under the inert carrier conditions, within the 25°C - 750°C TPD range. In contrast with ceria, this phenomenon is observed over lanthana even following the room temperature CO adsorption. The desorption

temperature, (for both adsorption temperature experiments), is observed to occur at approximately 600°C, as opposed to approximately 300°C for the analogous desorption over ceria. This demonstrates that the oxidative adsorption of the carbonaceous residue is much stronger over lanthana than ceria, as would be expected from the CO₂ TPD experimental results, (section 4.3.1). It can also be deduced that only one adsorption site exists for the oxidised carbonaceous residual, on the lanthana surface. The observed thermal activation of the carbonaceous residual adsorption sites can be explained in terms of cationic adsorption sites (with single possible valence), with thermal activation being via a progressive dehydroxylation of the cation sites with increasing adsorption temperature.

The carbonaceous residue following CO adsorption and the inert carrier TPD accounts for approximately 12% of the total desorption at both temperatures. This suggests that the ratio between the sites responsible for the He carrier desorptions and the sites responsible for the Heliox carrier desorptions is constant, reflecting the activation of both adsorption sites by a progressive dehydroxylation of the surface of lanthana with temperature, and the irreducibility of surface cations. Again it is possible that the carbonaceous residue from the adsorbed CO species may be deposited carbon following a Boudouard reaction type disproportionation, as mentioned in section 4.3.3.3.1

4.3.3.3.3 Summary

The results of this section demonstrate the effects of oxygen on the desorption of adsorbed CO species over materials in the ceria/lanthana solid solution system. There are several observations from this work which are worthy of note.

The adsorption of CO on both materials was found to result in oxidative and non-oxidative desorption under inert carrier gas TPD conditions. As the oxidation must be via reaction with some surface species, the adsorption site resulting in oxidative desorption was assigned to surface oxygen species. This proposal was supported by the observations that the oxidative adsorption/desorption process was activated with increasing temperature over reducible ceria, but not over irreducible

lanthana. In the case of ceria, it can be surmised that subsurface oxygen is also involved in the oxidation process increasingly with CO adsorption temperature, whilst the lanthana system is limited in its source of oxygen to capping oxygen only.

Non-oxidative adsorption/desorption of CO was thus assigned to surface cation sites. This was supported by the observation of a single non-oxidative desorption in the He carrier TPD over lanthana, and two separate non-oxidative desorptions for the analogous experiment over ceria. This was explained in terms of a single adsorption over lanthana on La^{III} , and two possible adsorptions over ceria on Ce^{III} and Ce^{IV} . On both materials, the non-oxidative adsorption/desorption of CO was determined to be activated with temperature. This was explained in terms of a progressive dehydroxylation of the surface cation sites with increasing CO adsorption temperature over lanthana, coupled with a progressive reduction of the surface in the case of ceria, also with increasing CO adsorption temperature.

Perhaps the most important observation from these results is the requirement for gas phase oxygen to enable complete desorption of adsorbed CO - a condition met under the catalytic reaction conditions. The proportion of carbonaceous residue following CO adsorption, in comparison with the total CO adsorption, (following the He carrier TPD), was found to increase with temperature in the case of ceria, but to be invariant with temperature in the case of lanthana. It can be inferred from this observation that the carbonaceous residual is related to the extent of reduction of the ceria surface, further suggesting that the Ce^{III} surface cations are the residual species adsorption sites. The irreducibility of lanthana accounts for the invariance in the proportion of residual adsorbed CO with CO adsorption temperature. It is proposed that under the inert carrier gas conditions, a Boudouard reaction type disproportionation ($2\text{CO} \rightarrow \text{C} + \text{CO}_2$) could result in carbon deposition, the deposited carbon being subsequently oxidised in the presence of gaseous oxygen. Under high oxygen partial pressure conditions, (e.g., CO catalytic oxidation reaction conditions in the present study), such a process could be an intermediate step in the CO catalytic oxidation reaction mechanism.

4.3.3.4 The Effect of Catalyst Composition.

In this set of experiments, the effect of lanthanum concentration in the catalyst materials was investigated with respect to CO adsorption/desorption properties. Materials investigated were selected due to specific variations in CO and CH₄ oxidation catalytic properties, as determined in the parallel study reported later in this chapter (section 4.5 and subsections therein). The materials investigated were CeO₂, Ce_{0.95}La_{0.05}O_{1.975}, Ce_{0.7}La_{0.3}O_{1.85}, Ce_{0.4}La_{0.6}O_{1.7}, Ce_{0.2}La_{0.8}O_{1.6}, Ce_{0.05}La_{0.95}O_{1.525} and La₂O₃. All materials were tested following pre-TPD in Heliox followed by CO adsorption. Adsorptions were completed at 25°C and 340°C in order to determine the effects of adsorption temperature at a reference temperature, and a typical CO catalytic oxidation reaction temperature, respectively. TPD spectra for adsorptions at 25°C and 340°C are shown in figures 4.46 and 4.47, respectively.

For this set of experiments quantification was only completed for CO₂, as under the Heliox carrier conditions CO desorption was not observed. In order to make meaningful comparison between the adsorption/desorption properties of the various compositions, the quantified CO₂ desorptions shown in table 4.31 can be expressed as specific CO adsorptivity by allowing for the specific surface area of the materials. Specific CO adsorptivity can then be plotted against surface composition in order to determine true variations in the material surface adsorption properties with surface composition.

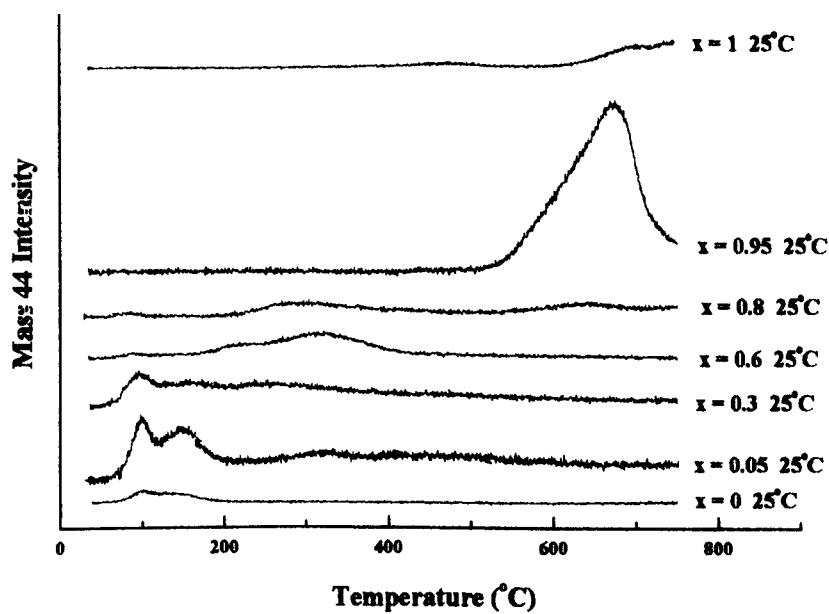
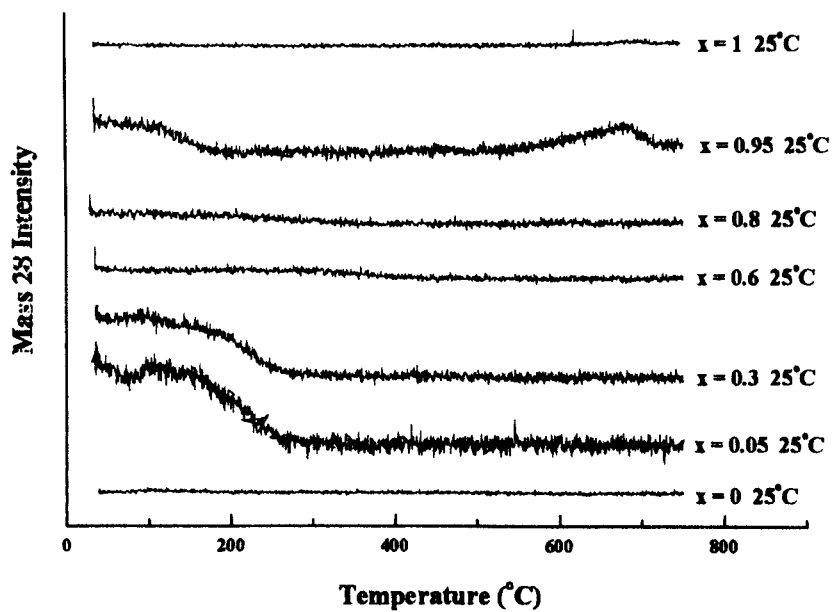
Figure 4.46 TPD spectra for CO (mass 28) and CO₂ (mass 44), adsorbed at 25°C.

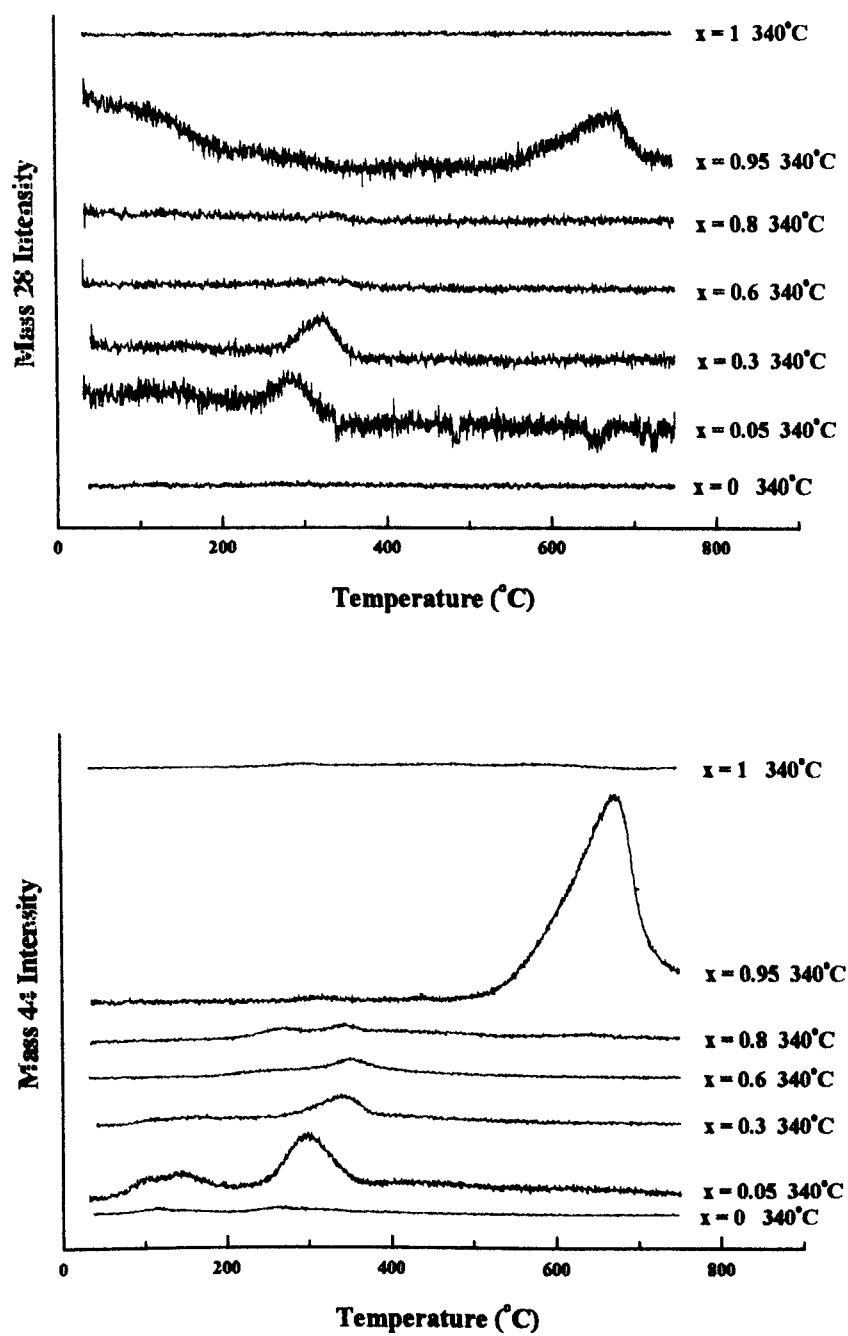
Figure 4.47 TPD spectra for CO (mass 28) and CO₂ (mass 44), adsorbed at 340°C.

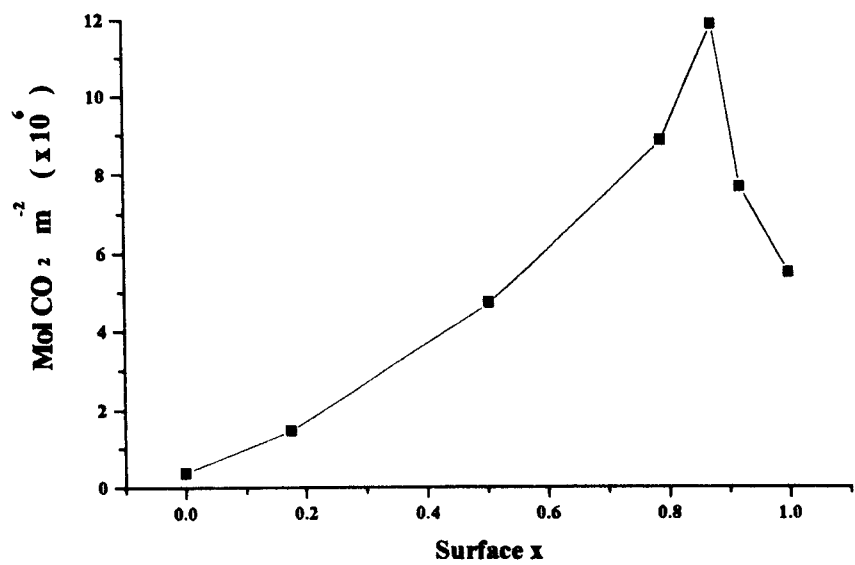
Table 4.31 Quantification of CO₂ desorptions with bulk and surface lanthanum concentrations, with adsorption temperature.

La Fraction (Bulk)	La Fraction (Surface)	Specific Surface Area m ² g ⁻¹	CO ₂ desorption 25°C adsorption Mol CO ₂ g ⁻¹	CO ₂ desorption 340°C adsorption Mol CO ₂ g ⁻¹
0	0	15.185	5.55×10 ⁻⁶	18.60×10 ⁻⁶
0.05	0.176	12.356	18.02×10 ⁻⁶	50.39×10 ⁻⁶
0.3	0.504	12.802	60.64×10 ⁻⁶	70.85×10 ⁻⁶
0.6	0.79	10.826	95.96×10 ⁻⁶	91.71×10 ⁻⁶
0.8	0.876	8.716	101.25×10 ⁻⁶	149.10×10 ⁻⁶
0.95	0.92	13.598	104.73×10 ⁻⁶	163.75×10 ⁻⁶
1	1	5.894	32.6×10 ⁻⁶	68.8×10 ⁻⁶

The general trends observed from the CO₂ desorption figures in table 4.31 are increases in adsorption both with adsorption temperature, and with lanthanum concentration up to surface $x = 0.92$, beyond which there is a sharp decline, at both adsorption temperatures. The increase in adsorption with adsorption temperature has been previously discussed, therefore the following discussion concentrates on the variation in the surface composition dependency of specific CO adsorptivity, at the two selected adsorption temperatures. In figure 4.48, the variation in specific CO adsorptivity with surface composition is shown for CO adsorptions at 25°C.

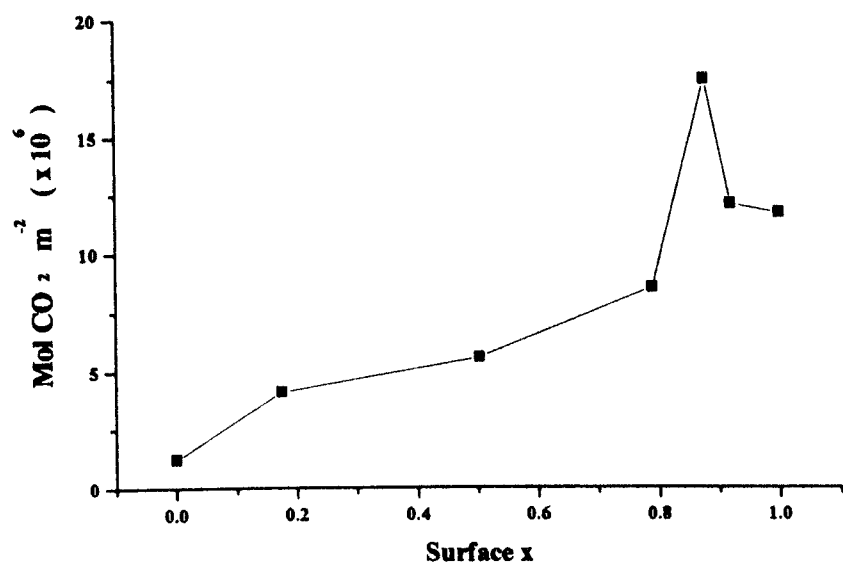
It can be observed that specific adsorption of CO increases with surface lanthanum concentration to a peak at a surface composition of $x = 0.876$; a Ce : La ratio of approximately 1 : 7. The peak corresponds well with the transition between single phase solid solution and the binary phase system at the surface, as determined previously in the XRD and XPS studies, (sections 4.1.4 and 4.2.3, respectively) to occur at surface concentrations between $x = 0.790$ and $x = 0.876$.

Figure 4.48 A plot showing the variation in the magnitude of specific CO adsorptivity (expressed as Mol CO₂ desorbed m⁻²), with surface composition, for CO adsorptions at 25°C.



In figure 4.49, the variation in specific CO adsorptivity with surface composition is shown for CO adsorptions at 340°C.

Figure 4.49 A plot showing the variation in the magnitude of specific CO₂ desorptions (expressed as Mol CO₂ m⁻²), with bulk and surface composition, for CO adsorptions at 340°C.



A near linear variation in CO adsorption with lanthanum concentration is observed, with the discontinuity in the linear plot clearly occurring at the solid solution limit (surface $x = 0.790$ to 0.876). A peak in the variation in specific CO adsorptivity with surface composition is observed at surface $x = 0.876$. This again corresponds to a surface Ce : La ratio of 1 : 7, in common with the 25°C CO adsorption experiments discussed previously.

From these experiments, it is observed that the variation in specific CO adsorptivity with composition is not significantly affected by variations in CO adsorption temperature. At 25°C and at 340°C, specific CO adsorptivity is observed to increase in a near linear fashion with surface lanthanum concentration up to a peak at the single phase solid solution limit, and then to fall with further successive increases in surface lanthanum concentration.

4.3.3.5 Summary

It can be concluded from these results that the specific CO adsorptivity is proportional to surface lanthanum concentration within the single phase solid solution region, peaking at the solid solution limit. This variation and the surface lanthanum concentration corresponding to peak specific CO adsorptivity was found to be almost invariant with CO adsorption temperature between 25°C and 340°C. Beyond the single phase solid solution concentration limit, further increases in the surface lanthanum concentration result in a progressive decrease in specific CO adsorptivity.

It can be deduced from these results that within the cubic solid solution materials CO is preferentially adsorbed on either trivalent lanthanum cations or an a surface site that increases in concentration in proportion with that of the lanthanum cations. It can further be deduced that lanthanum cations within the cubic fluorite structure surface provide a higher density of CO adsorption sites than in the two phase system beyond the solid solution limit.

4.4 Diffuse Reflectance Infrared FT Spectroscopy - An *in situ* Study.

In order to investigate species present at the catalyst surface under reaction conditions, experiments were performed to determine the variation in diffuse reflectance spectra with composition. Several materials were tested to give a good representation of compositional trend, including bulk compositions; $x = 0, 0.05, 0.1, 0.2, 0.3, 0.4, 0.5, 0.6, 0.7, 0.8, 0.9, 0.95$ and 1 . It should be noted that no quantification was done during this study, as the aim of the experiments was merely to identify surface species and determine the qualitative variations in the surfaces of the catalyst materials with catalyst composition under inert and catalytic reaction conditions.

4.4.1 Experimental Methodology

Following the collection of background scans over KBr, samples were introduced to the environment cell as finely ground powders. Samples were heated to 340°C in flowing He in order to dry samples of moisture adsorbed from the atmosphere, and desorb any carbon dioxide similarly adsorbed. The materials were then scanned under these conditions in order to provide an initial analysis of the surface before exposure to reaction conditions.

Materials were subsequently exposed to the standard CO/Heliox reaction mixture, supplied from and metered by the micro-reactor apparatus. This consisted of 1.75% CO, 17.3% O₂, balance He, at a flow rate of 143.5 ml min^{-1} , giving an environment cell flushing time of approximately 40–45 seconds, based on an estimated cell volume of 100 ml. Materials were allowed to equilibrate with the flowing gas mixture at 340°C for one hour before recording the diffuse reflectance spectra.

Following the CO catalytic oxidation reaction conditions experiment, the gas mixture was changed by replacing the 1.75% CO with 1.75% CH₄ in order to replicate the methane catalytic oxidation reaction conditions. The cell temperature was also increased to 500°C which was more typical of methane oxidation reaction temperatures. As with the CO oxidation conditions experiments, the diffuse reflectance

spectra were recorded after one hour equilibration time in the reaction gas mixture. (The standard temperature for the measurement of methane oxidation rate in the catalytic study was 560°C, however the maximum operating temperature for the environment cell was 500°C due to various thermally degradable seals used in the cell construction).

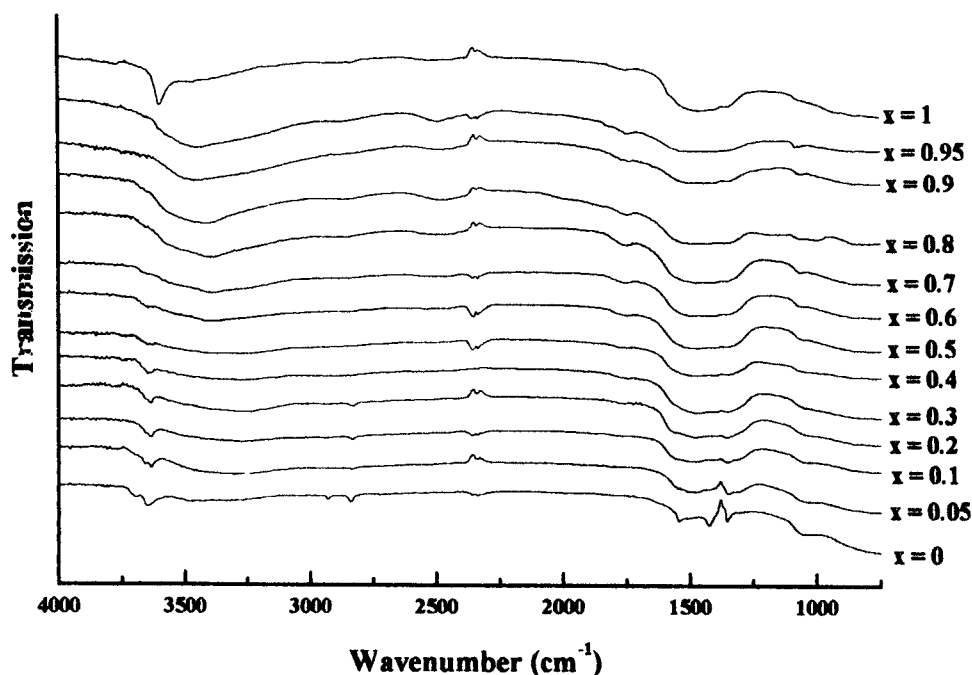
Finally, the methane oxidation reaction mixture was replaced with He after the temperature had been reduced to 340°C, under the reaction conditions. The temperature change was not made under flowing He, as the elevated temperature would have undoubtedly resulted in reduction of the ceria based materials under the inert gas. After a further one hour equilibration under He, a final diffuse reflectance scan was recorded. The purpose of this final scan was to determine whether any use dependent changes had occurred in the material surfaces, following exposure to CO and CH₄ oxidation reaction conditions.

4.4.2 Results analysis

4.4.2.1 Initial Spectra - Composition Variations.

In this set of spectra, the differences and trends in surface species with catalyst lanthanum concentration were determined in order to provide a pre-reaction-conditions analysis of the surfaces of the materials, and a baseline to determine whether use dependent changes occurred following exposure of the materials to CO and CH₄ oxidation reaction conditions. The spectra are presented in figure 4.50.

Figure 4.50 A plot of the variation in initial He spectra with composition.



Beginning at the high frequency end of the spectra, three sharp bands are observed in the pure ceria spectrum at 1356cm^{-1} , 1427cm^{-1} and 1543cm^{-1} . These correspond well to unidentate and bulk polydentate carbonates, and inorganic carboxylates, as reported in the literature and summarised in figure 2.11 in section 2.2.1 in the literature review. As the lanthanum concentration in the catalysts is increased, the bands at 1356cm^{-1} , 1427cm^{-1} and 1543cm^{-1} are observed to reduce in intensity, until they are no longer observed beyond $x = 0.3$ to $x = 0.4$, (surface $x = 0.504$ - $x = 0.609$). By this level of lanthanum, the three bands become swamped by a broad absorption envelope in the 1250cm^{-1} - 1600cm^{-1} range which persists through to $x = 1$. The broad adsorption corresponds to reported ranges for all of the reported surface carbonate species and the inorganic carboxylate. The presence of such a wide intense absorption band in the 1200cm^{-1} - 1800cm^{-1} is common for most untreated oxides, and is known as the fundamental absorption region (lattice vibration region). This is caused by admixtures adsorbed on the catalyst surface, made up of adsorbed water, carbon dioxide and assorted organic contaminants. These can only be completely removed by heating to 500°C under vacuum.¹¹⁶ As such a treatment was not possible using the apparatus available, further experimentation was completed in

the knowledge that surface adspecies were present on all catalyst materials before treatment under reaction conditions.

From these observations it can be concluded that the presence of lanthanum in the surface of the catalyst materials stabilises several different forms of adsorbed CO_2 species, including carbonate and carboxylate. In the case of pure ceria, only unidentate and bulk polydentate carbonates and carboxylate species were determined to be stable at 340°C under flowing He.

Moving toward the lower frequency end of the spectra, the appearance of a peak at 1750cm^{-1} was observed with the addition of lanthanum, which corresponds to bridged carbonate species. This band was observed to persist between $x = 0.05$ to $x = 1$, (surface $x = 0.176$ to $x = 1$), indicating that the presence of lanthanum is required in order to form the bridged carbonate species.

The formate species was also evident at $x = 0$ with characteristic peaks at 2840cm^{-1} and 2932cm^{-1} . The band at 2932cm^{-1} was observed to disappear on the introduction of lanthanum to the catalyst materials, whilst the band at 2840cm^{-1} persisted to lanthanum levels of $x = 0.2$ to $x = 0.3$, (surface $x = 0.407$ to $x = 0.504$). Clearly, the formate species is favoured by the presence of cerium cations in the surface under the experimental conditions.

Finally, two further absorption bands were observed on pure ceria, at 3650cm^{-1} and 3698cm^{-1} , both of which were attributed to surface hydroxyl species and were observed to decline with increasing lanthanum concentration. The 3650cm^{-1} band disappeared by approximately $x = 0.05$ (surface $x = 0.176$), whilst the 3698cm^{-1} band was observed to persist to approximately $x = 0.6$ (surface $x = 0.79$), which corresponds to the previously determined solid solution limit. A further absorption band in this region was observed only on pure lanthana, at 3600cm^{-1} , and was also attributed to surface hydroxyls. The shift to higher frequency in the case of pure lanthana suggests hydrogen bonding between the surface hydroxyls. This in turn could be caused by the formation of bulk lanthanum hydroxide at the surface of the lanthana material on exposure to atmospheric moisture, which is a known phenomenon for the material.

In summary, it is clear that following pre-treatment at 340°C in flowing He, the surface of the ceria/lanthana materials contains various species, formed by the adsorption of water and carbon dioxide, resulting in typical untreated oxide spectra.

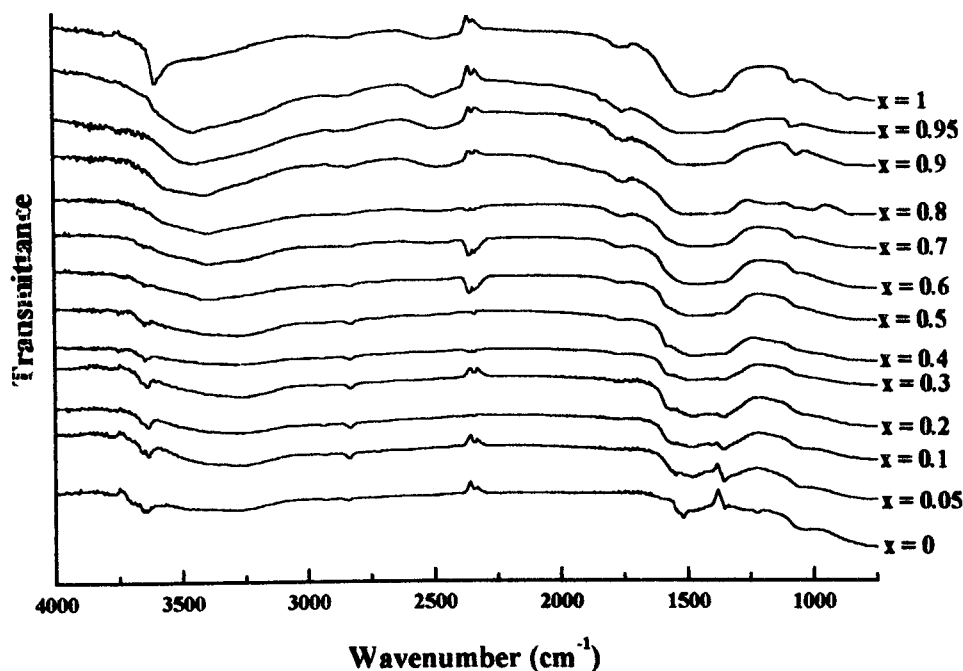
4.4.2.2 Final Spectra - Composition Variations

It is fitting at this point to compare the final spectra (after exposure to CO and CH₄ catalytic oxidation reaction conditions), with the initial spectra. The aim of the comparison being to determine whether there are any use dependent changes in the catalyst material surfaces. The resulting spectra are shown in figure 4.51. General observations indicate that there is little difference between the pre- and post-reaction spectra recorded at 340°C under He, adsorptions in the fundamental absorption region remaining unchanged. The only significant difference was a new band at 1225cm⁻¹ which was only observed for x = 0. This band is tentatively assigned to a bridged carbonate species.

Other notable differences between the two sets of spectra include an increase in the persistence of bands at 2840cm⁻¹ and 2932cm⁻¹ (assigned to the formate species) to x = 1 (from x = 0.2 - 0.3), and to x = 0.5 (from x = 0), respectively. This indicates that exposure to reaction conditions results in the formation of surface formate species on the catalyst surfaces which are stable at 340°C in the presence of He.

Finally, the bands observed previously at 3650cm⁻¹ and 3698cm⁻¹ are now both shown to persist with lanthanum concentration up to approximately x = 0.6, which has been determined to be the solid solution limit of lanthanum in ceria; the reason for this change is unclear. The continued presence of the band at 3600cm⁻¹ for x = 1 is observed after reaction conditions, indicating that the species it represents, (thought to be bulk lanthanum hydroxide at the surface of the material), is unchanged after exposure to reaction conditions. (It should be noted that the presence of bulk La(OH)₃ has been observed in X-ray diffraction patterns for lanthana which had been exposed to atmospheric air for prolonged periods of time). It can be concluded from this set of pre- and post-reaction conditions spectra that there are no significant changes in the material surfaces which persist after the catalytic reaction testing.

Figure 4.51 A plot of the variation in IR spectra with catalyst composition following exposure to catalytic oxidation reaction conditions.



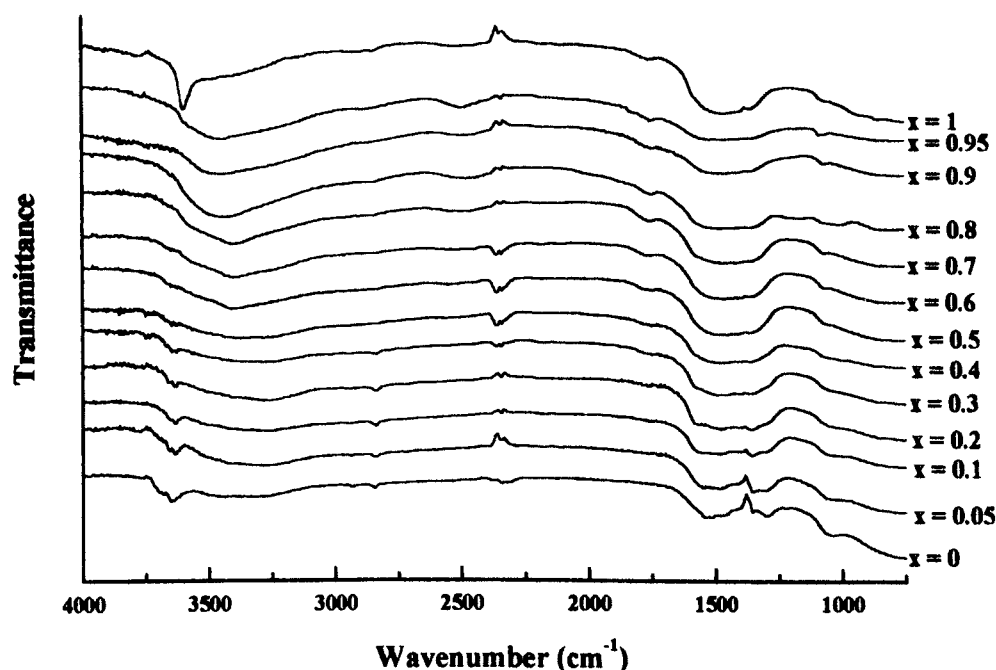
4.4.2.3 CO Oxidation Reaction Conditions - Compositional Variations

In this set of experiments, scans were conducted under the CO oxidation reaction conditions, as mentioned previously. Each material was allowed one hour to reach equilibrium with the surrounding reaction gas mixture before scanning. The resulting spectra are shown in figure 4.52.

Over ceria, in addition to the original bands at 1354cm^{-1} , 1545cm^{-1} , 2840cm^{-1} and 2932cm^{-1} (as discussed previously for the initial spectra), several new bands were evident under the CO oxidation reaction conditions. New bands at 1028cm^{-1} , 1214cm^{-1} , 1294cm^{-1} , 1463cm^{-1} , and shoulders at 1562cm^{-1} and 1582cm^{-1} were observed which were attributed to a bidentate carbonate surface species. There was no evidence for the formation of a surface carbonite species, except a very weak band at 1150cm^{-1} , which was only observed over pure lanthana. This is as expected in the presence of dioxygen.¹²¹ As the lanthanum concentration was increased, further bands were observed to appear. A band was observed to appear at 1380cm^{-1} and increase with lanthanum concentration up to $x = 0.2 - 0.3$. Above this concentration, a broad absorption was observed in the fundamental absorption region between 1200cm^{-1} and

1800 cm^{-1} , as was observed in the case of the initial scans under He. Similarly, a further band was observed to develop with increasing lanthanum concentration at 1750 cm^{-1} , which has previously been assigned to a bridged carbonate species. The formate bands at 2840 cm^{-1} and 2932 cm^{-1} were observed to persist until approximately surface $x = 0.609$.

Figure 4.52 A plot of the variation of *in situ* CO oxidation reaction spectra, with composition.



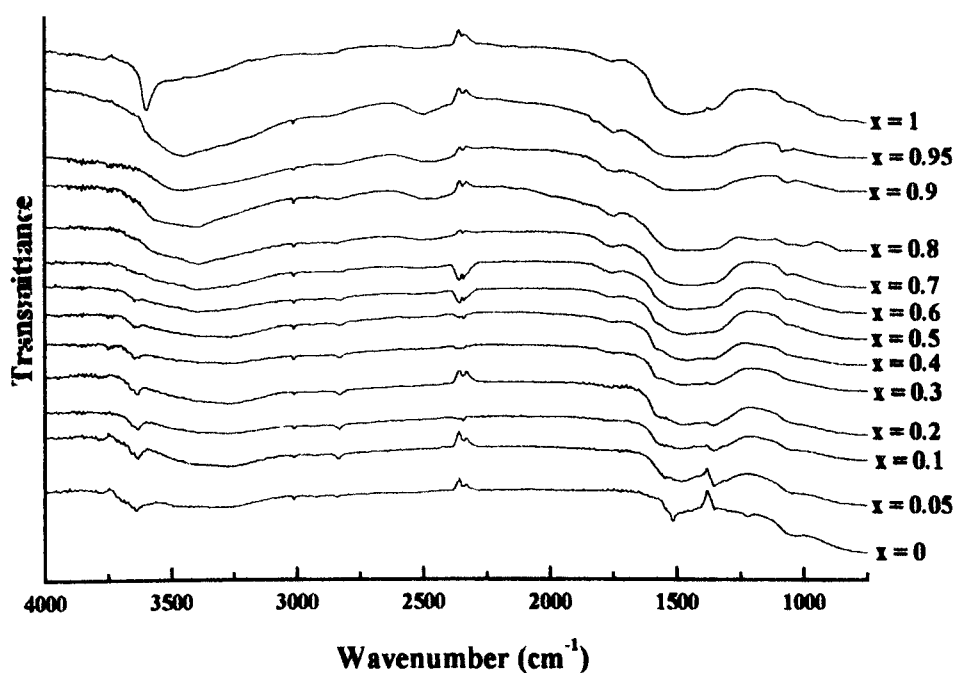
4.4.2.4 CH_4 oxidation conditions - Compositional Variations

The scans under CH_4 oxidation reaction conditions at 500°C are presented in figure 4.53. It can be observed that the carbonate and carboxylate species seen previously were all present. The main difference between the surface species observed under the methane oxidation conditions was that the individual carbonate/carboxylate species demonstrate a higher sensitivity to surface lanthanum concentration than observed previously. This is observed for the bidentate carbonate species band (854 cm^{-1}) appearing from $x = 0.1$, the bridged carbonate species band (1223 cm^{-1}) and the inorganic carboxylate species band (1514 cm^{-1}), both disappearing on the introduction of lanthanum. As with the CO reaction conditions experiments and the inert (He

carrier) runs, with increasing lanthanum concentration the resolution of peaks in the 1200cm^{-1} - 1600cm^{-1} region decreased, until a broad absorption common to most oxides (the fundamental absorption) was observed. The onset of this broad absorption band was complete by approximately $x = 0.6$, which corresponds well to the solid solution limit of lanthanum in ceria. The bands associated with the surface hydroxide species, in the range 3600cm^{-1} - 3700cm^{-1} were not observed to be significantly different from previous experiments, under methane oxidation reaction conditions.

The main result of the methane oxidation reaction conditions experiments was the observation of new absorption bands corresponding to methane adsorbed on coordinatively saturated ceria, and to a lesser extent, methane adsorbed on coordinatively unsaturated ceria. The new bands were observed at 3010cm^{-1} (strong), 1304cm^{-1} (weak), 2990cm^{-1} (weak) and 2875cm^{-1} (very weak). According to the literature, Li and Xin (1992)¹³² determined that methane adsorbed on coordinatively saturated ceria resulted in bands at 3008cm^{-1} and 1308cm^{-1} , whilst on coordinatively unsaturated ceria, in a band at 2990cm^{-1} , 2875cm^{-1} and 1308cm^{-1} . These reported bands correspond well to those observed in the present study.

Figure 4.53 A plot showing the variation of *in situ* CH_4 oxidation spectra, with composition



The trends observed in these newly observed absorption bands were also studied. The bands at 2875cm^{-1} and 2990cm^{-1} were always of low intensity and were not observed due to signal noise except on $x = 0$ and 0.05 samples, and therefore will not be discussed further. The major band at 3010cm^{-1} is observed for all catalyst compositions. The intensity of the band appears to be maximised at approximately bulk $x = 0.05$, further successive increases in catalyst lanthanum concentration resulting in a decline in band intensity. The weaker band observed at 1304cm^{-1} is only observed between $x = 0$ and $x = 0.3$, decreasing with successive increases in lanthanum concentration in the catalyst materials.

It can be concluded in accordance with the literature¹³² that methane is indeed adsorbed on surface anions exclusively. The high oxygen partial pressure under the methane reaction conditions accounts for the low intensity of bands associated with coordinatively unsaturated ceria. These bands were much more pronounced in the study by Li and Xin (1992)¹³², as the outgassing procedure would most likely result in reduction of the ceria surface to some extent, and therefore to a higher degree of coordinative unsaturation.

4.4.2.5 Variations in Spectra with Gaseous Environment

In this section, the variation in the DRIFTS spectra of selected catalyst compositions, under inert conditions, under CO and CH₄ oxidation reaction conditions, and again under inert conditions post-reaction are examined over ceria, lanthana and over dilute solid solutions of lanthanum in ceria and cerium in lanthana..

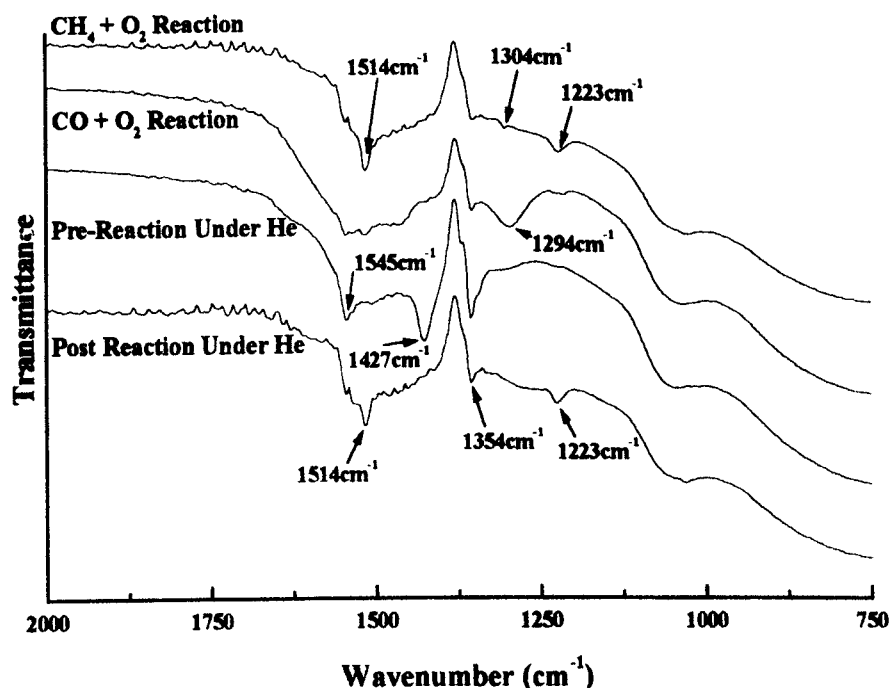
4.4.2.5.1 Ceria

Figures 4.54 and 4.55 show the scans resulting from the different gas environments between 750cm^{-1} and 2000cm^{-1} , and between 2500cm^{-1} and 3250cm^{-1} , respectively.

The first observations to be made regard the changes occurring on introduction of CO + O₂. The appearance of a weak band at 1223cm^{-1} (indicating the formation of a

bridged carbonate species), and a strong broad band in the 1250cm^{-1} - 1330cm^{-1} region, centred at 1294cm^{-1} . This second broad band is difficult to assign to individual species due to a lack of resolution of individual bands within the broad envelope, however the envelope does encompass possible bands for bidentate carbonate and carbonite species. Further investigation of secondary absorption bands for these species does confirm the formation of the bidentate carbonate species (bands observed at 854cm^{-1} (weak), 1028cm^{-1} (broad), 1562cm^{-1} (shoulder), 1478cm^{-1} (weak), 1461cm^{-1} (weak), 1464cm^{-1} (weak), 1354cm^{-1} (strong)). Further observations include the reduction in intensity of bands at 1354cm^{-1} and 1545cm^{-1} , attributed to inorganic carboxylate, and the disappearance of the band at 1427cm^{-1} , attributed to unidentate- and bulk poly-carbonate.

Figure 4.54 Ceria under CO and CH_4 oxidation reaction conditions, and under He both before and after reaction conditions testing in the 750cm^{-1} - 2000cm^{-1} range.

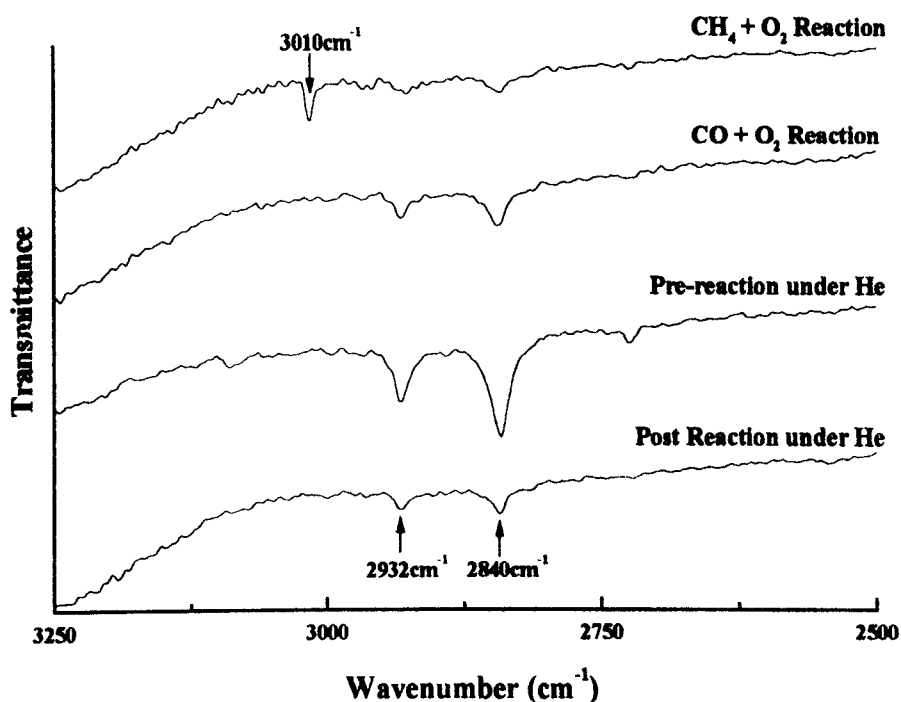


On introduction of $\text{CH}_4 + \text{O}_2$ and elevation of sample temperature to 500°C , the first observations are the disappearance of the bands at 1294cm^{-1} and 1354cm^{-1} , previously assigned to unidentate- and bidentate carbonate and carboxylate species. This is most likely due to the thermal decomposition of a large proportion of these

species at the elevated temperature. Conversely, the band at 1223cm^{-1} attributed to the bridged carbonate species is observed to increase in intensity, even at the elevated temperature.

The most significant observation is the appearance of the band at 1304cm^{-1} , which is attributed to the adsorption of methane on coordinatively saturated ceria. The adsorption of CH_4 on ceria also results in a characteristic absorption at 3010cm^{-1} , which is observed in figure 4.55 which focuses on the 2500cm^{-1} - 3250cm^{-1} range. The band at 3010cm^{-1} is observed only for the scan under the methane oxidation reaction conditions. The other characteristic peaks in this region are at 2840cm^{-1} and 2932cm^{-1} , both of which are characteristic of surface formate species. These species are observed to be present in all of the gaseous environments tested, although the intensity is reduced significantly after exposure to CO oxidation reaction conditions.

Figure 4.55 Ceria under CO and CH_4 oxidation reaction conditions, and under He both before and after reaction conditions testing in the 2500cm^{-1} - 3250cm^{-1} range.



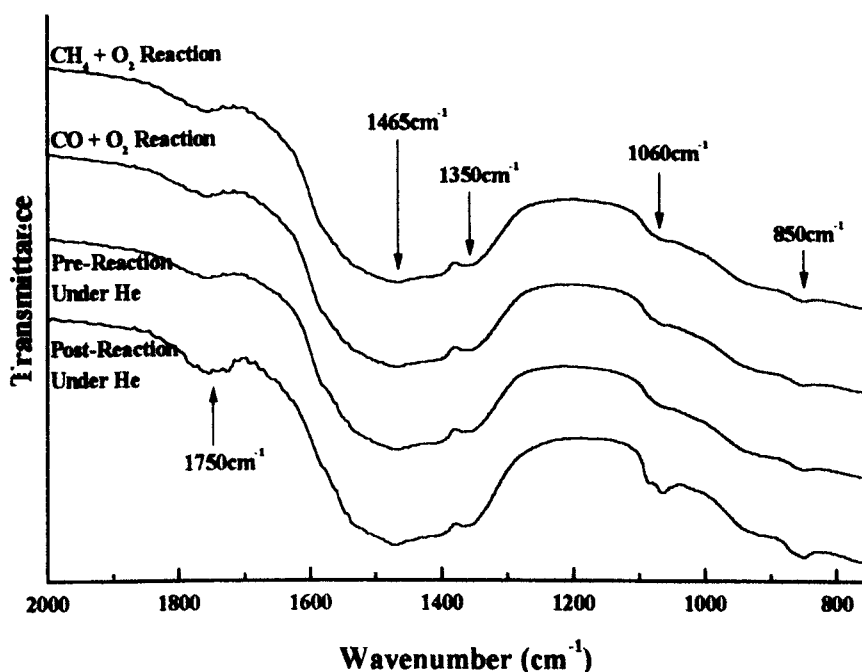
Post reaction conditions under He at 340°C , several differences between the pre- and post-reaction material can also be observed. The 1223cm^{-1} bridged carbonate

band remains, in contrast to the pre-reaction material, and the band at 1354cm^{-1} attributed to other carbonate species and inorganic carboxylate reappears, although at a much lower intensity than in the pre-reaction material. The bands at 1304cm^{-1} and 3010cm^{-1} also disappear, indicating that adsorbed methane does not remain adsorbed, except in the presence of gaseous methane. The band at 1514cm^{-1} (attributed to inorganic carboxylate), which was formed under the methane oxidation conditions was found to persist under inert conditions. The band at 1427cm^{-1} observed on the pre-reaction ceria surface (unidentate- and bulk poly-carbonate), was not observed post-reaction.

4.4.2.5.2 Lanthana

A similar comparative analysis of variation in surface species with environment is now possible over lanthana. Figure 4.56 shows scans for lanthana (comparable with figure 4.54 for ceria), in the 750cm^{-1} - 2000cm^{-1} range.

Figure 4.56 Lanthana under CO and CH_4 oxidation reaction conditions, and under He both before and after reaction conditions testing in the 750cm^{-1} - 2000cm^{-1} range.

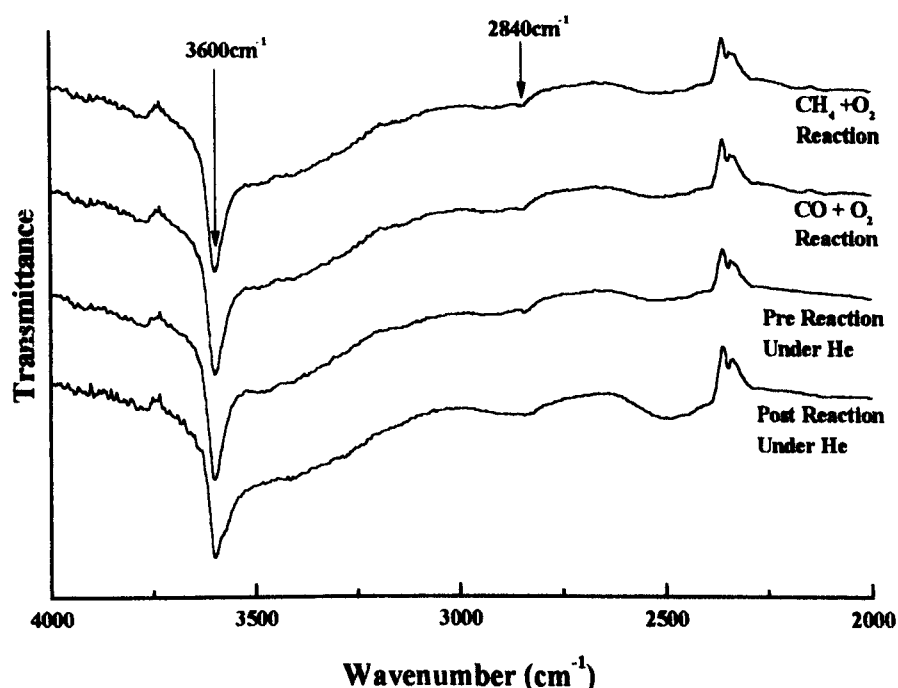


There are rather less features of interest in the lanthana scans, in comparison with the analogous scans for ceria. In the 750cm^{-1} - 2000cm^{-1} range, observed peaks are 850cm^{-1} (weak), 1060cm^{-1} (broad), 1350cm^{-1} (broad), 1465cm^{-1} (very broad) and 1750cm^{-1} (broad). These bands have been discussed previously in terms of assignment and were determined to represent a mixture of surface unidentate-, bidentate-, bridged-, and bulk polydentate-carbonates. The observation that there is little change in the carbonate spectra, even at high temperatures indicates that the surface carbonates are more stable over lanthana in comparison with over ceria. This effect is most likely due to the relatively higher basicity of the lanthana, and/or possibly due to reaction of the carbonate species over ceria with bulk oxygen, at higher temperatures. The two bands observed at 1060cm^{-1} and 1065cm^{-1} under the post reaction conditions inert scan can be assigned to bulk polydentate- and unidentate-carbonate species, respectively, although the reason for the increased resolution of these two species under these conditions is unclear. In the 2000cm^{-1} - 4000cm^{-1} region (figure 4.57), bands are observed at 2840cm^{-1} (weak) and 3600cm^{-1} (strong). The first of these two bands is characteristic of the formate species, the second is attributed to bulk $\text{La}(\text{OH})_3$.

In summary, the surface species present on lanthana are shown to be far less sensitive to their environment than ceria, probably due to the irreducibility of lanthana. The variable oxygen stoichiometry of the ceria allows the surface of the ceria to be much more responsive to the environment, and to accommodate different adsorption sites than in the case of lanthana. The most obvious example of this is in the lack of evidence for any methane adsorption on lanthana, whereas strong absorptions were observed at 1404cm^{-1} and 3010cm^{-1} for methane adsorbed on ceria.

Having highlighted the main differences between the surface species present on the ceria and lanthana surfaces under CO oxidation, CH_4 oxidation and inert conditions, it is now interesting to focus on the effects of small levels of each in the other.

Figure 4.57 Lanthana under CO and CH₄ oxidation reaction conditions, and under He both before and after reaction conditions testing in the 2000cm⁻¹ - 4000cm⁻¹ range.



4.4.2.5.3 Ce_{0.95}La_{0.05}O_{1.975}

The first composition of interest is 5 cation % lanthanum in ceria. Under He (pre-reaction conditions), the resolution of the bands at 1354cm⁻¹, 1427cm⁻¹, 1545cm⁻¹, 2840cm⁻¹ and 2932cm⁻¹ (which are attributed to carbonate, inorganic carboxylate and formate species), are observed to be significantly reduced on introduction of lanthanum into the surface, although the surface carbonate broad absorption at 1200cm⁻¹ - 1600cm⁻¹ increases with lanthanum concentration. This observation suggests that the introduction of lanthanum into the surface of ceria results in a stabilisation of several carbonate species, such that the individual bands are lost in the fundamental absorption region. On the introduction of CO and O₂, the band at 1514cm⁻¹, (attributed to inorganic carboxylate present on the ceria surface), was found to disappear in the lanthanum containing material. This was also observed under the methane oxidation reaction conditions, again demonstrating the destabilisation of a surface species on ceria by the introduction of lanthanum into the surface. The bands attributed to the formate species at 2840cm⁻¹ and 2932cm⁻¹ vary similarly with

environment as with the pure ceria material and the adsorption of methane appears to be relatively unaffected by the presence of lanthanum in the surface.

4.4.2.5.4 $\text{Ce}_{0.05}\text{La}_{0.95}\text{O}_{1.5+x}$

In the case of 5 cation % Ce doped lanthana, there are far fewer differences in the observed spectra under the different environments, than in the case of the ceria rich material. There are two main differences between the undoped lanthana and 5 cation % cerium doped lanthana; the appearance of a band at 1065cm^{-1} (attributed to unidentate, bidentate and bulk polydentate carbonate species), and the disappearance of the sharp $\text{La}(\text{OH})_3$ peak at 3600cm^{-1} on the introduction of cerium cations into the surface. The presence of cerium in the surface of lanthana appears to stabilise (particularly) unidentate and bidentate carbonate species, and other carbonaceous species at the surface of the material. The more basic lanthana is known to form bulk carbonate materials easily on the action of carbon dioxide, thus accounting for the loss of resolution of the individual carbonate bands with increasing surface lanthanum concentration.

4.4.2.6 Summary

The results of the *in situ* DRIFTS studies can be summarised in terms of the variation in the stabilisation of surface species with surface dopant concentration. The pure ceria and lanthana have quite different surface characteristics; in the case of ceria specific surface carbonate species can be observed, whereas in the case of the lanthanum rich doped ceria surfaces, a broad absorption in the 1200cm^{-1} - 1600cm^{-1} region indicates the presence of a large surface concentration of surface carbonaceous species.

Under CO oxidation reaction conditions, there is little conclusive evidence for any particular changes in the spectra with catalyst surface composition, although a broad band at 1294cm^{-1} is observed to appear which is attributed to the bidentate carbonate species on a cerium cation. This species was not observed under methane

oxidation conditions, but bands attributed in the literature to methane adsorbed on coordinatively saturated ceria were observed. Under methane oxidation conditions, the adsorption of methane on predominantly coordinatively saturated ceria was observed as absorption bands at 1304cm^{-1} and 3010cm^{-1} on all materials containing cerium. No bands were observed for the adsorption of methane on pure lanthana.

The main differences between the pre- and post-reaction conditions inert scans of the materials were generally attributed to thermal decomposition of the surface carbonate species. The unidentate and bidentate carbonates apparently decomposing at the expense of the bridged carbonate species, which was observed under the methane oxidation reaction conditions at 500°C . The presence of lanthanum in the surface of materials was found to cause a reduction in the resolution of the individual carbonate bands, probably due to the formation of a carbonaceous overlayer over the lanthanum rich surfaces.

4.5 Catalytic Study Results

In this section the results of the carbon monoxide and methane oxidation studies are presented and discussed in the light of the catalyst material characterisation data presented in the earlier sections of this chapter. Initial experiments were carried out in order to optimise the reaction conditions in terms of measurable reaction rate, and to avoid diffusion limitation of the catalytic reaction rate. This included testing materials made by the ceramic and coprecipitation methods in which it was determined that the ceramic materials were unsuitable for catalytic testing due to low specific surface areas, as discussed previously in section 4.1.1. All reported catalytic studies were therefore completed using materials made by the standard coprecipitation method. Initial experiments were completed in order to validate the experimental results by reproduction of experimental data reported in the literature, the results of which are presented and discussed in Appendix 4.1. The catalytic studies then focused on the ceria/lanthana catalyst system.

Reaction rates have been determined for both reactions over the ceria/lanthana series under standard oxygen excess conditions (approximately 10 : 1 oxygen : CO or

CH₄) over a range of temperatures such that conversions were in the range 2 - 12%. Activity per unit catalyst weight, and specific activity (activity per unit surface area of catalyst), was determined at standard temperatures (310°C for CO oxidation and 560°C for CH₄ oxidation). Activation energies and pre-exponential factors were determined using the Arrhenius method, by plotting \ln rate vs. $1/T$ for each material in the reaction temperature range tested. Finally, further tests were carried out on selected materials within the ceria/lanthana series in order to determine the order of the reaction with respect to the reactants, and to investigate possible retardation of the reactions by the main reaction product, CO₂.

4.5.1 Preliminary experiments

4.5.1.1 Investigation of Diffusion Limitations on Reaction Rate

The aim of this set of experiments was to determine the experimental conditions required in order to eliminate the effects of diffusion limitations on the measured catalytic reaction rate. Initial experiments had determined that production of reproducible results required that the thermocouple used for the measurement of the catalyst bed temperature and control of the furnace apparatus, be placed within the reaction tube, inside an α -alumina sheath. This in turn necessitated the use of 4mm internal diameter quartz reaction tube. Using the standard rules for the elimination of wall effects (as described in Appendix 3.6), this diameter was sufficient for catalyst samples with a particle size distribution of 200–400 μ m, providing a minimum catalyst bed length of 10mm was used. This condition was generally satisfied with a catalyst bed mass of approximately 0.2g. In order to determine that a catalytic reaction system measured rate is free of diffusion limitations, it is generally necessary to simultaneously increase both linear gas velocity of the reactant gas mixture, and bed length proportionally in order to ensure that the rate remains constant. Although this method is the only true test for this criteria (due to constant residence times), it is often simplified experimentally¹³⁵ such that the catalyst bed length remains constant, and linear gas velocity alone is varied, in order to determine the transition point between

rate increasing with linear gas velocity, and constant rate with linear gas velocity. In the present study, the positioning of the thermocouple within the apparatus, and the small furnace (and therefore small constant heating zone) rendered variations in catalyst bed length impractical, and therefore the simplified method was used.

The ratio of the reactant gases used was adopted from the Mackrodt patent⁹⁹ which was investigated in the preliminary ternary oxide study reported in Appendix 4.1, as the primary aim of the study at that point was reproduction of literature data. This ratio was approximately 1 : 10 of reactant gas (CO or CH₄) to O₂. The balance of gases was made up of helium for the CH₄ oxidation reaction and helium and nitrogen for the CO oxidation reaction. For each reaction, the variation in rate with linear gas velocity was determined with the ratio of gases in the reactant mixture held constant. The experiments were performed at lower than typical reaction temperatures (200°C and 500°C for CO and CH₄ oxidation reactions respectively), in order to keep total conversion below 100% at the lowest linear gas velocities. The experiments were conducted using a pure ceria catalyst, which was determined to have the highest surface area (and therefore porosity), of materials in the ceria/lanthana series, and was therefore deemed to present a 'worst case' with respect to diffusion limitations on reaction rate. The results of these experiments are shown graphically in figure 4.58.

For both CO and CH₄ catalytic oxidation reactions, the rate is observed to increase rapidly with initial increases in linear gas velocity (which is directly proportional to volumetric flow rate). For both reactions, the rate of increase in rate with linear gas velocity declined, until beyond approximately 15 cm s⁻¹, rate was observed to be invariant with further increases in linear gas velocity, indicating that mass transfer limitation of rate could be assumed to be insignificant beyond this point. It was therefore possible to standardise reaction conditions for future experiments with respect to gas flow. These standard conditions are summarised below.

Methane Oxidation

25.0 ml min⁻¹ 10% CH₄ / He

118.5 ml min⁻¹ 21% O₂ / He

Total Flow = 8.61 litres hour⁻¹

Linear Gas Velocity = 19.0323 cm s⁻¹

CO Oxidation

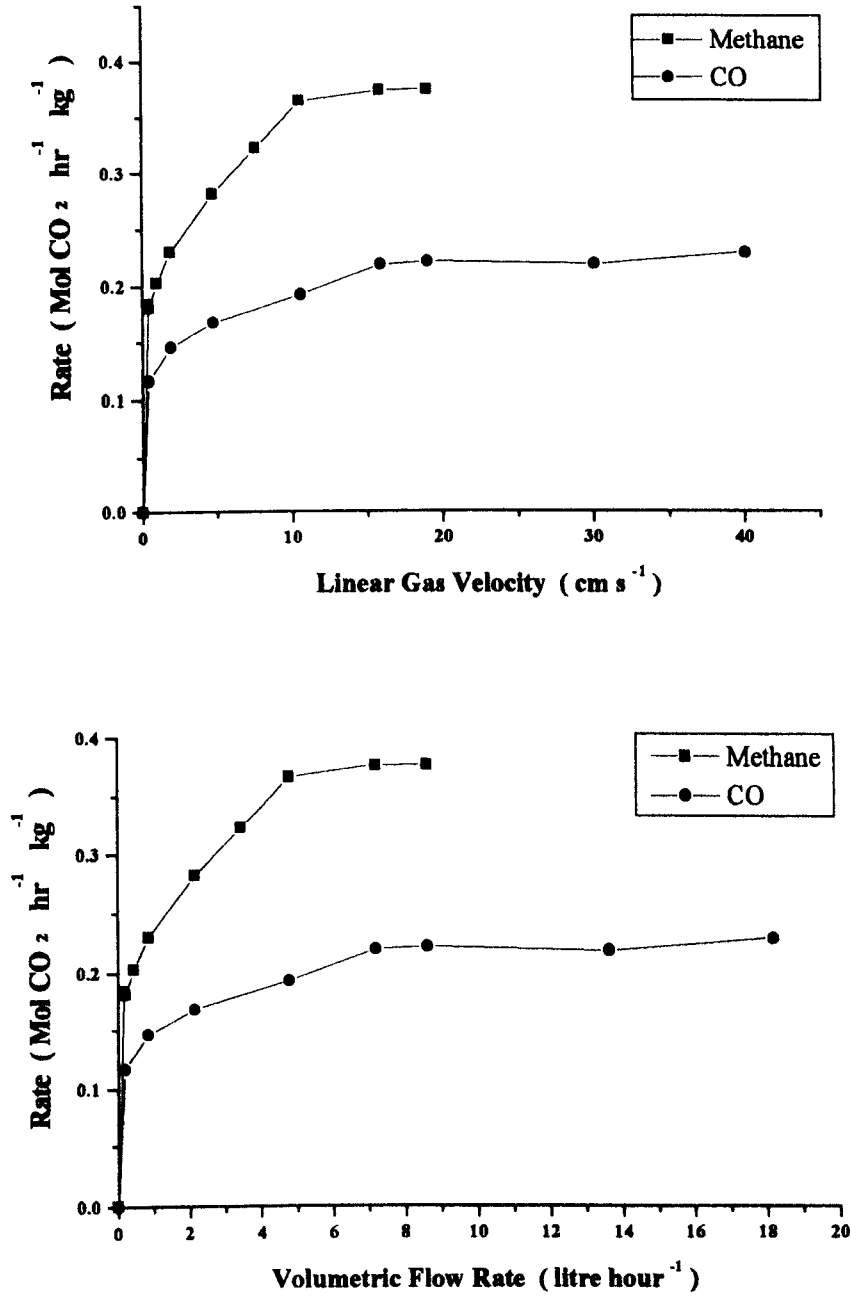
25.02 ml min⁻¹ 10% CO / N₂

118.5 ml min⁻¹ 21% O₂ / He

Total Flow = 8.61 litres hour⁻¹

Linear Gas Velocity = 19.0323 cm s⁻¹

Figure 4.58 Plots of the variations in rate with linear gas velocity and volumetric flow rate, for CO and CH₄ catalytic oxidation reactions over ceria.



Following this study all reaction studies were completed using these standard conditions, unless otherwise stated, and where alternative conditions were necessary, the linear gas velocity was always greater than the minimum value derived in this study. All experimentally derived rates are therefore considered to be true chemical rates, insofar as to be free from gross diffusion (mass transfer) limitation effects.

4.5.2 Ternary Oxide Study

The ternary oxide study was completed in order to validate the experimental set-up and methodology by attempting to reproduce literature data, the results of which are presented and discussed in Appendix 4.1. The literature data used was a patent by Mackrodt, W. C., (1990)⁹⁹ in which catalytic oxidation of methane was reported to be promoted over a ceria catalyst by the doping of with lanthanide oxides, and a further synergistic promotion of catalytic activity was claimed for a combination of lanthanum and praseodymium dopants. The literature data was reproduced empirically thus validating the experimental measurements of catalytic activity in the present study. The promotion of methane catalytic oxidation activity by doping ceria with lanthanide oxides was determined to be a true chemical effect, however the synergistic effect was determined to be a function of catalyst morphology dependence on dopant type, rather than a true chemical effect. CO oxidation was also investigated over the same materials and the addition of lanthanum dopants was found to have a detrimental effect on catalytic oxidation activity, in contrast to the analogous methane oxidation results. As lanthanum doping of ceria was determined to result in contrasting promoting and detrimental effects on CH₄ and CO oxidation activity, respectively, it was concluded that further systematic investigation of the effect of dopant concentration was necessary in order to elucidate the true dopant effects. The lanthanum dopant was determined to have a stronger influence over catalytic properties than praseodymium and was therefore chosen as the dopant for a systematic binary oxide study, (sections 4.5.3 and 4.5.4). Other advantages of the ceria/lanthana system were that lanthanum is not subject to the facile 3+ ↔ 4+ redox, as is praseodymium, therefore simplifying the binary oxide system. There is also far more ceria/lanthana binary oxide system literature data regarding catalytic measurements and other characterisation data than for the ceria/praseodymia system.

4.5.3 CO Oxidation - Systematic Study.

Following the ternary oxide material study discussed in the previous section and in Appendix 4.1, it was apparent that in order to better understand the variations in catalytic activity over doped ceria materials, a study of the systematic variations in catalytic properties with catalyst composition was necessary. A parallel study of both methane and CO oxidation properties was therefore completed over the $\text{Ce}_{1-x}\text{La}_x\text{O}_{2-x/2}$ series using the standard conditions as detailed previously. Activity and specific activity were determined for the materials at the standard temperatures (310°C for CO oxidation and 560°C for CH_4 oxidation), and the response of catalytic reaction rate to temperature was also determined by variation of the reaction temperature, in order to generate Arrhenius plots and activation data. The results of these studies for the CO oxidation reaction are presented in table 4.32. (The errors associated with the activation energies and $\ln A$ values were determined from the statistical analysis following a linear fit of the Arrhenius plot data).

In order to analyse the variations in catalytic properties with catalyst composition the variations in activity, specific activity, Arrhenius method derived activation energy and specific pre-exponential factor were plotted and discussed for the CO oxidation reaction in the following section. The catalyst composition can be expressed in terms of both bulk and surface composition (as determined in the XPS study), and observed trends can be further correlated with the results from the other characterisation methods, as reported previously in this chapter.

The simplest comparison between the catalytic activity of a series of materials is between activity per unit weight of catalyst at a given temperature. The inherent deficiency with comparison in terms of activity per unit weight of catalyst is that the influence of variations in specific surface area are neglected, rendering activity comparisons using the technique somewhat inaccurate and possibly even misleading, as shown in the case of the Mackrodt patent⁹⁹ (Appendix 4.1). For this reason, the comparison of activities between different catalysts in the present systematic study are in terms of specific activity measurements, as well as activity per unit weight of catalyst.

Table 4.32 Summary of the variation in CO catalytic oxidation rate data with composition for the series Ce_{1-x}La_xO_{2-x/2}.

1-x	x	Surface Area m ² g ⁻¹	Activity at 310°C MolCO ₂ hr ⁻¹ kg ⁻¹	Specific Act. 310°C Mol CO ₂ hr ⁻¹ m ⁻² (×10 ³)	Ea Kcal mol ⁻¹	Ea error	ln A	ln A error	A	A / SA
1	0	15.2	1.59343	0.104935	19.103	0.444	16.98842	0.39056	2.3877 e 7	1572397
0.999	0.001	9.3	0.68961	0.074553	21.881	0.008	18.58336	0.00695	1.1767 e 8	12720640
0.99	0.01	13.2	0.67309	0.051092	23.043	0.084	19.56781	0.06966	3.1491 e 8	23904202
0.975	0.025	12.9	0.60326	0.046670	22.589	0.399	18.91436	0.32103	1.6383 e 8	12674710
0.95	0.05	12.4	0.38279	0.030980	23.748	0.140	19.61582	0.11528	3.3040 e 8	26740190
0.90	0.10	13.4	0.31164	0.023201	23.276	0.088	18.99427	0.07097	1.7746 e 8	13211921
0.80	0.20	13.9	0.34699	0.025001	22.003	0.245	17.99040	0.19881	6.5033 e 7	4685687
0.70	0.30	12.8	0.24601	0.019217	19.966	0.496	15.86415	0.40066	7.7573 e 6	605947
0.60	0.40	11.4	0.27034	0.023281	16.967	0.306	13.35872	0.24266	6.3331 e 5	55466
0.50	0.50	11.7	0.15981	0.013639	18.372	0.224	13.65483	0.16931	8.5156 e 5	72678
0.40	0.60	10.8	0.10366	0.009575	16.360	0.456	11.73185	0.34419	1.2447 e 5	11498
0.35	0.65	6.3	0.15862	0.025046	16.077	0.332	11.9832	0.24487	1.6004 e 5	25271
0.25	0.75	9.1	0.15703	0.017183	13.054	0.210	9.89315	0.15489	1.9794 e 4	2166
0.20	0.80	8.7	0.41022	0.047065	16.971	0.988	13.86084	0.77290	1.0464 e 6	120052
0.10	0.90	7.7	0.09101	0.011854	21.003	0.453	15.76491	0.35793	7.0245 e 6	915002
0.05	0.95	13.6	0.15249	0.011214	23.270	0.276	17.83782	0.21256	5.5830 e 7	4105743
0.025	0.975	7.2	0.15215	0.021094	19.882	0.550	15.13314	0.41324	3.7346 e 6	517754
0.01	0.99	7.7	0.07016	0.009065	17.073	0.243	12.15014	0.18351	1.8912 e 5	24434
0.005	0.995	5.7	0.15005	0.026213	21.583	0.366	16.76069	0.28993	1.9014 e 7	3321816
0	1	5.9	0.37672	0.063916	11.713	0.561	9.17579	0.43585	9.6604 e 3	1639

4.5.3.1 CO Oxidation - Standard Activity Measurements

The variation in CO catalytic oxidation rate per unit weight of catalyst is shown in figure 4.59, with respect to both bulk and surface composition. The rate is observed to decrease rapidly with initial additions of lanthanum, with a systematic reduction in the decline of the rate for further lanthanum additions up to the solid solution limit, (bulk $x = 0.6$). Curve fitting of the data results in an approximate exponential decline in rate with lanthanum concentration within the solid solution limit. Beyond the solid solution limits ($x = 0.6$ and $x = 0.8$ in the variations with bulk and surface compositions, respectively), the observed variations are complex and no real trends can be determined in this region.

This result is in good agreement with the trends observed by Rienäcker,³³ as discussed previously in the literature review chapter (section 2.2.4), and clearly demonstrate that the introduction of the lanthanum dopant has a poisoning effect with regards the active sites for CO oxidation. From this it is possible to conclude that the concentration of active sites for CO oxidation is proportional to the concentration of cerium cations within the lanthanum in ceria solid solution range, ($0 < \text{bulk } x < 0.6$). Similar plots of variations in specific activity with bulk and surface composition are shown in figure 4.60.

The trends observed in the variation in specific activity for CO catalytic oxidation are notably similar to those observed for activity per unit weight, as would be expected from the similar order of surface areas for all of the materials within the systematic series. The general trend within the materials as prepared was previously determined to be a gradual decrease in surface area with lanthanum concentration in section 4.1.4, (although at higher sintering temperatures (section 4.1.3), the presence of lanthanum was found to stabilise the materials with respect to sintering, thus preserving higher surface areas). The effect of the gradual decline in surface area results in a moderating effect on the variation in specific activity with composition plot, in comparison with the analogous variation in activity per unit weight of catalyst. The progressive decline in activity with increasing lanthanum concentration for materials within the lanthanum in ceria solid solution range was again evident in the

specific activity plots, supporting the previous conclusion that the decline in activity was a true chemical effect which could be effectively described as the poisoning of active sites by the introduction of the lanthanum dopant within the solid solution range $0 < \text{bulk } x < 0.6$.

Figure 4.59 A plot of the variation in CO oxidation reaction rate per unit weight of catalyst with catalyst bulk and surface lanthanum concentration.

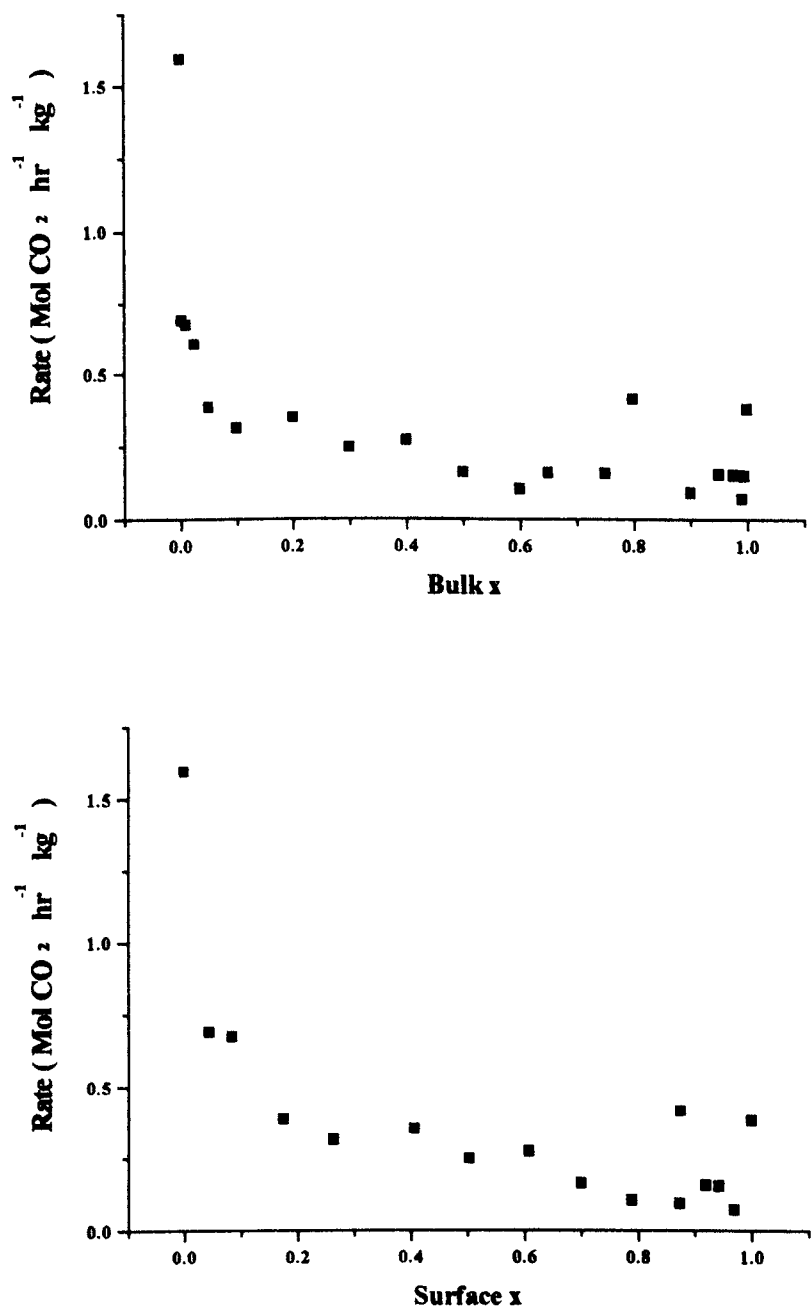
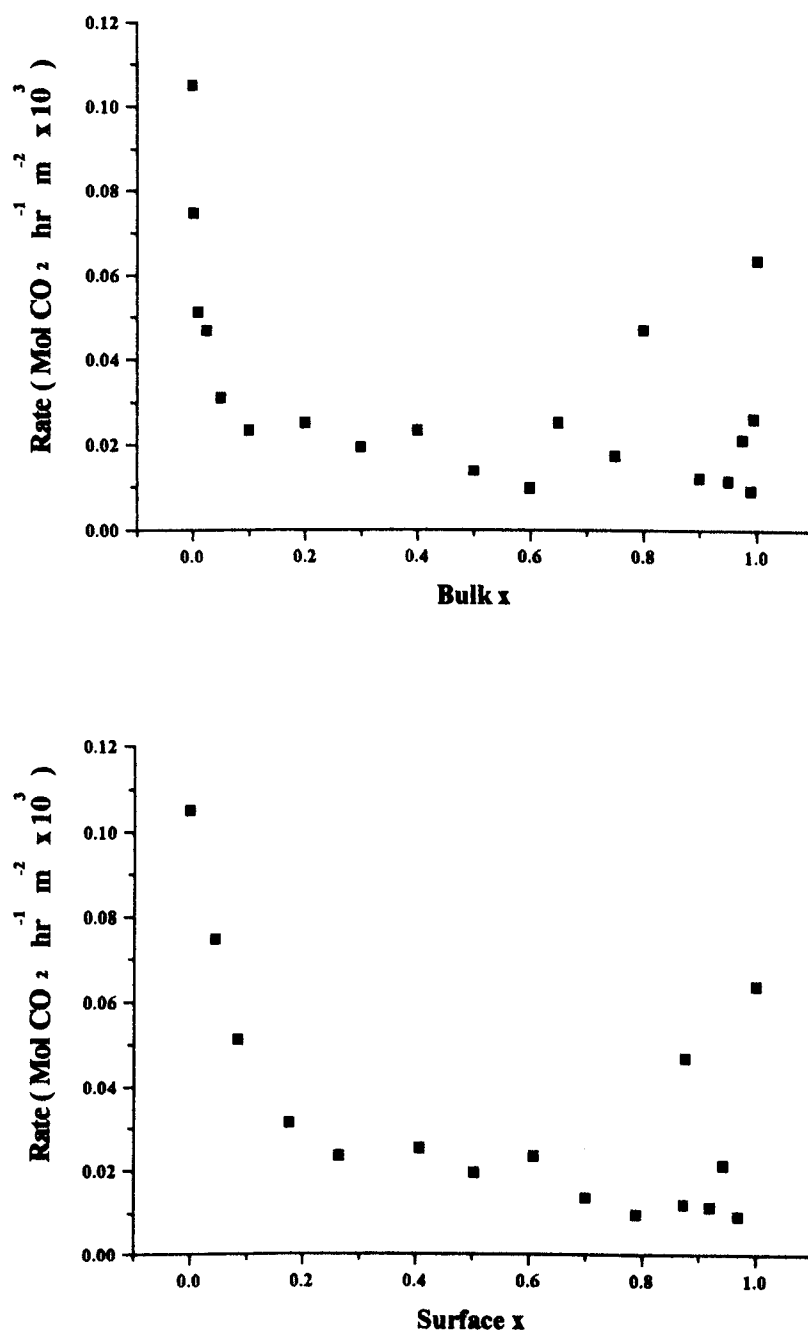


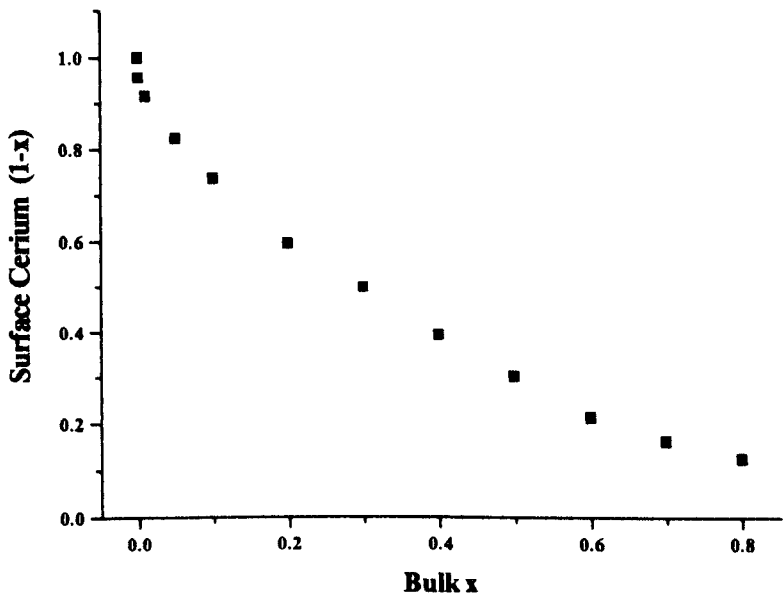
Figure 4.60 A plot of the variation in CO oxidation reaction rate per unit surface area of catalyst with catalyst bulk and surface lanthanum concentration.



The surface composition studies (section 4.2.3 and subsections therein), have previously demonstrated the non-linear variation in surface composition with bulk composition for these materials, and the significant levels of enrichment of lanthanum in the surface of the lanthanum in ceria solid solutions, particularly at low bulk concentrations. The variation in specific activity does not vary similarly as the concentration of surface cerium cations (surface 1-x) with bulk lanthanum concentration, as shown in figure 4.61. The variation in surface cerium with bulk

lanthanum has already been determined to approximate to an exponential decay function by the good fit of a power function similar in form to the Freundlich isotherm. It would appear that the incorporation of lanthanum into ceria results in a poisoning of the active sites which cannot be explained simply in terms of moderation of activity by displacement of active surface cerium cations by lanthanum.

Figure 4.61 A plot of the variation in surface cerium concentration with bulk x



4.5.3.2 CO Oxidation - Arrhenius Studies

For CO oxidation, reaction rates were determined at a series of temperatures, such that the total conversion was always in the 2 - 12% range. For each material, $\ln(\text{reaction rate})$ vs. $1/T$ plots (Arrhenius method), were used to determine the apparent activation energy (E_a) for the reaction (slope of plot), and the pre-exponential factor (A), ($\ln A$ is equal to the intercept on the $\ln(\text{reaction rate})$ axis at $1/T = 0$). The pre-exponential factor is assumed to be proportional to the number of active surface sites for the reaction. When divided by the specific surface area, a specific pre-exponential factor (A/SA) is derived which can be assumed to be proportional to the number of active sites for the reaction per unit area of each catalyst material. Thus, it is possible to compare materials in the systematic series in terms of catalytic active site density, and in terms of the activity temperature response.

The Arrhenius data for the CO oxidation reaction have been presented earlier in this section in the results summary table on page 4.32. The variations in E_a with bulk and surface composition are shown in figure 4.62 and the variations in specific pre-exponential factor with bulk and surface lanthanum concentration are shown in figure 4.63.

Figure 4.62 Plots of the variations in E_a with bulk and surface lanthanum concentration for the CO oxidation reaction.

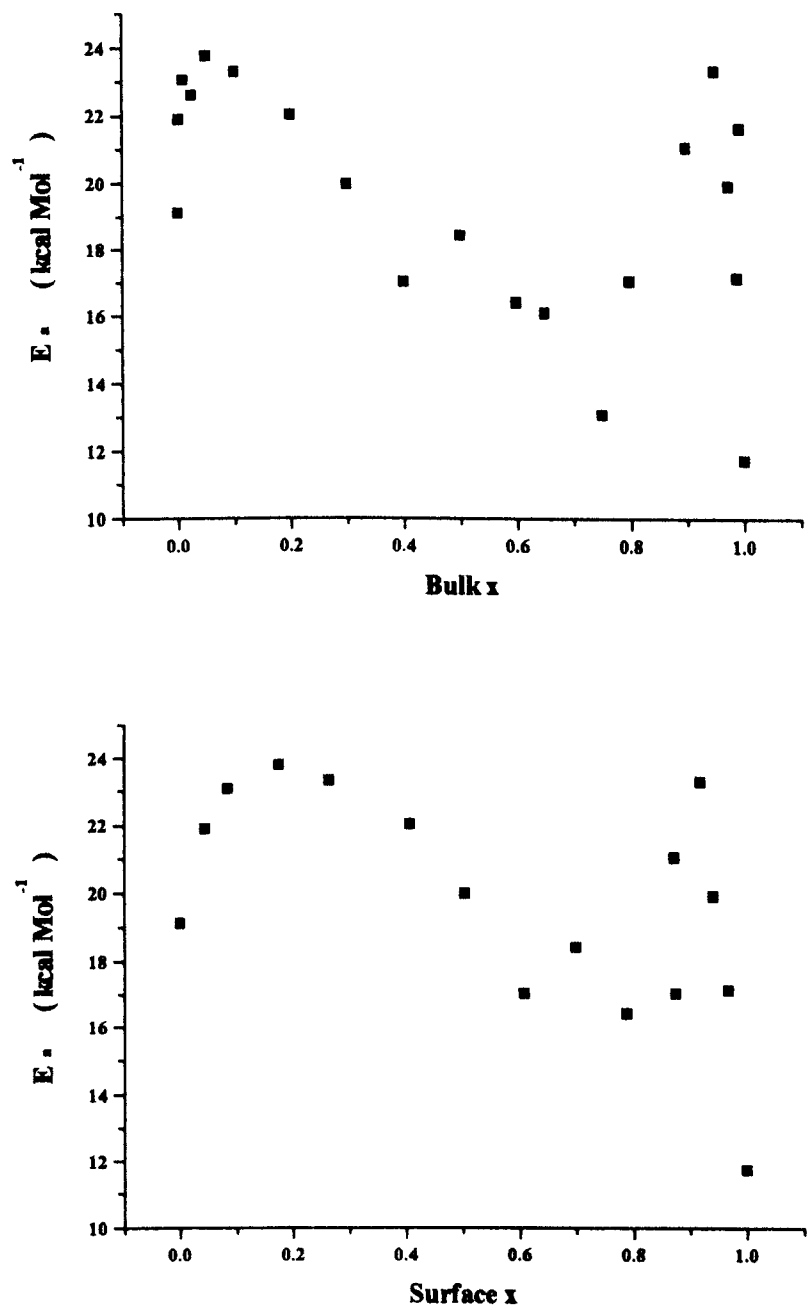
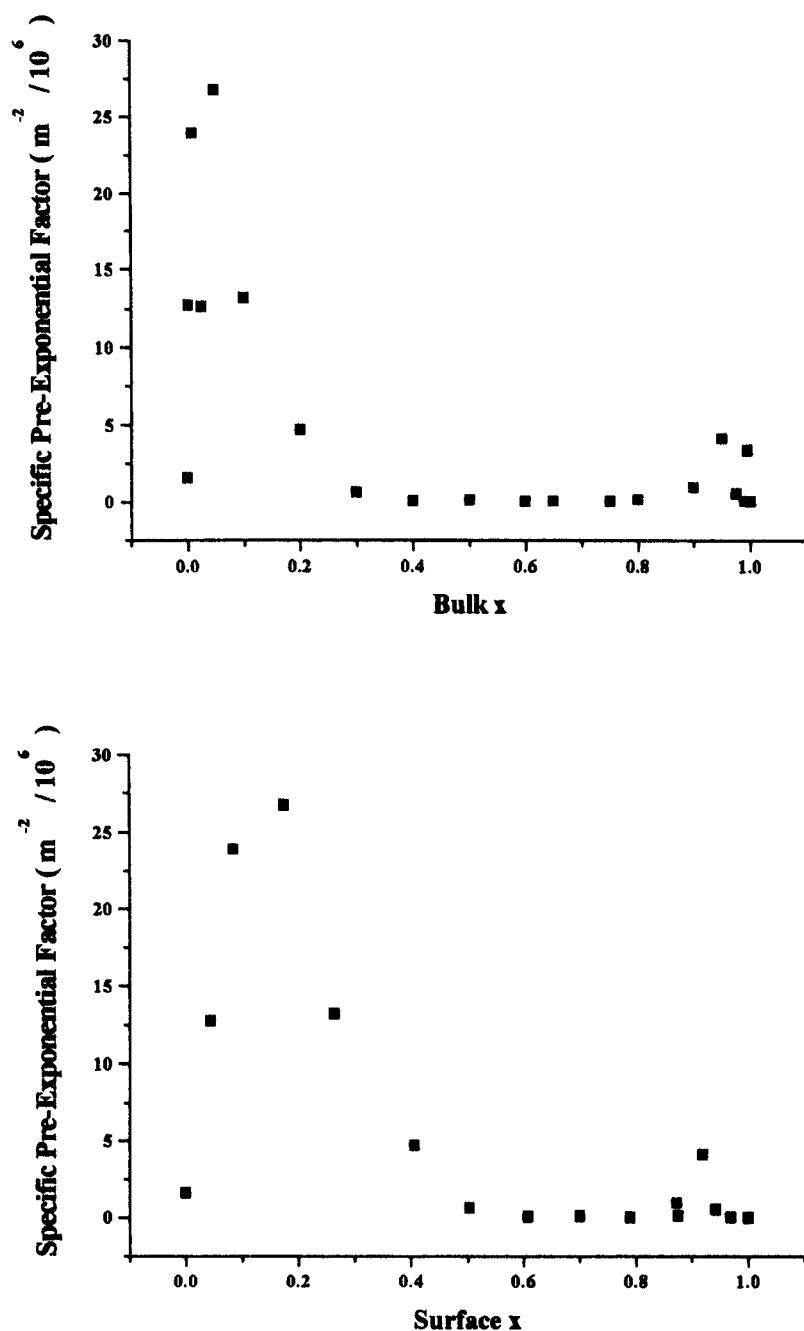


Figure 4.63 A plot of the variations in specific pre-exponential factor with Bulk and Surface lanthanum concentration for the CO oxidation reaction.



The observed maxima in specific pre-exponential factor (figure 4.63) are far more defined than the corresponding E_a maxima in figure 4.62, although the peak positions are near incident. It can therefore be concluded that the number of active sites is maximised at a surface La : Ce ratio of between approximately 0.08 and 0.17 in the La in ceria solid solution range, and (less significantly) at a surface Ce : La ratio of between approximately 0.1 and 0.05 at the lanthanum rich end of the systematic series.

The increases in the specific pre-exponential factor with composition (which would increase reaction rate) are therefore observed to be compensated for by simultaneous increases in E_a (which would decrease reaction rate). The compensation effect is discussed further in the next section.

There are several interesting features of the plots of the variations in E_a and specific pre-exponential factor with bulk and surface lanthanum concentration. With initial additions of low levels of lanthanum to ceria, a rapid increase in apparent activation energy is observed from approximately 19 to 24 kcal Mol⁻¹ (79.6 to 100.5 kJ mol⁻¹), up to the bulk lanthanum concentration range $x = 0.01$ to 0.05. Further increases in lanthanum concentration within the solid solution range result in near linear decline to approximately 13 kcal Mol⁻¹ (54.4 kJ Mol⁻¹), at approximately bulk $x = 0.6$ to 0.75. When the variation in apparent activation energy with surface lanthanum concentration is plotted, the variation within the solid solution region is observed to follow a more gentle peak, with a maximum corresponding to the surface lanthanum concentration range of $x = 0.085$ to 0.176. This observation is of particular interest, as the surface concentration range at which E_a is observed to be maximised in the La in ceria solid solution region correlates well with the concentration of lanthanum in ceria for which anionic mobility is maximised, as reported in the literature review, section 2.1.2.3.2. Although bulk cationic conductivity generally requires temperatures in the region of >500°C to become significant, the presence of conduction pathways at the surface (grain boundary) conductivity which require lower temperatures to become active is possible.

In data reported by Takahashi (1972)⁵³ which has been discussed in the literature review chapter, (section 2.1.2.3.2), a clear composition dependence of conductivity was demonstrated for lanthanum doped ceria solid solutions. At a measurement temperature of just 400°C, a clear maximum in the plot of conductivity with composition was reported between $0.1 < \text{bulk } x < 0.2$, from which the bulk x corresponding to peak conductivity can be estimated as 0.12. The observed trend in the composition corresponding to the maximum conductivity with measurement temperature allows the maximum conductivity at 310°C to occur at an estimated bulk lanthanum concentration range of $0.10 < x < 0.11$. The composition dependence of

conductivity observed at 400°C is also evidence of low temperature conductivity pathways within the material. The peak conductivity composition range determined by Takahashi is in good agreement with other literature studies, such as Rienäcker and Wu (1962) also investigating lanthanum doped ceria, and Balazs (1995) who investigated yttrium doped ceria. Both of these studies also reported that the activation energy for the conductivity process was also minimised at compositions in the range $0.04 < x_{\text{bulk}} < 0.18$. This variation is observed to be the converse of that observed for the catalytic oxidation of CO. It would appear that the measured CO oxidation activity does not vary similarly to conductivity at 310°C due to dominance of the activation energy term. At higher temperatures the variation in activity would become progressively dominated more by the variation in specific pre-exponential factor, and thus more akin to the variations in conductivity with composition. The minimum in the conductivity activation energy variation with composition can be explained in terms of an optimisation of the concentration of unbound vacancies exhibiting a minimal response to temperature. Thermal vacancy-dopant dissociation at higher and lower dopant concentrations results in a larger response to temperature for these compositions. Further details regarding the optimisation of anionic conductivity in doped ceria materials can be found in the literature review chapter in section 2.1.2.3 and subsections therein.

Beyond bulk $x = 0.6$ (the solid solution limit), progressive increases in the concentration of lanthanum results in peaks in apparent activation energy and specific pre-exponential factor at between $x = 0.9$ and 0.95 (surface also approximately $x = 0.9$ to 0.95). As regards conductivity in the Ce in lanthana solid solution region, Rienäcker also observed a peak in conductivity in this compositional range which was explained in terms of a promotion of semiconductivity by the incorporation of Ce into lanthana, rather than ionic conductivity. It would therefore appear that there is a correlation between material surface conductivity maxima, and maxima in both apparent activation energy and specific pre-exponential factor derived from the CO catalytic oxidation study.

The observed correlations of apparent activation energy and specific pre-exponential factor with both anionic and semi-conductivity made determination of the

conductivity of the catalyst material, and particularly of surface/grain boundary conductivity a desirable characterisation for the present study. The measurement of material conductivity using ac impedance spectroscopy and 4-probe dc techniques was attempted on materials prepared using the standard coprecipitation technique. However following calcination at 800°C (necessary in order to preserve the surface/bulk cation ratios as in the catalysts), materials were found to be structurally unsuitable for testing. As further experimental work to pursue this correlation directly was not possible, the correlations made are based on bulk conductivity data from literature sources.

It is reasonable to assume that based on simple physical concepts, the conductivity of the surface/grain boundary varies similarly with composition, as does bulk conductivity. It can be deduced based on surface composition measurements and lanthanum surface segregation modelling completed within the present study, that the maximum surface conductivity at the CO standard reaction temperature (340°C), should occur for catalysts such that $0.01 < \text{bulk } x < 0.05$. This range of bulk compositions was determined to correspond to a surface composition range of $0.085 < \text{surface } x < 0.176$. The observed maxima in CO oxidation reaction activation energy and specific pre-exponential factor in this exact compositional range supports the proposal that surface conductivity, and specifically the population of free oxide anion vacancies in the surface exhibits a direct correlation with measured catalytic properties for CO oxidation over lanthanum doped ceria.

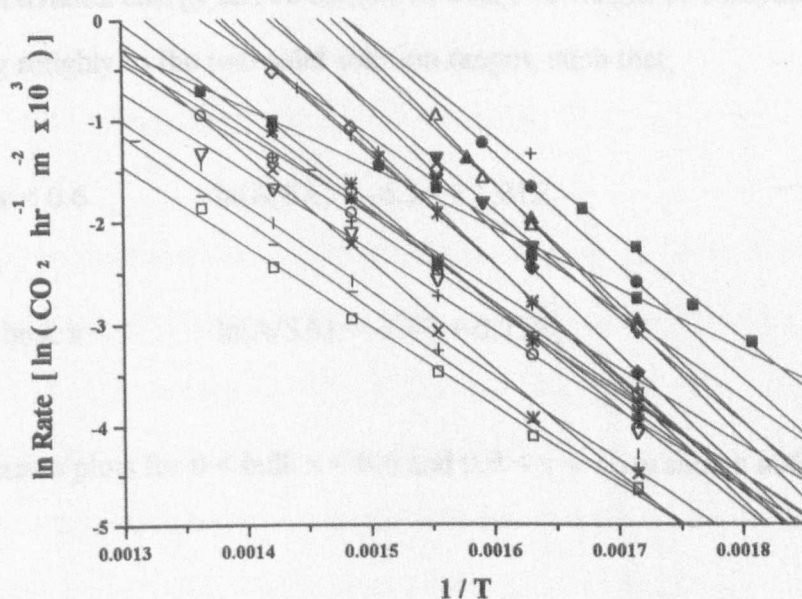
Sayle et al (1994)¹¹⁹ used computer simulation techniques to predict that the optimisation of surface conductivity in ceria would result in enhanced CO oxidation activity, by optimisation of the redox mechanism. This result is in marked contrast to other literature data,^{58, 73, 112, 128} in which activity was generally correlated with bulk composition. It is possible that the lack of good correlation of catalytic properties with conductivity up to now has been a consequence of the surface segregation processes. As surface conductivity and bulk conductivity will be maximised at different bulk compositions for a given preparative method, unless full characterisation of the surface segregation processes occurring are available, it would be impossible to correlate the two accurately. These results have indicated a fresh avenue for further

research to investigate the correlation of catalytic properties with surface conductivity. The results of such work could potentially be applied to optimise catalysts for surface conductivity limited reactions in a far more precise way than before, using bulk correlations only.

4.5.3.3 CO Compensation Effect

All of the CO oxidation data are plotted in figure 4.64 to show an overview of the Arrhenius data for CO catalytic oxidation for the entire $\text{Ce}_{1-x}\text{La}_x\text{O}_{2-x/2}$ series.

Figure 4.64 A plot of Arrhenius data for CO oxidation over the $\text{Ce}_{1-x}\text{La}_x\text{O}_{2-x/2}$ series.



There is no evidence for the presence of an isokinetic point in this plot which would reduce the validity of an observed compensation effect. The proportionality of specific pre-exponential factor to apparent activation energy is a phenomenon known as the compensation effect and can generally be represented by the equation $\ln A = m E_a + C$, where m and C are constants.¹⁶⁰ This effect is often observed for a given reaction over a series of catalysts, or indeed a series of related reactions over a given catalyst material. The origin of the effect stems from the fact that the activation energy

derived using the Arrhenius method is an apparent activation energy (E_a), rather than a true activation energy (E_{true}), where it can generally be stated that;

$$E_{\text{True}} = E_a - \Delta H_{\text{ads}}^{\circ} \quad (4.26)$$

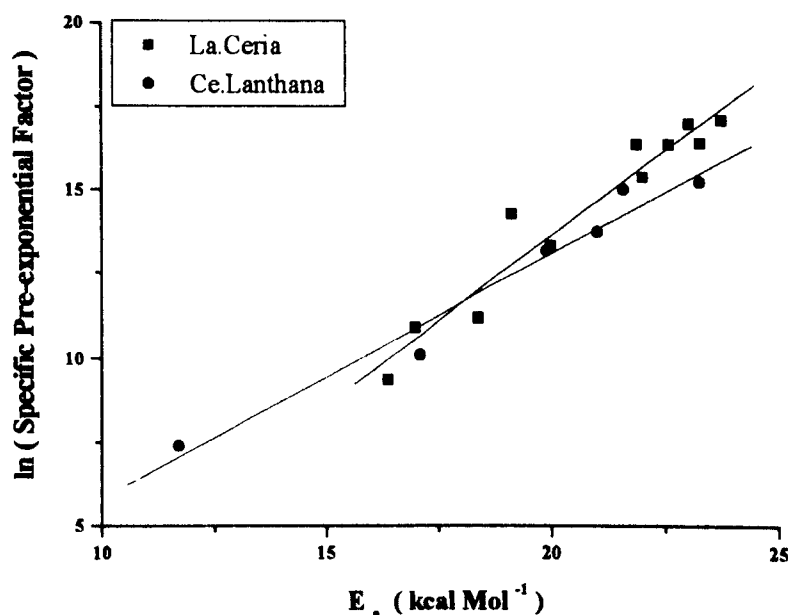
As most experimental measurements are performed such that the surface coverage of the adsorbed species lies in the range $0 < \theta < 1$, it is likely that the adsorption enthalpy term is significant. For a series of catalysts, it is likely that the adsorption enthalpy will vary from material to material, thus resulting in the observed variations in E_a , although E_{true} is generally assumed to remain constant. This variation in adsorption enthalpy is generally assumed to account for the observed compensation effects.¹⁶⁰ In the case of the present study, the plot of specific pre-exponential factor vs. apparent activation energy can be compared over two ranges of composition corresponding roughly to the two solid solution ranges, such that;

$$\text{for } 0 < \text{bulk } x < 0.6 \quad \ln(A/SA) = -6.54 + 1.01E_a \quad (4.27)$$

$$\text{and for } 0.9 < \text{bulk } x < 1 \quad \ln(A/SA) = -1.47 + 0.73E_a \quad (4.28)$$

The compensation plots for $0 < \text{bulk } x < 0.6$ and $0.9 < x < 1$ are shown in figure 4.65

Figure 4.65 Plots of \ln specific pre-exponential factor vs. E_a for the two solid solution compositional ranges; $0 < \text{bulk } x < 0.6$ and $0.9 < \text{bulk } x < 1$.



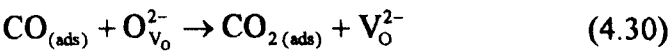
4.5.3.4 CO Catalytic Oxidation - Kinetic Studies

In this section, the effect of reactant and product partial pressure on reaction rate was investigated. The purpose of the study was to provide further data, pertinent to the elucidation of the reaction mechanism(s) occurring at the surface. Further correlation with data from the other methods of characterisation was used to lend support to the mechanistic arguments presented. Experimentally, the variation in rate with concentration of CO, O₂ and CO₂ was determined. For each experiment, computer curve fitting was then used to determine the order of the reaction with respect to the reactant.

For the variations in concentration of CO and O₂, experiments were possible under the standard reaction conditions and temperature by appropriate use of He balance gas. In the case of studies of the variation in CO₂ concentration, it was necessary to slightly increase the overall volumetric flow rate to accommodate the additional gas in the reactant stream, and by default, proportionally reduce the concentrations of reactants in the reactant mixture. However, the concentrations of CO and O₂ remained constant. Due to the high CO₂ concentrations caused by addition of

CO₂ to the reactant gas, reaction rate was determined by CO consumption. The reaction rate was then expressed in terms of Mol CO₂ hr⁻¹ kg⁻¹ for reasons of continuity.

A mechanism for the oxidation of CO, comprising alternating oxidation and reduction of ceria was presented by Breysse et al (1972).¹³⁵ The kinetics of the catalytic oxidation of CO and the electrical conductivity were derived from a four step mechanism;



In the Breysse study, the order on P_{CO} was determined to be 0.84, and the order on P_{O₂} was determined to be zero. Low levels of CO₂ were found to retard the reaction, but the degree of retardation was not affected by further increases in P_{CO₂}.

4.5.3.4.1 Oxidation of CO over CeO₂ Catalyst

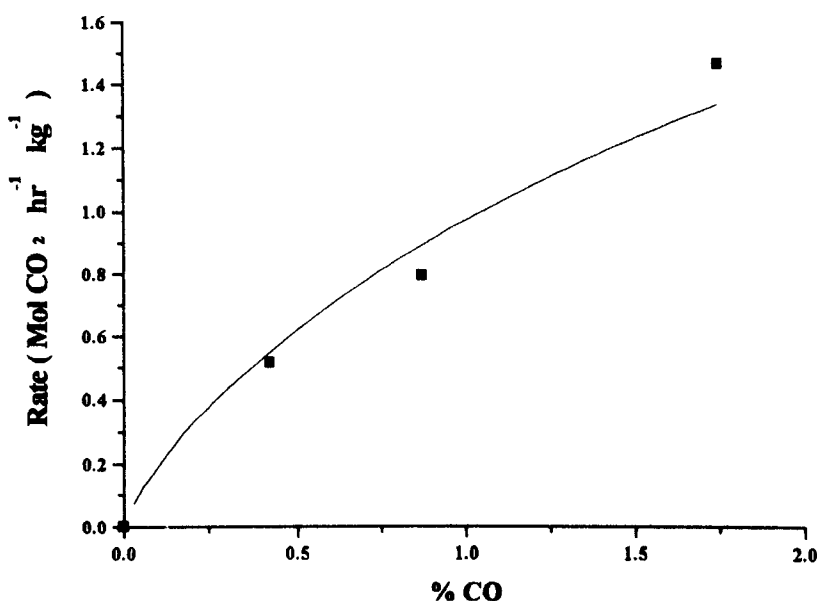
4.5.3.4.1.1 The effect of P_{CO}

Experimental Conditions: Total flow = 8.6112 l hr⁻¹ % O₂ = 17.340

Table 4.33 Results

% CO	Rate at 310°C (Mol CO ₂ hr ⁻¹ kg ⁻¹)
1.743	1.468119
0.870	0.795217
0.418	0.516628
0	0

Figure 4.66 A plot of the variation in CO oxidation rate with CO feed concentration



The apparent order on CO partial pressure is approximately 0.8, which is in good agreement with that reported by Breysse.¹³⁵ In the preferred interpretation, the reaction may be interpreted as pseudo-first order on CO, combined with the Langmuir-type adsorption isotherm arising from a progressive site-blocking effect of adsorbed CO in proportion to CO partial pressure. On this basis the effect of CO partial pressure on the rate of CO oxidation can be represented by the Langmuir-type isotherm expression;

$$\text{Rate} = \frac{1.29P_{\text{CO}}}{(1 + 0.32P_{\text{CO}})} \quad (4.33)$$

The adsorption of CO on ceria was found to obey a Langmuir type adsorption isotherm in an infrared adsorption/desorption study by Li et al,¹¹⁷ as discussed in section 2.2.1. Equation 4.33 is also similar in form to that presented by Liu and Flytzani-Stephanopoulos^{112, 128} for CO oxidation over La doped ceria supported copper oxide

The effect of the variable P_{CO_2} which ranged up to 0.14% in these reactions was determined in the CO₂ retardation study (next section), to retard the reaction by less than 2% at the highest P_{CO_2} level attained. The effect of product retardation was

accordingly neglected in this analysis. It is therefore concluded that the active form of CO is a single adsorbed CO molecule.

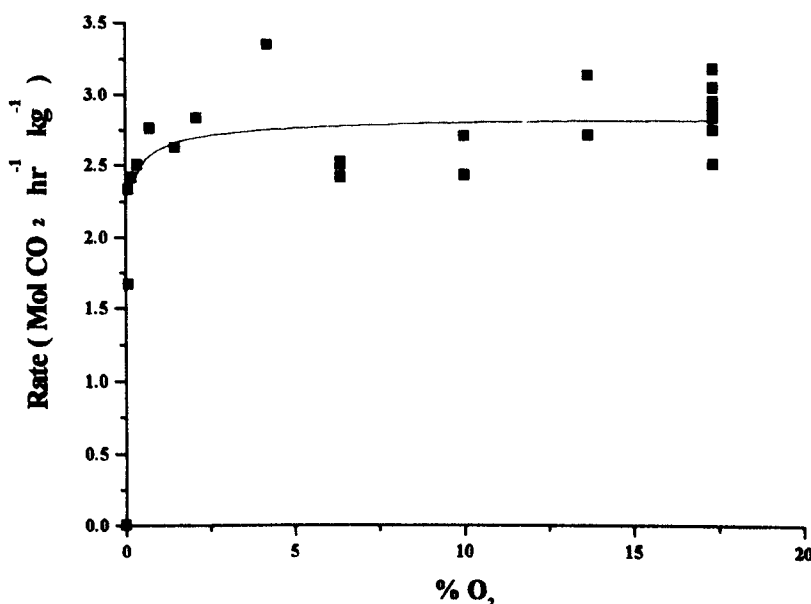
4.5.3.4.1.2 The effect of P_{O_2}

Experimental conditions Total flow = 8.6112 l hr⁻¹ % CO = 1.742

Table 4.34 Results

% O₂ (In Chronological Order)	Rate at 310°C (Mol CO₂ hr⁻¹ kg⁻¹)
17.339	2.511671
6.365	2.418611
4.211	3.350569
2.099	2.834046
1.482	2.625710
17.339	2.894119
6.365	2.502382
10.023	2.706553
13.681	3.136390
0.7107	2.757832
0.3561	2.500392
0.1772	2.411335
0.08846	1.665190
17.339	2.959723
17.339	2.839516
0.08846	2.330179
17.339	2.753912
6.365	2.522423
17.339	3.183949
13.681	2.712011
17.339	3.054429
17.339	2.905078
10.023	2.429709

Figure 4.67 A plot of the variation in CO oxidation rate with O₂ feed concentration



At low oxygen partial pressures, the rate of the CO oxidation reaction is found to increase in proportion to $\sqrt{P_{O_2}}$. Further increases in P_{O_2} have progressively less effect on the reaction rate, eventually establishing apparent zero order on P_{O_2} at higher partial pressures. The effect of the full range of P_{O_2} can be represented by the expression;

$$\text{Rate} = \frac{26.89\sqrt{[O_2]}}{(1 + 9.28\sqrt{[O_2]})} \quad (4.34)$$

This expression represents the long-term response to changes in P_{O_2} .

In the short-term, raising the P_{O_2} at constant P_{CO} was found to generate higher activities than predicted by the long term response expression. This would suggest the formation of short-lived high activity oxidants, or higher concentrations of the active oxidant under low P_{O_2} conditions. A partial reduction of the ceria surface is possible under low P_{O_2} which would create an increase in the concentration of sites for the activation of oxygen at the surface of the material. This would account for the observed increase in rate following the exposure to the more reducing conditions. At high P_{O_2} a gradual decrease in the reaction rate is observed toward that predicted by the long-term response expression which can be explained in terms of the re-oxidation of the surface. This explains the variation in the observed rates at 17.339 % O₂. Over

the P_{O_2} range 6.365 % to 17.339 %, the long term response rate of CO oxidation over CeO_2 is essentially independent of P_{O_2} .

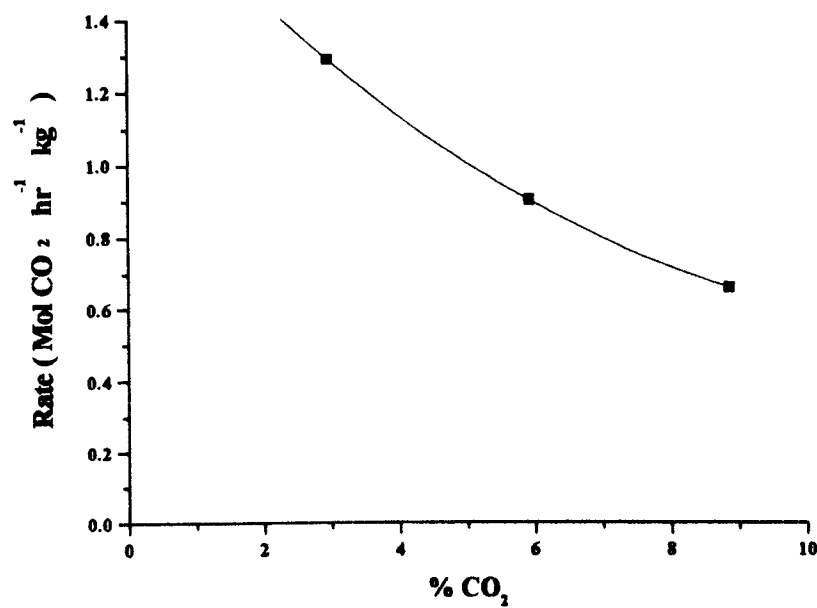
4.5.3.4.1.3 The effect of P_{CO_2}

Experimental conditions Flow rate = 10.1112 l hr⁻¹ %CO = 1.484 %O₂ = 14.769

Table 4.35 Results

% CO ₂	Rate at 310°C (Mol CO ₂ hr ⁻¹ kg ⁻¹)
2.973	1.286636
5.934	0.899578
8.871	0.656453

Figure 4.68 A plot of the variation in CO oxidation rate with CO₂ feed concentration



Increases in P_{CO_2} are observed to have a progressive and distinct retarding effect on the rate of CO oxidation. This observation is in contrast with that reported by Breyse et al (1972)¹³⁵ in which it was concluded that the total CO oxidation rate comprised a marginally CO₂ retarded component and a P_{CO_2} independent component.

The present activity study was completed under conditions such that the orders on CO and O₂ were 1 and zero, respectively. It therefore seems most likely that the retardation effect of CO₂ is due to competition between CO₂ and CO for adsorption sites. To distinguish positively between CO and O₂ as the competitor with CO₂ for adsorption sites, measurement of the retarding effect of CO₂ as a function of P_{CO} and P_{O₂} would be required. Such studies were however beyond the scope of the present study. The response of the rate of CO oxidation to P_{CO₂} can be represented by the expression;

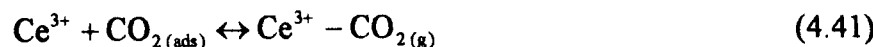
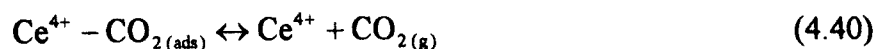
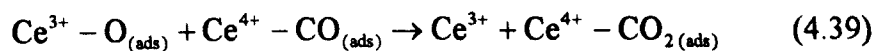
$$\text{Rate} = \frac{1.769}{(1 + 0.1[\text{CO}_2] + 0.01[\text{CO}_2]^2)} \quad (4.35)$$

4.5.3.4.1.4 Mechanistic Discussion.

At low P_{O₂}, the rate of catalytic oxidation of CO exhibits a dependence on oxygen partial pressure, indicating the reactivity of some form of adsorbed oxygen at 310°C. The following reaction scheme is presented to provide a generalised representation of oxygen adsorption on partially reduced ceria;



The extent of these reactions depends on the electron donor power of the surface of the ceria, which in turn depends on the extent of reduction of the surface. The half-order on O₂ suggests that atomic oxygen is the active oxidant. It is proposed that the activity hysteresis on changing from low O₂ : CO ratios to high originates from the variation in the concentration of reduced cerium cations at the surface, and by default the concentration of adsorbed atomic oxygen - the proposed active oxidant species. The following reaction scheme is therefore proposed;



A concerted reaction mechanism is proposed to operate under the low temperature conditions used here, although the mechanism may be superseded by a redox mechanism (see literature review, section 2.2.4), at higher temperatures.

For Ce^{3+} sites;

$$\theta_{\text{O}_2} = (\text{K}_{\text{O}_2} \text{P}_{\text{O}_2})^{0.5} (1 - \sum \theta^{\text{Ce}^{3+}}) \quad (4.42)$$

$$\theta_{\text{CO}_2}^{\text{Ce}^{3+}} = \text{K}_{\text{CO}_2}^{\text{Ce}^{3+}} \text{P}_{\text{CO}_2} (1 - \sum \theta^{\text{Ce}^{3+}}) \quad (4.43)$$

hence

$$(1 - \sum \theta^{\text{Ce}^{3+}}) = \frac{1}{(1 + (\text{K}_{\text{O}_2} \text{P}_{\text{O}_2})^{0.5} + \text{K}_{\text{CO}_2}^{\text{Ce}^{3+}} \text{P}_{\text{CO}_2})} \quad (4.44)$$

For Ce^{4+} sites;

$$\theta_{\text{CO}} = \text{K}_{\text{CO}} \text{P}_{\text{CO}} (1 - \sum \theta^{\text{Ce}^{4+}}) \quad (4.45)$$

$$\theta_{\text{CO}_2}^{\text{Ce}^{4+}} = \text{K}_{\text{CO}_2}^{\text{Ce}^{4+}} \text{P}_{\text{CO}_2} (1 - \sum \theta^{\text{Ce}^{4+}}) \quad (4.46)$$

hence

$$(1 - \sum \theta^{\text{Ce}^{4+}}) = \frac{1}{(1 + \text{K}_{\text{CO}} \text{P}_{\text{CO}} + \text{K}_{\text{CO}_2}^{\text{Ce}^{4+}} \text{P}_{\text{CO}_2})} \quad (4.47)$$

Assuming that the rate of the CO catalytic oxidation reaction is proportional to the product of the coverages of adsorbed CO and adsorbed atomic oxygen, and that the sites are randomly distributed on the surface, then from the expressions above;

$$\text{Rate} = k \theta_{\text{O}_2} \theta_{\text{CO}}$$

$$\text{Rate} = \frac{k(K_{O_2} P_{O_2})^{0.5} K_{CO} P_{CO}}{(1 + (K_{O_2} P_{O_2})^{0.5} + K_{CO_2}^{Ce^{3+}} P_{CO_2}) \times (1 + K_{CO} P_{CO} + K_{CO_2}^{Ce^{4+}} P_{CO_2})} \quad (4.48)$$

At constant P_{O_2} and P_{CO_2} , equation 4.48 reduces to;

$$\text{Rate} = \frac{k_{Eq4.49} P_{CO}}{(1 + K_{Eq4.49} P_{CO})} \quad (4.49)$$

which is similar in form to equation 4.33.

At constant P_{CO} and P_{CO_2} , equation 4.48 reduces to;

$$\text{Rate} = \frac{k_{Eq4.50} P_{O_2}^{0.5}}{(1 + K_{Eq4.50} P_{O_2}^{0.5})} \quad (4.50)$$

which is similar in form to equation 4.34.

At constant P_{CO} and P_{O_2} , equation 4.48 reduces to;

$$\text{Rate} = \frac{k_{Eq4.51}}{(1 + K_{Eq4.51} P_{CO_2} + K_{Eq4.51}' (P_{CO_2}^2))} \quad (4.51)$$

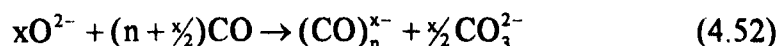
which is similar in form to the P_{CO_2} dependent component of equation 4.35.

4.5.3.4.2 Oxidation of CO over La_2O_3 Catalyst

This section addresses the CO oxidation reaction kinetics over lanthana, which is the other end member of the $Ce_{1-x}La_xO_{2-x/2}$ catalyst series. Of the lanthanide oxides, lanthana is known to exhibit the highest basic strength.^{141, 145 - 146} Among the rare-earth oxides, lanthana shows the highest activity and C_2 selectivity for the catalytic oxidative

coupling of methane reaction, in which a surface acid-base pair is known to activate adsorbed methane by abstraction of a proton.¹⁴⁶

Carbonate formation is often consequential to the adsorption of CO on strongly basic sites, as shown by the surface reaction of CO with the heavier alkaline earth oxides;



On strongly basic surfaces, the degradation of the carbanionic clusters $(CO)_n^{x-}$ is considered to be a possible route for the Boudouard reaction.¹²⁴



In a study of CO oxidation over mixed oxides of ceria and lanthana,³³ pure lanthana was found to exhibit the lowest activity of the series, mainly due to a low activation energy. It is known that CO catalytic oxidation can occur by two separate routes: a stepwise mechanism comprising alternating oxidation and reduction of the catalyst surface, or a concerted mechanism in which CO_2 is formed directly from an interaction between surface compounds formed from CO and molecular oxygen.¹⁷² Chromium and zinc oxides are two examples of catalysts which exhibit this dichotomy. The transition from the concerted mechanism to the stepwise mechanism is due to the increase in the reactivity of the lattice oxide with increasing temperature.

4.5.3.4.2.1 The effect of P_{CO}

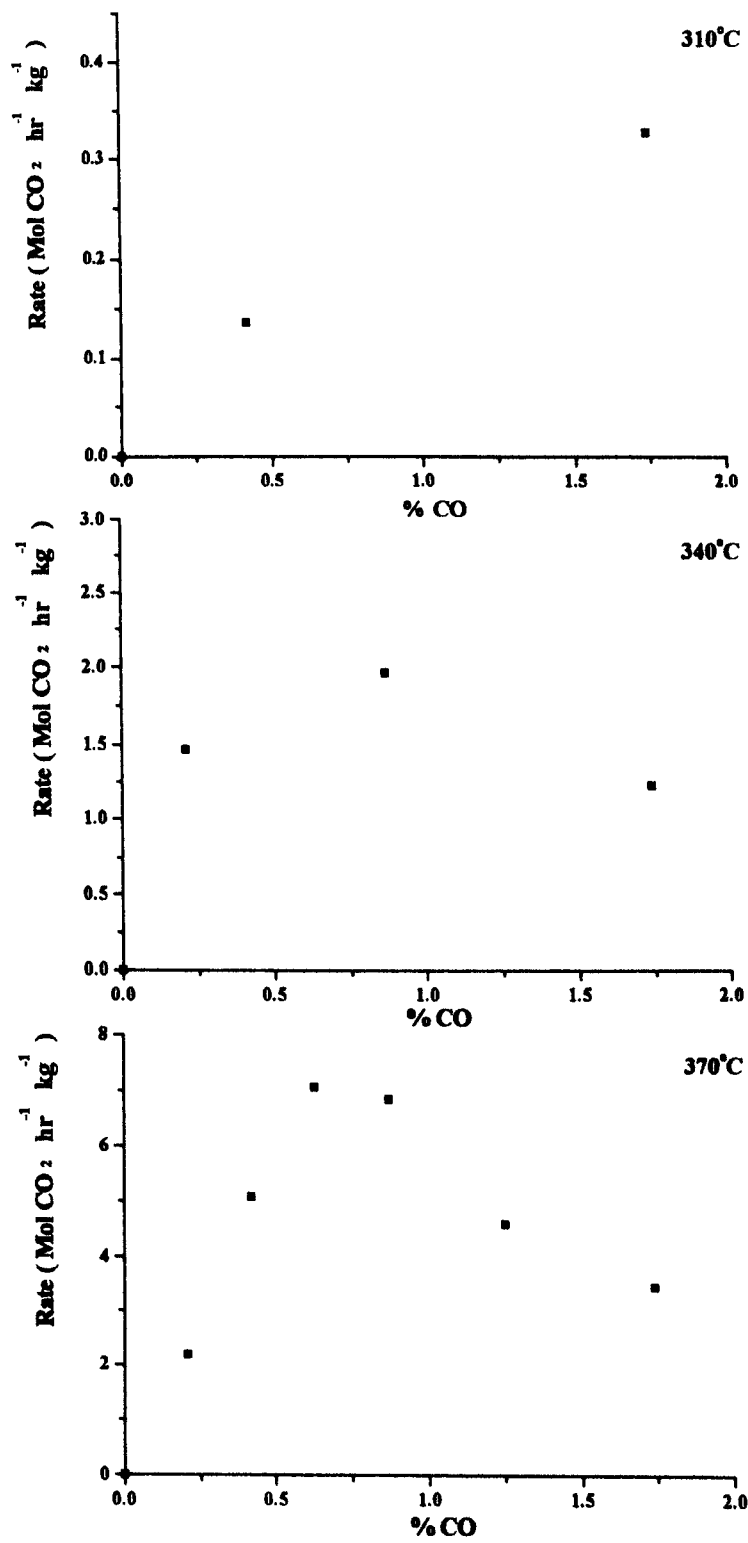
Experimental Conditions: Total flow = 8.61 l hr⁻¹ % O₂ = 17.339

Table 4.36 Results

Temperature (°C)	% CO	Rate (Mol CO ₂ hr ⁻¹ kg ⁻¹)
310	1.743	0.327490
"	0.418	0.135070
"	0	0
340	1.743	1.228615
"	0.870	1.957924
"	0.209	1.460583
"	0	0
370	1.743	3.418853
"	1.254	4.565090
"	0.870	6.830735
"	0.627	7.043140
"	0.418	5.061184
"	0.209	2.167685
"	0	0

From the experiments performed at 310°C to determine the response of CO oxidation reaction rate with P_{CO} it was determined that there was a positive order on CO partial pressure. However, as lanthana exhibits low activity for the CO oxidation reaction at the standard temperature, it was necessary to increase the standard measurement temperature of the kinetic study in order to reduce analytical instrument error, and therefore to better define the response curve. These further experiments were performed at 340°C and 370°C which were more typical of reaction temperatures for the reaction rate temperature dependency experiments over the less active materials.

Figure 4.69 A plot of the variation in CO oxidation rate with CO feed concentration at 310°C, 340°C and 370°C



The response to changes in P_{CO} at 340°C and 370°C exhibits dichotomous behaviour. At low P_{CO} , reaction rate increases with increasing P_{CO} , but at high P_{CO} , further increases in P_{CO} result in a progressive decrease in rate. Over the temperature range 340°C to 370°C, the rate of CO oxidation is observed to decrease by approximately one third to one half of the measured rates at 0.87 % CO after increasing the concentration of CO in the reactant gas to 1.743 %. It is assumed that the same reaction rate response to changes in P_{CO} observed at 340°C and 370°C would also be observed at 310°C.

The temperature programmed adsorption/desorption experiments presented and discussed earlier in this chapter (section 4.3.3 and subsections therein), determined that adsorption of CO on lanthana occurs on two separate sites. These adsorptions consist of a reversible (non-oxidative) adsorption and to a lesser extent, an irreversible (oxidative) adsorption resulting in CO_2 desorption (both determined under inert carrier TPD conditions). It is proposed that in the low range of temperature studied in the catalytic reaction, that it is the reversibly adsorbed species that is the active form towards oxidation by oxygen gas. Cognisant of the higher basicity of lanthana, and following Stone's^{123 - 124} proposal that basic sites can adsorb CO in carbanionic form ranging from dimers to short chain oligomers, the reactive form of adsorbed CO is proposed to conform to the equilibrium;



In order to account for the dichotomous response to CO partial pressure, it is further proposed that a particular value of n in equation 4.54 results in the active adsorbed CO species, the concentration of which can be optimised at a given CO partial pressure under reaction conditions. This proposal is further investigated in the subsequent mechanistic discussion, (section 4.5.3.4.2.4).

The quantity of CO_2 desorbed in the Heliox-carrier TPD over lanthana was found to increase with CO adsorption temperature, becoming significant at temperatures below 340°C. This desorption was subsequently factorised by repeating the TPD experiment with two desorptions, firstly under an inert carrier gas (He), and

then under Heliox. The first desorption was observed to consist of predominantly CO, although a small (but significant) CO₂ desorption was also observed. The second desorption under Heliox completed the desorption of carbon oxides as CO₂. Within experimental error, the one and two step desorptions were both found to release the same quantity of carbon oxides. At 340°C, (a typical CO oxidation reaction temperature), CO formed the major part of the desorbed oxides under the He carrier gas. It is therefore plausible to interpret the kinetic expressions in terms of adsorbed CO which is subsequently oxidised in the presence of gaseous molecular oxygen. The half-order on oxygen (see next section) suggests that the active oxygen species is atomic in nature, formed by dissociative adsorption of molecular O₂.

The adsorption of CO on lanthana may be analogous to that on the alkaline earth oxides, as reported by Stone.¹²⁴ He proposed that the electron donating property of the alkaline earths originated from the reduced Madelung potential of coordinatively unsaturated surface oxygen being destabilised relative to bulk ions, therefore inducing the release of electronic charge. Besides CO, it is here proposed that molecular oxygen is adsorbed by the same process.

It was further suggested in the TPD studies that the residual carbonaceous species following CO adsorption and TPD under the inert carrier gas conditions, which was subsequently desorbed as CO₂ in the presence of gaseous oxygen, could be deposited carbon formed in a Boudouard reaction type disproportionation ($2\text{CO} \rightarrow \text{CO}_2 + \text{C}$). Under reaction conditions, such a disproportionation was cited as a possible intermediate step in the reaction mechanism.

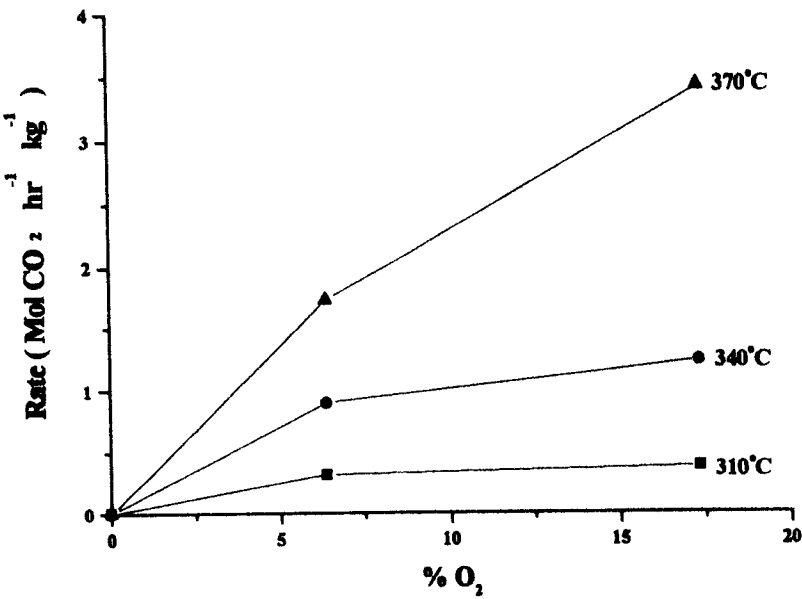
4.5.3.4.2.2 The effect of P_{O_2}

Experimental conditions Total flow = 8.61 l hr⁻¹ % CO = 1.742

Table 4.37 Results

Temperature (°C)	% O ₂	Rate (Mol CO ₂ hr ⁻¹ kg ⁻¹)
310	17.339	0.370488
"	6.365	0.313150
"	0	0
340	17.341	1.228615
"	6.365	0.899394
"	0	0
370	17.339	3.418855
"	6.365	1.730351
"	0	0

Figure 4.70 A plot of the variation in CO oxidation rate with O₂ feed concentration



As in the analysis of the CO oxidation reaction rate response to P_{CO} over the lanthana catalyst, the analysis of CO oxidation reaction rate response to P_{O_2} is also based on data collected at 340°C and 370°C, as at 310°C the reaction rate showed little response to P_{O_2} . From the experimental data at 340°C and 370°C which was chosen as a typical reaction temperature for the less active catalysts such as lanthana,

the order on P_{O_2} was found to range from 0.29 to 0.68, with a mean value of 0.485. From this it is taken that the reaction is half order on P_{O_2} as was found to be the case over the ceria catalyst.

It is also worthy of note that the apparent order on P_{O_2} was observed to increase with temperature, indicating that the reaction is retarded by oxygen (which is adsorbed more strongly at lower temperatures). This suggests that oxygen is competitively adsorbed on the active sites along with CO.

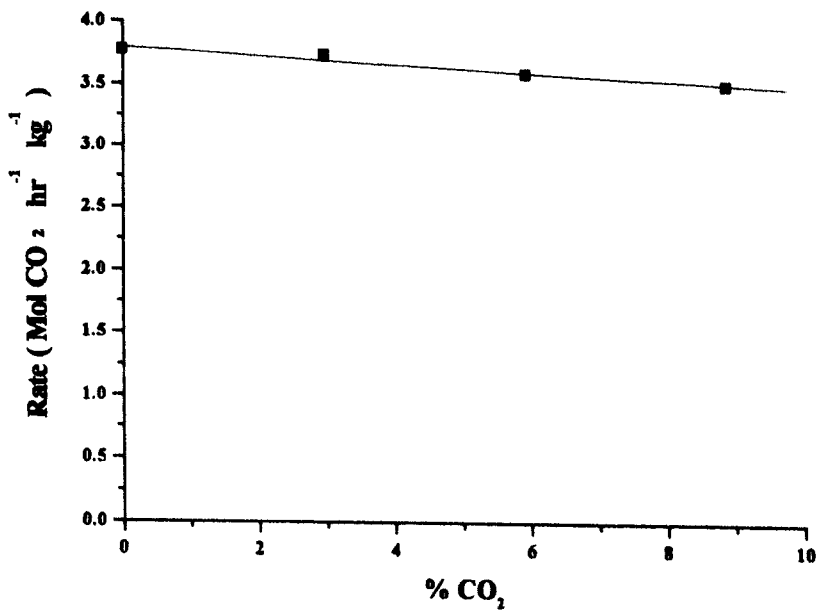
4.5.3.4.2.3 The effect of P_{CO_2}

Experimental conditions: Total flow = 8.61 l hr⁻¹ % CO = 1.742 % O_2 = 17.341

Table 4.38 Results

% CO ₂	Rate at 430°C (Mol CO ₂ hr ⁻¹ g ⁻¹)
0	3.766323
2.973	3.725760
5.934	3.569163
8.871	3.460380

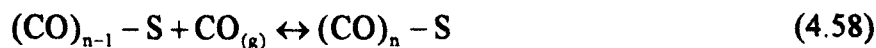
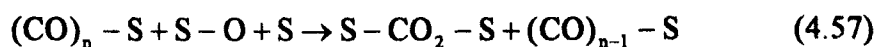
Figure 4.71 A plot of the variation in CO oxidation rate with CO₂ feed concentration



The catalytic oxidation of CO over lanthana is only very weakly retarded by CO₂. Further experiments were also completed to determine whether the presence of high concentrations of CO₂ affected the reaction response to temperature, as it was found to be adsorbed with range of strengths on lanthana in the TPD studies (section 4.3.3 and subsections therein). It was also found that the CO oxidation reaction activation energy was hardly changed by the presence of CO₂. It can be concluded from this observations that CO₂ either adsorbs on different sites to either CO or O₂, or, that the CO_{2(ads)} ↔ CO_{2(g)} equilibrium lies well to the right hand side on the active sites. TPD studies also showed that over lanthana a range of CO₂ adsorption sites exists with discernible broad desorption peaks occurring at approximately 350°C, 450°C and strong desorption peaks at 650°C and 725°C. Desorptions were observed to occur from temperatures of 200°C, upwards. The influence of CO₂ can therefore be neglected. The weak retardation by CO₂ does not support the Boudouard reaction type disproportionation intermediate theory as suggested in section 3.5.3.4.2.2.

4.5.3.4.2.4 Mechanistic Discussion

A concerted oxidation process is proposed comprising the following steps;



In the reaction scheme above, S represents a site capable of adsorbing molecular oxygen dissociatively to form atomic surface oxygen species, and of adsorbing CO in states such that n is greater than or equal to 2. Reaction occurs between the adsorbed CO and adsorbed oxygen, provided there is an adjacent S-site to adsorb the resulting CO₂, for example, as a (transient) carbonite species. Reactions 4.58 and 4.59 represent the equilibria between adsorbed and gas phase CO and CO₂,

respectively. The weak dependence on P_{CO_2} over lanthana confirms that the equilibrium in equation 4.59 lies well to the right hand side under reaction conditions, and can therefore be neglected.

Using the Langmuir isotherm, the fraction of S-O sites covered by CO, $(\text{CO})_2$, $(\text{CO})_3$,..... $(\text{CO})_n$ is derived from the adsorption/desorption equilibrium, such that;

$$k_{\text{CO}}(1 - \sum \theta)P_{\text{CO}} = k'_{\text{CO}}\theta_{\text{CO}} \quad (4.60)$$

where $\sum \theta$ is the fraction of sites covered by CO, $(\text{CO})_2$, $(\text{CO})_3$,..... $(\text{CO})_n$

It is assumed that oxygen dissociates on adsorption and associates on desorption. It is further assumed that for dissociative adsorption to occur, gaseous molecular oxygen must collide with the surface at a location comprising two adjacent sites. The concentration of such sites is proportional to the square of the concentration of single sites. Thus the rate of dissociative adsorption of oxygen is given by;

$$\text{Adsorption Rate} = k_1 P_{\text{O}_2} (1 - \sum \theta)^2 \quad (4.61)$$

It is further assumed that desorption occurs following the association of two neighbouring oxygen atoms, the rate of which can be expressed as;

$$\text{Desorption Rate} = k_2 \theta_{\text{O}_2}^2 \quad (4.62)$$

Combining equations 4.61 and 4.62;

$$\theta_{\text{O}_2} = (k_1/k_2)^{\frac{1}{2}} P_{\text{O}_2}^{\frac{1}{2}} (1 - \sum \theta) \quad (4.63)$$

Hence

$$\theta_{\text{O}_2} = k_3 P_{\text{O}_2}^{\frac{1}{2}} (1 - \sum \theta) \quad (4.64)$$

where

$$k_3 = (k_1/k_2)^{\frac{1}{2}}$$

$$\theta_{CO} = K_{CO} P_{CO} [1 - (\theta_{CO} + \theta_{(CO)_2} + \dots + \theta_{(CO)_n} + \theta_O + \theta_{CO_2})] \quad (4.65)$$

$$\theta_{(CO)_2} = K_{(CO)_2} P_{CO}^2 [1 - (\theta_{CO} + \theta_{(CO)_2} + \dots + \theta_{(CO)_n} + \theta_O + \theta_{CO_2})] \quad (4.66)$$

$$\theta_{(CO)_n} = K_{(CO)_n} P_{CO}^n [1 - (\theta_{CO} + \theta_{(CO)_2} + \dots + \theta_{(CO)_n} + \theta_O + \theta_{CO_2})] \quad (4.67)$$

$$\theta_O = k_3 P_{O_2}^{\frac{1}{2}} [1 - (\theta_{CO} + \theta_{(CO)_2} + \dots + \theta_{(CO)_n} + \theta_O + \theta_{CO_2})] \quad (4.68)$$

$$\theta_{CO_2} = K_{CO_2} P_{CO} [1 - (\theta_{CO} + \theta_{(CO)_2} + \dots + \theta_{(CO)_n} + \theta_O + \theta_{CO_2})] \quad (4.69)$$

Adding equations 4.65, 4.66, 4.67, 4.68 and 4.69;

$$\Sigma \theta = (K_{CO} P_{CO} + K_{(CO)_2} P_{CO}^2 + \dots + K_{(CO)_n} P_{CO}^n + k_3 P_{O_2}^{\frac{1}{2}} + K_{CO_2} P_{CO_2}) \times [1 - (\theta_{CO} + \theta_{(CO)_2} + \dots + \theta_{(CO)_n} + \theta_O + \theta_{CO_2})] \quad (4.70)$$

Subtracting both sides of equation 4.70 from unity and rearranging;

$$(1 - \Sigma \theta) = \frac{1}{(1 + K_{CO} P_{CO} + K_{(CO)_2} P_{CO}^2 + \dots + K_{(CO)_n} P_{CO}^n + k_3 P_{O_2}^{\frac{1}{2}} + K_{CO_2} P_{CO_2})} \quad (4.71)$$

In accordance with the product forming reaction in equation 4.57 of the concerted mechanism, it is necessary for an empty site to be present, adjacent to the reacting CO, in order to accommodate the product CO₂ in the adsorbed form. In this event the rate of the reaction can be expressed as;

$$\text{Rate} = k \theta_{(CO)_n} \theta_O (1 - \Sigma \theta) \quad (4.72)$$

where $\theta_{(CO)_n}$ refers to the active oligomer of adsorbed CO

Combining Equations 4.67, 4.71 and 4.72 gives;

$$\text{Rate} = \frac{k K_{(\text{CO})_n} P_{\text{CO}}^n k_3 P_{\text{O}_2}^{\frac{1}{2}}}{(1 + K_{\text{CO}} P_{\text{CO}} + K_{(\text{CO})_2} P_{\text{CO}}^2 \dots + K_{(\text{CO})_n} P_{\text{CO}}^n + K_1 P_{\text{O}_2}^{\frac{1}{2}} + K_{\text{CO}_2} P_{\text{CO}_2})^2} \quad (4.73)$$

hence;

$$\text{Rate} = \frac{k_4 P_{\text{CO}}^n P_{\text{O}_2}^{\frac{1}{2}}}{(1 + K_{\text{CO}} P_{\text{CO}} + K_{(\text{CO})_2} P_{\text{CO}}^2 \dots + K_{(\text{CO})_n} P_{\text{CO}}^n + K_1 P_{\text{O}_2}^{\frac{1}{2}} + K_{\text{CO}_2} P_{\text{CO}_2})^2} \quad (4.74)$$

where;

$$k_4 = k k_3 K_{(\text{CO})_n}$$

At constant P_{O_2} and P_{CO_2} equation 4.74 reduces to;

$$\text{Rate} = \frac{k_5 P_{\text{CO}}^n}{(1 + K_6 P_{\text{CO}} + K_7 P_{\text{CO}}^2 \dots + K_n P_{\text{CO}}^n)^2} \quad (4.75)$$

Application of equation 4.75 to experimental data using a computer curve fitting software package resulted in negative values being attributed to K_6 (associated with the monomeric $\text{CO}_{(\text{ads})}$) and K_n (associated with the adsorbed species $(\text{CO})_3$ and $(\text{CO})_4$, etc). As the negative values are unrealistic, this result was taken as an indication that catalytic activity of $\text{CO}_{(\text{ads})}$ and the associated species $(\text{CO})_{3(\text{ads})}$ and $(\text{CO})_{4(\text{ads})}$ were insignificant in comparison with that of $(\text{CO})_{2(\text{ads})}$. Accordingly, equation 4.75 can be rewritten;

$$\text{Rate} = \frac{k_2 P_{\text{CO}}^n}{(1 + K_{(\text{CO})_2} P_{\text{CO}}^m)^2} \quad (4.76)$$

Application of equation 4.76 to experimental data using a computer curve fitting software package allowed evaluation of k_2 , $K_{(\text{CO})_2}$, n and m . The results of this evaluation for the P_{CO} variation data at 370°C are presented in table 4.39.

Table 4.39 Coefficient evaluation results for equation 4.76, using computer curve fitting technique for P_{CO} variation data at 370°C.

Evaluation	k_2	n	$K_{(CO)_2}$	m	r^2
1	56	1 - 3	2	2	0.99
2	15	Fixed at 1	0.5	Fixed at 2	0.95
3	56	Fixed at 2	2	Fixed at 2	0.99
4	415	Fixed at 3	7	Fixed at 2	0.95

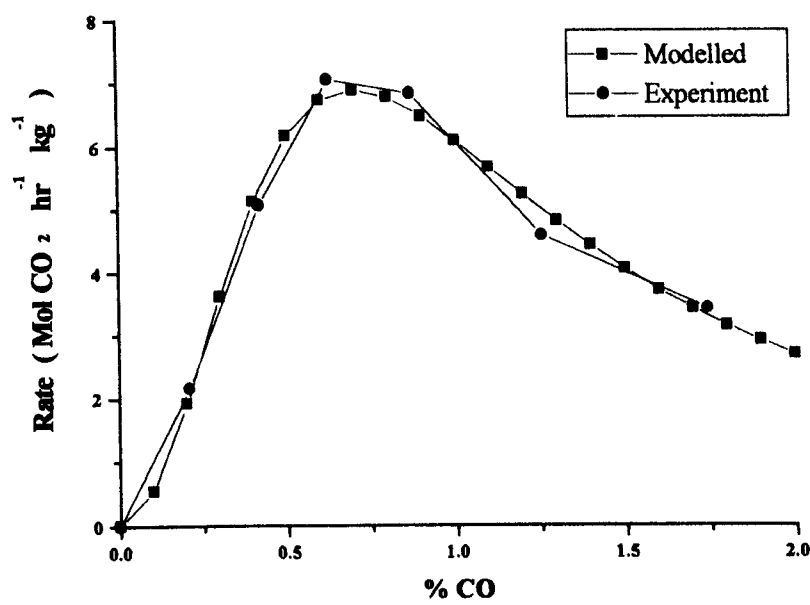
In the first evaluation, all parameters were freely floated with the result that at the 95% confidence level n fell in the range 1 - 3, and m fell in the range 1.8 - 2.2. The value of m was therefore taken to be 2. Consequently, in the subsequent evaluations m was fixed at 2 and n was varied through 1, 2 and 3. The degree of fit was optimal when n was 2. Further evaluations varied the power of the denominator between 0 and 3. The fit was optimal when the power of the denominator function was 2. It is therefore concluded that the best representation of equation 4.75 can be written;

$$\text{Rate} = \frac{k_2 P_{CO}^2}{(1 + K_{(CO)_2} P_{CO}^2)^2} \quad (4.77)$$

where $k_2 = 56$ and $K_{(CO)_2} = 2$

This result suggests that the active form of adsorbed CO over the lanthana catalyst is the dimer species; $(CO)_2$. The experimental data and data modelled using equation 4.77 for the CO oxidation reaction rate response to P_{CO} are compared in figure 4.72.

Figure 4.72 A comparative plot of the experimental and modelled CO oxidation reaction rate response to P_{CO} at 370°C.



It is observed that the model provides an excellent fit to the experimental data.

At constant P_{CO} , constant P_{CO_2} and at low P_{O_2}

$$\text{Rate} = k_{Eq4.78} P_{O_2}^{\frac{1}{2}} \tag{4.78}$$

The experimental results from the kinetic study are consistent with this.

At constant P_{CO} and P_{O_2}

$$\text{Rate} = \frac{k_{Eq4.79}}{(1 + K_{Eq4.79} P_{CO_2} + K_{Eq4.79} P_{CO_2}^2)} \tag{4.79}$$

The experimental results show slight retardation by CO_2 which is consistent with this.

**4.5.3.4.3 The kinetics of the catalytic oxidation of CO over the
Ce_{1-x}La_xO_{2-x/2} system.**

In this section, the orders of the CO catalytic oxidation reaction with respect to CO and O₂ over a mixed oxide catalyst have been determined similarly to the previous studies over ceria and lanthana. The experiments were conducted over the x = 0.05 material which was of particular interest following the catalytic activity study as it was determined as maximising CO catalytic oxidation activation energy and specific pre-exponential factor.

4.5.3.4.3.1 The effect of P_{CO}

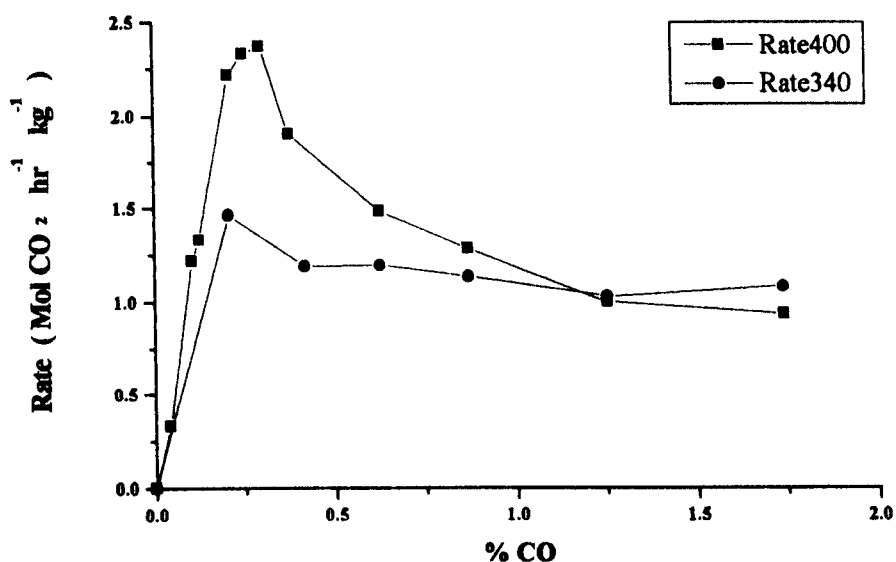
Experimental Conditions: Total flow = 8.61 l hr⁻¹ % O₂ = 17.339

Table 4.40 Results

Temperature (°C)	% CO	Rate (Mol CO ₂ hr ⁻¹ kg ⁻¹)
340	1.743	1.066187
340	1.254	1.012838
340	0.870	1.125192
340	0.627	1.187661
340	0.418	1.181953
340	0.209	1.458726
340	0	0
400	1.743	0.917
400	1.254	0.985
400	0.87	1.274
400	0.627	1.477
400	0.376	1.896
400	0.297	2.365
400	0.251	2.327
400	0.209	2.211
400	0.125	1.33
400	0.1045	1.218
400	0.0418	0.329
400	0	0

The data in table 4.40 is plotted in figure 4.73. It can be observed that the 400°C data clearly exhibits the dichotomous behaviour observed over lanthana, as does the 340°C data, albeit to a lesser extent.

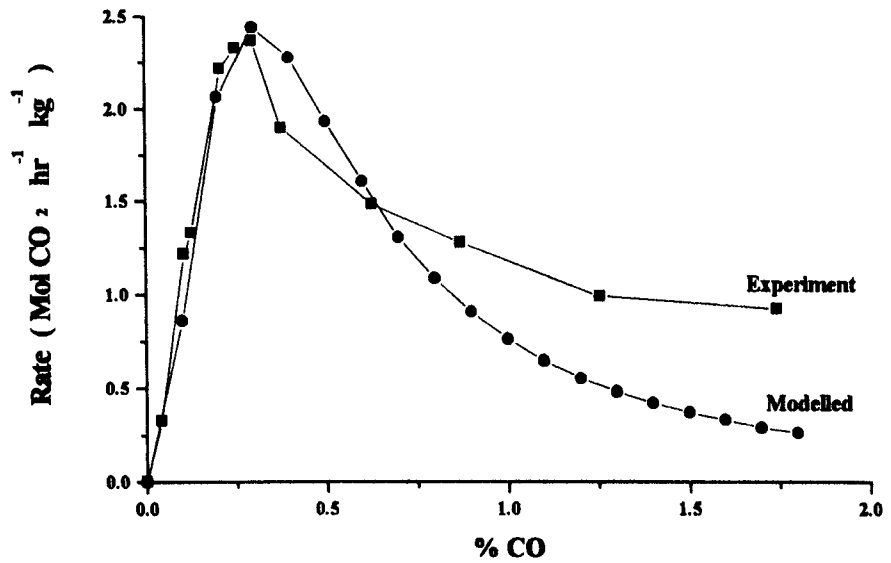
Figure 4.73 A plot of the variation in CO oxidation rate with CO feed concentration at 340°C and 400°C.



In order to characterise the response to P_{CO} the experimental data at 400°C was fitted to the model based on equation 4.77, which was observed to give an excellent interpretation of the data variation over lanthana. The experimental and modelled data are compared in figure 4.74.

It can be observed from figure 4.74 that the degree of retardation by CO at higher CO partial pressures is less than would be predicted by the equation 4.77 model, which is based on the CO reaction rate response to P_{CO} over lanthana. It is therefore proposed that the observed CO reaction rate response to P_{CO} over the mixed oxide could be characterised in terms of two contributions; one exhibiting the dichotomous behaviour determined over lanthana, the other exhibiting the Langmuir adsorption isotherm type response as determined over ceria.

Figure 4.74 A comparative plot of the experimental data measured at 400°C, and data modelled using equation 4.77.



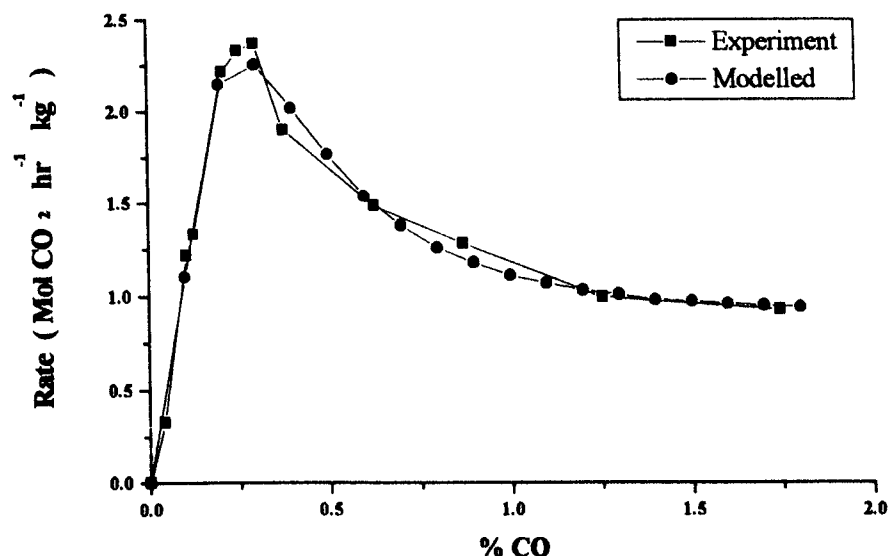
The suggested combined CO oxidation reaction rate P_{CO} response model can be expressed;

$$\text{Rate} = \frac{aP_{CO}^2}{(1 + bP_{CO}^2)^2} + \frac{cP_{CO}}{(1 + dP_{CO})} \quad (4.80)$$

where a , b , c and d are constants.

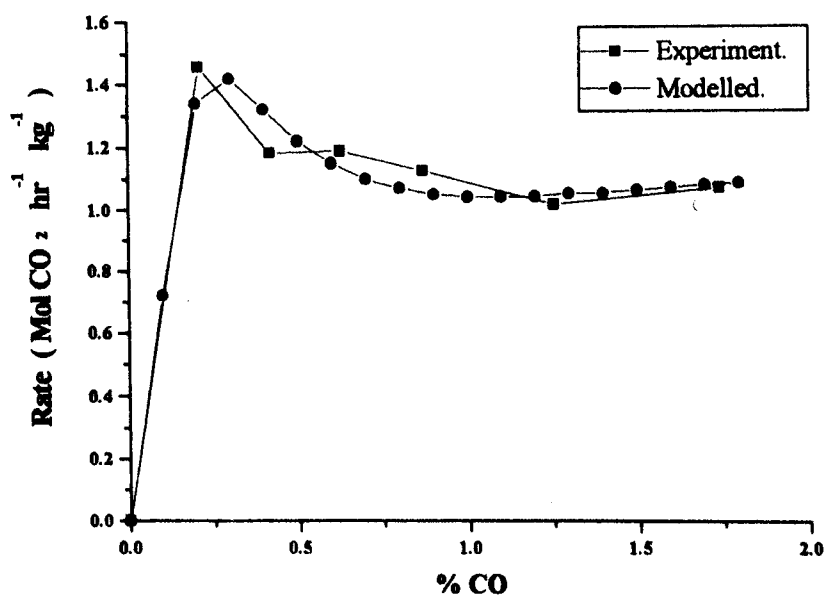
The 400°C experimental data was re-modelled using equation 4.80. The fit of the new model based on equation 4.80 was found to be significantly better than that of the model based on equation 4.77, returning evaluated constants; $a = 124$, $b = 16.2$, $c = 2.3$ and $d = 2.4$. The experimental data and the data modelled using equation 4.80 are compared in figure 4.75.

Figure 4.75 A comparative plot of the experimental and (equation 4.80) modelled CO oxidation reaction rate response to P_{CO} at 400°C.



The model based on equation 4.80 was also applied to the 340°C experimental data. Again the model was a reasonable fit to the experimental data returning evaluated constants; $a = 75$, $b = 18$, $c = 2.1$ and $d = 1.5$. The 340°C experimental data and the modelled data based on equation 4.80 are compared in figure 4.76.

Figure 4.76 A comparative plot of the experimental and (equation 4.80) modelled CO oxidation reaction rate response to P_{CO} at 340°C.



It can be concluded from the results of the model fitting that the activation and retardation of CO oxidation reaction rate with P_{CO} over the mixed oxide can be well represented by an expression consisting of components determined for the response of CO oxidation rate to P_{CO} over each of the component oxides. This indicates that at the catalyst surface, the oxidation of CO occurs simultaneously by two separate mechanisms - effectively oxidation over ceria active centres and lanthana active centres, respectively. The differences between the experimental data determined at 340 °C and 400°C can be explained in terms of the relative activity of the two pure oxides. At the lower temperature, the major contribution toward the total CO oxidation rate will be from the ceria component. At the higher temperature the lanthana component contribution to the total rate is more significant, thus accounting for the more pronounced retardation effect at higher CO partial pressures, as observed. It is expected that the model based on equation 4.80 would fit all materials within the series, the coefficients varying such that the lanthanum component becomes more significant with increases in both temperature and surface lanthanum concentration.

4.5.3.4.3.2 The effect of P_{O_2}

Experimental Conditions: Total flow = 8.61 l hr⁻¹ % O₂ = 17.339

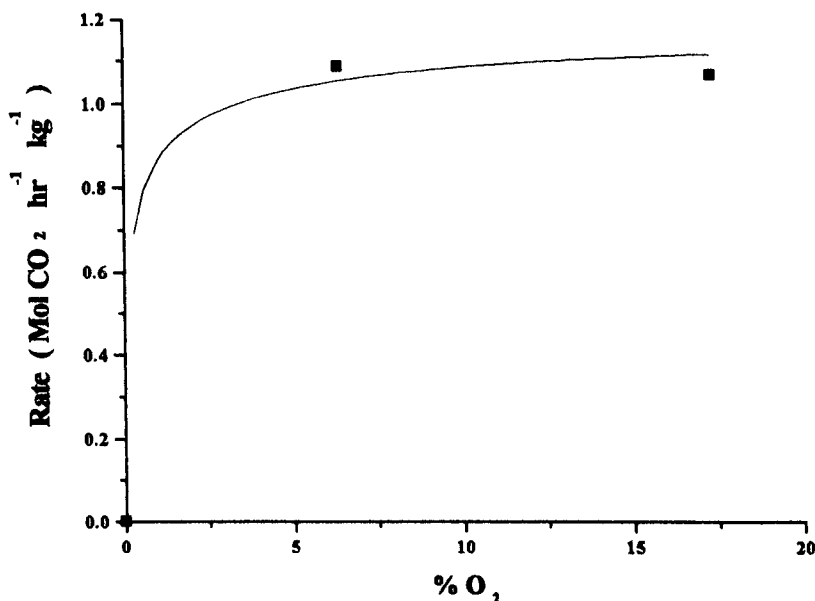
Table 4.41 Results.

% CO	%O ₂	Rate at 340°C Mol CO ₂ hr ⁻¹ kg ⁻¹
1.743	17.339	1.066187
1.743	6.365	1.085115
1.743	0	0

The variation in CO oxidation reaction rate with P_{O_2} at 340°C over the mixed oxide was found to be similar to the analogous variations over ceria and lanthana. At low oxygen partial pressures, the CO oxidation rate is found to increase in proportion

to $\sqrt{P_{O_2}}$. Further increases in P_{O_2} have progressively less effect on the reaction rate, eventually establishing zero order on oxygen at higher partial pressures.

Figure 4.77 A plot of the variation in CO oxidation reaction rate with P_{O_2} at 340°C



The effect of P_{O_2} can be represented by the expression;

$$\text{Rate} = \frac{2.935\sqrt{P_{O_2}}}{(1 + 2.393\sqrt{P_{O_2}})} \quad (4.81)$$

The CO oxidation rate response to oxygen partial pressure was thus determined to be invariant over the $\text{Ce}_{1-x}\text{La}_x\text{O}_{2-x/2}$ series.

4.5.3.4.4 Summary - The Nature of the Active Species

Over the whole range of compositions of the pure and mixed oxide catalysts the dependence of the CO oxidation reaction rate was determined to be half order on oxygen partial pressure at low partial pressures, tending toward zero order under the standard activity measurement conditions.

The retarding effect of carbon dioxide was determined to range from a strong progressive retarding effect observed over ceria to a weak (negligible) retarding effect over lanthana. The strong retarding effect was explained in terms of competitive

adsorption between CO and CO₂ on the active sites. The retardation of reaction rate over ceria was suitably expressed in terms of a Langmuir isotherm type expression. The weak retardation of reaction rate over lanthana was explained in terms of CO₂ adsorption on a non-active site or alternatively, by an adsorption/desorption equilibrium favouring the gas phase.

The CO oxidation rate response to CO partial pressure was determined to be the main distinguishing feature between ceria and lanthana. Over ceria, the CO oxidation rate response to CO partial pressure was pseudo first order, returning an apparent order of 0.8, which was found to be suitably represented by a Langmuir isotherm type expression. The active form of CO was therefore determined to be an adsorbed CO molecule. On the other hand, over lanthana the CO oxidation rate response to CO partial pressure was shown to exhibit a dichotomous dependence which was explained in terms of competitive adsorption of CO and oxygen resulting in a retardation of reaction rate for CO partial pressures above an optimal value. The active form of CO over the lanthana catalyst was determined to be adsorbed (CO)₂. The dimeric anion C₂O₃²⁻ was observed over lanthana by Bailes et al (1996)¹²³, even in the presence of dioxygen. The reported IR bands corresponding to the dimeric anion were not observed in the *in situ* DRIFTS studies, although this may have been due to their transient nature as an adsorbed intermediate under reaction conditions.

A Boudouard reaction type intermediate step consisting of a disproportionation of (CO)₂ to give CO₂ and deposited C (which is rapidly oxidised under high oxygen partial pressure), has been previously suggested by TPD results, although mild retardation of the oxidation reaction rate by CO₂ over lanthana did not lend support to this mechanism.

In the case of a mixed oxide, the CO oxidation rate response to CO partial pressure was best represented in terms of an expression consisting of contributions based on the summation of both of the analogous expressions determined for the pure oxides. From this it can be concluded that over the mixed oxides, both the active molecular CO and active CO dimer adsorbed species are being oxidised, each with the aforementioned kinetics over ceria centres and lanthana centres, respectively. It is not possible in the case of the mixed oxide to specify the oxidising species for either of the

active CO species, although the half order reaction rate on P_{O_2} indicated that it is likely to be atomic oxygen.

Under the standard activity measurement conditions, the constant low CO and high O_2 partial pressures, and the restriction of CO_2 partial pressure (achieved by operating at high space velocity and at low conversions), results in what is empirically a measurement of the net activity of the two concomitant mechanisms of CO oxidation, the magnitude of the contribution of each mechanism varying with catalyst composition.

4.5.4 CH_4 Oxidation - Systematic Study

As mentioned previously, a study of CH_4 oxidation over the $Ce_{1-x}La_xO_{2-x/2}$ systematic series was carried out in parallel with the CO oxidation study. The results of the CH_4 oxidation study are summarised in table 4.42. Initial observations of the data in table 4.42 must be confined to the Arrhenius data for comparisons with the CO oxidation data, as the standard activity measurements for CH_4 oxidation were completed at 560°C rather than at 310°C, as in the CO oxidation study. The activation energies and pre-exponential factors are notably higher for CH_4 oxidation, in the 30 - 40 kcal Mol⁻¹ and 10^7 - 10^9 ranges respectively, whereas for CO oxidation, typical analogous values are in the 12 - 20 kcal Mol⁻¹ and 10^3 - 10^7 ranges, respectively. These differences immediately emphasise the differences between the two mechanisms over the catalyst series.

In the following section the CH_4 oxidation results are discussed and compared with the analogous CO oxidation results. The results of the XRD study (section 4.1.4) suggest that the results are again best analysed in terms of two compositional regions; The solid solution region ($0 < x < 0.6$ bulk, $0 < x < 0.79$ surface) and the two-phase region ($0.6 < x < 1$ bulk, $0.79 < x < 1$ surface).

Table 4.42 Summary of the variation in CH₄ catalytic oxidation rate data with composition for the series Ce_{1-x}La_xO_{2-x/2}.

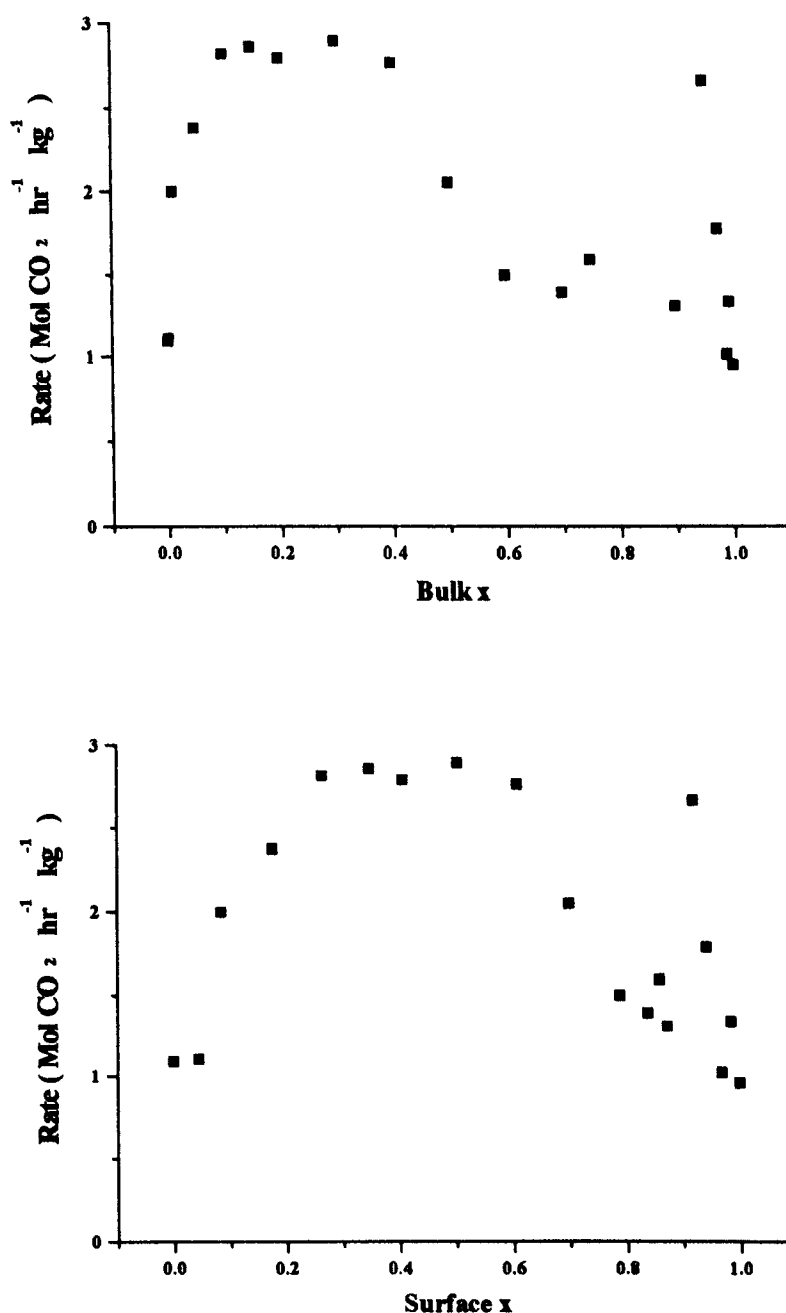
Ce Cation fraction	La Cation fraction	Surface Area m ² g ⁻¹	Activity at 560°C Mol CO ₂ hr ⁻¹ kg ⁻¹	Specific activity at 560°C Mol CO ₂ hr ⁻¹ m ⁻² (×10 ³)	Ea kcal mol ⁻¹	Ea error kcal mol ⁻¹	ln A	Ln A error	A	A / SA
1	0	15.2	1.08740	0.071610	32.118	0.246	19.56904	0.15227	3.1530 e 8	2.0764 e 7
0.999	0.001	9.3	1.10577	0.119543	31.982	0.131	19.49844	0.08099	2.9381 e 8	3.1763 e 7
0.99	0.01	13.2	1.99419	0.151373	34.035	0.360	21.31831	0.22372	1.8131 e 9	1.3763 e 8
0.95	0.05	12.4	2.37500	0.192214	33.451	0.128	21.14807	0.08056	1.5293 e 9	1.2377 e 8
0.90	0.10	13.4	2.81227	0.209370	35.463	0.413	22.52243	0.25624	6.0446 e 9	4.5001 e 8
0.85	0.15	14.5	2.85566	0.196454	38.075	0.786	24.14554	0.49525	3.0639 e 10	2.1078 e 9
0.80	0.20	13.9	2.78768	0.200856	37.662	0.695	23.86949	0.43781	2.3248 e 10	1.6751 e 9
0.70	0.30	12.8	2.88912	0.225677	37.945	0.172	24.07247	0.10385	2.8480 e 10	2.2247 e 9
0.60	0.40	11.4	2.75742	0.241498	33.681	0.416	21.44601	0.26097	2.0601 e 9	1.8042 e 8
0.50	0.50	11.7	2.04526	0.174555	33.842	0.249	21.24208	0.15444	1.6800 e 9	1.4338 e 8
0.40	0.60	10.8	1.49168	0.137787	36.167	0.884	22.33128	0.54736	4.9929 e 9	4.6119 e 8
0.30	0.70	10.4	1.37983	0.132256	32.691	0.380	20.15113	0.23436	5.6432 e 8	5.4090 e 7
0.25	0.75	9.1	1.58552	0.173490	32.967	0.074	20.44821	0.04473	7.5953 e 8	8.3109 e 7
0.10	0.90	7.7	1.30054	0.169408	33.362	0.264	20.50221	0.15910	8.0167 e 8	1.0443 e 8
0.05	0.95	13.6	2.65419	0.195189	33.409	0.197	21.22129	0.12131	1.6455 e 9	1.2101 e 8
0.025	0.975	7.2	1.77423	0.245976	36.139	0.667	22.50107	0.40313	5.9168 e 9	8.2030 e 8
0.01	0.99	7.7	1.00738	0.130153	38.489	0.364	23.35681	0.21894	1.3923 e 10	1.7988 e 9
0.005	0.995	5.7	1.32818	0.232037	38.152	0.482	23.39393	0.28990	1.4450 e 10	2.5243 e 9
0	1	5.9	0.94527	0.160378	39.388	0.317	23.83049	0.19178	2.2359 e 10	3.7935 e 9

(1 kcal = 4.187 kJ)

4.5.4.1 CH₄ Oxidation - Standard Activity Measurements

The variations in CH₄ catalytic oxidation rate per unit weight of catalyst with bulk and surface lanthanum concentration are presented in figure 4.78.

Figure 4.78 A plot of the variations in CH₄ catalytic oxidation activity per unit weight of catalyst with bulk and surface lanthanum concentration.



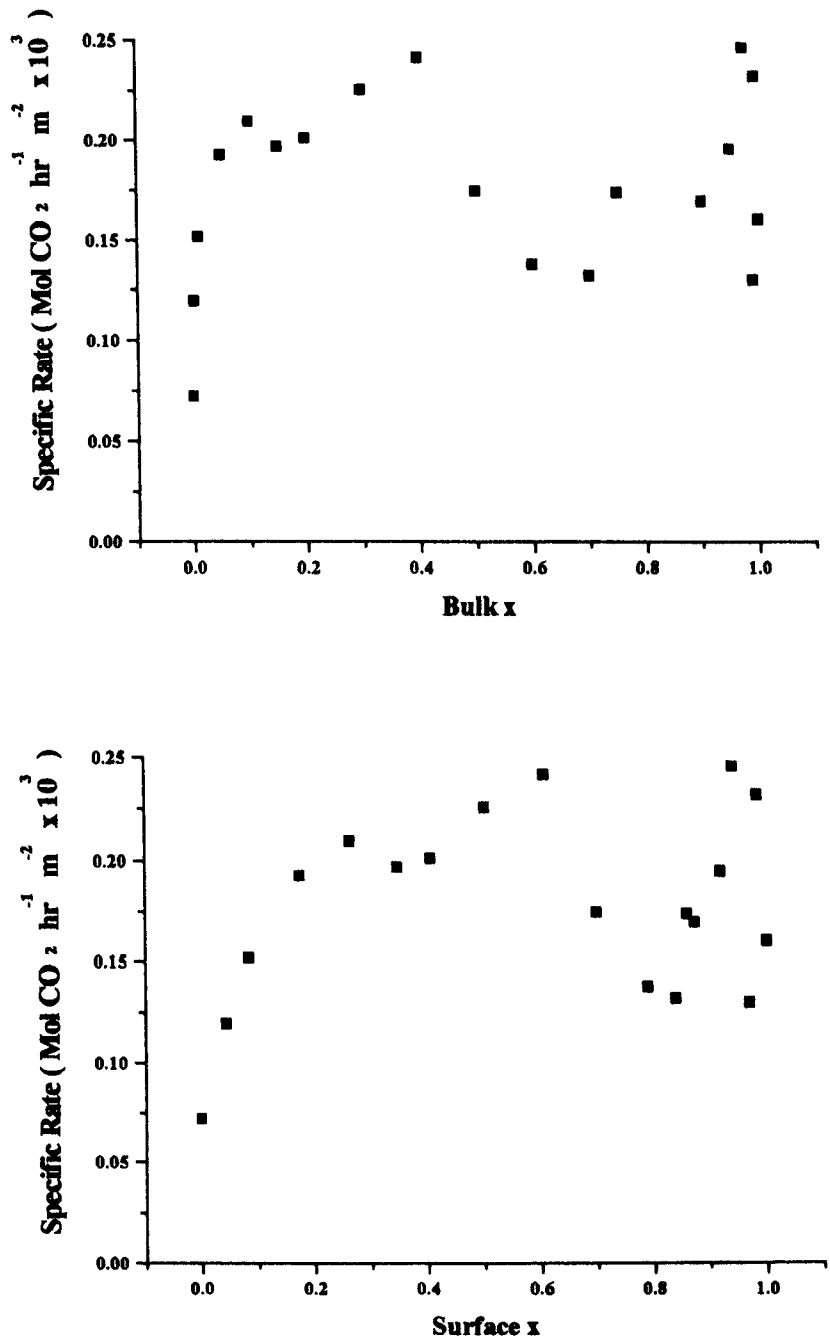
It can be observed in figure 4.78 that within the solid solution range, the variation in activity with lanthanum concentration forms a broad, roughly symmetrical

peak, with maximum activity corresponding to a bulk lanthanum concentration of approximately $x = 0.2$ to 0.3 (surface approximately $x = 0.4$ to 0.5). Quantitatively, the peak activity corresponds to a surface Ce : La ratio of approximately unity. This observation is significant if the reaction mechanism for CH_4 oxidation requires two concerted steps involving a basic site step (lanthanum promoted), such as activation of the methane by abstraction of a proton, and a subsequent redox step facilitated by the facile $\text{Ce}^{\text{III}} \leftrightarrow \text{Ce}^{\text{IV}}$ redox reaction at the surface.

Beyond the solid solution limit, the variation in activity with further increases in the concentration of lanthanum is complex and is therefore not discussed further at this point except that the presence of small amounts of (segregated) cerium in a lanthana host also seems to promote CH_4 oxidation activity with respect to pure ceria or lanthana. A similar effect of low concentrations of cerium in lanthana on activity was also observed with CO oxidation, as discussed in the previous section.

The variation in specific activity with bulk and surface lanthanum concentration is presented in figure 4.79. On comparison with activity per unit weight of catalyst, the variations in specific activity with bulk lanthanum concentration show a stronger increase in activity with increasing lanthanum concentration between $0 < \text{bulk } x < 0.1$. The shape of the curve between $0.1 < \text{bulk } x < 0.35$ is not well defined, although it would appear that the peak in the specific activity curve in the solid solution region remains at approximately $x = 0.2$ to 0.3 (surface approximately $x = 0.4$ to 0.5), as the effect of factoring in surface area is moderating rather than radical. The specific activity variation with composition is therefore quite similar to the activity per unit weight of catalyst variation with composition, again demonstrating an apparent synergistic promotion of catalytic activity which is observed to be optimised at 1 Ce : 1 La surface ratio. The variations in specific activity with composition beyond the La in ceria solid solution limit are not further resolved by analysis in terms of specific activity, although apparent promotion of activity by low levels of cerium in lanthana compared with pure ceria or lanthana is observed.

Figure 4.79 Plots of the variations in specific activity for methane oxidation with bulk and surface lanthanum concentration.



Inspection of both the activity and specific activity variations with material composition with respect to the selection of some form of parametric response model leads to the conclusion that there would be a significant level of uncertainty implicit in any such model due to poor peak definition. A generalised approach was therefore utilised, based on the assumption that there were three major contributions to the activity derived from cerium, lanthanum, and a specific interaction between cerium and lanthanum cations. This general relationship can be represented with an equation;

$$\text{Rate} = \alpha[\text{Ce}]^{\beta} + \chi[\text{La}]^{\delta} + \varepsilon[\text{Ce}]^{\phi}[\text{La}]^{\varphi} \quad (4.82)$$

Computer curve fitting of the experimental data using equation 4.82 returned the following values $\alpha = 0.07$, $\beta = 0.16$, $\chi = -1.3$, $\delta = 0.6$, $\varepsilon = 1.6$, $\phi = 0.1$, $\varphi = 0.6$. The curve generated was observed to be a good fit to the data returning a statistical r^2 of 0.91 and a peak maximum corresponding to surface $x = 0.46$. In order to identify the dominant contribution(s) to the variation in specific activity with surface composition, simplification of equation 4.82 by omission of the [Ce] and [La] terms in turn, was tested. Omission of the [Ce] term was found to have a detrimental effect on the overall curve fit of the data to the model, whereas omission of the [La] term resulted in a relatively insignificant change. It is therefore reasonable to discard the [La] term to produce a further simplification of the model, such that;

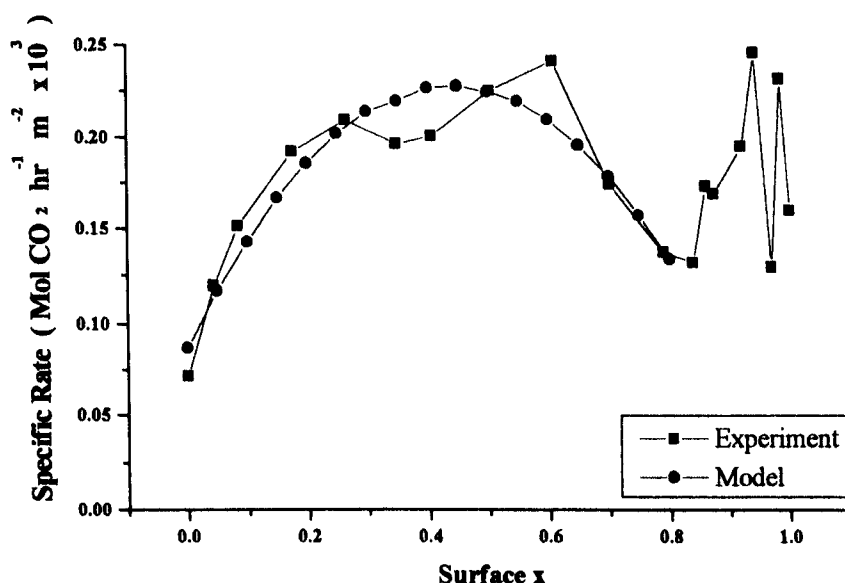
$$\text{Rate} = 0.07[\text{Ce}]^{0.8} + 0.48[\text{Ce}]^{0.72}[\text{La}]^{0.71} \quad r^2 = 0.90 \quad (4.83)$$

Equation 4.83 was further refined by assuming that the orders on each of the cation concentrations were most likely 1, rather than fractions near unity. Thus, a final simplification of the model compelled all of the reaction orders to be one, resulting in the model;

$$\text{Rate} = 0.09[\text{Ce}] + 0.73[\text{Ce}][\text{La}] \quad r^2 = 0.87 \quad (4.84)$$

Specific rate data evaluated using this final model is compared with the experimental data in figure 4.80.

Figure 4.80 A comparative plot of experimentally derived and modelled specific rate behaviour.



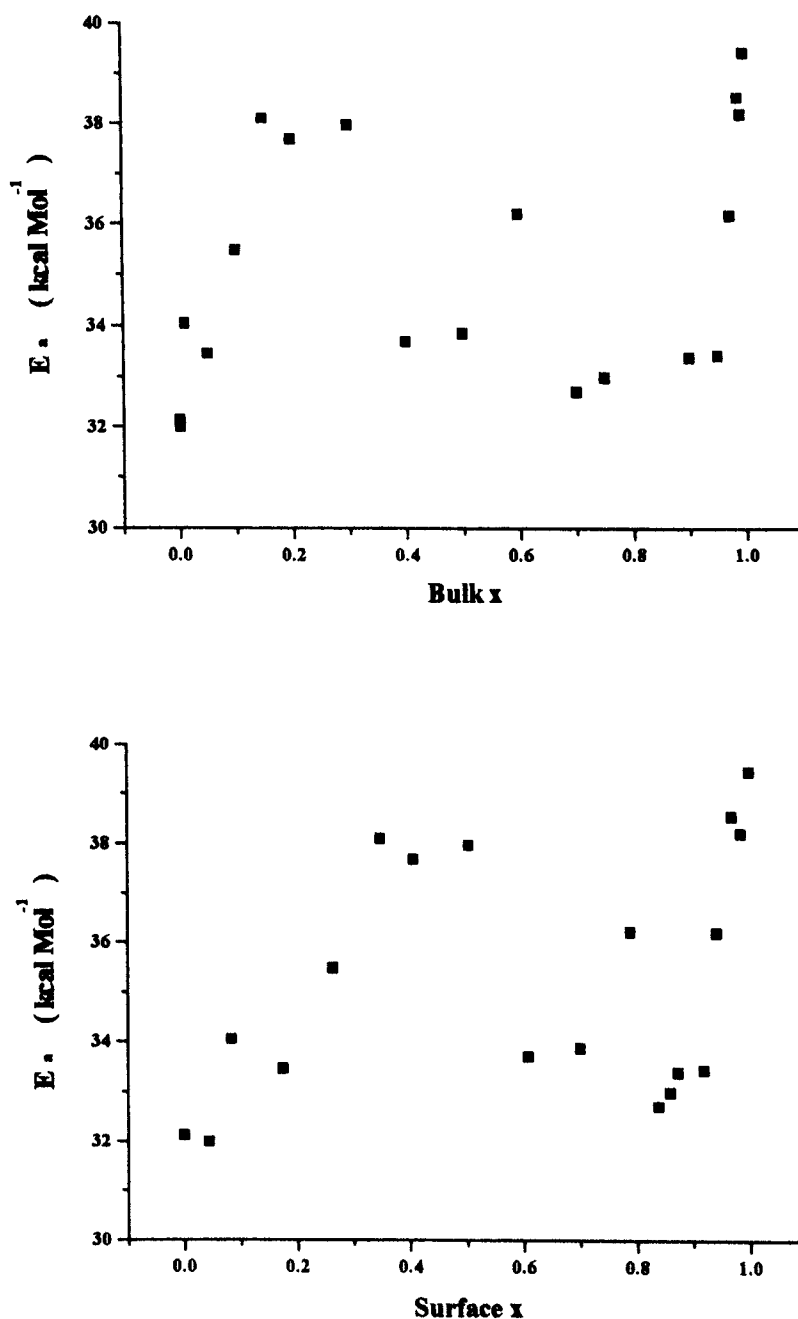
The dominance of the term comprising both [Ce] and [La] was determined. It is therefore proposed that Ce and La act synergistically in the catalytic mechanism for the oxidation of methane over ceria/lanthana solid solution catalysts. This is supported by the observation of the peak in specific activity corresponding to the equicationic surface composition.

4.5.4.2 CH₄ Oxidation - Arrhenius Studies

As in the CO oxidation reaction studies, for the CH₄ oxidation reaction, rates were determined at a series of temperatures, such that the total conversion was always in the 2 - 12% range. For each material, $\ln(\text{rate})$ vs. $1/T$ plots (Arrhenius method), were used to determine the apparent activation energy (E_a) for the reaction (slope of plot), and the pre-exponential factor (A). Again, the pre-exponential factor is assumed to be proportional to the number of active sites. When divided by the specific surface area, a specific pre-exponential factor (A/SA) is derived which is proportional to the number of active sites per unit area of each catalyst material. Thus, once more it is possible to compare materials in the systematic series in terms of catalytic active site density, and in terms of the response of activity to temperature.

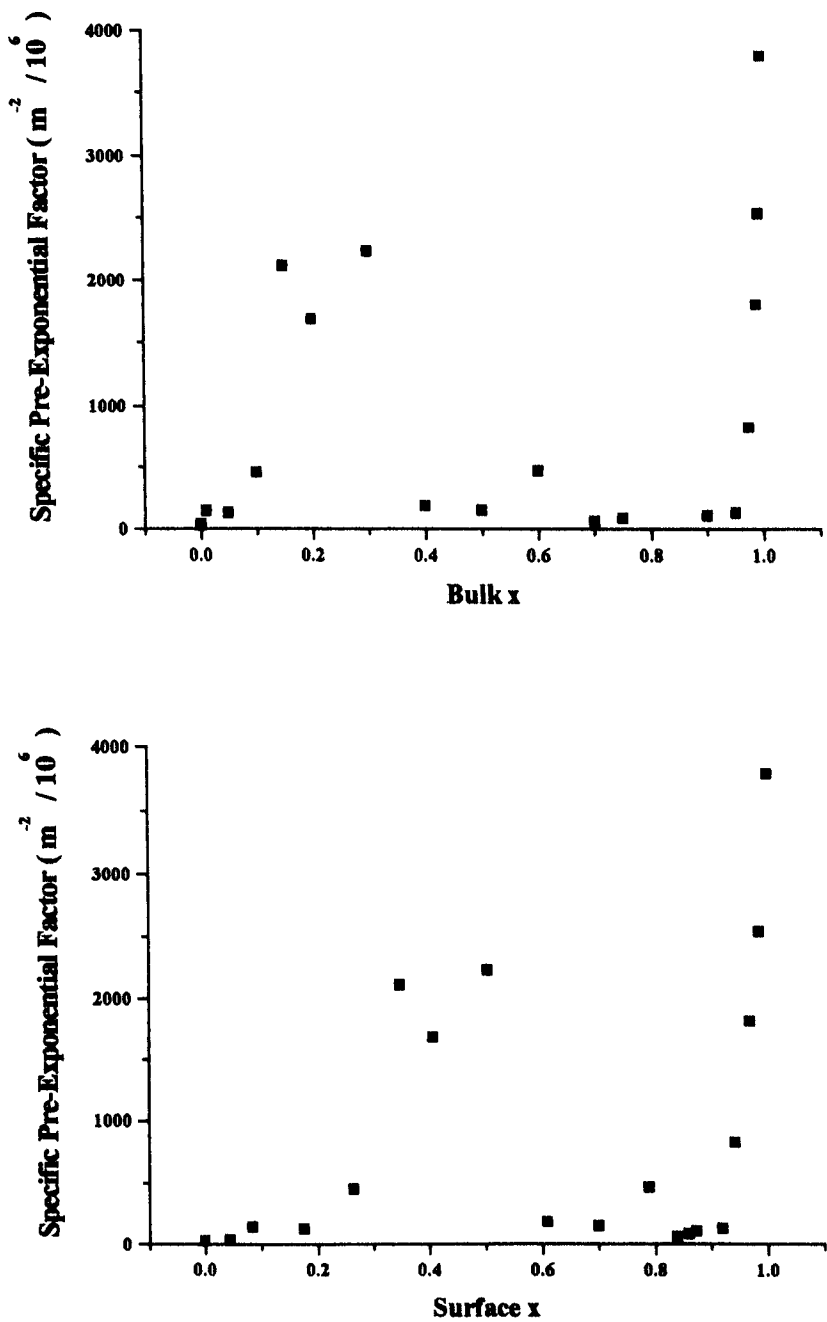
The variations in apparent activation energy with bulk and surface lanthanum concentration are shown in figure 4.81. Within the La in ceria solid solution range a near-symmetrical peak in E_a is observed with a maximum at approximately surface $x = 0.5$, similarly to as was observed previously for the peak in the curve representing the variation in specific activity with surface composition. The surface Ce : La ratio of 1 : 1 again proving to be significant with regards the CH_4 catalytic oxidation properties.

Figure 4.81 Plots of the variation in E_a with bulk and surface lanthanum concentration for the CH_4 oxidation reaction.



In the case of the Ce in lanthana solid solution region, E_a is observed to rise linearly with increasing surface lanthanum concentration.

Figure 4.82 Plots of the variation in Specific Pre-Exponential Factor with bulk and surface lanthanum concentration for the CH_4 oxidation reaction



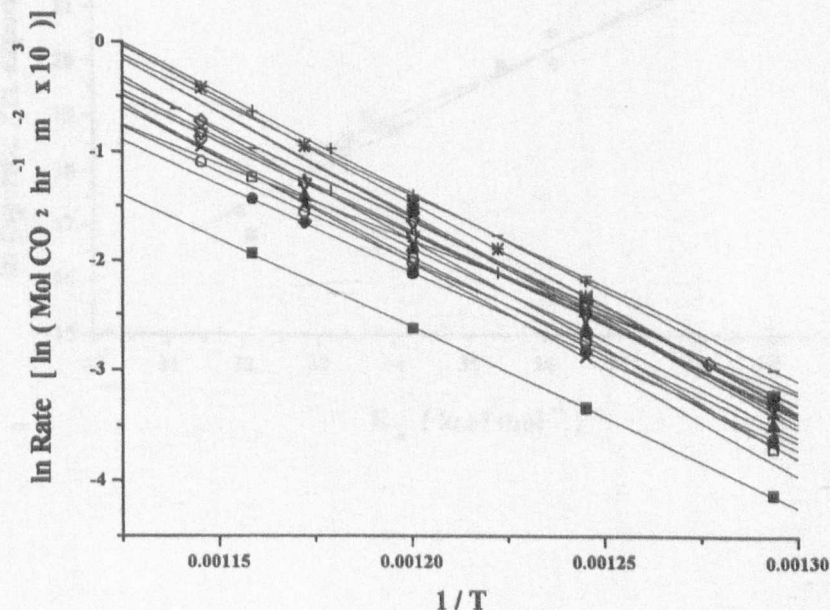
Finally, the variations in specific pre-exponential factor with bulk and surface lanthanum concentration are presented in figure 4.82. Assuming that the specific pre-exponential factor is proportional to the density of active sites on the surface of each of the catalyst materials tested, then within the solid solution range it can be observed that

the addition of lanthanum to ceria results in a significant increase in the density of active sites. The active site density is observed to peak at a surface Ce : La ratio of 1 : 1, similarly as with the variations in E_a . Beyond surface $x = 0.5$, the active site density is observed to fall to levels approaching that of the undoped ceria material and then remain relatively constant with further increases in lanthanum concentration up to surface $x = 0.92$, corresponding well to the Ce in lanthana solid solution limit. Between $0.92 < x < 1$, the active site density is observed to increase in a near linear fashion with lanthanum concentration to its highest level ($3.8 \times 10^9 \text{ m}^{-2}$) at $x = 1$. This variation reflects that of E_a within the Ce in lanthana solid solution range.

4.5.4.3 Compensation Effect

All of the CH_4 oxidation data are plotted in figure 4.83 to show an overview of the Arrhenius data for CH_4 catalytic oxidation for the entire systematic series of $\text{Ce}_{1-x}\text{La}_x\text{O}_{2-x/2}$ materials. It is observed that there is no evidence for the presence of an isokinetic point, and the near parallel nature of most of the plots suggests a narrow range of apparent activation energies.

Figure 4.83 A plot of Arrhenius data for CH_4 oxidation over the $\text{Ce}_{1-x}\text{La}_x\text{O}_{2-x/2}$ series.



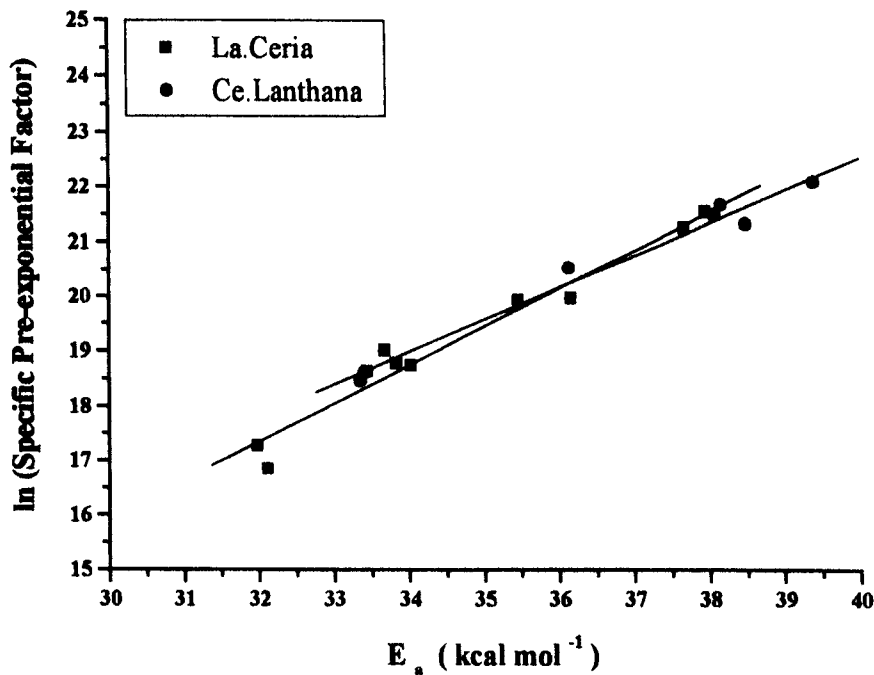
The similar trends within the E_a and specific pre-exponential factor variations with bulk and surface composition point to a significant compensation effect, as was observed with the CO catalytic oxidation reaction over the same materials. This is demonstrated by the straight line plots of the variation in \ln specific pre-exponential factor with E_a , for the two solid solution ranges: $0 < \text{bulk } x < 0.6$ and $0.9 < \text{bulk } x < 1$, which can be expressed;

$$0 < \text{bulk } x < 0.6$$
$$\ln (A/SA) = - 4.930 + 0.696 \times E_a$$
(4.85)

$$0.9 < \text{bulk } x < 1$$
$$\ln (A/SA) = - 0.914 + 0.585 \times E_a$$
(4.86)

These compensation plots over the two solid solution ranges are compared in figure 4.84.

Figure 4.84 A compensation effect plot of the variation of \ln specific pre-exponential factor with E_a for the CH_4 oxidation reaction.



4.5.4.4 CH₄ Catalytic Oxidation - Kinetic Studies

In this study, the effect of reactant and product partial pressure on reaction rate was investigated. The purpose of the study was to provide further data pertinent to the elucidation of the reaction mechanism(s) occurring at the surface. Further correlation with data from the other methods of characterisation was used to lend support to the mechanistic arguments presented. Experimentally, the variation in rate with the concentration of CH₄, O₂ and CO₂ was determined. For each experiment, computer curve fitting was then used to determine the order of the reaction with respect to the reactant.

For P_{CH₄} and P_{O₂} variations, the experiments were possible under the standard reaction conditions and temperature by use of He balance gas. In the case of the P_{CO₂} studies it was necessary to increase the overall volumetric flow rate to accommodate the additional gas in the reactant stream, and by default, proportionally reduce the concentrations of reactants in the reactant mixture. However, the CH₄ : O₂ ratio remained constant at 1 : 10 despite this experimental modification. Additionally, due to the high CO₂ concentrations caused by addition of CO₂ to the reactant gas, rate was determined by CH₄ consumption. The reaction rate was then expressed in terms of Mol CO₂ hr⁻¹ kg⁻¹ for reasons of continuity.

4.5.4.4.1 Oxidation of CH₄ over CeO₂ Catalyst

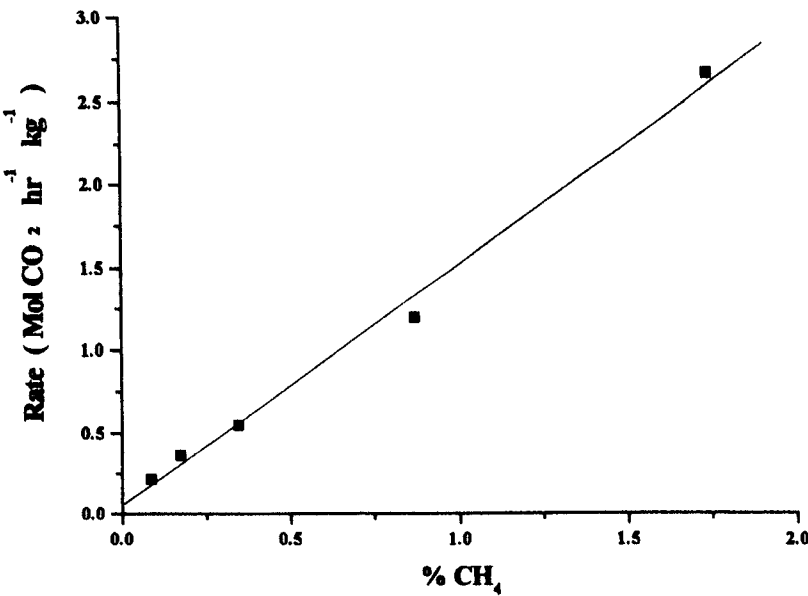
4.5.4.4.1.1 The effect of P_{CH₄}

Experimental Conditions: Total flow = 8.61 l hr⁻¹ % O₂ = 17.34

Table 4.43 Results

% CH ₄	Rate at 600°C (Mol CO ₂ hr ⁻¹ kg ⁻¹)
1.742	2.671330
0.871	1.194135
0.348	0.547583
0.174	0.358853
0.087	0.211912
0	0

Figure 4.85 A plot of the variation in CH₄ oxidation rate with CH₄ feed concentration



The rate is approximately first-order with respect to methane partial pressure;

Rate = 1.468 × [CH₄]

(4.87)

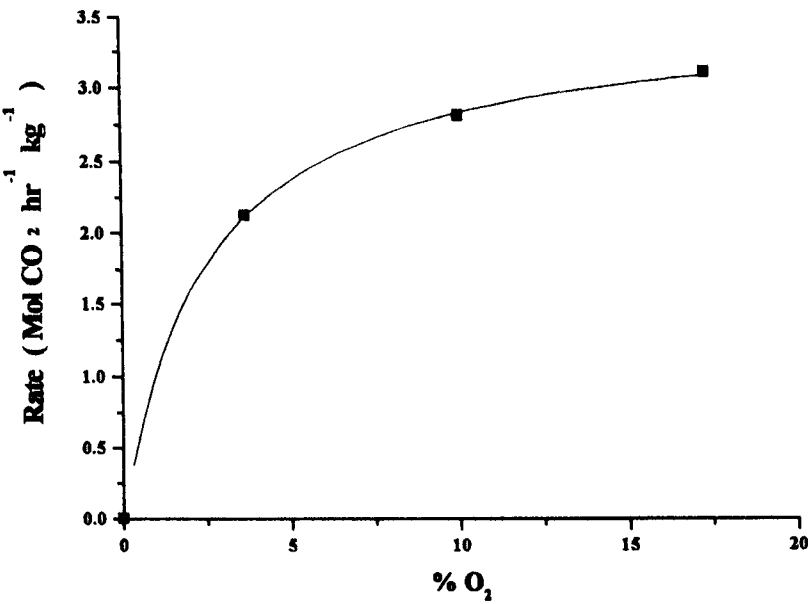
4.5.4.4.1.2 The effect of P_{O_2}

Experimental conditions Total flow = 8.61 l hr⁻¹ % CH₄ = 1.742

Table 4.44 Results

% O ₂	Rate at 600°C (Mol CO ₂ hr ⁻¹ kg ⁻¹)
17.340	3.105977
10.024	2.809831
3.659	2.117762
0	0

Figure 4.86 A plot of the variation in CH₄ oxidation rate with O₂ feed concentration



Analysis according to a power law shows a small positive order on oxygen concentration. The experimental data exhibits a good fit to a Langmuir type expression;

$$\text{Rate} = 1.44 \frac{P_{O_2}}{(1 + 0.41P_{O_2})} \tag{4.88}$$

4.5.4.4.1.3 The effect of P_{CO_2}

Experimental conditions Flow rate = 10.11 l hr⁻¹ %CH₄ = 1.484 %O₂ = 14.769

Table 4.45 Results

% CO ₂	Rate at 600°C (Mol CO ₂ hr ⁻¹ kg ⁻¹)
14.837	1.340038
2.967	1.312689
1.484	1.364654
0.742	1.673675
0.303	2.064880
0	2.299408

Figure 4.87 A plot of the variation in CH₄ oxidation rate with CO₂ feed concentration

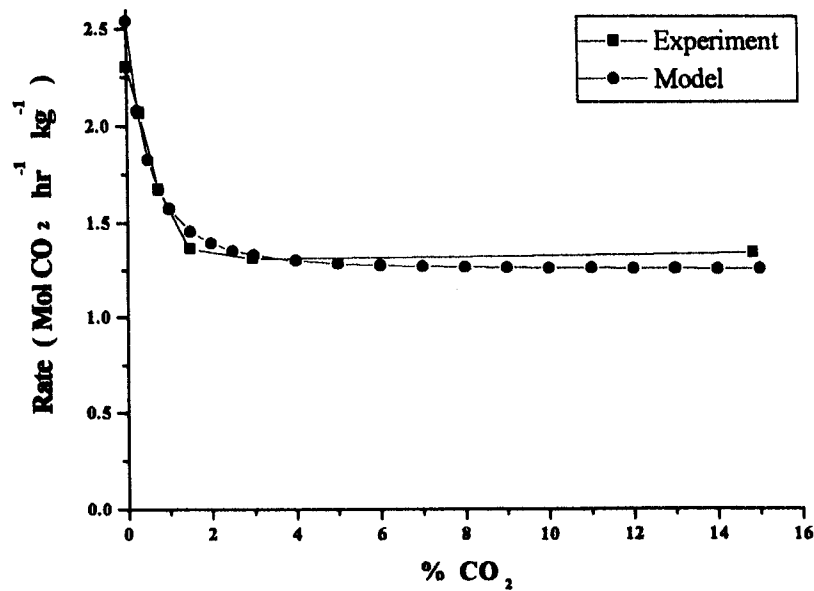


Figure 4.87 shows strong retardation by CO₂, the retardation becoming progressively larger with increasing CO₂ concentration, until the rate reaches a limiting value above approximately 3% CO₂. The experimental data may be fitted to a model equation such that;

$$\text{Rate} = 1.25 + \frac{1.29}{(1 + 0.93[\text{CO}_2])^2} \quad (4.89)$$

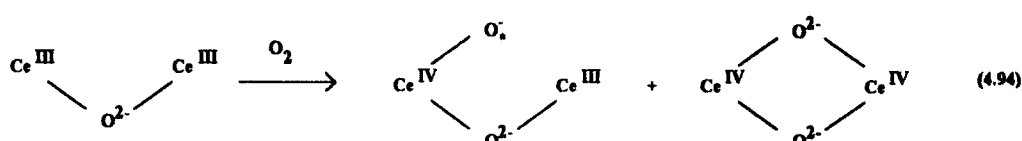
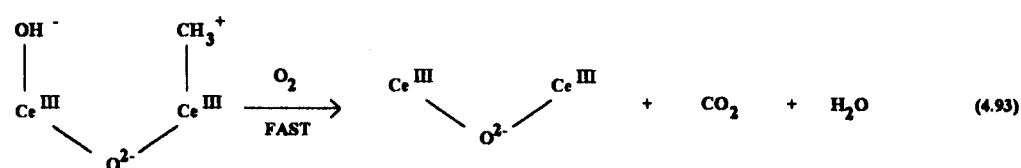
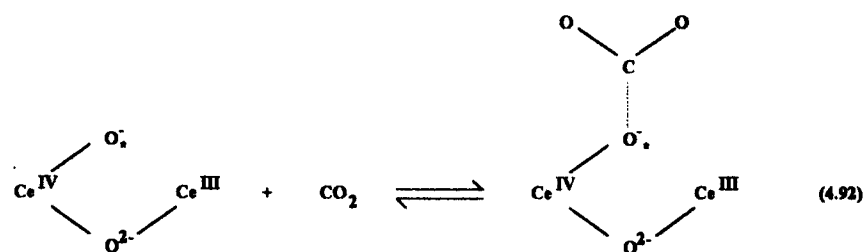
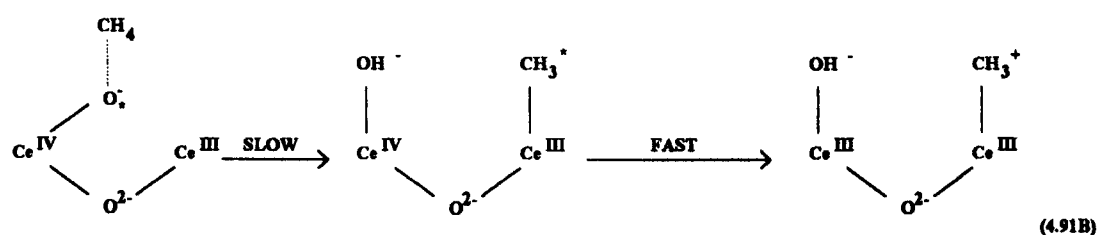
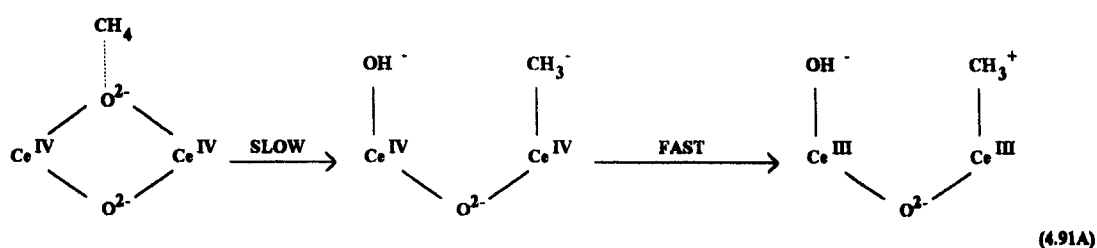
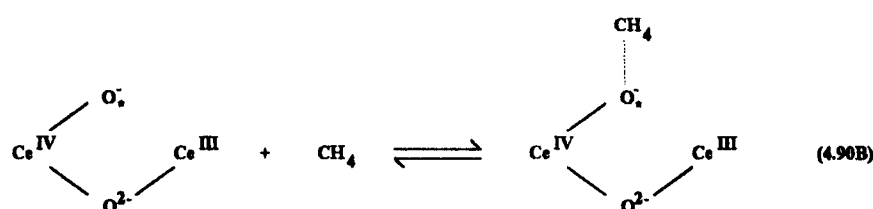
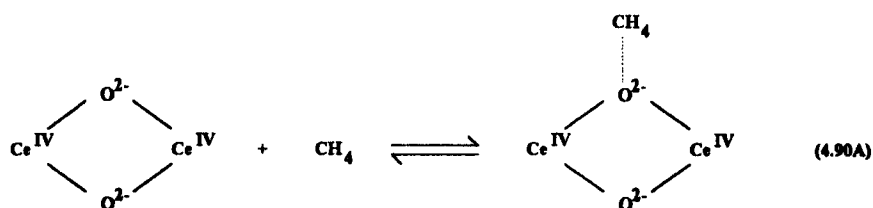
It is possible to conclude from this that the rate is comprised of two components, one of which is retarded by the presence of CO_2 , whilst the other is not. In the present case, the unretarded contribution to rate is constant (at $1.25 \text{ Mol CO}_2 \text{ hr}^{-1} \text{ kg}^{-1}$), whilst the retarded contribution varies in proportion to $1/[\text{CO}_2]^2$ (between $1.09 \text{ Mol CO}_2 \text{ hr}^{-1} \text{ kg}^{-1}$ and approximately zero $\text{Mol CO}_2 \text{ hr}^{-1} \text{ kg}^{-1}$), over the concentration range $14.9\% > [\text{CO}_2] > 0\%$. It is concluded from this result that two sites exist which are capable of methane activation. Activation of methane over one of these sites is retarded by CO_2 , and is therefore assumed to be basic in nature. Activation of methane on the second site is not retarded by CO_2 , and conversely it is assumed to be of a comparatively less basic nature.

4.5.4.4.1.4 Mechanistic Discussion.

The form of the observed parametric responses may be accommodated in the following reaction scheme, overpage. There are two separate sites available for adsorption of methane on the surface of ceria,¹³² a coordinatively saturated site and a coordinatively unsaturated site. These methane adsorption sites are shown in equations 4.90A and 4.90B, respectively. The competitive adsorption of CH_4 and CO_2 on the (more basic) coordinatively unsaturated site is proposed in equations 4.90B and 4.92, respectively, and is supported by the observed reduction in the amount of methane adsorbed on the coordinatively unsaturated site following CO_2 , as reported by Li and Xin (1992).¹³² An analogous reduction in the amount of adsorbed methane by pre-adsorption of CO_2 , from the (less basic) coordinatively saturated site was not reported. This is consistent with the observation two parallel methane activation mechanisms on the ceria surface, one of which is retarded by CO_2 . In the Li and Xin paper¹³² H_2O and CO_2 were reported as reacting preferentially with surface coordinatively unsaturated oxygen to produce hydroxyls and carbonate species, accounting for the absence of methane adsorption bands corresponding to adsorption on the coordinatively saturated sites. It should be noted that at the reaction temperatures used in the present study,

thermal decomposition of the carbonate species accounts for the observed progressive retarding effect with P_{CO_2} , whereas at temperatures of -100°C to 0°C (as used by Li and Xin), the CO_2 adsorption would result in a much stronger site blocking effect.

Reaction Scheme



The activation of CH_4 over the coordinatively unsaturated oxygen over ceria was also cited by Kundakovic and Flytzani-Stephanopoulos (1998)¹⁵². In this literature study, surface anionic conductivity/reducibility was also cited as important in the determination of total activity. In the present study, both bulk and surface lanthanum concentrations are well beyond the level required for maximum anionic conductivity casting doubt on the requirement for enhanced surface conductivity claimed by Kundakovic and Flytzani-Stephanopoulos.

The rate determining step for the catalytic oxidation of methane is proposed as the activation of methane by the abstraction of a proton, as represented in equations 4.91A and 4.91B, a process which is proposed to be concomitant with the subsequent oxidation of the resulting methyl fragment by the Ce^{IV} species. It is proposed that the oxidation can proceed by an ionic mechanism or a radical mechanism, depending on the nature of the activating site. Reaction 4.94 is a composite representation of the proposed fast oxidation of reduced cerium back to the higher oxidation state, thus regenerating the proposed active sites, the relative proportions of which are determined by surface composition, structure and heterogeneity. The subsequent rapid oxidation of the methyl cation produced over both active sites is represented by equation 4.93.

The adsorption of methane on ceria, studied by Li and Xin (1992)¹³² has previously been discussed in the literature review (section 2.2.3), in which two separate adsorptions were determined on coordinatively unsaturated and coordinatively saturated ceria by use of infra-red techniques. In the present study, only the characteristic IR bands due to methane adsorbed on coordinatively saturated ceria (3010cm^{-1} and 1304cm^{-1}), were observed to be strong under methane oxidation reaction conditions in the *in situ* DRIFTS study (section 4.2.2.4) The low intensity of the IR bands due to methane adsorption on coordinatively unsaturated ceria may be due to the short lifetime of this transient precursor at reaction temperatures, in comparison with the lower measurement temperatures used by Li and Xin (-100°C to 0°C). This is consistent with the proposed adsorption of methane in equations 1A and 1B, and with the scheme proposed by Li and Xin.¹³²

Choudhary and Rane (1991)¹⁴⁶ also proposed that methane is adsorbed on ceria on acid-base pair sites of low coordination. Given sufficient strength, activation of CH₄ by heterolytic fission of a C-H bond results in a carbanion species which is then subsequently oxidised. The form of the dependency of rate on oxygen partial pressure reported, suggests that at low P_{O₂}, adsorbed molecular oxygen could be involved in the rate determining step. The assumption that the rate determining step in the methane oxidation mechanism is two-electron oxidation of adsorbed methane by ceria is consistent with the observed first order dependency on P_{CH₄} and the near zero order on P_{O₂}. Further, it is logical to assume that the active centre comprises two adjacent cerium species. Both of these latter studies are consistent with the experimental observations within the present study.

Using the Langmuir adsorption isotherm, the fraction of surface sites covered by adsorbed CH₄ and CO₂ can be derived from the adsorption/desorption equilibrium to be;

$$k\text{CH}_{4_{\text{ads}}} \times P_{\text{CH}_4} \times (1 - \theta_{\text{Total}}) = k\text{CH}_{4_{\text{des}}} \theta_{\text{CH}_4} \quad (4.95)$$

where θ_{Total} is the fraction of available sites covered with CH₄ and CO₂.

The fraction of available surface sites covered with CH₄ and CO₂ can therefore be expressed as;

$$\theta_{\text{CH}_4} = K_{\text{CH}_4} \times P_{\text{CH}_4} \times (1 - \theta_{\text{Total}}) \quad (4.96)$$

and

$$\theta_{\text{CO}_2} = K_{\text{CO}_2} \times P_{\text{CO}_2} \times (1 - \theta_{\text{Total}}) \quad (4.97)$$

Adding equations 4.96 and 4.97

$$\theta_{\text{Total}} = (1 - \theta_{\text{Total}}) \times (K_{\text{CH}_4} P_{\text{CH}_4} + K_{\text{CO}_2} P_{\text{CO}_2}) \quad (4.98)$$

Hence

$$(1 - \theta_{\text{Total}}) = \frac{1}{(1 + K_{\text{CH}_4} P_{\text{CH}_4} + K_{\text{CO}_2} P_{\text{CO}_2})} \quad (4.99)$$

As an immediate consequence of the adsorption of CH_4 , the formation of two adsorbed species is proposed ($\text{CH}_3^+ + \text{H}^+$). Accordingly it is further proposed that an empty site adjacent to the activated methane is required. The adsorbed species are likely to be oxidised by oxygen derived from oxygen transfer from surface oxide sites, associated with ceric sites. Thus:

$$\text{Rate} = k_{\text{Eq4.100}} \times \theta_{\text{CH}_4} \times (1 - \theta_{\text{Total}}) \quad (4.100)$$

In order to accommodate the partial retardation by CO_2 , it has been proposed that the coordinatively saturated and coordinatively unsaturated sites operate simultaneously, but only the coordinatively unsaturated site adsorbs CO_2 . Allowing for this and substituting for $(1 - \theta_{\text{Total}})$ in equation 4.99 and θ_{CH_4} in equation 4.96;

$$\text{Rate} = \frac{k_{\text{Eq4.101}} \times K_{\text{CH}_4} \times P_{\text{CH}_4}}{(1 + K_{\text{CH}_4} P_{\text{CH}_4} + K_{\text{CO}_2} P_{\text{CO}_2})^2} + \frac{k'_{\text{Eq4.101}} \times K'_{\text{CH}_4} \times P_{\text{CH}_4}}{(1 + K'_{\text{CH}_4} P_{\text{CH}_4})^2} \quad (4.101)$$

At constant CH_4 partial pressure

$$\text{Rate} = \frac{k_{\text{Eq4.102}}}{(1 + K_{\text{CO}_2} P_{\text{CO}_2})^2} + k'_{\text{Eq4.102}} \quad (4.102)$$

and at constant CO_2 partial pressure

$$\text{Rate} = \frac{k_{\text{Eq4.103}} K_{\text{CH}_4} P_{\text{CH}_4}}{(1 + K_{\text{CH}_4} P_{\text{CH}_4})^2} + \frac{k'_{\text{Eq4.103}} K'_{\text{CH}_4} P_{\text{CH}_4}}{(1 + K'_{\text{CH}_4} P_{\text{CH}_4})^2} \quad (4.103)$$

which at low methane partial pressures approximates to

$$\text{Rate} = k_{\text{Eq4.104}} P_{\text{CH}_4} \quad (4.104)$$

The observed orders of reaction with respect to CO_2 and CH_4 are consistent with equations 4.102 and 4.104, respectively.

4.5.4.4.2 Oxidation of CH₄ over La₂O₃ Catalyst

Rare earth oxides and alkaline earth oxides promoted with rare earths are active catalysts for the oxidative coupling of methane reaction (OCM).¹⁴⁶ Accordingly, rare earth oxides have been indexed with regards their acid/base site densities and strengths, and of the rare earth oxides, lanthana was determined to be the strongest base.

In the presence of molecular oxygen, methyl radicals are formed from adsorbed methane interacting with acid/base pair sites on the surface of the rare earths. Abstraction of a proton activates the adsorbed methane, forming an adsorbed methyl carbanion. This in turn donates an electron to molecular oxygen to yield a methyl radical which subsequently desorbs and reacts in the gas phase.

The OCM reaction is selective only within a narrow range of CH₄/O₂ partial pressures. In the absence of molecular oxygen, methyl radicals are not formed, and the adsorbed carbanion undergoes surface reactions leading to combustion products. At high partial pressures of molecular oxygen, the coupling reaction rate is reduced at the expense of combustion.

The present study is an investigation of the catalytic combustion of CH₄, and consequently has employed large a stoichiometric excess of oxygen relative to CH₄. Conversions were minimised by use of short contact times and reaction temperatures only marginally higher than the reaction threshold.

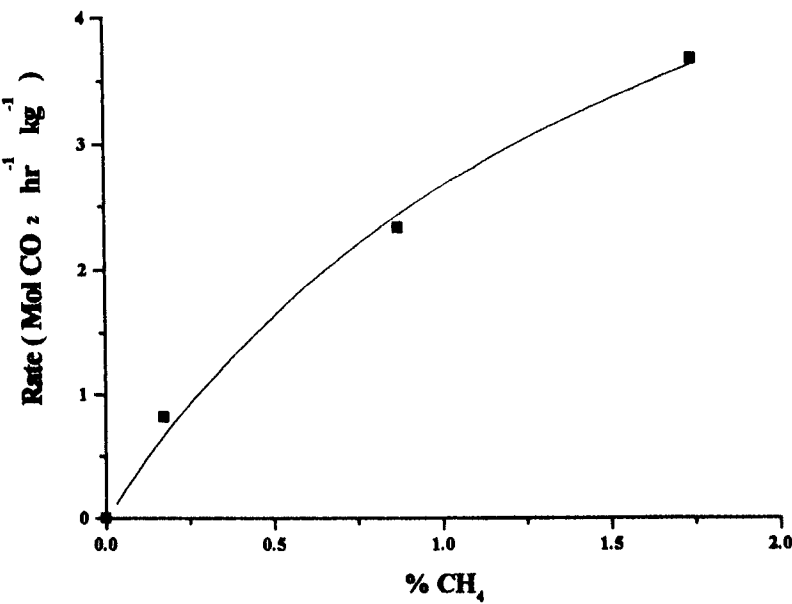
4.5.4.4.2.1 The effect of P_{CH_4}

Experimental Conditions: Total flow = 8.61 l hr⁻¹ % O₂ = 17.34

Table 4.46 Results

% CH ₄	Rate at 600°C (Mol CO ₂ hr ⁻¹ kg ⁻¹)
1.742	3.683844
0.871	2.335142
0.174	0.816581
0	0

Figure 4.88 A plot of the variation in CH₄ oxidation rate with CH₄ feed concentration



Curve fitting the data using a power law function generates an apparent order of 0.66. Assuming a Langmuir-type adsorption isotherm and that adsorbed CH₄ is the surface intermediate (as was determined previously for CeO₂), then the response of rate to P_{CH_4} may be represented by the equation;

$$\text{Rate} = \frac{4.22 \times P_{CH_4}}{(1 + 0.58 \times P_{CH_4})} \tag{4.105}$$

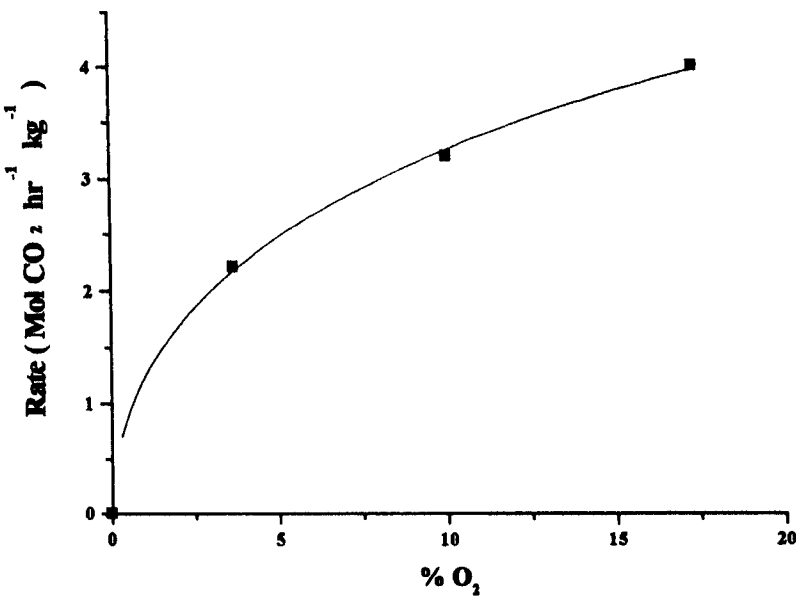
4.5.4.4.2 The effect of P_{O_2}

Experimental conditions Total flow = 8.61 l hr⁻¹ % CH₄ = 1.742

Table 4.47 Results

% O ₂	Rate at 600°C (Mol CO ₂ hr ⁻¹ kg ⁻¹)
17.341	4.021519
10.024	3.209031
3.659	2.214392
0	0

Figure 4.89 A plot of the variation in CH₄ oxidation rate with O₂ feed concentration



A power law curve fitting of the rate vs. P_{O_2} data shown in figure 4.89 above, returns an apparent order of 0.39. Again assuming a Langmuir-type adsorption isotherm for an adsorbed form of oxygen, the response of rate to P_{O_2} may be represented by;

$$\text{Rate} = \frac{k_1 [O_2]^n}{1 + k_2 [O_2]^n} \tag{4.106}$$

The experimental data are consistent with the value of n being in the range 0.5 to 1. Modelled rates obtained from 'best-fit' curve equations with n compelled to be 0.5 and

1 both approximate well to the experimental data, but based on a higher statistical fit the half order expression is preferred;

$$\text{Rate} = \frac{1.36P_{\text{O}_2}^{0.5}}{1 + 0.1P_{\text{O}_2}^{0.5}}$$

(4.107)

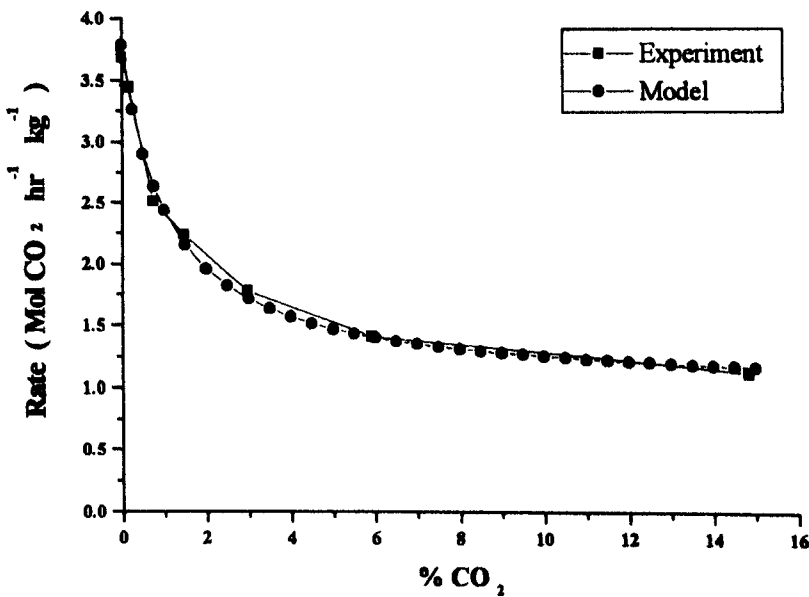
4.5.4.4.2.3 The effect of P_{CO₂}

Experimental conditions Total flow = 8.61 l hr⁻¹ % CH₄ = 1.742

Table 4.48 Results

% CO ₂	Rate at 600°C (Mol CO ₂ hr ⁻¹ kg ⁻¹)
0	3.683844
0.169	3.445722
0.742	2.509782
1.480	2.234453
2.970	1.775646
5.930	1.413154
14.84	1.114933

Figure 4.90 A plot of the variation in CH₄ oxidation rate with CO₂ feed concentration



Increases in P_{CO_2} progressively retards the rate of methane oxidation over lanthana up to a concentration of approximately 15 %, beyond which, further increases in P_{CO_2} have little further effect. The reciprocal of the oxidation rate rises with $P_{\text{CO}_2}^{0.36}$. Further analysis in terms of the Langmuir adsorption isotherm allows the experimental data to be represented by the relationship;

$$\text{Rate} = 0.967 + \frac{2.82}{1 + 0.92P_{\text{CO}_2}} \quad (4.108)$$

The form of this equation indicates that there are two contributions to methane oxidation rate over lanthana, similarly as observed for the same reaction over ceria. Again, one of the contributions to the total rate is retarded by CO_2 according to a first order effect, whilst the other is independent of P_{CO_2} . However, in the near absence of CO_2 , the contribution toward the total rate of the CO_2 retarded component represents approximately 70% of the total rate, which can be compared with an analogous figure of approximately 40% over ceria. This suggests that the adsorbed CO_2 retards the reaction step occurring on the basic site; i.e., the abstraction of a proton from CH_4 .

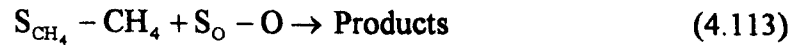
4.5.4.4.2.4 Mechanistic Discussion

From these studies of the effect of P_{CH_4} , P_{O_2} and P_{CO_2} , it is evident that the CH_4 oxidation rate over lanthana is not wholly controlled by any one of the three components, as changes in any of these three parameters has a significant influence on reaction rate.

A possible reaction scheme based on the adsorption of CH_4 and O_2 on different sites can be explored. As in the case of methane oxidation over ceria, methane activation can again be assumed to occur by proton abstraction over an acid/base pair site, resulting in carbanion formation. The retardation of the methane oxidation reaction by CO_2 can therefore be attributed to its adsorption on the base site, either then blocking the site for CH_4 adsorption or weakening the polarisation of any adsorbed methane. It is further assumed that oxygen is activated by adsorption, and that dissociated oxygen is the active species. Activation of oxygen over lanthana has

been variously described in terms of both associated and dissociated oxygen. The current results marginally favour interpretation of the dependence of methane oxidation rate as half order on P_{O_2} .

For simplicity, the scheme for a half order response to P_{O_2} is analysed:



For site S_{CH_4}

$$\begin{aligned} \theta_{CH_4} &= K_{CH_4} P_{CH_4} \{1 - (\theta_{CH_4}^{S_{CH_4}} + \theta_{CO_2}^{S_{CH_4}})\} \\ &= K_{CH_4} P_{CH_4} (1 - \sum \theta^{S_{CH_4}}) \end{aligned} \quad (4.114)$$

$$\theta_{CO_2}^{S_{CH_4}} = K_{CO_2}^{S_{CH_4}} P_{CO_2} (1 - \sum \theta^{S_{CH_4}}) \quad (4.115)$$

hence

$$(1 - \sum \theta^{S_{CH_4}}) = \frac{1}{(1 + K_{CH_4}^{S_{CH_4}} P_{CH_4} + K_{CO_2}^{S_{CH_4}} P_{CO_2})} \quad (4.116)$$

Similarly for site S_O

$$\begin{aligned} \theta_O &= K_O P_{O_2}^{\frac{1}{2}} \{1 - (\theta_O^{S_O} + \theta_{CO_2}^{S_O})\} \\ &= K_O P_{O_2}^{\frac{1}{2}} (1 - \sum \theta^{S_O}) \end{aligned} \quad (4.117)$$

$$\theta_{CO_2}^{S_O} = K_{CO_2}^{S_O} P_{CO_2} (1 - \sum \theta^{S_O}) \quad (4.118)$$

hence

$$(1 - \sum \theta^{S_O}) = \frac{1}{(1 + K_O^{S_O} P_{O_2}^{\frac{1}{2}} + K_{CO_2}^{S_O} P_{CO_2})} \quad (4.119)$$

If the rate of reaction is proportional to the product of adsorbed CH_4 and O_2 molecules, and assuming that sites are randomly distributed, then from equations 4.114, 4.116, 4.118 and 4.119;

$$\begin{aligned} \text{Rate} &= k\theta_{\text{CH}_4}^{S_{\text{CH}_4}}\theta_{\text{O}}^{S_{\text{O}}} \\ &= \frac{kK_{\text{CH}_4}^{S_{\text{CH}_4}}P_{\text{CH}_4}K_{\text{O}}^{S_{\text{O}}}P_{\text{O}_2}^{\frac{1}{2}}}{(1 + K_{\text{CH}_4}^{S_{\text{CH}_4}}P_{\text{CH}_4} + K_{\text{CO}_2}^{S_{\text{CH}_4}}P_{\text{CO}_2}) \times (1 + K_{\text{O}}^{S_{\text{O}}}P_{\text{O}_2}^{\frac{1}{2}} + K_{\text{CO}_2}^{S_{\text{O}}}P_{\text{CO}_2})} \end{aligned} \quad (4.120)$$

At constant P_{O_2} and P_{CO_2} , equation 4.120 may be simplified to;

$$\text{Rate} = \frac{k_{\text{Eq4.121}}P_{\text{CH}_4}}{(1 + K_{\text{Eq4.121}}P_{\text{CH}_4})} \quad (4.121)$$

which is similar in form to equation 4.105.

At constant P_{CH_4} and P_{CO_2} , equation 4.120 may be simplified to;

$$\text{Rate} = \frac{k_{\text{Eq4.122}}P_{\text{O}_2}^{\frac{1}{2}}}{(1 + K_{\text{Eq4.122}}P_{\text{O}_2}^{\frac{1}{2}})} \quad (4.122)$$

which is similar in form to equation 4.107.

At constant P_{CH_4} and P_{O_2} , equation 4.120 may be simplified to;

$$\text{Rate} = \frac{k_{\text{Eq4.123}}}{(1 + K_{\text{Eq4.123}}P_{\text{CO}_2} + K_{\text{Eq4.123}'}P_{\text{CO}_2}^2)} \quad (4.123)$$

The experimental data analysed according to equation 4.123, together with a P_{CO_2} independent term (as in equation 4.108), shows $K_{\text{Eq4.123}'}$ to be vanishingly small.

Hence, equation 4.123 may be further simplified to;

$$\text{Rate} = \frac{k_{\text{Eq4.124}}}{(1 + K_{\text{Eq4.124}}P_{\text{CO}_2})} \quad (4.124)$$

which is similar in form to the P_{CO_2} dependent part of equation 4.108.

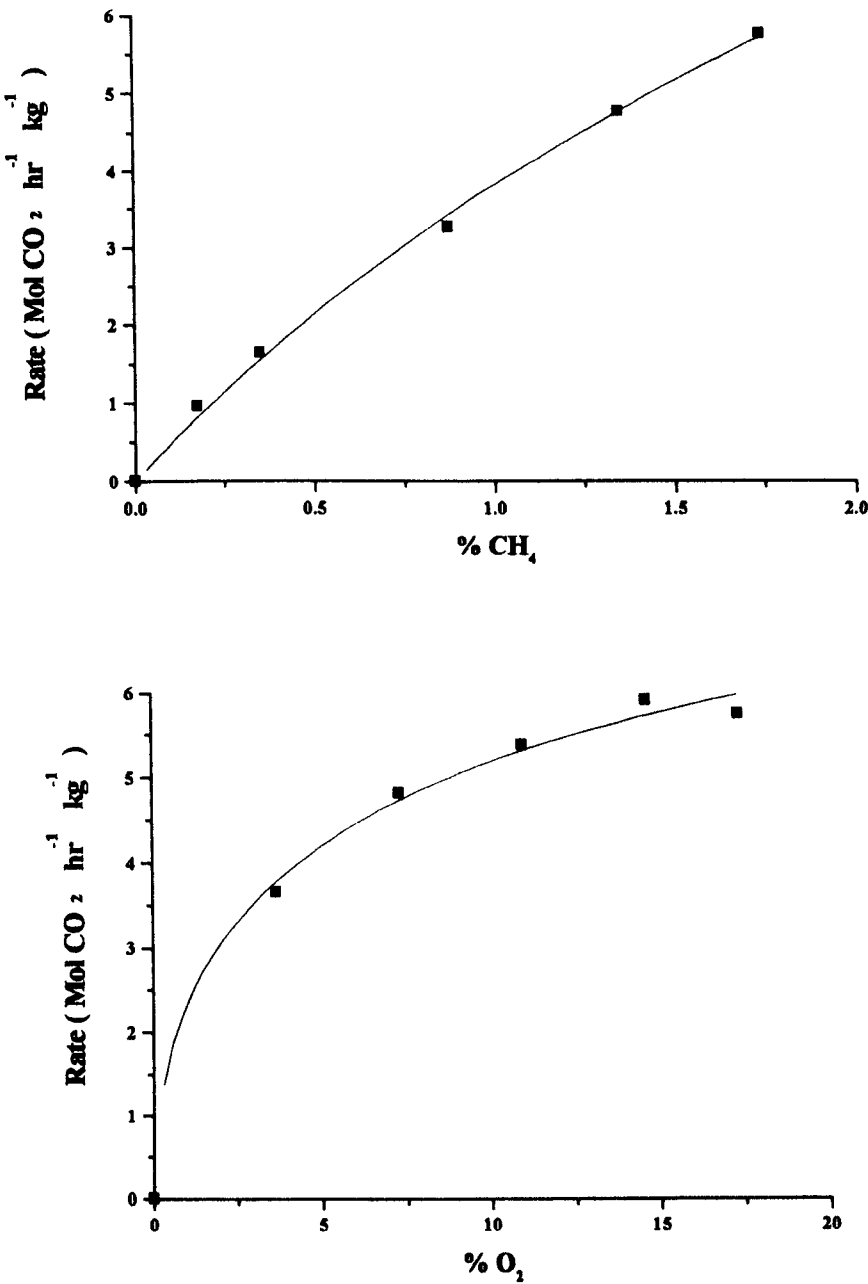
4.5.4.4.3 The kinetics of the catalytic oxidation of CH_4 over the $\text{Ce}_{1-x}\text{La}_x\text{O}_{2-x/2}$ system.

In this section, the variation in the order of the methane catalytic oxidation reaction with respect to P_{CH_4} and P_{O_2} with catalyst composition has been determined, similarly to the previous studies over the series end-members. The experiments were conducted over catalysts which were of particular interest following the catalytic activity study. The effect of small amounts of lanthanum dopant was tested with a surface $x = 0.044$ material, (a dopant level which was observed to result in a significant increase in methane oxidation reaction rate at 560°C), at surface $x = 0.176$ (a dopant level chosen to provide a comparison between the CH_4 and CO oxidation reactions over the $\text{Ce}_{1-x}\text{La}_x\text{O}_{2-x/2}$ system - the level of maximum CO catalytic oxidation activity) and finally, at surface $x = 0.504$ (the dopant level found to maximise CH_4 catalytic oxidation activity). Experiments were conducted similarly to the kinetic studies over ceria and lanthana, and the results are presented in table 4.49. The results for surface $x = 0.176$ were collected over a wide range of CH_4 and O_2 partial pressures and are shown in figure 4.91.

Table 4.49 Results of kinetic studies for $\text{Ce}_{0.95}\text{La}_{0.05}\text{O}_{1.975}$, surface $x = 0.176$

Surface x	% CH_4	% O_2	Rate at 600°C Mol CO_2 $\text{hr}^{-1} \text{ kg}^{-1}$
0.176	1.742	17.341	5.764287
0.176	1.347	17.341	4.780754
0.176	0.871	17.341	3.268085
0.176	0.348	17.341	1.647087
0.176	0.174	17.341	0.966986
0.176	0	17.341	0
0.176	1.742	14.634	5.920271
0.176	1.742	10.976	5.384623
0.176	1.742	7.317	4.808842
0.176	1.742	3.659	3.654274
0.176	1.742	0	0

Figure 4.91 Plots of the variation in CH₄ oxidation rate with P_{CH₄} and P_{O₂} for surface x = 0.176 at 600°C



For surface x = 0.176 (bulk x = 0.05), the orders on methane and oxygen are approximately 1 and 0.5, respectively. Assuming Langmuir style adsorption isotherms the data can be expressed rather more accurately as;

$$\text{Rate (with respect to } P_{\text{CH}_4} \text{)} = \frac{4.9P_{\text{CH}_4}}{(1 + 0.29P_{\text{CH}_4})} \quad (4.125)$$

and

$$\text{Rate (with respect to } P_{\text{O}_2} \text{)} = \frac{2.9P_{\text{O}_2}^{\frac{1}{2}}}{(1 + 0.24P_{\text{O}_2}^{\frac{1}{2}})} \quad (4.126)$$

The inclusion of lanthanum into ceria, such that surface $x = 0.176$ was observed to enhance the specific reaction rate by almost a factor of three. It is possible that the order on P_{O_2} decreased from approximately 1 (as observed over ceria), to 0.5 (similar to that observed over lanthana). It can therefore be concluded that inclusion of lanthanum into ceria, even at this relatively small bulk concentration, has resulted in a switching of the reaction mechanism from that of ceria toward that of lanthana. This is reasonable on the assumption that the base promoted abstraction of a proton from methane is the reaction rate limiting step.

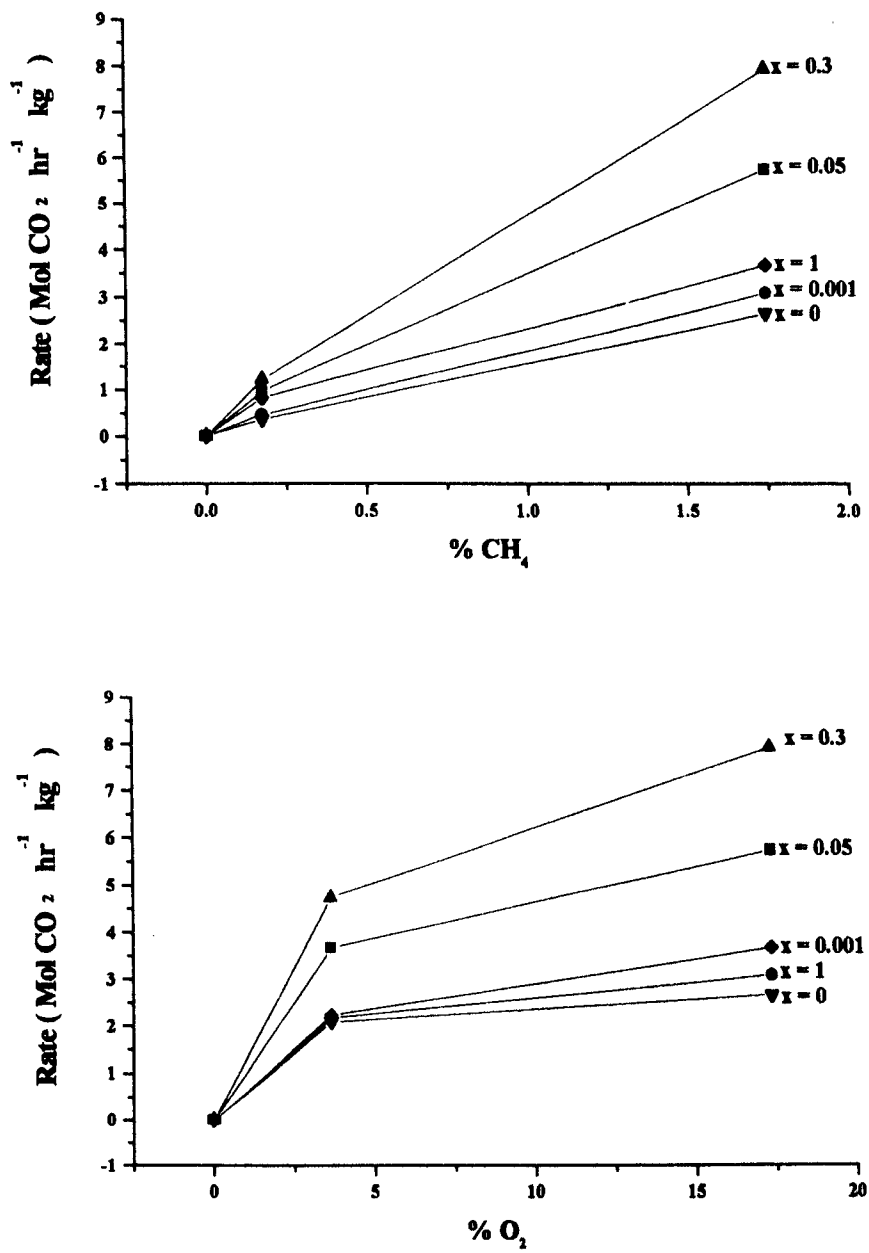
The other mixed oxide materials, as mentioned previously were studied in slightly less detail than the surface $x = 0.176$ example, in order to determine the variation in mean order with respect to P_{CH_4} and P_{O_2} , with catalyst composition. These results are presented in table 4.50.

Table 4.50 Results of CH_4 oxidation kinetic studies over mixed ceria/lanthana catalysts

x	% CH_4	%O_2	Rate at 600°C Mol CO_2 hr⁻¹ kg⁻¹
0.001	1.742	17.341	3.096274
0.001	0.174	17.341	0.462685
0.001	0	17.341	0
0.001	1.742	3.659	2.155286
0.001	1.742	0	0
0.3	1.743	17.341	7.930502
0.3	0.174	17.341	1.213591
0.3	0	17.341	0
0.3	1.743	3.659	4.724912
0.3	1.743	0	0

Plots to determine the mean order of the reaction with respect to CH_4 and O_2 over the mixed oxides studied are shown in figure 4.92, along with data from the analogous studies over ceria and lanthana, as discussed previously.

Figure 4.92 Plots of the variation CH₄ oxidation rate with P_{CH₄} and P_{O₂} with lanthanum concentration at 600°C



The progressive changes in the calculated mean orders of reaction at 600°C with respect to CH₄ and O₂ with variation in catalyst lanthanum concentration is presented in table 4.51.

Table 4.51 CH₄ oxidation reaction mean orders with respect to CH₄ and O₂ over ceria doped with several different concentrations of lanthanum.

Bulk x	Surface x	Mean order on CH ₄	Mean order on O ₂	% Rate CO ₂ Retardation
0	0	1.1	0.24	41.7
0.001	0.044	0.82	0.23	-
0.05	0.176	0.75	0.30	-
0.3	0.504	0.80	0.33	-
1	1	0.65	0.39	69.7

It is generally observed that with increasing lanthanum concentration, the order on CH₄ is generally reduced, whilst the order on oxygen is increased. This implies that increasing the lanthanum concentration progressively lowers the activity of adsorbed oxygen relative to that of absorbed methane. These effects can be explained by the increase in the concentration of base pair sites with surface lanthanum concentration resulting in a net increase in the activity of adsorbed methane and a progressive change in the oxygen activation stage. From the methane oxidation rate CO₂ retardation results, it is clear that the base site catalysed contribution to total rate over lanthana is approaching twice that of ceria. It is reasonable to assume that the increase in the retarding effect of CO₂ with lanthanum concentration in the surface of the mixed oxide is progressive.

The essential conclusion from these results is that under the methane oxidation standard conditions, the reaction kinetics dependence on catalyst composition is effectively constant at first order on P_{CH₄} and zero order on P_{O₂}. This result was one of the original objectives of the study, effected by the selection of the threshold temperature for catalytic activity as the standard reaction temperature. Adsorption of a low partial pressure of methane, a high partial pressure of oxygen and use of low conversions were also used in order to meet these objectives.

4.5.4.4.4 **Summary - Nature of the Active Species**

There are three main features characteristic of the methane oxidation reaction over the ceria/lanthana series of catalysts. The first characteristic feature of the catalyst series is the surface composition dependency of specific activity, specific pre-exponential factor and activation energy, all exhibiting a prominent peak at the equicationic Ce/La ratio. The second major characteristic is that over the entire catalyst series, the rate limiting step is the activation of methane. The third characteristic is that methane oxidation reaction rate retardation by CO₂ is higher over lanthana than ceria.

It is proposed that there is a synergistic effect arising from the equicationic combination of Ce and La in the surface of the tested materials, with respect to methane oxidation rate. Furthermore, it is proposed that surface lanthanum cations provide a basicity function, capable of methane activation by abstraction of a proton, and that surface cerium cations provide a redox function, capable of oxidising the carbanion formed on activation of the methane on the basic sites.

Within the tested catalyst composition range, it is possible to estimate the reaction orders on CH₄ and O₂ under the standard reaction conditions (1.742% CH₄, 17.341% O₂). These results are summarised in table 4.52. It is observed that the order on methane is always higher than that on oxygen. It can therefore also be proposed that the activation of methane makes the major contribution to the rate limiting step over the series of catalysts studied.

Table 4.52 Methane oxidation reaction orders on CH₄ and O₂ under standard reaction conditions.

Bulk x	Surface x	Order on CH ₄	Order on O ₂
0	0	1.1	0
0.05	0.176	0.62	0.16
0.3	0.504	0.70	0.18
1	1	0.68	0.22

The synergistic effect between the cerium and lanthanum cations arises principally from their combined effect on methane activation. It is also noted however, that there is an increasing dependence on P_{O_2} with increasing lanthanum concentration. The kinetics are shown to change from zero order on P_{O_2} to an appreciable dependency with catalyst surface lanthanum content. This suggests that the addition of lanthanum to the catalyst material results in a change in the nature of the rate determining step so as to include a contribution from the activation of oxygen. This points to a slowing of the oxidation stage, relative to the reduction stage in the reaction mechanism. The increases in E_a due to this are more than compensated for by a simultaneous increase in the pre-exponential factor. The overall effect of increasing the catalyst lanthanum content is therefore to increase both the apparent activation energy and pre-exponential factor.

The probable chemical explanation for these phenomena is the activation of methane over basic (cation) sites. In the case of ceria, the coordinatively unsaturated cerium cations are most likely the active sites for the abstraction of a proton from methane. Under the standard reaction conditions, activation of oxygen is facile due to the $Ce^{III} - Ce^{IV}$ redox, and therefore not rate limiting, hence the observed zero order. Addition of lanthanum cations up to surface $x = 0.504$ increases both the density of basic surface sites facilitating activation of methane, hence the observed decrease in the order on methane with lanthanum addition. The reduction in the concentration of easy redox sites for oxygen activation (cerium cations), with lanthanum addition results in the activation of oxygen becoming rate limiting, as observed in the increasing order on oxygen.

It was determined that the promotion of activity was due to the increase in the pre-exponential factor of the rate expression. As the number of active sites is maximised at $x = 0.504$. It can therefore be concluded that the active centre for the Ce/La synergistic CH_4 oxidation mechanism consists of one cerium cation and a neighbouring lanthanum cation. The basicity enhancement by incorporation of lanthanum into the ceria surface is responsible for the enhanced CH_4 activation activity, whilst the cerium cation is responsible for activation of the oxygen. Further increases in the lanthanum concentration in the surface can therefore be predicted to result in a

decrease in the order on methane and an increase in the order on oxygen as the concentrations of their activation sites increase and decrease, respectively, with catalyst lanthanum concentration.

Further analysis of the reaction beyond the solid solution limit concentration of lanthanum in ceria would require further experimental data and is beyond the scope of this thesis.

Chapter 5 Summary and Conclusions

5.1 Solid State Studies

Initial experiments were completed using a ceramic processing method for catalyst preparation, (section 4.1.1). The solid solution limit for a fluorite structured solid solution of lanthanum in ceria of the type $\text{Ce}_{1-x}\text{La}_x\text{O}_{2-x/2}$ was determined to fall in the range $0.55 < x < 0.60$ by application of Vergard's Law to the variation in lattice parameter with composition. This was in good agreement with literature data. The substitutional incorporation of lanthanum into the ceria lattice up to $x = 0.2$ was shown to have a retarding effect on the sintering rate for the ceria structured materials, by determination of the variation in crystallite size with composition. Surface area measurements of the ceramic materials were found to be relatively constant within the fluorite structured solid solution compositional range, and were not observed to correlate with variations in crystallite size. The specific surface areas were determined to be less than $1 \text{ m}^2\text{g}^{-1}$ for the whole series of materials, which rendered them unsuitable for further testing due to experimental limitations of other characterisation methods.

Further experiments were performed using catalyst materials prepared by a coprecipitation method, (section 4.1.2), adopted from a patent by Mackrodt (1991).⁹⁹ Preliminary experiments determined that such materials were more suitable for testing in the present study due to specific surface areas approximately one to two orders of magnitude higher than the ceramic analogues. It was also determined that material morphology was significantly influenced by dopant type, dopant concentration, material purity and by variations in calcination parameters such as time, temperature, isostatic pressing. Calcination temperature and the effect of pelletisation were investigated first in order to optimise the catalyst preparation method, (section 4.1.3). All calcinations were completed in air over 8 hours, as in the Mackrodt patent (1991).⁹⁹ The effect of dopant concentration was also tested using pure ceria and $x = 0.2$ lanthanum doped ceria. The calcination procedure was standardised as calcination for 8 hours in powder form for 8 hours in air. The calcination temperature was determined to be the best compromise between preservation of surface area and material stability under catalytic reaction

conditions. Unfortunately, the structural stability of pelleted samples intended for direct conductivity measurements of the catalyst materials was compromised at the standard catalyst calcination temperature (800°C).

The surface area of catalyst materials prepared using the standard method were found to exhibit an inverse proportionality to crystallite size, as would be generally expected. The sintering process was investigated in terms of the variation in crystallite size with calcination temperature. A pseudo-activation energy for the sintering process was determined (by the Arrhenius method), for both 20 cation % doped and undoped ceria to be approximately 6.5 kcal mol⁻¹ (27.2 kJ mol⁻¹), which is typical of ionic diffusion processes.

A series of catalysts were subsequently made incorporating a systematic variation in bulk composition between $0 < x < 1$, using the standard preparation method, (section 4.1.4). Phase and lattice parameter analysis (using Vergard's Law) again determined that the fluorite structured solid solution limit for lanthanum in ceria was $0.55 < x < 0.60$, which was in good agreement with that determined for the ceramic materials, and literature data. Additionally, limited evidence for the formation of substitutional solid solution of cerium in lanthana (HCP structure) was observed in the form of dopant induced shifts in the single phase HCP lattice parameter. The solid solution limit of cerium in lanthana was not investigated in great detail, but was estimated to lie in the 10 to 20 cation % cerium range.

The effect of composition on crystallite size was investigated over the coprecipitated systematic series and a strong stabilisation with respect to sintering was observed, even at the $x = 0.1$ level. The observed stabilisation effect was similar to that observed for the ceramic materials, but of a greater magnitude. The increase in the stabilisation effect continues up to the solid solution limit, but the rate of increase in the stabilisation effect decreases progressively with increasing lanthanum concentration. The coprecipitated materials were thus determined to be far more sensitive to dopant concentration than the ceramic materials, with respect to morphological properties. Beyond the solid solution limit, the linear variation in crystallite size suggests a dilution of the saturated solid solution in the second phase. This phenomenon was observed for both the ceramic and coprecipitated materials. The surface areas of the coprecipitated

materials were between 1 and 2 orders of magnitude greater than those determined for the ceramic materials, rendering them ideal for characterisation by the other techniques available.

Further investigation of the influence of calcination parameters was completed in the form of a sintering properties study, (section 4.1.5). The effect of calcination temperature was investigated for a range of catalyst compositions. No variation in lattice parameter was observed with increases in calcination temperature beyond 800°C, even at a dopant level as high as 0.5, thus confirming complete formation of the solid solution at this temperature for an 8 hour calcination. For all samples, crystallite size was observed to increase in a near linear fashion between 600°C and 1000°C. All doped materials were stabilised with respect to sintering at all calcination temperatures tested, in comparison with ceria and lanthana. The sintering rate retardation effect was observed to increase with dopant concentration, and with increased calcination temperature. This suggested that the sintering retardation by the lanthanum dopant was a grain-boundary effect in which cation diffusion was the rate limiting step, rather than a grain boundary oxide anion mobility retardation effect, as had been previously proposed in the literature.³⁵ The effect of calcination time was investigated under the standard preparation conditions. Lattice parameters were found to reach a constant value after just 1 hour at 800°C, whilst crystallite size was determined to be near constant after approximately 10 hours. From these results, the catalyst samples were assumed to be at thermodynamic equilibrium with respect to solid solution formation and sintering processes following the standard preparation method treatment.

5.2 Surface Studies

Following the determination of bulk solid state properties, a study of the surface composition variations of lanthanum doped ceria materials was completed, (section 4.2). The surface composition of lanthanum doped ceria is known to differ significantly from bulk composition,⁹⁷⁻⁹⁸ and as heterogeneous catalysis is a surface phenomenon it was deemed necessary to characterise the catalysts in such terms, using X-ray photoelectron spectroscopy. Initial experiments determined that following the standard preparation

method, the La doped ceria solid solutions were significantly enriched in segregated lanthanum, in comparison with the bulk composition. For fixed bulk compositions, the surface lanthanum fraction was generally observed to increase with increasing calcination temperature between 600°C and 1200°C. In order to determine whether the surface segregation process was kinetically limited, a series of experiments were conducted to determine the effect of variations in calcination time for a series of samples of varying bulk composition. After the standard (8 hour), calcination time, the surface compositions of all compositions tested were determined to be within 1 % of the steady state surface composition. All samples prepared using the standard method were therefore assumed to have thermodynamic equilibrium surface compositions.

Surface composition as a function of bulk composition was subsequently determined for the systematic compositional series of catalysts prepared by the standard method, (section 4.2.3). All surfaces were determined to be lanthanum enriched with respect to the bulk composition, within the bulk compositional range $0 < x < 0.8$. Similarly, surfaces were determined to be cerium enriched with respect to the bulk composition, within the bulk compositional range $0.9 < x < 1$. Accordingly, the data was split into these two compositional ranges, (corresponding approximately to the two solid solution ranges), for further analysis.

For the $0 < x < 0.8$ bulk compositional range, the degree of enrichment is observed to decrease in an approximately logarithmic fashion with increasing bulk lanthanum concentration. The segregation process was analysed using known solid state segregation models. The first model applied to the data was the McLean Regular Solution Model (equation 4.2, section 4.2.3.1.1), which is based on the Langmuir adsorption isotherm; the underlying assumption of the model being that the free energy of segregation is independent of composition. The model did not provide an adequate fit to the experimental data and was rejected on the grounds that the free energy of segregation was composition dependent. The model was of course suitable to be used however, to determine the free energy of segregation for each individual catalyst. The free energy of segregation, thus derived, was determined to be strongly composition dependent, confirming that rejection of the model was justified. The free energy of segregation was determined to decrease rapidly in magnitude with surface coverage of

the segregant, for both the segregation of La from a ceria-host solid solution, and for the segregation of Ce from a lanthana-host solid solution.

The segregation data thus far generated was analysed in terms of several alternative isotherm models, of which, the Freundlich (empirical) isotherm model, (based on a power law), was found to provide a reasonable representation of the data. This suggested that the variation in the free energy of segregation was approximately logarithmic. The best representation of the experimental data in both of the solid solution ranges within the catalyst series, was by a non-Arrhenius statistical thermodynamic model based on electrostatic theory. The model, proposed by Mackrodt and Tasker (1989)¹⁰⁴ was specifically designed for the analysis of two component systems comprising a single type of surface and bulk site, modified to accommodate solute-solute interactions at the surface. The model (equation 4.5, section 4.2.3.1.1.2), was found to give an excellent representation of the coverage dependence of the free energy of lanthanum segregation from the ceria-host solid solution, with a minimisation in the free energy of segregation at the solid solution limit, (figure 4.30). The model was also shown similarly to give an excellent description of the coverage dependence of the free energy of cerium segregation from the lanthana-host solid solution, again with a minimisation in the free energy of segregation at the solid solution limit, (figure 4.31). It was observed that in the case of segregation of cerium from the lanthana-host solid solution, that the model coefficients describing both the driving force for the segregation process, and the solute-solute interactions, were much smaller than for the segregation of lanthanum from the ceria-host solid solution. The driving force difference was explained in terms of the large cationic radius of the lanthanum cation in comparison with the Ce^{IV} cation resulting in a much larger amount of lattice strain when substitutionally incorporated into the ceria lattice, than for cerium incorporated into the lanthana lattice. The electrostatic effect was explained in terms of the fixed aliovalency of the lanthanum cation in the ceria lattice resulting in the formation of charge compensating species and inevitably strong coulombic interactions between various species within the doped solid solution lattice. In the case of cerium doped lanthana, the facile $\text{Ce}^{\text{III}} \leftrightarrow \text{Ce}^{\text{IV}}$ redox results in far weaker electrostatic interactions.

Finally, the Mackrodt and Tasker model¹⁰⁴ was compared and contrasted with an alternative model based on macroscopic properties, such as surface energy and strain energy arising from solute incorporation. This model proposed by Wynblatt and Ku (1977)¹⁰⁶ is based on a lattice model, in which the energy of the system is calculated in terms of nearest neighbour bond energies. Thus, the average energy change of a solute atom moving to the surface, and the solute/solvent interaction energy can be calculated. The surface energies of the solid solutions can also be similarly estimated in terms of the surface energies of the pure materials. A series of approximations and simplifications were made which incorporated empirical expressions for the variations in specific surface area and surface composition, which subsequently allow the free energy of segregation to be expressed in terms of the bulk lanthanum concentration and three constants (equation 4.25, section 4.2.3.1.1.3). Application of the expression to the full set of experimental data was found to give an adequate description of the experimentally determined variation in free energy of segregation, (figure 4.32), however the model was determined to be inferior to the Mackrodt and Tasker model. It was however possible to factorise the variation in free energy of segregation with bulk composition, in terms of the aforementioned three constants in the Wynblatt and Ku expression. The constants were representative of the net contribution to the total free energy of segregation of solute strain, surface and solute-solvent interaction energies, respectively.

Solute strain was determined to be independent of composition, whereas the magnitude of the surface energy and the solute-solvent interaction energy contributions were observed to decrease as the surface became progressively enriched with lanthanum. The strain energy was evaluated as favouring segregation, but was invariant with composition. The surface energy term was determined as not favouring segregation, but only exhibited a weak dependence on composition. The solute-solvent interaction energy was evaluated as favouring segregation, and was determined to be strongly dependent on the solid solution bulk composition. This contribution was determined to decline in an approximately logarithmic fashion with bulk lanthanum concentration.

It can be concluded that the main determinant of the dependency of the free energy of segregation on composition, is the solute-solvent interaction energy. This contribution is in turn dependent on the coulombic interactions between the aliovalent

lanthanum dopant cations, charge compensating lattice defects, and the ceria host lattice. This conclusion supports the interpretation of the segregation phenomenon using the Mackrodt and Tasker model¹⁰⁴ which is based on the variations in such electrostatic interactions with composition, as the main determinant of the variation in the free energy of segregation with composition.

Further investigations of catalyst surface properties were completed using Temperature Programmed Desorption (TPD) and in situ Diffuse Reflectance Infrared FT Spectroscopy (DRIFTS). The TPD studies were completed in order to determine the variations in surface basicity (CO₂ TPD), and in CH₄ and CO adsorption/desorption properties, with catalyst surface composition.

Initial basicity measurements determined that several different CO₂ adsorption sites existed on both ceria and lanthana, (section 4.3.1). The adsorptions were generally observed to be stronger on lanthana than on ceria which was attributed to higher basicity, in agreement with literature data. Pre-reduction of ceria resulted in enhanced basicity which was attributed to the Ce^{IV} → Ce^{III} redox at the surface. Basicity measurements for a range of catalyst composition were completed using a heliox carrier gas in order to simulate the reaction conditions. CO₂ adsorption strength was observed to increase with lanthanum concentration, and at a fixed dopant level, with the known order of lanthanide oxide basicity for different dopants. Quantitative analysis of the CO₂ TPD data determined that specific basicity increased by more than one order of magnitude with surface lanthanum concentration, from ceria to lanthana. The variation in specific basicity with surface composition was observed to increase in a near linear fashion up to the solid solution limit, beyond which a further more rapid linear increase in basicity with surface composition was observed, (figure 4.38). This suggested that the CO₂ adsorption site is a particular arrangement of lanthanum cations in the surface, rather than lanthanum cations alone. The concentration of this species is favoured beyond the solid solution limit.

The CH₄ TPD experiments, (section 4.3.2), did not detect any adsorbed CH₄ under the experimental conditions. It was therefore concluded that transient adsorption of methane was easily reversible, and that no adsorption occurred in the absence of gas phase methane. In contrast to methane adsorption, CO adsorption was determined to be

an activated process over both ceria and lanthana, with two well resolved desorptions for ceria, and three well resolved desorptions for lanthana, at typical CO oxidation reaction temperatures. Quantification of the adsorption properties determined that lanthana adsorbed over 1 order of magnitude more CO than ceria, even at room temperature, and that the adsorption process was more rapidly thermally activated over lanthana, (section 4.3.3.2).

The effect of oxygen on the CO adsorption/desorption properties was also investigated, by use of a double desorption technique in which an inert carrier gas TPD is immediately followed by a further TPD under heliox, (section 4.3.3.3). In summary, oxidative and non-oxidative adsorption was determined to occur over both ceria and lanthana under the inert carrier gas TPD, (section 4.3.3.3.3). Oxidative adsorption sites were determined to be surface oxygen sites, as supported by the observed strong activation of oxidative adsorption over (reducible) ceria, but not over (irreducible) lanthana. This further suggested the involvement of the oxygen sublattice in the case of ceria. Non-oxidative adsorption was assigned to cation sites. This was supported by the observation of single and double non-oxidative desorptions over lanthana and ceria, respectively, (irreducible La^{III} and $\text{Ce}^{\text{III}} \leftrightarrow \text{Ce}^{\text{IV}}$). The thermal activation of the adsorption processes were generally explained in terms of a progressive reduction of the ceria surface, and a progressive dehydroxylation of the lanthana surface with increasing CO adsorption temperature. This was supported by quantification of the carbonaceous residue, which was found to increase with CO adsorption for temperature over ceria, but was found to be invariant with CO adsorption temperature over lanthana. A Boudouard reaction-type disproportionation of CO; $2\text{CO} \rightarrow \text{CO}_2 + \text{C}$, was proposed to occur on the cation (non-oxidative) adsorption sites. The subsequent oxidation of the carbonaceous residue species in the presence of gaseous oxygen suggested a possible intermediate step in the total oxidation reaction mechanism. Significantly, the presence of gas phase oxygen was determined to be necessary to effect complete desorption of CO from the surfaces of both materials - a condition met under the oxidation reaction conditions.

The variation in specific CO adsorptivity with surface composition was also determined, (section 4.3.3.4). It was observed that specific CO adsorptivity increased in

a near linear fashion with surface lanthanum concentration, up to the solid solution limit. It was concluded that within the fluorite structure solid solution range, CO is adsorbed on a site that increases in concentration in proportion with the surface lanthanum concentration. Lanthanum cations within the cubic fluorite structured surface were determined to result in a higher CO adsorption site density, than in the hexagonal close packed structure of lanthana.

The final study of surface adsorption properties was completed using Diffuse Reflectance FT-IR Spectroscopy in combination with a temperature controlled environment cell, which allowed the examination of the surfaces of catalysts under reaction conditions, (section 4.4). The aim of the study was a qualitative determination of the variation in surface species present before, during and after exposure to oxidation reaction conditions, with catalyst composition. In outline, several forms of surface carbonate were shown to exist on the catalyst surfaces: the populations of the various forms of carbonate were shown to vary with catalyst surface composition. Several forms of carbonate species, formate and hydroxyl species were observed to be stable on all of the catalysts. The observed surface spectra of all of the catalysts were typical of untreated oxide materials, (section 4.4.2.1). The spectra of the surfaces of the catalysts were determined to undergo negligible change following exposure to reaction conditions, thus supporting the choice of catalyst calcination temperature, such that the catalyst surfaces were stable under reaction conditions, (section 4.4.2.2).

Under the CO oxidation reaction conditions a bidentate carbonate species was observed to be formed on ceria, (section 4.4.2.3). A further bridged carbonate species was observed to form with increasing surface lanthanum concentration, giving way to a broad absorption band in the fundamental region (section 4.4.2.1), beyond the equicationic Ce : La ratio. Characteristic absorption bands for the carbonate species were only observed over pure lanthana, and were of a very low intensity.

Under CH₄ oxidation conditions, the characteristic absorptions of the carbonate and inorganic carboxylate species were generally observed. The stability of individual carbonate species was observed to be more sensitive to catalyst surface composition than was the case in the analogous CO oxidation reaction conditions experiments, (section 4.4.2.4). This was attributed to the higher temperature of the CH₄ oxidation

conditions resulting in significant thermal decomposition of carbonate species. The main observation under the CH_4 oxidation reaction conditions was that there were two forms of adsorbed methane: the characteristic absorption bands of CH_4 adsorbed on coordinatively saturated, and to a lesser extent, coordinatively unsaturated ceria surfaces, (sections 2.2.3 and 4.2.2.4). It was concluded that CH_4 is adsorbed in two forms on surface anions under the oxidation reaction condition. The relative proportions of coordinatively saturated and coordinatively unsaturated surface species being a function of surface composition, morphology and heterogeneity.

Comparison of the ceria and lanthana surfaces under pre-, post- and under reaction conditions showed that the species on the surface of lanthana were far less sensitive to the environment, than the ceria surface species, (section 4.4.2.5). This is likely to originate from the variable oxygen stoichiometry of ceria. The effect of small concentrations of La in ceria and of Ce in lanthana was the stabilisation of additional surface carbonate species compared with the two pure oxide surfaces, under both oxidation reaction conditions.

5.3 Catalytic Studies

The catalytic studies were conducted using a series of catalysts with a systematic compositional variation, made by the standard coprecipitation method, (section 4.5). Activities were determined in terms of number of moles of CO_2 produced per unit mass, and per unit surface area of catalyst (known as specific activity), under standard conditions. The standard conditions included an approximately 10 : 1 ratio of oxygen to either CO or CH_4 , and reaction temperatures of 310°C and 560°C for the CO and CH_4 oxidation reactions, respectively. The variation in rate with temperature was also determined for both reactions allowing the determination of activation energy and specific pre-exponential data, the latter of which is assumed to be proportional to the active site density. Finally, kinetic studies were completed in order to determine the variation in reaction rate order with respect to reactant and product concentrations, with catalyst surface composition.

Initial experiments were completed in order to determine the experimental conditions required to ensure mass transfer limitation of reaction rate was avoided, (section 4.5.1.1). From these experiments, a standard experimental method was determined for catalytic activity measurements for both of the test reactions. The standard methods were further validated by the successful reproduction of literature data (section 4.5.2 and appendix 4.1). These experiments were based on investigation of data reported in a patent by Mackrodt (1991)⁹⁹ A further aim of the initial experiments was to investigate a synergistic promotion of CH₄ catalytic oxidation activity by simultaneous La and Pr doping of ceria. Both CO and CH₄ oxidation reactions were investigated to enable comparison of the variation in catalytic properties with catalyst composition, for two reactions with vastly different mechanisms. For the CH₄ oxidation reaction, the claimed promotion effect of the lanthanide dopants in ceria were reproduced, as was the synergistic promotion effect of the combination of La and Pr dopants in approximately the specified proportions. However, expression of catalytic activity data in terms of specific activity rather than activity per unit mass of catalyst, determined that the synergistic effect claimed was due to a catalyst morphological dependence on dopant type, rather than a true promotion in terms of surface chemistry, (section A4.1.2.2.1). In contrast with the activity promoting effect observed with CH₄ oxidation, the presence of lanthanide dopants in ceria was determined to have a detrimental effect on CO catalytic oxidation activity, (section A4.1.2.2.2). It was concluded from the initial experiments that the effect of a systematic variation in dopant concentration in ceria, on both CH₄ and CO oxidation activity was necessary. Lanthanum was chosen as the dopant for the systematic studies due to the observed influence over catalytic properties being significantly greater than that of praseodymium.

5.3.1 CO Oxidation Systematic Study

The catalytic oxidation of CO was investigated with respect to variations in activity with lanthanum concentration in ceria, (section 4.5.3). The rate was observed to decrease progressively with increments in the surface concentration of lanthanum, up to the solid solution limit, (section 4.5.3.1). Beyond the solid solution limit, the variation in

specific rate with surface composition was observed to be complex, with no obvious trends. The results were found to be in good agreement with literature data, and it was concluded that the introduction of lanthanum into the ceria surface effectively poisons or dilutes the concentration of the active sites for CO oxidation. The variation in the specific rate was found to vary similarly to the surface concentration of cerium cations, leading to the conclusion that the active sites were intimately related to surface cerium cations.

Arrhenius studies, (section 4.5.3.2), showed that simultaneous peaks in activation energy (E_a) and specific pre-exponential factor (A/SA) occurred at La surface fractions of approximately 0.08 to 0.17, in the La in ceria solid solution range, and at Ce surface fractions of approximately 0.05 to 0.1 in the Ce in lanthana solid solution range. The simultaneous peaks in both E_a and A/SA were shown to be characteristic of a compensation effect. Two separate compensation plots were shown corresponding to the two solid solution compositional ranges within the ceria/lanthana system, (section 4.5.3.3).

The surface lanthanum concentration range corresponding to the maximum in E_a and A/SA in the La in ceria solid solution range, was observed to coincide with the bulk concentration range of lanthanum in ceria for which bulk anionic mobility is also maximised. Estimation of the variation in surface/grain-boundary conductivity with lanthanum concentration was effected based on the reasonable assumption that the conductivity in the surface varies similarly with composition, as does bulk conductivity. Using the surface segregation data and analysis presented in section 4.2 it was therefore possible to model the variation in surface conductivity with bulk composition, based on analysis of bulk conductivity literature data.⁵³ It was determined that the observed peaks in the catalytic properties occur at a surface composition at which surface conductivity is also maximised. Since conductivity has been related to the population of mobile vacancies within such ionic conductors, it was concluded that the CO oxidation catalytic properties are directly related to the population of mobile vacancies in the surface of the solid solution materials. This conclusion has several implications for the field of heterogeneous catalysis of such oxide materials, for reactions in which catalyst conductivity may influence the rate limiting step of the reaction mechanism. In previous

studies, the correlation of bulk conductivity and catalytic properties has been rather hit and miss, despite theoretical predictions of a correlation between the two properties. The influence of surface segregation processes on the surface conductivity (on which the catalytic reaction occurs), has not previously been allowed for, thus accounting for poor correlations between conductivity and catalytic properties in the past. This study has shown that a correlation does exist between CO oxidation catalytic properties and surface conductivity. Potentially, the application of surface conductivity optimisation techniques could be of use in the development of more efficient catalysts.

The peak in E_a and A/SA in the Ce in lanthana solid solution region also agreed well with data reported in the previously mentioned literature.³³ In the literature study³³, a further second maximum in bulk conductivity was observed in the Ce in lanthana solid solution region, which was explained in terms of a semi-conductivity, rather than ionic conductivity effect. Again it is tempting to relate the observed catalytic properties to a conductivity property of the materials. Although desirable, direct conductivity measurements within the present study were found to be impossible on the catalyst materials due to structural instability of test pellets following calcination at 800°C. As determined in the surface composition studies, calcination at higher temperatures would have resulted in enhanced surface lanthanum enrichment, and results would not have been comparable with catalytic study results. A possible avenue for future work would be the direct correlation between surface conductivity, (determined using ac. impedance spectroscopic techniques), and CO catalytic properties. The crucial factor in such a study would be the catalyst preparation method, so as to produce workable catalysts and samples suitable for conductivity measurements within a single preparative procedure. Such a study would also require custom designed apparatus for characterisation and catalytic activity testing of the suitably sintered materials.

Kinetic studies were completed for the CO oxidation reaction over ceria, lanthana and ceria/lanthana catalysts, (section 4.5.3.4). Over ceria, the reaction was determined to be pseudo first-order on P_{CO} , the reaction rate being well described in terms of P_{CO} by a Langmuir type isotherm expression. It was concluded that the active form of CO was an adsorbed CO molecule. With respect to P_{O_2} , the reaction rate was determined to vary between half-order at low P_{O_2} and zero-order at high P_{O_2} . The active

form of oxygen was concluded to be dissociated oxygen. A short and long term response to P_{O_2} was observed which was explained in terms of partial reduction of the ceria surface at low P_{O_2} . The resulting increase in the concentration of sites capable of dissociatively adsorbing (and therefore activating oxygen), was cited as explanation for the observed temporary increase in reaction rate following exposure to low P_{O_2} . The response of the reaction rate to P_{CO_2} was also tested and it was determined that there was a progressive and distinct retardation of reaction rate over ceria. This result was in marked contrast to previously reported literature data.¹³⁵ Under reaction conditions the orders on P_{CO} and P_{O_2} were effectively one and zero, respectively. It was therefore concluded that the retardation effect was most likely due to competitive adsorption between CO and CO_2 . A reaction mechanism was subsequently proposed in which adsorbed CO and dissociatively adsorbed oxygen are the active species, (section 4.5.3.4.1.4). Under the low temperature reaction conditions used in the study, a concerted reaction mechanism was proposed in which oxygen is adsorbed on Ce^{III} and CO is adsorbed on Ce^{IV} . The CO_2 product is capable of being adsorbed on Ce^{III} and Ce^{IV} , but is more strongly adsorbed on the more basic Ce^{III} . The kinetic expressions derived from the proposed mechanism were consistent with those derived experimentally. At higher temperatures it is expected that the concerted mechanism proposed would be superseded by a redox mechanism. The correlation between peaks in activation energy, specific pre-exponential factor and surface conductivity, provide limited evidence for the catalyst surface composition dependent onset of the redox mechanism; the enhanced surface conductivity resulting in increased surface reoxidation efficiency.

In the case of CO oxidation over lanthana, reaction rate was observed to exhibit dichotomous behaviour: at low P_{CO} the rate was observed to increase with increasing P_{CO} ; at high P_{CO} , the rate was observed to decrease with increasing P_{CO} . This phenomenon has not previously been reported in the literature for this catalyst/reaction system. It was proposed that the active CO species was a carbanionic dimer or short chain oligomer. In order to account for the dichotomous response of the reaction rate to P_{CO} , it was further proposed that the active CO species corresponded to a particular value of n for the $(CO)_n$ oligomer, (see later). A reaction rate order of 0.5 was

determined with respect to P_{O_2} , suggesting that the active oxygen species is dissociated oxygen, as was the case over ceria. The order on P_{O_2} was determined to increase with increasing reaction temperature, suggesting that oxygen is competitively adsorbed on the active site. TPD results further suggested that a Boudouard reaction type disproportionation ($2CO \rightarrow C + CO_2$) could be a possible intermediate stage in the oxidation reaction mechanism. The response of the reaction rate to P_{CO_2} was also tested and it was determined that CO_2 resulted in only very weak retardation of the reaction rate. It was concluded from this kinetic data that CO_2 adsorbs either on different sites to CO and O_2 , or that the $CO_{2(ads)} \leftrightarrow CO_{2(gas)}$ equilibrium lies well over to the right-hand-side under reaction conditions. The weak CO_2 reaction rate retardation effect did not lend support to the CO disproportionation reaction being an intermediate step in the oxidation reaction mechanism.

A further concerted oxidation mechanism was proposed incorporating the above points, where the active surface adsorption site is capable of adsorbing molecular oxygen dissociatively, and $(CO)_n$, such that n is greater than or equal to 2, (section 4.5.3.4.2.4). Reaction was proposed to occur between $(CO)_{n(ads)}$ and $O_{(ads)}$, providing there is an adjacent empty site capable of adsorbing the CO_2 product. Curve fitting of the derived kinetic rate expression to the experimental data determined that the $(CO)_{2(ads)}$ species produced the best model to fit the experimental data. It was therefore proposed that the active CO species was the adsorbed CO dimer. The other kinetic expressions derived from the proposed reaction mechanism were consistent with those derived experimentally. The existence of such a dimer species has been reported in the literature, but the characteristic IR bands reported were not observed in the *in situ* DRIFTS study. This may be due to the transient nature of such species.

Finally, further kinetic studies were completed for the bulk $x = 0.05$ sample, which was of particular interest following the determination of the maximisation of both E_a and A/SA at this composition, in the systematic study. A dichotomous response of reaction rate to P_{CO} was again observed, similarly as to the reaction over lanthana. The kinetic model derived in the lanthana study was shown to give a reasonable description of the experimental data over the bulk $x = 0.05$ sample, however the model predicted a far stronger retardation by P_{CO} than was observed experimentally. It was therefore

proposed that the observed reaction rate response to P_{CO} could be better represented in terms of two contributions to the total reaction rate: one exhibiting the dichotomous behaviour as determined over lanthana, the other exhibiting a Langmuir type adsorption isotherm type response, as determined over ceria. This revised model, (equation 4.80) was shown to give an excellent description of the bulk $x = 0.05$ catalyst experimental data. It can be concluded that at the surface of the mixed oxide catalysts, the oxidation of CO occurs by two separate mechanisms - effectively oxidation over ceria dominated centres and lanthana dominated centres, (section 4.5.3.4.3.1). The relative contribution of each mechanism to the total rate can reasonably be expected to vary proportionally with composition and the relative activity of the pure oxides. Accordingly, it is assumed that the model presented would provide a reasonable description of the behaviour of all of the materials within the ceria/lanthana system. These observations and the subsequent description of the CO oxidation reaction kinetics in terms of $CO/(CO)_2$ parallel mechanisms has not been previously reported in the literature.

In summary, (section 4.5.3.4.4), the response of reaction rate to P_{O_2} was determined to be half-order for all catalyst compositions. The CO_2 reaction rate retardation effect observed over ceria was found to decrease with surface lanthanum concentration and was attributed to competitive adsorption between CO and CO_2 . The retardation effect was determined to become weaker with increasing surface lanthanum concentration due to either adsorption of CO_2 on an alternative (inactive) site, or an equilibrium favouring desorption of CO_2 under reaction conditions. The variation in the reaction rate order on P_{CO} was determined to be the main distinguishing feature between reaction over ceria and lanthana. Over ceria, molecular CO was determined to be the active adsorbed species, whilst over lanthana the active adsorbed species was determined to be $(CO)_2$. A disproportionation reaction suggested by TPD results as an intermediate step in the CO oxidation reaction could thus be expressed as $(CO)_2 \rightarrow CO_2 + C$. The adsorbed carbon is assumed to be rapidly oxidised in the presence of gaseous oxygen by adsorbed molecular oxygen. Over the mixed ceria/lanthana oxides it was concluded that both molecular CO and $(CO)_2$ adsorbed species are oxidised simultaneously, each with the aforementioned kinetics. It was not possible in the case of

the mixed oxide to specify the oxidising species, but it can be reasonably be assumed to be dissociatively adsorbed molecular oxygen, in common with ceria and lanthana.

5.3.2 CH₄ Oxidation Systematic Study.

The systematic study of methane oxidation was completed generally at higher temperatures than the CO oxidation study. The standard activity measurements were completed at 560°C and therefore activities cannot be directly compared with CO measurements. Methane oxidation activity at 560°C was determined to be promoted by lanthanum doping, with respect to the activity of undoped ceria, (section 4.5.4.1). Activity per unit weight and specific activity measurements showed a broad peak in reaction rate under the standard conditions centred around an equicationic surface Ce : La ratio. This observation was of particular interest as literature data has suggested a possible two-step concerted reaction mechanism involving activation of methane by proton abstraction over a basic site, subsequently followed by a redox step. As was observed for the analogous CO oxidation results, variations in activity with composition beyond the solid solution limit are complex. The apparent synergistic effect of the equicationic Ce : La surface ratio was further investigated using a parametric response model. The promotion effect was thus determined to rely on a [Ce] dependent component and a [Ce][La] component, of which the latter was dominant. It was determined that surface cerium and lanthanum act synergistically in the catalytic oxidation of methane reaction mechanism over lanthanum doped ceria solid solution catalysts.

The response of reaction rate to temperature was analysed with systematic variation in catalyst composition using the Arrhenius method, to produce Activation energy (E_a) and specific pre-exponential (A/SA) data, (section 4.5.4.2). A non-symmetrical peak was observed in the methane oxidation reaction E_a and A/SA variations with catalyst composition. The peak was centred on the equicationic Ce : La surface composition, as was observed for the analogous variation in activity at the standard temperature. Beyond the solid solution limit, E_a and A/SA are both observed to rise in a linear fashion from surface $x = 0.92 - 1$. The two compensation effects

observed corresponding to the two solid solution regions in the ceria/lanthana series were demonstrated, (section 4.5.4.3).

Kinetic studies were completed in order to elucidate mechanistic data, similarly as was done for the CO oxidation reaction, (section 4.5.4.4). Over ceria the reaction rate was observed to be first-order with respect to P_{CH_4} , and a small positive order on P_{O_2} , well represented by a Langmuir adsorption isotherm type expression. It was concluded that adsorbed CH_4 was the active CH_4 species. (Adsorption of CH_4 was subsequently confirmed in the *in situ* DRIFTS studies, section 4.4.2.4). The reaction rate was observed to exhibit a strong retardation effect with P_{CO_2} , up to a limiting value. The observed reaction rate was concluded to be comprised of two components, one of which is retarded by CO_2 . The retardation was characterised by a half-order expression. It was therefore concluded that two sites exist, both capable of methane activation over ceria, one of which is activation rate retarded by CO_2 , and the other not. The existence of two components of total rate, one of which is retarded by CO_2 has not previously been reported in the literature.

A reaction scheme was proposed in which the two sites for methane adsorption were assumed to be coordinatively saturated (CS) and coordinatively unsaturated (CUS) anions sites¹³², (section 4.5.4.4.1.4). Competitive adsorption of CH_4 and CO_2 was proposed on the more basic CUS site, which was consistent with the observed two-component rate, one of which is retarded by CO_2 . The rate determining step (RDS) was proposed to be the activation of methane by proton abstraction. The methyl fragment formed by proton abstraction from methane was proposed to be either ionic or radical depending on whether activation occurred on the CS or the CUS site, respectively. The methyl fragment is proposed to be subsequently rapidly oxidised by the Ce^{IV} species, which is subsequently regenerated by dissociatively adsorbing oxygen from the gas phase. No requirement for reoxidation of the active sites by lattice oxygen was suggested by the kinetic studies, as has been claimed previously in the literature.¹⁵² Accordingly, no correlations between catalytic and conductivity properties were observed in this study of CH_4 oxidation.

The adsorption of CH_4 on the CS and CUS sites was confirmed under reaction conditions in the *in situ* DRIFTS study, (section 4.4.2.4), although evidence for the

adsorption CH_4 adsorption on the CUS site was weaker than for on the CS site. It was assumed that the active site on ceria comprises two adjacent cerium cations. A series of kinetic expressions were subsequently derived from the model which were found to be consistent with the experimental data.

In the case of methane oxidation over the lanthana catalyst, reaction rate was shown to depend on P_{CH_4} with an apparent order of 0.66 and was well described with a Langmuir adsorption isotherm type expression. A half order dependence of reaction rate on P_{O_2} was demonstrated, indicating that atomic oxygen is the active oxygen species. The response of reaction rate to P_{CO_2} was determined to be similar to that observed over ceria. The observed rate was shown to be comprised of two components, one of which is retarded in the presence of CO_2 . The methane oxidation reaction rate was therefore shown to be significantly influenced by P_{CH_4} , P_{O_2} and P_{CO_2} . A novel reaction scheme was proposed assuming CH_4 and dissociative O_2 adsorption on different sites, (section 4.5.4.4.2.4). Methane activation was assumed to occur by proton abstraction, and the rate retardation by CO_2 was assumed to be by competitive adsorption on the basic site, either blocking CH_4 adsorption, or weakening the polarisation of adsorbed CH_4 . A series of kinetic expressions were derived based on the proposed model, which were found to be consistent with analogous expressions derived from the experimental data.

The kinetics of the methane oxidation reaction were also investigated over mixed oxides. The bulk $x = 0.05$ catalyst was observed to show significant promotion of activity with respect to undoped ceria, and was of particular relevance for comparison with the CO oxidation reaction study. It was shown that the reaction mechanism of the bulk $x = 0.05$ sample was more akin to that of lanthana than ceria. Further investigation of other catalyst compositions revealed a progressive change in the calculated mean orders of reaction with respect to P_{CH_4} and P_{O_2} . On increasing the concentration of surface lanthanum, the reaction rate order on CH_4 was reduced, whilst the order on O_2 increased, thus implying that the increasing surface lanthanum concentration progressively lowers the activity of adsorbed O_2 , relative to that of adsorbed CH_4 . This effect was explained in terms of an increase in the concentration of base sites with surface lanthanum concentration resulting in a net increase in the activity of adsorbed methane and a progressive change in the oxygen activation stage.

In summary, (section 4.5.4.4.4), the synergistic effect arising from the equicationic Ce : La ratio is due to optimisation of the methane activation function enhancement provided by the enhanced basicity of surface lanthanum, in combination with the redox function provided by surface cerium, subsequently oxidising the carbanion formed by the activation of the methane over the basic lanthanum sites. Over the range of catalyst compositions tested, the reaction rate order on P_{CH_4} is always observed to be higher than on P_{O_2} . It is therefore proposed that the activation of methane is the major contribution toward the rate determining step throughout the whole range of catalyst compositions. However, the observed increase in the reaction rate order on P_{O_2} with increasing surface lanthanum suggests that the nature of the rate determining step does contain some contribution from the activation of oxygen. This points to a slowing of the oxidation stage relative to the reductive stage of the mechanism, with increasing surface lanthanum concentration.

It was determined that the promotion of activity was due to the increase in the pre-exponential factor of the rate expression, the number of active sites being maximised at $x = 0.504$. It can therefore be proposed that the active centre for the Ce/La synergistic CH_4 oxidation mechanism consists of one cerium cation and a neighbouring lanthanum cation. The basicity enhancement by incorporation of lanthanum into the ceria surface is responsible for activation of the methane, whilst the cerium cation is responsible for activation of the oxygen. Further increases in the lanthanum concentration in the surface can therefore be predicted to result in a decrease in the order on methane and an increase in the order on oxygen as the concentrations of their activation sites increase and decrease, respectively, with catalyst lanthanum concentration. These predicted variations were observed in the experimental data.

Chapter 6 References

- 1 N. N. Greenwood, A. Earnshaw, *Chemistry of the Elements*, 1984, Pergamon Press, Oxford, 1423, ISBN 0-08-022057-6.
- 2 N. N. Greenwood, A. Earnshaw, *Chemistry of the Elements*, 1984, Pergamon Press, Oxford, 1102, ISBN 0-08-022057-6.
- 3 Y-M Chiang, D. P. Birnie, W. D. Kingery, *Physical Ceramics : Principles for Ceramic Science and Engineering*, 1997, J. Wiley & Sons, Inc., USA, ISBN 0-471-59873-9.
- 4 B. G. Hyde, J. G. Thompson, R. L. Withers, *Materials Science and Technology - A Comprehensive Treatment*, Eds, R. W. Cahn, P. Haasen, E. J. Kramer, Volume 11, *Structure and Properties of Ceramics*, Volume Ed. M. V. Swain, 1994, VCH, Germany, 1, ISBN 3-527-26813-8.
- 5 E.C. Subbarao, H. S. Maiti, *Solid State Ionics*, 1984, **11**, 317.
- 6 G. Adachi, N. Imanaka, *Chem. Rev.*, 1998, **98**, 1479.
- 7 Hj. Matzke, *Nonstoichiometric oxides*, Ed. O. Toft Sørensen, 1981, Academic Press Inc., 155, ISBN 0-12-655280-0.
- 8 S. J. Hong, A. V. Virkar, *J. Am. Ceram. Soc.*, 1995, **78**, [2], 433.
- 9 B. Touzelin, *J. Nuclear Materials*, 1981, **101**, 92.
- 10 M. G. Sanchez, J. L. Gazquez, *J. Catal.*, 1987, **104**, 120.
- 11 B. C. H. Steele, J. M. Floyd, *Proc. Br. Ceram. Soc.*, 1971, **19**, 55.
- 12 E. C. Subbarao, H. S. Maiti, *Solid State Ionics*, 1984, **11**, 317.
- 13 H. L. Tuller, A. S. Nowick, *J. Electrochem. Soc.*, 1979, **126**, 209.
- 14 F. Millot, N. A. Younes, P. Gerdanian, *High Temperatures - High Pressures*, 1982, **14**, 725.
- 15 R. N. Blumenthal, P. W. Lee, R. J. Panlener, *J. Electrochem. Soc.*, 1971, **118**, [1], 123.
- 16 J. Jr. Faber, M. A. Seitz, M. H. Müller, *J. Phys. Chem. Solids*, 1967, **37**, 903
- 17 J. Jr. Faber, M. A. Seitz, M. H. Müller, *J. Phys. Chem. Solids*, 1967, **37**, 909
- 18 N. Giordano, V. Antonucci, J. C. J. Bart, R. Maggiore, *Z. anorg. allg. Chem.*, 1982, **484**, 195.
- 19 C. R. A. Catlow, *Nonstoichiometric oxides*, Ed., O. Toft Sørensen, 1981, Academic Press (London) - Materials Science Series, 61, ISBN 0-12-655280-0.
- 20 P. A. Cox, *Transition Metal Oxides*, 170, ISBN 0-19-855570-9.
- 21 Z. C. Kang, L. Eyring, *J. Alloys Compd.*, 1997, **249**, 206.
- 22 R. Korner, M. Ricken, J. Nölting, I. Riess, *J. Solid State Chem.*, 1989, **78**, 136.
- 23 A. Trovarelli, *Catal. Rev.*, 1996, **38**, [4], 439.
- 24 F. M. Z. Zotin, L. Tournayan, J. Varloud, V. Perrichon, R. Fréty, *Appl. Catal. A : General*, 1993, **98**, 99.

- 25 R. J. Friauf, *Physics of Electrolytes, Volume 2, Thermodynamics and Electrode Processes in Solid State Electrolytes*, Ed., J. Hladik, 1972, Academic Press - London, 1103, ISBN 0-12-349802-3.
- 26 B. D. Cullity, *Elements of X-ray diffraction*, 1959, Addison-Wesley Publishing Company Inc.
- 27 J. Hladik, *Physics of Electrolytes, Volume 2 - Thermodynamics and Electrode Processes in Solid State Electrolytes*, 1972, Academic Press - London, 867, ISBN 0-12-349802-3
- 28 J. D. Cawley, W. E. Lee, *Materials Science and Technology - A Comprehensive Treatment*, Eds., R. W. Cahn, P. Haasen, E. J. Kramer, Volume 11 - *Structure and Properties of Ceramics*, Volume Ed., M. V. Swain, 1994, 47, ISBN 3-527-26813-8
- 29 D.-J. Kim, *J. Am. Ceram. Soc.*, 1989, **72**, [8], 1415.
- 30 H. Inaba, H. Tagawa, *Solid State Ionics*, 1996, **83**, 1.
- 31 K. E. Adham, A. Hammou, *Solid State Ionics*, 1983, **9&10**, 905.
- 32 H. Arai, T. Kunisaki, Y. Shimizu, T. Seiyama, *Solid State Ionics*, 1986, **20**, 241.
- 33 G. Rienäcker, Y. Wu, *Z. Anorg. Allg. Chem.*, 1962, **315**, 121.
- 34 R. G. Haire, L. Eyring, *Handbook on the Physics and Chemistry of Rare Earths*, 1994, North Holland, Amsterdam, **18**, 413.
- 35 M. Pijolat, M. Prin, M. Soustelle, O. Touret, P. Nortier, *Solid State Ionics*, 1993, **63-65**, 781.
- 36 O. Toft Sørensen, *Nonstoichiometric oxides*, Ed., O. Toft Sørensen, 1981, Academic Press - London, Materials Science Series, 1, ISBN 0-12-655280-0.
- 37 L. Manes, *Nonstoichiometric oxides*, Ed., O. Toft Sørensen, 1981, Academic Press - London, Materials Science Series, 99, ISBN 0-12-655280-0.
- 38 J. A. Kilner, B. C. H. Steele, *Nonstoichiometric oxides*, Ed., O. Toft Sørensen, 1981, Academic Press - London, Materials Science Series, 233, ISBN 0-12-655280-0.
- 39 J. A. Kilner, *Solid State Ionics*, 1983, **8**, 201.
- 40 B. T. Kilbourn, *Cerium - A Guide to its Role in Chemical Technology* (undated promotional material published by Molycorp, Inc., NY. USA).
- 41 R. D. Shannon, *Acta Cryst*, 1976, **A32**, 751.
- 42 T. Kudo, H. Obayashi, *J. Electrochem. Soc.*, 1975, **122**, [1], 142.
- 43 A. R. West, *Solid State Chemistry and its Applications*, 1987, Wiley and Sons, Great Britain, 4, ISBN 0-471-90337-9.
- 44 A. Atkinson, *Materials Science and Technology - A Comprehensive Treatment*, Eds., R. W. Cahn, P. Haasen, E. J. Kramer, Volume 11 - *Structure and Properties of Ceramics*, Volume Ed., M. V. Swain, 1994, 295, ISBN 3-527-26813-8.
- 45 Y. M. Chiang, P. B. Dunbar, D. W. Kingery, *Physical Ceramics - Principles for Ceramic Science and Engineering*, 1997, Wiley and Sons, New York, 185.

- 46 *Nonstoichiometric Oxides*, Ed. O. Toft Sørensen, 1981, Academic Press - London, Materials Science Series, ISBN 0-12-655280-0.
- 47 A. B. Lidiard, *Handbuch der Physik*, 1957, **20**, 246.
- 48 A. R. Cooper, J. H. Heasley, *Acta Metall.*, 1966, **49**, 280.
- 49 R. Gerhardt, A. S. Nowick, *J. Am Ceram. Soc.*, 1986, **69**, [9], 641.
- 50 J. Tanaka, J-F. Baumard, P. Abelard, *J. Am. Ceram. Soc.*, 1987, **70**, [9], 637.
- 51 S. P. S. Badwal, *Materials Science and Technology - A Comprehensive Treatment*, Eds, R. W. Cahn, P. Haasen, E. J. Kramer, Volume 11, Structure and Properties of Ceramics, Volume Ed. M. V. Swain, 1994, VCH, Germany, 567, ISBN 3-527-26813-8
- 52 K. S. Goto, W. Pluschkell, *Physics of Electrolytes, Volume 2 - Thermodynamics and Electrode Processes in Solid State Electrolytes*, Ed. J. Hladik, 1972, Academic Press - London, 539, ISBN 0-12-349802-3.
- 53 T. Takahashi, *Physics of Electrolytes, Volume 2 - Thermodynamics and Electrode Processes in Solid State Electrolytes*, Ed. J. Hladik, 1972, Academic Press - London, 989, ISBN 0-12-349802-3.
- 54 C. R. A. Catlow, *Solid State Ionics*, 1993, **8**, 89.
- 55 J. A. Kilner, C. D. Waters, *Solid State Ionics*, 1982, **6**, 253.
- 56 C. R. A. Catlow, *Solid State Ionics*, 1984, **12**, 67.
- 57 D. K. Hohnke, *Solid State Ionics*, 1981, **5**, 531.
- 58 R. Gerhardt-Anderson, A. S. Nowick, *Solid State Ionics*, 1981, **5**, 547.
- 59 G. B. Balazs, R. S. Glass, *Solid State Ionics*, 1995, **76**, 155.
- 60 A. S. Nowick, D. Y. Wang, D. S. Park, J. Griffith, *Fast Ion Transport in Solids*, Eds., P. Vashishta, J. N. Mundy, G. K. Shenoy, 1979, Elsevier - Amsterdam, 673.
- 61 H. L. Tuller, *Nonstoichiometric Oxides* Ed., O. Toft Sørensen, 1981, Academic Press - London, Materials Science Series, 271, ISBN 0-12-655280-0.
- 62 T. Takahashi, K. Ito, H. Iwahara, *Proc. J. Intl. Piles, Combust.*, 1965, **1-3**, 42.
- 63 D. Y. Wang, D. S. Park, J. Griffith, A. S. Nowick., *Solid State Ionics*, 1981, **2**, 95.
- 64 H. Yahiro, K. Eguchi, H. Arai, *Solid State Ionics*, 1989, **36**, 71.
- 65 H. L. Tuller, A. S. Nowick, *J. Electrochem. Soc.*, 1979, **122**, 255.
- 66 I. K. Naik, T. Y. Tien, *J. Electrochem. Soc.*, 1979, **126**, 562.
- 67 C. Ftikos, M. Nauer, B. C. H. Steele, *J. Europ. Ceram. Soc.*, 1993, **12**, 267.
- 68 M. R. DeGuire, M. J. Shingler, E. Dincer, *Solid State Ionics*, 1992, **52**, 155.
- 69 J. A. Kilner, R. J. Brook, *Solid State Ionics*, 1982, **6**, 237.
- 70 R. T. Dirstine, R. N. Blumenthal, T. F. Kuech, *J. Electrochem. Soc.*, 1979, **126**, [2], 264.
- 71 K. Eguchi, T. Setoguchi, T. Inoue, H. Arai, *Solid State Ionics*, 1992, **52**, 165.
- 72 N. N. Greenwood, A. Earnshaw, *Chemistry of the Elements*, 1984, Pergamon Press - Oxford, 1497, ISBN 0-08-022057-6.

- 73 V. Butler, C. R. A. Catlow, B. E. F. Fender, J. H. Harding, *Solid State Ionics*, 1983, **8**, 109.
- 74 K. E. Adham, A. Hammou, *Progress in Solid Electrolytes*, Eds., T. A. Wheat, A. Ahmad, A. K. Kuriakose, 1983, Ottawa: Energy Mines and Resources, ERP/MSL **83-94**, 313.
- 75 J. Nowotny, J. B. Wagner, Jr., *Oxid. Metals*, 1981, **15**, 169.
- 76 Z. Adamczyk, J. Nowotny, *J. Phys. Chem. Solids*, 1986, **47**, 11.
- 77 J. Nowotny, *Science of Ceramic Interfaces*, Ed., J. Nowotny, 1991, Elsevier - Amsterdam, 79.
- 78 P. Menon, P. S. R. Prasada Rao, *Catal. Rev.*, 1981, **20**, [1], 97.
- 79 J. Nowotny, *Solid State Ionics*, 1988, **28-30**, 1235.
- 80 M. C. Kung, H. H. Kung, *Surf. Sci.*, 1981, **104**, [1], 253.
- 81 P. J. Jorgensen, *J. Am. Ceram. Soc.*, 1965, **48**, [4], 207.
- 82 A. E. Hughes, *Science of Ceramic Interfaces II*, Materials Science Monographs, **81**, Ed., J. Nowotny, 1994, Elsevier - Amsterdam, 183.
- 83 W. Hartweck, H. J. Crabke, *Surf. Sci.*, 1979, **89**, 174.
- 84 M. P. Seah, *Surf. Sci.*, 1975, **53**, 168.
- 85 K. Myoshi, D. H. Buckley, M. Srinivasan, *Ceramic Bulletin*, 1983, **62**, [4], 494.
- 86 P. Wynblatt, R. C. McCune, *Surface and Near Surface Chemistry of Oxide Materials*, Eds., J. Nowotny, L.-C. Dufour, 1988, Elsevier - Amsterdam, 247.
- 87 A. J. Burggraaf, A. J. A. Winnubst, *Surface and Near Surface Chemistry of Oxide Materials*, Eds., J. Nowotny, L.-C. Dufour, 1988, Elsevier - Amsterdam, 449.
- 88 J. Nowotny, *Solid State Ionics*, 1991, **49**, 119.
- 89 E. D. Hondros, M. P. Seah, *Intern. Metals. Rev.*, 1977, **222**, 262.
- 90 D. McLean, *Grain Boundaries in Metals*, 1957, Oxford University Press, London, 116
- 91 C. Lea, M. P. Seah, *Philosophical Magazine*, 1977, **35**, [1], 213.
- 92 G. Rowlands, D. P. Woodruff, *Philosophical Magazine A*, 1979, **40**, [4], 459.
- 93 D. Y. Wang, A. S. Nowick, *J. Solid State Chem.*, 1980, **35**, 325.
- 94 M. Kleitz, E. Siebelt, J. Fouletier, *Chemical Sensors*, Eds., T. Seiyama, K. Fueki, J. Shiokawa, S. Suzuki, 1988, Kodansha/Elsevier - Japan, 105.
- 95 D. L. Maricle, T. E. Swarr, S. Karavolis, *Solid State Ionics*, 1992, **52**, 173.
- 96 B. G. Pound, *Solid State Ionics*, 1992, **52**, 183.
- 97 P. G. Harrison, D. A. Creaser, B. A. Wolfindale, K. C. Waugh, M. A. Morris, W. C. Mackrodt, *Catalysis and Surface Characterisation*, Eds., T. J. Dines, C. H. Rochester, J. Thomson, 1992, ISBN 0-85186-335-3.
- 98 P. G. Harrison, *Catalysis Today*, 1993, **17**, 483.
- 99 W. C. Mackrodt, U.S. Patent No 3, 070, 165, 1991
- 100 *Interfacial Segregation*, Eds., Johnson, W. C., Blakely, J. M., 1979, USA, ISBN 0-87170-004-2.

- 101 J. W. Gibbs, *The Scientific Papers of J. Willard Gibbs*, 1961, 1, Dover, New York, 219.
- 102 A. M. Stoneham, P. W. Tasker, *Surface and Near Surface Chemistry of Oxide Materials*, Eds., J. Nowotny, L.-C. Dufour, 1988, Elsevier - Amsterdam, 1.
- 103 T. X. T. Sayle, S. C. Parker, C. R. A. Catlow, *J. Phys. Chem.*, 1994, **98**, 13625.
- 104 W. C. Mackrodt, P. W. Tasker, *J. Am. Ceram. Soc.*, 1989, **72**, [9], 1576.
- 105 P. W. Tasker, E. A. Colbourn, W. C. Mackrodt, *J. Am Ceram. Soc.*, 1985, **68**, [2], 74.
- 106 P. Wynblatt, R. C. Ku, *Surf. Sci.*, 1977, **65**, 511.
- 107 V. D. Sokolovskii, *Catal. Rev.-Sci. Eng.*, 1990, **32**, [1&2], 1.
- 108 C. N. Satterfield, *Heterogeneous Catalysis in Industrial Practice*, 1991, 267, ISBN 0-07-054886-2
- 109 C. N. Satterfield, *Heterogeneous Catalysis in Industrial Practice*, 1991, 53, ISBN 0-07-054886-2
- 110 H. C. Yao, Y. F. Yu Yao, *J. Catal.*, 1984, **86**, 254.
- 111 J. C. Summers, S. A. Ausen, *J. Catal.*, 1979, **58**, 131.
- 112 W. Liu, M. Flytzani-Stephanopoulos, *J. Catal.*, 1995, **153**, 304.
- 113 F. Zamar, A. Trovarelli, C. de Leitenburg, G. Dolcetti, *J. Chem. Soc. Chem. Commun.*, 1995, 965.
- 114 Z. Yu, X. Yang, J. H. Lunsford, M. P. Rosynek, *J. Catal.*, 1995, **154**, 163.
- 115 P. J. Gellings, H. J. M. Bouwmeester, *Catalysis Today*, 1992, **12**, 1.
- 116 A. A. Davydov, *Infrared Spectroscopy of Adsorbed Species on the Surface of Transition Metal Oxides*, 1984, Wiley and Sons, UK, 6, ISBN 0-471-91813-X.
- 117 C. Li, Y. Sakata, T. Arai, K. Domen, K. Maruya, T. Onishi, *J. Chem. Soc. Faraday Trans. I*, 1989, **85**, [4], 929.
- 118 F. Bozon-Verduraz, A. Bensalem, *J. Chem. Soc. Faraday Trans.*, 1994, **90**, [4], 653.
- 119 T. X. T. Sayle, S. C. Parker, C. R. A. Catlow, *Surface Science*, 1994, **316**, 329.
- 120 T. Arai, K. Maruya, K. Domen, T. Onishi, *J. Catal.*, 1993, **141**, 533.
- 121 C. Binet, A. Badri, M. Boutonnet-Kizling, J-C. Lavalley, *J. Chem. Soc. Faraday Trans.*, 1994, **90**, [7], 1023.
- 122 C. Li, Y. Sakata, T. Arai, K. Domen, K. Maruya, T. Onishi, *J. Chem. Soc. Chem. Commun.*, 1991, 410.
- 123 M. Bailes, S. Bordiga, F. S. Stone, A. Zecchina, *J. Chem. Soc. Faraday Trans.*, 1996, **92**, [23], 4675.
- 124 A. Zecchina, F. S. Stone, *J. Chem. Soc. Faraday Trans. I*, 1978, **74**, 2278.
- 125 M. Che, A. J. Tench, *Adv. Catal.*, 1982, **31**, 77.
- 126 M. Che, A. J. Tench, *Adv. Catal.*, 1983, **32**, 1.
- 127 J. J. Spivey, *Ind. Eng. Chem. Res.*, 1987, **26**, [11], 2165.

- 128 W. Liu, M. Flytzani-Stephanopoulos, *J. Catal.*, 1995, **153**, 317.
- 129 X. Zhang, K. J. Klabunde, *Inorg. Chem.*, 1992, **32**, 1706.
- 130 C. Li, K. Domen, K-I. Maruya, T. Onishi, *J. Am. Chem. Soc.*, 1989, **111**, 7683.
- 131 C. Li, K. Domen, K-I. Maruya, T. Onishi, *J. Catal.*, 1990, **123**, 436.
- 132 C. Li, Q. Xin, *J. Phys. Chem.*, 1992, **96**, 7714.
- 133 T. Ito, T. Watanabe, T. Tashiro, K. Toi, *J. Chem. Soc., Faraday Trans. I*, 1989, **85**, [8], 2381.
- 134 J. M. Thomas, W. J. Thomas, W. J., *Introduction to the Principles of Heterogeneous Catalysis*, 1967, Academic Press - London, 365.
- 135 M. Breysse, M. Guenin, B. Claudel, H. Latreille, J. Véron, *J. Catal.*, 1972, **27**, 275.
- 136 J. Castiglioni, R. Kieffer, F. J. Botana, J. J. Calvino, J. M. Rodríguez-Izquierdo, H. Vidal, *J. Alloys and Compounds*, 1992, **180**, 295.
- 137 W. Liu, A. F. Sarofim, M. Flytzani-Stephanopoulos, *J. Appl. Catal. B: Environmental*, 1994, **4**, 167.
- 138 W. Liu, A. F. Sarofim, M. Flytzani-Stephanopoulos, *Chem. Eng. Sci.*, 1994, **49**, [24A], 4871.
- 139 K. S. Chan, J. Ma, S. Jaenicke, G. K. Chuah, J. Y. Lee, *Appl. Catal. A: Gen.*, 1994, **107**, 201.
- 140 T. Hattori, J-I. Inoko, Y. Murukami, *J. Catal.*, 1976, **42**, 60.
- 141 A. M. Maitra, *Appl. Catal. A : General*, 1993, **104**, 11.
- 142 K. D. Campbell, H. Zhang, J. H. Lunsford, *J. Phys. Chem.*, 1988, **92**, 750.
- 143 C-H. Lin, K. D. Campbell, J-X. Wang, J. H. Lunsford, *J. Phys. Chem.*, 1986, **90**, 534.
- 144 V. D. Sokolovskii, O. V. Buyevskaya, S. M. Aliev, A. A. Davydov, *Stud. Surf. Sci. Catal.*, 1990, **55**, 437.
- 145 A. M. Maitra, *J. Therm. Anal.*, 1990, **36**, 657.
- 146 V. R. Choudhary, V. H. Rane, *J. Catal.*, 1991, **130**, 411.
- 147 A. M. Maitra, I. Campbell, R. J. Tyler, *Appl. Catal. A : General*, 1992, **85**, 27.
- 148 S. Lacombe, H. Zanthoff, C. Mirodatos, *J. Catal.*, 1995, **155**, 106.
- 149 S. Lacombe, C. Geantet, C. Mirodatos, *J. Catal.*, 1994, **151**, 439.
- 150 K. Otsuka, A. A. Said, K. Jinno, T. Komatsu, *Chemistry Letters*, 1987, 77.
- 151 K-I. Machida, M. Enyo, *J. Chem. Soc. Chem. Commun.*, 1987, 1639.
- 152 Lj. Kundakovic, M. Flytzani-Stephanopoulos, *J. Catal.*, 1998, **179**, 203.
- 153 A. Guinier, *X-Ray Crystallographic Technology*, 1952, Hilger and Watts Ltd. - London.
- 154 B. E. Warren, *X-Ray Diffraction*, 1969, Addison-Wesley Publishing Company, Inc. - USA.
- 155 A. J. C. Wilson, *Elements of X-Ray Crystallography*, 1970, Addison-Wesley Publishing Company, Inc. - USA.
- 156 A. Guinier, D. L. Dexter, *X-Ray Studies of Materials*, 1963, Wiley and Sons, USA.

- 157 L. V. Azároff, *Elements of X-Ray Crystallography*, 1968, McGraw-Hill Book Company - USA.
- 158 G. H. Stout, L. H. Jensen, *X-Ray Structure Determination - A practical Guide*, 1968, Collier-Macmillan Ltd. - London.
- 159 M. M. Woolfson, *An Introduction to X-Ray Crystallography*, 1978, Cambridge University Press - Great Britain, ISBN 0-521-29343-X
- 160 G. C. Bond, *Heterogeneous Catalysis - Principles and Applications*, 2nd Edition, Eds. P. W. Atkins, J. S. E. Holker, A. K. Holliday, 1987, Oxford University Press, ISBN 0-19-855525-3.
- 161 J. R. Anderson, K. C. Pratt, *Introduction to Characterisation and Testing of Catalysts*, 1985, Academic Press - London, ISBN 0 12 058320 8.
- 162 T. Edmonds, *Characterisation of Catalysts*, Eds., J. M. Thomas, R. M. Lambert, 1980, J. Wiley and Sons - Great Britain, (1980), 30, ISBN 0-471-27874-2.
- 163 *Catalyst Characterisation Science - Surface and Solid State Chemistry*, Eds., M. L. Deviney, J. L. Gland, ACS Symposium Series, (1985), USA, ISBN 0-8412-0937-5.
- 164 *Surface and Near-Surface Chemistry of Oxide Materials*, Materials Science Monographs, Eds., J. Nowotny, L.-C. Dufour, 1988, 47, Elsevier, Amsterdam, ISBN 0-444-42954-9.
- 165 *Science of Ceramic Interfaces II*, Materials Science Monographs Ed., J. Nowotny, 1994, Elsevier - Amsterdam, ISBN 0-444-81666-6.
- 166 G. A. Somorjai, *Introduction to Surface Chemistry and Catalysis*, 1994, J. Wiley and Sons, Inc., USA, 382, ISBN 0-471-03192-5.
- 167 J. M. Thomas, W. J. Thomas, *Introduction to the Principles of Heterogeneous Catalysis*, 1967, Academic Press - London, 451.
- 168 C. N. Satterfield, *Heterogeneous Catalysis in Industrial Practice*, 2nd Edition, 1991, McGraw-Hill, Inc., USA, 471, ISBN 0-07-054886-2.
- 169 S. Y. Lui, M. H. King, *Surf. Sci.*, 1981, 110, 504.
- 170 R. Defay, I. Prigogine, A. Bellmans, D. H. Everett, *Surface Tension and Adsorption* 1966, J. Wiley and Sons - New York, 158.
- 171 *Interfacial Segregation*, Eds., W. C. Johnson, J. M. Blakely, 1977, Seminar of the Materials Science Division, American Society for Metals, 115.
- 172 A. A. Davydov, *Infrared Spectroscopy of Adsorbed Species on the Surface of Transition Metal Oxides*, Ed. C. H. Rochester, 1990, Wiley and Sons, 174.
- 173 F. A. Kröger, *The Chemistry of Imperfect Crystals*, 1964, North-Holland Publ., Amsterdam, Wiley, New York.
- 174 F. A. Kröger, H. J. Vink, *Solid State Phys.*, 3, 307
- 175 Nat. Bur. Stand. (U.S.) Monogr. 25; 20 38; 1983
- 176 Natl. Bur. Stand. (U.S.), Circ. 539; 3 33; 1954; Swanson, Fuyat.
- 177 I. Langmuir, *J. Am. Chem. Soc.*, 38, 2221

- 178 B. C. Gates, *Catalytic Chemistry*, 1992, J. Wiley & Sons, ISBN 0-471-55914-8
- 179 G. C. Bond, *Heterogeneous Catalysis - Principles and Applications*, 2nd Edition, Eds. P. W. Atkins, J. S. E. Holker, A. K. Holliday, 1987, Oxford University Press, 12, ISBN 0-19-855525-3
- 180 S. Brunauer, P. H. Emmett, E. Teller, *J. Am. Chem. Soc.*, 1938, **60**, 309.
- 181 K. S. W. Sing, D. H. Everett, R. A. W. Haul, L. Moscou, R. A. Pierotti, J. Rouquérol, T. Siemieniewska, *Pure and Applied Chem.*, 1985, **57**, [4], 603.
- 182 J. C. Rivière, *Practical Surface Analysis*, 2nd Edition, Volume 1 - *Auger and X-ray Photoelectron Spectroscopy*, Eds., D. Briggs, M. P. Seah, 1990 J. Wiley and Sons - Great Britain, ISBN 0-471-92081-9
- 183 C. N. Satterfield, *Heterogeneous Catalysts in Industrial Practice*, 2nd Edition, 1991, McGraw-Hill Inc. - New York, 165, ISBN 0-07-054886-2
- 184 *Spectroscopy in Heterogeneous Catalysis*, W. Nicholas Delgass, G. L. Haller, R. Kellerman, J. H. Lunsford, 1979, Academic Press - United Kingdom, 267.
- 185 C. R. Brundle, *Surface Science*, 1975, **48**, 99.
- 186 M. P. Seah, W. A. Dench, *Surf. Int. Anal.*, 1979, **1**, 2.
- 187 *Principles of Instrumental Analysis*, 4th edition, D. A. Skoog, J. J. Leary, 1992, Saunders College Publishing, ISBN 0-03-075398-8
- 188 J. M. Scofield, *J. El. Spec. Rel. Ph.*, 1976, **8**, 129.
- 189 R. F. Reilman, A. Msegane, S. T. Manson, *J. El. Spec. Rel. Ph.*, 1976, **8**, 389.
- 190 M. P. Seah, *Surf. Int. Anal.*, 1980, **2**, [6], 2222.
- 191 *Photoemission and the Electronic Properties of Surfaces*, Eds., B. Feuerbacher, B. Fitton, R. F. Willis, 1978, J. Wiley and Sons, Great Britain, ISBN 0-471-99555-X.
- 192 *Practical Surface Analysis*, 2nd Edition, Volume 1 - *Auger and X-ray Photoelectron Spectroscopy*, Eds., D. Briggs, M. P. Seah, 1990, J Wiley and Sons - Great Britain, ISBN 0-471-92081-9.
- 193 W. A. Fraser, J. V. Florio, W. N. Delgass, W. D. Robertson, *Surface Sci.*, 1973, **36**, 661.
- 194 G. Kortum, *Reflectance Spectroscopy, Principles, Methods and Applications*, 1969, Springer-Verlag, Berlin and New York.
- 195 R. W. Frei, M. M. Frodyma, V. T. Lieu, *Comprehensive Analytical Chemistry*, Volume 4, Eds., Svehla, G., 1975, Elsevier, Amsterdam, 263, ISBN 0-444-41163-1
- 196 W. N. Delgass, G. L. Haller, R. Kellerman, J. H. Lunsford, *Spectroscopy in Heterogeneous Catalysis*, 1979, Academic Press - London, 86, ISBN 0-12-210150-2
- 197 P. Kubelka, F. Munk, *Z. Tech. Phys.*, 1931, **12**, 593.

Appendix 2.1

Kröger Vink Notation^{173 - 174}

Kröger Vink notation is a means by which defects can be defined relative to a "perfect" crystal and consists of three separate elements. Firstly, the defect is identified by either the chemical symbol for the defective species or a "V" if the defect is a vacancy. Subsequently, a subscript is used to denote the site occupied by the defect, either the normal atom sites within the host lattice (denoted by the chemical symbol for such) or by an "i" for an interstitial defect. Finally the relative charge of the defect with respect to a "perfect" lattice is denoted by a superscript. Generally dashes (') are used to represent negative effective charges and dots (*) are used to represent positive effective charges. If there is no effective relative charge then the superscript is generally left blank, although occasionally a subscript x is used. The following are illustrative examples pertinent to species encountered in this study of the fluorite structured ceria/lanthana solid solution system:-

O_O or O_O^x An oxygen in an oxygen lattice site - no relative charge.

V_O^{**} An oxygen vacancy with an effective double positive charge relative to a "perfect" lattice.

Ce_{Ce} or Ce_{Ce}^x A cerium atom in a cerium lattice position - no relative charge.

La'_{Ce} A lanthanum cation in a cerium cation site with an effective single negative charge relative to a "perfect" lattice.

Ce'_{Ce} A reduced cerium ion (Ce^{III} rather than Ce^{IV}) in a cerium cation site with an effective single negative charge relative to a "perfect" lattice.

The Kröger Vink notation provides a useful descriptive tool for the solid state chemist to define defects within ionic materials in a precise manner. The association of defects can also be denoted with the use of parentheses, the effective charge of the associated defects represented by a superscript outside the parentheses. Similarly, the concentration of a particular defect can be denoted with the use of square brackets, as is the usual convention.

The limitations of the Kröger Vink notation system is that in complex systems with several cationic species and alternative lattice sites, the notation can only be considered to be arbitrary at best, a situation which is further complicated by the presence of cationic species with variable valence states. However, in relatively simple, consistent systems, such as the fluorite ceria/lanthana solid solutions which are isostructural over a wide range of dopant levels, the system is adequate and of great use.

Appendix 3.1

Raw materials

For all materials prepared by the ceramic method, the following raw materials were used;

Ce(NO₃)₃ · 6H₂O	99.99%	Mw = 434.25
	Johnson Matthey (Alfa) Batch 1129 6/2/96	

La(NO₃)₃ · 6H₂O	99.99%	Mw = 433.02
	Aldrich	Batch MN09816AN 24/1/96

For all materials prepared by the coprecipitation method, the following raw materials were used;

NH₄HCO₃	99%	Mw = 79.06
	Aldrich	

Ce(NO₃)₃ · 6H₂O	99.99%	Mw = 434.25
	Johnson Matthey (Alfa) Batch 1129 6/2/96	
	Aldrich	Batch 01128TW

La(NO₃)₃ · 6H₂O	99.99%	Mw = 433.02
	Aldrich	Batch MN09816AN 24/1/96

Pr(NO₃)₃ · 6H₂O	99.99%	Mw = 326.92
	Johnson Matthey (Alfa) Batch P1122	6/2/96
	Aldrich	Batch 15909BX

Appendix 3.2

The following account of the history, theory, development and use of X-ray powder diffraction techniques is based on several general review publications and common text-books.^{26, 43, 153 - 159}

A3.2.1 The Production of X-Rays

X-rays were first discovered accidentally in the summer of 1895 by W. C. Röntgen, a physics professor at the University of Wurzburg, in Bavaria. Whilst experimenting with a cathode-ray tube, a screen made from barium platinocyanide crystals, placed some distance away from the tube was observed to fluoresce each time he sent a pulse of cathode-rays through the tube. It was clear to Röntgen that the cathode rays were not responsible for the observed fluorescence, as they would be absorbed by the glass tube. Further experimentation determined that the radiation responsible for the fluorescence originated from the glass tube where the cathode-rays were incident, that it was propagated in a straight line, and was absorbed by matter to a much smaller extent than cathode-rays. He also determined that this new radiation was produced more efficiently by a metal target for the cathode-rays, rather than the wall of the glass tube. His most renowned achievement was probably the production of the first radiograph of the human hand, from which was spawned the invaluable medical applications of such radiation. As the true nature of these new rays was unknown, Röntgen called them X-rays.

Over the following years, research into X-rays increased in both the fields of physics and medicine, the most notable discoveries being the discovery of crystal back-scattering (Winkelmann and Straubel, 1896), the transverse wave nature of X-rays (Barkla, 1905), and the strong target-metal characteristic components of X-rays which were later related to the K and L electrons in the target atoms, in accordance with the Bohr atomic model, (also Barkla, 1909).

It was not until 1912, however, that diffraction of X-rays by a crystal was demonstrated (Friedrich and Knipping). Subsequently, Max Laue applied his

knowledge of the diffraction theory of light by gratings to the problem of three dimensional grating X-ray diffraction by a crystal, which was published in 1912, and for which he received the Nobel prize in 1914.

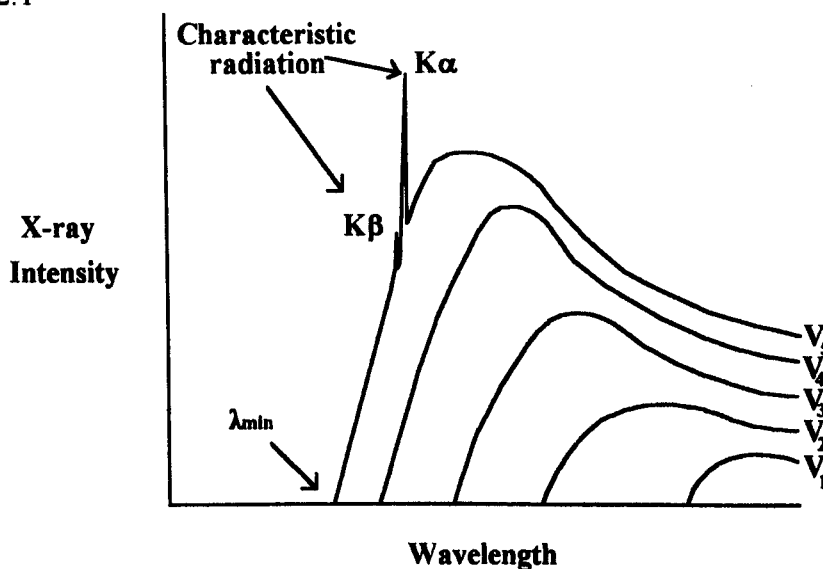
X-rays are now known to be electromagnetic radiation with wavelengths in the region of 1 \AA (10^{-10} m), the X-rays used for diffraction studies having wavelengths between $5 \times 10^{-11}\text{ m}$ and $2.5 \times 10^{-10}\text{ m}$.

X-rays are produced when charged particles with high kinetic energy (usually electrons) are decelerated on collision with matter. The X-radiation is generally produced in an X-ray tube which contains a source of electrons (produced by thermionic emission), and two metal electrodes. An voltage of the order of tens of thousands of volts across the electrodes accelerates the electrons toward a metal anode (target), which they impact with high kinetic energy, (for modern X-ray diffraction studies, copper is generally the target material used). On impact, most of the kinetic energy lost by the electrons is converted to heat, however a proportion of the energy lost in the deceleration process (less than 1%), is converted to electromagnetic radiation. The resulting rays are found to consist of many different wavelengths, the variation in intensity with wavelength depending on the tube voltage.

Such processes result in a continuous spectrum of X-rays known as "white radiation, which have wavelengths ranging upwards from a certain lower limiting value corresponding to the X-rays of highest energy. This occurs when all of the kinetic energy of the incident particles is converted to X-rays, and can be determined via $\lambda_{\min}(\text{\AA}) = 12400 / V$ where V is the accelerating voltage.⁴³ The origin of the continuous spectrum is due to the rapid deceleration of electrons hitting the target, however as not all electrons are decelerated in a single step (due to path deviations caused by target material atoms), fractions of kinetic energy are lost in a series of successive decelerations, thus resulting in a continuous spectrum of wavelengths above λ_{\min} .

When the accelerating voltage is raised above a certain target-metal characteristic value, sharp intensity maxima are observed at certain wavelengths, superimposed on the continuous spectrum, as shown in figure A3.2.1. Further increases in voltage results in increases in the intensity of the characteristic lines, the wavelengths remaining unchanged.

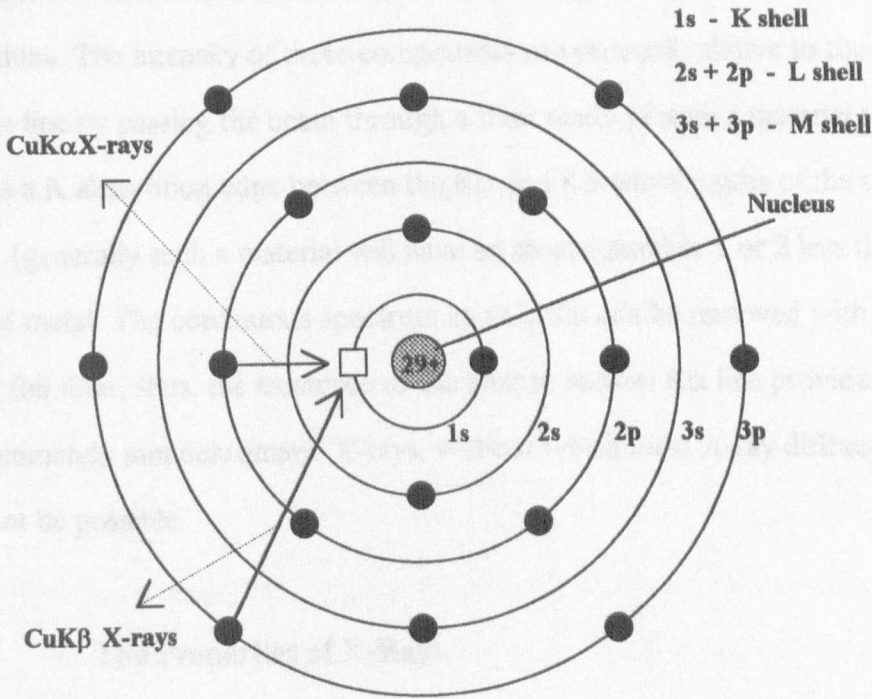
Figure A3.2.1



This figure shows the variation in X-ray intensity with wavelength as the accelerating voltage is increased from V_1 to V_5 . The total X-ray emitted per second is proportional to the area under each curve. The onset of the production of characteristic X-rays (K α and K β) is observed to occur for an accelerating voltage between V_4 and V_5 .

The origin of the characteristic X-rays stems from an initial ionisation of core level electrons within the target material (e.g., Cu 1s most commonly). An electron in an outer orbital immediately drops down to occupy the vacant core level and the resulting energy loss from the transition is emitted in the form of X-rays, (Figure A3.2.2). The K, L and M electronic shells can each be ionised and electron transitions down to these levels give rise to corresponding sets of lines of increasing emission wavelengths, respectively. Generally only the K lines have sufficiently high energy for use in diffraction studies, as the longer wavelengths are too easily absorbed. As these transitions have fixed energies for a given material, a material characteristic X-ray emission spectrum results.

Figure A3.2.2 The mechanism for the formation of Cu $K\alpha$ and Cu $K\beta$ X-rays.



X-rays are generated by the transition of an electron from a higher orbital to the vacancy in the 1s level (\square). Transition from the 2p level results in $K\alpha$ emission, transition from the 3p level results in $K\beta$ emission. The complete electronic structure of a copper atom is $1s^2 2s^2 2p^6 3s^2 3p^6 3d^{10} 4s^1$, but to avoid confusion the 3d and 4s orbitals are not shown in the figure.

The characteristic energies are primarily dependent on the causative electron transition, for example copper exhibits two characteristic peaks in its X-ray emission spectrum, the first at 1.5418\AA (known as Cu $K\alpha$), and a smaller peak at 1.3922\AA (known as Cu $K\beta$). The Cu $K\alpha$ originates from a $2p \rightarrow 1s$ transition and the Cu $K\beta$ originates from the less frequent $3p \rightarrow 1s$ transition. It is generally the more intense Cu $K\alpha$ that is used in diffraction experiments. It should be noted that due to the two possible spin states of the p electrons, relative to the spin of the vacant 1s orbital, the resulting Cu $K\alpha$ actually consists of a doublet, $K\alpha_1$ (1.54051\AA) and $K\alpha_2$ (1.54433\AA), therefore in diffraction experiments separate diffraction peaks may be therefore observed. It is possible to remove the weaker $K\alpha_2$ from the incident radiation, or (as in the present study), subtract the $K\alpha_2$ from the resulting diffraction patterns using instrument software techniques. There is a requirement for monochromatic (or near

monochromatic) X-radiation for most diffraction experiments. Thus, for the copper X-ray example it is desirable to remove the continuous spectrum and Cu $K\beta$ contributions. The intensity of these components can be reduced relative to the intensity of the $K\alpha$ line by passing the beam through a filter made of such a material that possesses a K absorption edge between the $K\alpha$ and $K\beta$ wavelengths of the target material. (generally such a material will have an atomic number 1 or 2 less than that of the target metal. The continuous spectrum and Cu $K\beta$ can be removed with the use of a Nickel foil filter, thus, the existence of the intense narrow $K\alpha$ line provides a source of approximately monochromatic X-rays, without which most X-ray diffraction work would not be possible.

A3.2.2 The Properties of X-Rays

In common with all electromagnetic radiation, for a monochromatic beam travelling in a direction x , there is an associated perpendicular electric field (E), and an associated magnetic field (H) which lies mutually perpendicular to both x and E . It is the interaction of the electric field associated with the X-ray with the electrons in a material that results in the diffraction phenomenon. If the electric field is plane polarised (i.e., restricted to the x E plane as the wave propagates, then E is found to oscillate in a regular manner with both time and distance in the direction of propagation, x . The exact form of the wave (e.g., sinusoidal, etc.), is not significant, the periodicity of the wave being of greater importance. Diffraction processes rely on the way monochromatic (identical wavelength) waves interfere with each other. Depending on the phase of the interfering waves the interference can be additive or destructive in terms of the combined electric field vector of the two waves. The two extreme cases occur when the waves are either in phase (constructive interference) where the two waves reinforce each other, or $\lambda/2$ out of phase (destructive interference), which results in a zero electric field vector. All other combinations caused by variation in phase differences between the interfering waves are possible, the classic demonstration of this phenomenon being the "Young's Slits" experiment, (originally performed by Thomas Young in the early nineteenth century). In this

experiment, light diffracted from two pinholes or two narrow parallel slits resulted in a series of light and dark bands, or *interference fringes* on a screen placed in the path of the light. The diffraction of X-rays by crystalline materials differs from this basic conceptual experiment in that X-rays are used as their wavelengths are of the same order of magnitude as the inter-atomic distances in crystalline materials, and that the crystal acts as a three dimensional diffraction grating rather than a two dimensional pair of slits.

A3.2.3 **Diffraction**

Diffraction is essentially a scattering phenomenon and a diffracted beam may be defined as a beam composed of a large number of scattered rays which constructively interfere with each other. In X-ray diffraction, the sinusoidal variation in the electric field associated with the incident electro-magnetic wave interacts with electrons in the crystal, resulting in the electron undergoing oscillatory motion around its mean position. The rapid acceleration and deceleration of the electron results in the emission of x-rays (in much the same way as with the production of the primary source X-rays, by high energy electron stimulation of a metal, as discussed previously). This radiated or *scattered* beam has by default the same wavelength and frequency as the incident X-ray beam, and has a fixed definite phase relationship (coherence) with the incident X-ray beam. The resulting scattered X-rays will be scattered in all directions, but depending on the relative phases of the diffracted rays in a given direction, the intensities of the diffracted X-rays will vary with the angle of diffraction.

Historically, there have been two approaches in dealing with diffraction by crystals, the von Laue and Bragg approaches. The von Laue approach treats diffraction from a three dimensional crystal similarly to the diffraction of light from a diffraction grating, giving an equation (equation A3.2.1), relating the atomic separation (S), the X-ray wavelength (λ), and the angle of diffraction (ϕ);

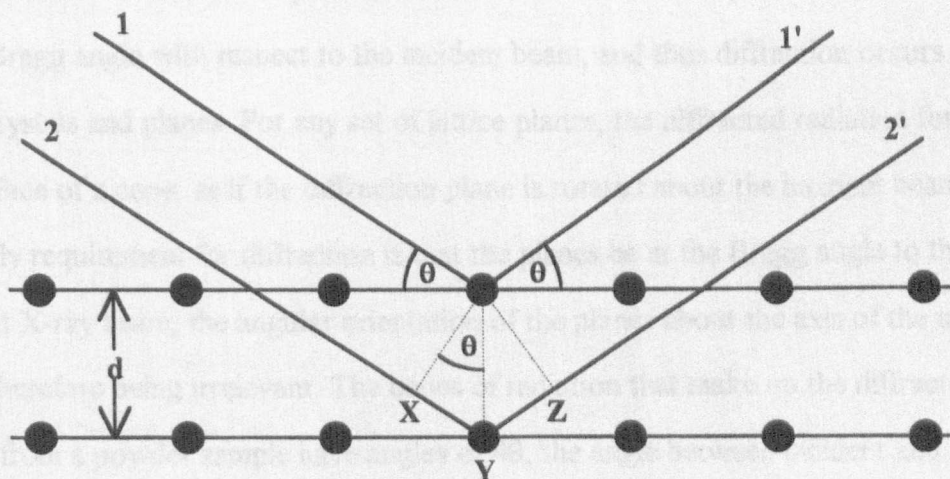
$$S \sin \phi = n \lambda \quad (\text{A3.2.1})$$

For a three dimensional arrangement, this results in a set of three simultaneous equations, each corresponding to a possible directional axis for rows of atoms in the crystal. All three equations must be satisfied for a diffracted beam to occur.

A3.2.4 The Bragg Law

The Bragg theory of diffraction is far simpler than that of von Laue, and regards crystals as built of layers of planes, each of which can act as a semi transparent mirror. Some of the incident X-rays are reflected from the plane with both angles of incidence and reflection equal, the rest being transmitted through the plane to be subsequently reflected by other planes. The basic derivation of the Bragg Law is shown in figure A3.2.3.

Figure A3.2.3 A schematic diagram of the diffraction of X-ray beams ($1 \rightarrow 1'$ and $2 \rightarrow 2'$) with angle of incidence θ to parallel adjacent planes of atoms, spacing d .



In the above schematic, it is observed that beam $2 \rightarrow 2'$ must travel the extra distance $XY + YZ$ compared with beam $1 \rightarrow 1'$. In order for the diffracted beams to interfere constructively, this extra distance ($XY + YZ$) must be equal to an integer (n) number of wavelengths. The d spacing and the angle of incidence θ , (the *Bragg Angle*), are related to the distance XY by;

$$XY = YZ = d \sin \theta \quad (\text{A3.2.2})$$

Thus, $XY + YZ = 2 d \sin \theta \quad (\text{A3.2.3})$

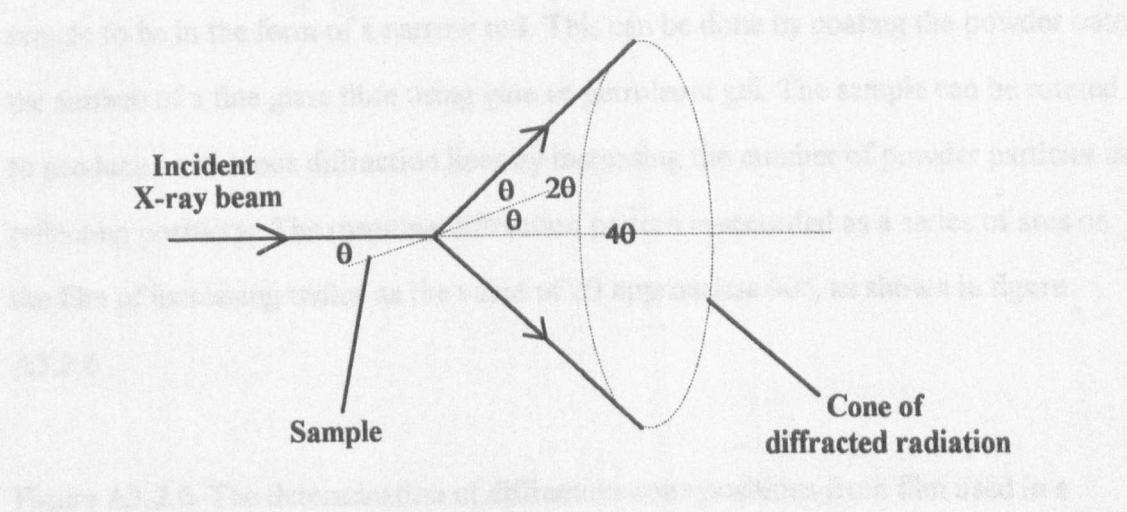
For constructive interference $XY + YZ = n \lambda \quad (\text{A3.2.4})$

Therefore $n \lambda = 2 d \sin \theta \quad \text{Bragg's Law} \quad (\text{A3.2.5})$

At angles of incidence other than the Bragg Angle, destructive interference occurs, such that annihilation is usually complete if the incident angle is just a few tenths of a degree out. Several solutions to Bragg's Law are usually possible, for $n = 1, 2, 3$, etc., therefore it is customary to set $n = 1$. Thus for $n = 2$ the d spacing is halved by doubling up the number of planes in the set, thus, $n = 1$ is maintained. n is known as the order of diffraction.

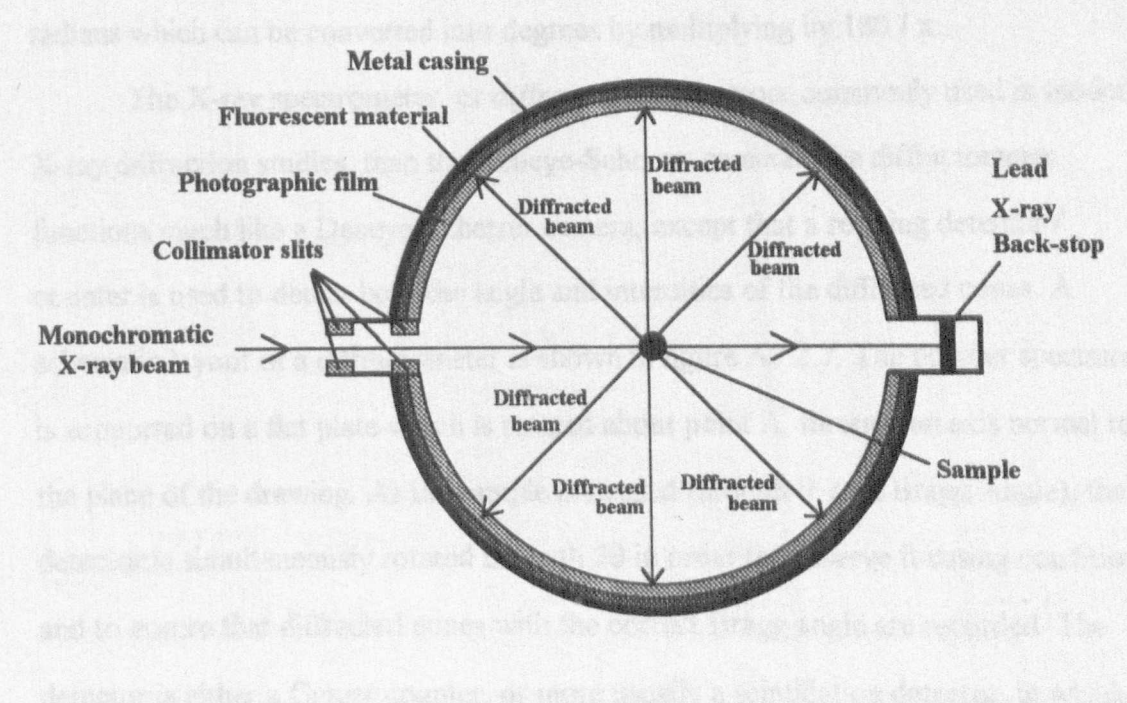
Bragg's law strictly applies to single crystals, but the majority of real samples analysed by X-ray diffraction are polycrystalline powders. Thus, the simple Bragg's Law model can be extended to deal with powder systems. Ideally, a powder sample has crystals randomly arranged in every possible orientation. In effect, a powder sample can be thought of as being equivalent to a single crystal rotated about all possible axes. For each set of planes, therefore, at least some crystals must be oriented at the Bragg angle with respect to the incident beam, and thus diffraction occurs for these crystals and planes. For any set of lattice planes, the diffracted radiation forms the surface of a cone, as if the diffraction plane is rotated about the incident beam axis. The only requirement for diffraction is that the planes be at the Bragg angle to the incident X-ray beam, the angular orientation of the planes about the axis of the incident beam therefore being irrelevant. The cones of radiation that make up the diffracted beams from a powder sample have angles of 4θ , the angle between incident and diffracted beams being 2θ . A separate cone is formed for each set of differently spaced lattice planes. This principle is shown in figure A3.2.4 for diffraction from a single lattice plane.

Figure 3.2.4 The formation of a cone of diffracted radiation by powder samples



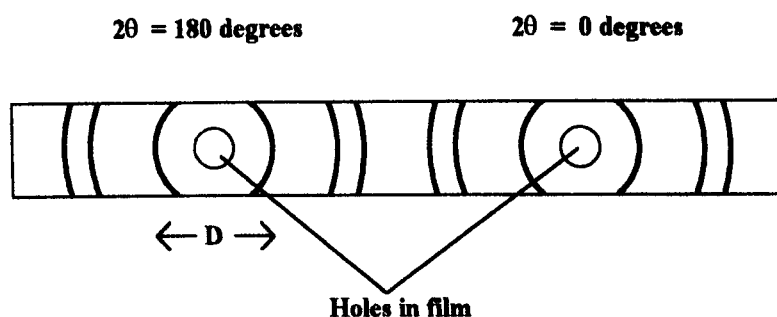
The most common powder diffraction technique is the Debye-Scherrer method, in which a narrow strip of film is curved into a cylindrical shape about the axis of the powder specimen with the incident beam at right angles to this axis. The cones of radiation form a pattern of lines on the film where the two intersect. Each line is made up of many spots, each originating from a single crystallite. θ can be determined from the measured position of a given diffraction line on the film, and as λ is known, d can be determined for each line produced. The schematic layout and operation of a Debye-Scherrer camera is shown in figure A3.2.5.

Figure A3.2.5 A schematic layout depicting the operation of a Debye-Scherrer camera



Use of the Debye-Scherrer camera for powder sample analysis requires the sample to be in the form of a narrow rod. This can be done by coating the powder onto the surface of a fine glass fibre using glue or petroleum gel. The sample can be rotated to produce continuous diffraction lines by increasing the number of powder particles in reflecting positions. The resulting diffraction pattern is recorded as a series of arcs on the film of increasing radius as the value of 2θ approaches 90° , as shown in figure A3.2.6

Figure A3.2.6 The determination of diffraction cone positions from film used in a Debye-Scherrer camera.

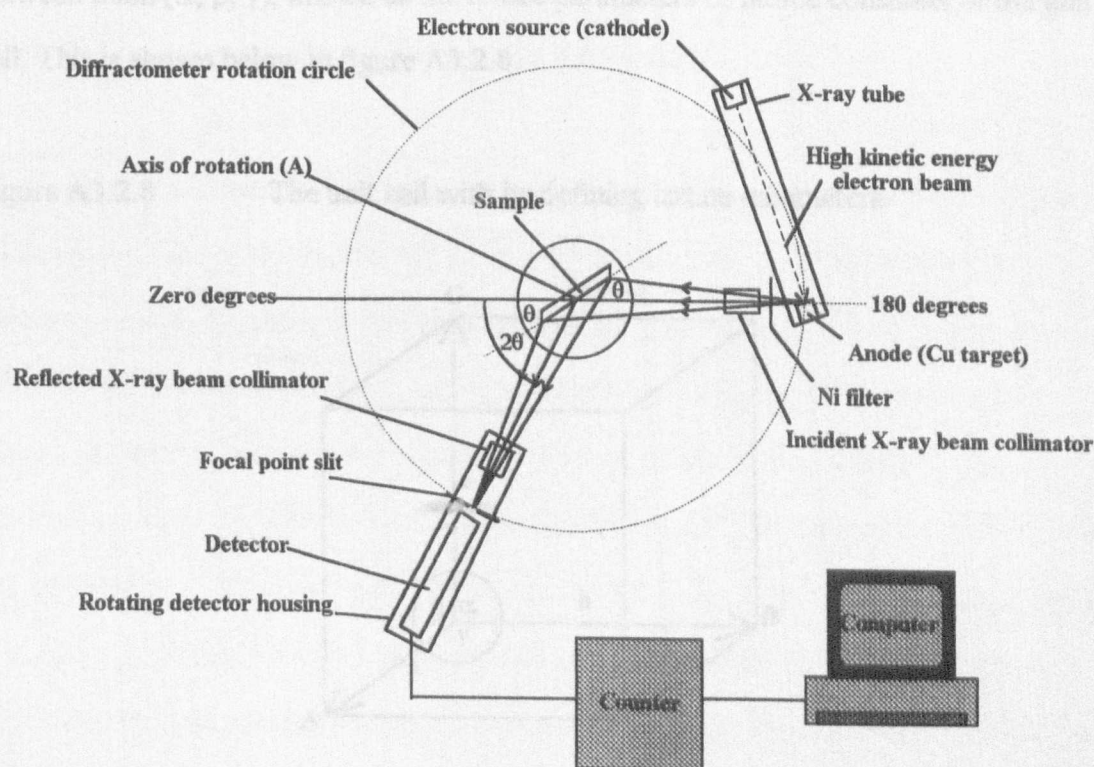


The values of 2θ for each of the diffracted cones can be derived from the diameter of the cone, by dividing the diameter of the cone by the radius of the film in the camera, i.e., $2\theta = D / \text{film radius}$. The value of 2θ thus derived has units of radians which can be converted into degrees by multiplying by $180 / \pi$.

The X-ray spectrometer, or *diffractometer*, is more commonly used in modern X-ray diffraction studies, than the Debye-Scherrer camera. The diffractometer functions much like a Debye-Scherrer camera, except that a rotating detector / counter is used to detect both the angle and intensities of the diffracted cones. A schematic layout of a diffractometer is shown in figure A3.2.7. The powder specimen is supported on a flat plate which is rotated about point A, through an axis normal to the plane of the drawing. As the sample is rotated through θ , (the Bragg Angle), the detector is simultaneously rotated through 2θ in order to preserve focusing conditions and to ensure that diffracted cones with the correct Bragg angle are recorded. The detector is either a Geiger counter, or more usually a scintillation detector, in which

incident X-rays cause fluorescence of a crystal, which is in turn converted to electric current pulses using a photo-multiplier.

Figure 3.2.7 A schematic showing the layout and operation of a modern X-ray diffractometer



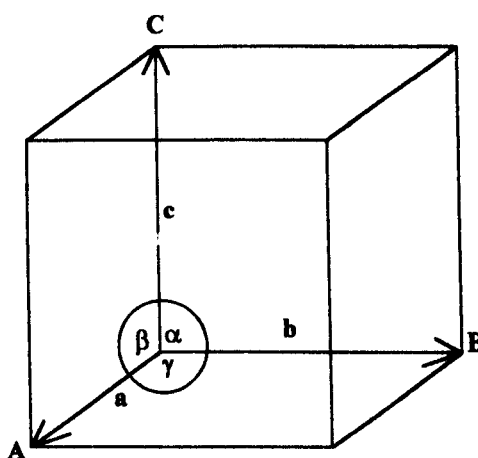
The operation of the instrument is generally by computer controlled servo-motors, and the count rate with angle data is stored digitally by computer for display and software manipulation. In normal use, the detector scans over a range of 2θ values at a constant angular velocity. The 10° to 80° 2θ range is generally sufficient to cover the most useful part of a powder pattern. The resulting patterns are subsequently presented graphically as the variation of intensity with 2θ .

A3.2.5 Crystallography

In order to make effective use of X-ray diffraction data, it is vital that the structures and geometries of crystals are considered. A crystal can be defined as a three dimensional solid structure consisting of identical three dimensional repeating arrangements of atoms. The smallest repeating three dimensional pattern which is

representative of the crystal structure is known as the unit cell. In describing crystals, it is convenient to think of the structure in terms of a fixed framework of imaginary points in three dimensional space. If space is divided into three planes, the unit cell can be described in terms of three vectors (A, B, C) from a given origin, (known as a point lattice), or more conveniently, in terms of three lengths (a, b, c), and the three angles between them (α , β , γ), known as the lattice parameters or lattice constants of the unit cell. This is shown below in figure A3.2.8.

Figure A3.2.8 The unit cell with its defining lattice parameters



The resulting shapes of the unit cell point lattices depend on the arrangement of the three planes. Thus, by giving different values to a, b, c, α , β and γ , and since the points are located at the cell corners, up to seven different shapes of point lattices, (and therefore unit cells) are possible. These seven point lattices correspond to the seven crystal systems into which all crystal systems are classified. As well as unit cells with only corner lattice points, known as primitive (P) structures, it is also possible for the unit cell to have lattice points in the centre (known as body centred (I)), and in the centres of each face (known as face centred (F)). It is also possible to have face centre points on only two opposite faces (also face centred (A, B or C)). In 1848, it was demonstrated by Bravais, a French crystallographer, that there are in fact only 14 possible point lattices, also known as Bravais lattices to commemorate his discovery.

The materials under investigation in this work are ceria which has the simple cubic structure known as fluorite where $a = b = c$ and $\alpha = \beta = \gamma = 90^\circ$, and lanthana

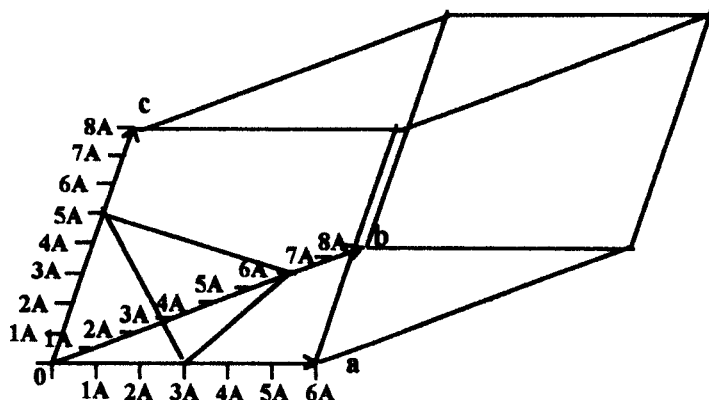
which has the simple hexagonal structure where $a = b \neq c$ and $\alpha = \beta = 90^\circ$, $\gamma = 120^\circ$.

Additionally, fluorite structured substitutional solid solutions with lanthanum ions incorporated into the ceria fluorite lattice, (and to a far lesser extent, HCP structured substitutional solid solutions of cerium in lanthana), which are formed by solid state reaction are also investigated.

A3.2.6 Crystal Planes Involved in Diffraction

Planes of atoms within crystals are identified and named symbolically using the Miller Index. The Miller Indices are defined as "the reciprocals of the fractional intercepts which the plane makes with the crystallographic axes". Use of Miller Indices involves the assignment of three numbers, (the Miller Indices) to each set of lattice planes. In order to assign Miller Indices to a set of planes, it is necessary to first consider an adjacent plane that passes through the origin. The intersection of this plane on the three axes of the unit cell can then be written as fractions of the cell edges, ($1/h$, $1/k$, $1/l$), or in terms of the lattice parameters, as a/h , b/k , c/l). The Miller Indices of a plane are then derived by taking the reciprocal of the three fractions and multiplying or dividing by a common factor as necessary, to express the set of three indices (hkl), as the smallest integers possible. A worked example for the determination of the Miller Indices of a plane is shown in figure A3.2.9.

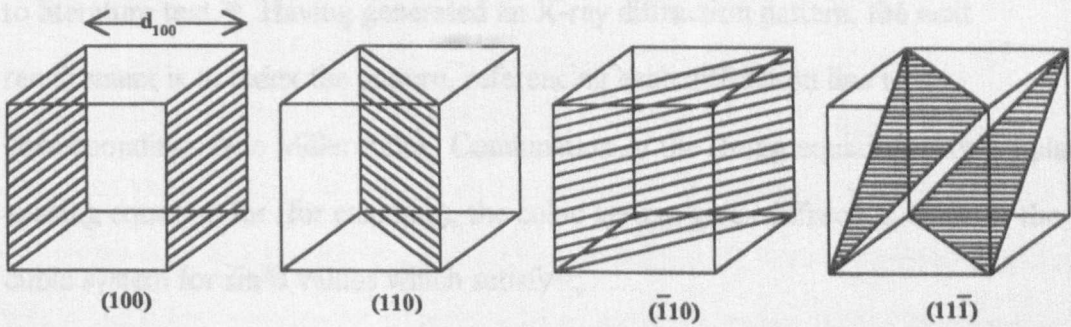
Figure A3.2.9



Cell Axis Length	6A	8A	8A
Intercept length	3A	6A	5A
Fractional intercept	1/2	3/4	5/8
Miller Indices	2	4/3	8/5
Clearing fractions	30	20	24
Divide by lowest common factor	15	10	12

Thus, the Miller Indices for the planes above are (15 10 12). For the cubic system, there are several simple and common planes, such as those illustrated in figure A3.2.10.

Figure A3.2.10 An illustration of four different planes in a cubic unit cell



All Miller Indices are derived in much the same way as in the example above, except for the hexagonal lattice category crystals. In this case, the unit cells are defined by 2 equal coplanar vectors with an angle of 120° between them, and a third vector normal to the plane of the first two. A different system known as the Miller-Bravais Index system is used in this case which refers to four axes, three in one plane, all at 120° to each other and a fourth normal to the plane defined by the first three.

In this study, although lanthana has a hexagonal lattice, the dominance of the cubic lattice throughout most of the solid solution range of primary interest, and the relative ease of analysis makes it a more suitable method for systematic analysis of the system. It can be fairly assumed in the ceria / lanthana system that once the solid solution limit of lanthanum in ceria is exceeded, further addition of lanthanum results in the precipitation of a second hexagonal lanthana phase along with a cubic saturated

solid solution phase. Further discussion of the hexagonal system is beyond the scope of this thesis and the reader is referred to literature texts for further details.²⁶

Miller indices are used in X-ray diffraction to relate diffraction peaks to defined crystal planes, and to calculate the value of the d spacing between planes. The d_{hkl} spacing depends on the type of lattice and the lattice parameters (a , b , c , α , β , γ) of the crystal and the plane indices. The simplest relationship exists for the cubic system (e.g., ceria and lanthanum doped ceria solid solutions) and can be expressed;

$$d_{hkl} = \frac{a}{\sqrt{h^2 + k^2 + l^2}} \quad (\text{A3.2.6})$$

For other systems, analogous expressions exist, but are far more complicated. For further information regarding expressions for the other systems, the reader is referred to literature text.²⁶ Having generated an X-ray diffraction pattern, the next requirement is to index the pattern, referencing each diffraction line to its corresponding plane Miller Index. Combination of the Bragg equation with the plane spacing equation for (for example), the cubic system gives diffraction lines for the cubic system for $\sin^2\theta$ values which satisfy²⁶;

$$\frac{\sin^2 \theta}{h^2 + k^2 + l^2} = \frac{\sin^2 \theta}{s} = \frac{\lambda^2}{4a^2} \quad (\text{A3.2.7})$$

In this equation, $h^2 + k^2 + l^2$ (and therefore s) is always an integral value and $\lambda^2 / 4a^2$ is a constant for a given pattern. Values of s are generally determined using computer software, rather than by hand, and the hkl of each line can then be determined. In this study, the hkl values of a library standard diffraction pattern of ceria were used to determine the hkl values of the experimentally determined ceria host solid solutions, by comparison. The pattern index were only determined for the cubic structured range within the solid solution limits, and were used to determine the variation in cubic lattice parameter with lanthanum content.

Thus far, only consideration to the line positions has been given account of. It should also be noted that the intensities of X-ray reflections are also of great

importance for any quantitative measurements and for qualitative measurements, particularly in the identification of an unknown material by its X-ray diffraction pattern "fingerprint". The mechanism of X-ray diffraction by electrons has been discussed previously and the intensity of the diffracted beam with respect to the incident beam can be determined by the Thomson equation, (also known as the polarisation factor);

$$I_{\text{diffracted}} \propto \frac{1}{2}(1 + \cos^2 2\theta) \quad (\text{A3.2.8})$$

(X-rays can also undergo Compton Scattering, which is analogous to an elastic collision process. Scattered X-rays are of longer wavelength and are out of phase with respect to the incident beam. This type of scattering is generally caused by X-rays interacting with valence electrons and is most significant with the lighter elements).

The scattered intensity of X-rays depends on the atomic (and therefore electron) content of the unit cell. The scattered beam intensity is a summation of the scattered beams from all of the electrons. As the electrons can occupy different positions within the atoms, interference between the scattered waves is inevitable which has the consequence of reducing the scattered amplitude. The relative efficiency of the scattering process for an atom, known as the scattering factor, or form factor (f), is proportional to the number of electrons the atom possesses. As well as the electrons occupying different positions within the atoms, the atoms can also occupy different positions within the unit cell which leads to a structure factor or structure amplitude (F_{hkl}) for the hkl reflection. Both f and F_{hkl} have a large influence over the scattered intensities for a given material unit cell.

As well as these factors, other notable influences on the scattered intensity include the Lorentz factor - an instrument and θ specific geometric factor, a multiplicity (of reflections) factor, which allows for the number of reflecting planes contributing to a given line in the pattern, a sample X-ray absorption factor, a temperature factor allowing for the decrease in scattered beam intensity and the increase in background scattering caused by thermal vibration of atoms, and in powder methods, the presence of any kind of preferred orientation of the crystallites.

Appendix 3.3

Powder X-Ray Diffractometer Reference Patterns.

All data cards below from Philips Electronic Instruments, INC., CD - ROM Database, (1987)

Reference Pattern 34 - 394 CeO_2 Cerium Oxide¹⁷⁵

Lambda = 1.5405981

System - Cubic

SG - Fm3m

Total d's = 16

Colour - Light grey/yellowish brown

Pattern temp 26°C

Lattice parameters - a - 5.411 b - 5.411 c - 5.411

D	RELATIVE INTENSITY	H	K	L	D	RELATIVE INTENSITY	H	K	L
3.123	100	1	1	1	1.104	14	4	2	2
2.705	30	2	0	0	1.041	11	5	1	1
1.913	52	2	2	0	0.9566	4	4	4	0
1.631	42	3	1	1	0.9147	13	5	3	1
1.562	8	2	2	2	0.9019	6	6	0	0
1.353	8	4	0	0	0.8556	9	6	2	0
1.241	14	3	3	1	0.8251	6	5	3	3
1.210	8	4	2	0	0.8157	5	6	2	2

Comments

This yttria stabilised phase was prepared at NBS, Gaithersburg, Maryland, USA, by Dragoo and Domingues (1982) from coprecipitation of the oxides. The powder was calcined at 620°C and then formed into a billet without binder, isostatically pressed, and then hot pressed in an alumina die for 30 minutes at 1350°C with an applied stress of 28M.Pa. The structure of fluorite was determined by Bragg (1914).

Reference Pattern 5 - 602 La_2O_3 **Lanthanum Oxide¹⁷⁶**

Lambda = 1.5405 System - hexagonal SG - P-3m1

Total d's = 39 Colour - colourless (white powder) Pattern temp 26°C

Lattice parameters - a - 3.937 b - 3.937 c - 6.130

D	RELATIVE INTENSITY	H	K	L	D	RELATIVE INTENSITY	H	K	L
3.410	34	1	0	0	1.090	7	2	1	3
3.063	31	0	0	2	1.065	4	3	0	2
2.980	100	1	0	1	1.022	1	0	0	6
2.278	58	1	0	2	0.9952	3	2	0	5
1.968	63	1	1	0	0.9840	3	2	2	0
1.753	52	1	0	3	0.9787	1	1	0	6
1.705	4	2	0	0	0.9459	1	3	1	0
1.656	24	1	1	2	0.9372	3	2	2	2
1.642	17	2	0	1	0.9345	5	3	1	1
1.532	3	0	0	4	0.9131	2	3	0	4
1.490	5	2	0	2	0.9070	2	1	1	6
1.398	2	1	0	4	0.8883	5	2	1	5
1.309	7	2	0	3	0.8766	1	2	0	6
1.289	2	2	1	0	0.8583	4	3	1	3
1.261	12	2	1	1	0.8480	2	1	0	7
1.209	6	1	1	4	0.8443	1	4	0	1
1.187	4	2	1	2	0.8283	2	2	2	4
1.153	4	1	0	5	0.8050	1	3	1	4
1.139	2	2	0	4	0.8007	2	2	1	6
1.136	4	3	0	0	-	-	-	-	-

Comments

Merck Index, 8th Ed., p. 608. Opaque mineral optical data on specimen from Nanseke, Uganda. Sample from Fairmount Chemical Company. Sample was annealed at 1200°C for 1 hour and mounted in petrolatum to prevent readsorption of CO_2 and H_2O .

Spectroscopic analysis: <0.01% Ca, Mg, Si; <0.001% Al, Cu, Fe, Pb.

Appendix 3.4

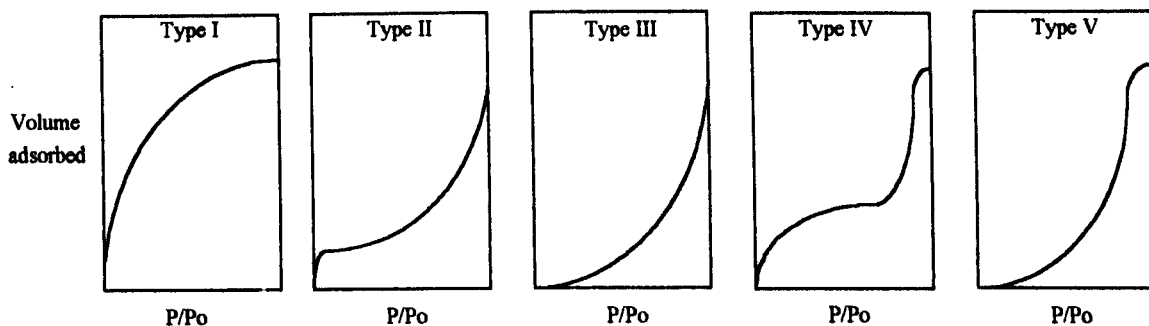
Surface Area Measurement by Gas Adsorption - Theory

A gas (adsorbate) and a solid (adsorbent) can interact in two ways, depending on the nature of the interactions. The strongest interaction is chemical adsorption (chemisorption) which requires the formation of chemical bonds between adsorbate and adsorbent surface, resulting in a single monolayer coverage. The highly specific nature of the chemical bonds varies from system to system and indeed between individual components in multi-component catalyst systems, thus rendering this type of interaction unsuitable for measurement of the total surface area of a solid. Physical adsorption (physisorption), on the other hand, relies on Van der Waals interactions to drive the adsorption process. These forces are much weaker than chemical bonds and due to non-specific adsorption characteristics are ideal for total surface area measurements by adsorption. The magnitude of the enthalpy of adsorption for physisorption is about the same as that for condensation (approximately 5 kcal mol^{-1} (21 kJ mol^{-1})).

In 1916, Langmuir¹⁷⁷ presented an adsorption isotherm which could be used to determine the surface area of a solid. The isotherm model relied on the adsorption of a gas at a temperature well above that at which it condenses as a liquid, in order to ensure monolayer coverage only. Knowledge of the surface area occupied by each molecule and the number of molecules adsorbed then allows the total surface area to be calculated. However, there are several problems associated with this ideal method. For instance, porous solids and the use of adsorption temperatures close to the condensation temperature of the adsorbate gas allow multi-layer adsorption to occur - as well as physisorption the total adsorption has some of the character of condensation. Also, the primary assumption of uniformity of the surface sites is usually invalid for inorganic solids which results in a marked decrease in the enthalpy of adsorption beyond a coverage of approximately one-third of a monolayer. This is most likely due to the sites of greatest coordinative unsaturation being energetically most favoured and occupied first, others of a lower coordinative unsaturation then becoming

occupied. There are also no allowances for steric effects of adsorbate interactions.¹⁷⁸ As a result of this several different adsorption isotherms have been observed which have been classified into five types as shown in figure A3.4.1.

Figure A3.4.1 The five common classifications of adsorption isotherm.¹⁷⁹



Of these, the greatest value isotherm for the determination of catalyst surface area is the Brunauer-Emmett-Teller (BET) isotherm.¹⁸⁰ Unlike the Langmuir isotherm the BET isotherm gives a good representation of physisorption as it accounts for multi-layer adsorption. The BET equation is based on the same assumptions as the Langmuir equation but allows for multiple layers of adsorbate to build up on top of the monolayer. Each adsorbed species is assumed to provide an adsorption site for a subsequent layer. The rate of adsorption onto the bare surface is assumed equal to the rate of desorption from the monolayer, and the enthalpy of adsorption to give layers beyond the monolayer is equal to the enthalpy of condensation of the adsorbing gas. The enthalpy of adsorption of the monolayer onto the bare surface was assumed to be greater than secondary layers.

The BET equation provides an adequate, if simplified description of the adsorption of gas on a solid surface, and can be written;

$$\frac{P/P_0}{V[1 - (P/P_0)]} = \frac{1}{V_m C} + \frac{C - 1}{V_m C} \times P/P_0 \quad (\text{A3.4.1})$$

where V is the volume at standard pressure and temperature (STP) of gas adsorbed at pressure P . P_0 is the saturation pressure which is equal to the vapour pressure of liquefied gas at the adsorbing temperature. V_m is the volume of gas at ST required to

form an adsorbed monolayer. C is a temperature dependent constant derived from the energy of adsorption of the first and higher layers. A plot of the left hand side of the equation vs. P/P_0 gives a straight line with intercept $1/V_m C$. Experimental results often conform to straight line plots for low values of P/P_0 . This linear plot allows a simple determination of V_m and the surface area of the solid can be estimated, assuming that the cross sectional area of an adsorbed nitrogen molecule is $16.2 \times 10^{-20} \text{ m}^2$.

The standard BET procedure requires the measurement of at least three and preferably five or more points in the appropriate pressure range on the N_2 adsorption isotherm at the normal boiling point of liquid nitrogen.¹⁸¹ For routine measurements of surface area, IUPAC stated in 1985 that a simplified procedure may be used involving the determination of only a single point on the adsorption isotherm, lying within the linear range of the BET plot. On many solids the value of C for N_2 , is usually sufficiently large to allow the assumption that the BET plot passes through the origin. This single point technique allows the advantage of simple apparatus requirements and high throughput whilst still producing accurate and reproducible results. This technique was used for all samples tested within this thesis using a Micromeritics Flowsorb II 2300 instrument.

It is possible to represent the surface area of the monolayer adsorbing sample as

$$S = \frac{V_m A N}{M} \quad (\text{A3.4.2})$$

where A is Avogadro's constant which is the number of molecules in 1 mole, M is the molar volume of the gas and N is the area covered by each molecule of the adsorbed gas.

The constant C of the BET equation is typically $\gg 1$ and allows the BET expression to be reduced to

$$\frac{P/P_0}{V[1 - (P/P_0)]} = \frac{1}{V_m} \times [(1/C) + (P/P_0)] \quad (\text{A3.4.3})$$

If it is now assumed that $P / P_0 \gg 1 / C$, the $1 / C$ term can be eliminated from equation A3.4.3

$$\frac{(P/P_0)}{V[1 - (P/P_0)]} = \frac{1}{V_m} \times \frac{P}{P_0} \quad (\text{A3.4.4})$$

Which can be rearranged

$$V_m = V[1 - (P/P_0)] \quad (\text{A3.4.5})$$

Equation A3.4.5 can now be substituted into equation A3.4.2 to give

$$S = \frac{VAN[1 - (P/P_0)]}{M} \quad (\text{A3.4.6})$$

The surface area of a sample can then be determined once the volume of gas adsorbed and/or desorbed is measured.

The experimental gas mixture used was 29.9 volume % nitrogen in helium. For nitrogen gas adsorbed from this mixture under the experimental conditions used (adsorption at liquid nitrogen temperature), the following values are derived:

V is converted to Standard Temperature and Pressure (STP) conditions (273.2 °, 760mmHg). The number of molecules present in the injected volume can then be calculated, as the Number of molecules per mole (Avogadro's number - 6.023×10^{23}) and the molar volume ($22414 \text{ ml mol}^{-1}$ at STP) are known. The total surface area covered by the injected volume can then be determined as the presently accepted value for the area occupied by an adsorbed nitrogen molecule is $16.2 \times 10^{-20} \text{ m}^2$. P is $0.29 \times$ atmospheric pressure ($0.29 \times 760 \text{ mmHg}$), and P_0 , the saturation pressure is typically 15mmHg greater than atmospheric pressure due to dissolved oxygen, thermal circulation and other factors (assumed to be 775mmHg).

The result of this calculation for the 29.9% nitrogen in helium gas mixture used experimentally is as follows:-

$$S = V \times \frac{273}{\text{Room Temp}} \times \frac{\text{Atm Press}}{760} \times \frac{6.023 \times 10^{23} \times 16.2 \times 10^{-20}}{22414} \times 1 - \frac{\%N_2}{100} \times \frac{\text{Atm Press}}{\text{Sat Vap Press}}$$

(A3.4.7)

Substituting actual values

$$S = V \times \frac{273.2}{295.2} \times \frac{6.023 \times 10^{23} \times 16.2 \times 10^{-20}}{22414} \times 1 - \frac{0.3 \times 760}{775}$$

$$S = 2.85 V$$

Where S is the surface area in square meters.

Thus for calibration performed at 22°C and at atmospheric pressure 760mmHg, The indicated surface area should register 2.85 m² ml⁻¹ N₂ injected. The experiments were performed in a room with a maintained temperature of 22°C, and atmospheric pressure was assumed to be constant.

Appendix 3.5

X-Ray Photoelectron Spectroscopy - General Theory

In XPS, the analyte is irradiated under ultra high vacuum (UHV) conditions with monochromatic X-rays, normally aluminium (AlK_α Energy = 1486.6 eV, line width = 0.85 eV) or magnesium (MgK_α Energy = 1253.6 eV, line width = 0.7 eV) characteristic X-ray lines. (Core electron binding energies go up to values of 1 keV or more). The requirement for UHV conditions is to minimise scattering (and therefore loss) of electrons by encounters with gas molecules as they travel from the sample surface toward the energy analyser.¹⁸² The X-rays are produced by bombarding the relevant anode with a high energy electron beam (approximately 15 keV or thereabouts). Soft X-rays generated pass through an aperture covered with a thin (approximately 2 μm) sheet of aluminium foil, (which screens the sample from stray electrons, heating effects and any contamination originating from the source), and then toward the sample. The X-rays stimulate photoemission from the core levels of the atoms present in the surface layers of the sample and due to their high penetrative power are able to penetrate to a depth of several microns. However, the photoelectrons produced can only escape from the sample material if they originate from atomic layers very near to the surface.

The distance into a material from which electrons are able to escape from the surface of a material is termed the Escape Depth which is characterised by the electron mean free path for inelastic scattering within the solid (λ). In order to interpret electron spectra, it is vital that this measure of sampling depth be known as a measure of the surface specificity of the technique for given materials. λ is found to vary with electron kinetic energy E_k (approximately as $\lambda \propto E_k^{-1/2}$ for E_k values greater than approximately 50 eV),¹⁸³ and as a function of the nature of the solid. Assuming that the electron intensity is attenuated by the exponential $e^{-x/\lambda}$, where x is the distance the electron travels through the solid, it is clear that the total intensity from a homogeneous solid is proportional to λ .¹⁸⁴ The mean free path of electrons for elastic scattering in solids as a function of the kinetic energy of the emitted electrons, when plotted, forms a curve

known as the *universal curve*¹⁸⁵ (because it is applicable to most solids), and provides a useful guide for the estimation of λ . At very low electron kinetic energy, insufficient energy is available to excite the major inelastic scattering mechanisms therefore λ increases. At very high kinetic energies the cross section for inelastic processes decreases as the electron energy is much higher than the resonance energy. The minimum in λ occurs between 10 and 500eV and can have a value as low as 0.4nm. At typical XPS energies, λ is of the order 1-3nm. The energy dependence of the inelastic mean free path factor in determining the elemental sensitivity for this study was calculated according to Seah and Dench (1979).¹⁸⁶

Figure A3.5.1 A schematic mechanistic comparison of XPS and AES¹⁸⁷

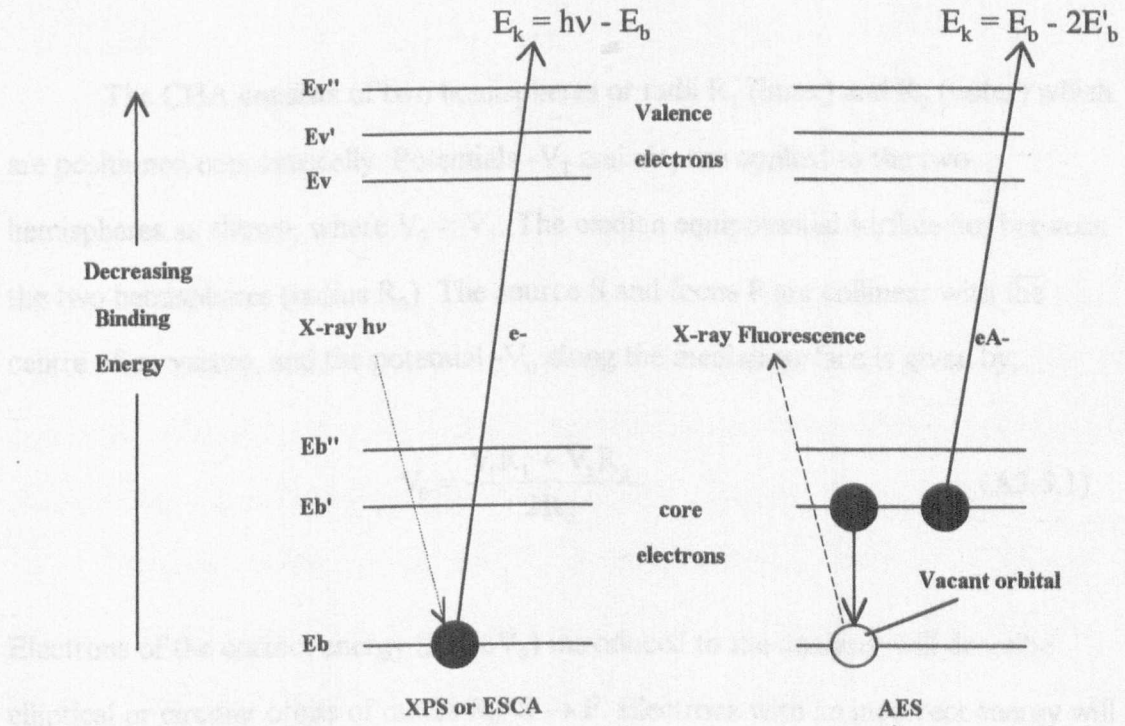
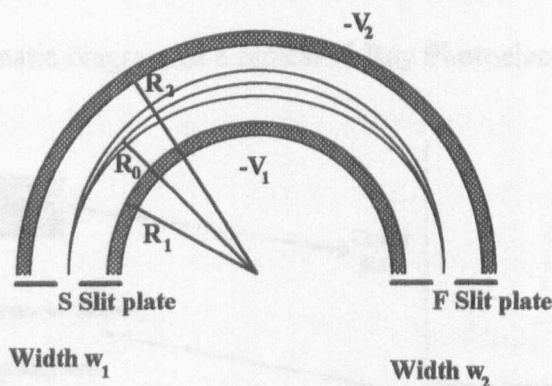


Figure A3.5.1 shows a schematic mechanistic comparison of XPS and Auger electron spectroscopies (AES). In both cases the lower three lines E_b , $E_{b'}$ and $E_{b''}$ represent energies of the inner K and L electrons. The upper three lines represent energy levels of some of the outer shell or valence electrons.

The resulting photoelectrons are detected and energy analysed to yield the photoelectron spectrum. Such an analysis is performed by an electron energy (or strictly speaking, an electron velocity analyser). The type of analyser used in most XPS

and AES spectrometers is known as a Concentric Hemispherical Analyser (CHA), the basic form of which is shown in schematic form in figure A3.5.2.

Figure A3.5.2 Schematic cross section of a Concentric Hemispherical Analyser.¹⁸²



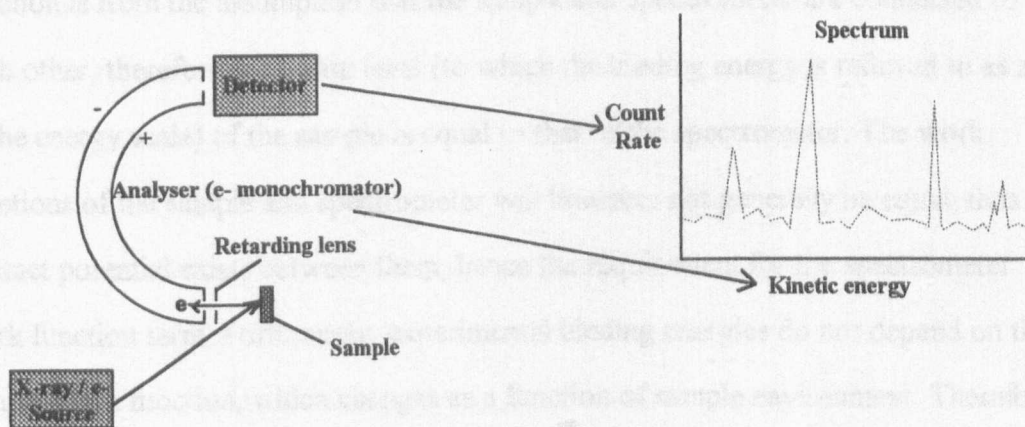
The CHA consists of two hemispheres or radii R_1 (inner) and R_2 (outer) which are positioned concentrically. Potentials $-V_1$ and $-V_2$ are applied to the two hemispheres as shown, where $V_2 > V_1$. The median equipotential surface lies between the two hemispheres (radius R_0). The source S and focus F are collinear with the centre of curvature, and the potential $-V_0$ along the median surface is given by;

$$V_0 = \frac{V_1 R_1 + V_2 R_2}{2R_0} \quad (\text{A3.5.1})$$

Electrons of the correct energy ($E = eV_0$) introduced to the analyser will describe elliptical or circular orbits of radius R_0 , $S \rightarrow F$. Electrons with an incorrect energy will be focused away from the focus slit. In effect, the CHA is an electron monochromator which for a fixed setting, passes only electrons of a fixed kinetic energy. A sweep of the analyser potentials, $-V_1$ and $-V_2$ sweeps a range of kinetic energies of emitted electrons. A plot of detected signal versus electron kinetic energy yields the photoelectron spectrum. w_1 and w_2 are the entrance and exit slit widths respectively, and are generally equal in most instruments. The intensity of the XPS signal is proportional to the entrance slit width w_1 , providing $w_2 > w_1$.¹⁸⁴ The general instrumentation of X-ray photoelectron (and Auger photoelectron) spectrometers is

therefore similar in most experimental set-ups and consists of five basic stages, a photoemission excitation source (X-ray or electron beam source), a sample, an electron analyser (monochromator), a detector, and a UHV system in which to house the apparatus. A schematic of the typical instrument set-up is shown in figure A3.5.3.

Figure A3.5.3 A schematic diagram of a typical X-Ray Photoelectron Spectrometer.



The kinetic energy of the photoelectron depends on the binding energy of the electrons in the core levels from whence photoemission was excited. Thus, each element produces a characteristic photoelectron spectrum with peaks at well defined characteristic energies. The measurement of these energies allows the determination of elemental composition of an analyte, and the measurement of the relative intensities of characteristic photoelectron peaks yields quantitative analysis.

In the case of XPS, an electron (e^-) is displaced from a core (K) level (E_b) by a photon from the incident monochromatic X-ray beam. The photon has a known energy ($h\nu$) therefore the process can be represented by the expression;



where A can be an atom, a molecule or an ion, and A^{+*} is an electronically excited ion with a positive charge one greater than that of A. The kinetic energy of the emitted electron E_k is measured in an electron spectrometer. The electron binding energy E_b (which may be visualised as the ionisation energy for that electron), can then be calculated by means of the equation

$$E_b = h\nu - E_k - w \quad (\text{A3.5.3})$$

In this equation w is the work function of the spectrometer. This term corrects the E_b for the electrostatic environment in which the electron is formed and measured and is a pre-determined instrument constant. The origin of the spectrometer work function is from the assumption that the sample and spectrometer are connected to each other, therefore the Fermi level (to which the binding energy is referred to as zero in the energy scale) of the sample is equal to that of the spectrometer. The work functions of the sample and spectrometer will however not generally be equal, thus a contact potential exists between them, hence the requirement for the spectrometer work function term. Fortunately, experimental binding energies do not depend on the sample work function, which changes as a function of sample environment. Therefore, providing the spectrometer work function remains constant (i.e., constant UHV conditions within the spectrometer), and electrical equilibrium is maintained, a reproducible experimental binding energy scale is obtained. It should be noted that the assumption in the theory of determining E_b is that the system is in a state of electrical equilibrium, i.e., that the Fermi level of the sample is constant and equal to that of the spectrometer. However, the process of photoemission by definition means that there is a constant loss of electrons from the sample. Thus equilibrium can only be established if electrons can flow readily from a ground source to neutralise the accumulated positive charge left by default on the sample by the photoemission process. The consequence of this for insulating samples is that there may be an observed increase in binding energy with charging. If this does occur, then the charging can be corrected for, or removed with the use of a Flood Gun which floods the region surrounding the sample with low energy electrons in order to negate photoemission induced charging effects.

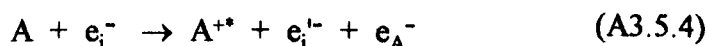
As well as the energy dependence of the inelastic mean free path, the value of E_k may also be modified by several atomic parameters that are associated with the photoemission process. In order to calculate the relative sensitivities for the elements studied, it is also necessary to take into account the photoelectrons cross section,¹⁸⁸

the angular asymmetry parameter¹⁸⁹ and the transmission of the energy analyser.¹⁹⁰ More detailed explanation of these factors is beyond the scope of this text, but several excellent reviews of electron spectroscopic theory are available which explore these and other aspects of the theories in great depth.¹⁹¹⁻¹⁹² However, a simple explanation is required as although the areas of XPS peaks carry quantitative information, their meaning is revealed only with the aid of a structural model of the surface layer. For a homogeneous solid with a flat surface the detected intensity of electrons emitted from a depth between x and $x+\delta x$ can be expressed most simply as the product of the flux of X-rays having range l at x below the free surface, the differential cross section per atom for production of electrons with energy E and solid angle Ω , the number of atoms in the differential element, the escape probability for an electron of inelastic mean free path $\lambda(E)$ and energy E , and the detection efficiency for electrons with energy E ¹⁸⁴ (from original reference¹⁹³). Under most circumstances the X-ray flux can be assumed to be constant unless the X-rays approach the surface from a glancing angle, otherwise the attenuation of the X-rays is negligible over the XPS sampling region. The cross section term cannot be easily measured and so is generally calculated, as previously mentioned in this paragraph. The angular dependence of the cross section term is generally insignificant for core levels, but is of greater importance for valence electrons. The term representing the number of atoms in the differential volume is the product of the number density of atoms at depth x and the volume of the differential element. The detection efficiency is determined by the take-off beam divergence angle and the detector slit area. The use of this relationship and equations derived from it can be used to model layer structures, such as may be expected for surface enriched materials.

In the resulting spectra, the binding energies for core (e.g., 1s) electrons are observed to increase with atomic number, because of the increased positive charge on the nucleus. Often more than one peak for each element is observed as other core level orbitals such as 2s and 2p are also XPS active. A large background is always observed (in addition to element characteristic peaks), which originates from ejected electrons which have lost part of their kinetic energy by undergoing inelastic collisions within the sample material. Such electrons are therefore detected with reduced kinetic energies,

and thus appear in the spectra at higher binding energies. Binding energies at the core levels of atoms are also slightly affected by their chemical environment, so as to cause a shift (known as Chemical Shift), of up to 10eV or more in the observed photoelectron energy.¹⁸³ The cause of this phenomenon is a distortion of valence electrons by chemical bonding which affects the degree of electrostatic screening of the core electrons

Auger electron spectroscopy, on the other hand, is based on a two step process, the first of which is the formation of an electronically excited ion A^{+*} , by exposure to either a beam of x-rays as in XPS, or an electron beam. With X-ray excitation, the equation for the excitation process is as with XPS. Excitation by an electron beam can be represented as;



where e_i^- represents an incident electron from the beam source, $e_i'^-$ represents the same electron after it has interacted with A and has therefore lost some of its energy, and e_A^- represents an electron that is ejected from one of the inner orbitals of A. As shown in figure 1, there are two ways in which the excitation of the excited ion A^{+*} can occur; the ejection of an Auger electron;



where e_A^- is an Auger electron and X-ray fluorescence, or;



where $h\nu_f$ is a fluorescence photon, the energy of which is independent of the excitation energy.

Auger emission therefore results from the energy evolved from the relaxation process causing the ejection of an Auger electron with a kinetic energy E_k . The kinetic energy of the Auger electron is independent of the excitation beam energy and is

determined by the difference between the evolved relaxation energy ($E_b - E_b'$) and the binding energy of the auger electron (E_b'). The energetic process can therefore be represented as

$$\begin{aligned} E_k &= (E_b - E_b') - E_b' \\ &= E_b - 2E_b' \end{aligned} \quad (\text{A3.5.7})$$

The nature of the Auger emission process means that the possible emissions are limited by the orbital transitions involved in the production of the Auger electron. Due to this, all Auger emissions are described in terms of the orbital transitions from whence they were derived. An example of such would be an LMM transition. This would involve the initial removal of an L electron followed by a transition of an M electron to the L orbital, with the simultaneous ejection of a second M electron. The resulting spectra are similar to those of XPS, consisting of a elemental characteristic peaks.

It should be noted that X-ray fluorescence and Auger electron emission are competitive processes, their relative rates depending on the atomic number of the element involved. For most materials (with atomic numbers greater than approximately 10), excitation of a sample by X-rays results in the simultaneous emission of X-ray photoelectrons, Auger electrons and X-ray fluorescence. The main difference between the XPS, AES and XRF techniques lies in the analysed species (electrons or X-rays) and the subsequent spectral analysis.

Appendix 3.6

A3.6.1 Experimental Theory and the Calculation of Reaction Rate¹⁶¹

There are two possible basic experimental modes of operation for a fixed bed micro-reactor. In temperature flux mode (known as "batch reactor" mode), the catalyst is exposed to a constant composition and flow rate feed-stream. The catalyst bed temperature is then increased at a constant heating rate (ramp-rate) with time in order to produce a reaction temperature profile in terms of the variation in conversion with temperature. Surface area characterisation data allows the comparison of catalysts in terms of specific activities at given temperatures. The product stream composition can be analysed throughout the experiment by mass spectrometry, or by gas chromatography at fixed temperature intervals, (determined by the ramp-rate and the GC column retention time). There are advantages and disadvantages to this mode of operation. As a method of screening many materials for a given reaction, this mode of operation allows a high throughput of materials and is a viable comparative technique. However, for the determination of accurate materials specific factors, such as activation energies and specific rates at standard temperatures, this method cannot be generally considered suitable as the constant temperature flux does not necessarily allow the catalysed reaction system to reach thermodynamic equilibrium rate values. Many catalysts can undergo chemical changes such as reduction under experimental conditions, which in turn can exert a significant influence over the catalytic reaction rate. The kinetics of the processes occurring in these use dependent changes can be relatively slow, (solid state reactions) and therefore rather than measuring the true activity of the reaction system under equilibrium conditions, the results may represent what is effectively an artificial transient system and therefore an "apparent" activity.

Due to the use of temperature feedback loops in the control of the ramp rate, there often exists a temperature lag between the measured and actual bed temperatures, (especially if the temperature probe is external to the catalyst bed). This may be manifest as a negative lag, where the thermal conductivity of the reaction tube is a limiting factor, or a positive lag, for example where an exotherm occurs in the

catalyst bed at reaction light off, which is not observed due to the location of the temperature probe.

Due to the nature of this study and the necessity of obtaining materials specific factors such as activation energies and kinetic data, and the known acute (kinetically limited) dependence of the oxygen stoichiometry of ceria based materials on temperature and gas environment, the temperature flux experimental technique was deemed unsuitable for use with this system, and will not be discussed further.

The second mode of operation of a micro-reactor involves the measurement of catalytic reaction rate under steady state temperature conditions. In this mode of operation, the catalyst is exposed to a constant composition and flow rate feed-stream. The catalyst bed temperature is then held at a series of constant temperatures until the catalytic reaction system reaches thermodynamic equilibrium at each temperature. The product stream composition can be analysed at each steady state temperature by mass spectrometry or gas chromatography, in order to determine the variation in reaction rate with steady-state temperature. As thermodynamic equilibrium rates can be calculated directly at each temperature, this mode of operation is most suitable for obtaining useful kinetic data. There are several other advantages of this experimental method, such as the rendering negligible of mass and heat transfer influences due to maintenance of low conversions and therefore low heat release. Under these adiabatic conditions the catalyst bed remains isothermal as any heat produced by an exothermic reaction is removed by the flowing gases. The effects of temperature and concentration (and / or pressure) may also be studied separately. There are some disadvantages of operation in this mode, primarily that conversions must be limited to approximately less than 10%, leading to the possibility of significant analytical errors. The reason for this maximum conversion limitation can be explained as follows.

In an ideal cylindrical fixed-bed reactor, it is generally assumed that there are no radial gradients of gas velocity or concentration, and that there is no axial mixing, and that the reactant concentration is a function of the catalyst bed length. This type of reactor bed is known as the plug flow model. The reaction under plug flow conditions is represented schematically in figure A3.6.1. By mass balance it can be stated that

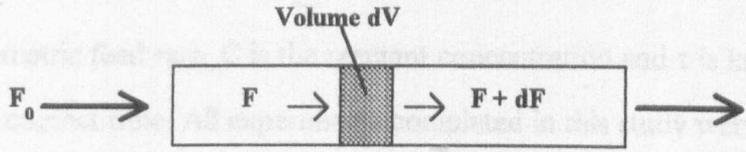
$$F = (F + dF) + r dV \quad (\text{A3.6.1})$$

therefore

$$r = \frac{-dF}{dV} \quad (\text{A3.6.2})$$

where r is the reaction rate per unit volume of catalyst, V is the volume of catalyst and F is the molar flow of reactant.

Figure A3.6.1 A schematic of the fixed catalyst bed in a micro-reactor.



If F_0 is the molar feed rate of reactant and x is the fractional conversion, then

$$F = F_0 (1 - x) \quad (\text{A3.6.3})$$

and

$$\frac{dF}{dV} = -F_0 \frac{dx}{dV} \quad (\text{A3.6.4})$$

thus

$$r = F_0 \frac{dx}{dV} \quad (\text{A3.6.5})$$

At low conversions dx may be replaced with Δx and direct measurements of rate may be made;

$$r = \frac{F_0}{V} \Delta x \quad (\text{A3.6.6})$$

Under these conditions the reactor operates in "differential mode" and the rate calculated from the above equation corresponds to the average reactant concentration in the catalyst bed. The reaction rate is proportional to the fractional conversion and low conversions are necessary.

Operation of the reactor at higher conversions is often unavoidable due to analytical problems associated with the low conversions necessary in the differential mode. At higher conversions, the rate varies with axial position in the reactor and operation in this region is known as integral mode. In this case rate is expressed as:-

$$r = F_0 \frac{dx}{dV} = C_0 \frac{dx}{d \frac{V}{Q_0}} \quad (\text{A3.6.7})$$

where

$$\frac{V}{Q_0} = \tau \quad (\text{A3.6.8})$$

Q_0 is the volumetric feed rate, C is the reactant concentration and τ is known as the space time or contact time. All experiments completed in this study were under differential mode conditions. In effect, the differential mode is an approximation of the integral mode which can be applied only under low conversion conditions.

The reciprocal of space time is known as space velocity and is defined as the number of catalyst bed volumes fed per hour (and has units of hours^{-1}). The space velocity is known as Gas Hour Space Velocity (GHSV) or in terms of a liquid volume Liquid Hour Space Velocity (LHSV). Another similar measure can be calculated in terms of mass flow and catalyst bed weight which is known as Weight Hour Space Velocity (WHSV). In this study, as the catalyst materials all have similar densities throughout the compositional series, and for convenience, an arbitrary term similar to space velocity has been used which is the ratio of volumetric flow to catalyst bed weight (units of $\text{litres hour}^{-1} \text{ kg}^{-1}$). The reasons for this were to standardise reactor loadings and to allow the determination of activity per square metre area of catalyst by a simple division of the calculated rate by the specific surface area. (In order to determine true GHSV (or LHSV) it is therefore necessary to divide by the average tap-packed density of the test materials). In order to determine the true WHSV it is necessary to multiply by the density of the gas mixture. For the sake of simplicity, the term WHSV is used throughout this text to represent the arbitrary non-density specific WHSV.

The calculation of rate for a given reaction is then expressed in moles of product formed (generally CO_2) per hour per kg of catalyst and is calculated as follows:-

$$\text{rate} = \frac{\text{WHSV} \times \% \text{CO}_2 \times 298}{24 \times 100 \times 393} \quad (\text{A3.6.9})$$

the units of rate as expressed above are moles CO_2 hour⁻¹ kg⁻¹. A temperature conversion factor (298/393) is included to allow the use of the 24 litre molar gas volume constant at room temperature and pressure (298K, 760 mmHg).

The other main limitation of the differential method is that it is very time consuming. Many experiments are necessary to determine the response to temperature and to reactant gas stoichiometry, thus the throughput is much lower than with the batch reactor. However, the kinetic data obtained is much more useful.

The measurement of rate with time under steady state conditions allows the equilibration time to be determined. The use of steady state temperature methods with a pre-determined equilibration time then allows the system to reach thermodynamic equilibrium before any rate measurements are made. The other advantage of the differential method is that use dependent effects such as product self poisoning (product retardation), or the effect on activity of the extent of reduction of a catalyst under reaction conditions can be assessed. In the lanthanum doped ceria system, both of these effects are known to occur.

A3.6.2 Limitations of the Plug Flow Model - Approximations and Assumptions.

A3.6.2.1 Wall effects

In a fixed-bed flow reactor, the lower packing density of the catalyst bed at the wall interface can result in the reactant gas stream bypassing the catalyst somewhat. In order to minimise this effect there is a general rule of thumb that the reaction tube internal diameter should be at least one order of magnitude larger than the catalyst

particle diameter. Thus, for a 200 - 400 μ m particle size fraction, (as used in this study), the reactor tube should be at least 3mm (10 times the average particle size diameter). To err on the safe side, a 4mm internal diameter reaction tube was chosen for these studies, using the maximum catalyst particle size as a reference. The minimum length of the catalyst bed likewise, should be approximately 25 times the particle diameter, in this case at least 10mm.

The other main deviations from ideal behaviour are generally due to heat and/or mass transfer limitations of the reactor apparatus. These deviations from ideal behaviour may be such that they hide the true intrinsic catalytic properties that are being investigated, the results obtained being characteristic of the limiting process only. There are several criteria which ideally must be met in the design of a catalytic reactor in order to avoid such limitations and to access true measurements of the intrinsic properties of catalyst materials. It is first necessary to define the heat and or mass transport mechanisms within such materials.

It can be assumed that all heterogeneous catalyst materials are porous solids. The surface of the catalyst material is separated from the bulk gas phase by a stationary gas phase boundary layer through which reactants must diffuse in order that reaction may occur. When the reactants enter the pore system of the catalyst consecutive processes of diffusion to an internal active surface, adsorption on active sites, chemical reaction, desorption of products, diffusion of products through pores to the boundary layer, and finally diffusion of the products out through the boundary layer, back into the bulk gas phase all must occur for a reaction to occur. Any of these individual steps in the reaction mechanism can be the rate determining step. Heat transfer occurs through similar gas diffusion pathways and by conduction through the catalyst material itself. In addition to these inter-phase processes, it is also necessary to take account of such mechanisms in the macro-domains on both the inter-particle scale and on the scale of the reactor. It should be noted that the exponential nature of the dependence of rate on temperature is generally of much greater significance than diffusion effects which generally vary linearly with rate.

Large radial temperature gradients within the catalyst bed are one of the major causes of error in rate measurement when using the integral mode of operation. The

presence of exotherms within catalyst beds with low thermal conductivity is the usual origin of such thermal gradients, but use of the isothermal differential mode eliminates this factor. The presence of axial concentration gradients is an unavoidable consequence of the catalytic reaction within the catalyst bed. The presence of axial concentration gradients can result in eddy diffusion and a reduction in conversion, although for vapour phase reactions, this effect is also generally considered negligible. A further complication can occur in the formation of pressure gradients across the catalyst bed. For solid/gas catalytic reactions performed at (near) atmospheric pressure, the pressure gradient across the catalyst bed is a function of fluid velocity, viscosity, particle size and bed voidage - a measure of free volume within the catalyst bed. Any observed increase in the pressure gradient is generally a useful sign of the deposition of fines or other materials in the interstices. In the present experimental set-up, there was no facility for pressure drop measurement, although any pressure build-up due to deterioration of the catalyst particles would have been indicated by "stalling" of the mass flow controllers.

There are several excellent review articles within the literature detailing the theoretical aspects of catalyst activity testing¹⁶¹ the design aspects of catalytic reactors¹⁶⁷ and experimental methods for catalyst testing,¹⁶⁸ a full account of which are beyond the scope of this text. One particular aspect of the reactor which must be addressed is the effect of mass transfer through the gas phase. This subject is dealt with in the experimental chapter (section 4.5.1 and subsections therein), with particular regard to the experimental determination of mass transfer limitations on reaction rate.

Appendix 3.7

A3.7.1 Diffuse Reflectance Infrared Spectroscopy - a General Description

Diffuse reflectance occurs where the incident radiation penetrates the surface layer of a material, excites characteristic vibrational modes of the analyte molecules, (and thereby loses intensity at certain corresponding characteristic frequencies), and is then scattered in all directions. The intensity of the reflected radiation is generally in the order of two orders of magnitude less than for transmission techniques, and therefore the signal must be intensified by the use of an integrating sphere surrounding the sample to accumulate as much of the scattered radiation as possible.

A3.7.2 Diffuse Reflectance Theory

The theory and application of diffuse reflectance spectroscopy has been extensively reviewed in the literature, the original and most complete of which by Kortüm in 1969.¹⁹⁴ Two other references of interest are by Frei et al¹⁹⁵ which covers practical experimental aspects as well as theory from the perspective of the analytical chemist, and Delgass et al¹⁹⁶ which reviews the application of diffuse reflectance spectroscopy to heterogeneous catalysts. These latter reviews are most applicable to the application of diffuse reflectance spectroscopy in this study. Other general information regarding general infrared spectroscopic techniques such as the use of Fourier transform techniques can be found in the excellent analytical review by Skoog and Leary.¹⁸⁷ The bulk of the theory within this section is derived from these references and others specifically cited within the text.

Reflected radiation from a powder solid consists of specular reflection and diffuse reflection components. The diffuse reflectance component is of greatest interest as it has penetrated the surface of the sample material and undergone partial absorption and multiple scattering within the surface layer of the material, before emergence. Specular reflectance, on the other hand, generally does not undergo any absorption

processes as there is no surface penetration. The specular reflectance intensity is generally much higher than the diffuse reflectance intensity thus causing the total reflected intensity to be anomalously high, effectively swamping the diffuse reflectance signal. Thus, the minimisation of specular reflectance is generally a major factor in the design of instruments and sample preparation.

The apparent absorption of light by scattering media is generally described by the phenomenological theory of Kubelka and Munk (1931)¹⁹⁷ in terms of an absorption parameter (K) and a scattering parameter (S). For an infinitely thick opaque layer the Kubelka-Munk equation can be written as;

$$F(R_{\infty}) \equiv \frac{(1 - R_{\infty})^2}{2 R_{\infty}} \equiv \frac{K}{S} \quad (\text{A3.7.1})$$

where R_{∞} is the diffuse reflectance relative to a non- or low-absorbing standard such as MgO, K is the molar absorption coefficient of the sample and S is the scattering coefficient.¹⁹⁵ If S remains constant, then $F(R_{\infty})$ and K should be proportional to each other. When the reflectance of a sample diluted with a non-absorbing powder is measured against the pure powder, the adsorption coefficient K may be replaced such that $K \equiv 2.303 \epsilon c$ where ϵ is the extinction coefficient and c is the molar concentration. As $F(R_{\infty}) \propto c$ under constant experimental conditions, the Kubelka Munk equation is seen to be comparable to the Beer-Lambert law of transmission spectroscopy;

$$I_{\text{out}} = I_{\text{incident}} e^{-\alpha c l} \quad (\text{A3.7.2})$$

where α is a proportionality constant, c is concentration of the absorbing species and l is the path length through the absorbing medium. In the Beer-Lambert equation, α can be replaced by 2.303ϵ ($\epsilon = \alpha / \ln 10$). ϵ is known as the molar absorption (extinction) coefficient. Deviations from Kubelka-Munk behaviour are generally attributable to associative or dissociative processes at the boundaries of the particles within the sample. Further detail regarding the Kubelka-Munk theory and its applications are beyond the scope of this text, and the reader is referred to the original publication.¹⁹⁷

A3.7.3 Kubelka -Munk Theory

The main pre-requisite for reliable diffuse reflectance results is that the incident radiation should be diffuse. This condition is easily met by for samples which scatter strongly and absorb weakly as the incident radiation is rendered diffuse by sample scattering before significant absorption occurs. The second precondition is that the sample should be of infinite thickness and extent in order that there is no loss of radiation via edge losses or by forward scattering through the thickness of the sample. In practice, this condition is met by a minimum sample thickness of 3mm. The other main factor is that the sample should be uniform - this is not generally a problem with catalyst samples which are generally of a disperse nature. It is also desirable to use as small a particle size as possible in order to reduce specular reflection as much as possible. Large particles with larger faceted crystals are far more likely to result in specular reflection at the sample surface. For strong absorbers, the effect of particle size is much reduced and absorption prevails for all particle sizes, however for weakly absorbing materials light scattering is inversely proportional to the particle size. It should be noted however that in cases where the particle size is of the same order of magnitude as the wavelength of the incident radiation, it is possible for the scattering coefficient, S , to exhibit a wavelength dependence. This effectively limits the lower particle size to approximately $25\mu\text{m}$ for this study where the minimum wavelength used is approximately $2.5\mu\text{m}$.

Other conditions worthy of note are that the sample should be only weakly absorbing in order to ensure that scattering predominates over absorption, effectively rendering diffuse the non-diffuse illumination. (This generally corresponds to pastel colours in the visible absorbance spectrum). The sample should also be non-fluorescent under the illuminating radiation.

A3.7.4 Fourier Transform Spectroscopy

The instrument used in this study was a Fourier Transform (or multiplex) device. In such a device, all elements of the observed signal are determined

simultaneously. In order to determine the magnitude of each element of the signal, the analyte signal is modulated in such a way as to permit the subsequent decoding of the signal in terms of each element. The Fourier Transform (FT) technique was first developed in the 1950's as a method of improving the signal to noise ratio for very weak signals. There are three main advantages of the FT technique, each of which are particularly advantageous to techniques with inherently poor signal to noise ratios. In the first instance, the relative lack of optical elements (in comparison to a dispersive instrument), results in a much larger proportion of the diffuse reflectance signal power reaching the detector, enhancing the signal to noise ratio. Secondly, the high precision of FT instruments allows the use of signal averaging techniques, again enhancing the signal to noise ratio. The random nature of noise signals results in their accumulation in proportion to the square root of the number of scans averaged. In this study 1024 scans were signal averaged for each spectrum, resulting in a theoretical signal to noise ratio enhancement factor of 32 in comparison with a single scan. The third advantage of use of FT techniques stems from the experimental time reduction gained by the analysis of all elements of the spectrum simultaneously. The reduction in scan time resulting allows signal averaging of many scans to be performed (thus improving the signal to noise ratio), in similar or shorter times as a dispersive instrument would require to record a single spectrum.

Fourier transform spectroscopy can be described as time domain spectroscopy. In contrast to conventional spectroscopy where signal intensity is recorded as a function of frequency, FT methods make use of the variation in signal intensity with time. Using FT techniques, it is possible to plot the complex variation in signal intensity with time of several different frequencies simultaneously. In such plots, a periodicity is generally observed (although this becomes increasingly less obvious as more frequencies are included in the time domain plot), which is characteristic of the wavelengths comprising the overall signal coming in and out of phase with time. The resulting time domain spectrum contains all of the information present in an analogous frequency domain spectrum, and both can be mathematically converted to the other. In the analysis of real spectra, conversion of time domain data to frequency domain spectra is very complicated and is always effected with the use of computer and

software which is generally supplied with the instrument and specific to that instrument. Further explanation of the mathematical processes involved are beyond the scope of this text.

The acquisition of time domain spectra presents a major experimental problem. The frequency response time of transducers within the detector in a spectrometer is several orders of magnitude less than the frequencies of the intensity variations under observation. In other words, the transducer signal is equivalent to the average intensity of a high frequency signal and contains no data regarding the periodicity of the signal. The solution to this problem requires the modulation of the signal to a lower (and therefore measurable) signal, whilst simultaneously preserving the time relationships and periodicity of the parent signal. There are several different techniques for circumventing this problem, the most commonly used being the Michelson Interferometer. The interferometer splits the radiation from the source using a mirror that reflects approximately 50% of the radiation and transmits the remainder. The beam splitter for the mid infrared region generally consists of thin films of germanium or silicon deposited on cesium iodide or bromide, sodium chloride or potassium bromide. The resulting split beams are again reflected back through the beam splitter mirror, one from a fixed mirror, the other from a movable mirror. These beams are again split by reflection and transmission, resulting in a combined beam consisting of a beam of fixed path length, and one of variable path length (both comprising approximately 25% of the source radiation), which then impinge on the sample and then on to the detector for analysis. For the mid infrared region triglycine sulphate pyro-electric detectors are widely used, or liquid N₂ cooled mercury cadmium telluride or indium antimonide photo-conductive detectors can be used where better sensitivity and faster response time is a necessity.

Horizontal motion of the mirror results in a known variation in path length with time. This in turn causes the two beams comprising the combined beam to pass in and out of phase, resulting in a predictable variation in the power of the beam reaching the detector. The power output of the detector can then be plotted against the difference in path lengths for the two beams comprising the combined beam (known as the retardation - δ). This type of plot is known as an interferogram. The frequency of the

interferogram f is related to the velocity of the moving mirror M_v and the wavelength of the radiation such that;

$$f = \frac{2M_v}{\lambda} \quad (\text{A3.7.3})$$

or in terms of the radiation wavenumber;

$$f = 2M_v \bar{\nu} \quad (\text{A3.7.4})$$

The optical frequency of the radiation thus be obtained by substitution of c/ν for λ in the equation such that;

$$f = \frac{2M_v}{c} \nu \quad (\text{A3.7.5})$$

As can be seen the frequency of the interferogram and the optical frequency are in direct proportion to one another and the proportionality constant (derived from the ratio of the mirror velocity and the velocity of light - typically 10^{-10}) is sufficiently small to modulate the frequency of the optical radiation into the measurable range.

The Fourier transformation of interferograms from time domain into frequency domain spectra, as mentioned previously is generally performed by computer algorithms supplied with the instrument. For a continuous source the resulting interferogram ($P\delta$), can be represented as the integral between zero and infinity of;

$$B(\bar{\nu}) \cos 2\pi \bar{\nu} \delta d\bar{\nu} \quad (\text{A3.7.6})$$

where $P(\delta)$ is the amplitude of the interferogram signal (- a measurement in the time domain), $B(\bar{\nu})$ is a (frequency domain) factor dependent on the radiant power of the beam incident upon the interferometer, the source beam splitting ratio, and the frequency dependence of both the detector and the amplifier responses. The corresponding Fourier transform of the integral, $B(\bar{\nu})$ is the integral between zero and infinity of;

$$P(\delta) \cos 2\pi \bar{\nu} \delta d\delta \quad (\text{A3.7.7})$$

A complete Fourier Transform requires both real (cosine) and imaginary (sine) components. Experimentally, $P(\delta)$ is recorded as a function of δ and is then mathematically transformed to give $B(\bar{\nu})$ as a function of $\bar{\nu}$.

The limitations of the technique stem from the finite sized digital sampling interval and the finite retardation (δ) range. The effect of these limiting factors is to limit the frequency range and resolution of the instrument. the resolution of the instrument is given by the reciprocal of the retardation. In other words the resolution of an instrument is improved with increasing mirror drive length.

The mirror drive mechanism is generally electromagnetic with the mirror mount generally floated on air bearings within close fitting guide sleeves. It is necessary to be able to sample the interferogram at precisely spaced δ intervals and to be able to determine the exact $\delta = 0$ position in order to allow signal averaging. These preconditions are met by use of two further interferometers running in parallel with the sampling beam interferometer. Sampling interval referencing is provided by a He/Ne laser-fringe reference system. This system has a cosine output of the variation in beam power as the mirror moves and the split beams move in and out of phase, resulting in constructive and destructive interference fringes. This signal is converted electronically to a square wave and sampling is then referenced to each zero intensity on the square wave. The $\delta = 0$ position is determined using the third parallel interferometer which incorporates a polychromatic (white light) tungsten source. The polychromatic source results in a large signal at the $\delta = 0$ position providing a highly reproducible trigger point for the beginning of the data sampling sweep. The mirror system for this interferometer is set so as to give a $\delta = 0$ before that of the analytical interferometer in order to ensure that the sample interferogram is recorded in its entirety.

Appendix 4.1

A4.1.1 Patent Study - Introduction

The first samples to be made using the coprecipitation method were used to investigate the findings of the Mackrodt patent.⁹⁹ The crucial compositions to be tested were $x = 0$ (to act as a baseline measurement in a catalysis study), $x = 0.2$ with a lanthanum dopant (to determine catalytic activity at the optimum concentration as determined in the patent), and a further sample with both lanthanum and praseodymium dopants, both at $x = 0.1$, giving a total dopant level of 0.2 (to investigate the synergistic effect of both dopants). The materials were calcined at 1200 °C for 8 hours, as specified in the patent.

The three samples were characterised by XRD and surface area measurements were made before catalytic activity testing. For these samples, scans were performed between 2θ values of 10° and 80° over a period of 10 minutes. The resulting data were used to determine phase composition, lattice parameter and to estimate crystallite size, all with respect to bulk composition. All samples were determined to be single phase with the cubic fluorite structure. The peak positions for the doped materials were observed to be shifted toward lower 2θ values in comparison with the doped material. The experimental results and calculations of the lattice parameters of the three samples are presented in table A4.1.1.

Table A4.1.1 Lattice parameter calculations for CeO_2 , $\text{Ce}_{0.8}\text{La}_{0.2}\text{O}_{1.9}$ and $\text{Ce}_{0.8}\text{La}_{0.1}\text{Pr}_{0.1}\text{O}_{1.9}$ (coprecipitated and calcined at 1200°C.

x	d111	d200	d220	d311	a111 (Å)	a200 (Å)	a220 (Å)	a311 (Å)	Average LP (Å)
0	3.1186	2.7016	1.9109	1.6302	5.402	5.403	5.405	5.407	5.404
0.2 La	3.1578	2.7354	1.9348	1.6500	5.469	5.471	5.472	5.472	5.471
0.1 La + 0.1 Pr	3.1342	2.7158	1.9213	1.639	5.429	5.432	5.434	5.436	5.433

It can be observed that lattice parameter varies such that $\text{Ce}_{0.8}\text{La}_{0.2}\text{O}_{1.9} > \text{Ce}_{0.8}\text{La}_{0.1}\text{Pr}_{0.1}\text{O}_{1.9} > \text{CeO}_2$. This is as would be expected from the relative cationic radii, La^{3+} (103.2 pm) $>$ Ce^{3+} (102 pm) $>$ Pr^{3+} (99 pm) $>$ Ce^{4+} (87 pm) $>$ Pr^{4+} (85 pm).⁷² It can be assumed that the +4 oxidation states of both cerium and praseodymium would predominate in the cubic fluorite structure. As the cationic radii of Ce^{4+} and Pr^{4+} are effectively equal, the lattice parameter shifts could be reasonably expected to vary proportionally as though only the lanthanum dopant concentration were present. In fact, the determined lattice parameter for $\text{Ce}_{0.8}\text{La}_{0.1}\text{Pr}_{0.1}\text{O}_{1.9}$ is very close to that determined for 10 cation % lanthanum doped ceria as determined for the ceramic material, (5.433 Å cf. 5.440 Å, respectively).

The variation in estimated crystallite size between the three samples was also investigated in order to gain valuable information regarding the effect of lanthanum and combined lanthanum and praseodymium doping on sintering properties. The method used for estimation of crystallite size and an error analysis can be found in the X-ray powder diffraction section of the experimental chapter in section 3.2 and subsections therein. The peak selected for analysis was the well resolved 220 reflection which is found in a range of 2θ values below the 47.6° of pure ceria. The summary of the calculations and results of the crystallite size estimation are presented in table A4.1.2.

Table A4.1.2 Crystallite size estimation calculations and results for CeO_2 ,

$\text{Ce}_{0.8}\text{La}_{0.2}\text{O}_{1.9}$ and $\text{Ce}_{0.8}\text{La}_{0.1}\text{Pr}_{0.1}\text{O}_{1.9}$ prepared using the coprecipitation method and calcined at 1200°C .

x	2θ	θ	$\cos \theta$	Constant	FWHM	Crystallite size (Å)
0	47.54	23.770	0.9152	79.44	0.132	658
0.2 La	46.919	23.460	0.9173	79.44	0.180	481
0.1 La + 0.1 Pr	47.265	23.633	0.9161	79.44	0.168	516

It can be observed that the addition of lanthanum and lanthanum plus praseodymium dopants results in a retardation in the sintering process in comparison with the undoped material. The degree of retardation of sintering seems to vary with some proportionality to the lanthanum concentration, although the lack of a systematic variation within just these three samples precludes further conclusions

Surface area measurements were also obtained using the single point method as described in the experimental chapter (section 3.3 and subsections therein). The surface area results are presented in table A4.1.3.

Table A4.1.3 Surface area results for CeO_2 , $\text{Ce}_{0.8}\text{La}_{0.2}\text{O}_{1.9}$ and $\text{Ce}_{0.8}\text{La}_{0.1}\text{Pr}_{0.1}\text{O}_{1.9}$ prepared using the coprecipitation method and calcined at 1200°C .

x	0	0.2 La	0.1 La + 0.1 Pr
Surface Area (m^2g^{-1})	0.6	2.7	2.4

The first observation from these results is that the surface areas of materials prepared by the coprecipitation method as specified in the Mackrodt patent⁹⁹ are approximately one order of magnitude higher than ceramic analogues. The retardation of the sintering process by the dopants as discussed in the previous section is reflected in the variation in specific surface area for the three samples. Both of the doped samples exhibit significantly higher surface area than the undoped material, as would be expected from the crystallite size estimation results.

From the XRD and surface area studies of these three samples, it was clear that the coprecipitation process resulted in materials which were more suited to characterisation and catalytic testing using the apparatus available in the present study. It was also clear that within the preparation parameters, there were several other experimental parameters of influence which required investigation, in order to optimise the material preparation method. These parameters were specific to the calcination step of the preparation and included dopant type and concentration, calcination temperature and pelletisation. (In the Mackrodt patent⁹⁹ it was not specified whether or not the materials were pelleted before calcination, as was specified in the ceramic preparation

method). The investigation of these factors in order to standardise the preparation process is discussed in section 4.1.3.

A4.1.2 Ternary Oxide Catalytic Study

The first catalytic experiments performed were designed to reproduce the results reported in the patent by Mackrodt, W. C., (1991)⁹⁹ In summary, the patent described a promotion of CH₄ oxidation activity by the addition of lanthanum or praseodymium to ceria to form a solid solution, such that the catalytic activity was found to be maximised at approximately $x = 0.25$ for both dopants. The measured reaction rates were determined to be approximately 27 and 24 times greater than for the undoped materials with $x = 0.25$ lanthanum and praseodymium, respectively. A further set of experiments determined that a combination of lanthanum and praseodymium dopants to give a total dopant level of $x = 0.25$ resulted in a synergistic increase in the measured catalytic activity, the combined dopants resulting in a measured reaction rate in excess of 40 times greater than that of undoped ceria. The materials tested in the patent were prepared using the coprecipitation technique which was adopted for use throughout the present study. Materials were calcined at 1200°C for 8 hours in air. No accurate surface area or surface composition data was presented in the patent pertaining to the relevant materials, and therefore the investigation of this promotion of activity in the binary and ternary metal oxide materials became the initial focus of investigation of the present study.

A4.1.2.1 Experimental

For this study, three coprecipitated samples were prepared and calcined for 8 hours in air at 800°C. This temperature was used instead of 1200°C, as used in the patent, in order to preserve a measurable surface area in the materials, as discussed previously in the solid state study of the sintering of lanthanum doped materials (section 4.1.3). The samples selected for testing were CeO₂, Ce_{0.8}La_{0.2}O_{1.9},

$\text{Ce}_{0.8}\text{Pr}_{0.2}\text{O}_{2-x}$ and $\text{Ce}_{0.8}\text{La}_{0.1}\text{Pr}_{0.1}\text{O}_{1.95-x}$, with the intent of reproducing a similar order of reactivity as reported in the Mackrodt patent.

A4.1.2.2 Results Summary

A4.1.2.2.1 Methane Oxidation

Methane oxidation rate was measured over a range of temperatures in order to determine the activation energies and specific pre-exponential factors for the reaction over each material. Reaction rates (expressed as $\text{Mol CO}_2 \text{ hr}^{-1} \text{ kg}^{-1}$) and specific rates (expressed as $\text{Mol CO}_2 \text{ hr}^{-1} \text{ m}^{-2} (\times 10^3)$), were also determined at a standard measurement temperature of 560°C to allow direct comparison of activities under reaction conditions. The results of the rate comparisons are shown below in table A4.1.4.

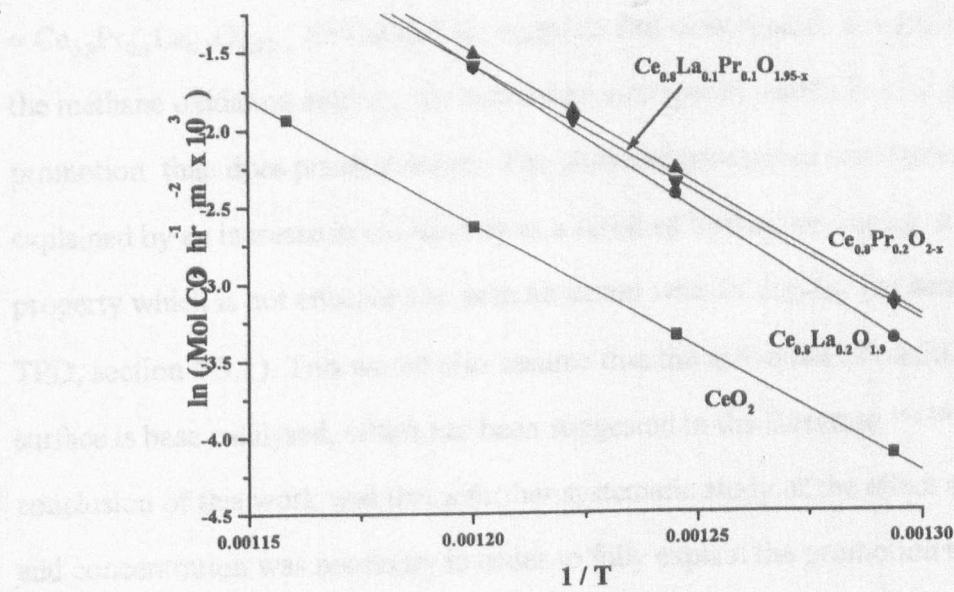
The first observations to be made regarding the reaction rate (per kg of catalyst) data, are that the doped materials are clearly more active than undoped ceria. In the present study there is at best a trebling of activity, rather than the factors of 26, 27 and 40 increases observed by Mackrodt et al, for $x = 0.2 \text{ Pr}$, $x = 0.2 \text{ La}$ and $x = 0.1\text{Pr} + 0.1\text{La}$, respectively. In the present study, the analogous factors were determined to be 2.81, 3.59 and 3.54. The differences between the magnitude in the dopant promotion of methane oxidation, and the relative order of promotion in this study and that of Mackrodt et al is possibly due to the lower calcination temperature used in the present study or other preparative variations, such as precursor purity. For this reason, the comparison of specific activities between materials was introduced as a development of the Mackrodt patent. It is observed that there is a significant increase in specific activity on doping, but at a constant doping level of $x = 0.2$, variation in the dopant ratio of La and Pr has little significant effect.

Table A4.1.4 Methane oxidation rate data

Ce	La	Pr	Surface area (m ² g ⁻¹)	Rate Mol CO ₂ hr ⁻¹ kg ⁻¹ 560°C	Specific Rate Mol CO ₂ hr ⁻¹ m ⁻² (×10 ³) 560°C
1	0	0	15.185	1.08740	0.071610
0.8	0.2	0	13.879	2.78768	0.200856
0.8	0	0.2	17.934	3.90510	0.217748
0.8	0.1	0.1	19.046	3.85030	0.202158

The resulting Arrhenius plots are shown in figure A4.1.1.

Figure A4.1.1 Arrhenius plots for methane oxidation



Data derived from the Arrhenius plots in figure A4.1.1 is presented in table A4.1.5.

Table A4.1.5 Arrhenius data for methane oxidation derived from figure A4.1.1

Ce	La	Pr	E _a kcal mol ⁻¹	E _a error kcal mol ⁻¹	ln A	ln A error	A	A / SA
1	0	0	32.118	0.246	19.569	0.152	3.153×10 ⁸	2.076×10 ⁷
0.8	0.2	0	37.662	0.695	23.869	0.438	2.325×10 ¹⁰	1.675×10 ⁹
0.8	0	0.2	34.189	0.479	22.105	0.300	2.982×10 ⁹	2.220×10 ⁸
0.8	0.1	0.1	33.101	0.448	21.421	0.281	2.009×10 ⁹	1.055×10 ⁸

The conclusion of this study therefore is that the observed increases in methane oxidation activity reported in the Mackrodt patent are entirely due to morphological differences between the materials. More specifically, the stabilisation of surface area of the ceria structured materials by the introduction of dopants was identified as the controlling factor with regards activity per unit weight of catalyst, (the comparative measurement used in the patent), rather than a synergistic chemical effect as proposed in the patent.

Analysis of the Arrhenius plots also lends support to a surface area based explanation of the Mackrodt et al results. The Arrhenius plots were observed to be near parallel, and consequently activation energies for all of the doped materials were found to be similar, suggesting similar catalytic reaction mechanisms. The order of specific pre-exponential factors (A/SA) was observed: $Ce_{0.8}La_{0.2}O_{1.9} \gg Ce_{0.8}Pr_{0.2}O_{2-x} \approx Ce_{0.8}Pr_{0.1}La_{0.1}O_{1.95-x} \gg CeO_2$. This suggests that with regards the true promotion of the methane oxidation activity, the lanthanum component results in a far greater promotion than does praseodymium. The observed promotion could possibly be explained by an increase in the basicity as a result of lanthanum doping, a surface property which is not enhanced to such an extent with Pr doping, (as determined in the TPD, section 4.3.1). This would also assume that the activation of methane at the surface is base catalysed, which has been suggested in the literature.^{141 146 - 147} The main conclusion of this work was that a further systematic study of the effect of dopant type and concentration was necessary in order to fully explain the promotion of the methane catalytic oxidation reaction over doped ceria.

A4.1.2.2.2 Carbon Monoxide Oxidation

In addition to the methane oxidation study, CO catalytic oxidation activity was also determined for the same materials in order to investigate a complimentary reaction system, and perhaps gain useful information with regards the reaction mechanism of methane oxidation (CO being a possible intermediate and product, along with CO_2). CO oxidation rate was measured over a range of temperatures in order to determine the activation energies and specific pre-exponential factors for the reaction over each

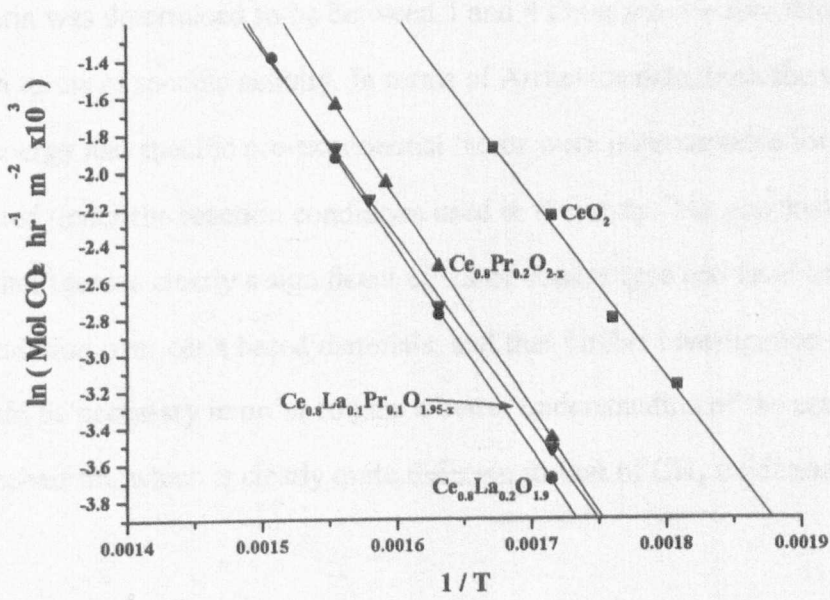
material, similarly as with methane oxidation. Reaction rates (expressed as Mol CO₂ hr⁻¹ kg⁻¹) and specific rates (expressed as Mol CO₂ hr⁻¹ m⁻² (×10³)), were also determined at a standard measurement temperature of 310°C to allow direct comparison of activities under reaction conditions. The results of the rate comparisons are shown below in table A4.1.6.

Table A4.1.6 CO oxidation rate data

Ce	La	Pr	Surface area (m ² g ⁻¹)	Rate Mol CO ₂ hr ⁻¹ kg ⁻¹ 310°C	Specific Rate Mol CO ₂ hr ⁻¹ m ⁻² (×10 ³) 310°C
1	0	0	15.185	1.59343	0.10494
0.8	0.2	0	13.879	0.34699	0.02500
0.8	0	0.2	17.934	0.55911	0.03118
0.8	0.1	0.1	19.046	0.56070	0.02944

The resulting Arrhenius plots are shown in figure A4.1.2.

Figure A4.1.2 Arrhenius plots for CO oxidation



Data derived from the Arrhenius plots in figure A4.1.2 is presented in table A4.1.7.

Table A4.1.7 Arrhenius data for CO oxidation derived from figure A4.1.2.

Ce	La	Pr	E_a kcal mol ⁻¹	E_a error kcal mol ⁻¹	ln A	ln A error	A	A / SA
1	0	0	19.103	0.444	16.988	0.391	2.387×10^7	1.57×10^6
0.8	0.2	0	22.003	0.245	17.990	0.199	6.503×10^7	4.69×10^6
0.8	0	0.2	22.623	0.190	19.011	0.156	1.805×10^8	1.01×10^7
0.8	0.1	0.1	20.378	0.772	17.048	0.632	2.535×10^7	1.33×10^6

Initial observations from this study are that the CO oxidation reaction is activated at much lower temperatures than the CH₄ oxidation reaction. This is reflected in the activation energies which were approximately one third less, and specific pre-exponential factors approximately two orders of magnitude less than those measured for the CH₄ oxidation reaction. This result was not unexpected, as the activation of methane is rather more difficult than the activation of CO due to the requirement for abstraction of a proton.

The most striking observation from the CO oxidation activity data is that the addition of lanthanum and praseodymium dopants to the ceria results in a significant decrease in activity - a complete contrast to the dopant effect in the methane oxidation reaction, suggesting distinctly different activation steps and reaction mechanisms. The undoped ceria was determined to be between 3 and 4 times more active than the doped materials, in terms of specific activity. In terms of Arrhenius data, both the variations in activation energy and specific pre-exponential factor were unremarkable for the samples tested under the reaction conditions used in the study. The conclusion of this study was that there is clearly a significant effect of dopant type and level on CO catalytic oxidation over ceria based materials, and that further investigation of these effects would be necessary in order to gain a better understanding of the catalytic reaction mechanism, which is clearly quite different to that of CH₄ oxidation.